Experimental Investigation on Heat Transfer and Pressure Loss Characteristics of Rotating Rectangular and Annular Ducts

Jin Woo Lee

Thesis submitted to the faculty of the Virginia Polytechnic Institute and State University
in partial fulfillment of the requirements for the degree of

Master of Science
In
Mechanical Engineering

Changmin Son - Chair
Rui Qiao,
Scott T. Huxtable
Thomas E. Diller

12th of August - 2022
Blacksburg, Virginia

Keywords: Heat Transfer, Pressure Loss, Rectangular Duct Parallel Axis Rotation,
Annular Duct Inner Surface Rotation

Experimental Investigation on Heat Transfer and Pressure Loss Characteristics of Rotating Rectangular and Annular Ducts

Jin Woo Lee

ABSTRACT

In a gas turbine, a small portion of air is bled from the compressor to provide cooling to keep the turbine at a safe operating temperature. The air flows through several passages in between where the components of the turbine are assembled. In this study, the heat transfer and pressure loss characteristics of two of these passages are investigated experimentally. The first of the two passages investigated is the passage in between the turbine blade root and disc. This passage has a unique geometry resembling an S-shape. The heat transfer and pressure loss characteristic of this passages in not well documented. For this study, a model of the realistic S-shaped passage has been made. In addition, a simplified rectangular duct with hydraulic diameter similar to that of the realistic S-shaped passage was constructed along with three other rectangular passages at aspect ratios, 17.33, 8.81, 3.93, and 2.02. This study aims to determine if rectangular duct correlations are valid for the realistic S-shaped model. Specifically, flow in low Reynolds number ranges of less than 3000 are of interest. With the effect or rotation and aspect ratio being of primary concern in the study, an experimental rig was constructed to measure the heat transfer and pressure loss in these models. The experiments were conducted with both clockwise and counterclockwise rotation to account for the passage on the pressure side and suction side of the passage.

The centerline Nusselt number distribution measured to check if the flow was fully developed. The effect of rotation caused swirling, increasing the entrance length in the duct and also enhanced heat transfer. The rotation also enhanced the heat transfer in the fully developed region. The fully developed experimental data for the simplified rectangular ducts showed good correlation with that of literature. However, the realistic S-shaped duct showed lower heat transfer values than the simplified rectangular ducts. Still, the effect of rotation is seen enhancing the rotation inf the realistic S-shaped duct. Additionally, the

friction factor which was measured using the cross-sectional average static pressure showed similar results for the realistic S-shaped duct and the simplified rectangular duct.

The passage between turbine disc bore and shaft is modeled as an annular duct with inner surface rotation. Flow in the turbulent region is studied and the test sections are made to have short length to hydraulic dimeter ratios. Along the centerline, the onset of Taylor vortices can be seen enhancing the Nusselt number in regions where the flow should be fully developed. This effect can also be seen enhancing the heat transfer in the fully developed region. The presence of Taylor vortices also adds resistance increasing the pressure loss across the duct.

Experimental Investigation on Heat Transfer and Pressure Loss Characteristics of Rotating Rectangular and Annular Ducts

Jin Woo Lee

GENERAL AUDIENCE ABSTRACT

Industrial gas turbines are designed to have an optimum overall pressure ratio for target temperatures rise. The demand for higher efficiency and power continues to push the operating pressure and temperature. Air systems is the flow network to provide necessary cooling to keep the machinery at a safe operating temperature.

In this study, two passages of the air system in the turbine are of interest. The passage between turbine blade root and disc, and the passage between the turbine disc and shaft. The effect of rotation on the flow through the two passages are of primary interest with focus on heat transfer and pressure loss characteristics. This experimental study presents unique results as a realistic model of the passage which resembles an S-shape was constructed and tested. The passage in between the turbine disc and shaft forms a rotating annular passage. There is limited data available representing the realistic geometrical shape of the annular passage under rotation. Therefore, the present study aims to present data for more realistic geometry and operating conditions. In addition, simplified rectangular ducts and annular ducts are also tested for comparison purpose.

The results of the study showed that the rotation does provide a significant increase in heat transfer and pressure loss in experiment modeling the passage between the turbine blade root and disc. Comparing the realistic S-shape passage and the rectangular passage with similar aspect ratio, the realistic S-shape passage showed less heat transfer and less sensitivity to the effect of rotation. The pressure loss characteristics on the other hand proved to be very similar. For the experiments modeling the passage between turbine disc and shaft, the effect of rotation once again showed to increase the heat transfer and pressure loss. The effect is more prominent when there is less axial flow.

Acknowledgements

I would like to first acknowledge Dr. Changmin Son my research advisor. I am grateful for the opportunity he has provided me to conduct research while pursuing my master's degree here at Virginia Tech. He has helped identify the areas of my education that need to be improved and also spared time to help me prepare myself for the next phase of life. He has challenged me to go above and beyond to produce high quality work striving for a degree of professionalism. I would also like to acknowledge Dr. Rui Qiao, Dr. Scott Huxtable, and Dr. Thomas Diller for serving on my advisory committee. During the review on my research progress, they have provided great feedback and suggestions on other things to explore in research.

Shinyoung Jeon and Jinsol Jung also deserve to be acknowledged. Both have been instrumental in helping me complete my research. They have spared many hours in manual labor to help me build and change out my test rig. They have also been great mentors to me in helping me adapt to the graduate student lifestyle. They showed me how to use many of the software and instrumentation I would need to conduct my research and have given me good feedback on papers I am writing. They have never turned me away when I had a question and always gave thorough answers helping me understand what they are explaining to me. In events where I would feel down because things were going wrong, I could always count on them to cheer me up or provide any assistance I would need. Needless to say, I would not have been able to complete my research without them.

Lastly, I would like to acknowledge Dr. Jungshin Park and Doosan Enerbility for sponsoring the project that I conducted my research in. Our bi-weekly meeting showed me what it is like to interact with an engineer in a professional environment. I am thankful for the patience showed to me as I learned how to conduct research and produce high quality results.

Table of Contents

Appendix A: Parallel Mode Rotation Data 139
Appendix B: Annular Duct Data 247

List of Figures

List of Tables

Nomenclature

Symbols

A	Duct cross-sectional area: A = Height x Width for rectangular duct, A = π(outer radius^2-inner^2) for annular duct (m^2)
D_h	Hydraulic Diameter: D_h = 2 x Height x Width/(Height + Width) for rectangular duct D_h = 2(outer radius - outer radius) for annular duct (m)
f	Friction Factor
h	Heat transfer coefficient (W/m^{2}K)
H	Duct height (m)
I	Current (A)
J	Rotational Reynold number
k	Thermal Conductivity of air (W/mK)
L	Length
$\dot{m}$	Mass flow rate (kg/s)
r	Annular Duct radius (m)
R	Rectangular Duct radius (m)
Ra	Rayleigh number
Re	Reynolds Number
Pr	Prandtl Number
u	Velocity (m/s), Uncertainty
p	Pressure (Pa)
Δp	Pressure drop across duct (Pa)
Q	Heat transferred (W)
q	Heat flux (W/m^2)
ε	Eccentricity (ε = R/D_h)
T	Temperature (K)
Ta	Taylor Number
W	Duct width (m)
x	Axial distance (m)
V	Voltage (V)
z	z-axis coordinate,

ρ	Density (kg/m^3)
μ	Viscosity (kg/ms)
ω	Angular velocity (rad/s)
Δr	Annular gap height Δr = outer radius – inner radius (m)

Abbreviations

TC	Thermocouple
AR	Aspect ratio AR = Width/Height
$\Delta r/r_1$	Radius Ratio

Subscripts

A01	Air temperature thermocouple
amb	Ambient
b	Bulk
Dh	Based on hydraulic diameter
e	Equivalent
h	Heater
m	Mean
mod	modified
t	Tangential
R01	Rotor wall temperature thermocouple
w	Wall
x	Based on axial distance
ω	Angular velocity
φ	Based on rotation

Chapter 1 Introduction

1.1 Gas Turbine Air System

Gas turbines are commonly used in applications such as aircrafts and power plants. They convert high temperature gases into mechanical energy. The efficiency and the power output of the turbine can be increased by increasing the operating gas temperatures. However, using high temperature requires cooling systems to keep the machinery at a safe operating temperature. The turbine is also designed with a cooling system referred to as the turbine internal air system. In this system air is bled from the upstream compressor and passes through several passages cooling the machinery. A typical layout of the air system is show in Figure 1-1. Of the various passages in the air system the present study focuses on two passages marked in red. These passages are the passage between the turbine blade and disc and the passage between the turbine disc and shaft.

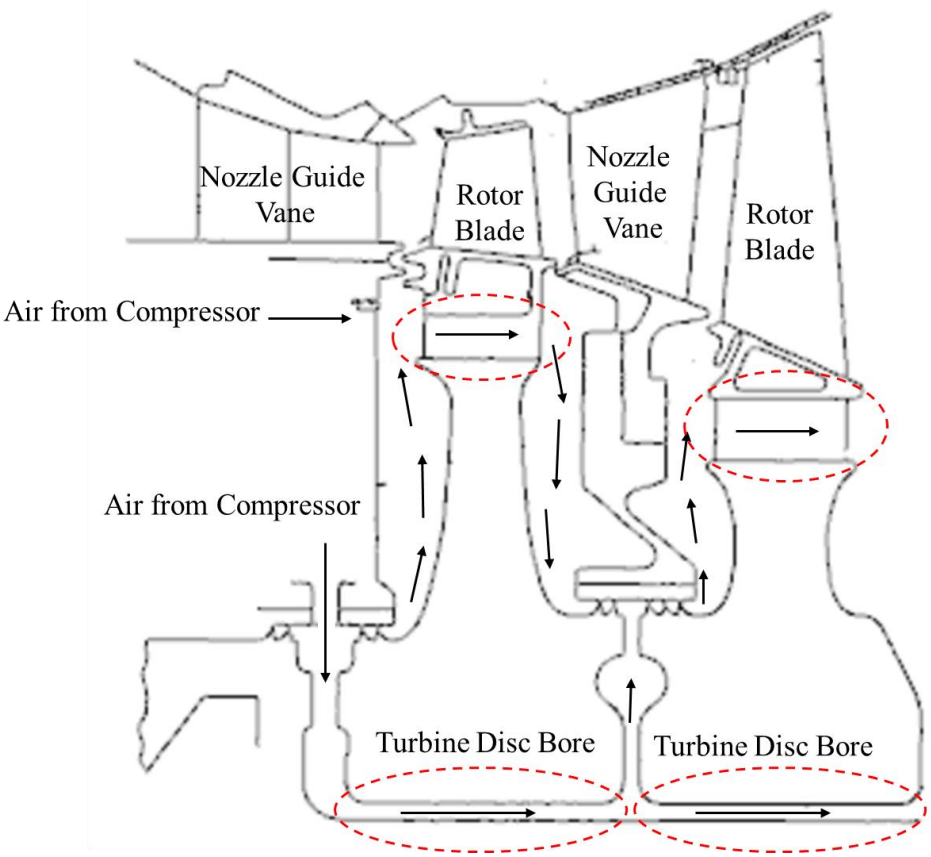

Figure 1-1 Typical Internal-Air System for an Industrial Gas Turbine Side View [1]

1.1.1 Passage Between the Turbine Blade Root and Disc

The turbine rotor is assembled by combining two components, the turbine blade and the turbine disc. The root of the turbine blade has a shape that resembles a firtree shape and dovetails into the grooves of the disc. The assembly is designed to include small gaps in between the blade root and disc which resembles an S-shape. The gaps help maintain mechanical integrity by creating a passage for cooling air to flow through so the blade and disc can survive high temperatures and pressures. Figure 1-2 shows the blade and disc assembly along with the air passage. As the rotor rotates about the x-axis, the cooling air flows through the S-shaped passage in the x direction. This passage is typically not exactly parallel to the shaft axis but can be simplified to a rectangular duct rotating about a parallel axis for study.

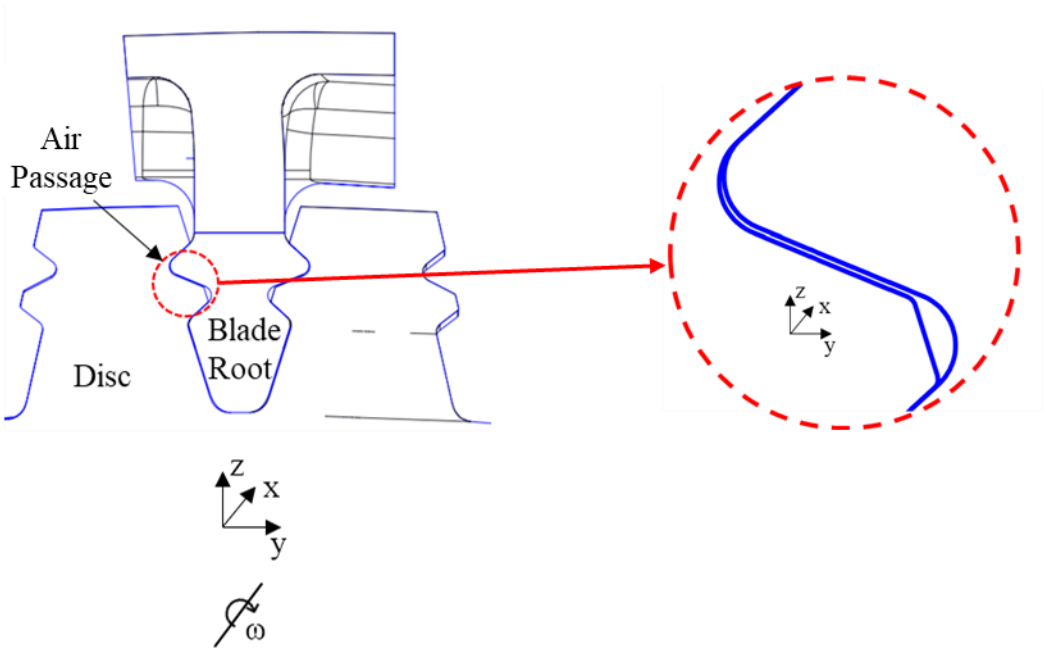

Figure 1-2 Passage Between Turbine Blade Root and Disc (Front View)

1.1.2 Passage between Turbine Disc Bore and Shaft

The rotor disc is also connected to the shaft which drives the rotation. The assembly is designed with a small clearance between the disc bore and shaft which creates an additional passage for cooling air to flow through. This passage can be modeled as an annular duct

undergoing rotation. Figure 1-3 shows the passage between turbine disc and shaft. As the rotor and shaft rotate about the x-axis, the cooling air also flows through the passage along the x direction. In an actual engine the turbine disc rotates with the shaft however due to limitations of the test facility, in this study the passage is simplified as an annular duct with inner surface rotation.

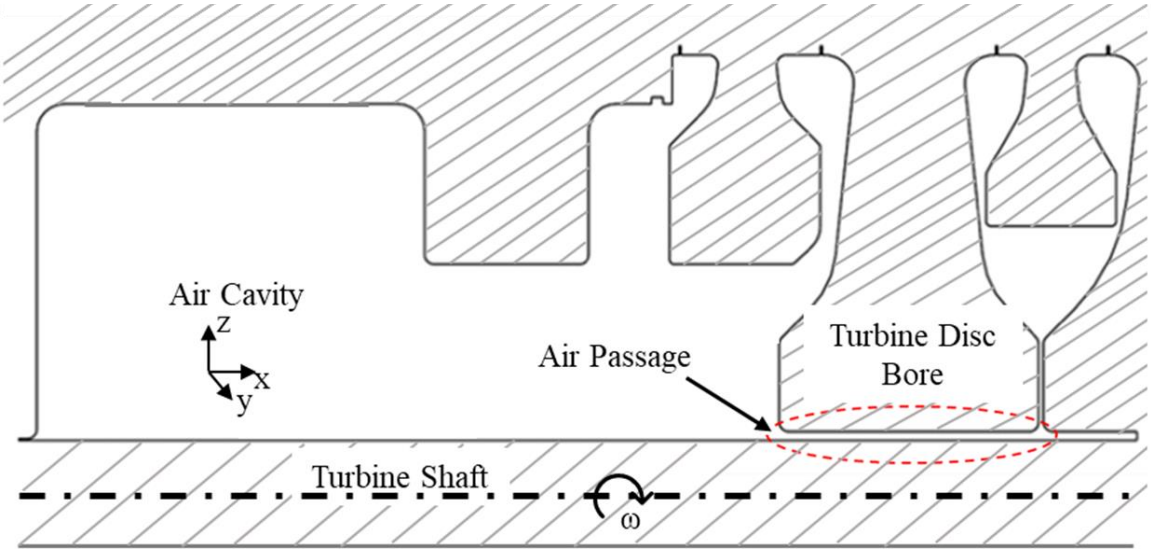

Figure 1-3 Passage Between Turbine Disc and Blade

1.1 Effect of Rotation

1.1.1 Coriolis Force

As a duct rotates about a parallel axis, often referred to as parallel mode rotation, secondary flow occurs due to Coriolis forces. The Coriolis force is defined as a force acting perpendicular to the direction of motion caused by rotation. The effect of rotation caused by the Coriolis forces has been quantified by Morris & Woods [2] by a rotational Reynolds number defined as

$$J = \frac{\rho \omega D_h^2}{\mu} \tag{1}$$

As the Coriolis effect induces secondary flow, it enhances heat transfer in a rotating duct. Figure 1-4 shows a summary of data and correlations from literature comparing the Nusselt number and the rotational Reynolds number.

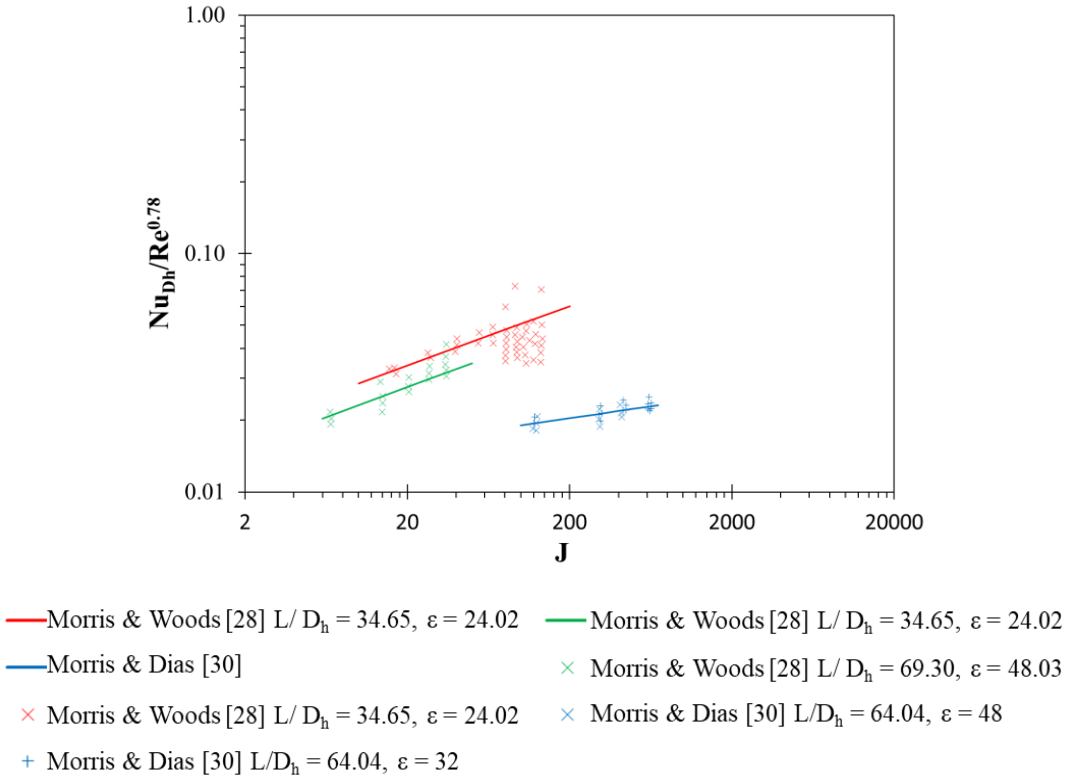

Figure 1-4 Comparison of Heat Transfer Data for Circular, and Rectangular Ducts with Rotation

1.1.2 Taylor Vortices

When fluid flows through an annular duct with inner surface rotation and stationary outer surface, secondary flow occurs in the form of Taylor vortices. Taylor vortices form when the radial pressure gradient and viscous forces cannot dampen out the changes in the centrifugal force induced by rotation, resulting in the flow becoming unstable [3]. G. I. Taylor [4] quantified the effect of the Taylor vortices with the Taylor number defined as

$$\mathrm{Ta} = \frac{\omega r_m^{0.5} \mathrm{b}^{1.5}}{\nu} \tag{2}$$

When the Taylor number surpasses a critical number, Taylor Vortices begin to form which enhances heat transfer by inducing mixing of the annular flow. In addition, G.I Taylor [4] noted that the heat transfer is also affected by a geometric parameter listed as

$$F_g = (\frac{\pi^4}{1697})(1 - \frac{z}{2r_m})^{-2} S^{-1} \tag{3}$$

$$S = 0.0571\left[1 - 0.652\left(\frac{b/r_m}{1 - b/2r_m}\right)\right] + 0.00056\left[1 - 0.652\left(\frac{b/r_m}{1 - b/2r_m}\right)\right]^{-1} \tag{4}$$

To offset the effect of the geometric factor most literature present the non-dimensional parameter for heat transfer, the Nusselt number as a function of a modified Taylor number

$$Ta_{mod} = \frac{Ta^2}{F_g} \tag{5}$$

Figure 1-5 shows this trend as data from experiments with rotation have higher Nusselt number values.

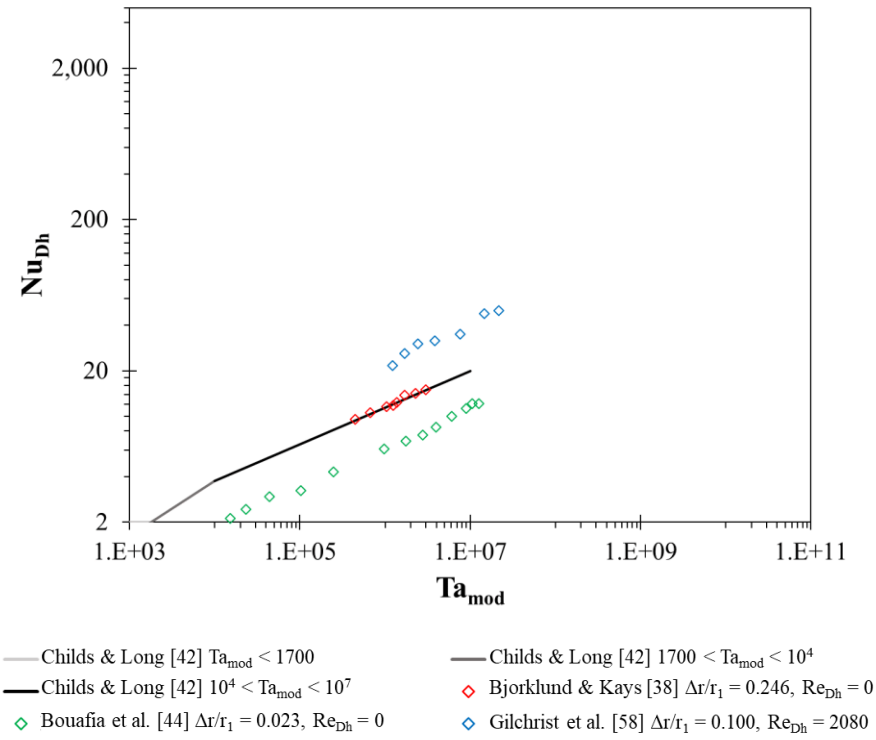

Figure 1-5 Comparison of Heat Transfer Data for Annular Ducts with Rotation

1.2 Research Objective & Scope

The purpose of this study is to experimentally investigate the heat transfer and pressure loss characteristics in the air passages between turbine blade root and disc and that of turbine disc and shaft. It is important understand these characteristics as these air passages play a significant role in keeping the machinery at safe operating temperatures in gas turbines. The experiments in this study are conducted at steady state and modeled after a uniform heat flux test.

The scope of the study is as follows

Passage 1: Passage Between Turbine Blade Root and Disc

- Experimental Design of test rig to investigate heat transfer and pressure loss characteristics in duct flow rotating about parallel axis
- Focus on laminar and turbulent regions to model real engine conditions

- Investigation of the effect of rotation on heat transfer and pressure loss characteristics of realistic S-shape and simplified rectangular ducts rotating about a parallel axis
- Investigation of the effect of aspect ratio on heat transfer and pressure loss characteristics of rectangular ducts

Passage 2: Passage Between Turbine Blade Root and Disc

- Experimental Design of test rig to investigate heat transfer and pressure loss characteristics in annular duct flow with rotating inner surface and stationary outer surface
- Focus on the turbulent region to model real engine conditions
- Investigation of effects of rotation on heat transfer and pressure loss characteristics on annular duct flow with inner surface rotation
- Investigation of effects of radius ratio on heat transfer and pressure loss characteristics on annular duct flow with inner surface rotation

Chapter 2 Literature Survey

2.1 Heat Transfer and Pressure Loss in Stationary Duct Flow

The heat transfer in the present study is driven by forced convection. Therefore, before analyzing the characteristics, it is important to understand the different regimes of convection. Metais & Eckert [5] created a chart outlining the different regimes. This chart contains a distinction between the laminar and turbulent regions and a distinction between forced convection and free conviction. Figure 2-1 shows the boundaries for forced and free convection and laminar vs turbulent regions. The figure compares the Reynolds number with the Grashof number multiplied by the Prandtl number often referred to as the Rayleigh number denoted by

$$Ra = \mathrm{GrPr} = \frac{g\beta(T_w - T_b)D_h^3}{\nu^2} \tag{6}$$

Most correlations and experimental data from literature operate in the forced convection zone. The characteristics in mixed or free convection differs from forced convection and therefore, it is important to verify that the experimental data lies within the forced convection region.

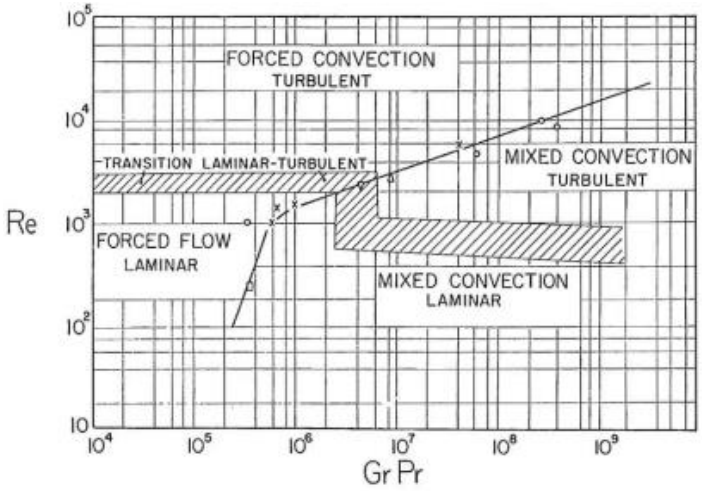

Figure 2-1 Regimes of Free, Forced, and Mixed Convection for Flow Trough Hozirontal Tubes [5]

The heat transfer is represented by means of heat transfer coefficient given by

$$h = \frac{q}{T_w - T_b} \tag{7}$$

The heat transfer coefficient is then presented in a non-dimensional form as the Nusselt number. The Nusselt number is a non-dimensional parameter that denotes the ratio between heat transfer from convection and conduction in a fluid defined as

$$Nu = \frac{hD_h}{k} \tag{8}$$

Several factors can influence the Nusselt number in internal flow starting with the boundary condition. Two of the most common boundary conditions for heat transfer are uniform wall temperature and uniform heat flux. As their names imply, the boundaries are defined as either having constant temperature at the walls or constant heat flux. As cooling systems in turbines mostly resemble heat flux boundary conditions, the present study will focus on the heat flux boundary condition. The boundary condition is important as the heat transfer is heavily influenced by the presence of a boundary layer in internal flow. When the boundary layer is developing, also known as the entrance region, the heat transfer is known to decrease exponentially along the axial direction. However, when the boundary layer is fully developed, also known as the fully developed region, the heat transfer is constant [6]

Another factor that can influence the heat transfer is the Reynolds number. In the laminar region, the Nusselt number is known to be constant, derived from an energy balance and Newton's law of cooling. However, in the turbulent region, the Nusselt number increases with Reynolds number. This trend has been well studied with several correlations available. Figure 2-2 shows a summary of the correlations and past experimental data. From this figure another parameter can be seen influencing the heat transfer. Geometric parameters such as the cross-section shape, aspect ratio or radius ratios all can also influence the heat transfer. Comparing the correlations and data, most follow similar trends with the absolute values varying based on aspect ratio but the data blue and green diamonds show different trends. This is because the experiments for this data included rotational effects while the rest of the references are stationary experiments.

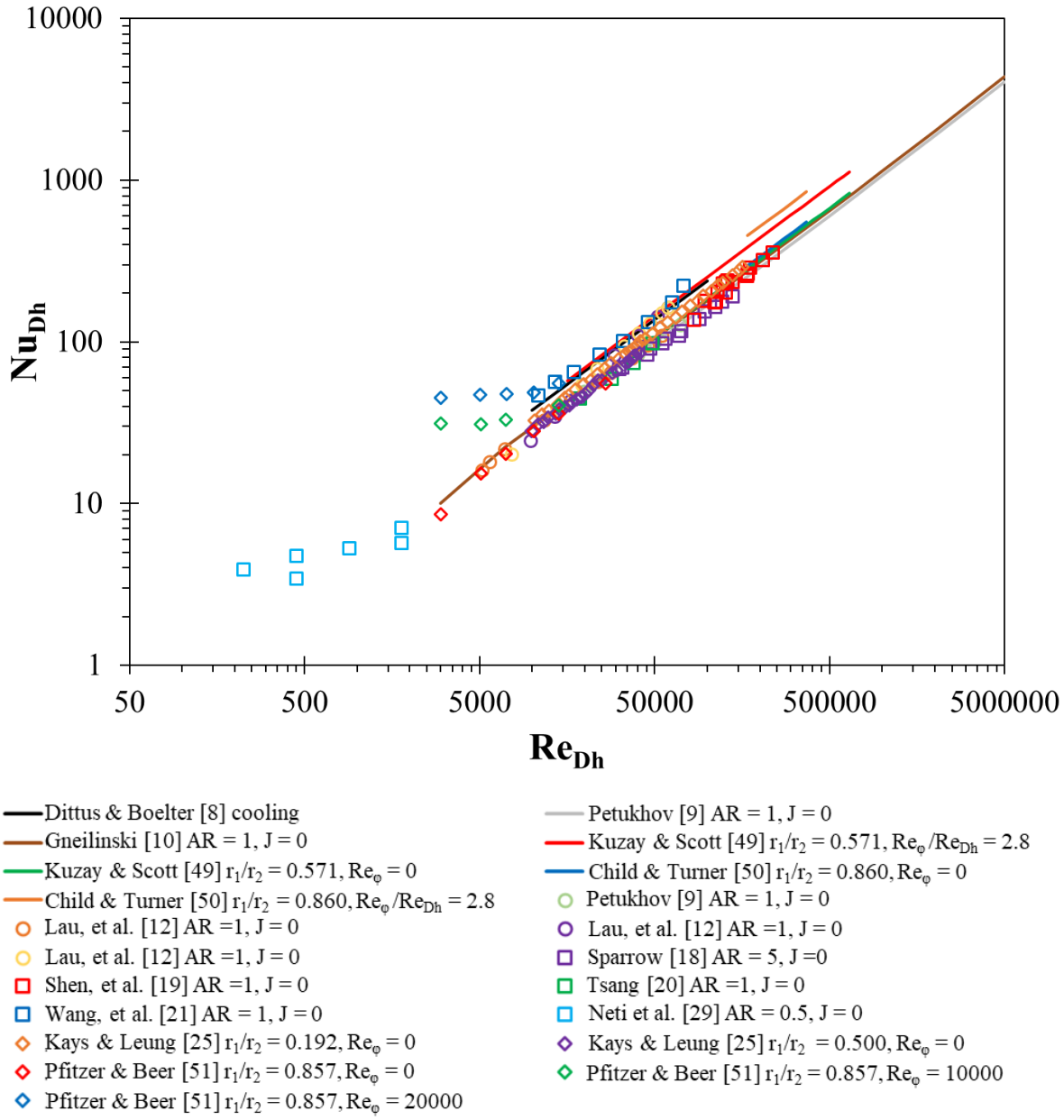

Figure 2-2 Comparison of Heat Transfer Data for Circular, Rectangular, and Annular Ducts

Pressure loss occurs in internal flow due to friction between the fluid and the walls at the boundary. Similar to the heat transfer the pressure loss behaves differently in the entrance region and the fully developed region. In the axial distribution of the pressure loss, this pressure loss decreases exponentially in the entrance region and decreases linearly in the entrance region [7]. The pressure loss can be represented in a non-dimensional term known as the Darcy friction factor defined as

$$f = \frac{2\Delta p D_h}{\rho u_x^2 L} \tag{9}$$

The friction factor is often correlated with the Reynolds number and the relative roughness. Figure 2-3 contains a summary of experimental data of smooth duct flow for friction factor. In general, as the Re_{Dh} increases the friction factor decreases on a linear trend in a log-log graph. The data that other factors such as rotation and L/D_h can also influence the friction factor.

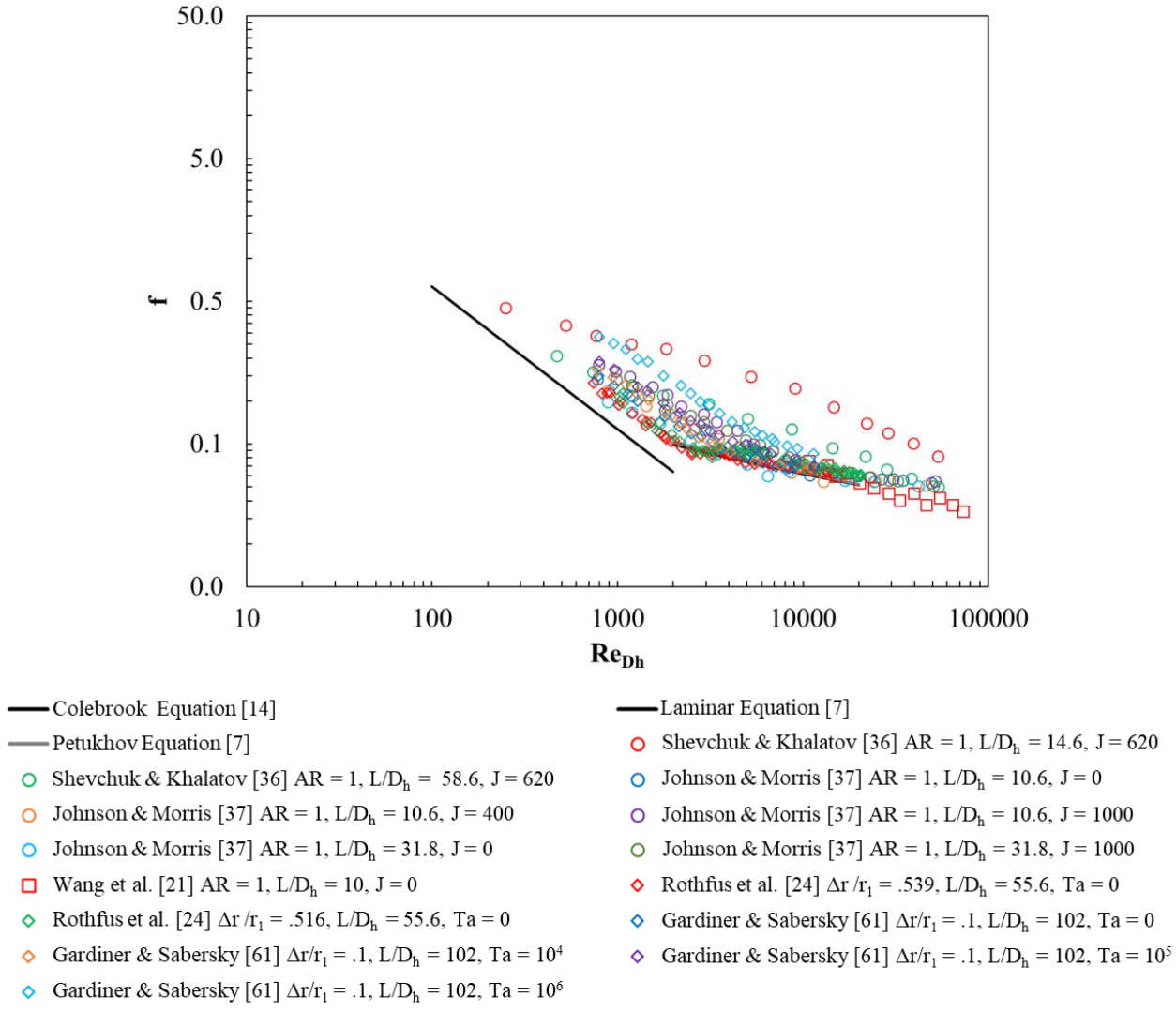

Figure 2-3 Comparison of Friction Factor Data for Circular, Rectangular, and Annular Ducts

2.1.1 Circular Cross-section

Heat transfer in circular ducts have been the most document and most of the correlations widely used today for heat transfer stem from experiments on circular ducts so they often serve as a baseline for comparison. The laminar Nusselt number of the fully developed region is derived theoretically to have a single value using an energy balance and Newton's law of cooling assuming incompressible, constant property fluid with negligible net axial conduction [6]. The values are listed below.

$$Nu_{Dh} = 3.66 \text{ (Uniform Wall Temperature)} \tag{10a}$$

$$Nu_{Dh} = 4.36 \text{ (Uniform Heat Flux)} \tag{10b}$$

While heat transfer in the laminar region can be calculated by theory the same cannot be done for the turbulent region. Therefore, several experiments have been conducted to develop empirical correlations for heat transfer in the turbulent region. Dittus & Boelter [8] studied heat transfer in a stationary circular duct and proposed the correlation valid for $Re_{Dh} \geq 10^4$ and $0.6 \leq Pr \leq 160$

$$Nu_{Dh} = 0.0265 Re_{Dh}^{.8} Pr^{.3} \text{ (Cooling)} \tag{11a}$$

$$Nu_{Dh} = 0.0243 Re_{Dh}^{.8} Pr^{.4} \ (Heating) \tag{11b}$$

Where PR is 0.71 for air and Re_{Dh} is given as

$$Re_{Dh} = \frac{\rho u_x Dh}{\mu} \tag{12}$$

This correlation is solely dependent on the Reynolds number and Prandtl number. It is known to have errors as great as 25%. More complex correlations have been developed with errors reduced

to 10%. Petukhov [9] developed a correlation basing the Nusselt number as a function of Reynolds number, Prandtl number and friction factor valid for $10^4 \leq Re_{Dh} \leq 5 \times 10^6$ and $0.5 \leq Pr \leq 200$

$$Nu_{Dh} = \frac{(f/8)Re_{Dh}Pr}{1.07 + 12.7(f/8)^{1/2}(Pr^{2/3} - 1)} \quad (13)$$

Gneilinski [10] expanded on the Petukhov [9] correlation replacing the Reynolds number with (ReDh -1000) modifying the correlation valid for $3{,}000 \leq Re_{Dh} \leq 5 \times 10^6$ and $0.5 \leq Pr \leq 2000$

$$Nu_{Dh} = \frac{(f/8)(Re_{Dh} - 1000)Pr}{1 + 12.7(f/8)^{1/2}(Pr^{2/3} - 1)} \quad (14)$$

Taler [11] further expanded the heat transfer correlation valid for both the transitional and turbulent region with ranges of $2{,}300 \leq Re_{Dh} \leq 10^6$ and $0.1 \leq Pr \leq 1000$

$$Nu_{Dh} = 4.36 + \frac{(f/8)(Re_{Dh} - 1000)Pr^{1.008}}{1.08 + 12.39(f/8)^{1/2}(Pr^{2/3} - 1)} x \left[1 + \left(\frac{Dh}{L}\right)^{2/3}\right]\left(\frac{T}{T_w}\right)^{0.45} \quad (15)$$

Lau et al. [12] conducted a series of experiments on smooth circular duct passages. While the focus of this study was the effect of plenum length and diameter on heat transfer and pressure loss, the study provides experimental data for heat transfer in circular ducts. Figure 2-4 shows the comparison between the experimental data with equation (14). The data shows excellent agreement with equation (14) regardless of the plenum length or diameter which is represented by L/d in the figure. The study also presents data on the heat transfer coefficients as seen in Figure 2-5. The experimental data shows the expected profile as the heat transfer coefficient decreases exponentially in the entrance region and is constant in the fully developed region.

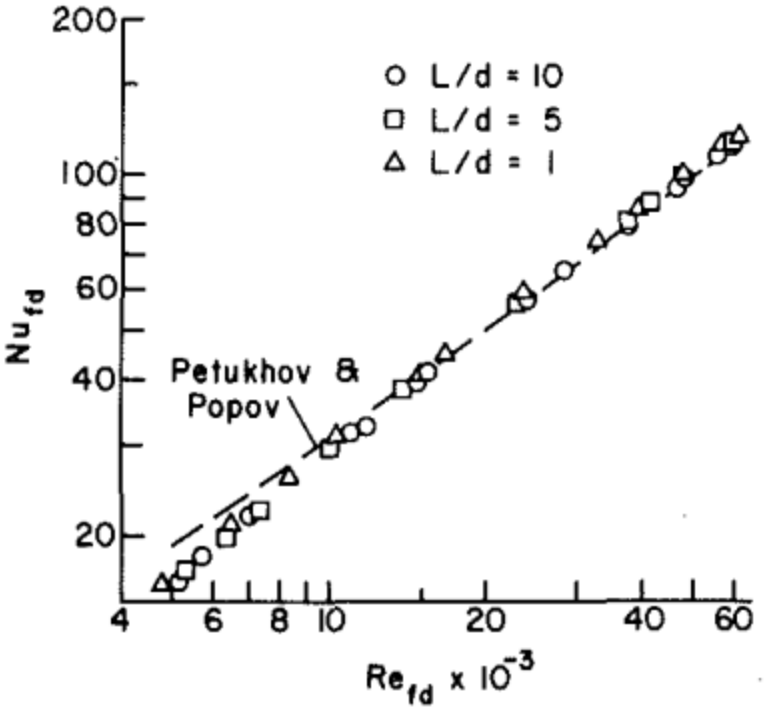

Figure 2-4 Fully Developed Nusselt Numbers for D/d = 3 [12]

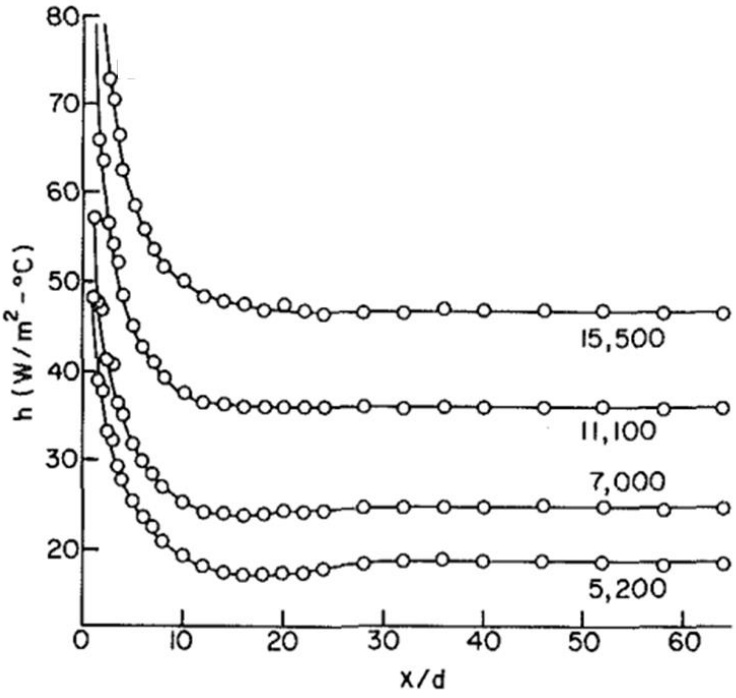

Figure 2-5 Illustrative Axial Distributions of the Heat Transfer Coefficient for Parametric Values of Reynolds Number, D/d = 3 [12]

The Pressure Loss characteristics are represented by the Darcy friction factor defined by Equation (9). Moody [13] created a simple chart to estimate the friction factor in a pipe based on the Reynolds number and the pipe roughness. For the laminar region, the friction factor is given as

$$f = \frac{64}{Re_{Dh}} \tag{16}$$

For the turbulent region, the Moody Diagram uses a correlation developed by Colebrook often reffered to as the Colebrook White equation [14] denoted by

$$\frac{1}{\sqrt{f}} = -2\log\left(\frac{2.51}{Re_{Dh}\sqrt{f}} + \frac{\frac{\varepsilon}{D_h}}{3.71}\right) \tag{17}$$

Petukhov [9] also presents a more simplified correlation for the friction factor given as

$$f = (1.82\log(Re_{Dh}) - 1.64)^{-2} \tag{18}$$

2.1.2 Rectangular Cross-section

The cross-sectional shape of the duct is also important parameter as this study presents three different cross-sections: the realistic geometry, rectangular, and annular. While studies on the realistic S-shaped geometry cross-section is rare, the effect on rectangular and annular ducts are well documented. Shah & London [15] preformed several experiments on the Nusselt number for laminar duct flow with various cross-sections. For laminar flow in a rectangular duct, the uniform heat flux Nusselt number is given as

$$Nu_{Dh} = 3.61 \tag{19}$$

Shah & London also included a study of the effect of aspect ratio and number of walls heated expanding on a study done by Schmit & Newell [16]. Schmidt & Newell calculated the Nusselt number with a hydraulic diameter defined using the heated perimeter. Shah & London corrected the definition to use the wetted perimeter instead. Figure 2-6 shows Shah & London's summary of the distribution of the Nusselt number based on the aspect ratio and the number of walls heated. In the present study the aspect ratio is defined as width over length so for Figure 2-6 $\alpha^* = 2a/2b$. Case 1 seems parabolic since all 4 walls are heated. Cases 2 and 5 also behave similarly but slightly skewed. Case 3 shows the Nusselt number increasing when aspect ratio increases and case 4 shows the Nusselt number decreasing when aspect ratio increases aspect ratio. It is important to note however, that the cross-sectional area is constant for the different aspect ratios in this study. C. Y. Wang [17] also studied the effect of aspect ratio and number of walls heated. This study shows a plot of the isotherms for a rectangular duct with all four walls heated in Figure 2-7. When all four walls are heated, the walls with shorter lengths generally have the highest temperatures.

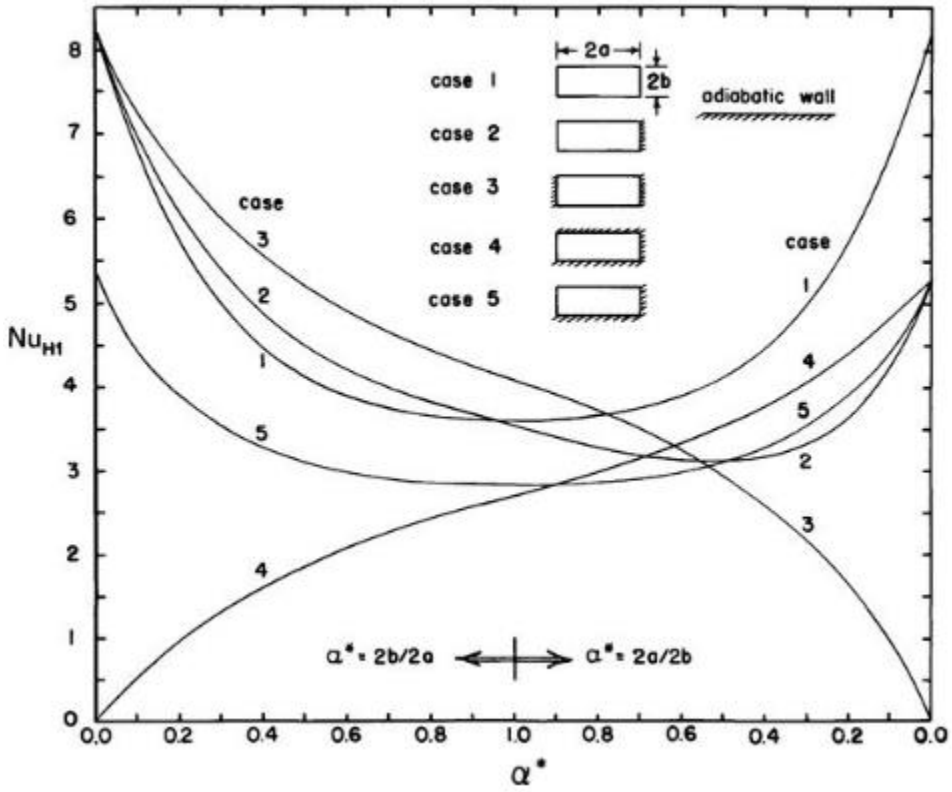

Figure 2-6 Laminar Nusselt Number Trends Based on Aspect Ratio and Number of Walls Heated [15]

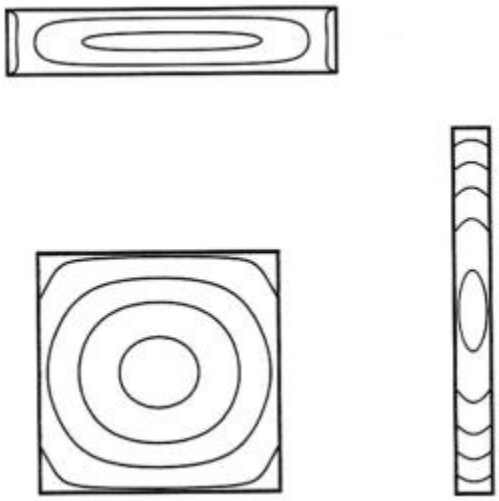

Figure 2-7 Typical Isotherms for Rectangular Ducts with All Walls Heated [17]

Several studies have also been conducted on turbulent flow in rectangular ducts. Sparrow et al. [18] conducted experiments on rectangular ducts with asymmetrically heated walls. Heat transfer in a symmetrically heated duct with opposing wall heated were compared to that of a duct with only one wall heated and that of one where one wall was provided half the heat flux as the other. Sparrow et al. showed that in cases where only one wall is heated the heat transfer can decrease up to 10-20 percent. Shen et al. [19], Tsang [20] effect of turbulators on rectangular duct flow but presented data for smooth passages as well. L. B. Wang et al. [21] studied turbulent flow in converging & diverging ducts. However, this study contains data for both heat transfer and pressure loss in rectangular ducts. Smith [22] studied rectangular serpentine passages but presented data for smooth rectangular passages with different aspect ratios.

2.1.3 Annular Cross-section

Shah & London [15] also provided data for heat transfer in the laminar region for annular ducts. Figure 2-8 shows the trend of the Nusselt number as the radius ratio changes. While here the radius ratio is defined as the inner radius divided by the outer, the trend shows that for a fixed inner cylinder radius, a larger annular passage height will produce a higher Nusselt number.

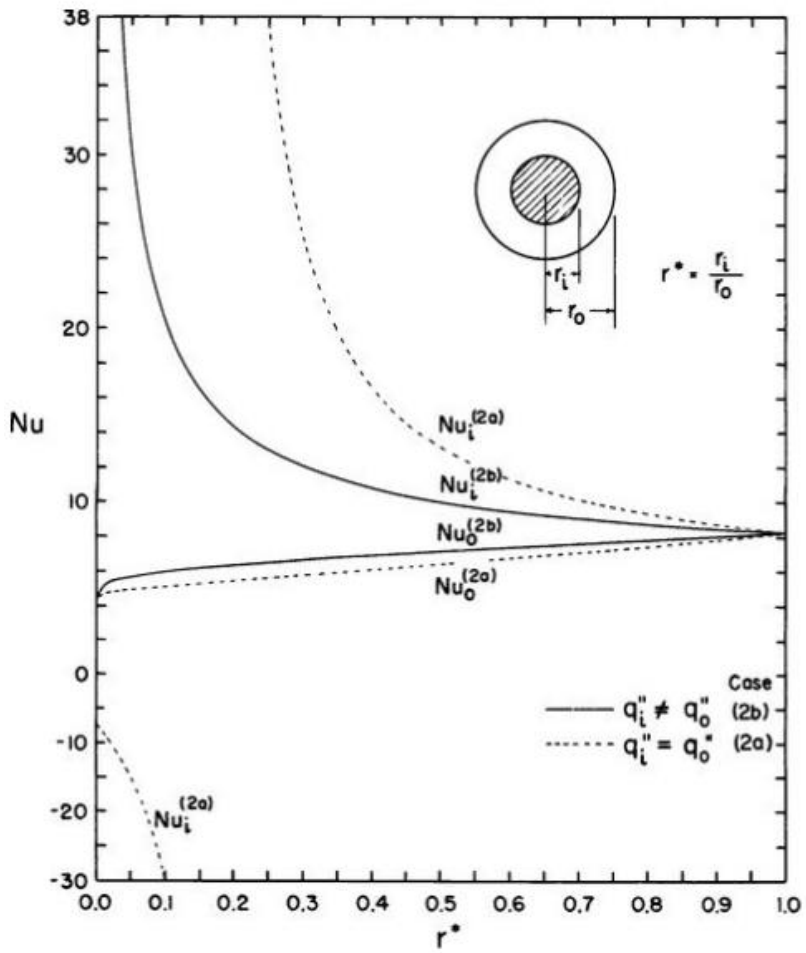

Figure 2-8 Nusselt Number for Uniform Heat Flux Laminar Flow in Annulus [15]

For the turbulent region, Roberts & Barrow [23] shows the development of the boundary layer in the annulus. The boundary layer forms along the walls of both the inner and outer surfaces. Rothfus et al. [24] Studies the velocity distributions and friction factor in turbulent annular flow. Figure 2-10 shows that for annular flow the friction factor along the outer wall still behaves similar to a circular duct. For heat transfer, Kays & Leung [25] preformed experiments for the effect of radius ratio in the turbulent region. The results show the same trend in the turbulent region as the laminar. Barrow [26] also conducted experiments on annular flow. This study concluded that the friction factor increases with the radius ratio and that the heat transfer behaves similarly to a circular duct.

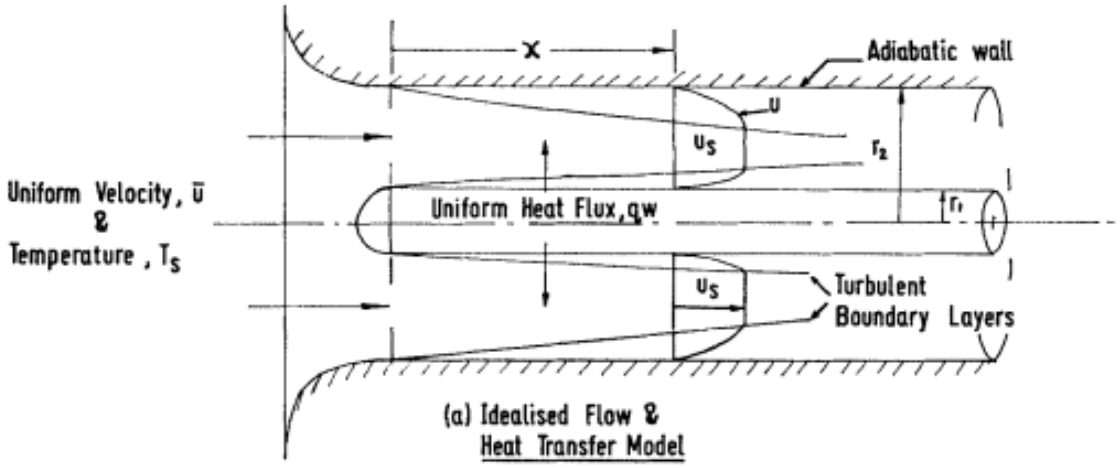

Figure 2-9 Idealized Flow in Annulus [23]

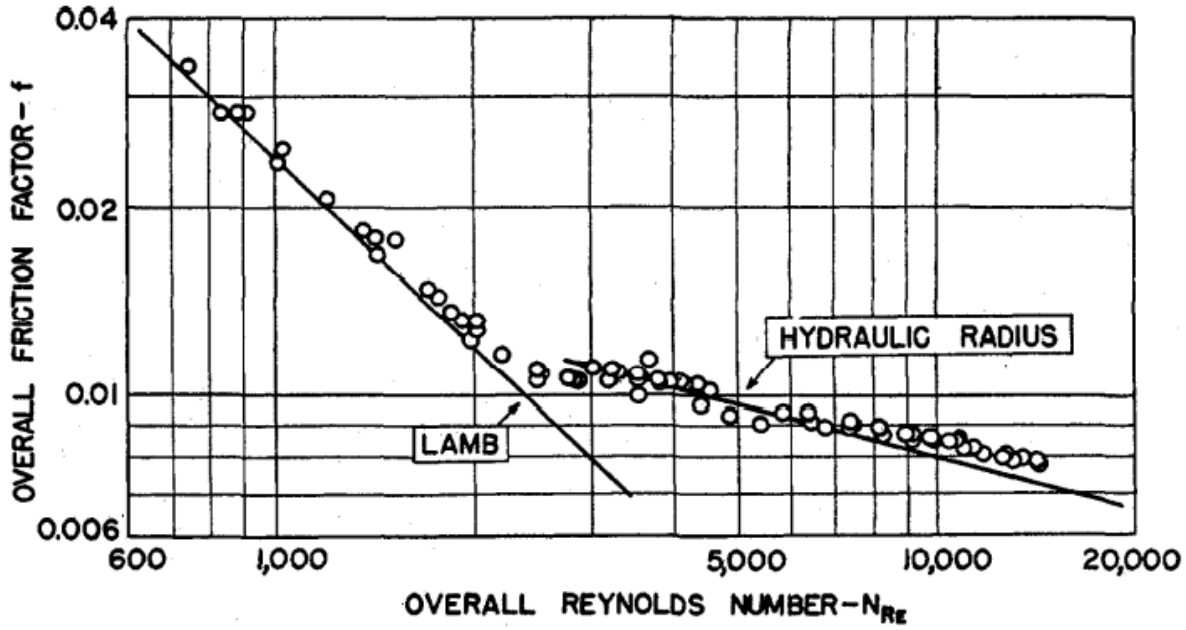

Figure 2-10 Fanning Friction Factor for Annular Flow [24]

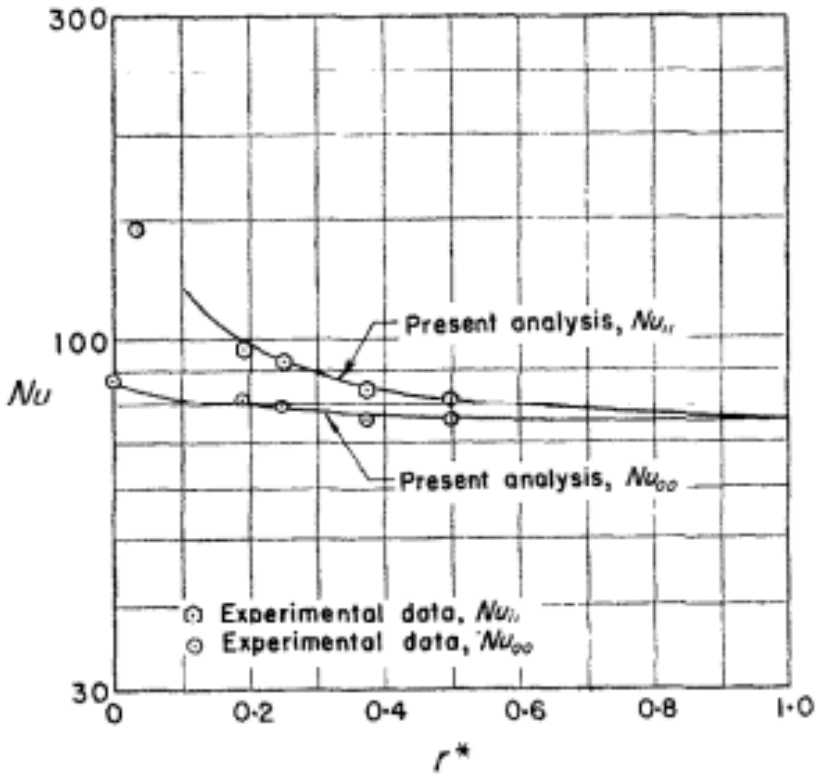

Figure 2-11 Nusselt Number for Uniform Heat Flux Turbulent Flow in Annulus [25]

2.2 Heat Transfer and Pressure Loss Characteristics in Rotating Duct flow

2.2.1 Duct in Parallel Mode Rotation

The effect of rotation is also key parameter in this study. When a duct undergoes rotation about its parallel axis, secondary flows occur due to centrifugal forces and Coriolis forces. The centrifugal forces occur in all instances of rotation while Coriolis forces occur when a system rotates but the velocity of the flow relative to the system does not coincide with the rotation. Mori & Nakayama [27]. Figure 2-12 shows the secondary flow induced by the rotating. The left side shows when the rotation is not strong, and the right side shows when the rotation effect is large. The secondary flow causes the boundary layer to become skewed towards the rotation direction due to the Coriolis forces. Woods & Morris [28] Conducted a similar study in the laminar region. Figure 2-13 shows the velocity and temperature profiles of a rotating duct in the cross-sectional view.

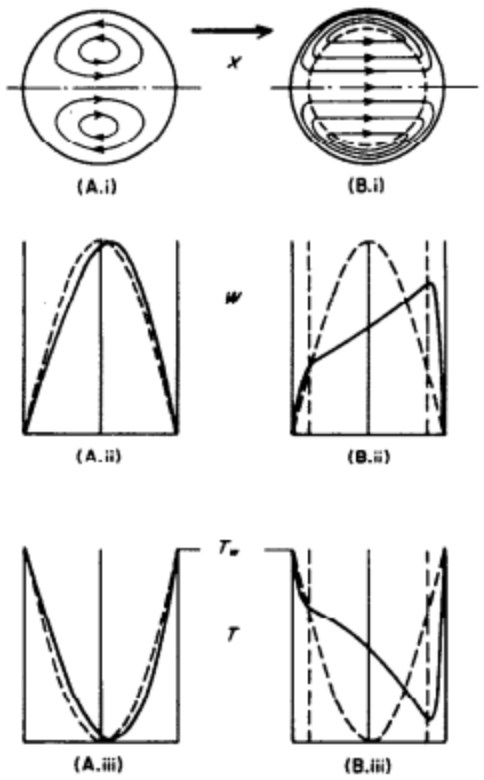

Figure 2-12 Secondary Flow Structure & Velocity Profiles of Duct Rotating about Parallel Axis [27]

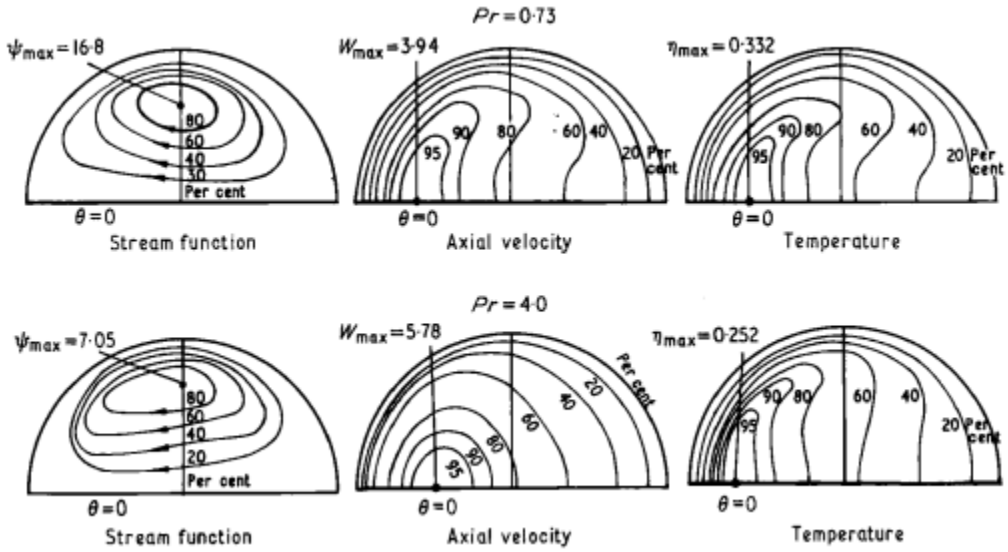

Figure 2-13 Velocity & Temperature Profiles for Circular Duct Rotating about Parallel Axis [28]

The non-symmetric profiles due to secondary flow can affect the heat transfer. Because of this, Morris & Woods [2] conducted experiments to develop a new correlation for duct flow rotating about a parallel axis. Morris & Woods [2] proposed the following correlation dependent on the axial and rotational Reynolds numbers.

$$Nu = nRe_{Dh}^{0.78}J^{0.25} \tag{20}$$

where n = 0.016 when $L/D_h = 34.65$, ε = 24.02 and n = 0.013 when $L/D_h = 69.30$, ε = 48.03. Figure 2-14 shows the correlation compared to their experimental data. In is important to note however, that the data does show very scattered results especially when the rotational Reynolds number is larger.

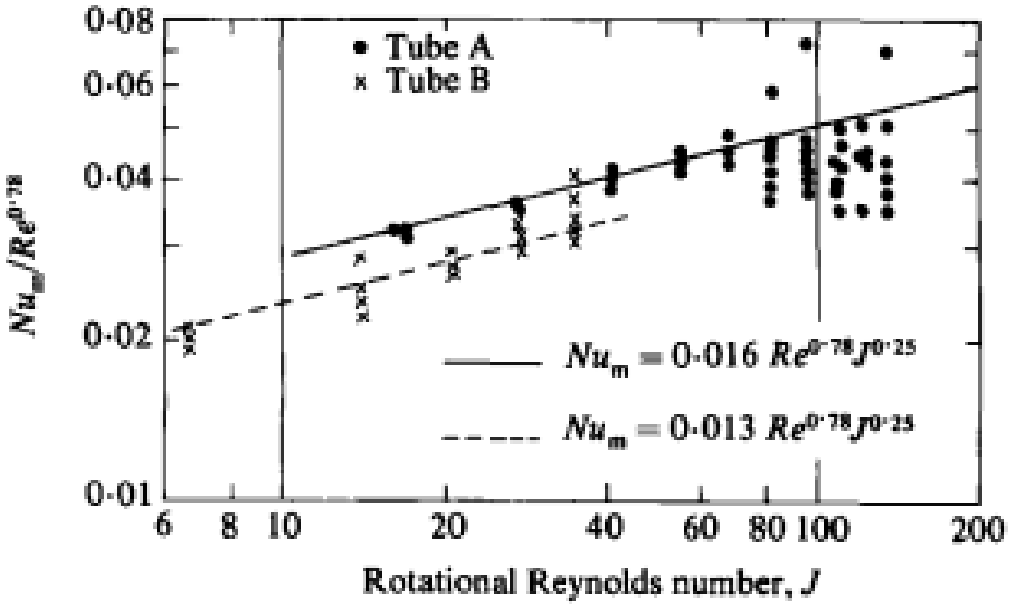

Figure 2-14 Comparison of Laminar Flow Data with Proposed Correlations [2]

Typically, flow passages in turbine air systems resemble a rectangular cross section instead of a circular one. Neti et al. [29] presented a numerical study on laminar heat transfer in a rectangular duct rotating about a parallel axis. Similar to the circular duct the velocity profile becomes skewed due to secondary flow. Figure 2-15 shows the comparison between the stationary and rotating velocity profiles.

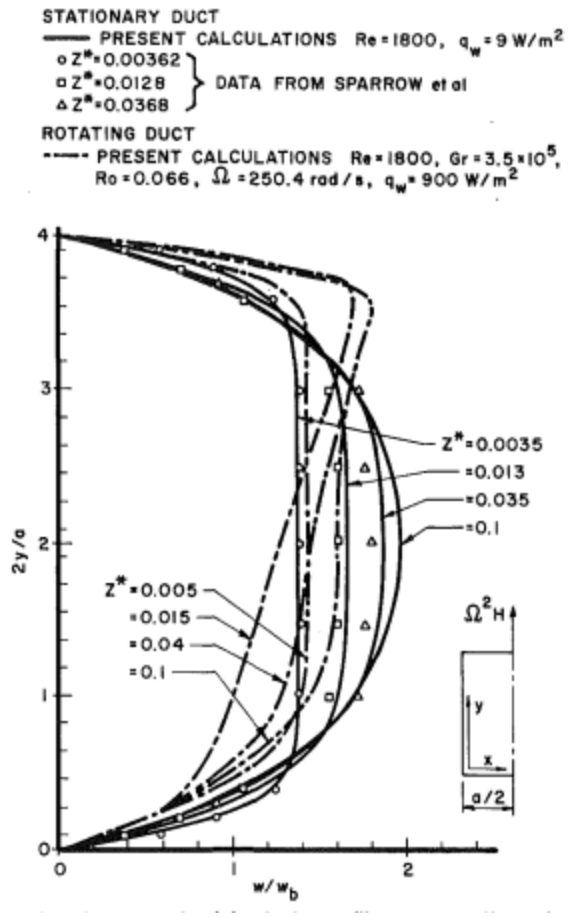

Figure 2-15 Comparison of Velocity Profiles for Rectangular Duct with and without Rotation [29]

Morris & Dias [30] preformed experiments on a rotating square duct and compared the results to that of data from rotating circular duct. This study concluded that while the square cross-section does exhibit an increase in Nusselt Number as the rotation speed increases, the heat transfer for the square duct is less sensitive to the effect than the circular duct. The correlation for a square duct is

$$Nu = 0.012 Re_{Dh}^{0.78} J^{0.1} \tag{21}$$

Levi et al. [31] investigated the effect of rotation in laminar heat transfer in a rotating rectangular duct using the Grashof number defined as

$$Gr = \frac{\rho \beta q R \omega^2 D_h^2}{\mu k} \tag{22}$$

This study revealed that when the Grashof number is less than 10^3 then the effects of rotation are negligible but when Gr > 10^6 The Nusselt Number is about twice that of flow without rotation. Hanafizadeh [32] also compared the effect of rotation using the Grashof number. This study concluded that while the effect of rotation does increase the heat transfer, the effect of is minimized as the Reynolds number increases. Mori et al. [33] also investigated the effect of rotation on rectangular duct flow. This study contradicts the results of Morris and Dias stating that the rectangular cross-section with an H/B range of 6 to 60 is similar to that of a circular duct. Sleiti & Kapat [34] showed that in parallel mode rotation, the leading, trailing, and radial outward walls have enhanced heat transfer however the radially inward wall experiences a decrease in heat transfer. Sarja et al. [35] further confirms this by stating that this tendency is due to the centrifugal buoyancy forces induced by rotation. From Figure 2-17 when all walls are heated, the top wall produces the highest Nusselt number while the bottom wall produces the least.

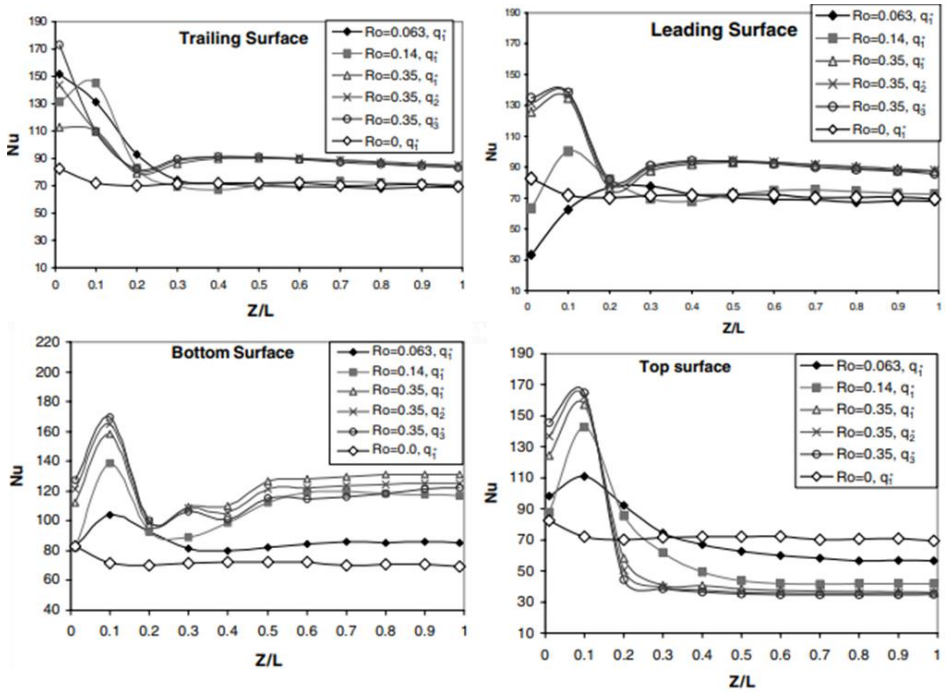

Figure 2-16 Nusselt Number Distributions for Rectangular Duct Walls [34]

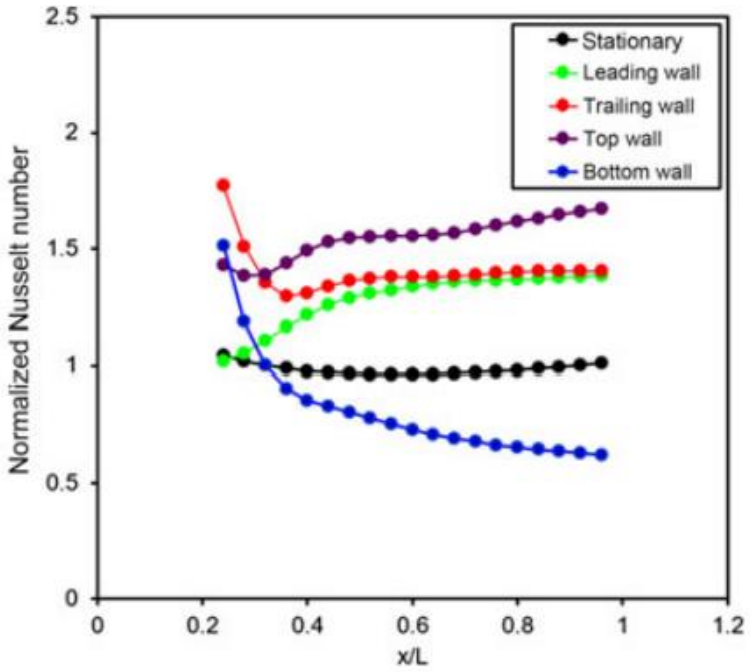

Figure 2-17 Comparison of Nusselt Number Distribution Along Rectangular Duct Walls [35]

Regarding the friction factor, Shevchuk & Khalatov [36] conducted a review studying the effects of rotation about a parallel axis on duct pressure. This study reviewed experimental data from Johnson & Morris [37] showing that compared to a stationary duct, rotation about the parallel axis causes the friction factor to increase. This increase is greater when the L/D_h is shorter. As for the effect of rotation, experimental data for a duct with L/D_h of 10.6 was compared with J equal to 450, 870 and 1200. The notation of the data in the Shevchuk & Khalatov [36] may be incorrect as the data from this paper shows that higher J values resulted in lover friction factor. However, in the Johnson & Morris [37] paper, the opposite trend is observed with the higher J values resulting in higher friction factor. Following the data from the original source [37], the effect of rotation is seen to be greater at lower Re_{Dh}. The study of Johnson & Morris [37] also showed that the effect of the eccentricity is negligible when comparing friction factors.

2.2.2 Annular Duct with Rotating Inner Surface and Stationary Outer Surface

Flow in an annulus with inner surface rotation and stationary outer surface has also been well documented. Bjorklund & Kays [38] conducted experiments on the effect of the rotation on annular flow. This study proposed that the Taylor vortices would enhance the heat transfer meaning the Nusselt number would increase with the Taylor number. This would be due to the vortices enhancing mixing of the flow adding energy to the fluid. Figure 2-18 shows thee suggested vortex patterns presented by Bjorklund & Kays. As the Taylor number increase, the vortices become more unstable further increasing the heat transfer. Becker & Kaye [39] expanded on the study providing experimental data to show when the effect of the Taylor vortices take effect. From Figure 2-19 the Nusselt number does not change with the Taylor number until the Taylor number is greater than 1700 which is the critical Taylor number. Ball et al. [40] and Aoki et al. [41] also conducted similar experiments verifying the critical Taylor number to occur at 1700. Child & Long [42] presents ca correlation using the modified Taylor number given as

$$Nu = 2 \tag{23a}$$

for $Ta_{mod} < 1700$

$$Nu = 0.128 Ta_{mod}^{0.367} \tag{23b}$$

for $1700 < Ta_{mod} < 10^4$

$$Nu = 0.409 Ta_{mod}^{0.241} \tag{23c}$$

for $10^4 < Ta_{mod} < 10^7$

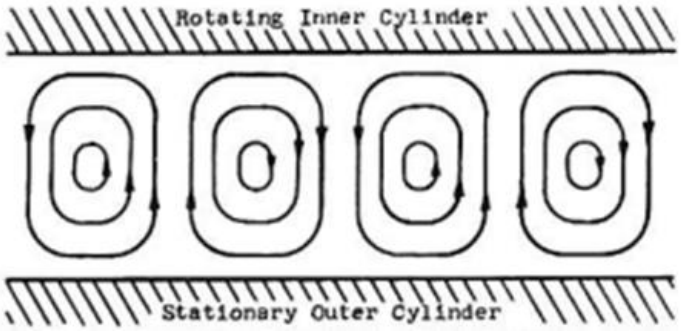

(a) Taylor Number Slightly Above Critical Value

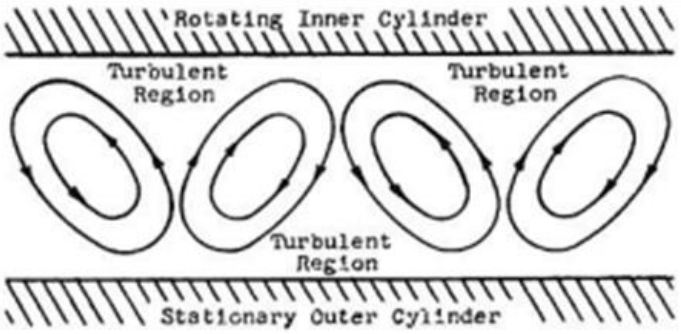

(b) Very High Value of Taylor Number

Figure 2-18 Taylor Vortices Structure [38]

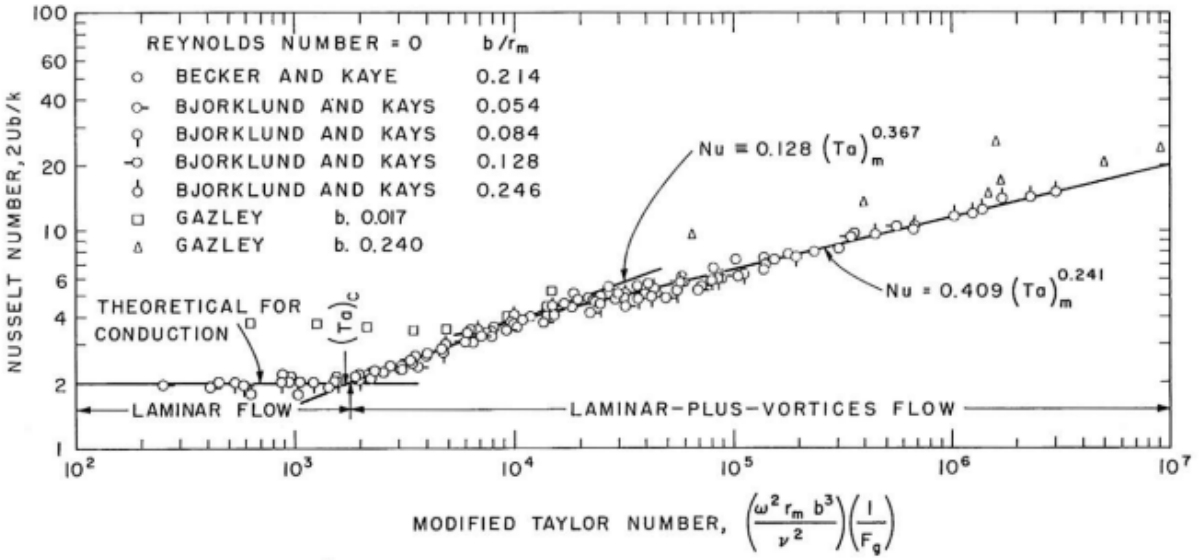

Figure 2-19 Effect of Taylor Number on Heat Transfer [39]

Abed et al. [43] shows the effect of the Taylor vortices on the temperature profile of various radius ratio annuli though CFD. From Figure 2-20 there is less difference between the temperature near the inner wall surface when the rotation speed is increased suggesting that the increased rotation has enhanced the heat transfer.

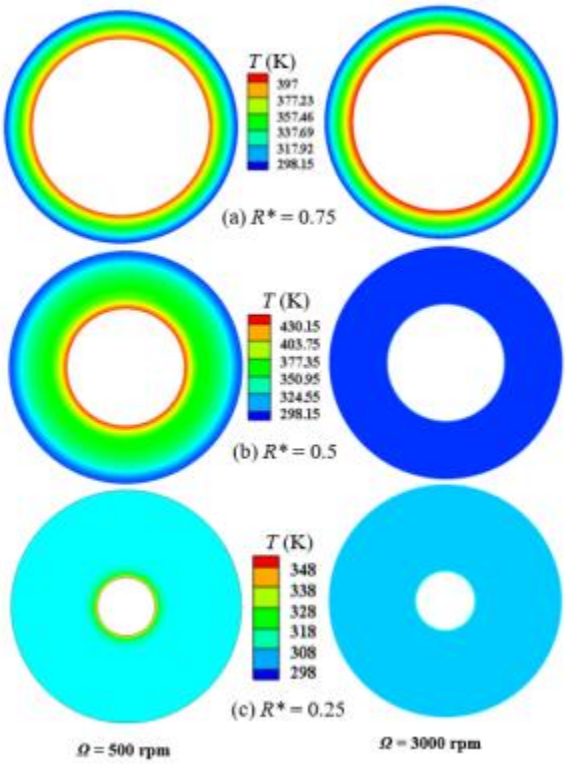

Figure 2-20 Temperature Distribution of Annular Ducts with Inner Surface Rotation and Stationary Outer Surface [43]

A rotational Reynolds number is also used to represent the effect of rotation on annular flow denoted by

$$Re_{\varphi} = \frac{\rho u_t D_h}{\mu} \tag{24}$$

$$u_t = r_1 \omega \tag{25}$$

This rotational Reynolds number is often combined with the axial Reynolds number into an equivalent Reynolds number defined as

$$Re_e = \frac{\rho D_h \sqrt{u_x^2 + \frac{u_t^2}{4}}}{\mu} \tag{26}$$

Boufia et al. [44] presents a correlation using the equivalent Reynolds number given as

$$Nu = 0.025 Re_e^{0.8} \tag{27}$$

for $1.1x10^4 < Re_e < 3.1x10^4$. Jalil et al. [45] expanded on this study suggesting a similar correlation given as

$$Nu = 0.02 Re_e^{0.7927} \tag{28}$$

for $2300 < Re_e < 23600$.

There are also many studies on annular flow with both rotational and axial flow. Child & Long [42], Dawood et al. [46], and Fénot et al. [47] present a review of experiments on heat transfer in an annular passage. These reviews concluded that there are many minor disparities between the results of the authors whose work was reviewed. These disparities can be attributed to factors such as radius ratios, duct lengths and other parameters that may affect the experimental data. However, the data from these reviews generally follow the same trends.

Tachibana & Fukui [48] showed the total heat rate is the sum of heat transfer due to turbulent axial flow and vortices formed by the effect of rotation. Kuzay & Scott [49] presented experimental data in a vertical duct with outer surface heated and an adiabatic rotor. This study concluded that the rotation causes the radial temperature was changed by having temperature decreased near the stator wall and increased near the rotor wall. Additionally, a correlation for the Nusselt number is presented as

$$Nu_{\varphi} = Nu_0 \left[1 + (\frac{2D_h u_t}{\pi D_i u_x})^2\right]^{0.8714} \quad (29)$$

Where Nu_0 is the Nusselt number when the annulus is not rotating calculated using equation (11a).

Childs & Turner [50] also presents a correlation for an annular duct with both axial flow and inner cylinder rotation given as

$$Nu_{\varphi} = Nu_0 + 0.068 Nu_0 (\frac{u_t}{u_x})^2 \quad (30)$$

Pfitzer & Beer [51], Tzeng [52] and Jakoby et al. [53] both showed the enhancement of Nusselt number as rotation speed increases. However, this effect is reduced at higher axial Reynold's number. Rao & Sastri [54] created a numerical model which shows good agreement with data from Becker & Kaye. El-Ghnam et al. [55] primarily investigated the effects of eccentricity on the heat transfer but also includes experimental data on concentric annuli. Abou-Ziyan [56] also focused on the effect of eccentricity but provided numerical analysis for both heat transfer and friction factor for concentric cylinders. Yanagida & Kawasaki [57], Gilchrist et al. [58], and Nouri-Borujerdi & Nakhchi [59] all focused on the effects of turbulators on heat transfer in rotating annulus but also presents data for smooth ducts. Molki et al. [60] studied the effect of rotation on the Nusselt Number across the duct. this study showed that the Taylor vortices cause a sudden increase in the mass transport which also cause a sudden increase in the heat transfer in the duct. This sudden increase occurs closer to the entrance of the duct at higher Taylor Numbers. Gardiner & Sabersky [61] in addition to including experimental data for heat transfer also included data on friction factor. This study showed that the friction factor does not show significant influence until the Taylor number > 10^4.

2.3 Effect of Entrance Geometry

2.3.1 Entrance Geometry

Experimental data from literature mostly involve test sections with bell-mouth entrances. In the present study the test sections have a sharp entrance which makes it important to understand how the differences can affect the heat transfer and pressure loss. The pressure loss due to entry effect is given as

$$\Delta p_{entry} = K_L \frac{1}{2} \rho u_x^2 \tag{31}$$

where K_L is the pressure loss coefficient and u_x is the average velocity of the cross section at the entrance [7]. With the entry effect quantified, it can be subtracted from the friction factor to determine the friction factor in only the fully developed region.

The effect of the entry loss on the heat transfer has been studied as well. Mills [62] conducted a series of experiments with 12 different entrance geometries. Of the 12 different geometries, two geometries of are interest for this study, the bell-mouth and the sharp edge. This is because most relevant studies use bell-mouth inlets to study heat transfer however in the present study a sharp entrance is used. Figure 2-21 shows the differing profiles between the bell-mouth and the sharp entrance. For the sharp entrance, the heat transfer coefficient initially increases then decreases into a plateau. This is because the sharp entrance causes a stagnate air pocket in the entrance which causes a larger pressure loss and lower heat transfer. As the flow reattaches after the pocket, the heat transfer is greater and declines in a similar fashion to Figure 2-5. For the bell-mouth entrance, the heat transfer coefficient initially drops. This represents the laminar section of the flow and as the flow transitions into turbulent, the heat transfer coefficients can be seen as increasing until it reaches the fully developed region where the heat transfer coefficient becomes constant. This is further validated by Tam & Ghajar [63] who compared reentrant sharp, and bell-mouth entrances. Ghajar & Tam [64] also presented a study of the effect of the entrance geometry on the transition region. Figure 2-22 shows the Reynolds number where each geometry starts their transition region. The reentrant entrance transitions at the lowest Reynolds number while the bell-

mouth the highest. Mohammed [65] studied the effects on the entrance geometry in the laminar region. This study also included the effect of buoyancy forces. This study shows the bell-mouth entrance having the highest Nusselt number as the bell-mouth inlet minimizes the losses increasing the heat transfer.

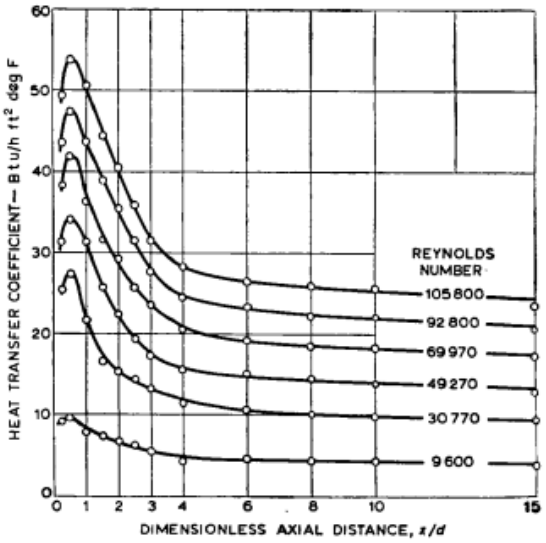

(a) Sharp Entrance

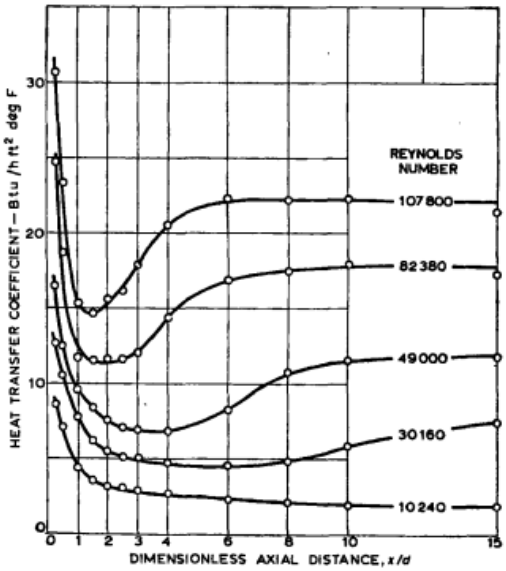

(b) Bell-mouth Entrance

Figure 2-21 Local Heat Transfer Coefficients [62]

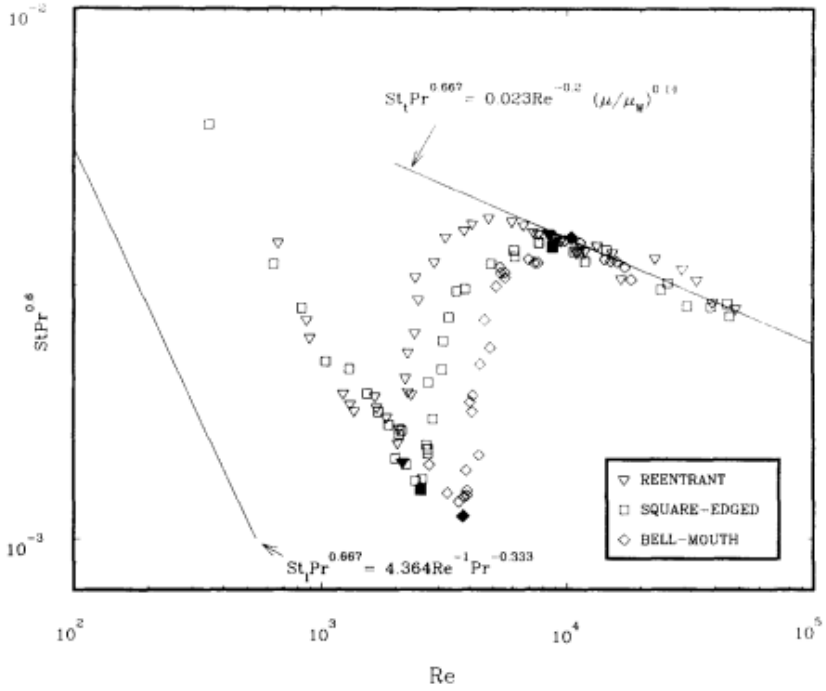

Figure 2-22 Transition Region for Different Entrance Geometries [64]

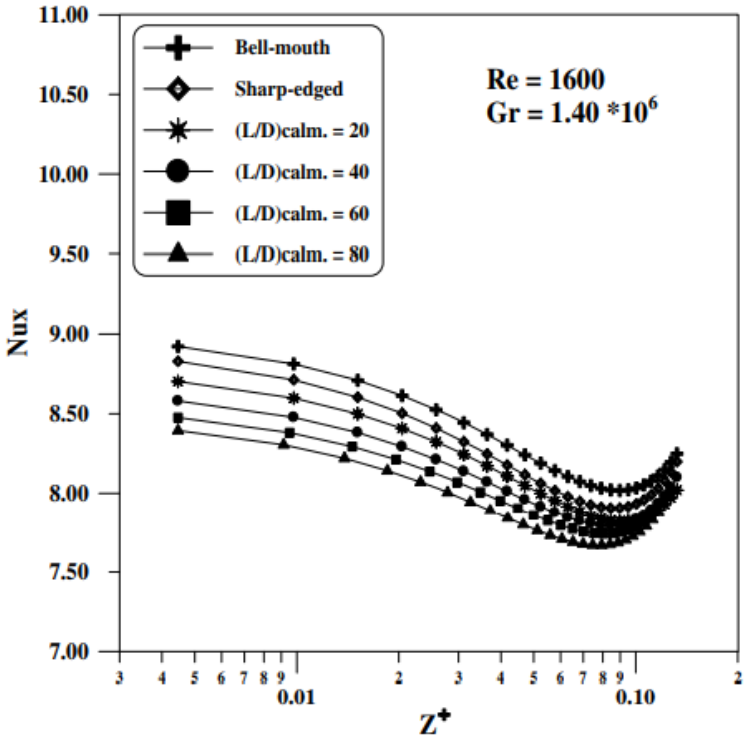

Figure 2-23 Nusselt Profile for Mixed Convection with Different Entrance Geometries [65]

Chapter 3 Experimental Approach

3.1 Experimental Rig & Test Models

3.1.1 Soft Disc Rotating Rig

The Soft Disc Rotating Rig was designed to test the heat transfer and pressure loss characteristics in rotating duct flow. The rig has two set ups; one to test duct flow rotating about a parallel axis and one to test flow in an annulus with inner surface rotation. Figure 3-1 shows the schematic for the set up to test duct flow in parallel mode rotation. A blower controlled by a 60 Hz frequency inverter is used to pull air through a slot in a Rohacell 31 IG-F soft disc, through the hollow shaft, through an orifice and exiting into atmospheric conditions as outlined by black arrows. The rotation speed is controlled by a motor using a 60 Hz frequency inverter and the mass flow rate is measured using an orifice designed following the British Orifice Standards [66]. In Figure 3-2a, the connection of the blower to the soft disc is shown. The plumbing is connected to the hollow shaft and a tachometer is placed to measure the rotation speed. Figure 3-2b, shows the rotational components of the rig. The soft disc is wrapped with shrink wrap to make the outer surface smooth and help hold the disc together. Additionally, in the section where the hollow shaft is marked, there is a section of the shafted wrapped in duct tape. This is where the sensors were fed through to measure the temperature and pressures of the duct.

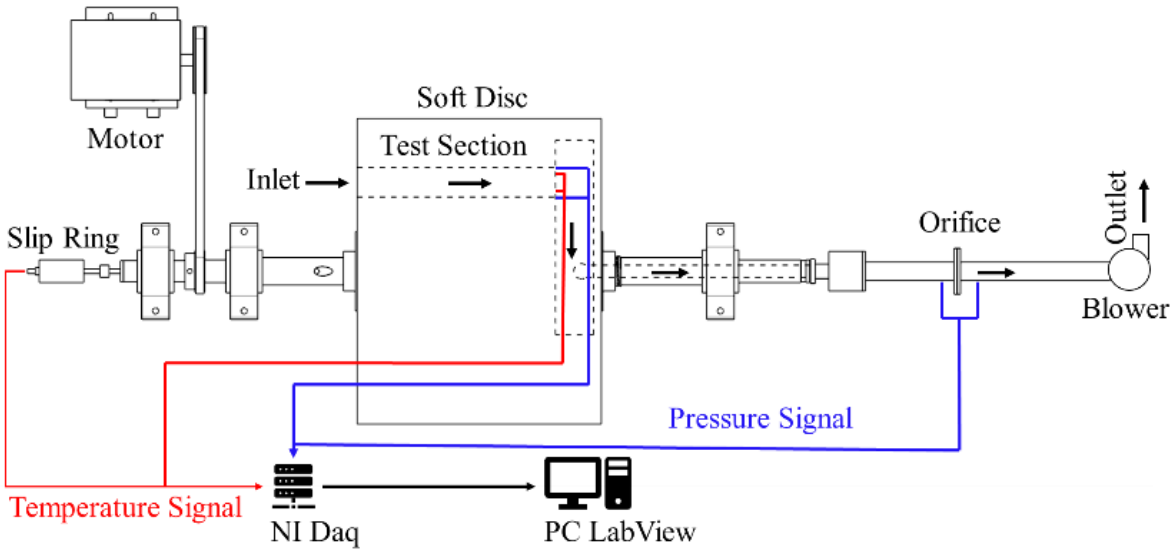

Figure 3-1 Schematic of Soft Disc Rotating Rig (Set up for Parallel Mode Rotation Test)

(a) Mass Flow Components

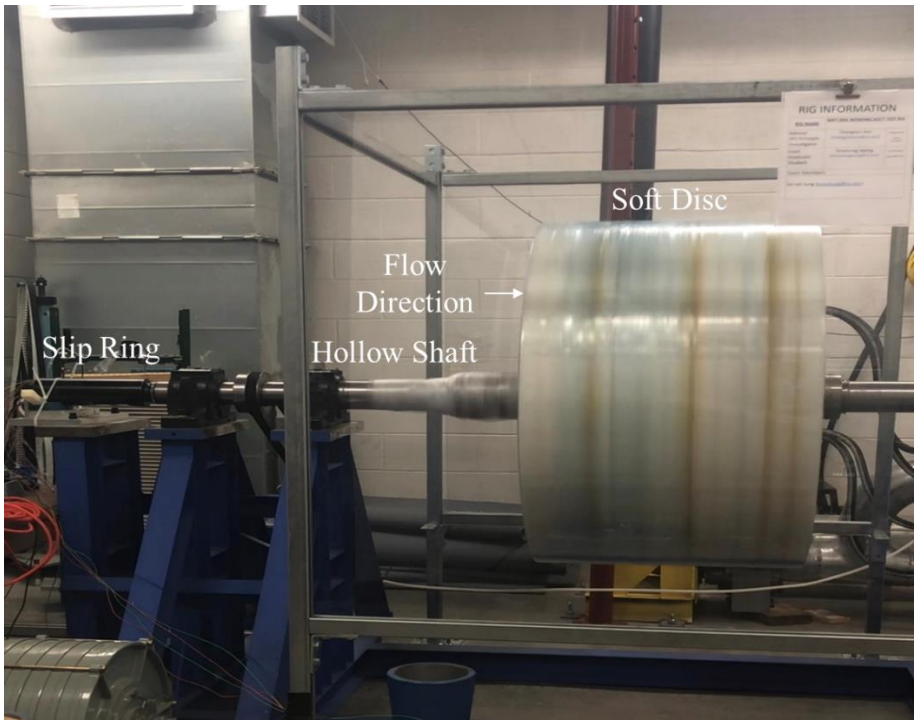

(b) Rotational Components

Figure 3-2 Photo of Parallel Mode Rotation Set Up

The schematic of annular duct configuration can be seen in Figure 3-3 with the flow path marked with black arrows. The rotation speed is controlled by a motor the same as for the parallel mode rotation set up. In terms of how the mass flow rate was controlled, air is supplied from a compressor and the mass flow is regulated by setting a reference pressure to a Parker R119-20J pressure regulator monitored by a Fluke 719 pro 150G pressure calibrator. A Valworx 529100A solenoid valve is included in the assembly to shut off the flow in case of emergencies. The mass flow is measured using orifices following British orifice standards [66] once downstream of the pressure regulator and once again upstream of the plenum to check for any air leakage. Figure 3-4a shows the rotational components of the rig. The rotor and stator can be seen along with sensors attached. The rotor is made of Rohacell 31 IG-F and has fixed dimensions while the stator is made from acrylic and is changed out for different radius ratios. Figure 3-4b shows the plumbing for the annular duct configuration. In the high-pressure regions, 2.5” stainless steel piping was used to ensure safety. After the pressure is regulated down, the piping is expanded to 6” and pvc piping is

used. The larger diameter piping allowed the pressure in the pvc to stay below the maximum operating pressure of the piping.

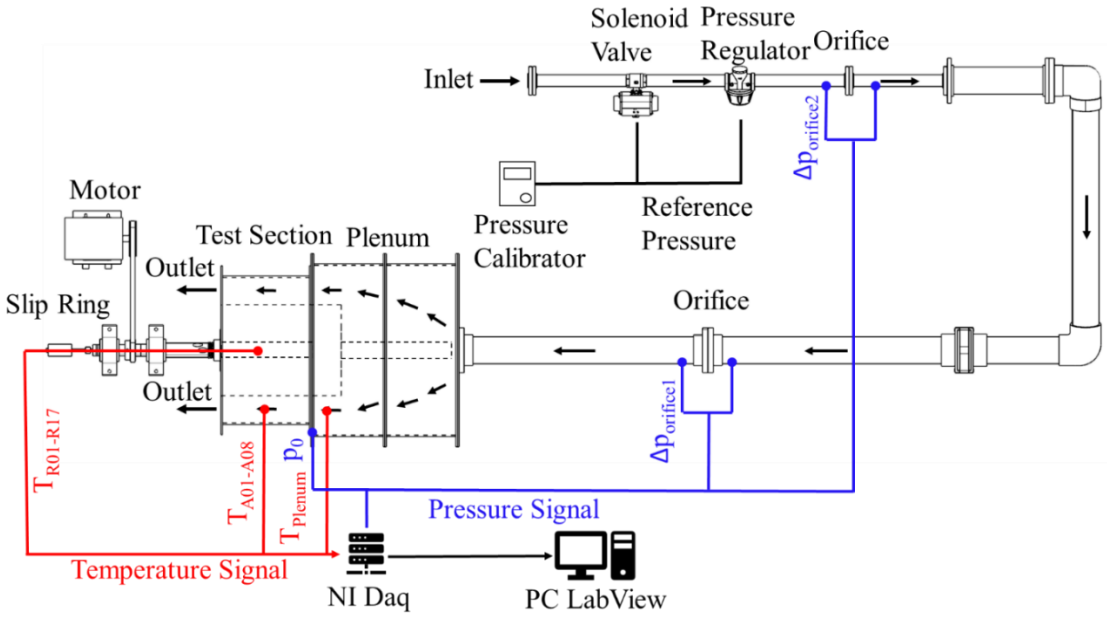

Figure 3-3 Schematic of Soft Disc Rotating Rig (Set up for Annular Duct Test with Rotating Inner Surface)

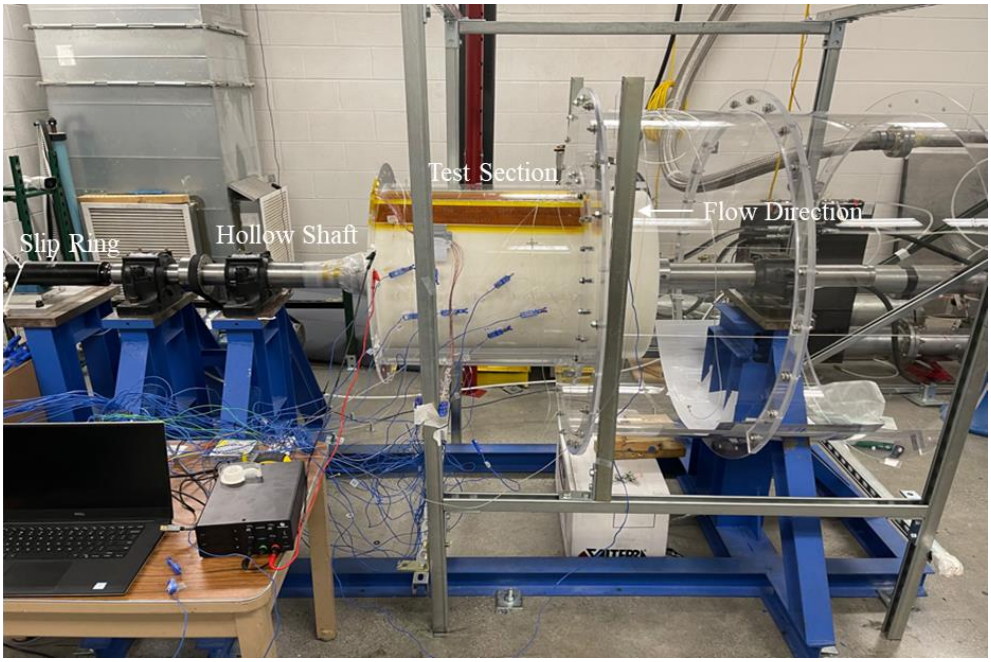

(a) Rotational Components

(b) Mass Flow Components

Figure 3-4 Photo of Annular Duct Set Up

3.1.2 Realistic S-shaped Model of Passage between Turbine Blade Root and Disc

The realistic S-shaped model test section is scaled from a real engine with the results listed in Table 3-1. Since the Nusselt number correlations and pressure loss correlations depend on the Re_{Dh} it was important to align is parameter. Also, since the L/D_h can also influence the heat transfer and pressure loss this parameter is also aligned. The radius is scaled down to one third and the hydraulic diameter is scaled up by a factor of 4. Scaling down the radius reduced cost of material and reduces the stress on the soft disc while under rotation. The hydraulic diameter is scaled up by a factor of four allowing easier machinability when creating the model. The entrance was also designed with a sharp edge to match what would typically be seen in a real engine.

Although much effort was placed into making the model accurately represent real engine parameters, there are still some limitations. Firstly, in a real engine the passage is slanted off the x-axis. This slant could not be modeled as the machining of the S-shaped geometry proved to be difficult. Additionally, since the assembly of the blade root and disc is that of sliding the blade root

into the dovetail of the disc, the blades root will move slightly as the rotor is rotating. This will cause the passage cross-sectional area to vary throughout operation.

Table 3-1 Scaling for Realistic S-shaped Model

Parameter	Real Engine	Scaled Model
R (m)	0.945	0.330
L (m)	0.119	0.476
D_h (m)	0.002	0.008
L/D_h	58.690	58.690
Re_{Dh}	3000	3000

The test sections for the parallel mode rotation tests are placed in a slot in the Rohacell soft disc as seen in Figure 3-5. The actual measurement for the radius varies slightly from the design. The realistic S-shaped passage was machined out of Rohacell 31 IG-F. An isometric drawing and cross-sectional view with dimensions listed are available in Figure 3-6. A photo of the duct cross-section can be seen in Figure 3-7. From the photo the two exit air thermocouples can be seen. They are placed halfway between the middle and edge of the flat portion of the top wall where the end of the flat portion is marked with lines from a black marker. Static pressure taps were also placed slightly upstream of but in line with the thermocouples. Figure 3-8 shows the locations of the thermocouples and pressure taps on the top wall. The pressure sensors were placed in line with the end of the heaters at 508 mm from the inlet or 17 mm from the outlet.

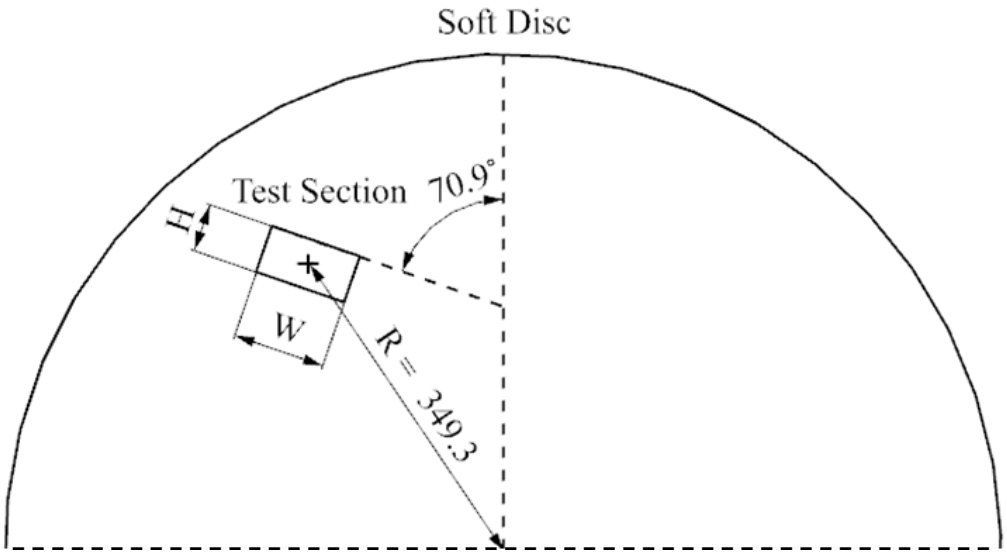

Figure 3-5 Test Section Slot in Soft Disc Front View (Units: mm)

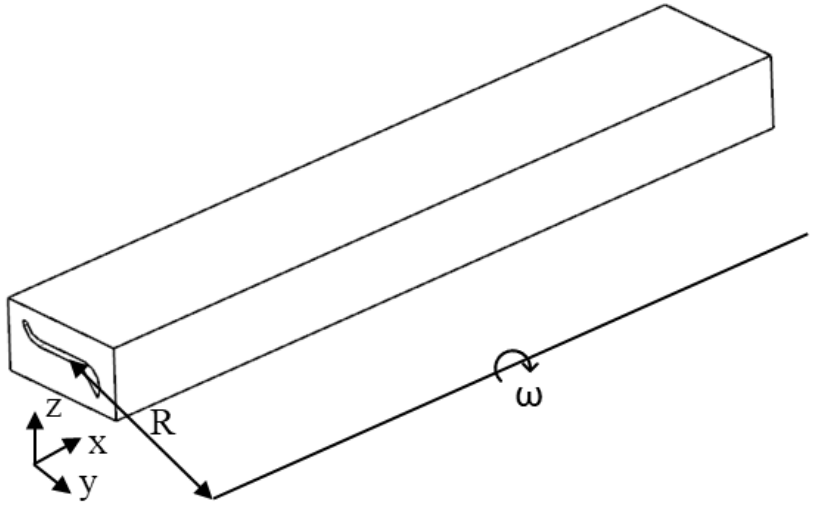

(a) Isometric View

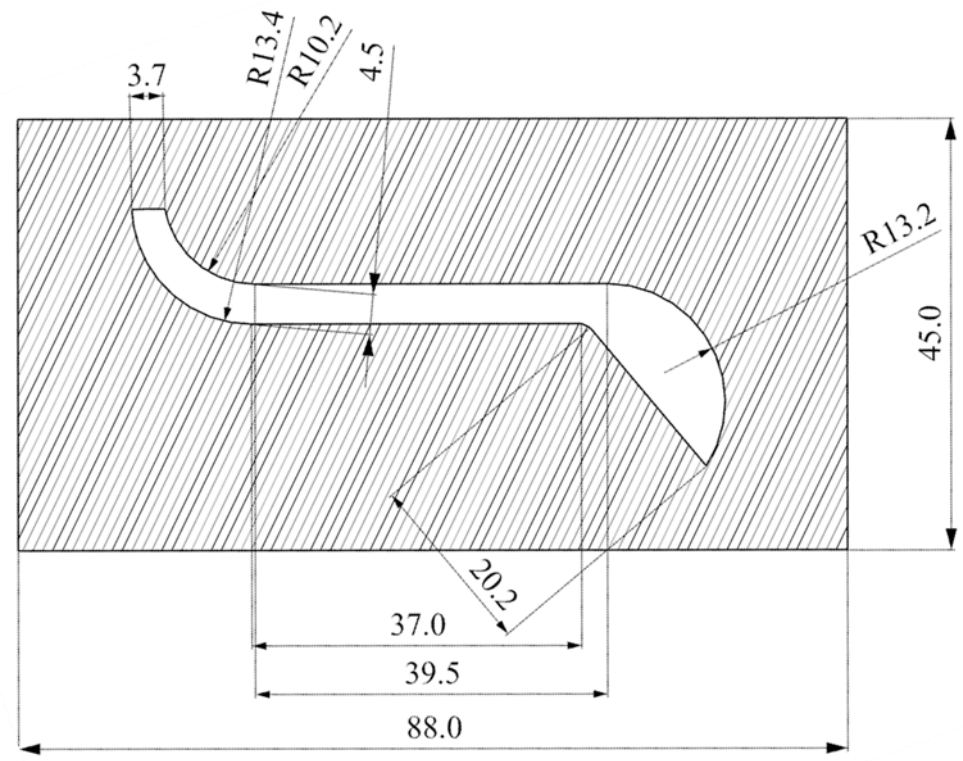

(b) Cross-sectional View

Figure 3-6 Realistic S-shaped Model Duct front view (Units: mm)

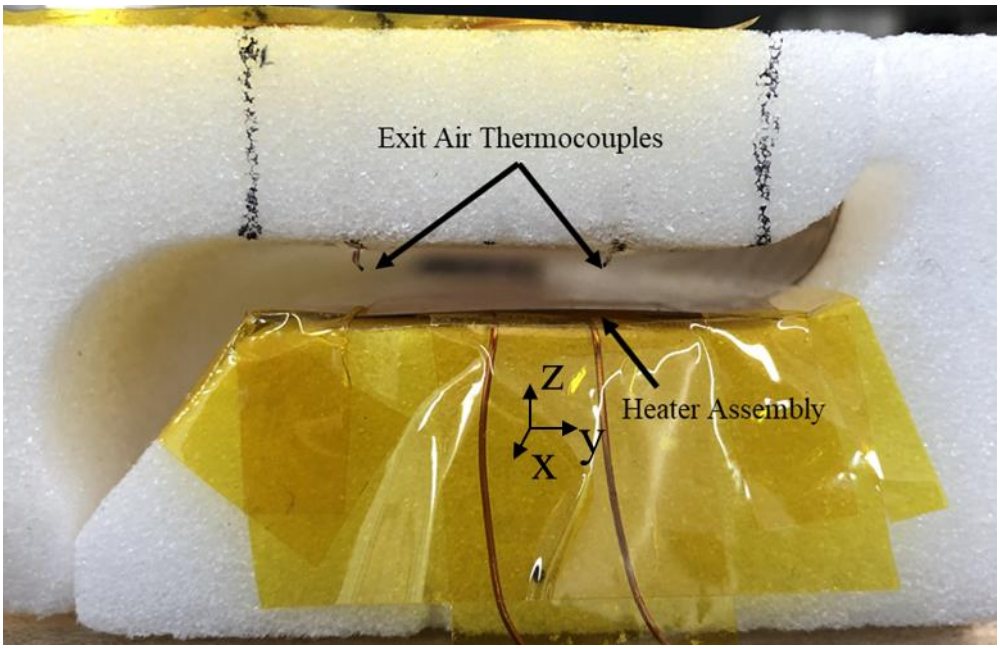

Figure 3-7 Photo of Realistic S-shaped Model Cross-section rear view

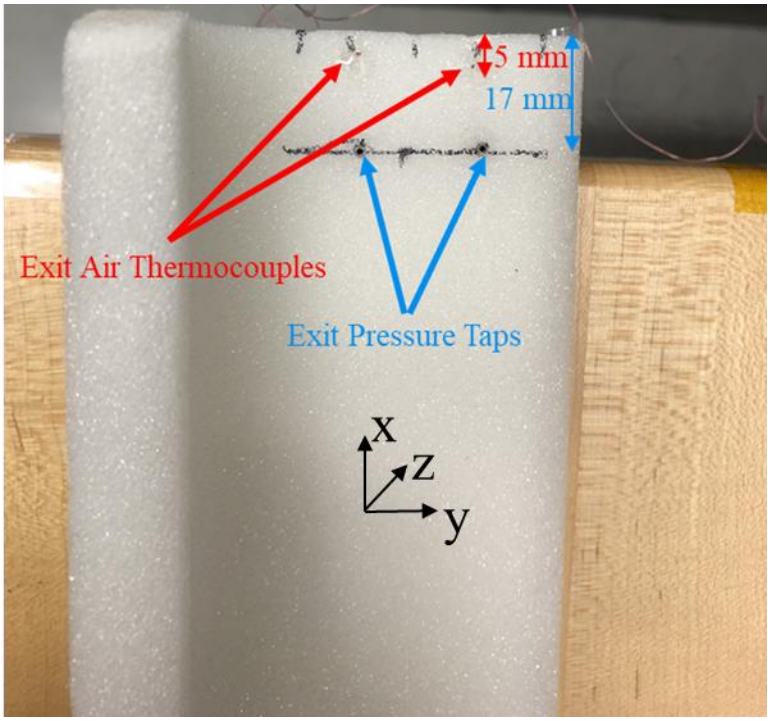

Figure 3-8 Exit Pressure Tap & Thermocouple Locations

3.1.3 Simplified Model of Passage between Turbine Blade Root and Disc

Rectangular ducts were also constructed to see if the correlations for the rectangular duct can be applied to the realistic S-shaped model. In Figure 3-9b, the coordinate system is included with the rotation axis in the isomeric view. A duct with an aspect ratio of 20 would have a hydraulic diameter similar to the realistic S-shaped model. For the other aspect ratios chosen, the assumption is that the realistic S-shaped model can be split into three sections: the curves section on the left, the rectangular section in the middle and the semi-circle on the right. Each of these sections can be represented by different aspect ratio ducts. For example, the middle section of the realistic S-shaped model would have an aspect ratio similar to 10. Lastly, two other aspect ratios of target value of 4 and 2 are also constructed. The dimensions can be seen in Table 3-2. Due to machining tolerances and tolerances in assembly, the measured aspect ratios differ from the design values. The rectangular duct aspect ratio 2.05 test section was constructed out of 4 acrylic plates. From this duct, the aspect ratio was adjusted by adding spacers made from Rohacell 31 IG-F as seen in Figure 3-10. Using the spacers, the height of the duct is reduced reducing the hydraulic diameter

and cross-sectional area. This also effects the duct length to hydraulic diameter ratio since the duct length is fixed by the design of the soft disc.

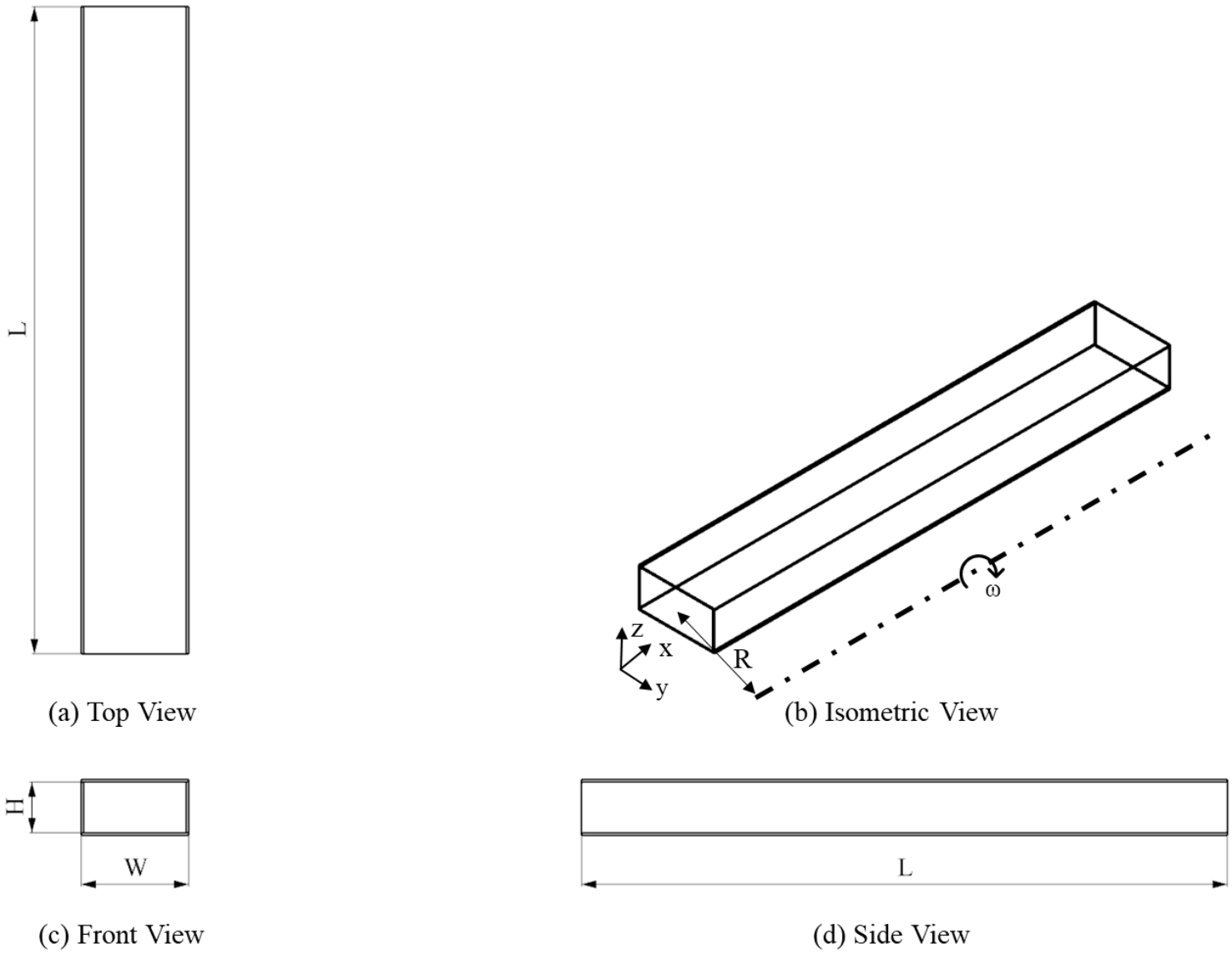

Figure 3-9 Simplified Rectangular Model AR = 2.02

Table 3-2 Non-Dimensional Parameters of Parallel Mode Rotation Test Sections

Geometry	Aspect Ratio = W/H	L/D_h	ε	$Re_{Dh} = \rho u_x D_h/\mu$	$J = (\rho\omega D_h^2)/\mu$
Realistic	-	52.71	35.04	169-3714	32-552
AR20	17.33	57.38	37.93	74-3170	27-450
AR10	8.81	30.7	20.41	291-5606	95-1543
AR4	3.93	17.48	10.35	443-10244	365-6148
AR2	2.05	9.55	6.31	630-19032	1014-16664

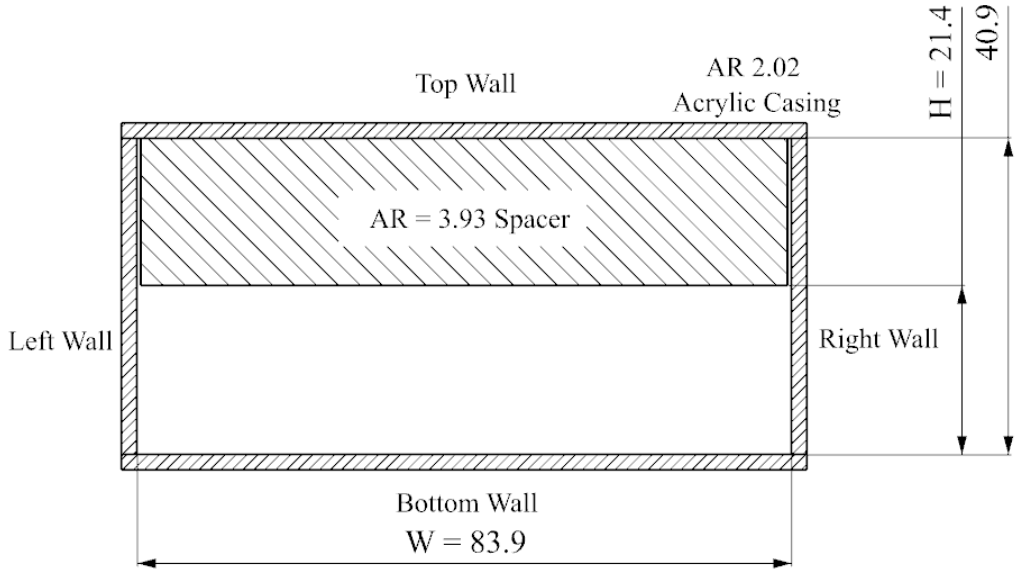

Figure 3-10 Front View of Simplified Rectangular Duct AR = 3.93 with Spacer Installed for Stationary Experiment

3.1.4 Simplified Model of Passage between Turbine Disc and Shaft

The annular duct test section is also scaled from a real engine; however, different turbines have different passage heights, so the radius ratios were varied. Table 3-3 lists the parameters of the real engine and scaled model. The rotor radius is twice the radius of the real engine, and the radius radios were ranged from 0.05 to 0.6. The target Re_{Dh} is too large for testing so the minimum to maximum Re_{Dh} was limited to that which can be safely operated in the facility.

In a real engine, the shaft and the disc typically rotate together. However, in this study, only the rotor could be rotated due to limitations of the rig. The rotor was made from Rohacell 31

IG-F and stator was made from acrylic casing. Figure 3-11 shows the drawing and coordinate system. The radius of the rotor is fixed, and the radius ratio is changed by changing the stator. Table 3-4 shows the dimensions of each test sections. Similar to the rectangular duct, changing the radius ratio changes the passage height thus changing the duct L/D_h.

Table 3-3 Scaling for Annular Duct Tests

Parameter	**Real Engine**	**Scaled Model**
r_1 (m)	0.141	0.282
r_2 (m)	0.161	0.332
$\Delta r/r_1$	0.1418	0.1418
L/D_h	7.100	7.100
Re_{Dh}	326000	32600

Table 3-4 Annular Duct Test Section Dimensions

$\Delta r/r_1$	r_1	r_2	$D_h = 2(r_2-r_1)$	L/D_h	$Re_{Dh} = \rho u_x D_{h/}\mu$
0.05	282	592	28.1	19.9	7792-41657
0.1	282	620	56.3	9.9	10026-40488
0.3	282	733	169.1	3.3	9868-40828
0.6	282	902	339.3	1.7	9764-41689

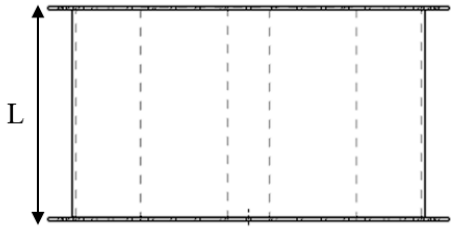

(a) Top View

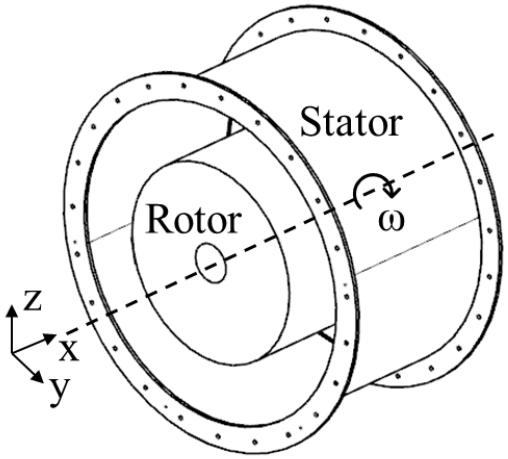

(b) Isometric View

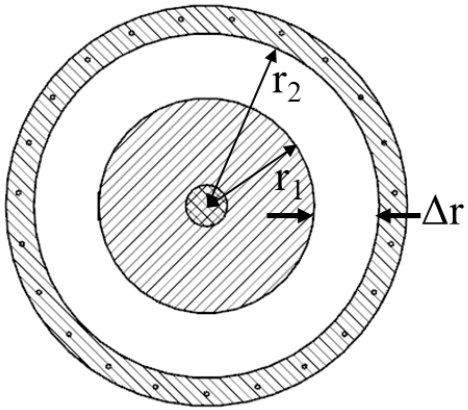

(c) Front View

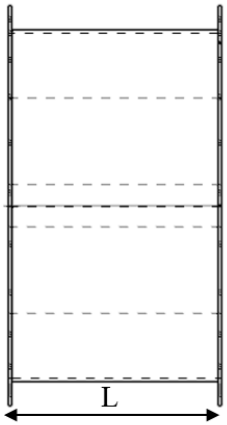

(d) Side View

Figure 3-11 Simplified Annular Model $\Delta r/r_1 = 0.6$

3.2 Data Acquisition System

3.2.1 Temperature Sensors

Temperature signals were measured using two different types of thermocouples. Temperature measurements for the air, ambient, and conduction were all measured by omega T-type thermocouples with a reference photo provided in Figure 3-12. The thermocouple was inserted into a 1.6 outer diameter stainless steel tube with the thermocouple junction slightly sticking out. This ensured that the thermocouple would not be moved by the flow during tests. For the wall temperatures, centerline temperatures were measured with thermocouples distributed at smaller intervals near the inlet and larger intervals towards the exit. To ensure that the thermocouples are all aligned along the centerline, a thin film thermocouple was designed, manufactured by FluxTech. This sensor contains a series of T-type thermocouples inside a polyimide film. A photo of the sensor is given in Figure 3-13.

Figure 3-12 Omega T-type Thermocouples

Figure 3-13 FluxTech Thin Film Thermocouple

Calibration for the Omega thermocouples were done using an Omega PT100 RTD Probe and a Sika electronic K325K Calibrator as seen in Figure 3-14 and Figure 3-15. Both the thermocouple and the Omega PT100 were placed into the chamber of the Sika electronic K325K Calibrator. The temperatures were varied from 0°C to 80°C. Figure 3-16 shows the calibration curves for the omega T-type thermocouples. The thermocouple data shows good correlation with the Omega PT100 RTD Probe. For the Thin film Thermocouple, the film is too large to fit into the calibrator. Therefore, a water bath was used to calibrate the thin film thermocouples. The results of the calibration for the thin film thermocouples are listed in Table 3-5. Using the calibration curves from Table 3-5, the temperatures read from the thermocouples (T_{TC}) are converted to the calibrated temperatures (T_{cal}).

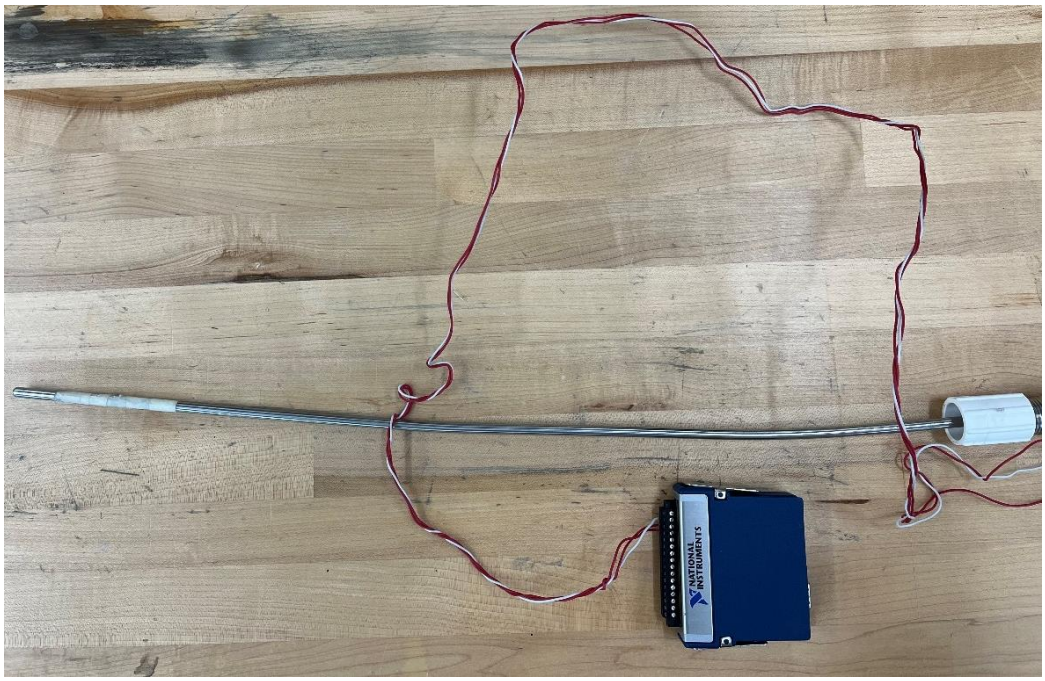

Figure 3-14 Omega PT100 RTD Probe

Figure 3-15 Sika electronic K325K

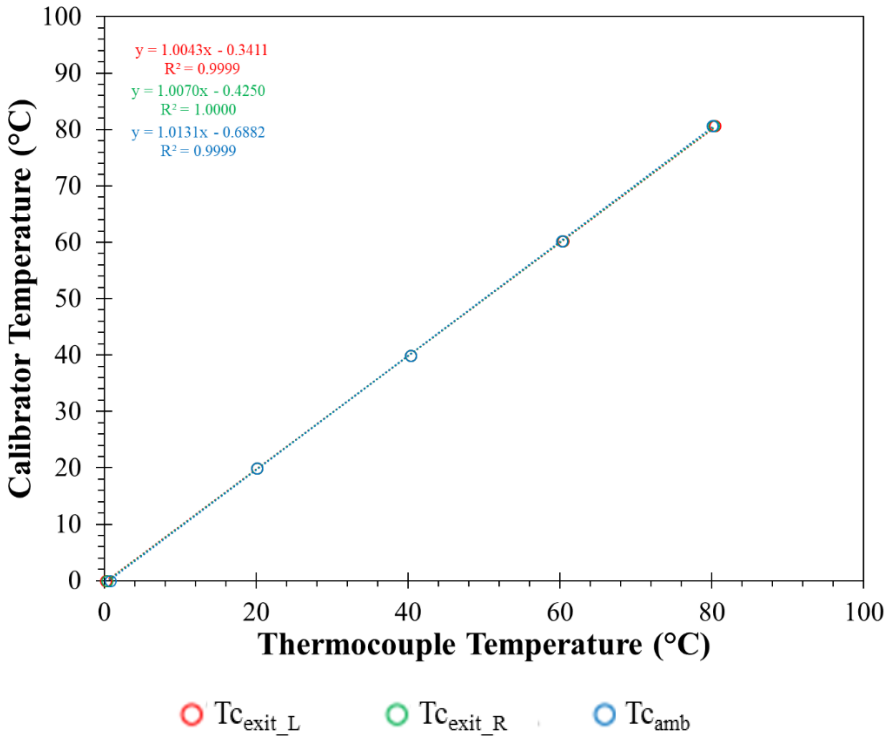

Figure 3-16 Thermocouple Calibrations

Table 3-5 Thin Film Thermocouple Calibration Curves

Calibration Curves $T_{cal} = a*T_{Tc}+b$								
TC #	**a**	**b**	**TC #**	**a**	**b**	**TC #**	**a**	**b**
TC_{01}	1.0346	-1.4909	TC_{07}	1.0322	-1.0548	TC_{13}	1.0344	-1.1781
TC_{02}	1.0349	-1.4515	TC_{08}	1.0289	-0.8903	TC_{14}	1.0461	-1.5637
TC_{03}	1.0352	-1.4104	TC_{09}	1.0258	-0.718	TC_{15}	1.0195	-0.7875
TC_{04}	1.0362	-1.4263	TC_{10}	1.0268	-0.6808	TC_{16}	1.0402	-1.4179
TC_{05}	1.0371	-1.406	TC_{11}	1.0257	-0.4043	TC_{17}	1.0547	-2.4244
TC_{06}	1.0368	-1.3722	TC_{12}	1.0284	-0.9955			

3.2.1 Sensor and Heater Assembly

With the experiments being designed after a uniform heat flux condition, the thin film thermocouple was attached to a thin film resistance heater in a manner to evenly distribute the heat flux and minimize heat loss through conduction. Figure 3-17 shows the components of the assembly for the rectangular duct. For the realistic S-shape model the components are the same but without the acrylic plate. The heater is attached to the acrylic plate using 3m double sided tape.

On the other side of the heater, thermally conductive double-sided tape (k = 1.5 w/mK) is used. This is because for the assembly from the heater to the sensor, conduction loss should be minimized. An aluminum plate (k = 250 w/mK) is placed on top of the heater because the high thermal conductivity would help spread the heat flux uniformly as possible. From the heater, thermally conductive tape is placed followed by the thin film sensor. Figure 3-18, shows the layout of the assembly from the top view. For the realistic S-shape and simplified rectangular assemblies, heat is provided using two Omega thin film heaters. Each heater is 254 mm long and places one after the other. The heaters do not fully cover the entire length of the duct as the duct is 525 mm long and the two heaters together are 508 mm long. The locations of the thin film sensors are also more visible in this figure with dimensions listed in Table 3-6. Since the heat transfer is expected to decrease exponentially in the entrance region, more thermocouples are located towards the inlet than the outlet. Figure 3-19 shows the photo of the assembly for the AR = 2.02. The locations of the exit air thermocouples and exit static pressure taps are shown with the locations listed in Table 3-6.

One limitation of this assembly is that only the centerline temperatures are measured. Each wall surface is expected to follow different trends however, for this experiment, at stationary conditions, the heated surface is the bottom wall, when rotating clockwise, the heated surface is the trailing wall, and for the counterclockwise test, the heated surface is the leading wall. Also, in this study, the heat transfer is assumed to be constant along the width of the duct.

Figure 3-20 shows the components of the annular duct assembly. Here the difference between the annular duct and the rectangular duct is that there is no acrylic plate as the assembly is placed on the Rohacell rotor. Additionally, the sensor is not placed in the center but on the edge of the heater. This is because there is no fixed centerline as the rotor is rotating. However, the assembly is extruded from the rotor, so the sensors is placed to the side to minimize influence of the extrusion tripping the boundary layer. Figure 3-21 and Figure 3-22 show the sensor locations like the rectangular duct with dimensions in Table 3-7. Here the difference is that since the stator is easily accessible, air temperatures at more locations were able to be measured. One air thermocouple is placed for every wall temperature thermocouple till near the inlet region where the wall thermocouples are too close to place one air thermocouple for each. Regarding the pressure sensors, the inlet pressure was measured in the plenum instead of assuming ambient pressure like the rectangular duct.

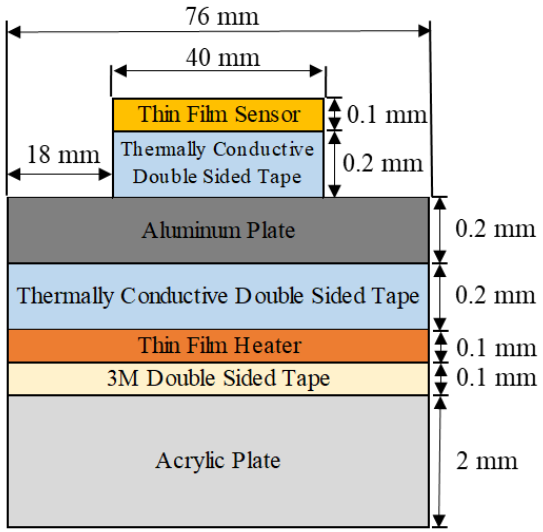

Figure 3-17 Components of Simplified Rectangular Duct Sensor Heater Assembly

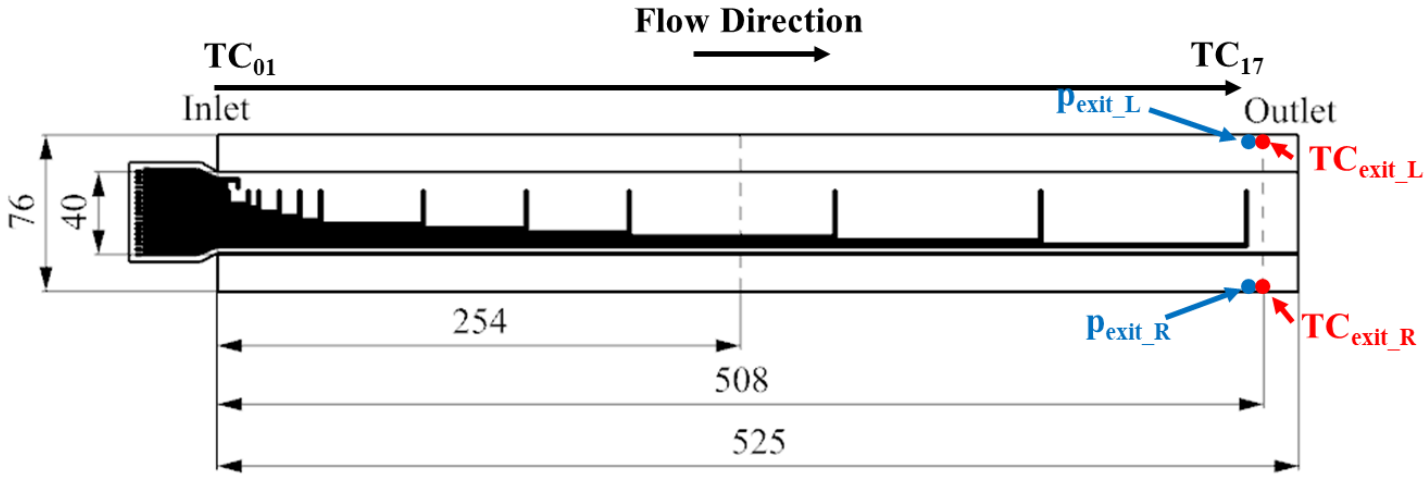

Figure 3-18 Top View of Simplified Rectangular Duct Sensor and Heater Assembly (Units: mm)

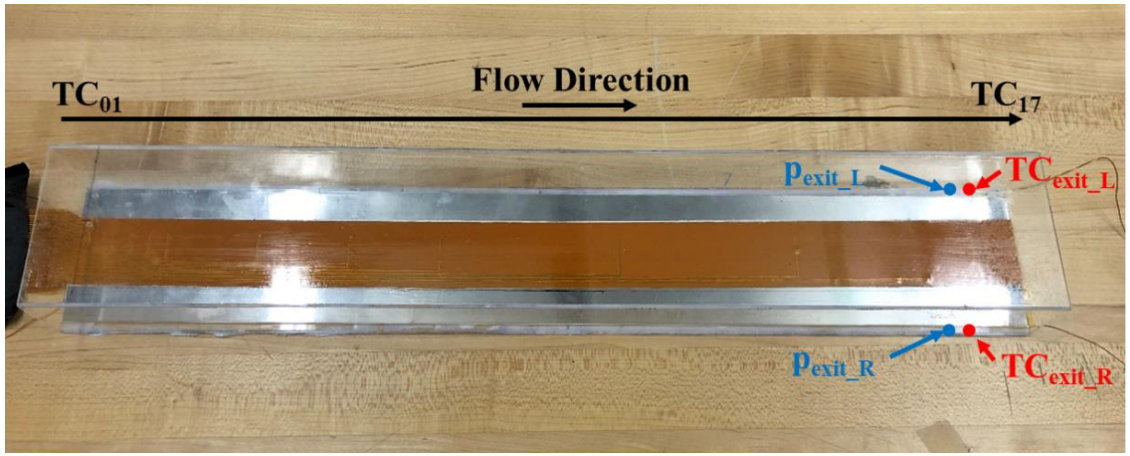

Figure 3-19 AR = 2.02 Sensor Locations

Table 3-6 Realistic S-shape & Simplified Rectangular Duct Sensor Locations

Thermocouple Name	x (Location mm from Inlet)
TC_{01}	1.5
TC_{02}	2.5
TC_{03}	3.5
TC_{04}	4.5
TC_{05}	5.5
TC_{06}	10
TC_{07}	15
TC_{08}	20
TC_{09}	30
TC_{10}	40
TC_{11}	50
TC_{12}	100
TC_{13}	150
TC_{14}	200
TC_{15}	300
TC_{16}	400
TC_{17}	500
TC_{exit_L}	508
TC_{exit_R}	508
p_{exit_L}	504
p_{exit_R}	504

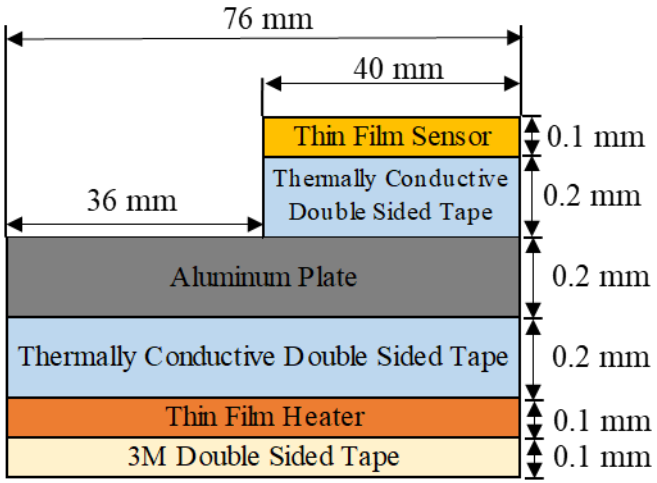

Figure 3-20 Components of Annular Duct Sensor Heater Assembly

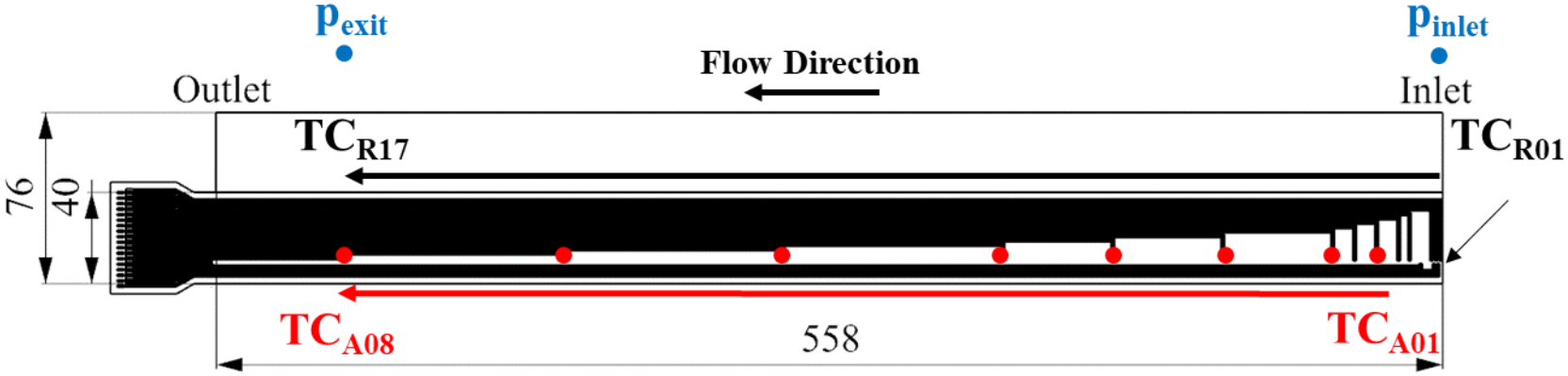

Figure 3-21 Top View of Annular Duct Heater Assembly (Units: mm)

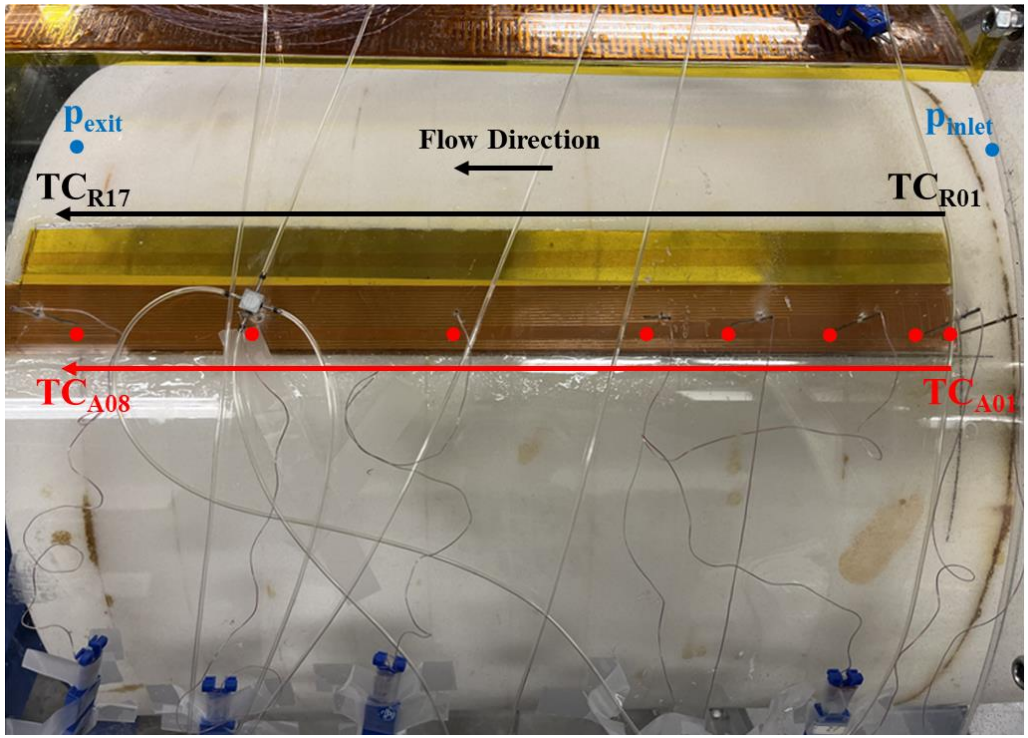

Figure 3-22 $\Delta r/r_1 = 0.05$ Sensor Locations

Table 3-7 Annular Duct Sensor Locations

Thermocouple Name	x (Location mm from Inlet)
TC_{R01}	1.5
TC_{R02}	2.5
TC_{R03}	3.5
TC_{R04}	4.5
TC_{R05}	5.5
TC_{R06}	10
TC_{R07}	15
TC_{R08}	20
TC_{R09}, TC_{A01}	30
TC_{R10}	40
TC_{R11}, TC_{A02}	50
TC_{R12}, TC_{A03}	100
TC_{R13}, TC_{A04}	150
TC_{R14}, TC_{A05}	200
TC_{R15}, TC_{A06}	300
TC_{R16}, TC_{A07}	400
TC_{R17}, TC_{A08}	500
p_{inlet}	0
p_{exit}	500

3.2.2 Heat Flux Distribution

While the experiments are modeled after a uniform heat flux boundary condition, due to 3D conduction losses at the ends, the heat flux distribution will need to be mapped out. The heat flux distribution was checked using a FLIR A325sc IR camera. Figure 3-23 shows the image of the heater assemblies. Figure 3-24 shows the comparison between the IR image and the thermocouple data. The absolute values of the IR image are not accurate due to the rests not being conducted on a blackbody. However, the IR image shows the axial distribution of the heat flux. Assuming the heat flux behaves similarly to the temperature profile, a curve fit of the temperature profile was made and adjusted to fit the heat flux. The heat flux profiles are shown in Figure 3-25. The heat flux has been normalized using the heat flux calculated assuming uniform boundary conditions defined as the total heat divided by the area. Since the Rectangular duct assembly consists of two heaters placed one after the other, the heat flux distribution is more exaggerated in the rectangular duct assembly than the annular duct, which only has one heater. The heat flux distribution is then used to calculate the local heat transfer along the centerline of the duct.

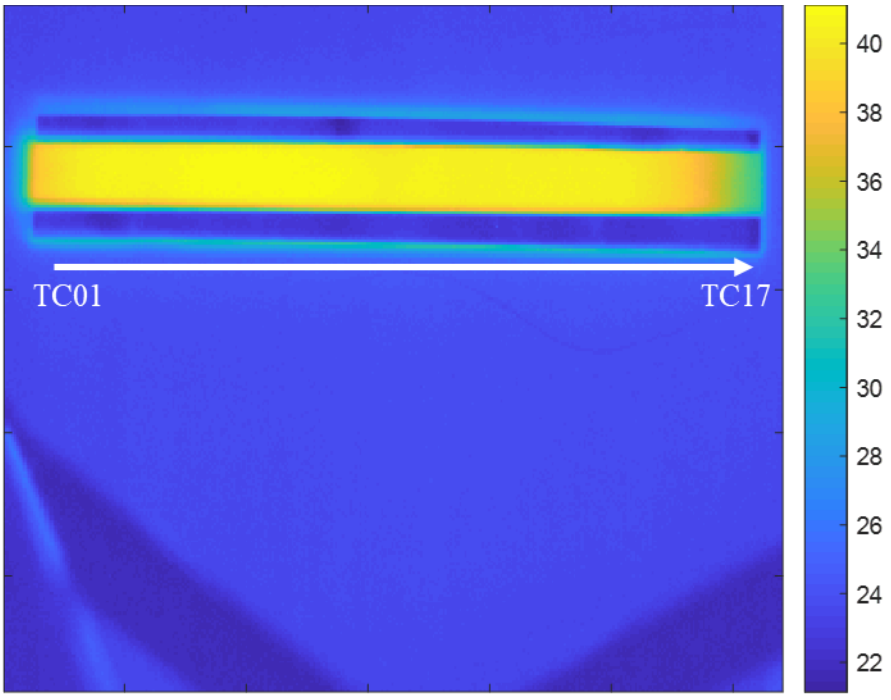

(a) Realistic S-shape & Simplified Rectangular Duct

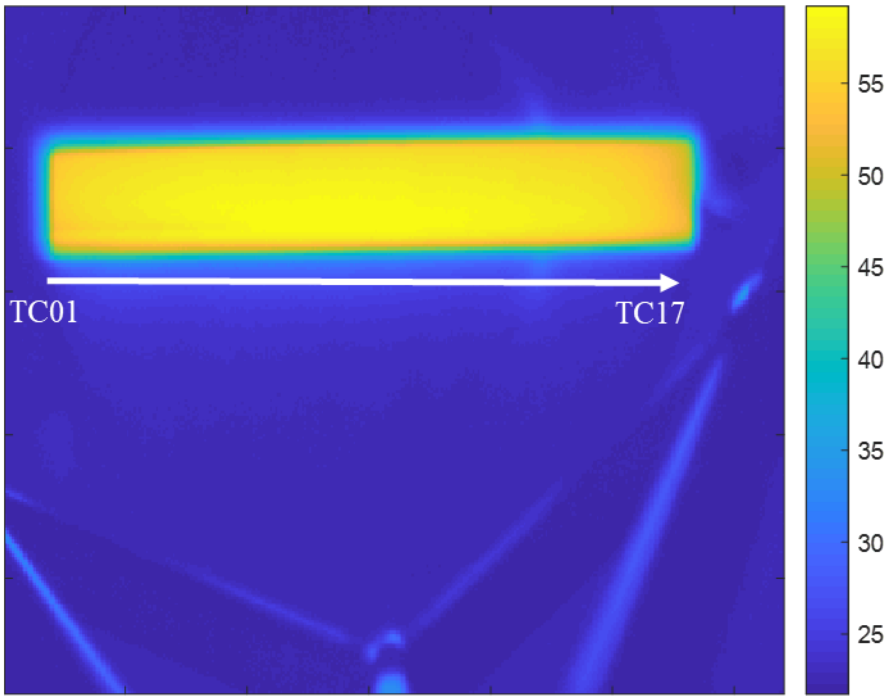

(b) Annular Duct

Figure 3-23 Heating Test IR Image (Units: °C)

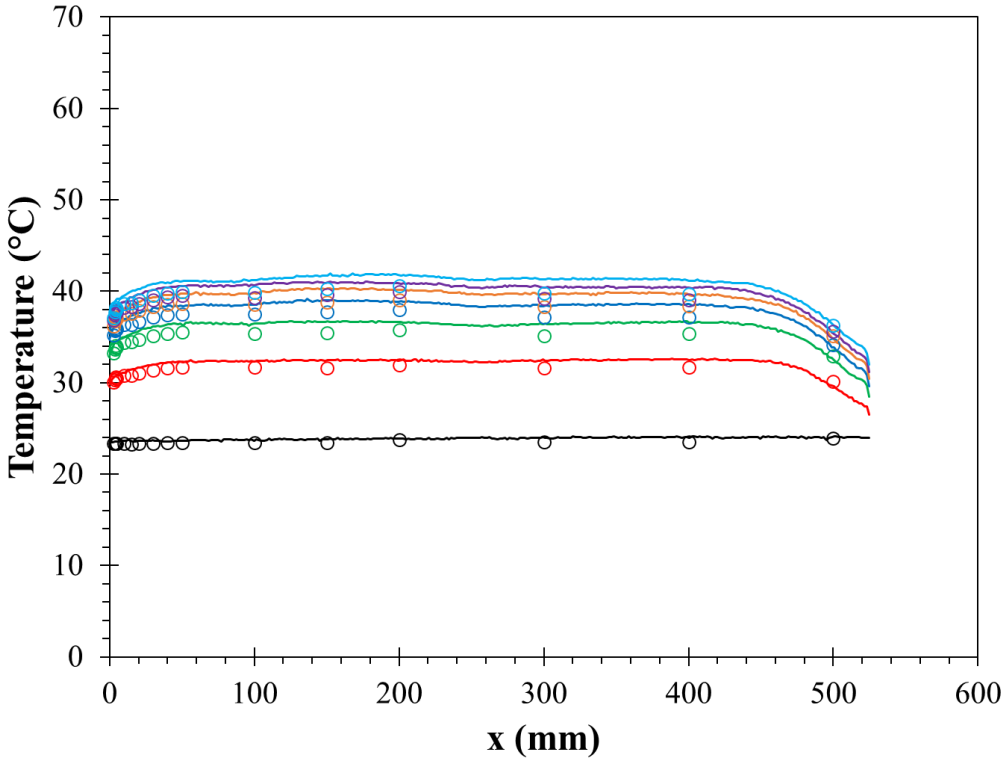

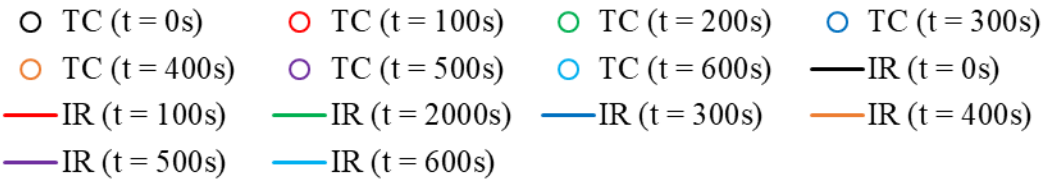

(a) Realistic S-shape & Simplified Rectangular Duct

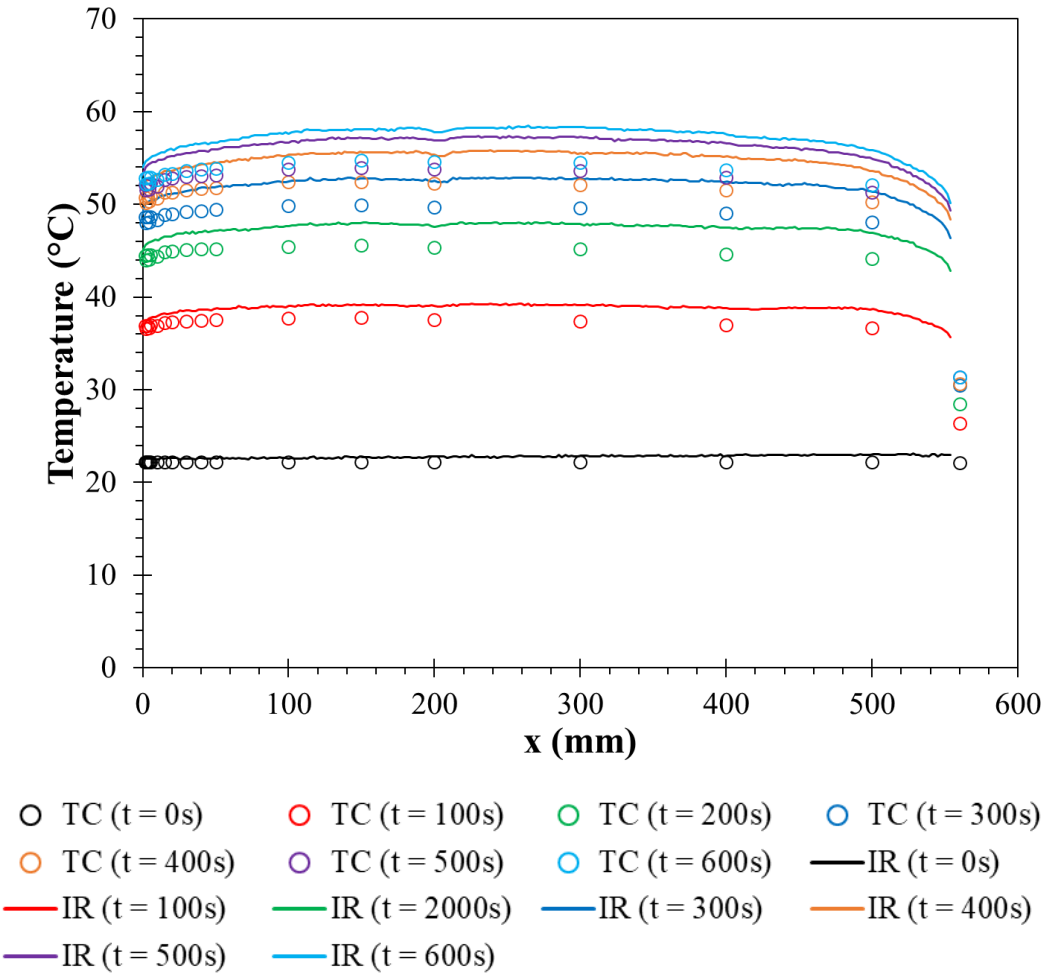

(b) Annular Duct

Figure 3-24 Sensor Heat Assembly Axial Temperature Distribution

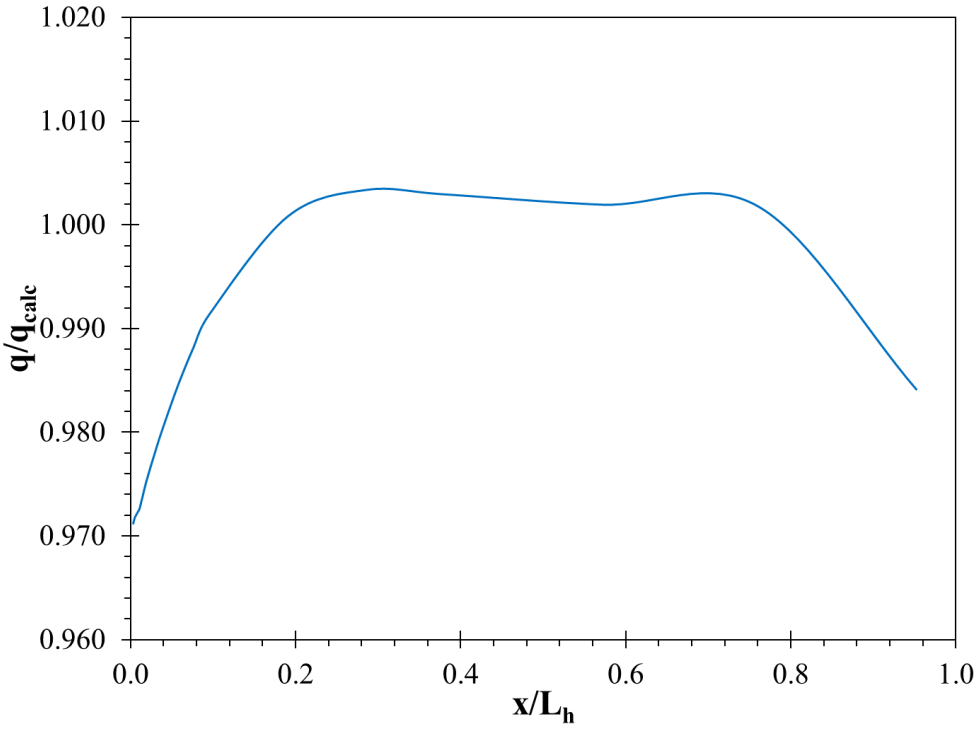

(a) Realistic S-shape & Simplified Rectangular Duct Assembly

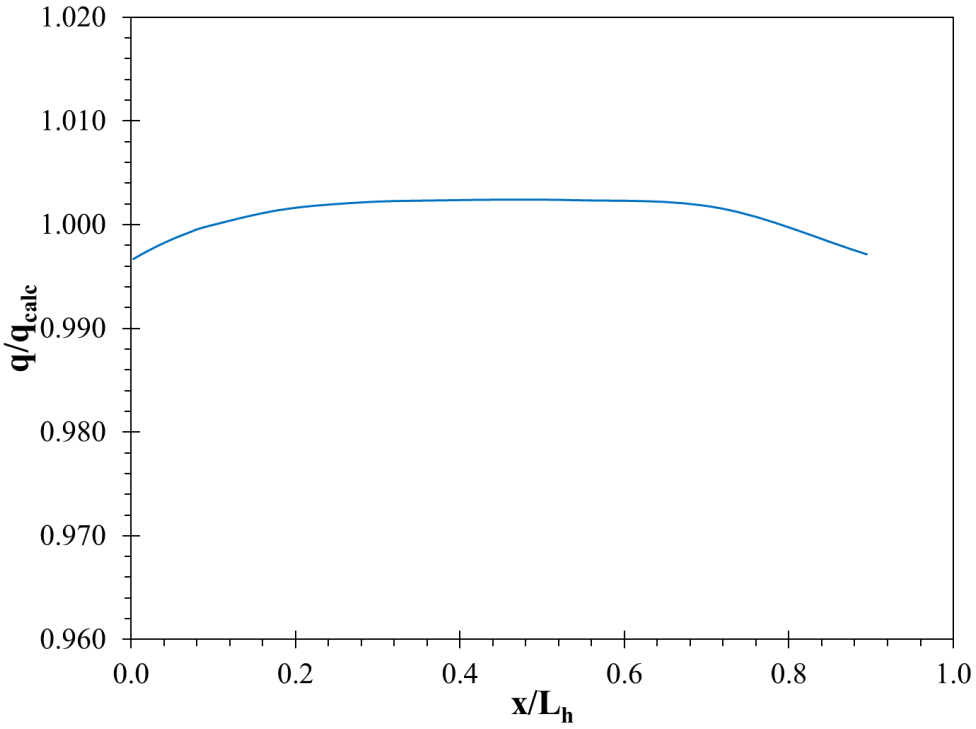

(b) Annular Duct Assembly

Figure 3-25 Sensor & Heater Assembly Heat Flux Distributions

3.2.3 Pressure Sensors

For pressure measurements, first sensor HDI series pressure sensors were used. Sensors with maximum operating pressures of 10 mbar, 50 mbar, 200 mbar, 500 mbar and 2 bar were used for this study. A photo of two 200 mbar pressure sensors is provided as a reference in Figure 3-26. Calibrations were done using a Fluke 719 Pro 150G pressure calibrator as seen in Figure 3-27. A reference pressure was set in the calibrator and the pressure sensor voltage reading was recorded. A linear curve fit was then made to convert the voltage signals into pressure readings. The results of the calibrations can be seen in Figure 3-28.

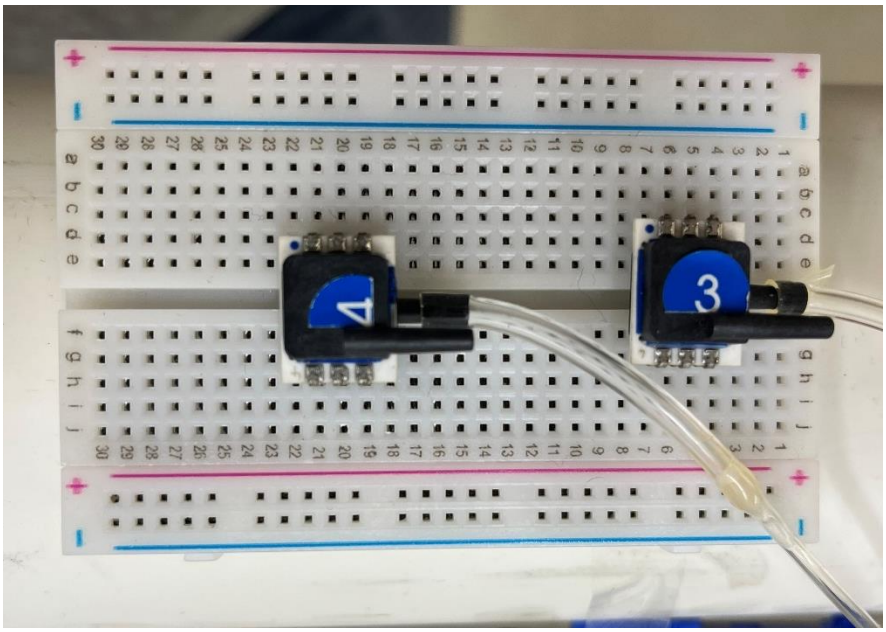

Figure 3-26 First Sensor HDIM200DUF8P5

Figure 3-27 Fluke 719 Pro 150G

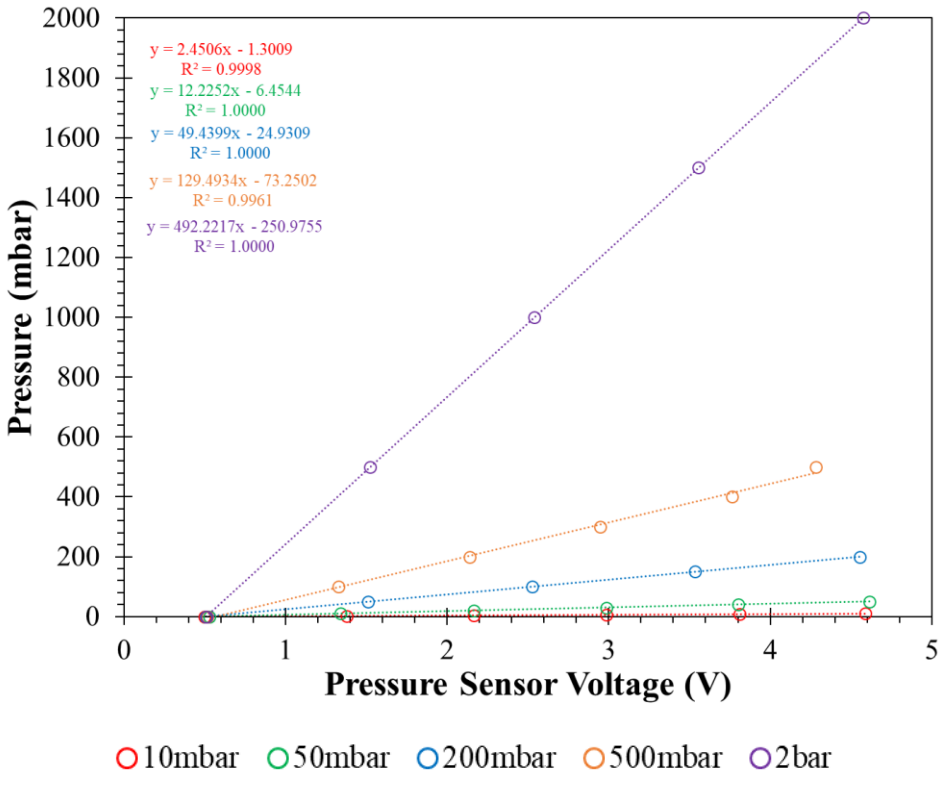

Figure 3-28 First Sensor Pressure Calibration Curves

3.2.4 Mass Flow Rate

The Mass flow rate was measured using orifices designed using British orifice standards [66] for D and D/2 taps. The equation for the mass flow rate is given as

$$\dot{m} = \frac{C}{\sqrt{1-\beta^4}} \varepsilon \frac{\pi}{4} d^2 \sqrt{2\Delta p \rho} \tag{32}$$

Where β is the ratio between pipe and orifice diameters and ε is the expansibility factor (1 for incompressible flow). The discharge coefficient C is defined as

$$C = 0.5961 - 0.0261\beta^2 + 0.000521\left(\frac{10^6\beta}{Re}\right)^{0.7} + (0.0188 + 0.0063A)\beta^{3.5}\left(\frac{10^6}{Re}\right)^{0.3} + ((0.043 + 0.080\mathrm{e}^{-10L_1} - 0.123\mathrm{e}^{-7L_1})(1 - 0.11A)\frac{\beta^4}{1-\beta^4} - 0.031\left(M_2' - 0.8{M_2'}^{1.1}\right)\beta^{1.3} \tag{33}$$

with the variables defined in the standards. The discharge coefficient is a function of the Reynolds number in the pipe where the orifice is located which depends on the axial velocity. The Reynolds number in a circular pipe can be rewritten as a function of the mass flow rate as

$$Re = \frac{4\dot{m}}{\pi\mu D} \tag{34}$$

The correct discharge coefficient is calculated by setting an initial guess value for the axial velocity and solving for the Reynolds number using equation (12). Then using this Reynolds number, the discharge coefficient and mass flow rate can be calculated. With the new mass flow rate calculated, the Reynold can be solved for using equation (34). If the Reynolds number calculated from equations (12) and (34) are within 1% error, the correct discharge coefficient has been calculated. Otherwise, the next iteration occurs with a new guess axial velocity. From the

correct mass flow rate, the mean axial velocity of the duct must be calculated using the following equation

$$u_x = \frac{\dot{m}}{\rho A} \tag{35}$$

For the parallel mode rotation test the orifice used a 76 mm ID pipe with an 8 mm diameter orifice giving a β = 0.1. For the annular duct, a 152.4 mm ID pipe was used with a 76.2 mm diameter orifice giving a β = 0.5. The orifice plates were manufactured in-house using aluminum. However, these orifices are not calibrated which calls into question the accuracy especially relating to the discharge coefficient. To ensure the accuracy of the mass flow rate measurements, professionally manufactured orifices have been purchased from USA Industries. Photos of the orifices are provided in Figure 3-29. Figure 3-30 shows the comparison between the pressure drop measurements between the orifice manufactured in-house and the calibrated orifice from USA Industries. The results show that both orifices produced similar results validating the data preformed with orifices machined in-house.

(a) In-house Orifice 152.4 mm ID pipe size, β = 0.5

(b) Calibrated Orifice from USA Industries 152.4 mm ID pipe size, β = 0.5

Figure 3-29 Photo of Orifices

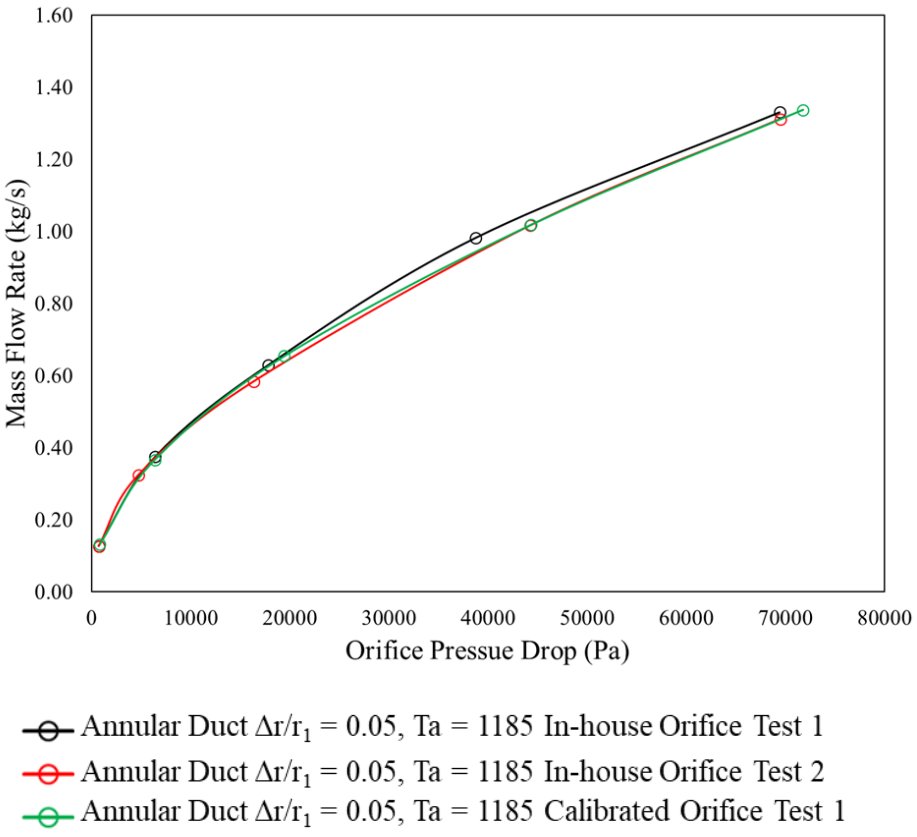

Figure 3-30 Comparison of Pressure Difference Measurements between Orifices in Annular Duct Tests

3.2.5 Rotation Speed

The rotation speed was measured using a Tachometer. A strip of reflective tape was placed on the shaft surrounded by black tape. The Tachometer uses a laser to measure the rotation speed in rpm by seeing how quickly the reflective tape completes one revolution. A photo of the Tachometer and shaft are provided in Figure 3-31.

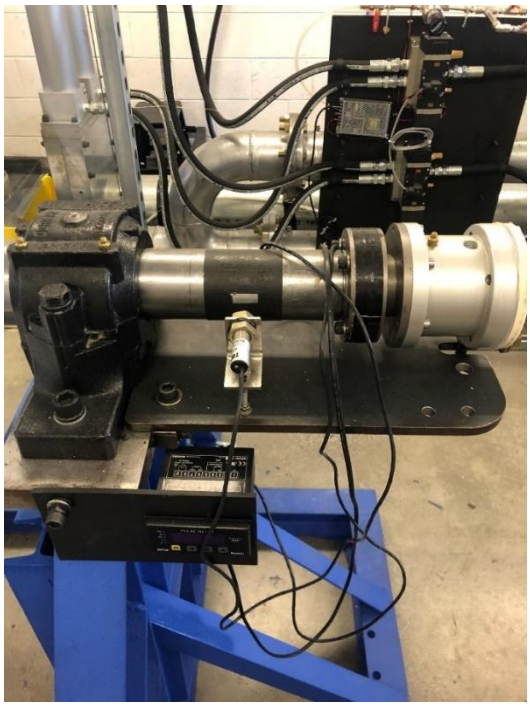

Figure 3-31 Photo of Tachometer

3.2.6 Slip Ring

In order to record data from a rotating frame a Moflon GT2586-S16-22T-3600RPM-FL01 slip ring was used with a photo and specifications listed in Figure 3-32 & Figure 3-33. This slip ring contains 22 T-type thermocouple channels and 16 American wire gage 22 teflon wire channels. It is able to operate at voltages from 0-300 VDC/VAC, rotation speed up to 3600 rpm, and temperatures from -30°C to 80°C. The slip ring does experience heating when operating at high rotation speeds. Therefore, it is necessary to add cooling air to the slip ring to maintain accurate measurements.

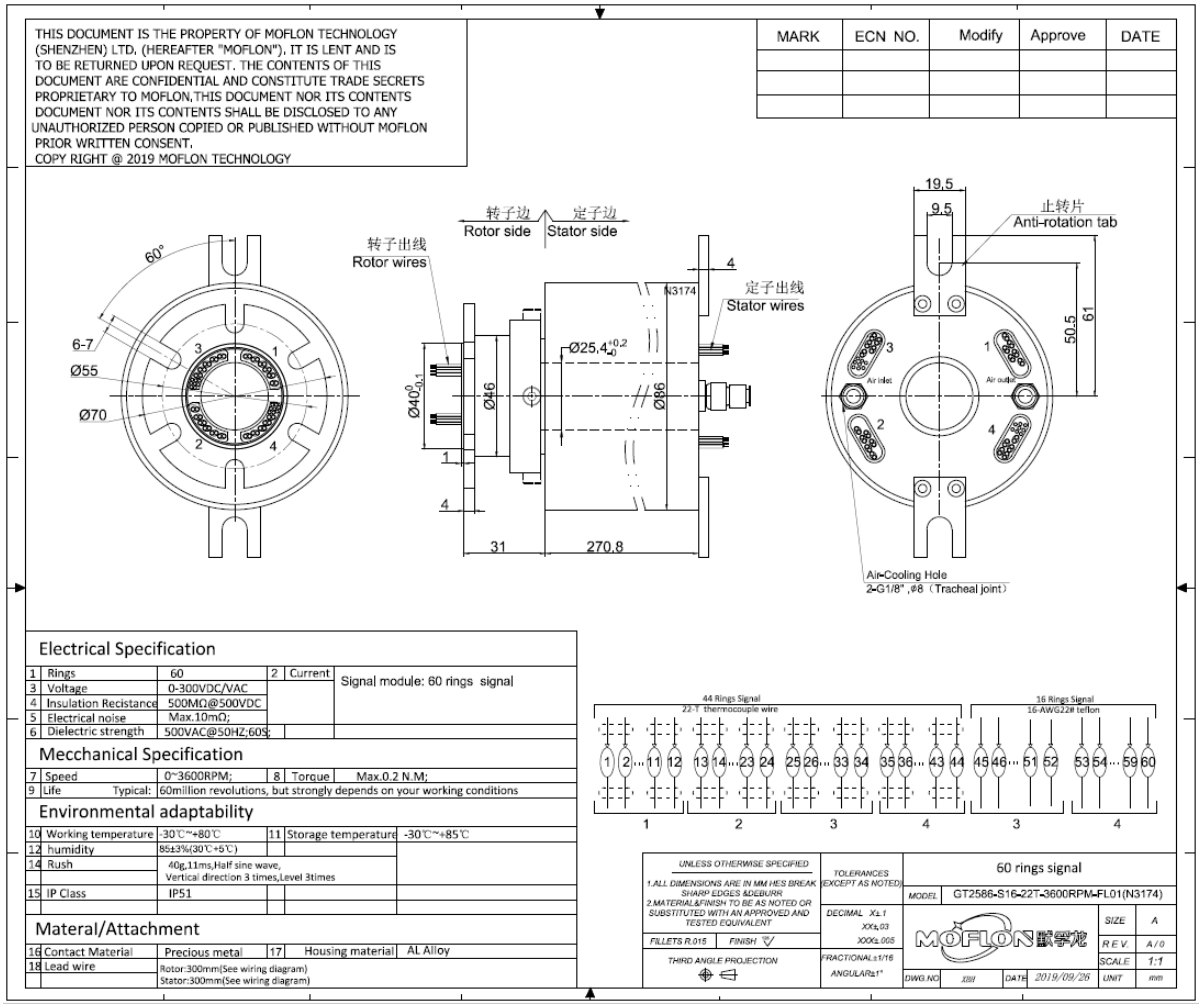

Figure 3-33 Moflon Slip Ring Specifications

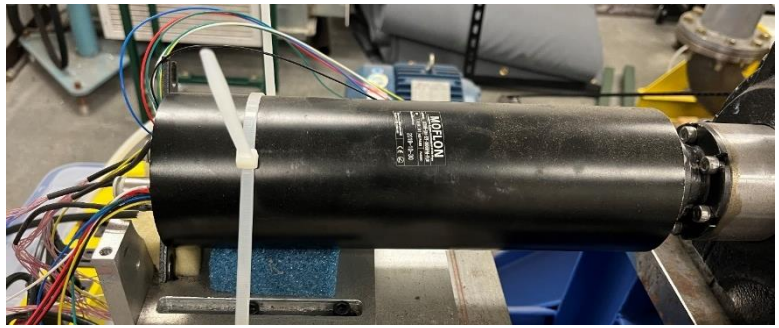

Figure 3-32 Photo of Moflon Slip Ring

3.2.7 LabView

Data is read into a LabView 2019 program using a NI Daq-9174. The temperature signals were read obtained using a NI 9213 module and the pressure signal was obtained using a NI 9201 module. A photo of the Daq is provided in Figure 3-34. The VI used to monitor the signals is shown in Figure 3-35 shows the VI for the Parallel mode rotation test and Figure 3-36 shows the block diagram. The temperature and pressure signals were displayed on the monitors seen in Figure 3-35 and continuously recorded into a .lvm file. While the pressure and temperature signals could be monitored on the VI, the mass flow rate and Reynolds number could not. Because of this, the .lvm file was periodically exported to check the mass flow rate using a MATLAB code. The signals were recorded with a sampling frequency of 10 Hz. Figure 3-37 and Figure 3-38 show the VI and block diagram for the annular duct test respectively. This configuration had to use two Daqs to collect the data. The rotor, and stator temperatures were measured along with the pressure loss across the duct using one Daq and the second Daq recorded the orifice pressures and temperatures along with the ambient temperature. The stator temperatures were recorded but not processed in this experiment.

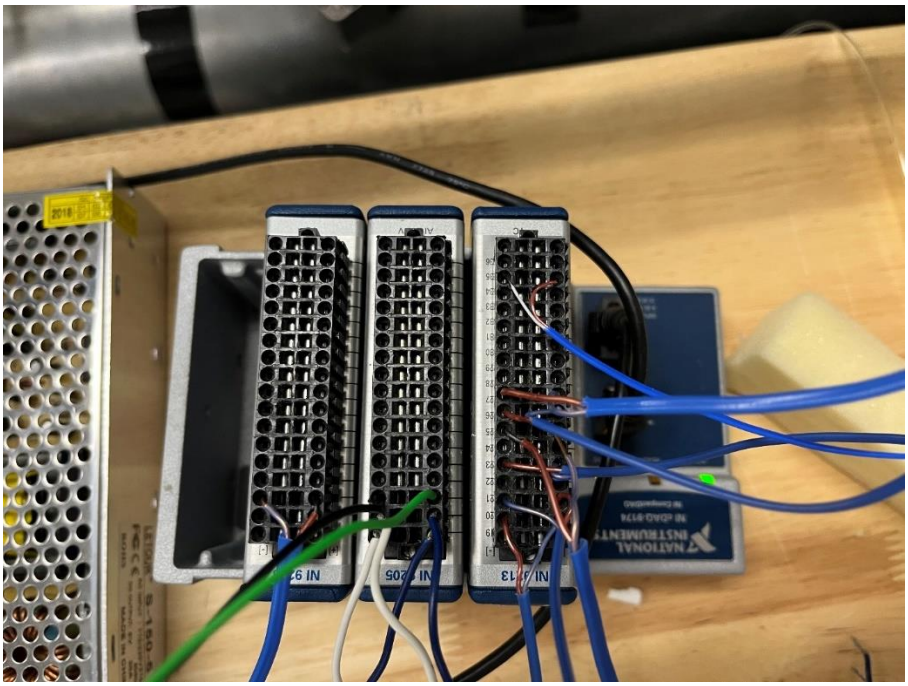

Figure 3-34 Photo of NI Daq System

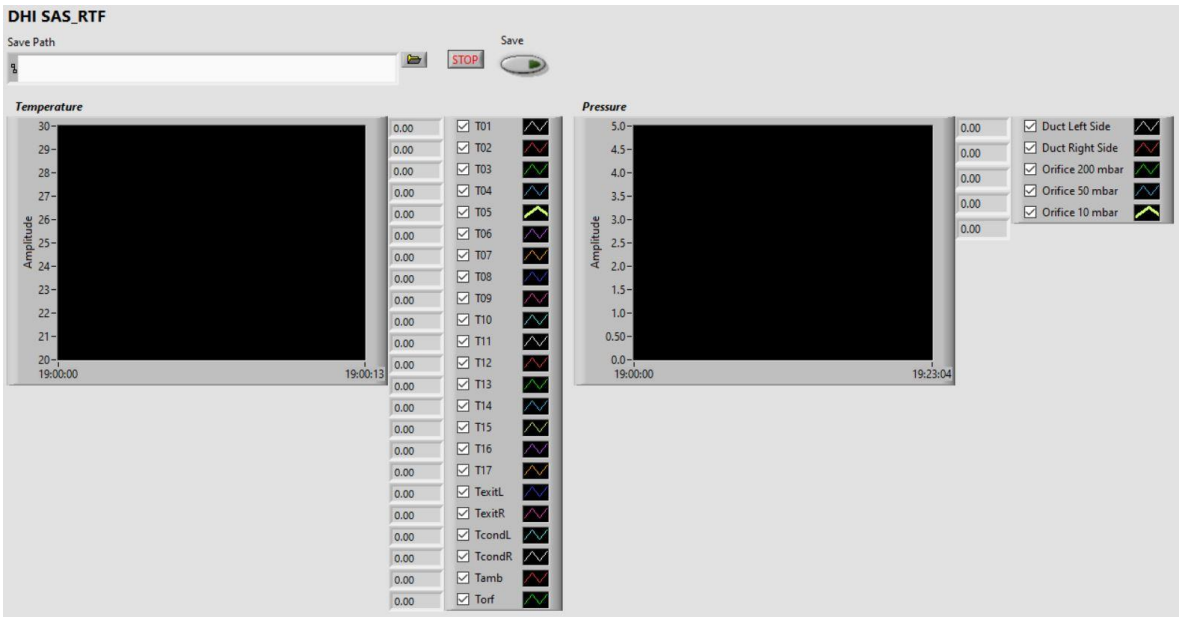

Figure 3-35 Parallel Mode Rotation Test LabView VI

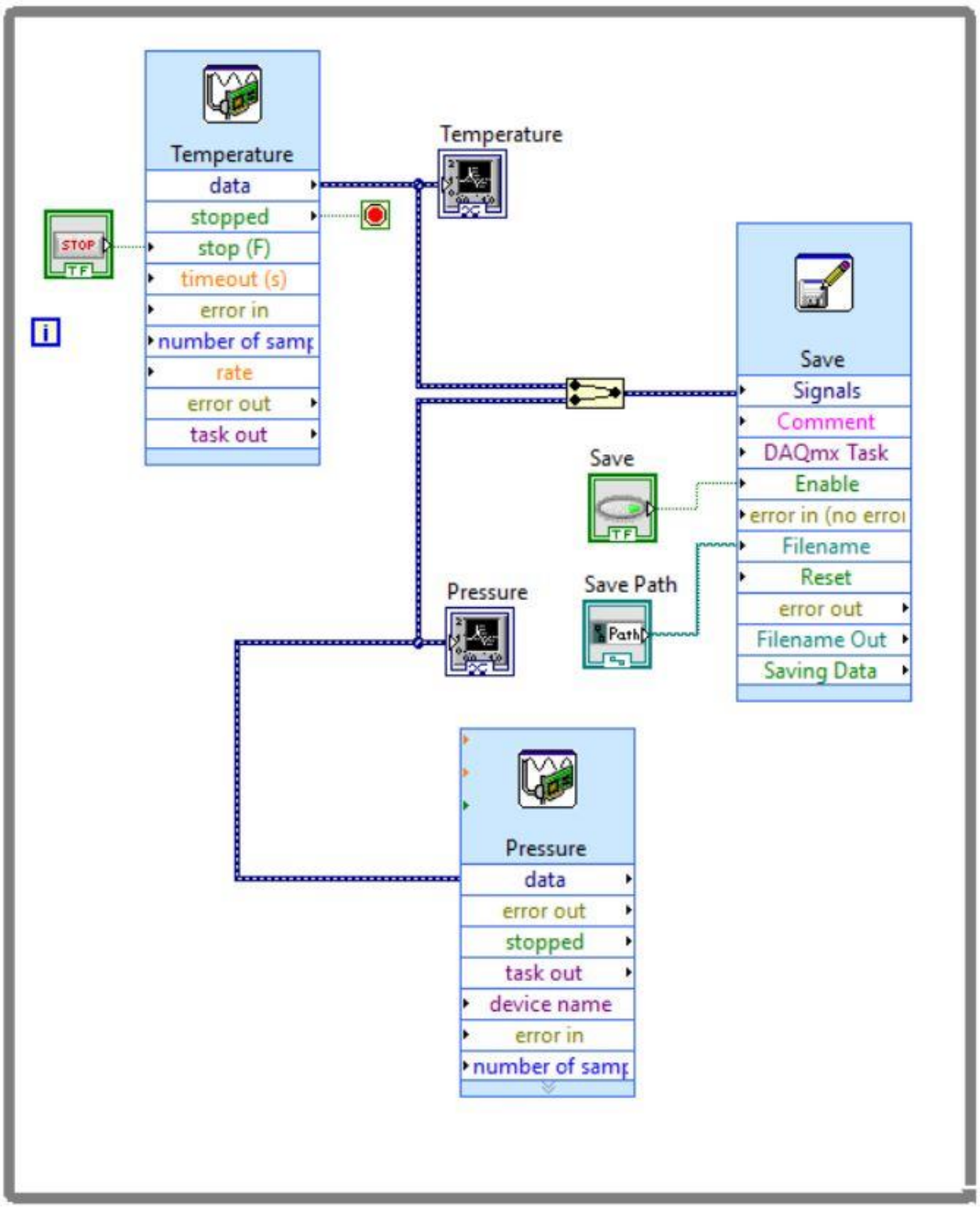

Figure 3-36 Parallel Mode Rotation Test LabView Block Diagram

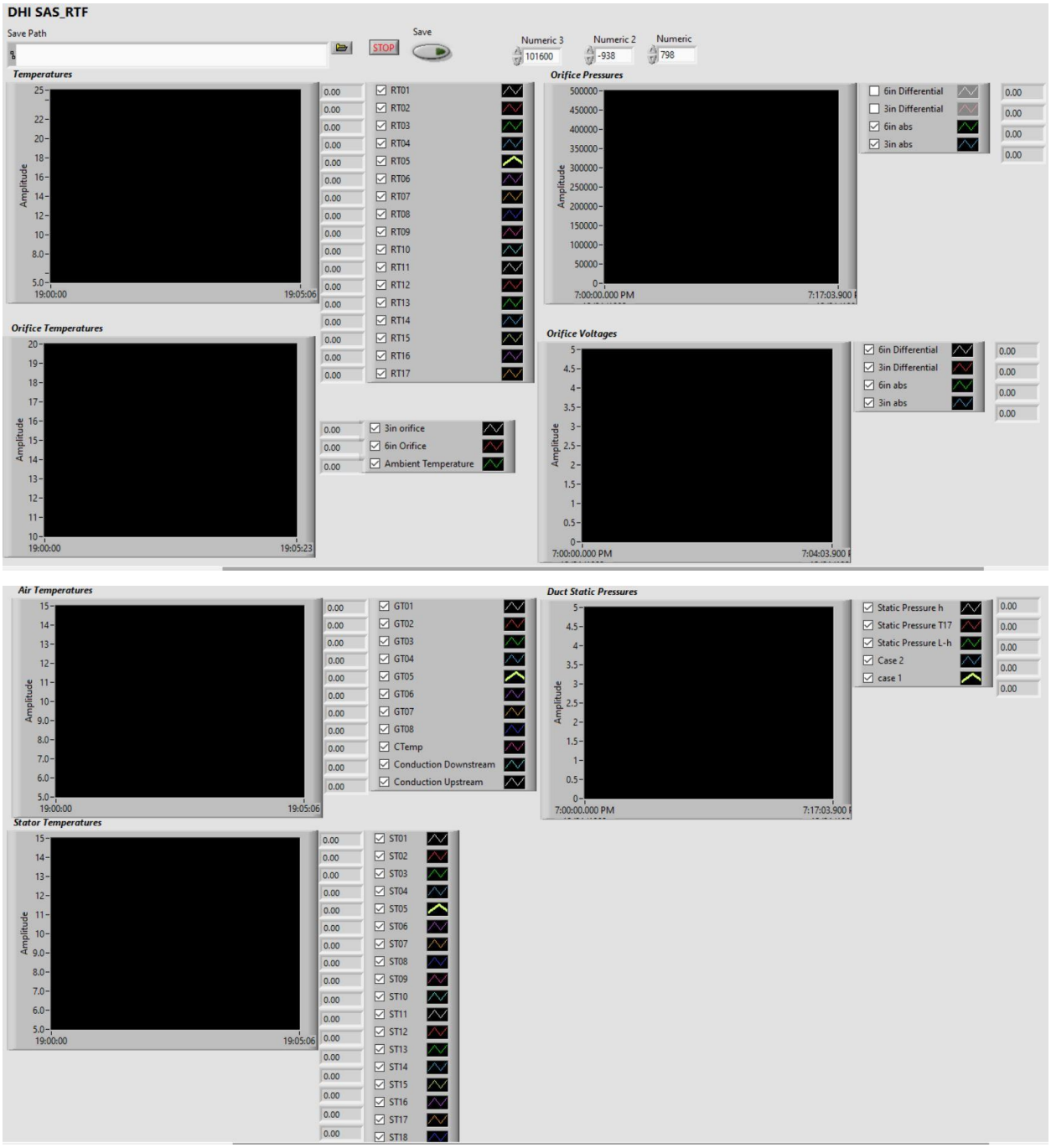

Figure 3-37 Annular Duct Test LabView VI

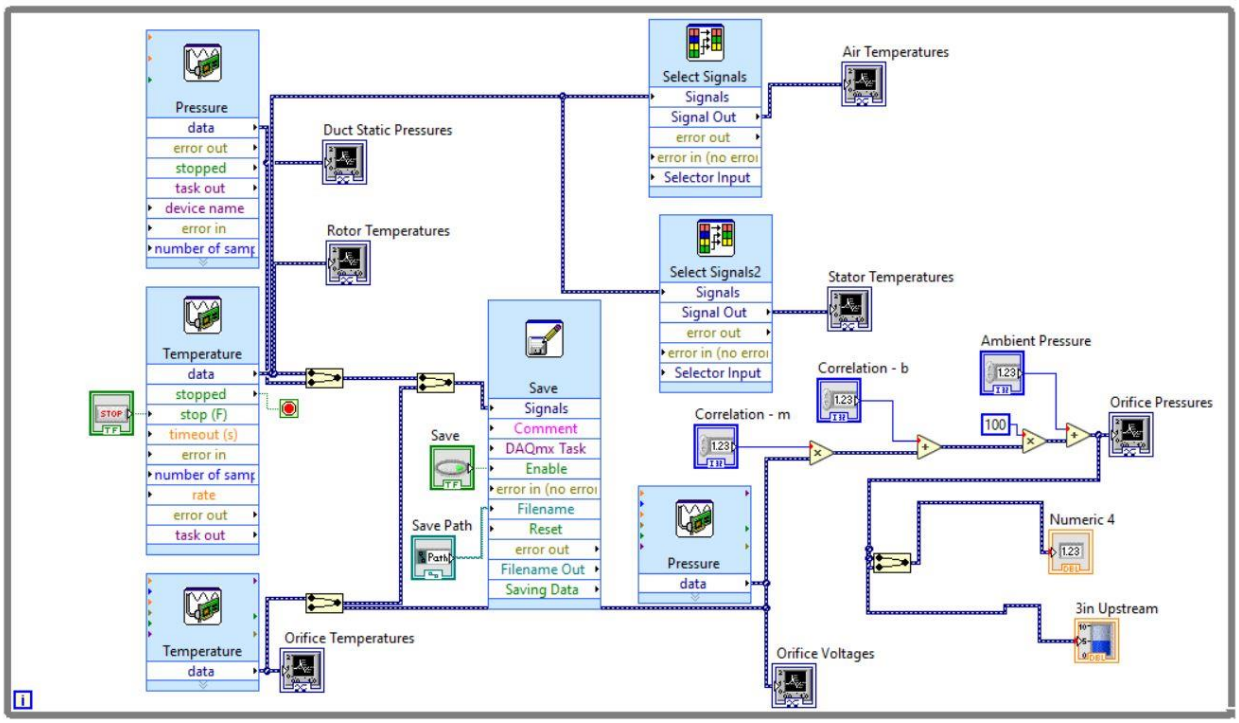

Figure 3-38 Annular Duct Test LabView Block Diagram

3.3 Experimental Procedures

3.3.1 Parallel Mode Rotation of Realistic S-shaped and Simplified Duct

For the parallel mode rotation test, the rotation speed is fixed, and the mass flow rate is changed. At the beginning of each test, three minutes of data with no flow, rotation or heating was collected to offset the pressure and temperature readings from the sensors connected to the slip ring with the ambient pressure and temperature. Following the initial three minutes, the motor is started rotating the soft disc at a fixed rotation speed and data is again recorded for three minutes. Since the pressure sensors for the exit static pressure are rotating, the recording pressure signals at stationary and rotating frames allows the effect of rotation on the pressure signal to be offset. Next, the Powerbes variable DC power supply is turned on providing a fixed power to the heaters is and the blower is set to the provide a mass flow rate resulting in the highest Re_{Dh}. After the temperature readings reached a steady state data is recorded for five minutes and then the blower frequency is adjusted reach a lower Re_{Dh}.

3.3.2 Annular Duct with Inner Surface Rotation

For the annular duct test, each test case was conducted by fixing the mass flow rate and varying the rotation speed. At the beginning of each test case, three minutes of data was collected with no flow, rotation, or heating. This data was used to offset pressure and temperature readings with that of the ambient pressure and temperature. Following the initial three minutes, the power to the heater is turned on and the axial flow is turned on set near the target Re_{Dh}. The wall and bulk temperature profiles were recorded as three-minute averages when the flow reached a steady state for at least five minutes. After the data for then stationary case is recorded, the motor is turned set at a rotation speed of 100 rpm and the process is repeated until a total of five rotation speeds up to 800 rpm is measured.

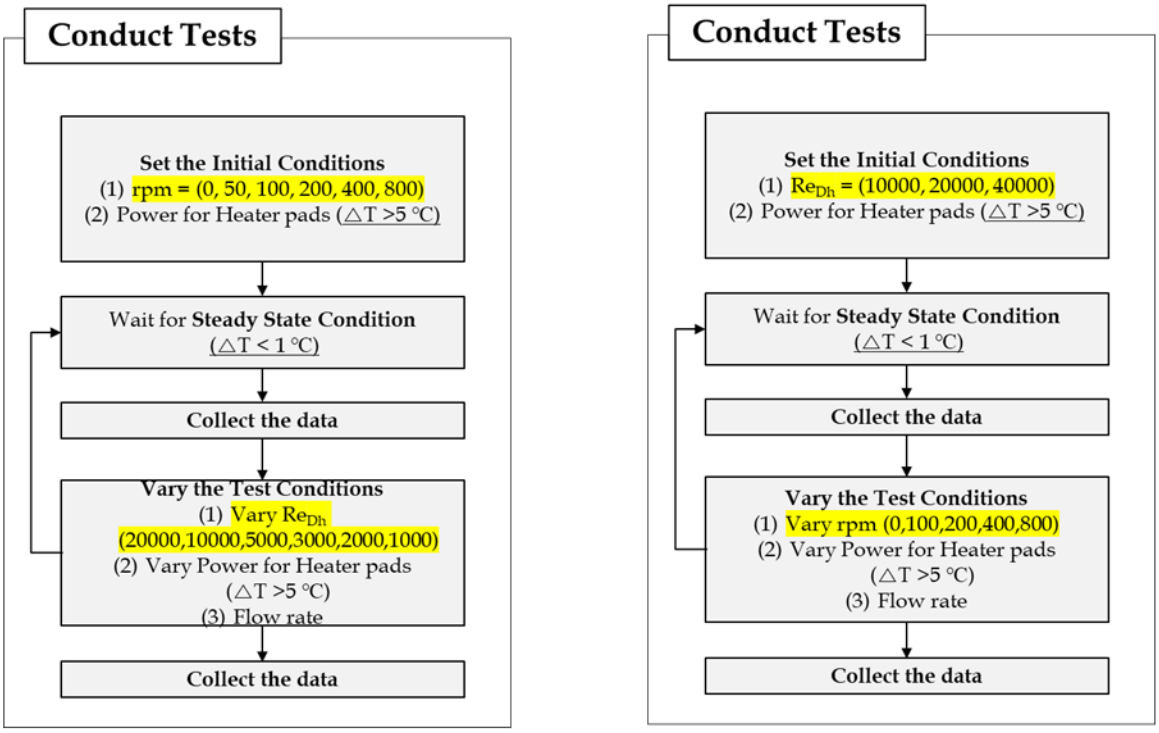

(a) Parallel Mode Rotation of Realistic S-shaped and Simplified Duct

(b) Annular Duct with Inner Surface Rotation

Figure 3-39 Block Diagram of Test Procedures

3.4 Data Processing

3.4.1 Signal Processing

The data processing is the same for the parallel mode rotation and annular duct test. The first step in the post processing was to analyze the temperature and pressure history of the test. Figure 3-40 and Figure 3-41 shows the time history of the thin film thermocouple and pressure sensors for the realistic S-shaped model test at the highest rotation speed tested. There is a significant amount of noise in the data, more evident in the pressure signal and thermocouples closer to the inlet. The signals were filtered using a second order low pass filter. To determine the cut-off frequency, the Fast Fourier Transform was applied to the data as seen in Figure 3-42. In this figure, significant noise can be seen even at frequencies less than 1 Hz. Therefore, an initial cut off frequency was set to 1 Hz then decreased until the signals started to also get cut off. For both temperature and pressure signals a cut off frequency of 0.005 Hz proved to clean the signal while retaining all important information.

Figure 3-43 and Figure 3-44 show the filtered data. In both cases the signals are cleaner while retaining all important information. Figure 3-45 shows the voltage history of the pressure sensors measuring the rectangular duct exit pressures. These pressure sensors were placed on the shaft and therefore experienced rotation. This rotation causes the sensor to measure higher voltages than what is accurate. To account for this, three minutes of data was collected with no flow, no heat, and no rotation. Then another three minutes of data was recorded with rotation but no heat or axial flow. The data from this period is used to offset the rest of the data set allowing for accurate pressure voltage signals to pass through.

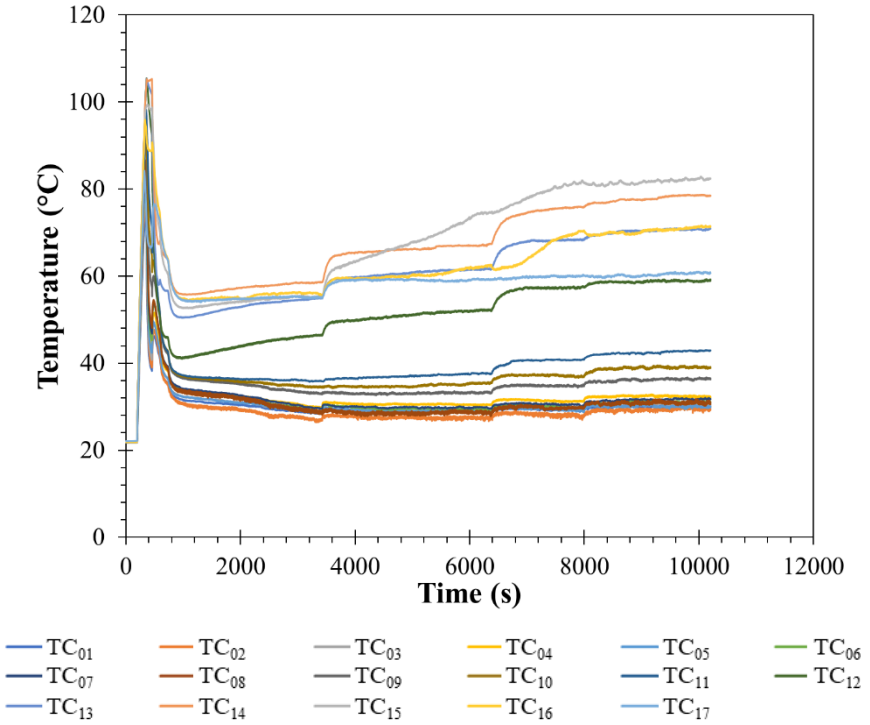

Figure 3-40 Realistic S-shaped model J = 522 ccw Temperature History (Raw)

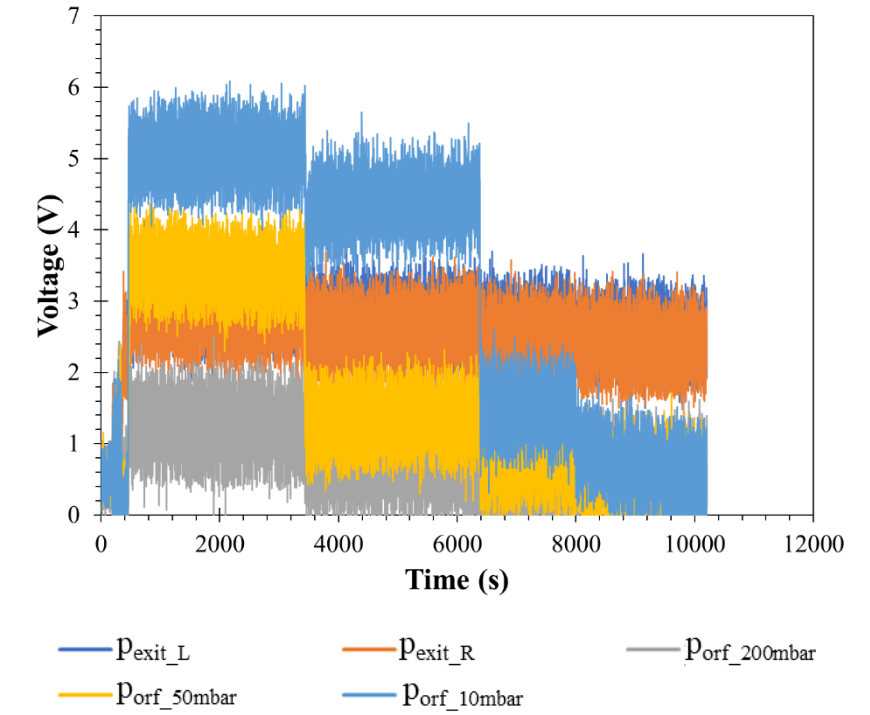

Figure 3-41 Realistic S-shaped model J = 522 ccw Pressure Sensor Voltage History (Raw)

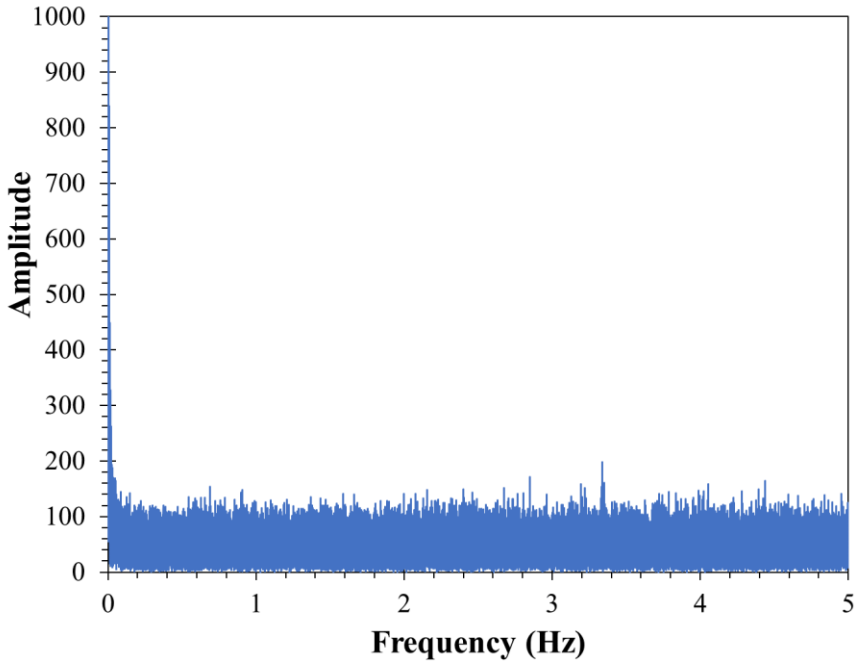

Figure 3-42 Fast Fourier Transform of Orifices Pressure Sensor Signal During Realistic S-Shape Test J = 522

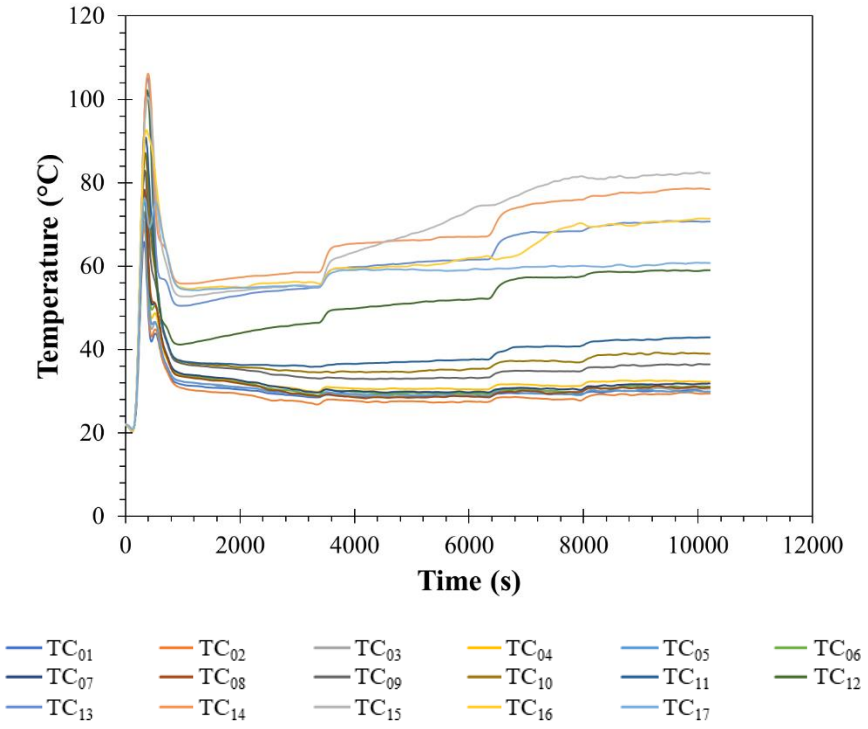

Figure 3-43 Realistic S-shaped model J = 522 ccw Temperature History (Filtered)

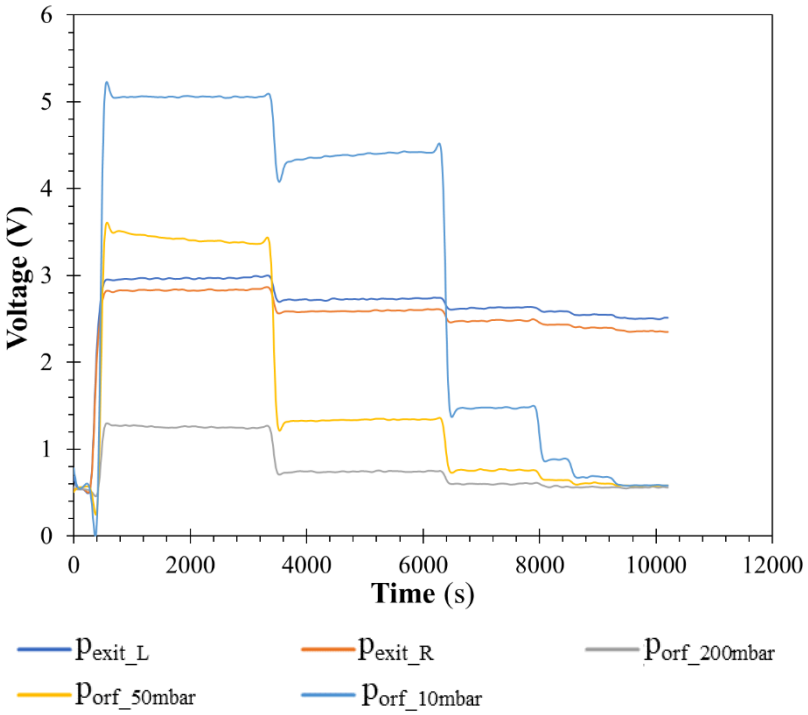

Figure 3-44 Realistic S-shaped model J = 522 ccw Pressure Sensor Voltage History (Filtered)

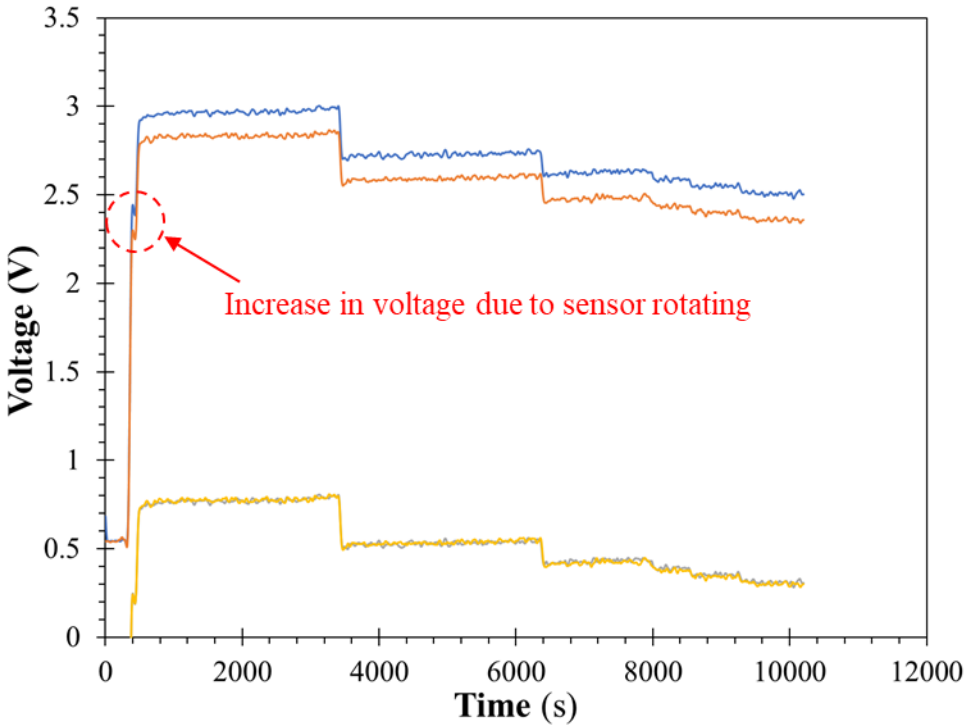

Figure 3-45 Pressure Sensor Voltage History for Rotating Sensors

3.4.2 Selection of Steady State Condition

With the data filtered, the steady state temperatures needed to be determined. At each test condition (mass flow rate for parallel mode rotation and rotation speed for the annular duct), there is a 5-minute interval where the temperature and pressure signals are plateau before switching to the next condition. The of these 5-minutes, data is recorded as the time average of a 3-minute window in the 5-minute plateau. The pressure drop measured from the orifice is used to calculate the mass flow rate using equation (32) and then from the mass flow rate the axial velocity in the duct and Reynolds number is calculated using equations (12) and (35). The local heat transfer coefficient and Nusselt numbers are calculated using equations (7) and (8).

3.4.3 Bulk Air Temperatures

While the wall temperatures are measured from the thin film thermocouple, there is no data recorded for the bulk temperature at each wall temperature measurement location. For a uniform heat flux test, the bulk temperature is expected to be linear across the duct. For the parallel mode rotation test, a linear curve fit is applied using ambient air temperature as the inlet temperature and an average of the two exit thermocouples as the exit temperature. For the annular duct test there are more thermocouples placed to measure air temperature across the duct. However, there still in not enough thermocouples near the inlet to measure the bulk temperature at every location of thin film thermocouple wall temperature. For the locations with both wall and air temperature measurements the difference was taken directly however for the near inlet area a curve fit was made to estimate the temperatures where air temperatures could not be taken. Figure 3-46 and Figure 3-47 show examples of the bulk temperature profiles for both the parallel mode rotation test and the annular duct test.

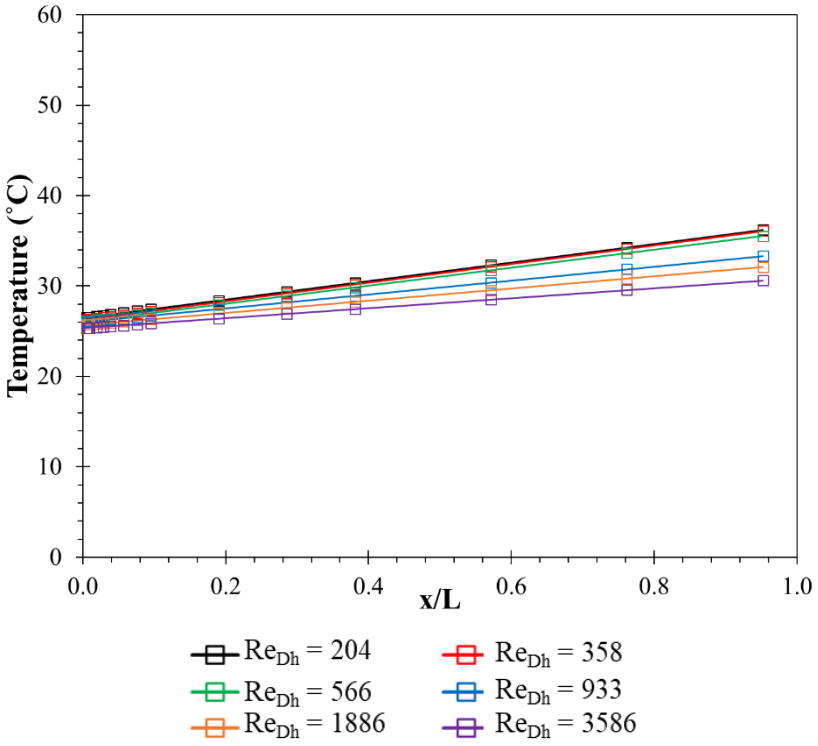

Figure 3-46 Bulk Temperature Curve for Realistic S-shaped model J = 522 ccw

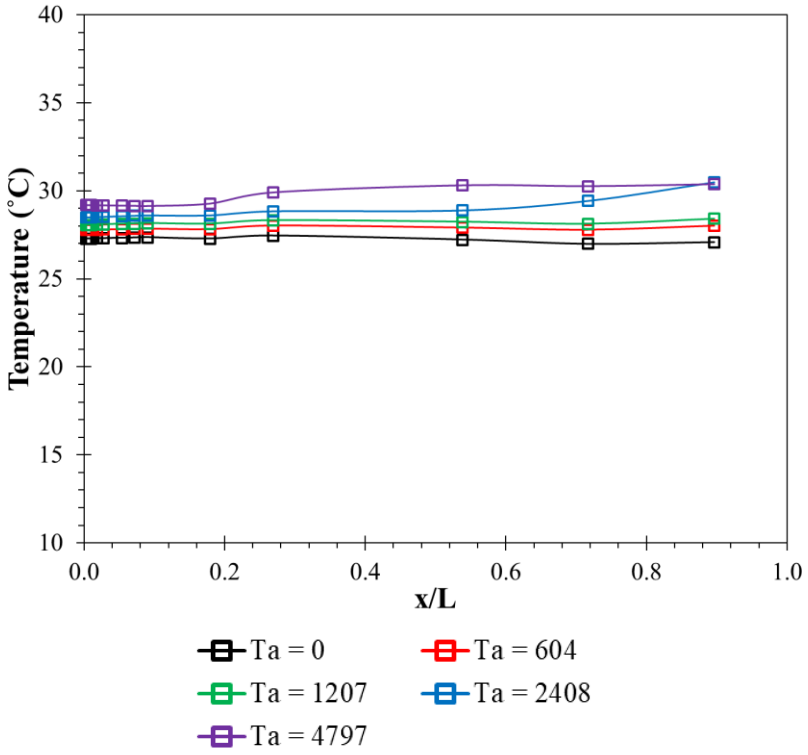

Figure 3-47 Bulk Temperature Curve for $\Delta r/r_1 = 0.05$ $Re_{Dh} = 7792$

3.4.4 Average Nusselt Number

After calculating the local Nusselt numbers, the average fully developed Nusselt number is also calculated. After looking at the Local Nusselt number distributions, the fully developed region is determined as where the Nusselt number is constant. Morris & Woods [2] showed that at the exit the end loss effects cause the wall temperature to drop significantly. This effect is accounted for, and the last thermocouple data point is neglected in the average Nusselt number calculation. For the realistic S-shaped and simplified rectangular the models, the fully developed Nusselt number was taken as the average of the Nusselt number from TC_{15} and TC_{16} while for the annular duct the Nusselt number in the fully developed region was taken as the average from TC_{15} to TC_{17}.

3.4.5 Friction Factor

Lastly, the friction factor is calculated for each test case. For the parallel mode rotation tests, the pressure loss was measured as the difference between the ambient inlet pressure and the exit static pressure of the duct. The entry loss was also accounted for, and the duct pressure loss is given by

$$\Delta p = p_{inlet} - p_{exit} - \Delta p_{entry} \tag{36}$$

With Δp_{entry} defined in equation (31). p_e is taken as the average of the pressure measured from the two exit static pressure taps. From the pressure loss, the friction factor can then be calculated using equation (9). For the annular duct the pressure loss is also calculated by equation (36) however the inlet pressure is taken as the circumferential average of the static pressure at the plenum right before the test section and the exit pressure is the circumferential average of pressure taps located at the last thermocouple in the thin film thermocouple located 500 mm from the inlet.

3.4.6 Uncertainty Analysis

To verify accuracy of the experimental results, a target value of the uncertainty in heat transfer measurement was set to 10%. This is due to the correlations available for heat transfer also having an error of 10%. In the experiment, the two sources of error regarding the heat transfer coefficient are the power supply which controls the voltage and the thermocouples that provide the temperature readings. The total heat transferred to the heater assembly is equal to the power by the adjustable dc power supply and can be written a

$$Q = IV \tag{37}$$

And the total heat is related to the heat transfer coefficient as such

$$Q = hA\Delta T \tag{38}$$

Combining equations (37) and (38) the heat transfer coefficient can be written as a function of the power supply voltage and the temperature as follows.

$$h = \frac{V^2/R}{A\Delta T}, \qquad h = f(V, R, A, \Delta T) \tag{39}$$

From equation (39) the Root-Sum-Squared method [67] is used to calculate the heat transfer coefficient uncertainty in percentage form

$$\delta h = \frac{\sqrt{\left(\frac{\partial h}{\partial V}u_V\right)^2 + \left(\frac{\partial h}{\partial \Delta T}u_{\Delta T}\right)^2 + \left(\frac{\partial h}{\partial A}u_A\right)^2 + \left(\frac{\partial h}{\partial R}u_R\right)^2}}{h} \text{x}100\% \tag{40}$$

where u_v and $u_{\Delta T}$ are the uncertainty values for the power supply and thermocouples. After an initial analysis the uncertainty attributed to the area and resistance were several magnitudes smaller

than the uncertainty due to Voltage and temperature difference therefore equation (40) can be simplified to

$$\delta h = \frac{\sqrt{\left(\frac{\partial h}{\partial V} u_V\right)^2 + \left(\frac{\partial h}{\partial \Delta T} u_{\Delta T}\right)^2}}{h} \text{x}100\% \tag{41}$$

$$\frac{\partial h}{\partial V} = \frac{2\,V/R}{A\Delta T} \tag{42}$$

$$\frac{\partial h}{\partial \Delta T} = -\frac{V^2/R}{A\Delta T^2} \tag{43}$$

In the experiments, the voltage since the voltage is fixed, the uncertainty in the heat transfer coefficient can be kept under 10% by ensuring that the minimum temperature difference between the wall and bulk temperatures is greater than 5˚C as shown in Figure 3-48.

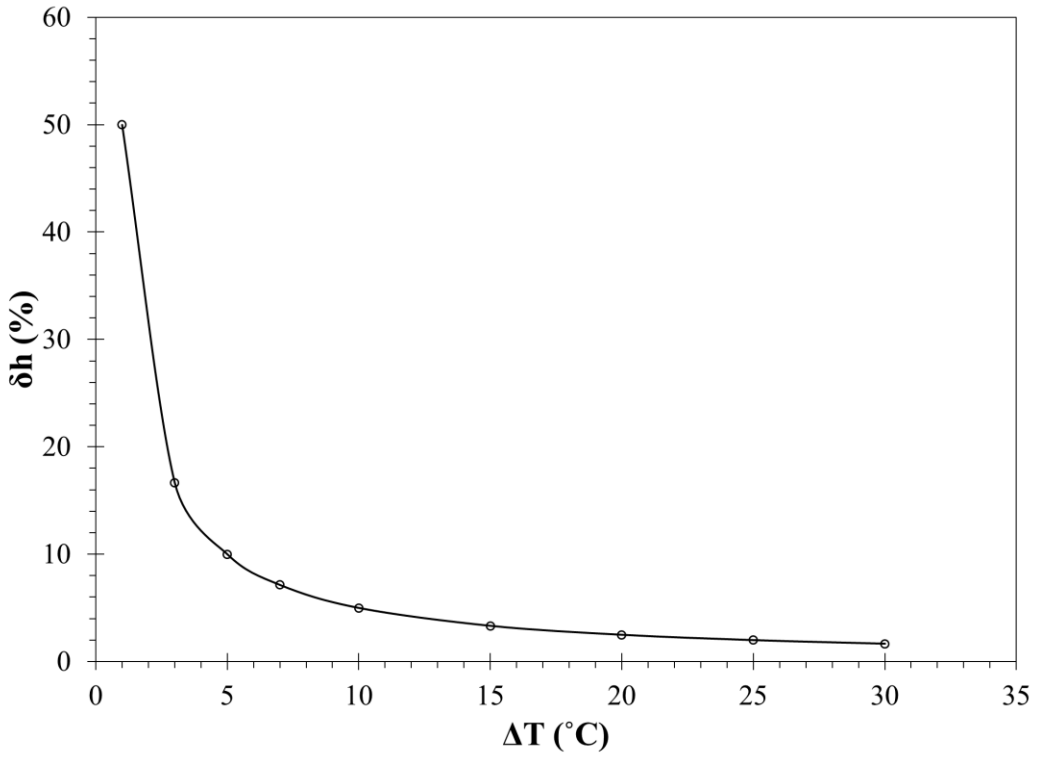

Figure 3-48 Uncertainty of Heat Transfer Coefficient vs Temperature Difference

Chapter 4 Results and Discussion

4.1 Parallel Mode Rotation of Realistic S-shaped and Simplified Rectangular Duct

4.1.1 Centerline Heat Transfer Distribution

As the rotation speed increases, the flow is expected to become more unstable. Table 4-1 shows the ranges of duct axial and tangential velocities. The effect of rotation becomes a factor when the ratio between the tangential and axial velocities exceeds unity. With the ratio between the tangential and axial velocities reaching up to 135, instabilities due to effect of rotation are expected. The instabilities are reflected in the heat transfer starting with the centerline temperature distributions as shown in Figure 4-1. The temperature distribution at different J but same Re_{Dh} were compared to see the effect of the rotation on the development of the flow. Typically, when flow in a duct is fully developed, the wall temperature shows a linear profile parallel to the bulk temperature [6]. The distributions shown in Figure 4-1 does not seem to follow this trend near the duct exit where the wall temperature can be seen decreasing at the exit. This decline, however, is consisted with experimental data from past literature and is attributed to end-loss effects according to Morris & Woods [2]. For the purposes of determining if the flow development this decline towards the exit is neglected. When the exit data points are neglected, fully developed profiles can be seen in the higher aspect ratio test cases. Additionally, the temperature profile for the ω = 800 rpm cases for the realistic S-shaped duct shown in Table 4-1e shows a strange trend from x/L = 0.6 and forward. After investigation, it is concluded that the adhesive on attaching the sensor to the Rohacell for the realistic S-shape model had become loose in this region causing the sensor to bubble out. This test was repeated and the results show the same trend as the other aspect ratios. The repeat test results are used for further analysis.

Table 4-1 Velocity Ranges for Realistic S-shape and Simplified Rectangular Model Tests

	AR = 2.02	**AR = 3.93**	**AR = 8.81**	**AR = 17.33**	**Realistic**
u_t (m/s)	0 ~ 28.97	0 ~ 28.49	0 ~ 27.95	0 ~ 27.94	0 ~ 29.24
u_x (m/s)	0.29 ~ 5.10	0.23 ~ 4.56	0.31 ~ 5.03	0.21 ~ 5.27	0.29 ~ 5.79
u_t/u_x	0 ~ 101	0 ~ 124	0 ~ 90	0 ~ 135	0 ~ 95

Table 4-2 Legend Key for Figure 4-1

			AR = 2.02			AR = 3.93			AR = 8.81		
T_w Marker	**T_b Marker**	**Rotation Direction**	**ω (rpm)**	**J**	**Re_{Dh}**	**ω (rpm)**	**J**	**Re_{Dh}**	**ω (rpm)**	**J**	**Re_{Dh}**
		-	0	0	19032	0	0	9981	0	0	5517
		cw	200	4082	13968	200	1495	10073	200	384	5561
		ccw	200	4180	13813	200	1518	10244	200	385	5547
		cw	400	8354	13843	400	2984	10003	400	755	5592
		ccw	400	8275	13698	400	3056	9975	400	760	5500
		cw	800	16664	13619	800	5917	9555	800	1515	5391
		ccw	800	16181	13627	800	6148	9889	800	1543	5502
			AR = 17.33			**Realistic S-shape**					
T_w Marker	**T_b Marker**	**Rotation Direction**	**ω (rpm)**	**J**	**Re_{Dh}**	**ω (rpm)**	**J**	**Re_{Dh}**			
		-	0	0	3138	0	0	3651			
		cw	200	110	3130	200	131	3712			
		ccw	200	108	3159	200	129	3676			
		cw	400	222	3162	400	259	3690			
		ccw	400	222	3170	400	261	3678			
		cw	800	442	3096	800	522	3609			
		ccw	800	450	3127	800	522	3641			

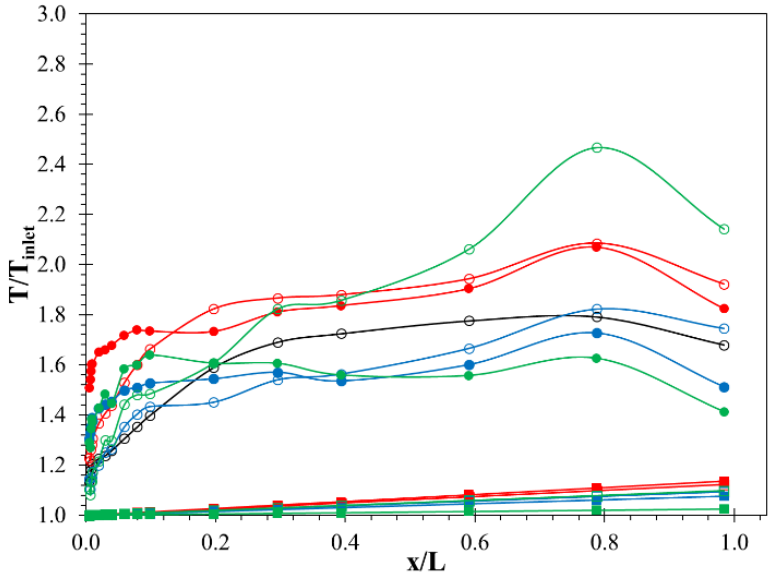

T_w Marker	T_b Marker	Rotation Direction	ω (rpm)	J	Re_{Dh}
		-	0	0	19032
		cw	200	4082	13968
		ccw	200	4180	13813
		cw	400	8354	13843
		ccw	400	8275	13698
		cw	800	16664	13619
		ccw	800	16181	13627

(a) AR = 2.02, $Re_{Dh,avg}$ = 13690, Re_{Dh} = 19032 for J = 0,

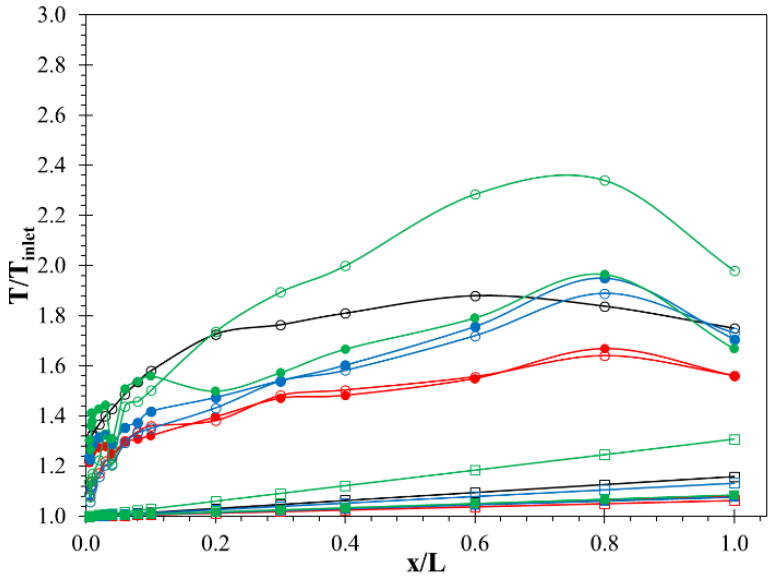

T_w Marker	T_b Marker	Rotation Direction	ω (rpm)	J	Re_{Dh}
		-	0	0	9981
		cw	200	1495	10073
		ccw	200	1518	10244
		cw	400	2984	10003
		ccw	400	3056	9975
		cw	800	5917	9555
		ccw	800	6148	9889

(b) AR = 3.93, $Re_{Dh,avg}$ = 10019

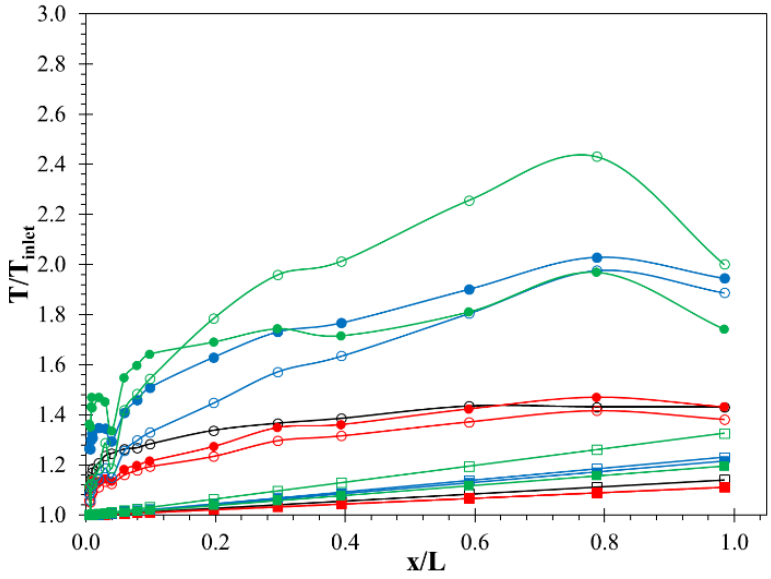

T_w Marker	T_b Marker	Rotation Direction	ω (rpm)	J	Re_{Dh}
		-	0	0	5517
		cw	200	384	5561
		ccw	200	385	5547
		cw	400	755	5592
		ccw	400	760	5500
		cw	800	1515	5391
		ccw	800	1543	5502

(c) AR = 8.81, $Re_{Dh,avg}$ = 5547

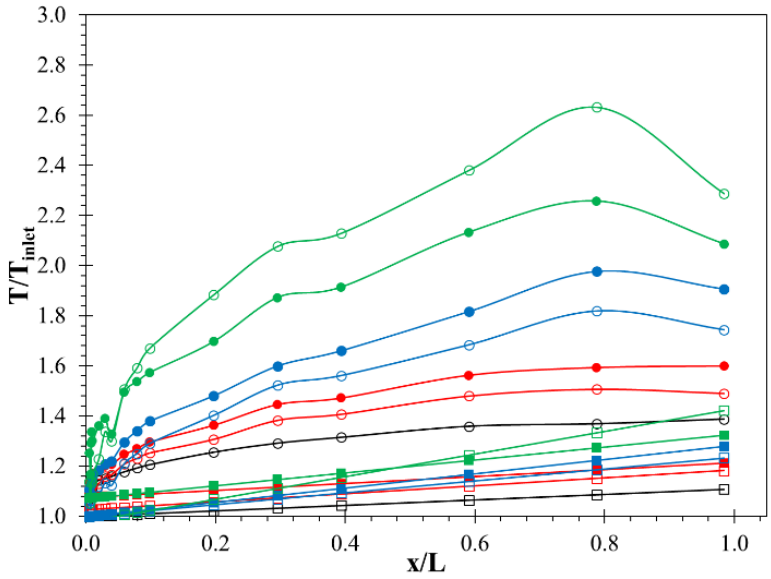

T_w Marker	T_b Marker	Rotation Direction	ω (rpm)	J	Re_{Dh}
		-	0	0	3138
		cw	200	110	3130
		ccw	200	108	3159
		cw	400	222	3162
		ccw	400	222	3170
		cw	800	442	3096
		ccw	800	450	3127

(d) AR = 17.33, $Re_{Dh,avg}$ = 3342

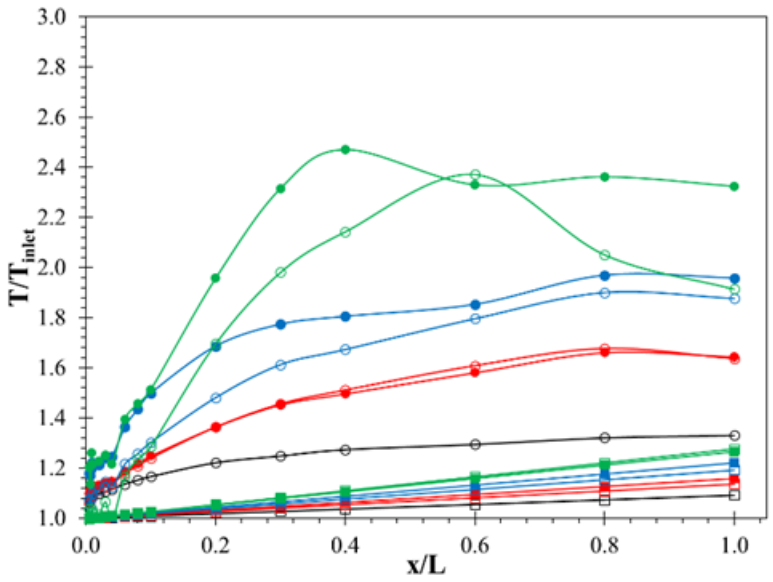

T_w Marker	T_b Marker	Rotation Direction	ω (rpm)	J	Re_{Dh}
		-	0	0	3651
		cw	200	131	3712
		ccw	200	129	3676
		cw	400	259	3690
		ccw	400	261	3678
		cw	800	522	3653
		ccw	800	522	3586

(e) Realistic S-shaped, $Re_{Dh,avg}$ = 3683

Figure 4-1 Axial Wall & Bulk Temperature Distribution

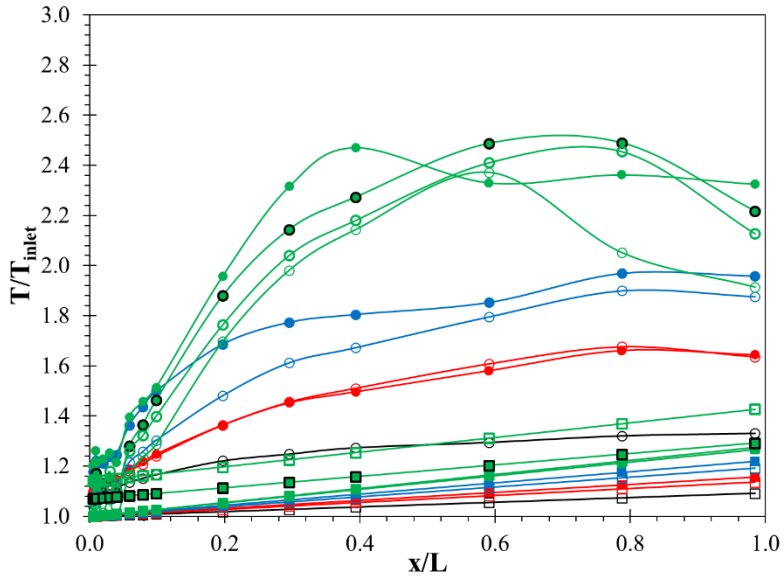

T_w Marker	T_b Marker	Rotation Direction	ω (rpm)	J	Re_{Dh}
		-	0	0	3651
		cw	200	131	3712
		ccw	200	129	3676
		cw	400	259	3690
		ccw	400	261	3678
		cw	800	522	3653
		ccw	800	522	3586
		cw	800	522	3609
		ccw	800	522	3641

Figure 4-2 Repeated Test for Realistic S-shape Model J = 522

The development of the flow is better monitored by Figure 4-3. Here when the flow is fully developed, the Nusselt Number will reach a plateau. The Nusselt number can be seen spiking up at x/L = 1.0. As mentioned before, this spike is caused by end loss effects and are neglected when determining fully developed behavior. By analyzing the points from x/L = 0.6 and x/L = 0.8 the

fully developed condition can be determined. Figure 4-3a-b show the Nusselt number constantly decreasing for all cases except the stationary case. However, Figure 4-3c-e show fully developed behavior for the stationary and low J cases. As J increases, the effect of rotation causes instabilities especially evident in the data in green in Figure 4-3. This make it difficult to claim that the flow reaches fully developed conditions for these cases. Additionally, as the rotation speed increases, the Nusselt number takes longer to reach a plateau. This suggests that the effect of rotation increases the entrance length possibly due to the boundary layer becoming skewed by the Coriolis forces and therefore taking longer to converge.

Table 4-3 Legend Key for Figure 4-3 ~ Figure 4-4

	AR = 2.02			AR = 3.93			AR = 8.81		
Marker	**ω (rpm)**	**J**	**Re_{Dh}**	**ω (rpm)**	**J**	**Re_{Dh}**	**ω (rpm)**	**J**	**Re_{Dh}**
	0	0	19032	0	0	9981	0	0	5517
	200	4082	13968	200	1495	10073	200	384	5561
	400	8354	13843	400	2984	10003	400	755	5592
	800	16664	13619	800	5917	9555	800	1515	5391
	AR = 17.33			**Realistic S-shape**					
Marker	**ω (rpm)**	**J**	**Re_{Dh}**	**ω (rpm)**	**J**	**Re_{Dh}**			
	0	0	3138	0	0	3651			
	200	110	3130	200	131	3712			
	400	222	3162	400	259	3609			
	800	442	3096	800	522	3641			

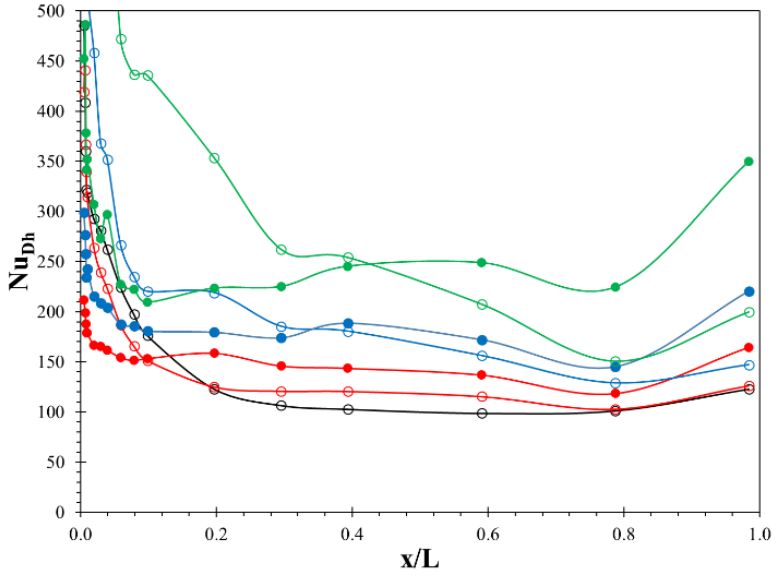

Marker	Rotation Direction	ω (rpm)	J	Re_{Dh}
	-	0	0	19032
	cw	200	4082	13968
	ccw	200	4180	13813
	cw	400	8354	13843
	ccw	400	8275	13698
	cw	800	16664	13619
	ccw	800	16181	13627

(a) AR = 2.02, $Re_{Dh,avg}$ = 13690, Re_{Dh} = 19032 for J = 0

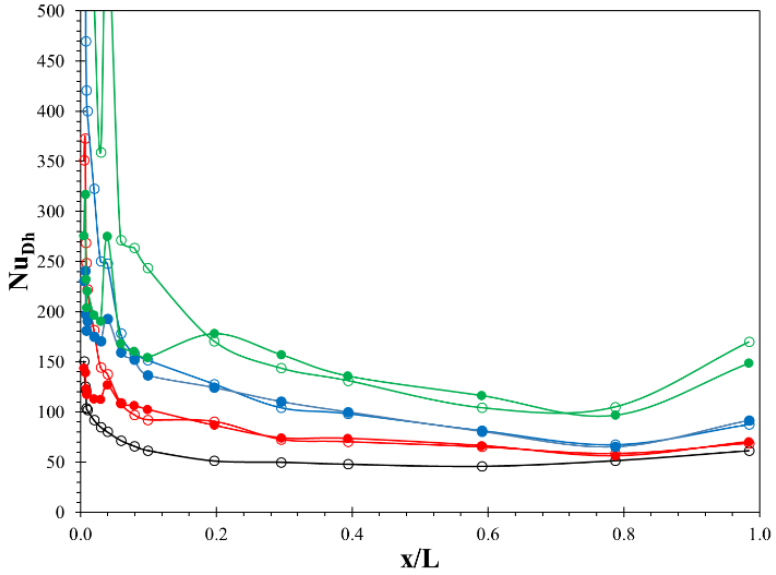

Marker	Rotation Direction	ω (rpm)	J	Re_{Dh}
	-	0	0	9981
	cw	200	1495	10073
	ccw	200	1518	10244
	cw	400	2984	10003
	ccw	400	3056	9975
	cw	800	5917	9555
	ccw	800	6148	9889

(b) AR = 3.93, $Re_{Dh,avg}$ = 10019

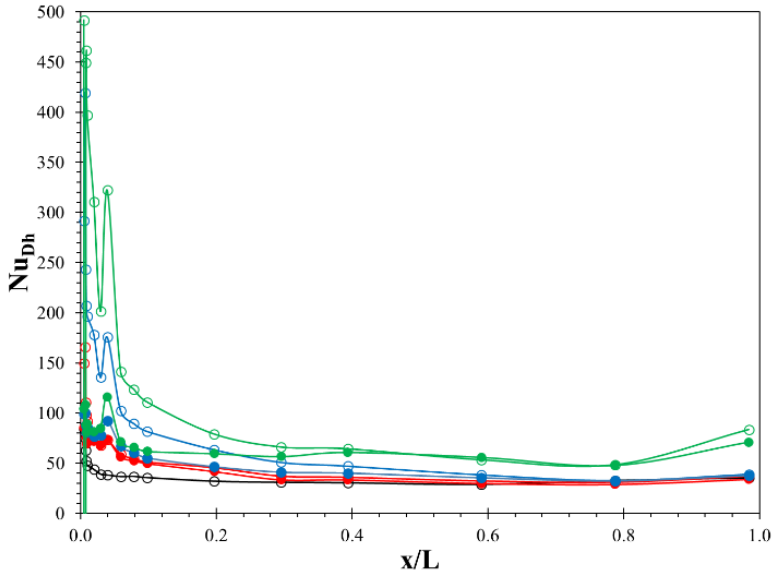

Marker	Rotation Direction	ω (rpm)	J	Re_{Dh}
	-	0	0	5517
	cw	200	384	5561
	ccw	200	385	5547
	cw	400	755	5592
	ccw	400	760	5500
	cw	800	1515	5391
	ccw	800	1543	5502

(c) AR = 8.81, $Re_{Dh,avg}$ = 5547

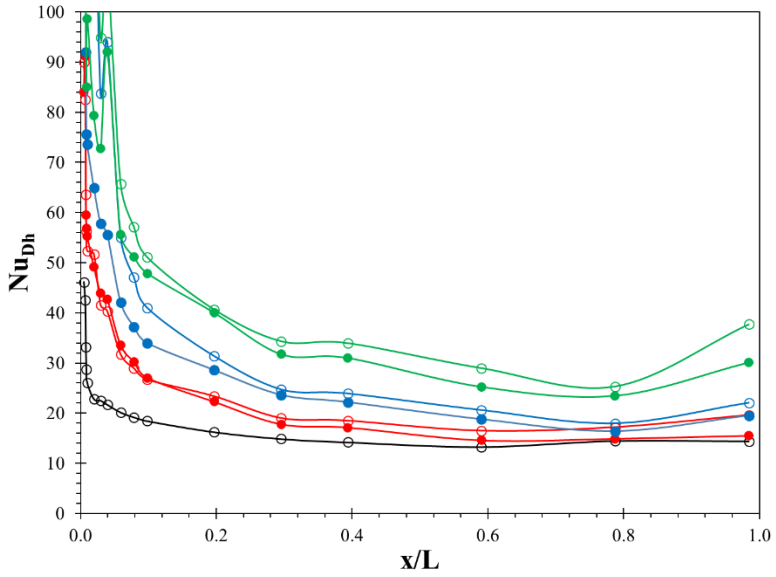

Marker	Rotation Direction	ω (rpm)	J	Re_{Dh}
	-	0	0	3138
	cw	200	110	3130
	ccw	200	108	3159
	cw	400	222	3162
	ccw	400	222	3170
	cw	800	442	3096
	ccw	800	450	3127

(d) AR = 17.33, $Re_{Dh,avg}$ = 3342

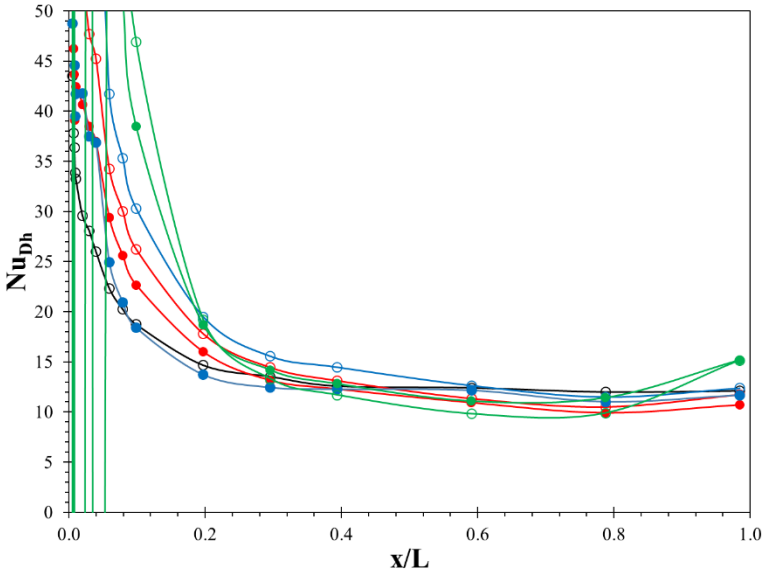

Marker	Rotation Direction	ω (rpm)	J	Re_{Dh}
	-	0	0	3651
	cw	200	131	3712
	ccw	200	129	3676
	cw	400	259	3690
	ccw	400	261	3678
	cw	800	522	3609
	ccw	800	522	3641

(e) Realistic S-shaped, $Re_{Dh,avg}$ = 3683

Figure 4-3 Realistic S-Shape and Simplified Rectangular Duct Axial Heat Transfer Distribution Normalized by Duct Length

Typical x/D_h for fully developed condition lies between $20 < L/D_h < 30$ [7]. For the turbulent region however, the criteria generally lie between $10 < L/D_h < 60$ [6]. This is reflected in the experimental data shown in Figure 4-4. In Figure 4-4a the x/D_h for the AR = 2.02 cases are shorter than 10 and the Nusselt number distribution is shown decreasing then increasing due to end loss effects. Similarly, in Figure 4-4b, the AR = 3.93 cases also do not reach a plateau. In Figure 4-4c the AR = 8.81 cases reach a plateau after $x/D_h = 10$. However, as the rotation speed increases the flow no longer meets the fully developed condition. A similar trend can be seen in Figure 4-4d and Figure 4-4e suggesting that the effect of rotation increase the length on the entrance region. This may be due to the Coriolis forces causing the boundary layer to become skewed and therefore taking longer to converge.

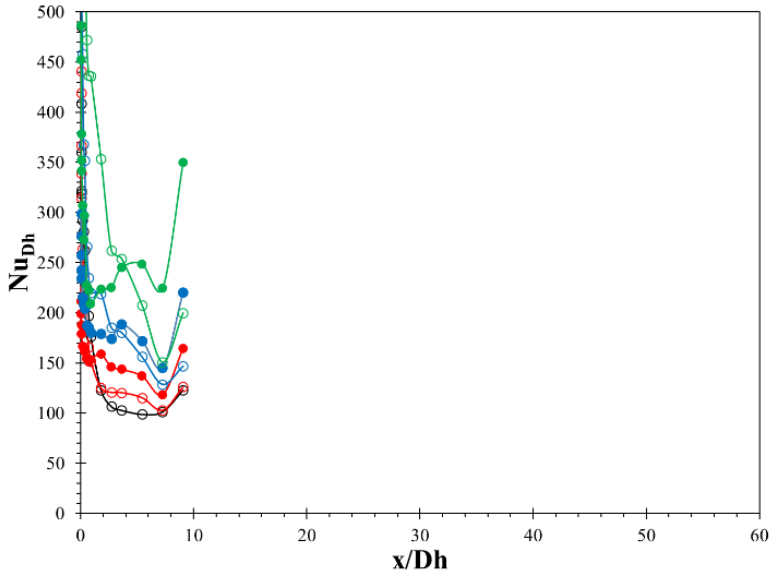

Marker	Rotation Direction	ω (rpm)	J	Re_{Dh}
	-	0	0	19032
	cw	200	4082	13968
	ccw	200	4180	13813
	cw	400	8354	13843
	ccw	400	8275	13698
	cw	800	16664	13619
	ccw	800	16181	13627

(a) AR = 2.02, $Re_{Dh,avg}$ = 13690, Re_{Dh} = 19032 for J = 0,

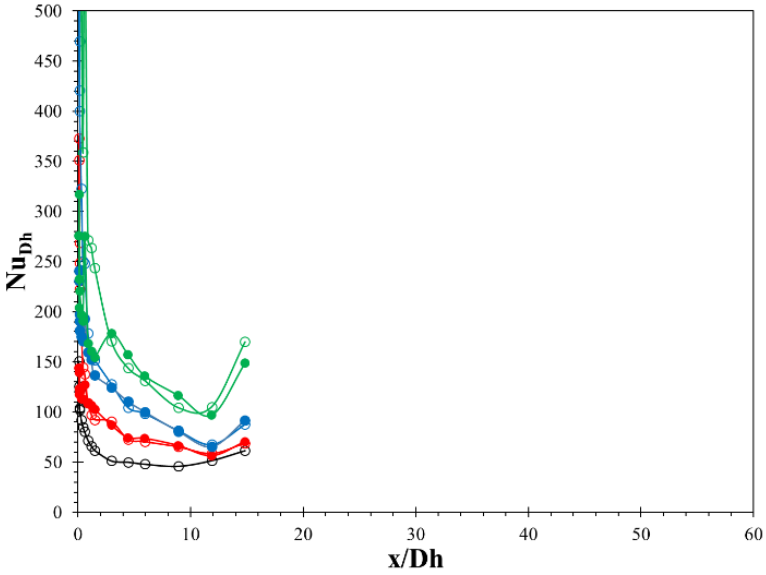

Marker	Rotation Direction	ω (rpm)	J	Re_{Dh}
	-	0	0	9981
	cw	200	1495	10073
	ccw	200	1518	10244
	cw	400	2984	10003
	ccw	400	3056	9975
	cw	800	5917	9555
	ccw	800	6148	9889

(b) AR = 3.93, $Re_{Dh,avg}$ = 10019

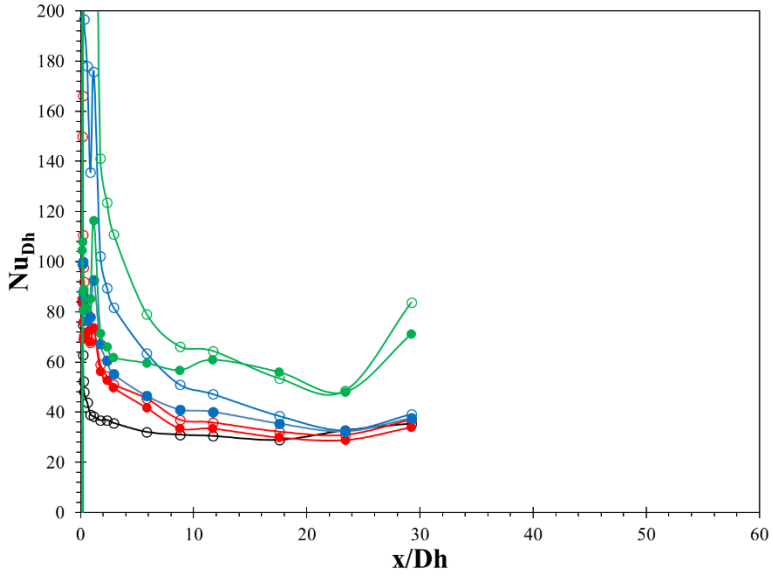

Marker	Rotation Direction	ω (rpm)	J	Re_{Dh}
	-	0	0	5517
	cw	200	384	5561
	ccw	200	385	5547
	cw	400	755	5592
	ccw	400	760	5500
	cw	800	1515	5391
	ccw	800	1543	5502

(c) AR = 8.81, $Re_{Dh,avg}$ = 5547

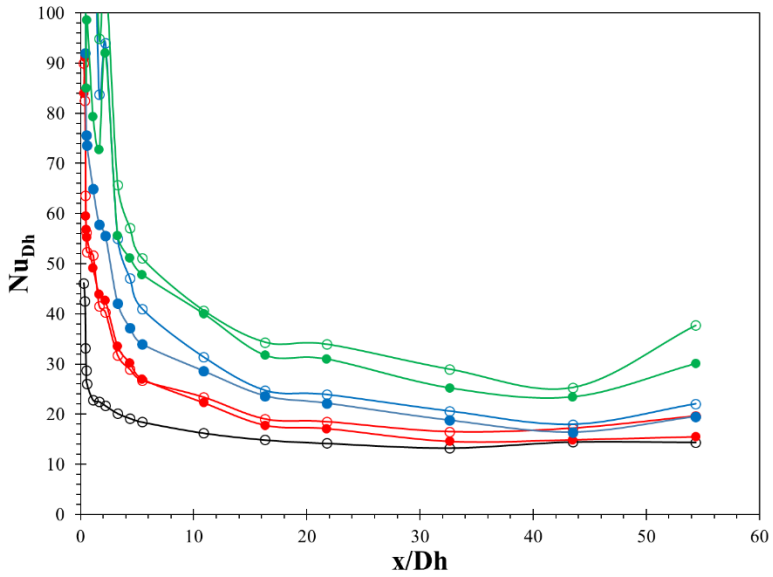

Marker	Rotation Direction	ω (rpm)	J	Re_{Dh}
	-	0	0	3138
	cw	200	110	3130
	ccw	200	108	3159
	cw	400	222	3162
	ccw	400	222	3170
	cw	800	442	3096
	ccw	800	450	3127

(d) AR = 17.33, $Re_{Dh,avg}$ = 3342

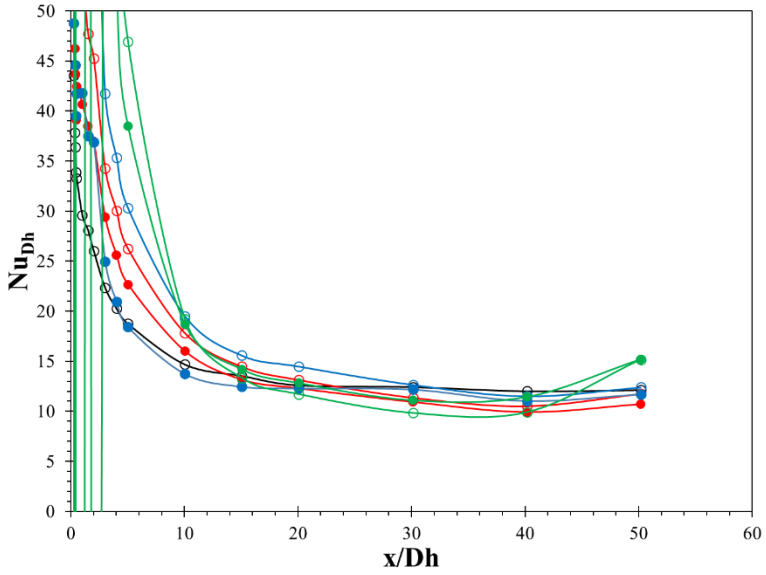

Marker	Rotation Direction	ω (rpm)	J	Re_{Dh}
	-	0	0	3651
	cw	200	131	3712
	ccw	200	129	3676
	cw	400	259	3690
	ccw	400	261	3678
	cw	800	522	3609
	ccw	800	522	3641

(e) Realistic S-shaped, $Re_{Dh,avg}$ = 3683

Figure 4-4 Realistic S-Shape and Simplified Rectangular Duct Axial Heat Transfer Distribution Normalized by Hydraulic Diameter

4.1.2 Investigation of Fully Developed Heat Transfer

Figure 4-5 shows the comparison between the axial Reynold's Number and the Rayleigh number. In the figure, the black line signifies the mixed convection boundary from Metais & Eckert [5], where data to the left of the boundary is in the forced convection region while the data to the right is in the mixed convection region. The area outlined in the grey region is the transition region between laminar and turbulent flow. This figure is used to validate that the experiments conducted were indeed in the forced convention zone where correlations for heat transfer are valid. All except for a few data points lie in the forced convection region. In Figure 4-5a there are a few data point from the AR = 2.02 case that lie in the mixed convection region however these data point do not show fully developed behavior due to the short L/D_h. Figure 4-5 (b) shows the reduced data set including only the data points that show fully developed behavior.

Table 4-4 Legend Key for Experimental Data in Figure 4-5 ~ Figure 4-7

Marker	AR	Rotation Direction	ω (rpm)	J	Marker	AR	Rotation Direction	ω (rpm)	J
	2.02	-	0	0		2.02	-	0	0
		CW	50	1014			CCW	50	1014
			100	1997				100	1997
			200	4082				200	4082
			400	8354				400	8354
			800	16664				800	16664
	3.93	-	0	0		3.93	-	0	0
		CW	50	372			CCW	50	365
			100	739				100	747
			200	1495				200	1518
			400	2984				400	3056
			800	5917				800	6148
	8.81	-	0	0		8.81	-	0	0
		CW	50	95			CCW	50	95
			100	190				100	189
			200	384				200	385
			400	755				400	760
			800	1515				800	1543
	17.33	-	0	0		17.33	-	0	0
		CW	50	27			CCW	50	27
			100	54				100	54
			200	110				200	108
			400	222				400	222
			800	442				800	450
	Realistic S-shape	-	0	0		Realistic S-shape	-	0	0
		CW	50	32			CCW	50	32
			100	64				100	64
			200	131				200	129
			400	259				400	261
			800	522				800	522

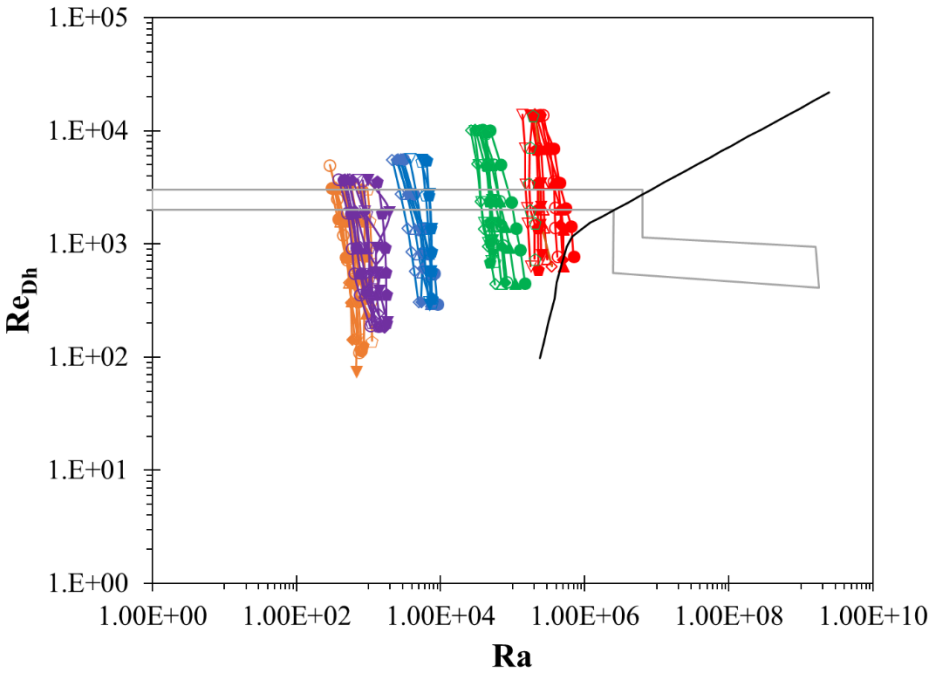

(a) All Experimental Data

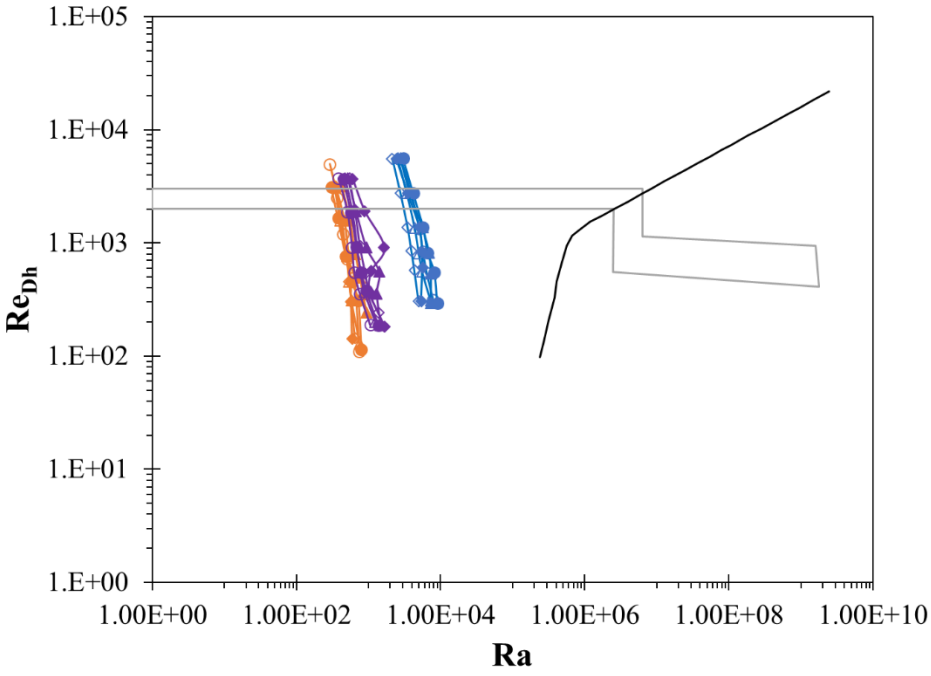

(b) Reduced to Data with Fully Developed Condition Met

Laminar to Turbulent Transition Region [5]

Mixed Convection Boundary [5]

Figure 4-5 Convection Regimes of Experimental data (Refer to Table 4-4)

The heat average heat transfer in the fully developed region is compared with data and correlations from literature. The average fully developed Nusselt number was taken as the average of the local Nusselt numbers (equation (8)) taken from x/L = 0.6 and x/L = 0.8. As many of the data and correlations from literature are given for the fully developed region, the data that does not meet the fully developed condition has been omitted the average Nusselt Number comparisons. This includes data all AR = 2.02 and AR = 3.93 data along with the data from AR = 8.81, AR = 17.33 and realistic S-shaped models at the highest J values. Figure 4-6 shows the comparison of the Nusselt Number vs the axial Reynolds number without rotation. The marker with no line connecting correspond to experimental data from literature circles for circular duct tests and squares for rectangular. The lines with no markers represent correlations from literature. The realistic S-shaped model shows good correlation to the data from literature in the turbulent region. The rectangular duct data also generally shows good correlation to data from literature with the trend in the turbulent region being very similar. However, the absolute value of the Nusselt numbers vary showing the effect of the duct aspect ratio on heat transfer. The smallest aspect ratio case shows the highest Nusselt number which is consistent with the data from Schmidt & Newell [16] for heat transfer in a duct with only one wall heated. Regarding the laminar region, the AR = 2.02, 3.93 and 8.81 cases show the data almost reaching a plateau. This is consistent with theory suggesting that the Nusselt number is constant in the laminar region. Since the rotational Reynolds number values are not comparable between aspect ratios the comparison is done between stationary data.

For the effect of the aspect ratio, the Nusselt number increases as aspect ratio decreases. This is contrary from literature, but this discrepancy is due to the data from literature all having the same cross-sectional area while the present study does not. Comparing stationary data of the AR = 17.33 and the AR = 8.81 cases, the Nusselt number for the AR = 8.81 case was generally between 40-50% greater than the AR = 17.33 cases. However, it is important to note, that this increase does not necessarily imply higher heat transfer as the cross-sectional areas are different and the Nusselt number is a function of the hydraulic diameter which is heavily influenced by cross-sectional area.

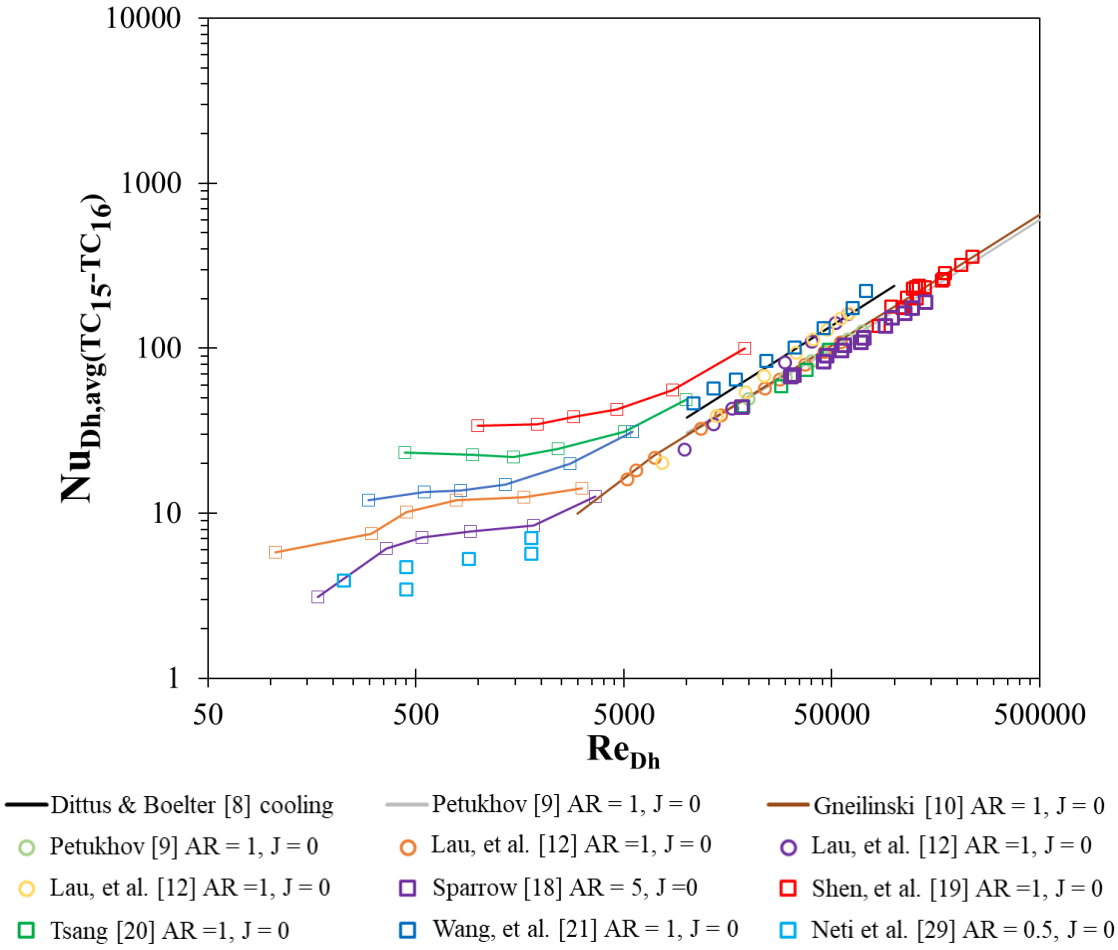

Figure 4-6 Stationary Heat Transfer Comparison in Realistic S-shaped & Simplified Rectangular Ducts (Refer to Table 4-4)

Figure 4-7 contains a summary of the Nu_{Dh} vs Re_{Dh} for all experimental work in the present study. Figure 4-7a shows the summary of all the data while Figure 4-7b omits the data that do not meet the fully developed condition as shown in Figure 4-4. It can be noted that as the rotation speed increases, so does the Nusselt number. However, the increase in Nusselt Number due to the rotations is greater in the lower Re_{Dh} range compared to the higher values. When comparing the stationary data with J = 260 for the realistic S-shaped model, at the lowest Re_{Dh} of 175, the Nusselt Number increased by 178% for clockwise rotation and 90% for counter-clockwise rotation. For the same comparison at the highest Re_{Dh} of 3695, the J = 260 data showed lower Nusselt number, but the decrease is less than 10% which can be attributed to the uncertainty. The real engine

operates at Re_{Dh} near 3000, and for this region, the results of the present study show the effect of rotation not having a significant effect the realistic S-shaped model when J < 260.

For the rectangular duct AR = 17.33 comparing the stationary to J = 222, at the lowest Re_{Dh} of 141, the Nusselt Number increases by 128% for clockwise rotation and 162% for the counterclockwise, however for the highest Re_{Dh} of 3142, the Nusselt Number increases by only 20% for both. For the AR = 17.33 the difference between the clockwise and counterclockwise rotation proved to be within the 10% uncertainty. For the AR = 8.81 experimental data, at Re_{Dh} = 300 the J = 760 Nusselt number is 104% higher than stationary for clockwise rotation and 145% higher when rotating counterclockwise. At Re_{Dh} = 2740, the Nusselt number increases by 56%. Repeatability tests were also conducted. Figure 4-8 shows the repeatability tests for the realistic S-shape at J = 522 and the stationary data for AR = 2.02. For the realistic S-shaped duct, the maximum difference in the repeatability was less than 10% for clockwise rotation and less than 20% for the counterclockwise. For the simplified rectangular duct AR = 2.02, the second and third tests show good repeatability with each other with a maximum difference of 6% but shows up to a 39% difference compared to the first test. Although the absolute values show differences greater than the 10% target uncertainty, the trends for the Nusselt number are the same for the data. This shows the trends are reliable and the differences in absolute value can be attributed to different atmospheric conditions as the tests were conducted on different days.

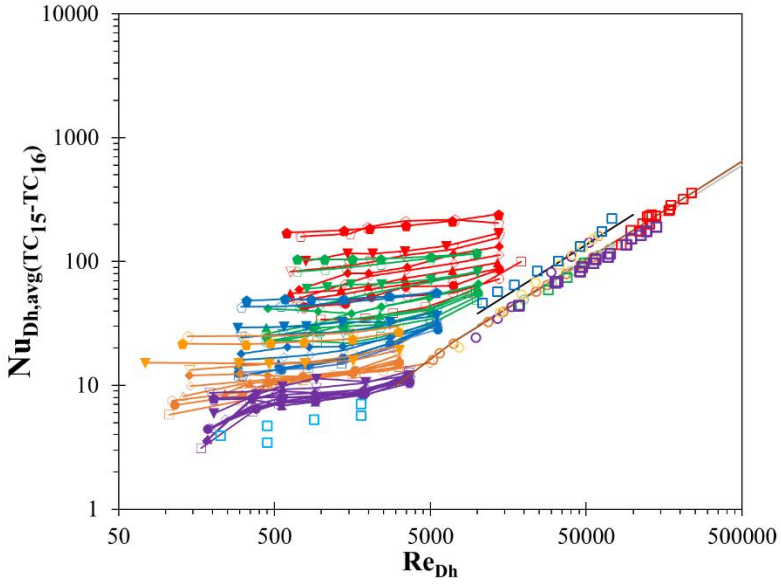

(a) All Experimental Data

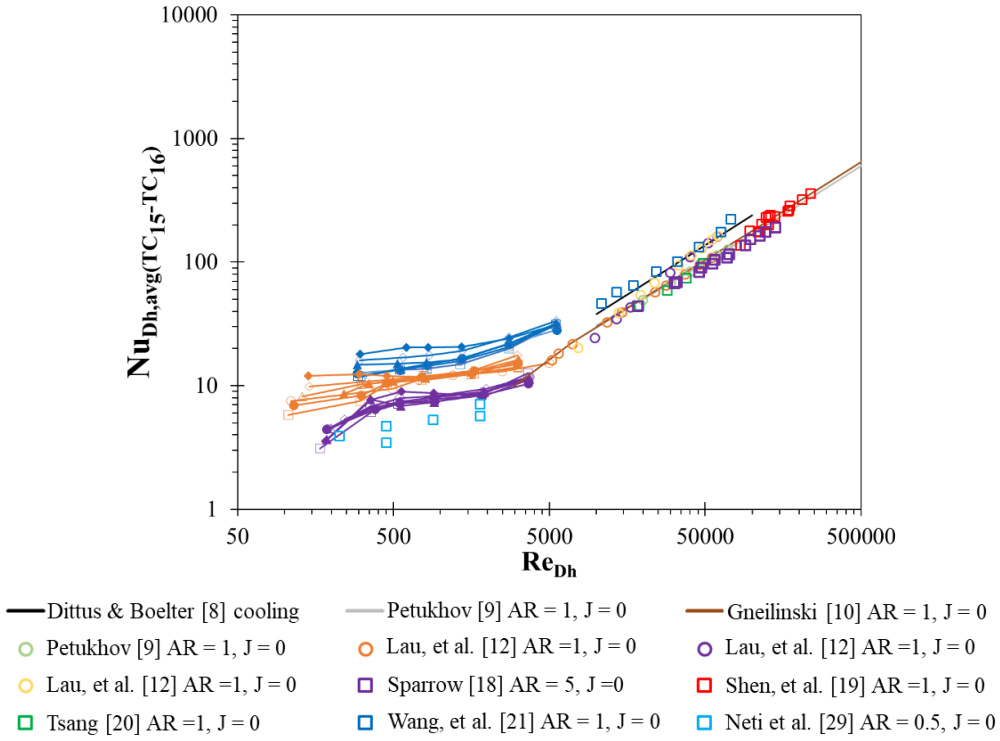

(b) Reduced to Data with Fully Developed Condition Met (Refer to Table 4-4)

Figure 4-7 Heat Transfer Comparison in Realistic S-shaped & Simplified Rectangular Ducts

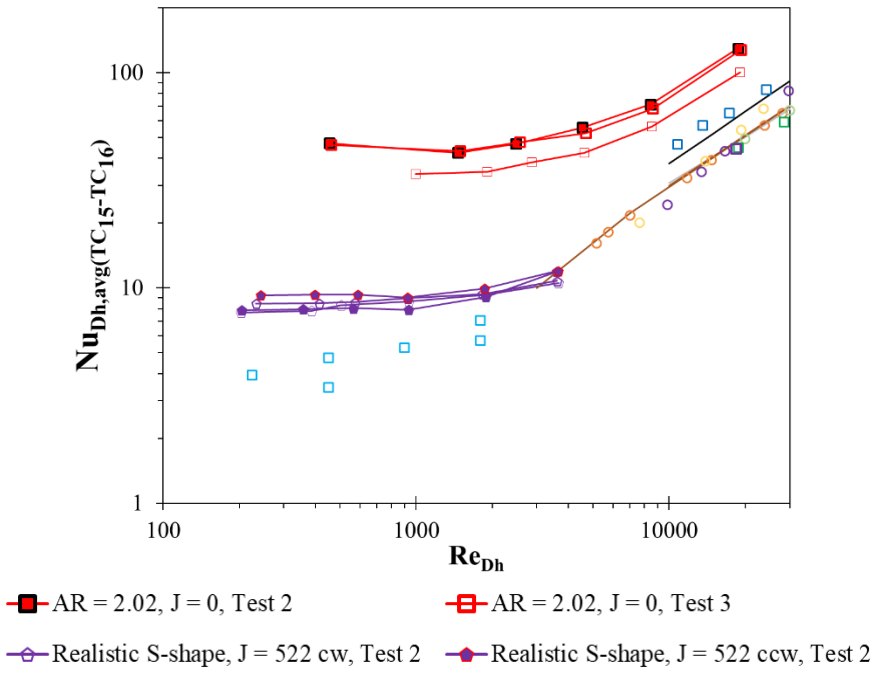

Figure 4-8 Repeatability Test for Realistic S-shaped Geometry (Refer to Table 4-5)

Figure 4-9 shows the variation of the Nusselt number based on the Rotation Reynold's number. The Nusselt number was divided by the Re_{Dh} so only the effect of rotation would be shown. Even though the Nusselt number is offset by the Re_{Dh}, in each data set, the data point with the highest Re_{Dh} produced the lowest modified Nusselt Number. Like the correlations from literature, the data shows that for cases when the aspect ratio and the Re_{Dh} are similar, a linear fit can be applied on a log-log scale. In this figure, the effect of the rotation direction is shown. As the duct rotates, when undergoing clockwise rotation, the bottom wall of the duct becomes the trailing surface, while when rotating counterclockwise, bottom wall is now the leading surface. The heat transfer is expected to have slight variation based on the rotation direction as the temperature gradient in the duct is expected to become skewed towards the leading surface.

Comparing the clockwise and counterclockwise Nusselt number for the realistic S-shaped model there is no clear trend. Comparing the clockwise and counterclockwise data for the rectangular duct, for the AR = 17.33 model, the differences in the data are within the 10% uncertainty. However, for the AR = 8.81, the counterclockwise data clearly shows higher heat transfer in the lower Re_{Dh} ranges. This suggests that the rotation direction is negligible for higher aspect ratios as the small distance between leading and trailing surfaces produces a smaller temperature gradient between the leading and trailing surfaces.

Table 4-5 Legend Key for Experimental Data in Figure 4-9

Marker	AR	Rotation Direction	ω (rpm)	Re_{Dh} Range	Marker	AR	Rotation Direction	ω (rpm)	Re_{Dh} Range
	2.02	-	0	995~19032		2.02	-	0	995~19032
		CW	50	773~13834			CCW	50	775~13882
			100	730~13535				100	632~13511
			200	633~13968				200	722~13813
			400	633~13843				400	792~13698
			800	736~13619				800	567~13617
	3.93	-	0	443~9981		3.93	-	0	443~9981
		CW	50	459~10182			CCW	50	446~10091
			100	445~10075				100	443~10061
			200	442~10073				200	455~10244
			400	705~10003				400	807~9975
			800	702~9555				800	698~9889
	8.81	-	0	297~5517		8.81	-	0	297~5517
		CW	50	313~5525			CCW	50	292~5588
			100	310~5613				100	293~5606
			200	304~5561				200	306~5547
			400	304~5592				400	291~5500
			800	307~5391				800	332~5502
	17.33	-	0	106~3138		17.33	-	0	106~3138
		CW	50	110~4981			CCW	50	115~3116
			100	130~3139				100	241~3170
			200	144~3130				200	142~3159
			400	143~3162				400	74~3170
			800	139~3096				800	128~3127
	Realistic S-shape	-	0	169~3651		Realistic S-shape	-	0	106~3138
		CW	50	189~3736			CCW	50	115~3116
			100	199~3708				100	241~3170
			200	242~3712				200	142~3159
			400	192~3690				400	74~3170
			800	203~3653				800	128~3127

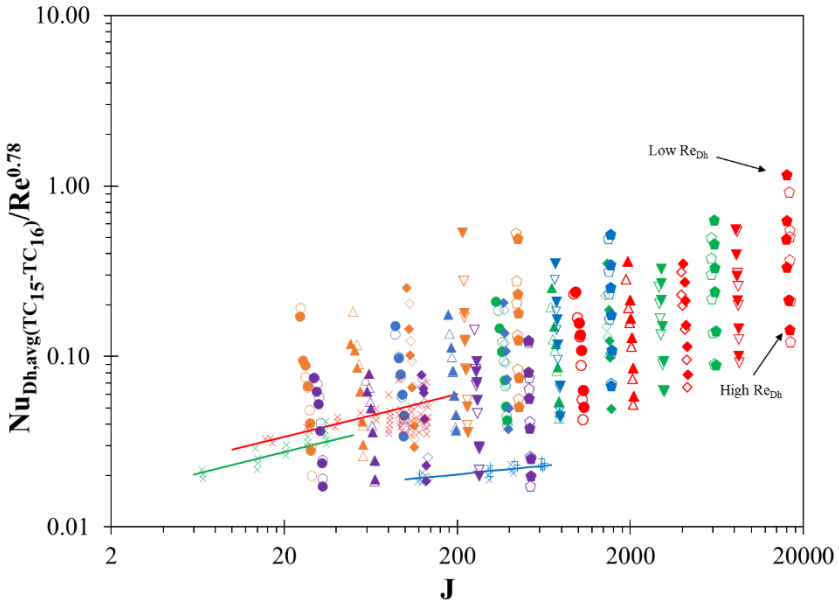

(a) All Experimental Data

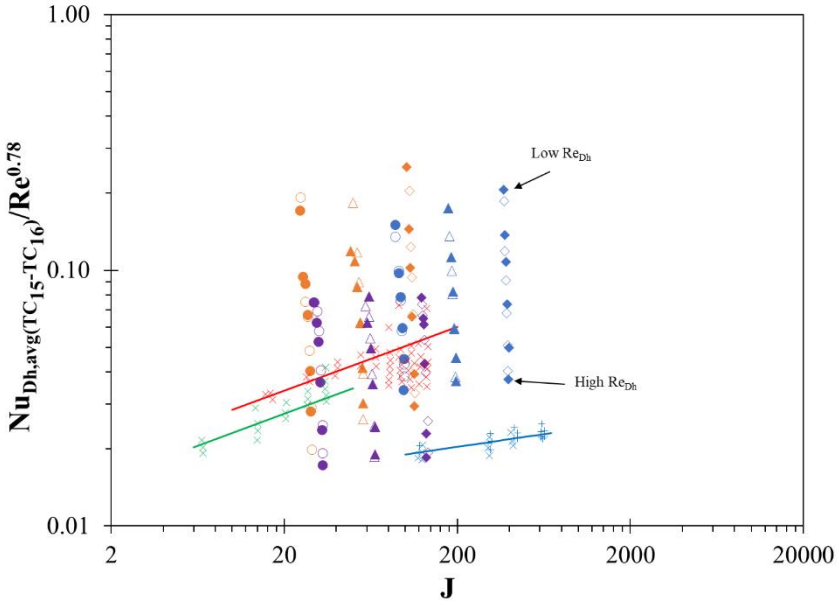

(b) Reduced to Data with Fully Developed Condition met

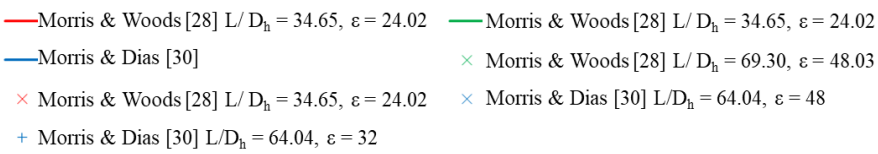

Figure 4-9 Heat Transfer Comparison in Realistic S-shaped & Simplified Rectangular Ducts with Effect of Rotation (Refer to Table 4-5)

The AR = 17.33 rectangular duct has the most comparable hydraulic diameter to the realistic S-shaped model. Figure 4-10 shows the comparison of Nusselt Numbers of the AR = 17.33 and realistic S-shaped models. The heat transfer characteristics proved to be quite dissimilar with the realistic geometry being less effected by the rotation especially in the turbulent region. At Re_{Dh} around 3600, the AR = 17.33 rectangular duct has 12% higher Nusselt number than the realistic S-shape at stationary conditions. The clockwise rotation data show similar trends however the absolute values of the realistic S-shaped model are lower. The counterclockwise data shows no clear trends suggesting that the instability is greater on the leading surface than the trailing surface. This comparison also has limitations as even though the hydraulic diameters were similar, since only the centerline temperatures were measured on a single surface, the Nusselt numbers presented cannot represent the cross-sectional average.

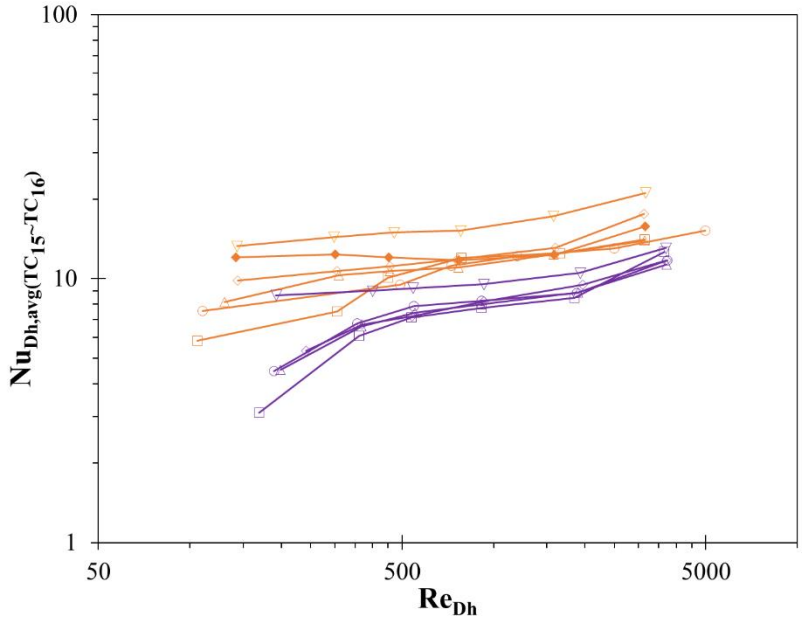

(a) Stationary & Clockwise Data (Heated Wall is on Trailing Surface for Clockwise, Bottom Wall for Stationary)

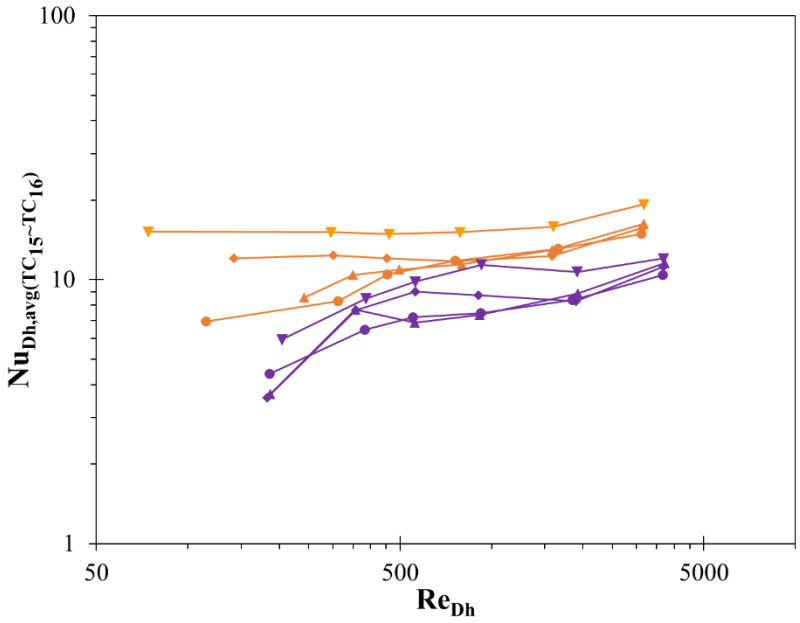

(b) Counter-clockwise Data (Heated Wall is on Leading Surface)

Figure 4-10 Comparison of Realistic S-shaped model & AR = 17.33- Nusselt Number vs Re_{Dh} (Refer to Table 4-4)

4.1.3 Investigation of Overall Pressure Loss

Figure 4-10 shows the plot of the friction factor (equation (9)) compared to data from literature. This friction factor was calculated using the pressure loss defined in equation (36). Here, neither the absolute value nor the trends match the correlations. Figure 4-10 shows an overall summary of the friction factor data. There are several data sets that do not show a clear trend in the data. These cases are due to the actual pressure in the duct is below the measurable range for the pressure sensors in some cases. Figure 4-10 gives a better picture with only the reliable data present. Overall, the data from the present study is aligned with the data from the literature. The trends in the data suggest that the friction factor decreases sharply then reaches a plateau however not enough data was collected at higher Re_{Dh} to confirm this trend. For the realistic S-shaped model, the at J = 130, Re_{Dh} = 3736, the effect of rotation increased the friction factor by 13% for clockwise rotation and 20% for counter-clockwise. For the most comparable rectangular duct at AR = 17.33 with J = 110 and Re_{Dh} = 3342, the effect of rotation increases the friction factor by

36% for clockwise rotation and 45% for counterclockwise. It is also of note that at lower J values, the slope of the data is less steep than the higher J values. Since only the stationary data can be compared for the effect of aspect ratio due to the J not being comparable between aspect ratios, no conclusions can be drawn about the effect or aspect ratio on friction factor for the rectangular duct as the AR = 8.81 stationary data is unreliable.

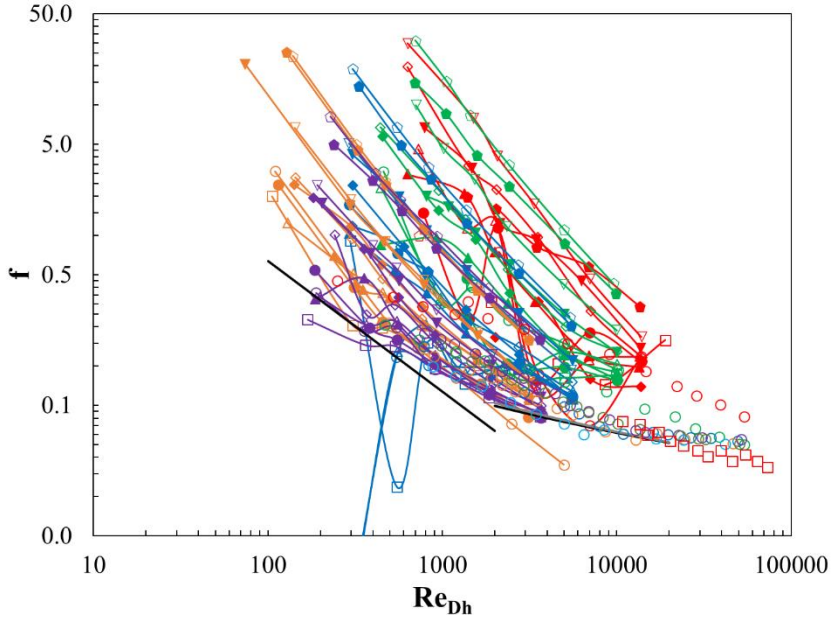

(a) All Experimental Data

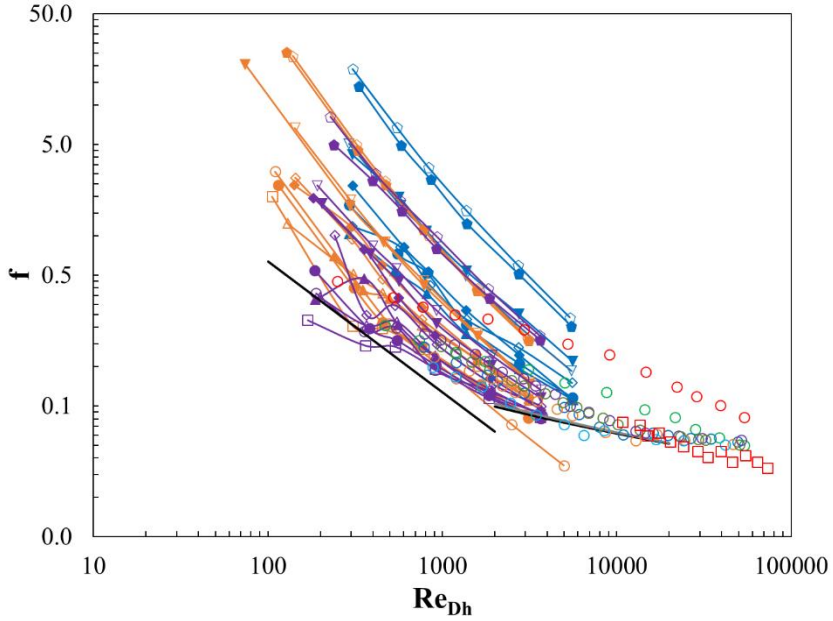

(b) Reduced to Data with Reliable Pressure Measurements

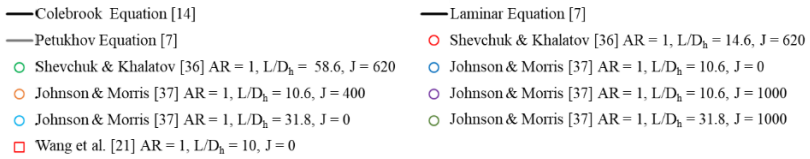

Figure 4-11 Pressure Loss Comparison in Realistic S-shaped & Simplified Rectangular Ducts (Refer to Table 4-4)

Comparing the realistic S-shape and the AR = 17.33 ducts, the pressure loss characteristics proved to be similar. Figure 4-12 shows the comparison of the friction factor data. The friction factor data proved to be similar as the pressure drop data was taken as the averaged between pressures measured at pressure taps on opposite sides of the duct. All data Re_{Dh} > 1000 showed the friction factors are within a 5% difference. At lower Re_{Dh}, there is slightly more variation. However, this variation is due to the pressure drop measurements in this area being close to the minimum pressure drop measurable by the pressure sensors.

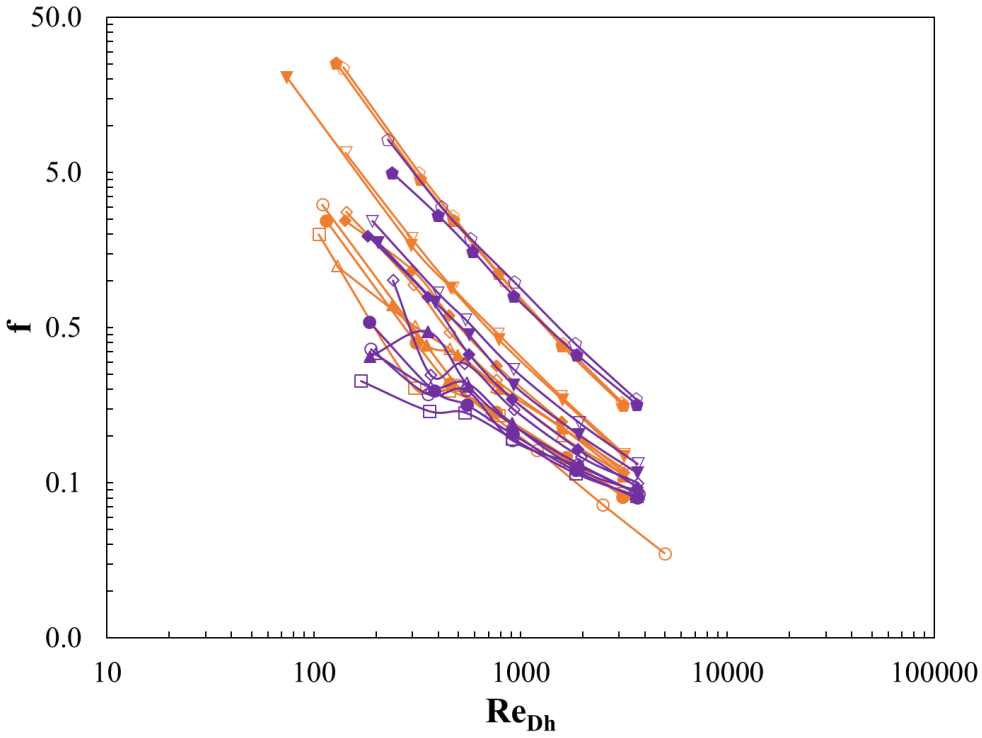

Figure 4-12 Comparison of Realistic S-shaped model & AR = 17.33– Friction Factor (Refer to Table 4-4)

4.2 Annular Duct with Inner Surface Rotation

4.2.1 Centerline Heat Transfer Distribution

To understand the effect of the rotation on the heat transfer first it is important to chart whether or not the axial flow or tangential flow is dominant. Kuzay & Scott [49] shows that this can be done comparing the axial velocity with the tangential velocity. Table 4-6 shows the ranges of the ratio between the tangential and axial velocities. For the $\Delta r/r_1 = 0.05$ and 0.1 cases, most of the ratios were below 1 which signifies axial flow dominance. The $\Delta r/r_1 = 0.3$ and 0.6 cases showed values greater than 1 for all cases except the stationary showing rotational flow dominance. In the cases where the ratio between the tangential and axial velocities are greater than 1 the possible onset of Taylor vortices can be seen similar to that seen in Molki et al. [60]. This trend can first be seen in the temperature distribution. Figure 4-13 shows the distribution of temperature profiles. For the stationary can cases where the ratio between the tangential and axial velocities are less than 1, the flow shows fully developed behavior past x/L = 0.54. However, as the rotation speed increases, the wall temperature profile starts to show fluctuations past x/L = 0.54.

Table 4-6 Velocity Ranges for Annular Duct Tests

	$\Delta r/r_1 = 0.05$	$\Delta r/r_1 = 0.1$	$\Delta r/r_1 = 0.3$	$\Delta r/r_1 = 0.6$
u_t (m/s)	0 ~ 23.62	0 ~ 23.62	0 ~ 23.62	0 ~ 23.62
u_x (m/s)	4.34 ~ 24.03	2.91 ~ 11.80	0.95 ~ 4.04	0.46 ~ 2.05
u_t/u_x	0 ~ 5.49	0 ~ 8.25	0 ~ 25.09	0 ~ 50.51

Table 4-7 Legend Key for Figure 4-13

		$\Delta r/r_1 = 0.05$			$\Delta r/r_1 = 0.1$		
T_w Marker	**T_b Marker**	**ω (rpm)**	**Re_φ**	**Re_{Dh}**	**ω (rpm)**	**Re_φ**	**Re_{Dh}**
		0	0	7970	0	0	10447
		100	5125	7825	100	10211	10464
		200	10228	7829	200	20022	10436
		400	20430	7664	400	39996	10071
		800	40929	7671	800	80158	10061
		$\Delta r/r_1 = 0.3$			$\Delta r/r_1 = 0.6$		
T_w Marker	**T_b Marker**	**ω (rpm)**	**Re_φ**	**Re_{Dh}**	**ω (rpm)**	**Re_φ**	**Re_{Dh}**
		0	0	9866	0	0	9795
		100	29960	9901	100	60131	9807
		200	59668	9766	200	120448	9533
		400	119260	9945	400	240530	9856
		800	237911	9862	800	480949	9827

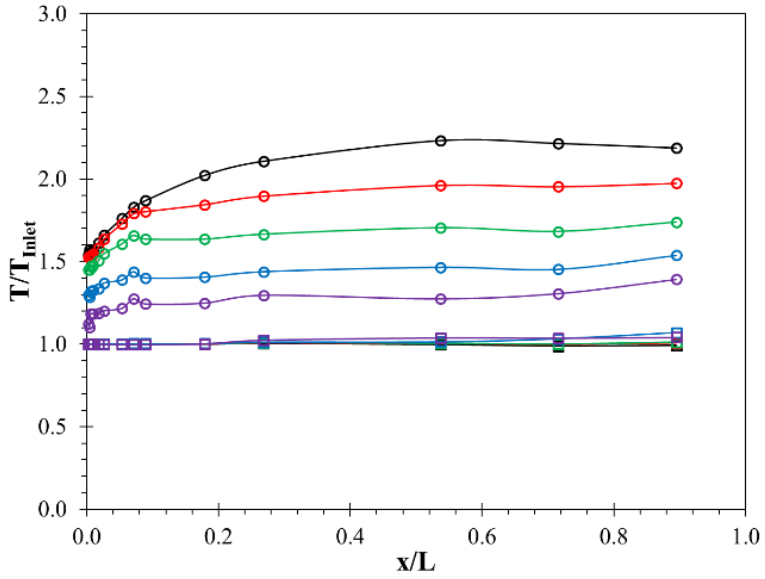

T_w Marker	T_b Marker	ω (rpm)	Re_φ	Re_{Dh}
		0	0	7970
		100	5125	7825
		200	10228	7829
		400	20430	7664
		800	40929	7671

(a) $\Delta r/r_1 = 0.05$, $Re_{Dh,avg} = 7792$

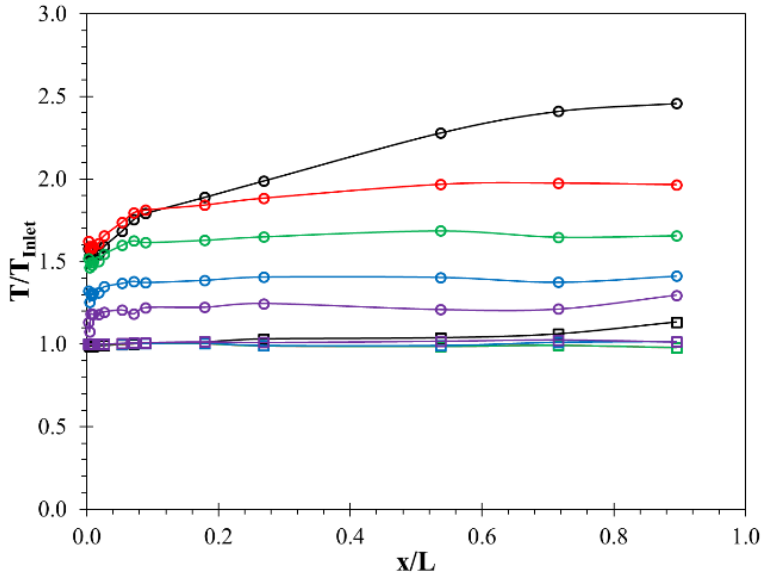

T_w Marker	T_b Marker	ω (rpm)	Re_φ	Re_{Dh}
		0	0	10447
		100	10211	10464
		200	20022	10436
		400	39996	10071
		800	80158	10061

(b) $\Delta r/r_1 = 0.1$, $Re_{Dh,avg} = 10296$

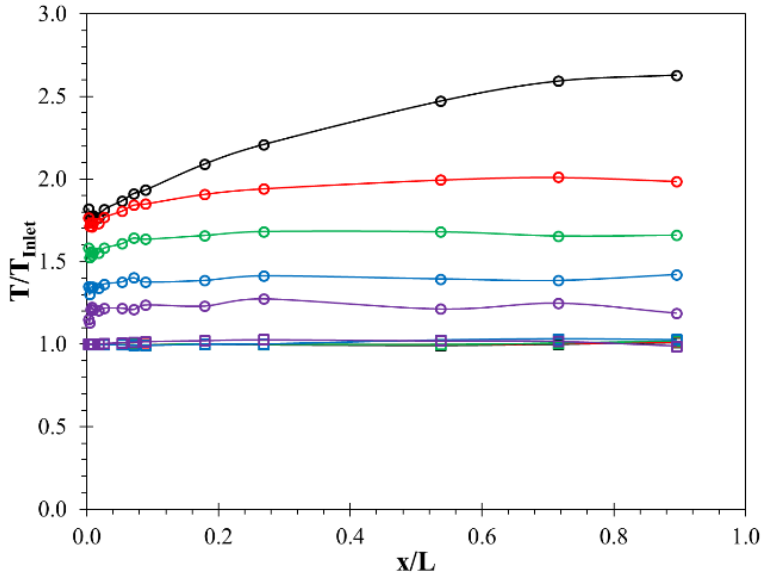

T_w Marker	T_b Marker	ω (rpm)	Re_φ	Re_{Dh}
		0	0	9866
		100	29960	9901
		200	59668	9766
		400	119260	9945
		800	237911	9862

(c) $\Delta r/r_1 = 0.3$, $Re_{Dh,avg} = 9868$

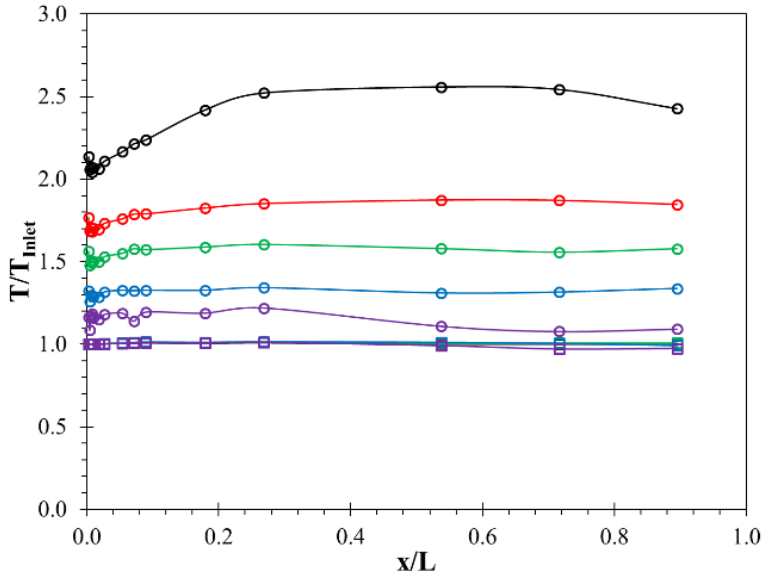

T_w Marker	T_b Marker	ω (rpm)	Re_φ	Re_{Dh}
		0	0	9795
		100	60131	9807
		200	120448	9533
		400	240530	9856
		800	480949	9827

(d) $\Delta r/r_1 = 0.6$, $Re_{Dh,avg} = 9764$

Figure 4-13 Annular Duct Axial Wall & Bulk Temperature Distributions

Table 4-8 Legend Key for Figure 4-14 ~ Figure 4-17

	$\Delta r/r_1 = 0.05$			$\Delta r/r_1 = 0.1$		
Marker	**ω (rpm)**	**Re_φ**	**Re_{Dh}**	**ω (rpm)**	**Re_φ**	**Re_{Dh}**
	0	0	7970	0	0	10447
	100	5125	7825	100	10211	10464
	200	10228	7829	200	20022	10436
	400	20430	7664	400	39996	10071
	800	40929	7671	800	80158	10061
	$\Delta r/r_1 = 0.3$			$\Delta r/r_1 = 0.6$		
Marker	**ω (rpm)**	**Re_φ**	**Re_{Dh}**	**ω (rpm)**	**Re_φ**	**Re_{Dh}**
	0	0	9866	0	0	9795
	100	29960	9901	100	60131	9807
	200	59668	9766	200	120448	9533
	400	119260	9945	400	240530	9856
	800	237911	9862	800	480949	9827

The fully developed behavior better shown in the plot of the Nusselt number. Figure 4-14 shows the Nusselt number plateauing after x/L = 0.54 for the cases where the velocity ratio is less than one. However, when the ratio is greater than 1, Nusselt Number suddenly increases then begin to decrease again. This is possibly evidence of the effect of the Taylor vortices mentioned in Molki et al. [60]. While generally the plots show similar patterns with the Nuseelt number suddenly increasing then decreasing, in Figure 4-14c shows an oscillatory profile. To investigate this difference further, repeated tests were conducted. In Figure 4-15 the repeated test results for the $\Delta r/r_1$ = 0.1 case are shown. The results of the repeated test for the $\Delta r/r_1$ = 0.1 show good repeatability verifying the increase in Nusselt number. Data was also collected at Re_φ = 68137 further validating the trend. Figure 4-16 shows a different case. The original data and one repeated test show the same oscillation in the Nusselt number profile. However, the other two repeated tests at Re_φ = 241878 show the trend where the Nusselt number increases and decreases. This shows that the effect of rotation causes the flow to have no clear trend however, it is possible that the onset of Taylor vortices creates the oscillatory behavior in the heat transfer distribution and more thermocouples are needed in this area to validate this trend.

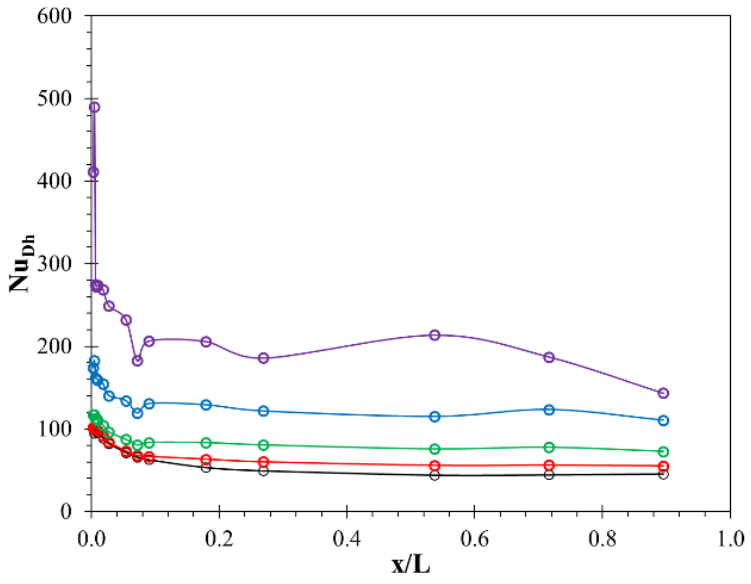

Marker	ω (rpm)	Re_φ	Re_{Dh}
	0	0	7970
	100	5125	7825
	200	10228	7829
	400	20430	7664
	800	40929	7671

(a) $\Delta r/r_1$ = 0.05, $Re_{Dh,avg}$ = 7792

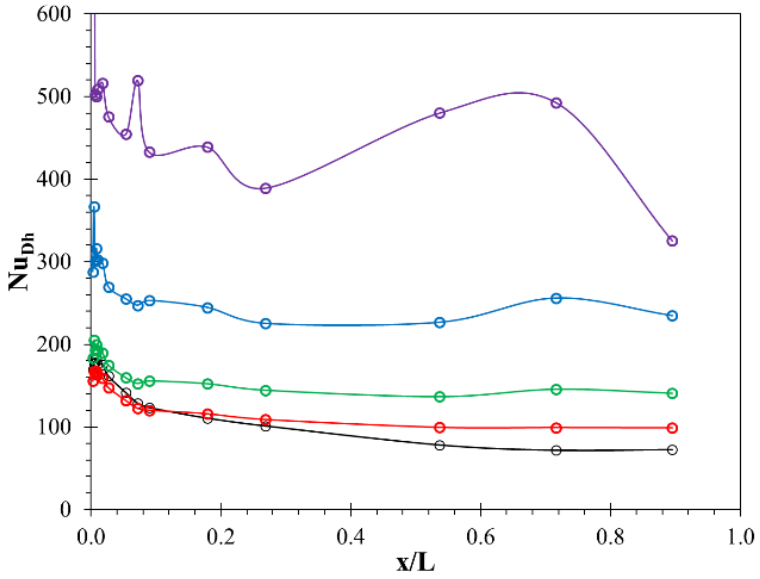

Marker	ω (rpm)	Re_{φ}	Re_{Dh}
	0	0	10447
	100	10211	10464
	200	20022	10436
	400	39996	10071
	800	80158	10061

(b) $\Delta r/r_1 = 0.1$, $Re_{Dh,avg} = 10296$

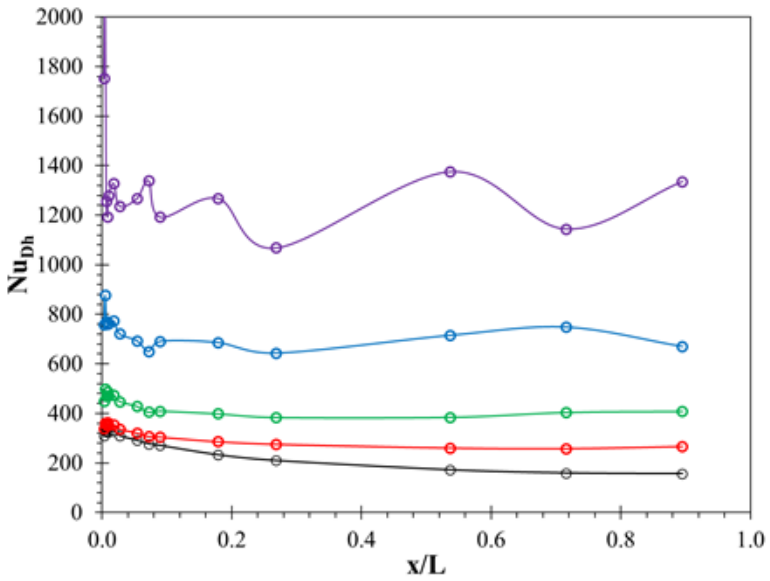

Marker	ω (rpm)	Re_{φ}	Re_{Dh}
	0	0	9866
	100	29960	9901
	200	59668	9766
	400	119260	9945
	800	237911	9862

(c) $\Delta r/r_1 = 0.3$, $Re_{Dh,avg} = 9868$

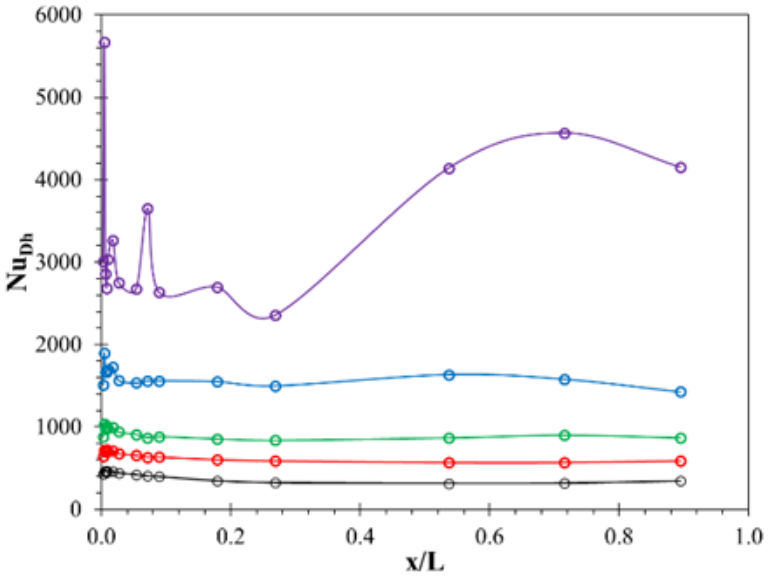

Marker	ω (rpm)	Re_φ	Re_{Dh}
	0	0	9795
	100	60131	9807
	200	120448	9533
	400	240530	9856
	800	480949	9827

(d) $\Delta r/r_1 = 0.6$, $Re_{Dh,avg} = 9764$

Figure 4-14 Annular Duct Axial Heat Transfer Distribution Normalized by Duct Length

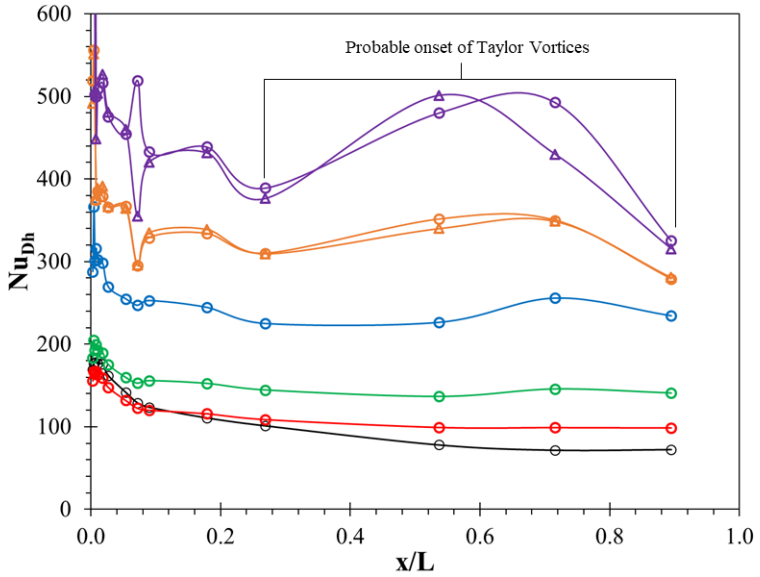

Marker	ω (rpm)	Re_φ	Re_{Dh}
	0	0	10447
	100	10211	10464
	200	20022	10436
	400	39996	10071
	800	80158	10061

$Re_\varphi = 566$, $Re_{Dh} = 9716$ $Re_\varphi = 68137$, $Re_{Dh} = 10874$

$Re_\varphi = 81778$, $Re_{Dh} = 10464$

Figure 4-15 Repeatability Test for $\Delta r/r_1 = 0.1$

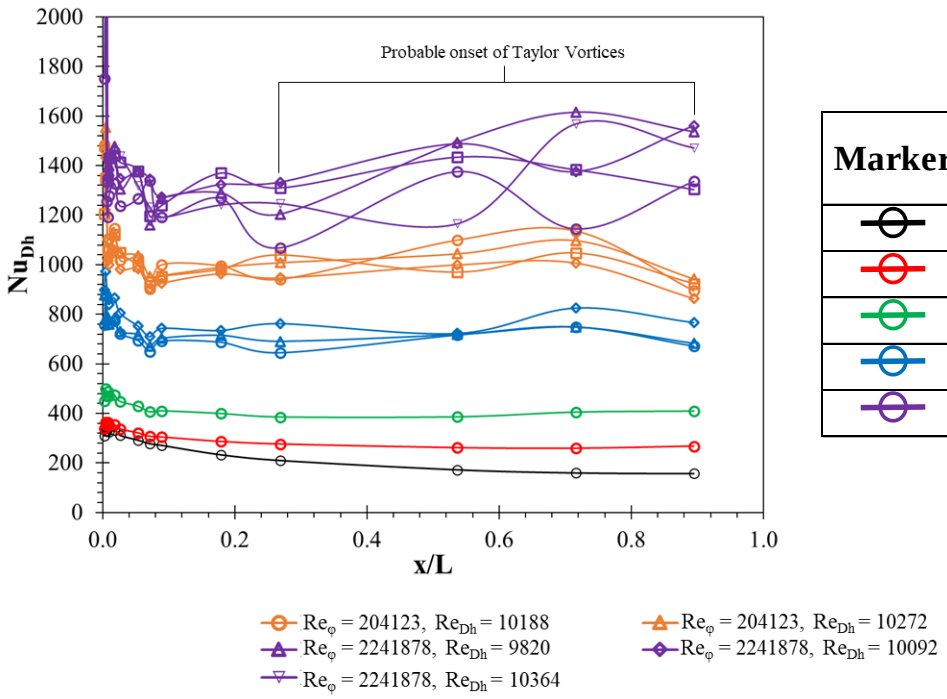

Marker	ω (rpm)	Re_φ	Re_{Dh}
	0	0	9866
	100	29960	9901
	200	59668	9766
	400	119260	9945
	800	237911	9862

Figure 4-16 Repeatability Test for $\Delta r/r_1 = 0.3$

The experimental data for the annular duct tests lies in the turbulent region. Therefore, the fully developed x/D_h is compared to that of the expected value of between 10 and 60 [6]. In Figure 4-17 even though the x/D_h is significantly less than 10, the for the $\Delta r/r_1 = 0.05$ and $\Delta r/r_1 = 0.1$ cases show fully developed behavior. For the $\Delta r/r_1 = 0.3$ and $\Delta r/r_1 = 0.6$ cases, the test section is not long enough to meet the fully developed condition. The flow may be reaching fully developed conditions at a shorter x/D_h due to having a smaller cross-sectional gap allowing the boundary layers to converge faster than if the cross-section was circular of a square.

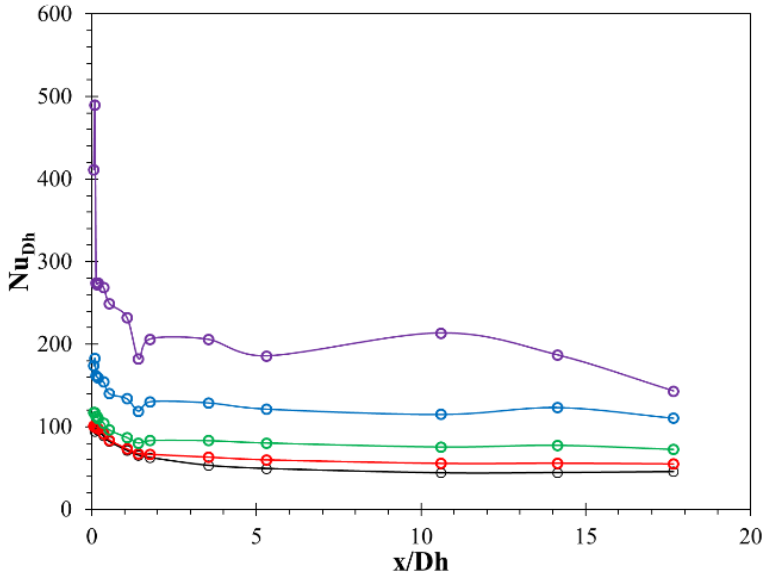

Marker	ω (rpm)	Re_{φ}	Re_{Dh}
	0	0	7970
	100	5125	7825
	200	10228	7829
	400	20430	7664
	800	40929	7671

(a) $\Delta r/r_1 = 0.05$, $Re_{Dh,avg} = 7792$

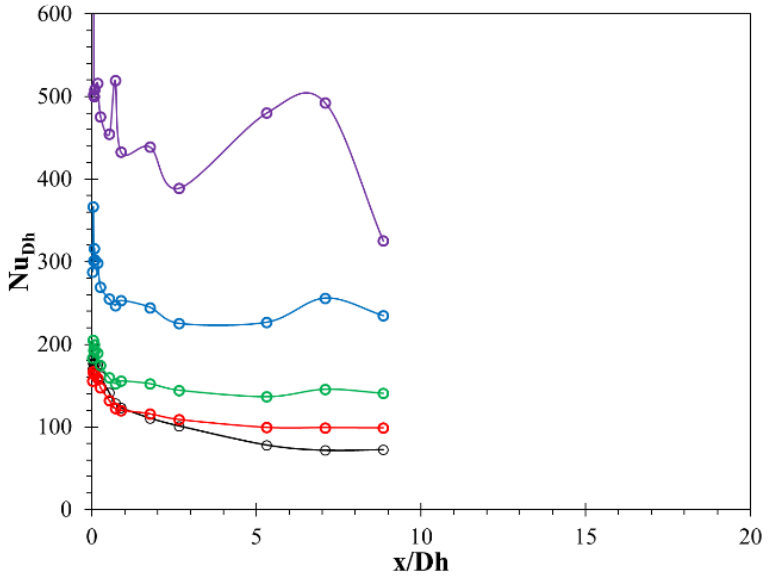

Marker	ω (rpm)	Re_{φ}	Re_{Dh}
	0	0	10447
	100	10211	10464
	200	20022	10436
	400	39996	10071
	800	80158	10061

(b) $\Delta r/r_1 = 0.1$, $Re_{Dh,avg} = 10296$

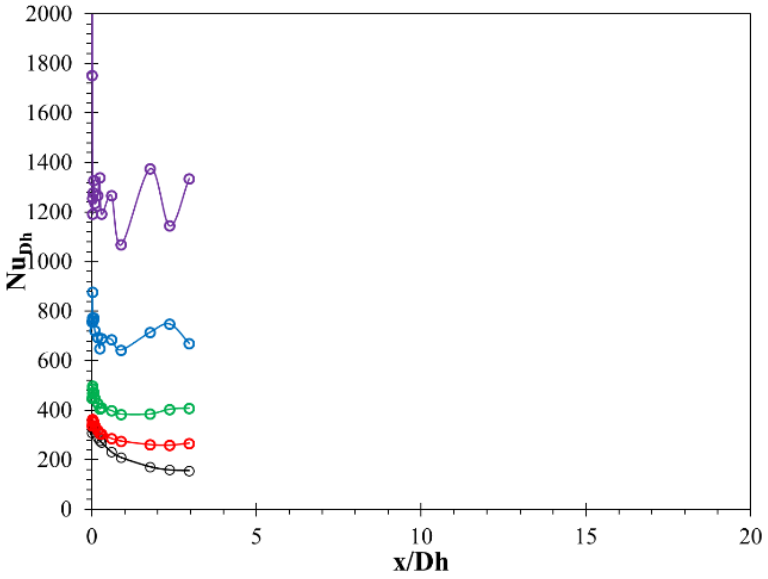

Marker	ω (rpm)	Re_{φ}	Re_{Dh}
	0	0	9866
	100	29960	9901
	200	59668	9766
	400	119260	9945
	800	237911	9862

(c) $\Delta r/r_1 = 0.3$, $Re_{Dh,avg} = 9868$

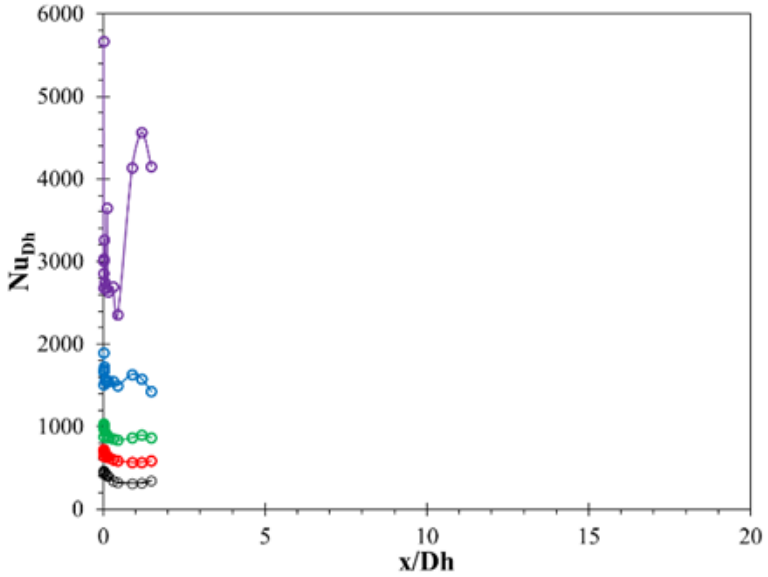

Marker	ω (rpm)	Re_{φ}	Re_{Dh}
	0	0	9795
	100	60131	9807
	200	120448	9533
	400	240530	9856
	800	480949	9827

(d) $\Delta r/r_1 = 0.6$, $Re_{Dh,avg} = 9764$

Figure 4-17 Annular Duct Axial Heat Transfer Distribution Normalized by Hydraulic Diameter

4.2.2 Investigation of Fully Developed Heat Transfer

The average Nusselt number in the fully developed region was taken as the average of local Nusselt numbers (equation (8)) from x/L = 0.54 and x/L = 0.72. Figure 4-18 compares the data at stationary flow conditions with that of correlations and experimental data from the literature review. The data from the $\Delta r/r_1 = 0.05$ test case lie within the 10% uncertainty when compared to the Dittus-Boelter correlation. The data from the other $\Delta r/r_1 = 0.05$ cases are higher than the correlations from literature however this is due to the heat transfer in annulus with larger radius ratios having higher heat transfer [6]. Since the Rotational parameters are not comparable, only the stationary data can be investigated to see the effect of radius ratio. Comparing the Nusselt number for the $\Delta r/r_1 = 0.05$ and $\Delta r/r_1 = 0.6$ cases, at Re_{Dh} approximately at 40,000 the Nusselt Number can increase by up to 520%.

Table 4-9 Legend Key for Figure 4-18 ~ Figure 4-19 & Figure 4-22 ~ Figure 4-23

Marker	$\Delta r/r_1$	ω (rpm)	Re_φ	Marker	$\Delta r/r_1$	ω (rpm)	Re_φ
	0.05	0	0		0.3	0	0
		100	5125			100	10211
		200	10228			200	20022
		400	20430			400	39996
		800	40929			800	80158
	0.1	0	0		0.6	0	0
		100	29960			100	60131
		200	59668			200	120448
		400	119260			400	240530
		800	237911			800	480949

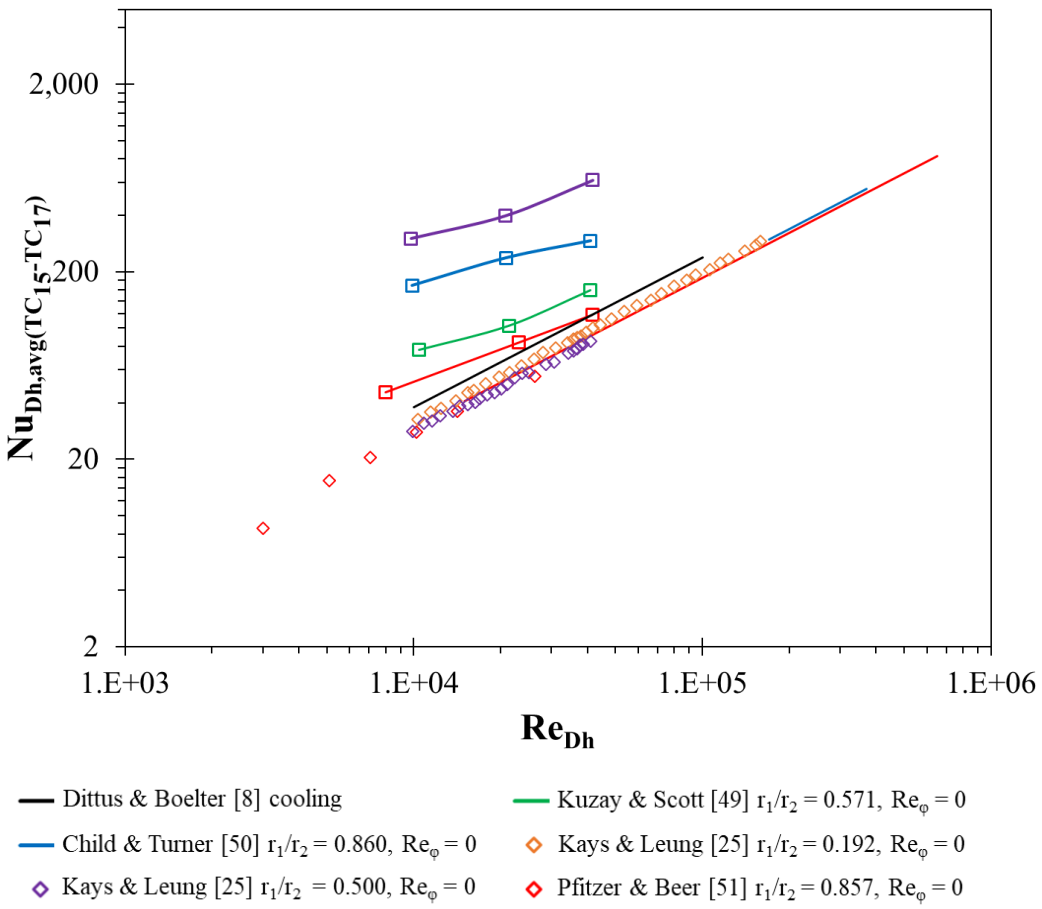

Figure 4-18 Stationary Heat Transfer Comparison for Annular Duct (Refer to Table 4-9)

Several of the experiments, especially with ω = 400 and ω = 400 showed the possible onset of Taylor vortices and therefore the fully developed condition cannot be claimed. However, since most passages in the turbine air system have short L/D_h the experimental data still proves valuable in providing information on the trends in heat transfer. Therefore, the experimental data was still included even if the fully developed condition cannot be claimed. In Figure 4-19, the effect of rotation can be seen as the formation of Taylor vortices enhances the heat transfer. The maximum increase in Nusselt number can be seen when at the $\Delta r/r_1 = 0.6$ case at the $Re_{Dh} = 9764$. Here the Nusselt number can be seen increasing by 380%. For the $\Delta r/r_1 = 0.05$ case the Nusselt Number increased by a factor of 160% when $Re_{Dh} = 7792$. It is also noted however, as the rotation speed increases, the slope of the trendline of the data decreases. For the $\Delta r/r_1 = 0.6$ case at the $Re_{Dh} = 41689$ the Nusselt Number increase only by 180% rather than increase of 380% at $Re_{Dh} = 9764$.

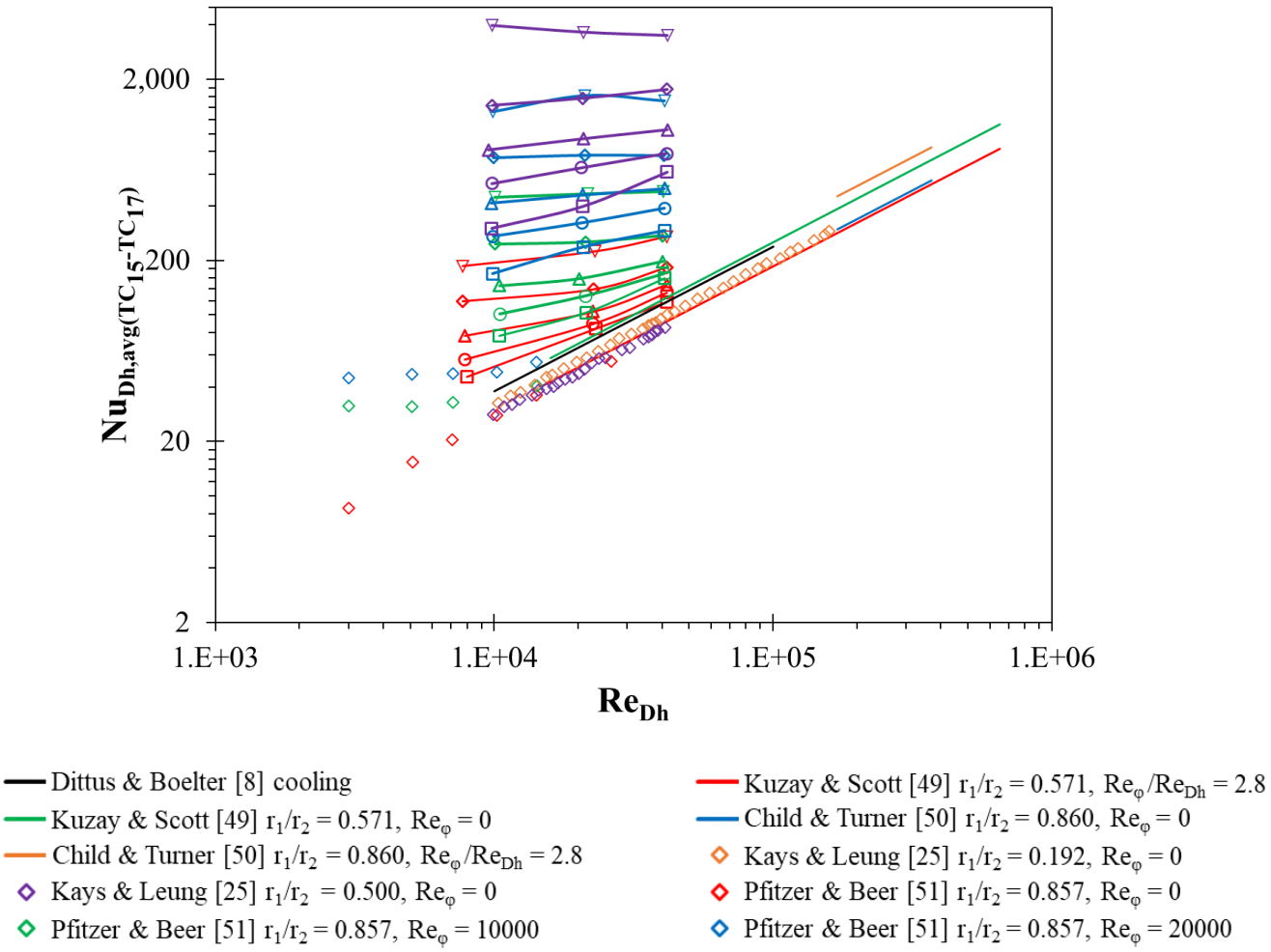

Figure 4-19 Stationary & Rotational Heat Transfer Comparison for Annular Duct (Refer to Table 4-9)

Figure 4-20 compares the Nusselt number with the modified Taylor number, this modified Taylor number is offset by a geometric factor which removes effect of the radius ratios which is reflected as data with differing radius ratios still having similar values of Nusselt number at similar Ta^2/Fg. Here only the effect of rotation and axial flow can be seen where at the lower Taylor numbers, there is more variation in the Nusselt number as the axial Reynold's number increases, however at the maximum Ta shown in the figure, the Nusselt number is almost identical for the three different axial Reynold's number. Additionally, when comparing the absolute value of the present study with that of the Childs & Long correlation [42], the absolute values are higher.

However, this is because the Childs & Long correlation [42] does not account for axial flow. Gilchrist [58] showed that the presence of axial flow superimposed to the rotational causes the Nusselt number to increase. While the absolute values differ, the trend is similar

Table 4-10 Legend Key for Figure 4-20 ~ Figure 4-21

Marker	$\Delta r/r_1$	Re_{Dh}	Marker	$\Delta r/r_1$	Re_{Dh}
	0.05	7792		0.3	9868
		22771			20934
		41657			40828
	0.1	10296		0.6	9764
		21128			20767
		40488			41689

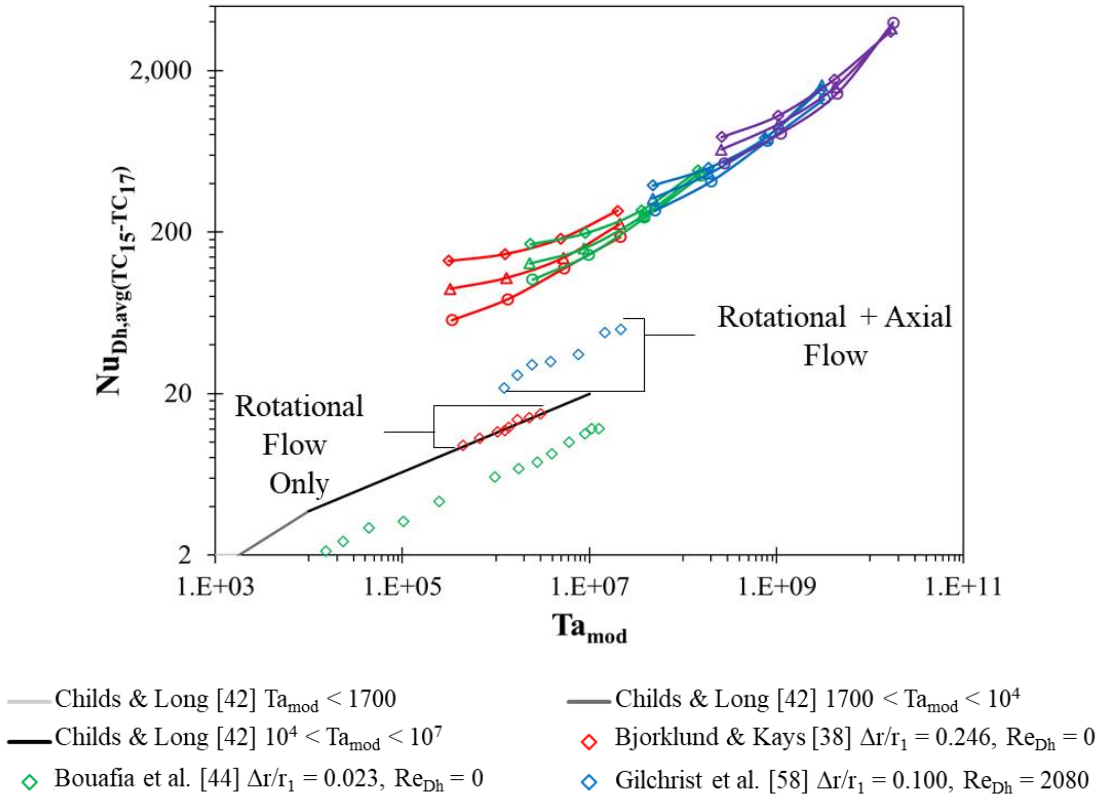

Figure 4-20 Heat Transfer Comparison for Annular Duct with the effect of rotation (Refer to Table 4-10)

In Figure 4-21, at first glance the data does seem very scattered however, similar to the experimental data from literature, the data in the present study shows variation based on whether the forced convection or natural convection is dominant. For the $\Delta r/r_1 = 0.05$ and $\Delta r/r_1 = 0.1$ cases, the forced convection is mostly dominant resulting in the slope of the trendline being more vertical while for the $\Delta r/r_1 = 0.3$ and $\Delta r/r_1 = 0.6$, the natural convection due to rotation is dominant resulting in the trendline being more horizontal. When the data is grouped by fixed Re_{Dh} the data does not follow the trend set by the correlations and data from literature. However, if the data is grouped by fixed Re_ϕ the data does seem to follow the trends.

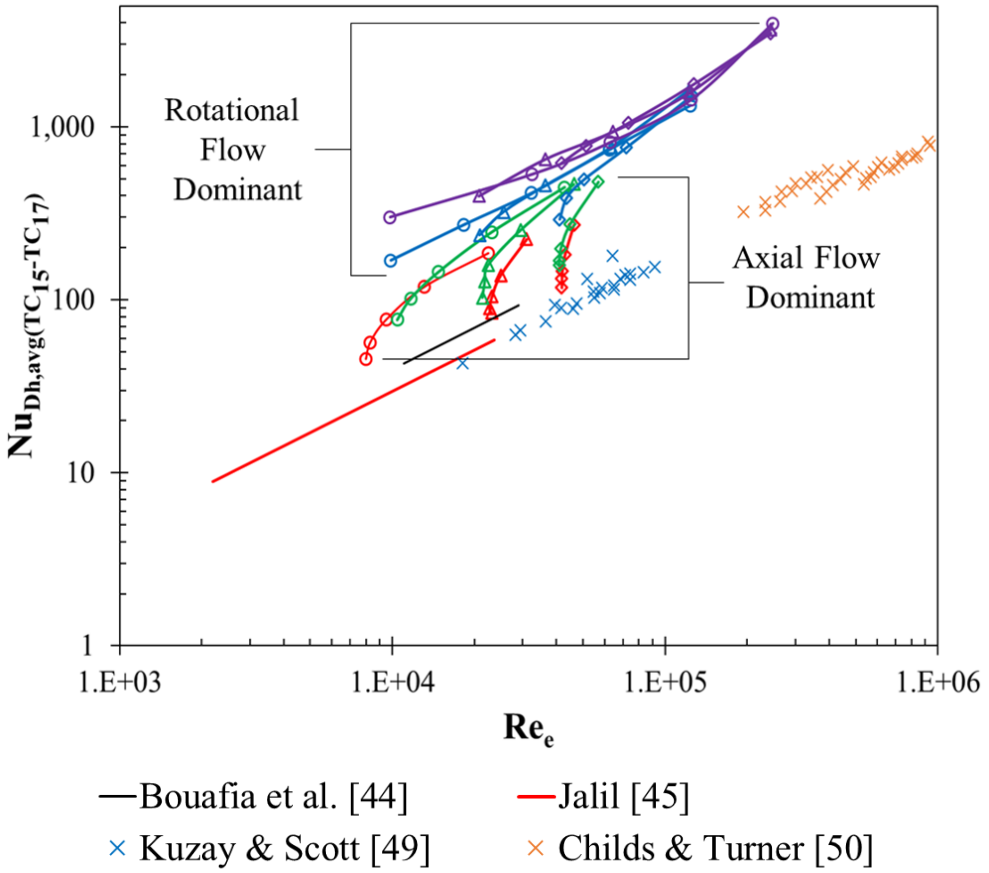

Figure 4-21 Heat Transfer Comparison Annular Duct with effect of Combined Axial and Rotational Flow (Refer to Table 4-10)

After the initial sets of tests, repeated tests were conducted for the $\Delta r/r_1 = 0.05$ case. This was to verify the accuracy of the data and to expand the Re_{Dh} to as much as possible. Figure 4-22

shows the results of the repeated tests. The data shows excellent repeatability with the maximum difference being less than 10%. The extended Re_{Dh} data shows good agreement with the correlations from literature. Lastly, one additional repeated test was conducted. However, for this test, no heat was applied to the heater assembly on the stator. The results show that the heat from the stator did not have any significant effect on the heat transfer of the rotor.

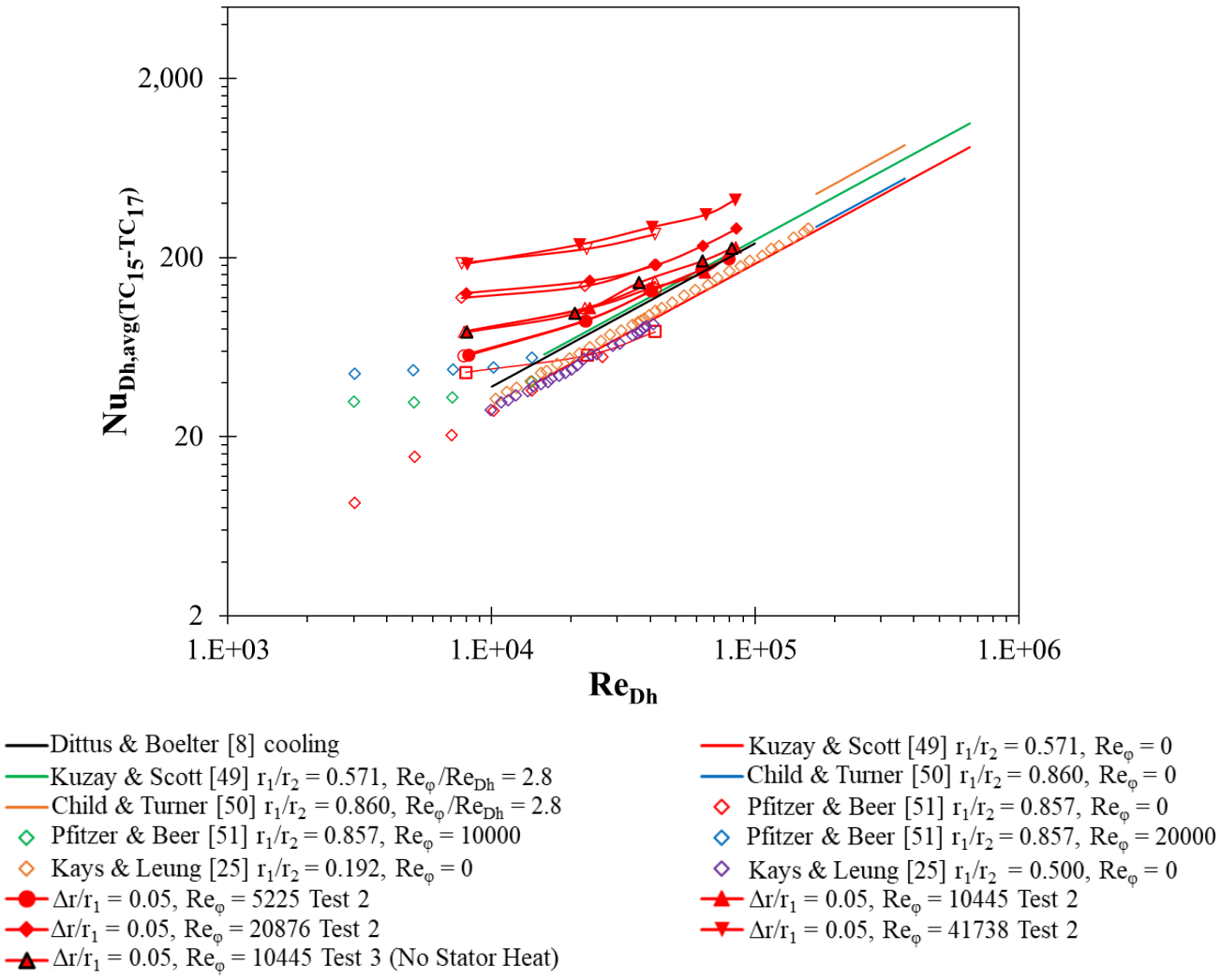

Figure 4-22 Repeated Tests for $\Delta r/r_1 = 0.05$ (Refer to Table 4-9)

4.2.3 Investigation of Overall Pressure Loss

In Figure 4-23 the friction factors (equation (9)) of the experimental data are compared correlations and data from literature. The friction factor in the present data is higher than the data from literature. This is possibly due to the short L/D_h ducts having more swirling as mentioned by Shechuk & Khalatov [36]. Additionally, compared to the Colebrook equation, the data here includes the entry loss which resulted in the friction factor of the present study being higher than that of the Colebrook equation. Figure 4-23a show the overall summary while Figure 4-23b shows the data reduced to include only the reliable data. The results of the study showed that, similar to the experimental data from literature, the friction factor decreases with Re_{Dh} and approaches a plateau. The present study shows that this plateau occurs somewhere near when $Re_{Dh} > 4x10^4$. It can also be observed that the effect of rotation is greater at lower Re_{Dh} where the results of the $\Delta r/r_1 = 0.05$ experiment show an increase of friction factor by 50% at $Re_{Dh} = 7792$ comparing the stationary and $Ta_{mod} = 5.2x10^6$ cases. However, when $Re_{Dh} = 41657$, the friction factor is almost identical. Comparing the radius ratios, the friction factor increases by 40% comparing the $\Delta r/r_1 = 0.05$ and $\Delta r/r_1 = 0.1$ cases for the stationary data.

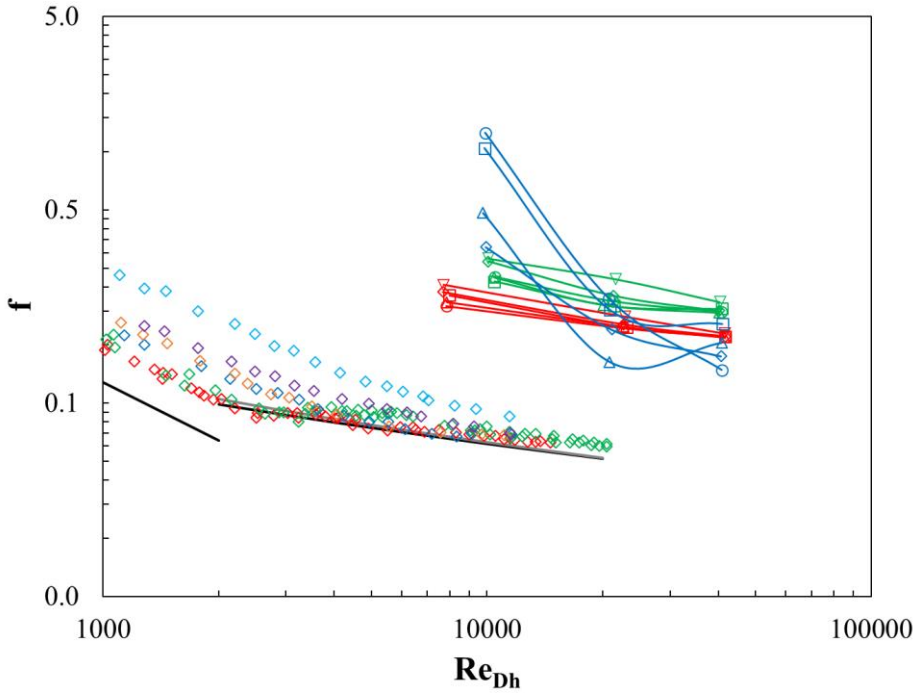

(a) All Experimental Data

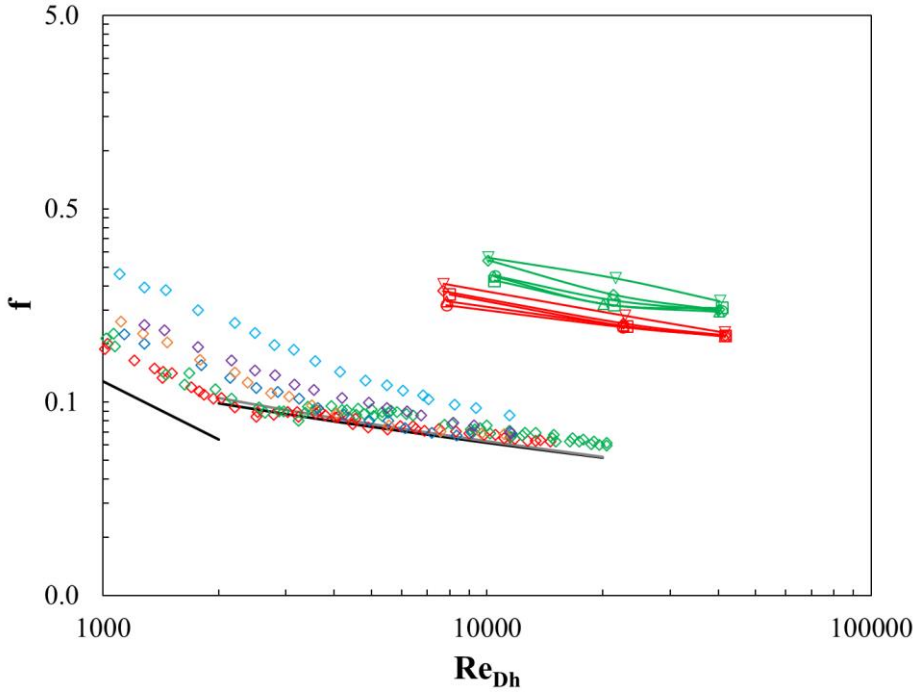

(b) Reduced to Data with Reliable Pressure Measurements

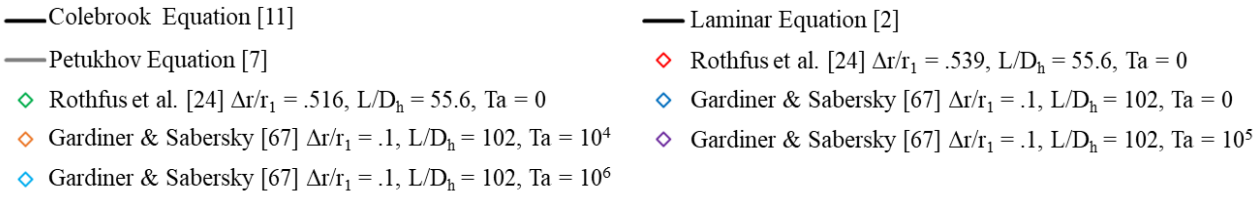

Figure 4-23 Pressure Loss Comparison for Annular Duct (Refer to Table 4-9)

Chapter 5 Conclusion

The heat transfer and pressure loss characteristics of the two passages have been investigated experimentally. A realistic S-shaped model of the passage between the turbine blade root and disc has been tested along with simplified rectangular models rotating about a parallel axis. The passage between a turbine disc and shaft has also been modeled as an annular duct with inner surface rotation.

5.1 Parallel Mode Rotation of Realistic S-shaped and Simplified Rectangular Duct

Flow through a realistic S-shaped model of the passage between turbine blade and disc was investigated along with simplified rectangular models with aspect ratios of 17.33, 8.81, 3.93, and 2.02. Effect of rotation and cross-sectional geometry was of focus in the study. The experiments were conducted with both counterclockwise and clockwise rotation to account for the pressure side and suction side of the passage. The centerline Nusselt number distribution was measured and checked to see if the flow reached a fully developed condition. The AR = 8.81, 17.33 and realistic S-shape test cases all had L/D_h greater than 10 and showed fully developed behavior. The fully developed data was compared to correlations and experiments from past literature. The study showed the following conclusions.

Centerline Characteristics

- The entrance length increases due to effect of rotation as the Coriolis forces skews the boundary layers, making it take longer for the boundary layers to converge.
- The realistic S-shaped duct had less heat transfer compared to the simplified rectangular duct because the complex geometry provided less air flow near the centerline than compared to a rectangular duct.
- Higher aspect ratios had smaller cross-sectional areas and thus larger L/D_h which provided sufficient length to reach fully developed conditions.
- In clockwise rotation (trailing wall) heat transfer is slightly higher as the Coriolis forces push the flow in a manner in which the radial temperature gradient is favored towards the

leading wall thus having slightly lower temperatures near the trailing wall producing higher heat transfer.

Fully Developed Characteristics

- Coriolis forces induce secondary flow which mixes the flow enhancing heat transfer in the fully developed region.
- Experimental data suggests that the correlations for rectangular ducts cannot be used for the realistic S-shaped due to the complex geometry producing different heat transfer behavior but this may be due to only the centerline Nusselt numbers being measured.
- The Nusselt number is shown to be higher at lower aspect ratios due to the cross-sectional areas not being constant however, the heat transfer is higher in higher aspect ratios due to the cross-sectional areas being larger and therefore more energy from the rotation is required to mix the flow to enhance heat transfer.
- The effect of rotation direction is minor on the fully developed heat transfer as the flow is well mixed as the boundary layers have converged.
- The effect of rotation increases the pressure loss as the increased swirling increases the resistance to the flow due to friction.
- The realistic S-shape and AR = 17.33 tests showed similar results with the difference being less than 10% due to the pressure measurements being an average of pressure sensors at opposite ends of the duct suggesting that if the average heat transfer was recorded the values would also be similar.
- The rotation direction did not show any effect as the pressure loss was taken as the average of the cross-section.

5.2 Annular Duct with Inner Surface Rotation

An annular duct was constructed to model real engine application with a sharp entrance and short L/D_h. The effect of rotation was studied for four different radius ratios of 0.05, 0.1, 0.3. and 0.6. Even though the L/D_h where shorted than the expected value of 10, fully developed behavior was seen possibly due to the smaller cross-sectional area allowing the boundary layers to converge quicker. The following conclusions are made after the study

Centerline Characteristics

- The onset of Taylor vortices in regions where the flow should be fully developed mixes the flow causing the Nusselt number to increase in these regions.
- Higher radius ratios had larger cross-sectional areas and thus larger L/Dh which shorter than typical values for fully developed condition, however compared to a circular pipe the cross-sectional areas are smaller meaning the boundary layer converges faster and fully developed behavior can be seen.

Fully Developed Characteristics

- Taylor vortices induce mixing enhancing the heat transfer however, when the rotational flow is dominant, the Nusselt number increases less with increasing axial Reynolds number
- The Nusselt number is shown to be higher at higher aspect ratios due to the cross-sectional areas not being constant however, the heat transfer is higher in lower aspect ratios due to the cross-sectional areas being smaller and therefore less energy from the rotation is required to mix the flow to enhance heat transfer.
- The effect of rotation increases the pressure loss as the increased swirling increases the resistance to the flow due to friction.
- The larger radius ratio showed higher friction factor due to the larger hydraulic diameter producing higher numbers for friction factor however in reality there is more resistance to the flow in the lower radius ratios due to the smaller cross-sectional area.

5.3 Future Work

As the present study showed that the heat transfer characteristics of the realistic S-shaped model are different from the rectangular duct even with similar hydraulic diameters additional study on this model can prove beneficial. For instance, in this study only the bottom wall of the model was heated. Studies with all four walls heated would produces insightful data however, to record data along all four walls is almost non-feasible currently as the rotating environment presents a challenge in installing sufficient sensor to measure the heat transfer. Similarly, for the annular duct, only a small section of the rotor was heated. Additional study can be performed

heating the whole rotor surface. Investigation on the heat transfer on the stator could also be conducted. Furthermore, for the annular duct, the turbine blade disc rotates with the shaft. Investigation of heat transfer with co-rotating can provide more accurate heat transfer data. Lastly, numerical investigation using CFD would also help further explain the results of the experiments.

References

[1] M. Wilson, R. Pilbrow, J. M. Owen, "Flow and Heat Transfer in a Preswirl Rotor - Stator System," *ASME Journal of Turbomachinery,* vol. 119, pp. 364-373, 1997.

[2] W. D. Moris, J. L. Woods, "Heat Transfer in the Entrance Region of Tubes that Rotate about a Parallel Axis," *Journal Mechanical Engineering Science,* vol. 20, no. 6, pp. 319-325, 1978.

[3] P. R. N. Childs, Rotating Flow, Butterworth-Heinemann, 2011.

[4] G. Taylor, "Stability of a Viscous Iiquid Contained Between Two Rotating Cylinders," *Philosophical Transactions, Royal Society (London), series A,* vol. 223, p. 289, 1923.

[5] B. Metais, E. R. G. Eckert, "Forced, Mixed, and Free Convection Regimes," *ASME Journal of Heat Transfer,* vol. 86, no. 2, pp. 295-296, 1964.

[6] T. L. Bergman, A. S. Lavine, F. P. Incropera, D. P. Dewitt, Fundamentals of Heat and Mass Transfer, Danvers, Ma: John Wiley & Sons, Inc, 2002.

[7] P.M. Gerhart, A. L. Gerhart, J. I. Hochstein, Munson, Young, and Okiishi's Fundamentals of Fluid Mechanics, Danvers: John Wiley & Sons Inc, 2016.

[8] F. W. Dittus, L. M. K. Boelter, "Heat Transfer in Automobile Radiators of the Tubular Type," *University of California Press, Berkeley, University of California Publications in Engineering,* vol. 2, pp. 443-461, 1930.

[9] B. S. Petukhov, "Heat Transfer and Friction in Turbulent Pipe Flow with Variable Physical Properties," Academy of Science of the USSR, Moscow, 1970.

[10] V. Gneilinski, "Neue Gleichungen für den Wärme- und den Stoffübergang in turbulent durchströmten Rohren und Kanälen," *Forsch. Ing.-Wes.,* vol. 41, pp. 8-16, 1975.

[11] D. Taler, "A New Heat Transfer Correlation for Transition and Turbulent Fluid Flow in Tubes," *International Journal of Thermal Sciences,* vol. 108, pp. 108-122, 2016.

[12] S.C. Lau, E.M. Sparrow, J.W. Ramsey, "Effect if Plenum Length and Diameter on Turbulent Heat Transfe in a Downstream Tube and on Plenum-Related Pressure Losses," *ASME Journal of Heat Transfer,* vol. 103, pp. 415-422, 1981.

[13] L. F. Moody, "Friction Factors for Pipe Flow," *Transactions of the A.S.M.E.*, pp. 671-684, 1944.

[14] C. F. Colebrook, "Turbulent Flow in Pipes, with Particular Reference to the Transition Region between the Smooth and Rough Pipe Laws," *Journal of the Institution of Civil Engineers*, vol. 11, pp. 133-156, 1939.

[15] R. K. Shah, A. L. London, Laminar Flow Forced Convection in Ducts, New York: Academic Press, Inc., 1978.

[16] F. W. Schmidt, M. E. Newell, "Heat Transfer in Fully Developed Laminar Flow Through Rectangular and Isosceles Triangular Ducts," *International Journal of Heat & Mass Transfer*, vol. 10, pp. 1121-1123, 1966.

[17] C. Y. Wang, "Mixed H1 and H2 Forced Convection in a Retangular Duct," *ASME Journal of Heat Transfer*, vol. 140, no. 3, 2018.

[18] E. M. Sparrow, J. R. Lloyd, C. W. Hixon, "Experiments on Turbulent Heat Transfer in an Asymmetrically Heated Rectangular Duct," *ASME Journal of Heat Transfer*, vol. 88, no. 2, pp. 170-174, 1966.

[19] J. R. Shen, Z. Wang, P. T. Ireland, T. V. Jones, A. R. Byerley, "Heat Transfer Enhancement Within a Turbine Blade Cooling Passage Using Ribs and Combination of Ribs with Film Colling Holes," *ASME Journal of Turbomachinery*, vol. 118, pp. 428-434, 1996.

[20] C. L. P. Tsang, *High Blockage Turbulators in Gas Turbine Cooling Passages (Ph.D. Thesis)*, Department of Engineering Science, University of Oxford, 2002.

[21] L. B. Wang, Q. W. Wang, Y. L. He, W. Q. Tao, "Experimental and Numerical Study of Developing Turbulent Flow and Heat Transfer in Convergent/Divergent Square Ducts," *Heat and Mass Transfer*, vol. 38, pp. 399-408, 2002.

[22] M. A. Smith, *Heat Transfer for High Aspect Ratio Rectangular Channels in a Stationary and Rotating Serpentine Passage with Turbulated and Smooth Surfaces (Thesis)*, 2012.

[23] A. Roberts, H. Barrow, "Turbulent Heat Transfer to Air in the Vicinity of the Entry of an Iternally Heated Annulus," *Proc Instn Mech Engrs*, vol. 68, pp. 268-276, 1967.

[24] R. R. Rothfus, C. C. Monrad, V. E. Senecal, "Velocity Distribution and Fluid Friction in Smooth Concentric Annuli," *Industrial and Engineering Chemistry,* vol. 42, no. 19, pp. 2511-2520, 1950.

[25] W. M. Kays, E. Y. Leung, "Heat Transfer in Annular Passages- Hydrodynamically Delevloped Turbulent Flow with Arbitrarily Prescribed Heat Flux," *International Journal of Heat and MassTransfer,* vol. 6, pp. 537-557, 1963.

[26] H. Barrow, "Fluid Flow and Heat Transfer in an Annulus with a Heated Core Tube," *Proceedings of the Institution of Mechanical Engineers,* vol. 169, no. 1, pp. 1113-1124, 1955.

[27] Y. Mori, W. Nakayama, "Forced Convection Heat Transfer in a Straight Pipe Rotating Around a Parallel Axis," *International Journal of Heat and Mass Transfer,* vol. 10, pp. 1179-1194, 1967.

[28] J. L. Woods, W. D. Morris, "An Investigation of Laminar Flow in the Rotor Windings of Directly-Cooled Electrical Machines," *Journal of Mechanical Engineering Science,* vol. 16, no. 6, pp. 408-417, 1974.

[29] S. Neti, A. S. Warnock, E. K. Levy, K. S. Kannan, "Computation of Laminar Heat Transfer in Rotating Rectangular Ducts," *ASME Journal of Heat Transfer,* vol. 107, pp. 575-582, 1985.

[30] W. D. Morris, F. M. Dias, "Turbulent Heat Transfer in a Revolving Square-Sectioned Tube," *Journal Mechanical Engineering Science,* vol. 22, no. 2, pp. 95-101, 1980.

[31] E. Levy, S. Neti, G. Brown, F. Bayat, V. Kadambi, "Laminar Heat Transfer and Pressure Drop in a Rectangular Duct Rotating about a Parallel Axis," *ASME Journal of Heat Transfer,* vol. 108, pp. 350-356, 1986.

[32] P. Hanafizadeh, S. Karbalaee M, R. Attarpour, M, Ashjee, "A Criterion for the Effect of Parallel Mode Rotation on Non-isothermal Flow Though Square Channel," *International Journal of Heat and Mass Transfer,* vol. 139, pp. 343-350, 2019.

[33] H. Mori, R. Shiobara, K. Hattori, "Heat Transfer Characteristic of a Rectangular Channel Rotating on a Parallel Axis (1st Report, Study on Flow and Heat Transfer Charateristics of a

Large Rotating Electrical Machine)," *Trans Japan Soc. Mech. Engrs,* vol. 66, no. 650, pp. 138-142, 1999.

[34] A. Sleiti, J. S. Kapat, "Heat Transfer in Channels in Parallel-Mode Rotation at High Rotation Numbers," *Journal of Thermophysics and Heat Transfer,* vol. 20, no. 4, pp. 748-753, 2006.

[35] A. Sarja, P. Singh, S. V. Ekkad, "Parallel rotation for negating Coriolis force effect on heat transfer," *The Aeronautical Journal,* vol. 124, no. 1274, pp. 581-596, 2020.

[36] I. V. Shevchuk & A. A. Khalatov , "Heat Transfer and Hydrodynamics in Straight Channels Rotating about a Parallel or Inclined Axis," *High Temperature,* vol. 34, no. 3, pp. 455-467, 1996.

[37] A. R. Johnson, W. D. Morris, "An Experimental Investigation into the Effects of Rotation on the Isothermal Flow Resistance in Circular Tubes Rotating about a Parallel Axis," *International Journal of Heat and Fluid Flow,* vol. 13, no. 2, pp. 132-140, 1992.

[38] I. S. Bjorklund, W. M. Kays, "Heat Transfer Between Concentric Rotating Cylinders," *ASME. Journal of Heat Transfer,* vol. 81, no. 3, pp. 175-183, 1959.

[39] K. M. Becker, J. Kaye, "Measurements of Diabatic Flow in an Annulus With an Inner Rotating Cylinder," *ASME Journal of Heat Transfer,* vol. 84, no. 2, pp. 97-104, 1962.

[40] K. S. Ball, B. Farouk and V. C. Dixit, "An experimental study of heat transfer in a vertical annulus with a rotating inner cylinder," *International Journal of Heat and Mass Transfer,* vol. 32, no. 8, pp. 1517-1527, 1989.

[41] H Aoki, H. Nohira, H. Arai, "Convective Heat Transfer in an Annulus with an Inner Rotating Cylinder," *Bullentin of JSME,* vol. 10, no. 39, pp. 523-532, 10.

[42] P. R. N. Childs, C. A. Long, "A Review of Forced Convection Heat Transfer in Stationary and Rotating Annuli," *Proceedings of the Institution of Mechanical Engineers, Part C: Journal of Mechanical Engineering Science,* vol. 210, no. 2, pp. 123-134, 1996.

[43] W. M. Abed, A. Al-Demook, W. H. Khalil, "Convective Heat Transfer in an Annulus of Concentric and Eccentric Cylinders with an Inner Rotating Cylinder," *International Journal of Heat and Technology,* vol. 39, no. 1, pp. 61-72, 2021.

[44] M. Bouafia, y. Bertin, J. B. Saulnier, "Analyse experimentale des transferts de chaleur en espace annulaire etroit et rainure avec cylindre interieur tournant," *International Journal of Heat and Mass Transfer*, vol. 41, no. 10, pp. 1279-1291, 1998.

[45] J. M. Jalil, A. O. Hanfash, M. R. Abdul-Mutaleb, "Experimental and Numerical Study of Axial Turbulent Fluid Flow and Heat Transfer in a Rotating Annulus," *Arab J. Sci Eng*, vol. 41, pp. 1857-1865, 2016.

[46] H. K. Dawood, H. A. Mohammed, N. A. C. Sidik, K. M. Munisamy, M. A. Wahid, "Forced, natural and mixed-convection heat transfer and fluid flow in annulus: a review," *International Communications in Heat and Mass Transfer*, vol. 62, pp. 45- 57, 2015.

[47] M. Fenot, y. Bertin, E. Dorignac, G. Lalizel, "A review of heat transfer between concentric rotating cylinders with or without axial flow," *International Journal of Thermal Sciences*, vol. 50, pp. 1138-1155, 2011.

[48] F. Tachibana, S. Fukui, "Convective Heat Transfer of the Rotational and Axial Flow between Two Concentric Cylinders," *Bulletin of JSME,* vol. 7, no. 26, pp. 385-391, 1964.

[49] T. M. Kuzay, C. J. Scott, "Turbulent Heat Transfer Studies in Annulus With Inner Cylinder Rotation," *ASME Journal of Heat Transfer*, vol. 99, no. 1, pp. 12-19, 1977.

[50] P.R.N Childs, A. B. Turner, "Heat Tansfer on the surface of a Cylinder Rotating in an Annulus at High Axial and Rotational Reynolds Number," *Heat Transfer,* vol. 3, pp. 13-18, 1994.

[51] H. Pfitzer & H. Beer, "Heat Transfer in an Annulus Between Independently Rotating Tubes with Turbulent Axial Flow," *International Journal of Heat and Mass Transfer*, vol. 35, no. 3, pp. 623-633, 1992.

[52] S. C. Tzeng, "Heat transfer in a small gap between co-axial rotating cylinders," *International Communications in Heat and Mass Transfer,* vol. 33, pp. 737-743, 2006.

[53] R. Jakoby, S. Kim, S. Wittig, "Correlations of the Convection Heat Transfer in Annular Channels With Rotating Inner Cylinder," *ASME J. Eng. Gas Turbines Power,* vol. 121, no. 4, pp. 670-677, 1999.

[54] K. V. Chalapathi Rao, V. M. K. Sastri, "Heat Transfer in an Annulus with Rotating Inner Cylider," *Chemical Engineering and Processing: Process Intensification,* vol. 26, no. 2, pp. 17-177, 1989.

[55] R. I. El-Ghnam, M. G. Ma=ousa, E. A. Abdel-Hadi, S. H. Taher, H. R. Elthan, "Analysis of Heat Transfer in an Annulus Between Two Horizontal Rotating Cylinders," *7th International Engineering Conference,* pp. 21-33, 2009.

[56] H. Abou-Zinyan, R. Ameen, K. Elsayed, "Fluid flow and convection heat transfer in concentric and eccentric cylindrical annuli of different radii ratios for Taylor-Couette-Poiseuille flow," *Advances in Mechanical Engineering,* vol. 13, no. 8, pp. 1-22, 2021.

[57] T. Yanagida, N. Kawasaki, "Pressure Drop and Heat Transfer Caracteristics of Axial Flow with a Deep-Slotted Outer Cylinder and a Rotating Inner Cylinder," *Transactions of the Japan Society of Mechanical Engineers Series B,* vol. 57, no. 538, pp. 2099-2103, 1991.

[58] S. Gilchrist, C. Y. Ching, D. Ewing, "Heat Transfer Enhancement in Axial Taylor-Couette Flow," *Proceedings of the ASME 2005 Summer Heat Transfer Conference collocated with the ASME 2005 Pacific Rim Technical Conference and Exhibition on Integration and Packaging of MEMS, NEMS, and Electronic Systems. Heat Transfer,* vol. 1, pp. 227-233, 2005.

[59] A. Nouri-Borujerdi, M. E. Nakhchi, "Friction factor and Nusselt number in annular flows with smooth and slotted surface," *Heat and Mass Transfer,* vol. 55, pp. 645-653, 2019.

[60] M. Molki, K.N. Astill, E.Leal, "Convective Heat-Mass Transfer in the Entrance Region of a Concentric Annulus having a Rotating Inner Cylinder," *International Journal of Heat and Fluid Flow,* vol. 11, no. 2, pp. 120-128, 1990.

[61] S. R. M. Gardiner, R. H. Sabersky, "Heat Transfer in an Annular Gap," *International Journal of Heat and Mass Transfer,* vol. 21, no. 1, pp. 1459-1466, 1978.

[62] A. F. Mills, "Experimetal Investigation of Turbulent Heat Transfer in the Entrance Region of a Circular Conduit," *Journal Mechanical Engineering Sciences,* vol. 4, pp. 63-77, 1961.

[63] L.M. Tam, A. J. Ghajar, "The Unusual Behavior of Local Heat Transfer Coefficient in a Circular Tube with a Bell-mouth Inlet," *Experimental Thermal and Fluid Sciences,* vol. 16, pp. 187-194, 1998.

[64] A. J. Ghajar, L. M. Tam, "Heat Transfer Measurements and Correlations in the Transition Region for a Circular Tube with Three Different Inlet Configurations," *Experimental Thermal and Fluid Sciences,* vol. 8, pp. 79-90, 1994.

[65] H. A. Mohammed, "The Effect of Different Inlet Geometries on Laminar Flow Combined Convection Heat Transfer Inside a Horizontal Circular Pipe," *Applied Thermal Engineering,* vol. 29, pp. 581-590, 2009.

[66] *Measurement of fluid flow by means of pressure differential devices inserted in circular cross-section conduits running full BS EN ISO 5167-2,* 2003.

[67] S. J. Kline, F. A. McClintock, "Describing Uncertainties in Single Sample Experiments," *Mechnical Engineering,* vol. 75, pp. 3-8, 1953.

Appendix A: Parallel Mode Rotation Data

Table A-1 Parallel Mode Rotation Test Matrix

ω (rpm)	Rotation Direction	AR = 2.02	AR = 3.93	AR = 8.81	AR = 17.33	Realistic
Stationary	cw & ccw	O	O	O	O	O
50	cw & ccw	O	O	O	O	O
100	cw & ccw	O	O	O	O	O
200	cw & ccw	O	O	O	O	O
400	cw & ccw	O	O	O	O	O
800	cw & ccw	O	O	O	O	O
Re_{Dh}	71 ~ 19032					
Note - cw: Clockwise, ccw: Counter Clockwise (from front view)						

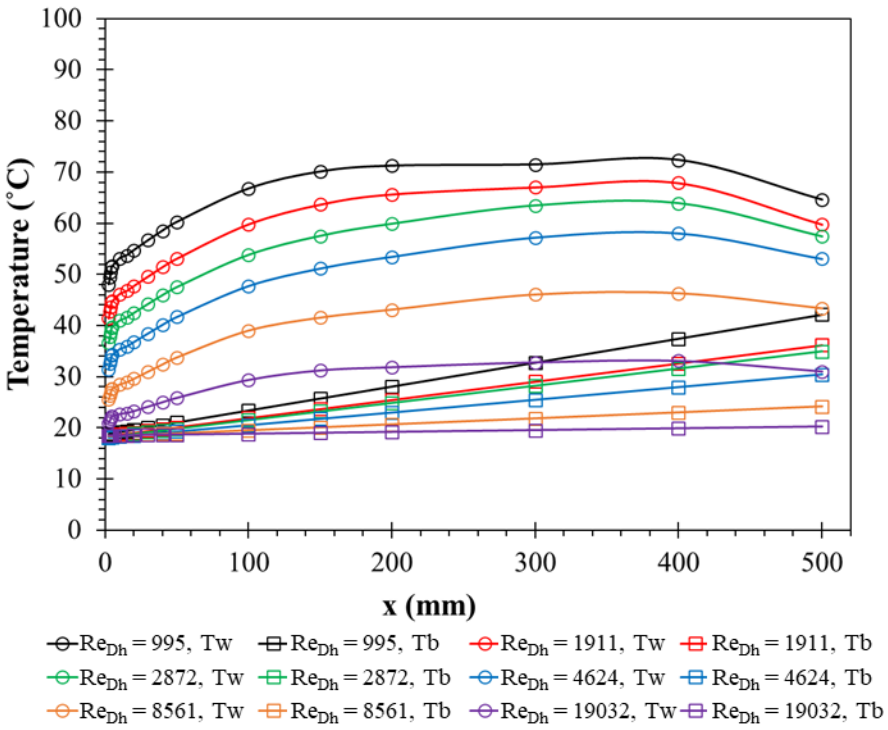

Figure A-1 AR = 2.02 J = 0, 31.4 V, (03/30/21), Temperature Profile

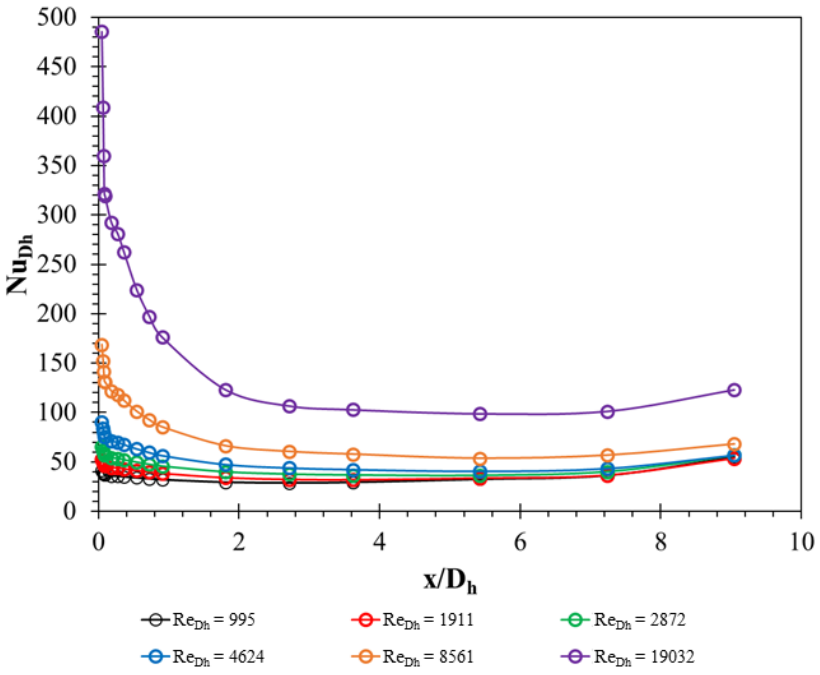

Figure A-2 AR = 2.02 J = 0, 31.4 V, (03/30/21), Nu_{Dh} Profile

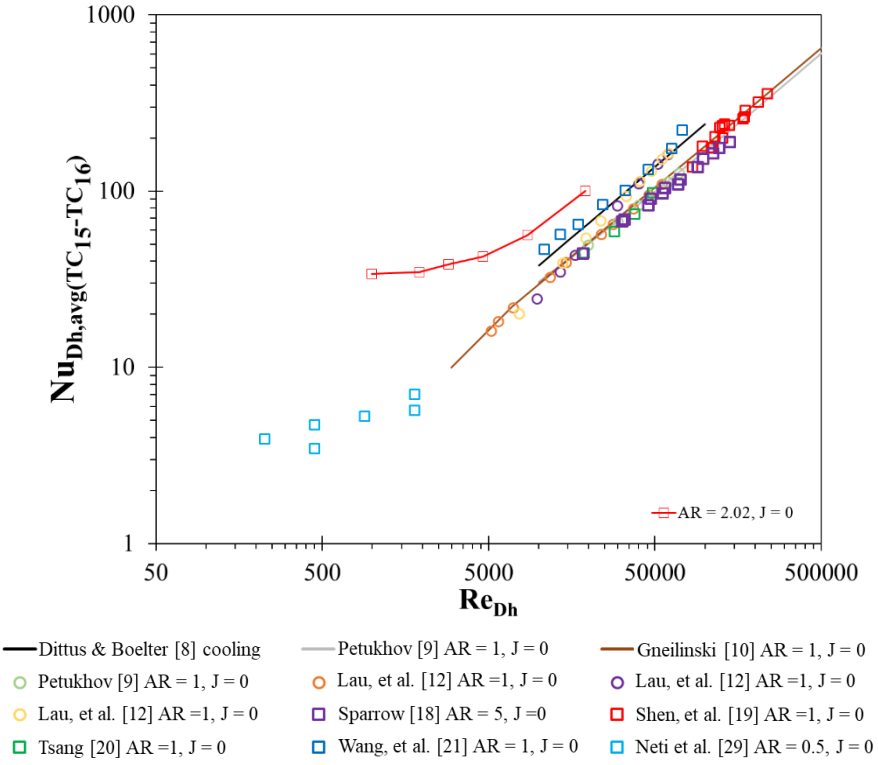

Figure A-3 AR = 2.02 J = 0, Nu_{Dh} vs Re_{Dh}

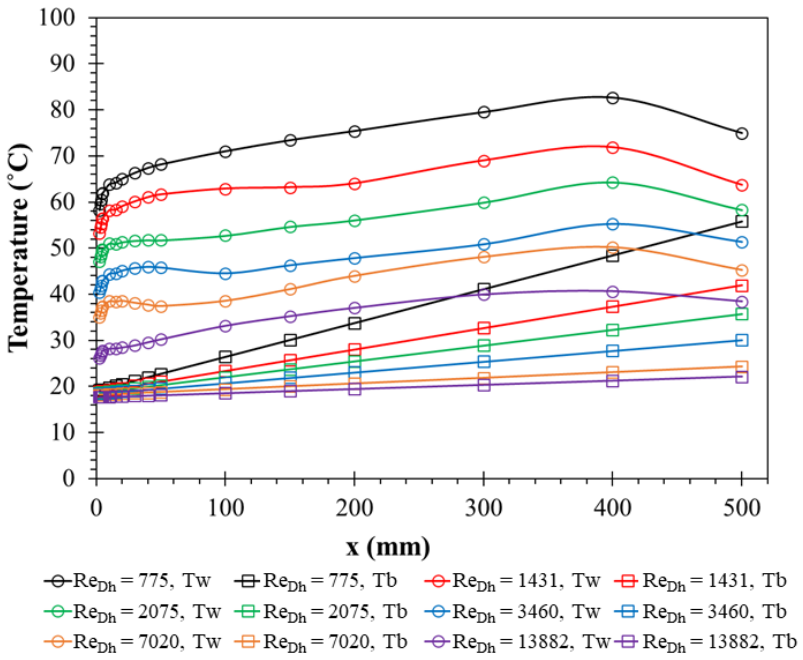

Figure A-4 AR = 2.02, J = 1030 ccw, 35 V, (04/26/21), Temperature Profile

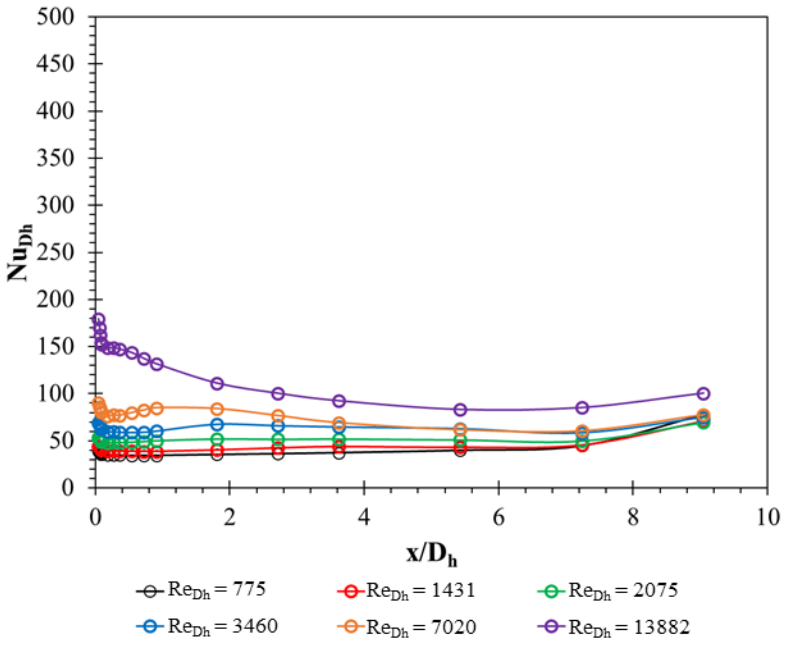

Figure A-5 AR = 2.02, J = 1030 ccw, 35 V, (04,26,21), Nu_{Dh} Profile

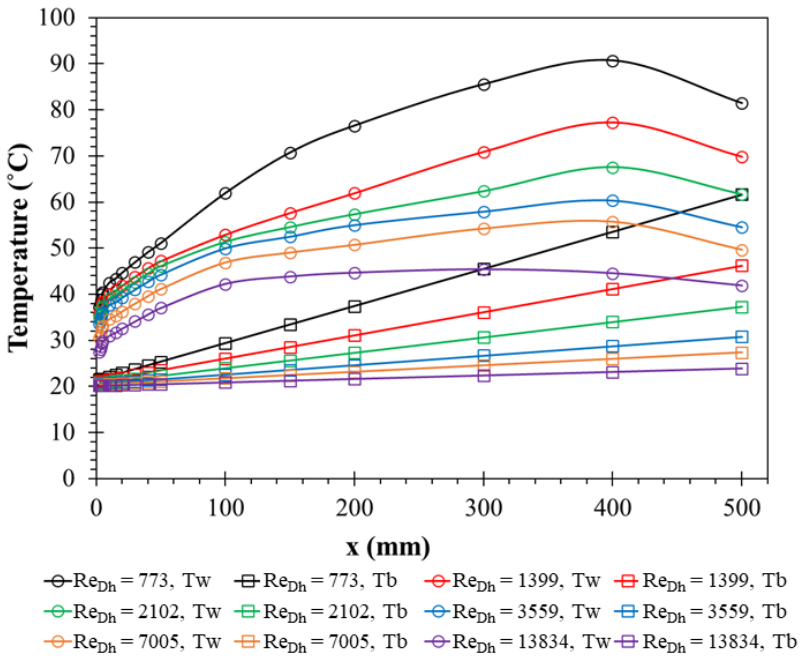

Figure A-6 AR = 2.02, J = 1014 cw, 35 V, (04/26/21) Temperature Profile

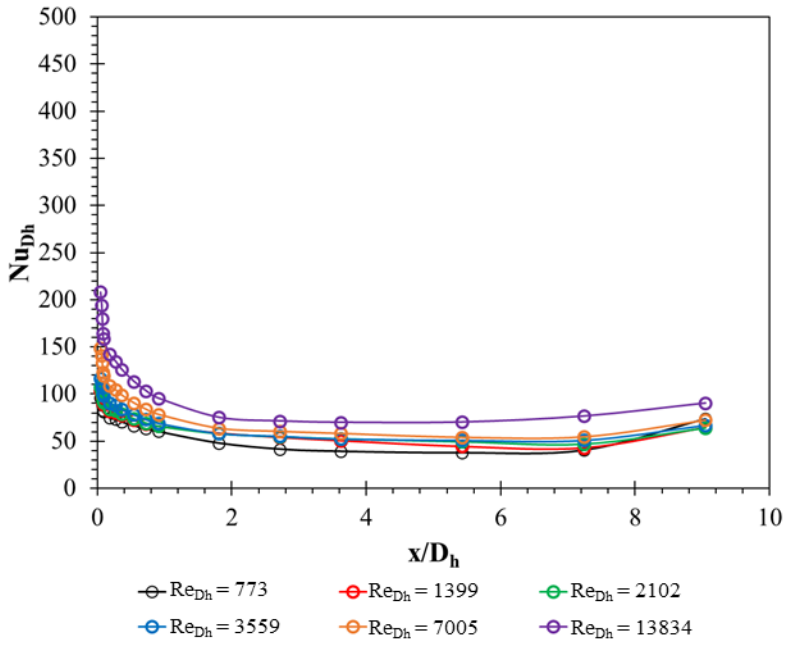

Figure A-7 AR = 2.02, J = 1014 ccw, 35 V, (04/26/21), Nu_{Dh} Profile

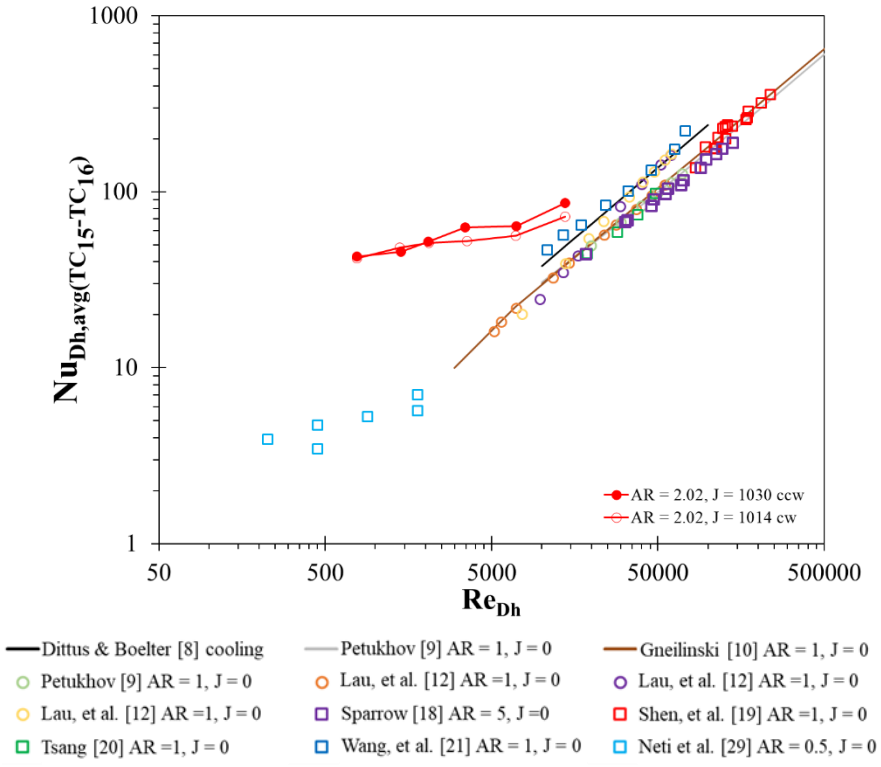

Figure A-8 AR = 2.02, J = 1014 cw, 1030 ccw, Nu_{Dh} vs Re_{Dh}

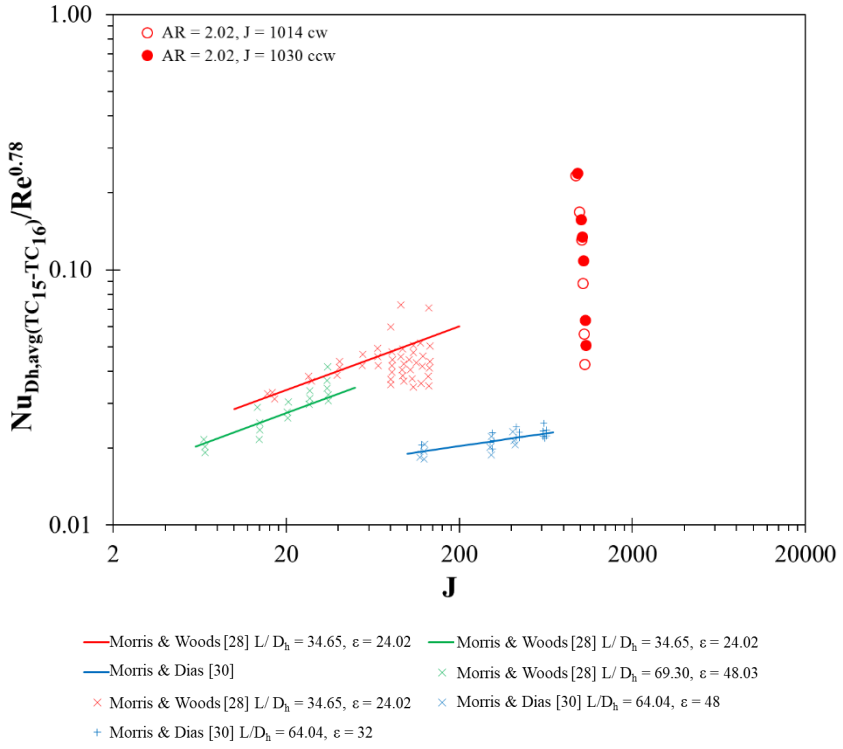

Figure A-9 AR = 2.02, J = 1014 cw, 1030 ccw, Nu_{Dh} vs J

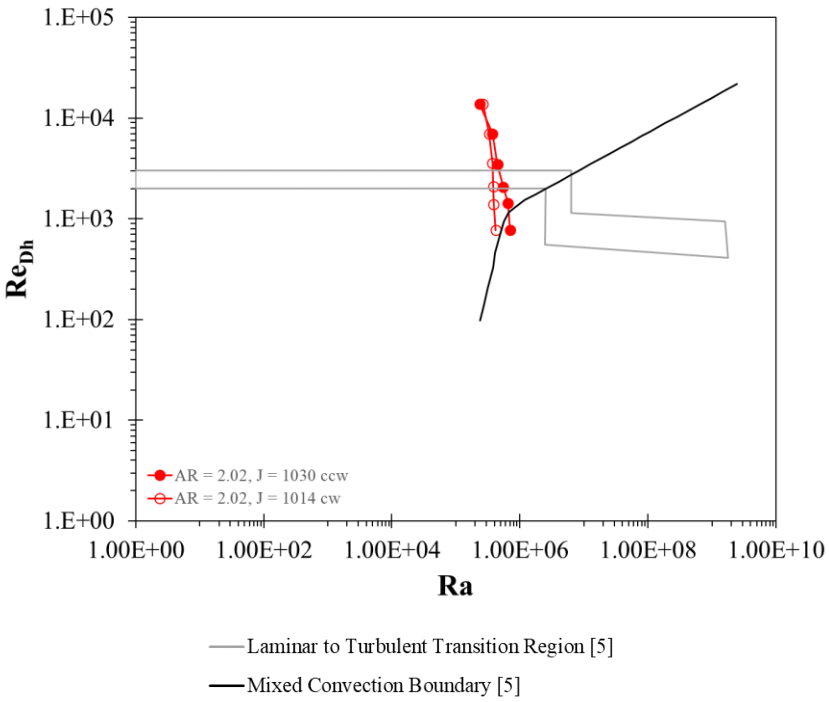

Figure A-10 AR = 2.02, J = 1014 cw, 1030 ccw, Re_{Dh} vs Ra

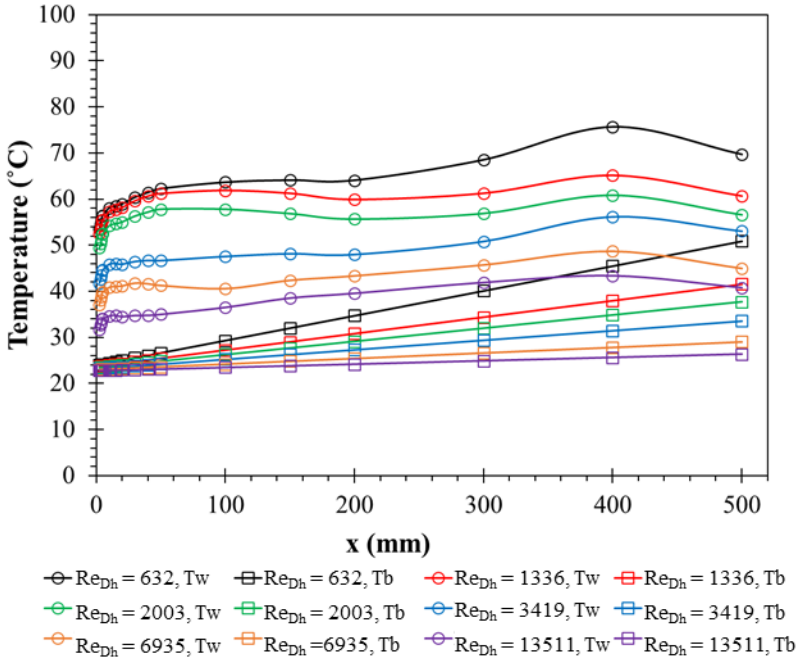

Figure A-11 AR = 2.02, J = 2026 ccw, 35V, (05/26/21) Temperature Profile

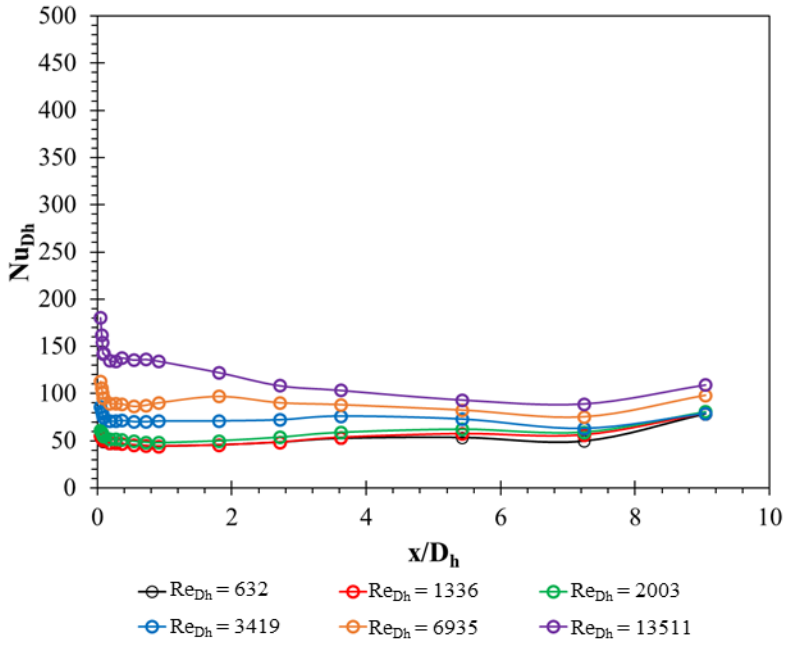

Figure A-12 AR = 2.02, J = 2026 ccw, 35V, (05/26/21), Nu_{Dh} Profile

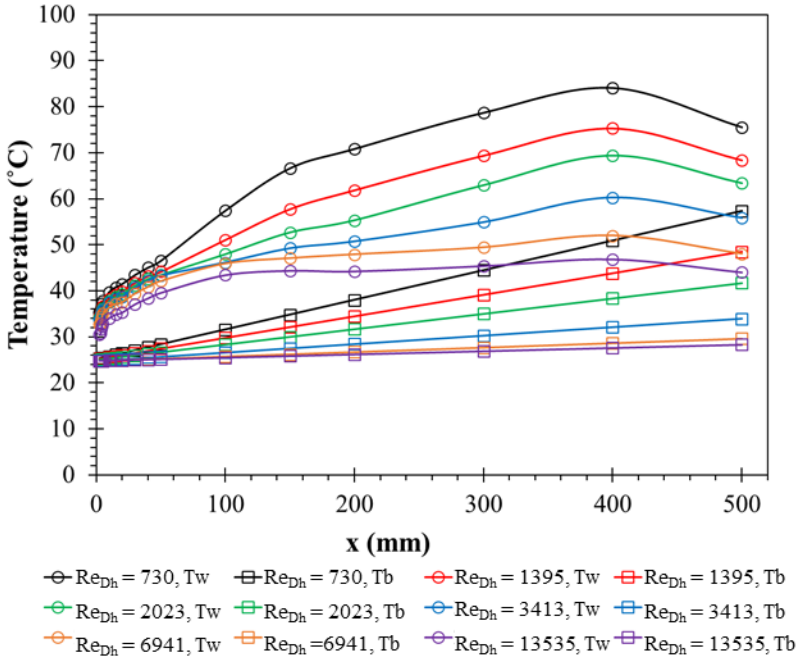

Figure A-13 AR = 2.02, J = 1997 cw, 35V, (05/26/21), Temperature Profile

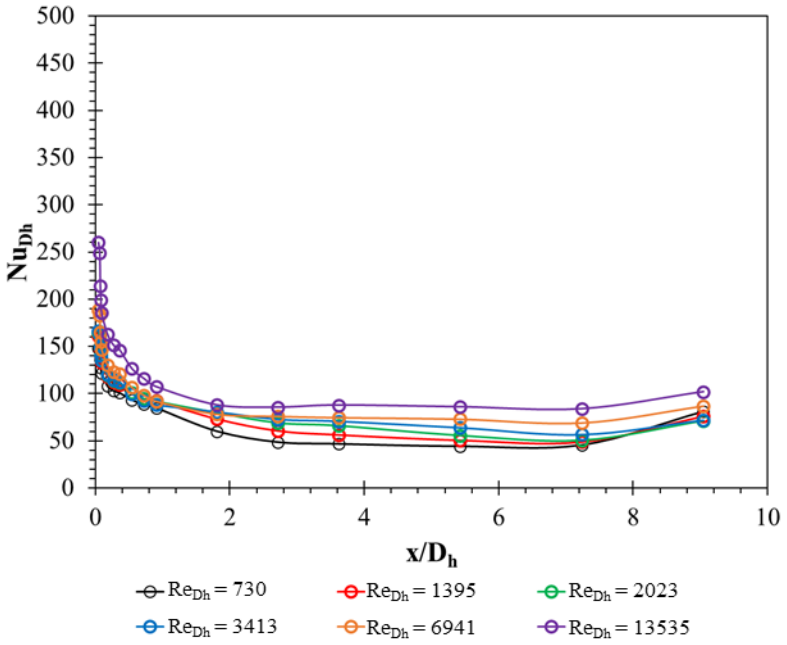

Figure A-14 AR = 2.02, J = 1997 cw, 35V, (05/26/21), Nu_{Dh} Profile

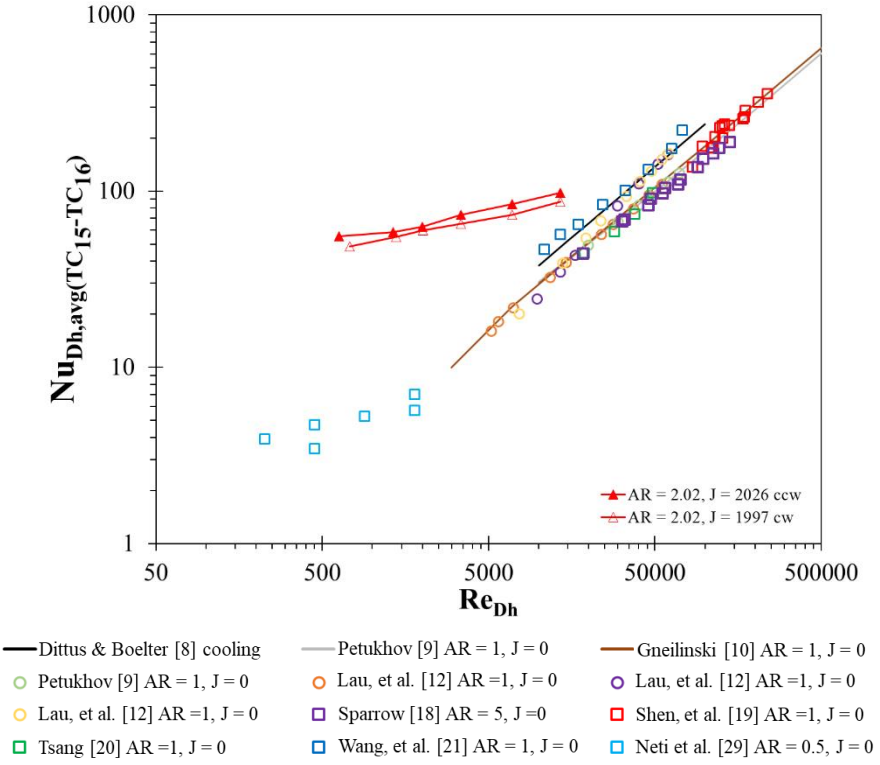

Figure A-15 AR = 2.02, J = 1997 cw, 2026 ccw, Nu_{Dh} vs Re_{Dh}

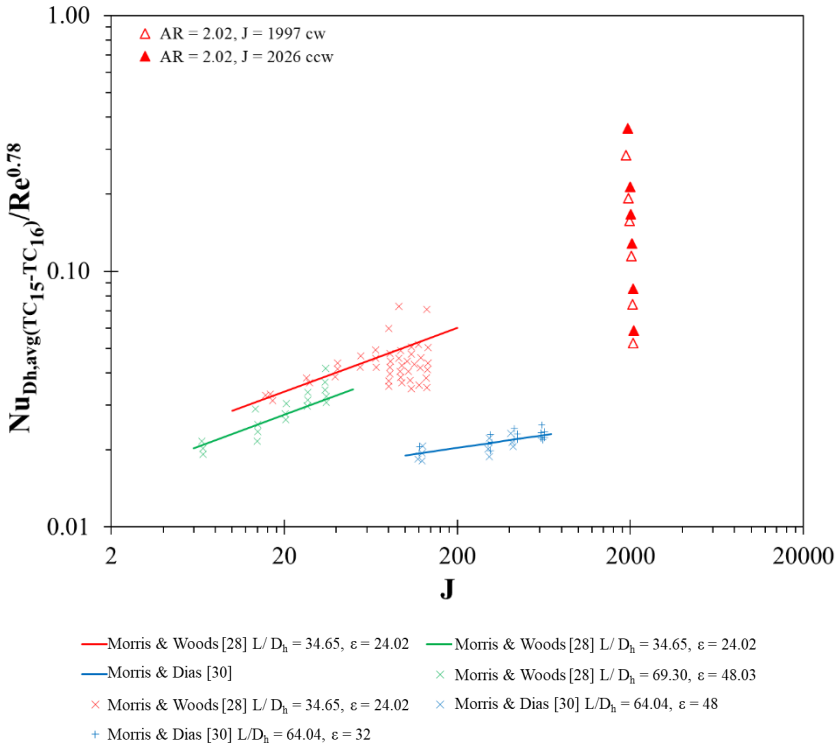

Figure A-16 AR = 2.02, J = 1997 cw, 2026 ccw, Nu_{Dh} vs J

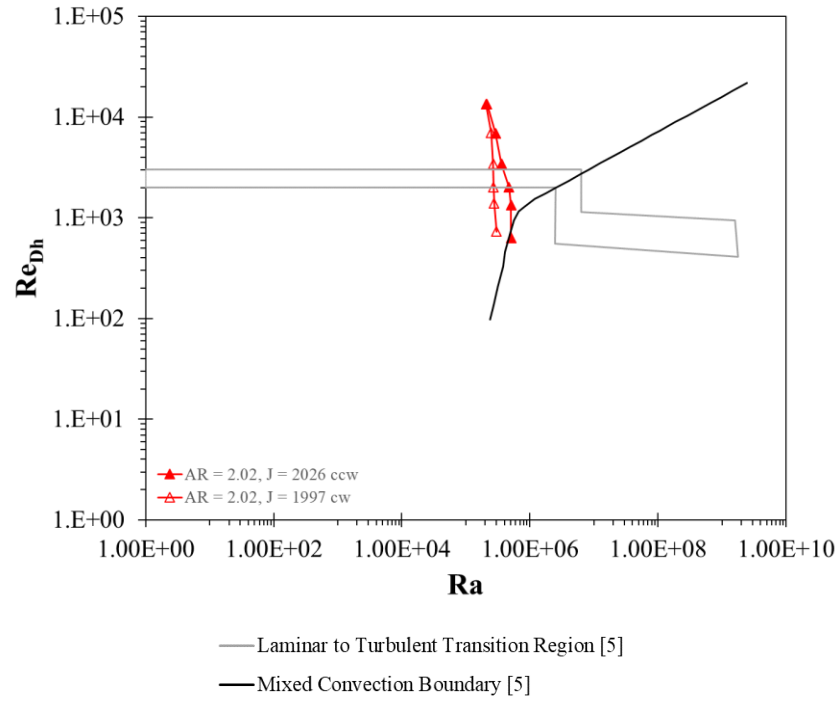

Figure A-17 AR = 2.02, J = 1997 cw, 2026 ccw, Re_{Dh} vs Ra

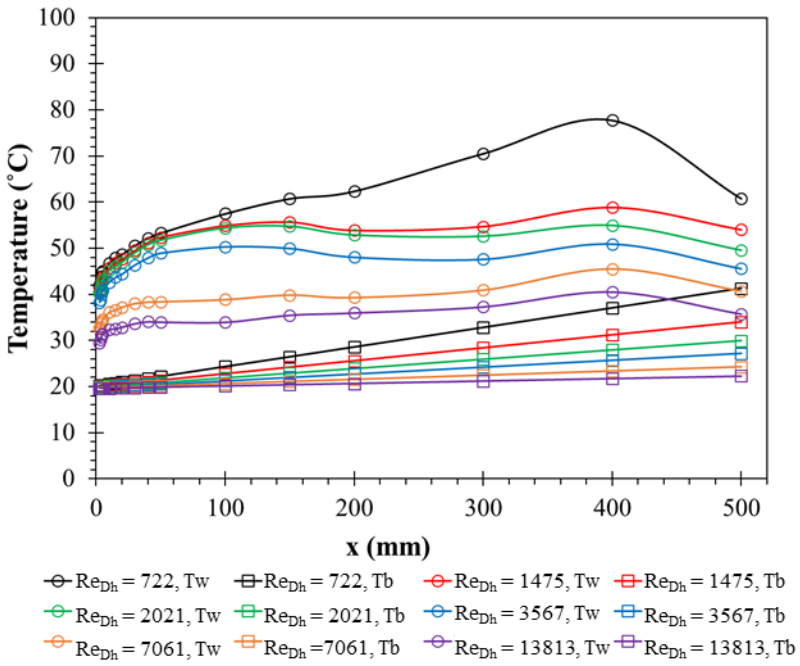

Figure A-18 AR = 2.02, J = 4180 ccw, 40V, (05/12/21), Temperature Profile

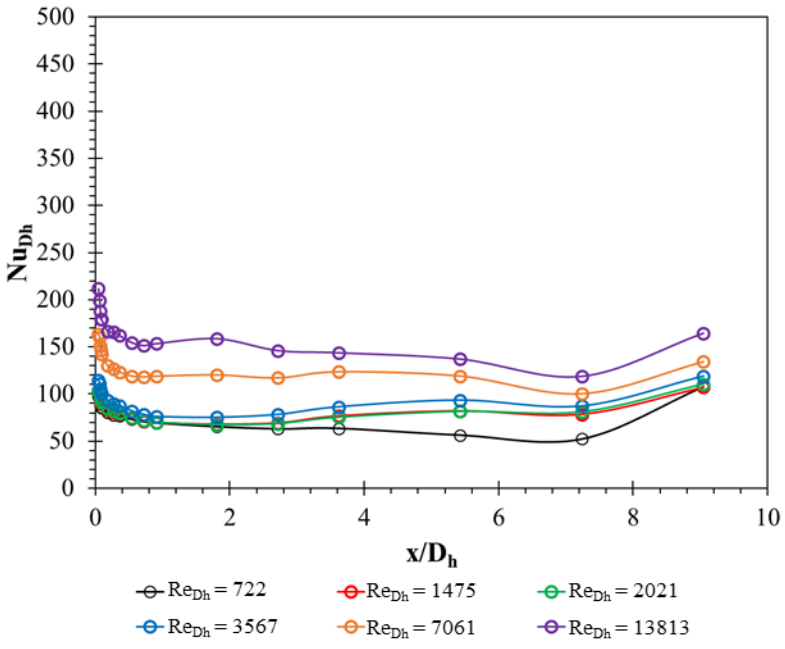

Figure A-19 AR = 2.02, J = 4180 ccw, 40V, (05/12/21), Nu_{Dh} Profile

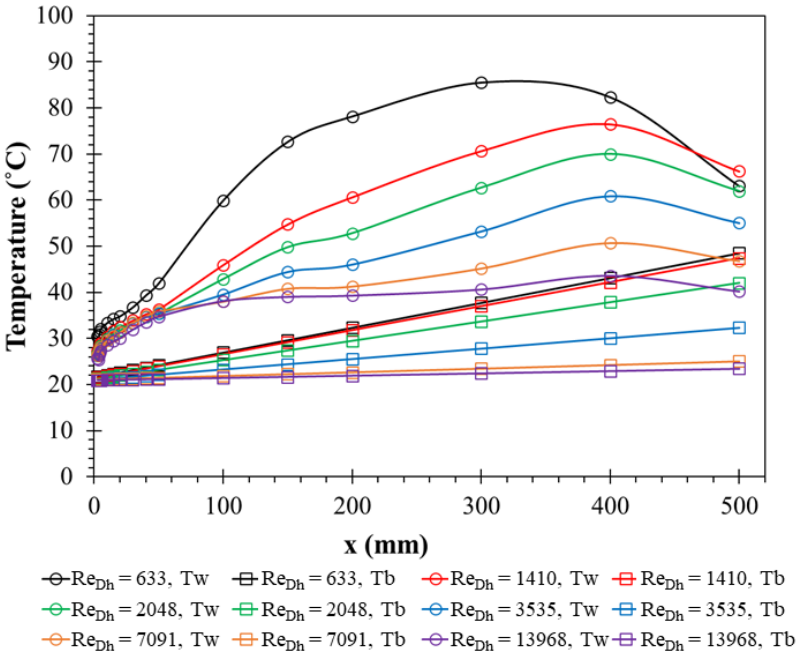

Figure A-20 AR = 2.02, J = 4083 cw, 40V, (05/12/21), Temperature Profile

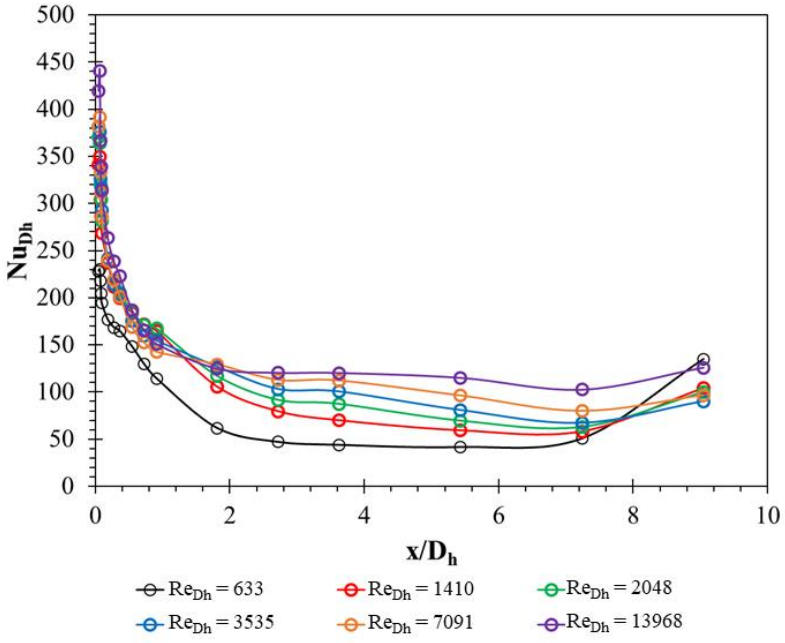

Figure A-21 AR = 2.02, J = 4083 cw, 40V, (05/12/21), Nu_{Dh} Profile

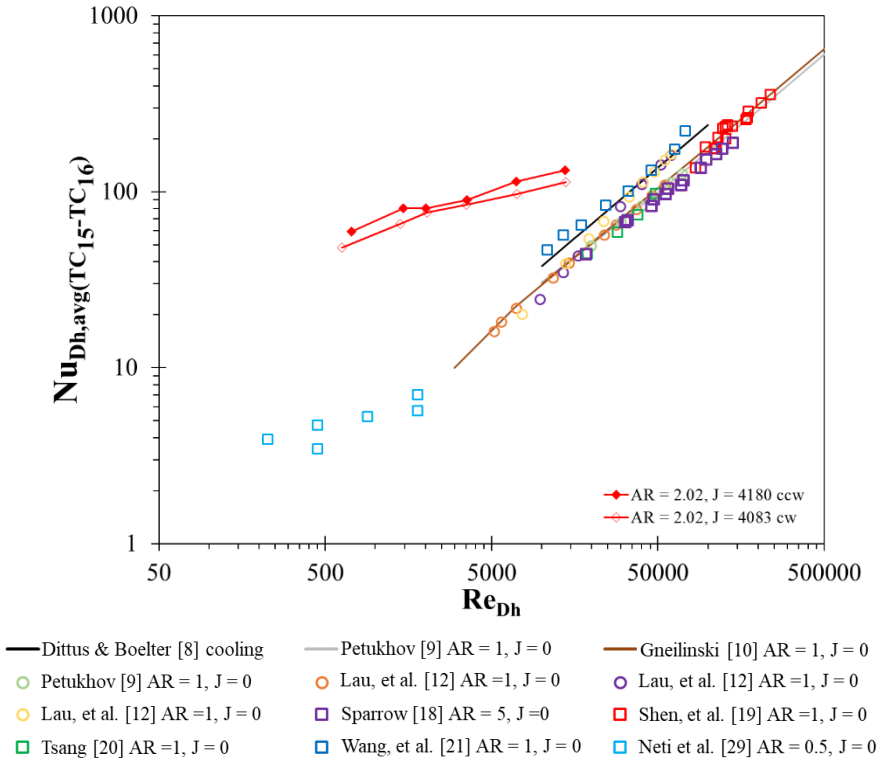

Figure A-22 AR = 2.02, J = 4083 cw, 4180 ccw, Nu_{Dh} vs Re_{Dh}

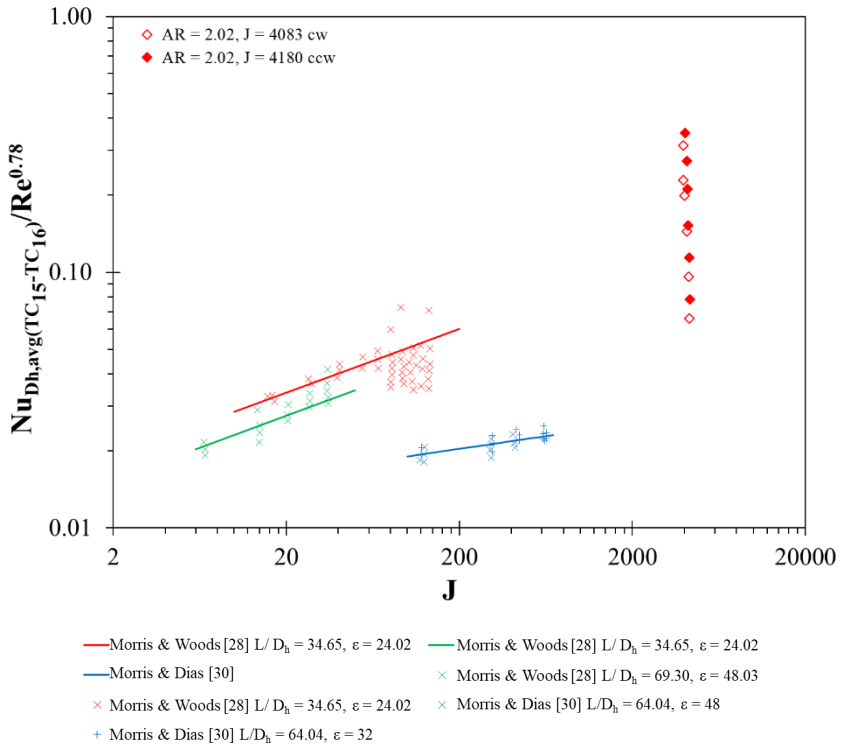

Figure A-23 AR = 2.02, J = 4083 cw, 4180 ccw, Nu_{Dh} vs J

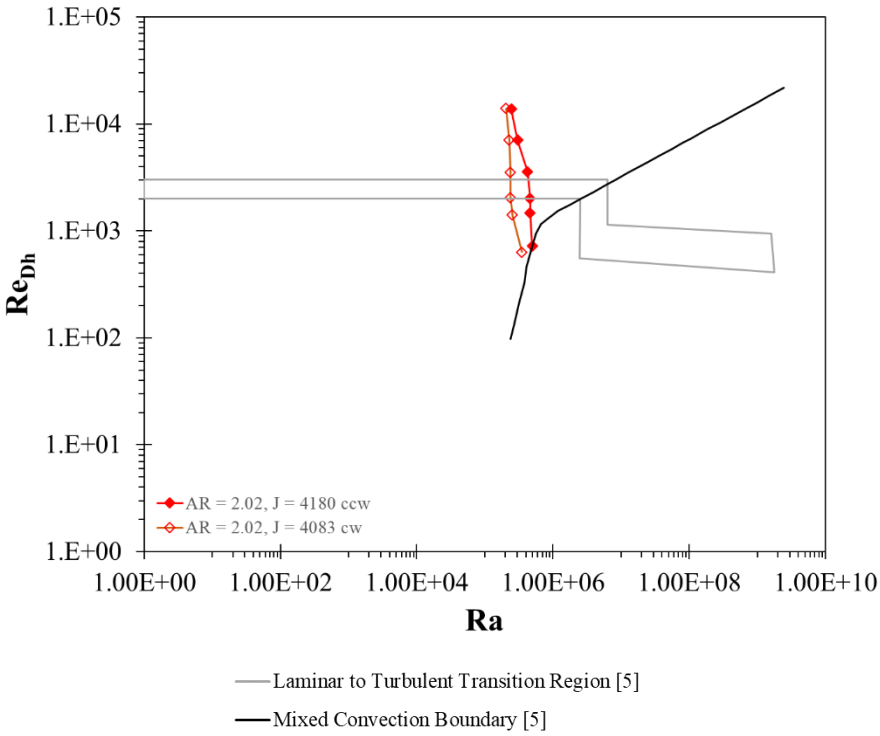

Figure A-24 AR = 2.02, J = 4083 cw, 4180 ccw, Re_{Dh} vs Ra

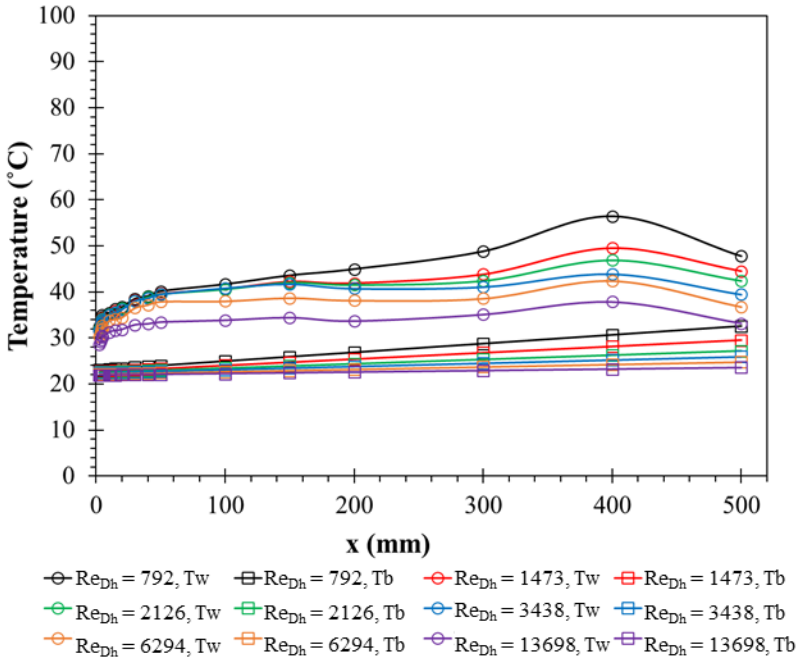

Figure A-25 AR = 2.02, J = 8276 ccw, 40V, (05/21/21), Temperature Profile

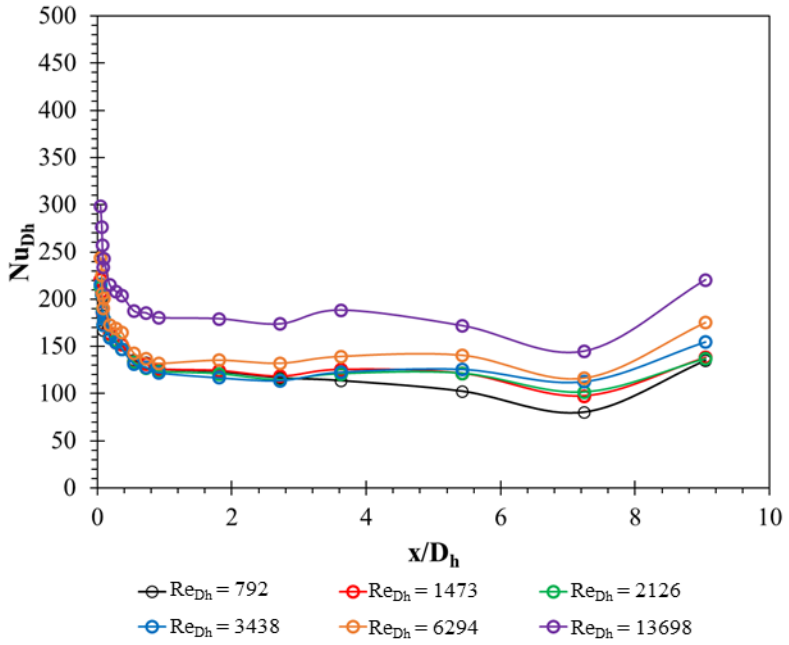

Figure A-26 AR = 2.02, J = 8276 ccw, 40V, (05/21/21), NuDh Profile

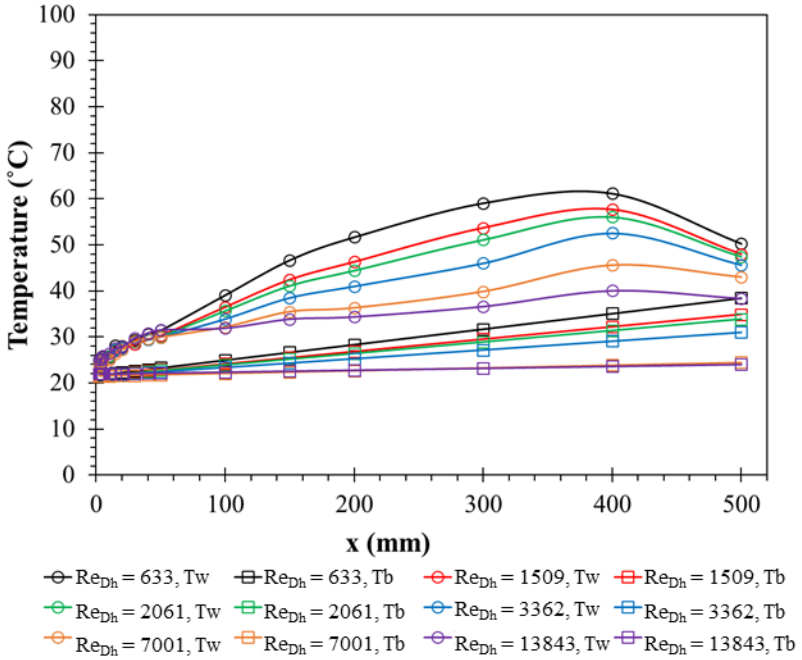

Figure A-27 AR = 2.02, J = 8355 cw, 40V, (05/14/21), Temperature Profile

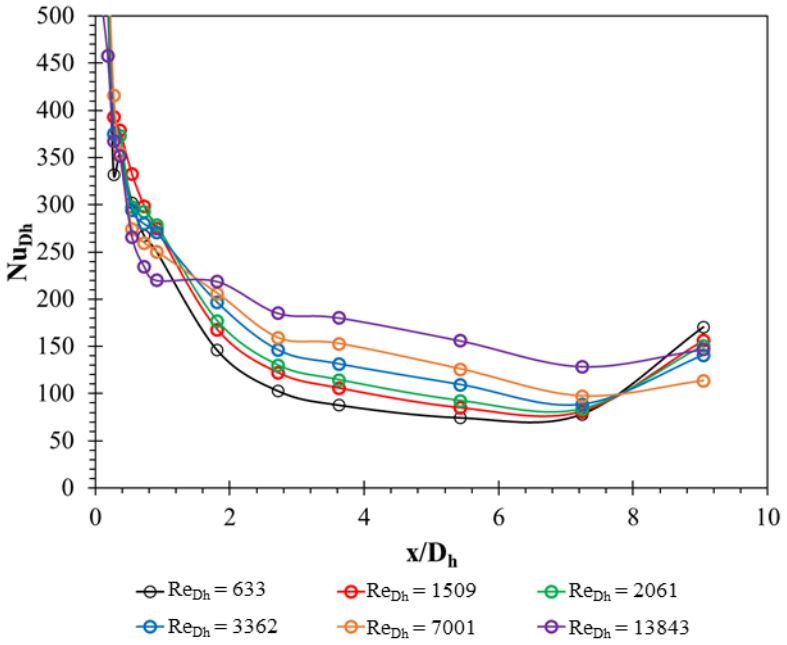

Figure A-28 AR = 2.02, J = 8355 cw, 40V, (05/14/21), Nu_{Dh} Profile

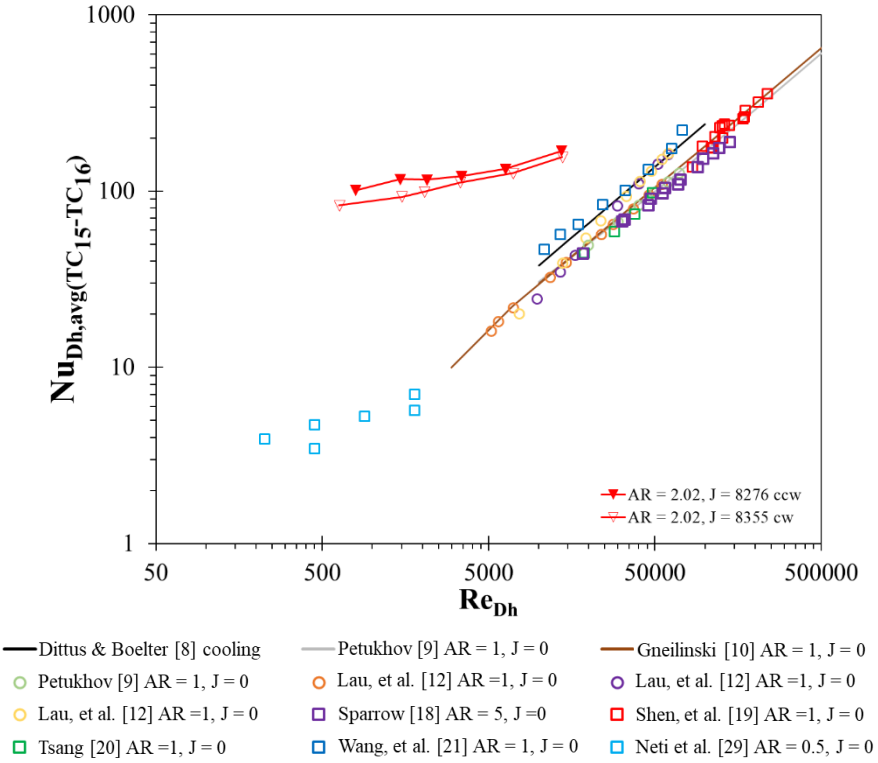

Figure A-29 AR = 2.02, J = 8355 cw, 8276 ccw, Nu_{Dh} vs Re_{Dh}

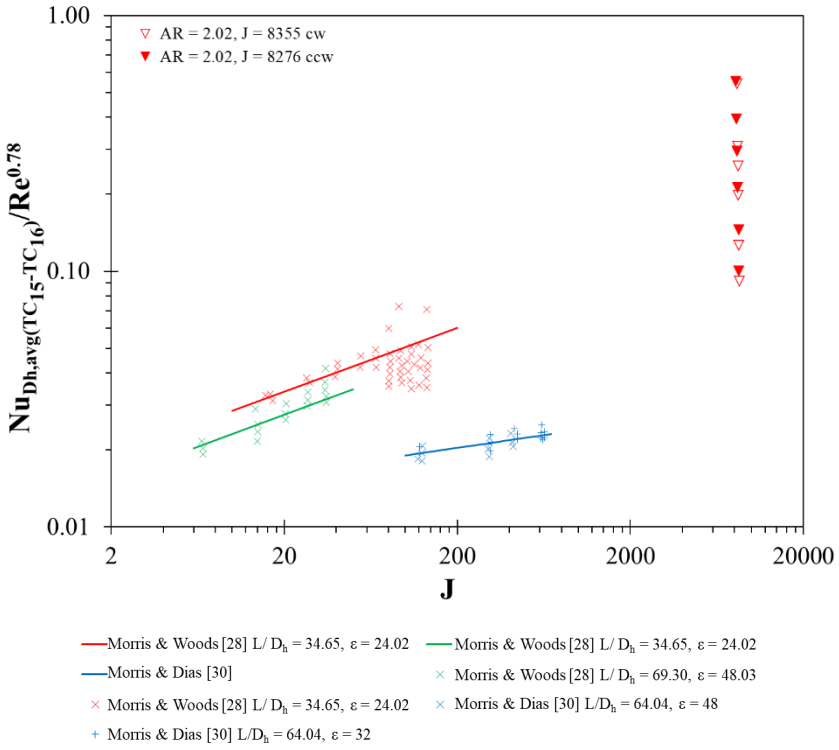

Figure A-30 AR = 2.02, J = 8355 cw, 8276 ccw, Nu_{Dh} vs J

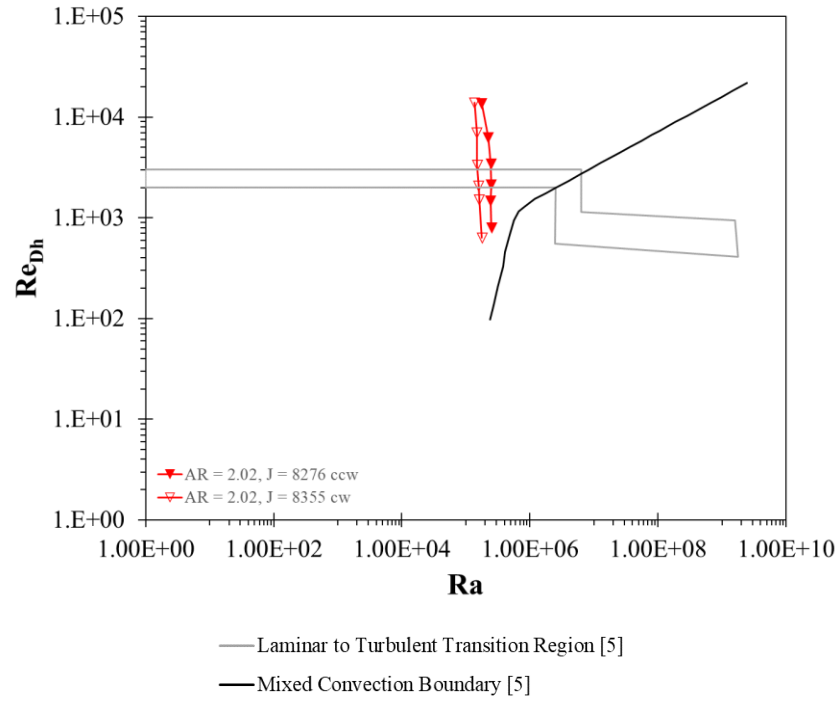

Figure A-31 AR = 2.02, J = 8355 cw, 8276 ccw, Re_{Dh} vs Ra

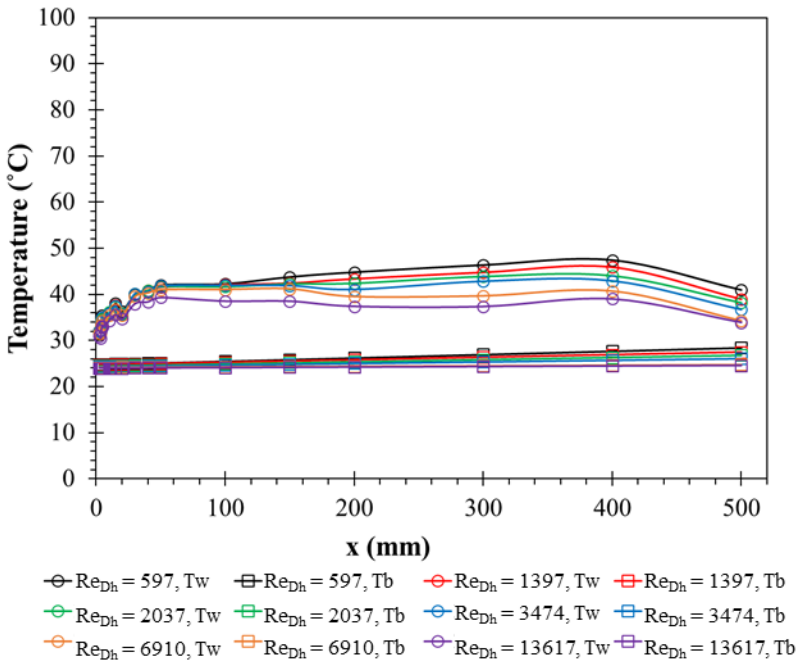

Figure A-32 AR = 2.02, J = 16182 ccw, 50V, (05/21/21), Temperature Profile

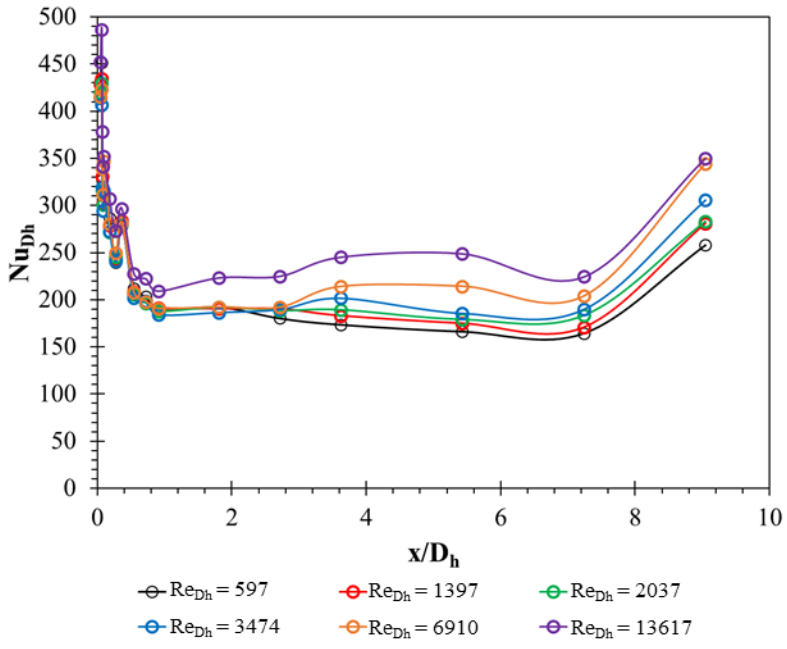

Figure A-33 AR = 2.02, J = 16182 ccw, 50V, (05/21/21), Nu_{Dh} Profile

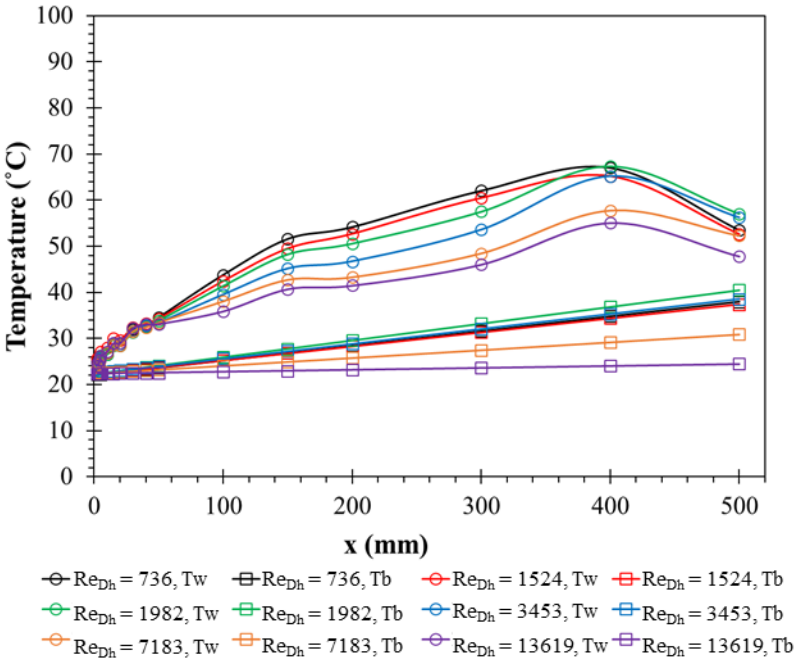

Figure A-34 AR = 2.02, J = 16664 cw, 60V, (05/11/21), Temperature Profile

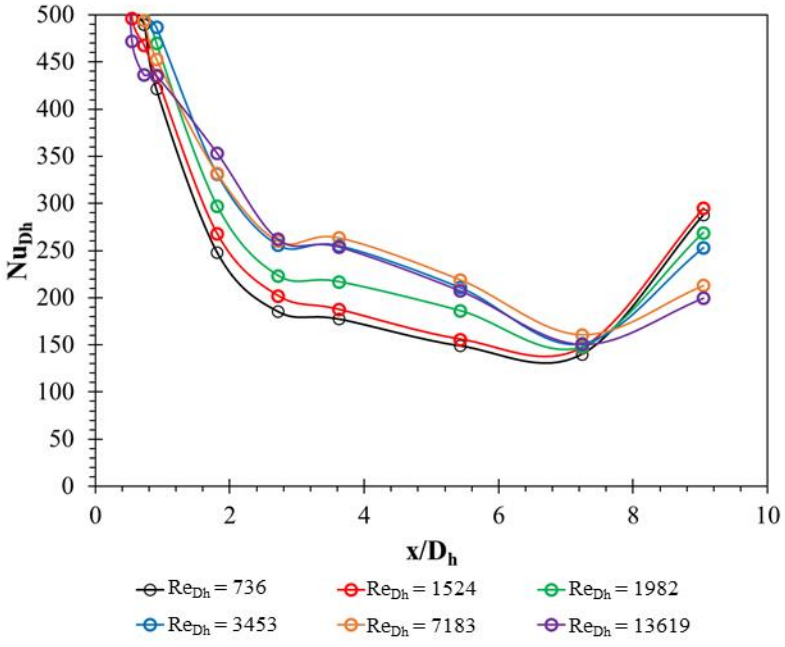

Figure A-35 AR = 2.02, J = 16664 cw, 60V, (05/11/21), Nu_{Dh} Profile

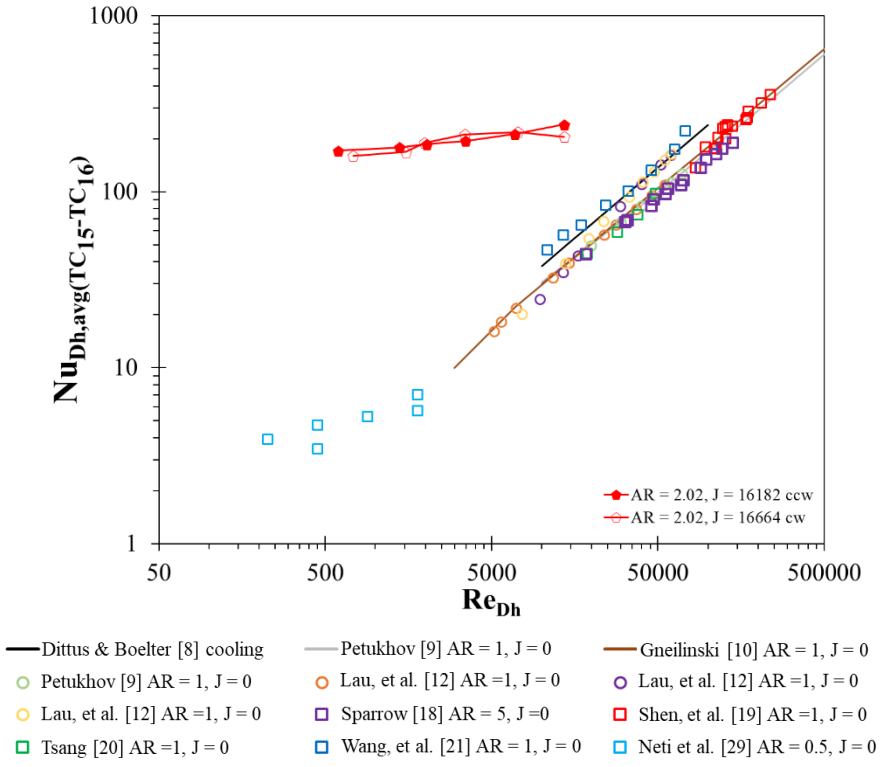

Figure A-36 AR = 2.02, J = 16664 cw, J = 16182 ccw, Nu_{Dh} vs Re_{Dh}

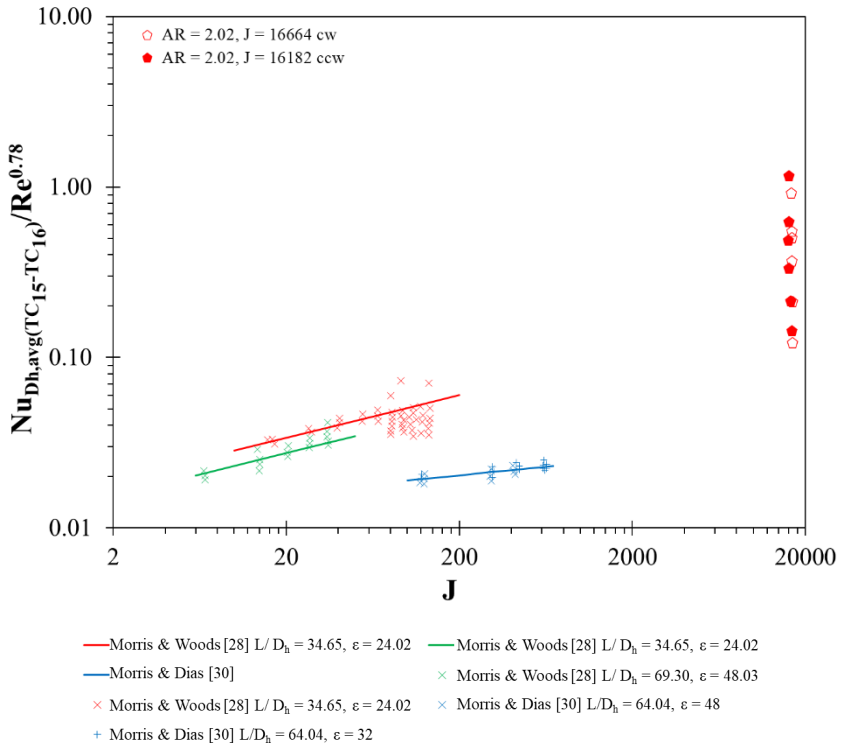

Figure A-37 AR = 2.02, J = 16664 cw, J = 16182 ccw, Nu_{Dh} vs J

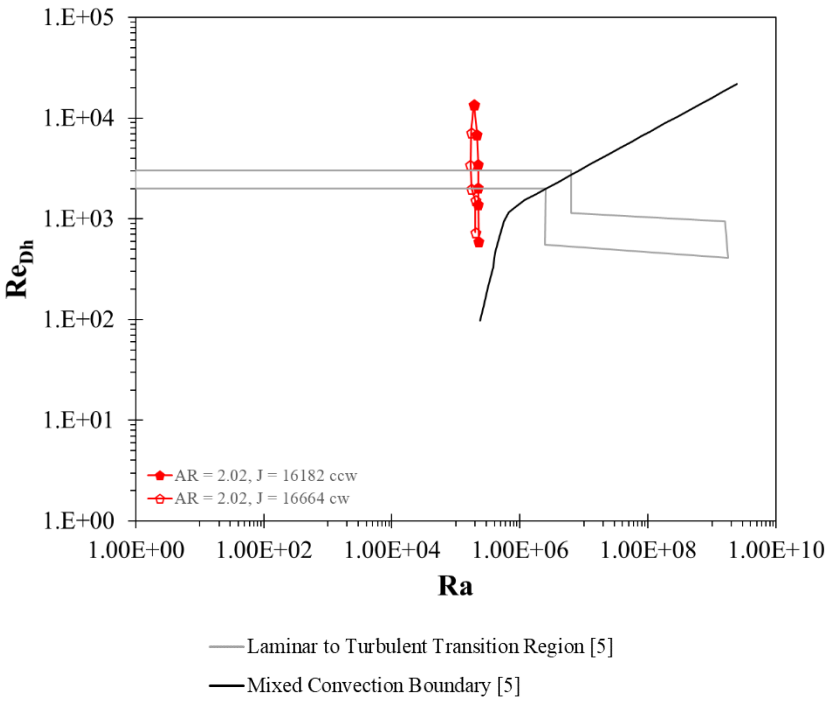

Figure A-38 AR = 2.02, J = 16664 cw, J = 16182 ccw, Re_{Dh} vs Ra

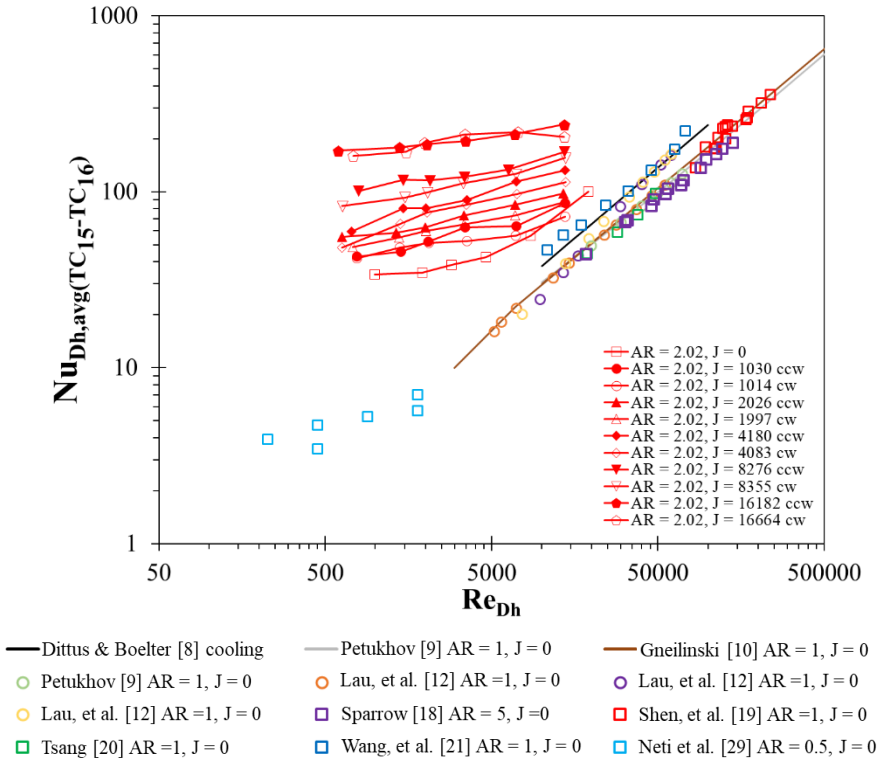

Figure A-39 AR = 2.02 Comparison, Nu_{Dh} vs Re_{Dh}

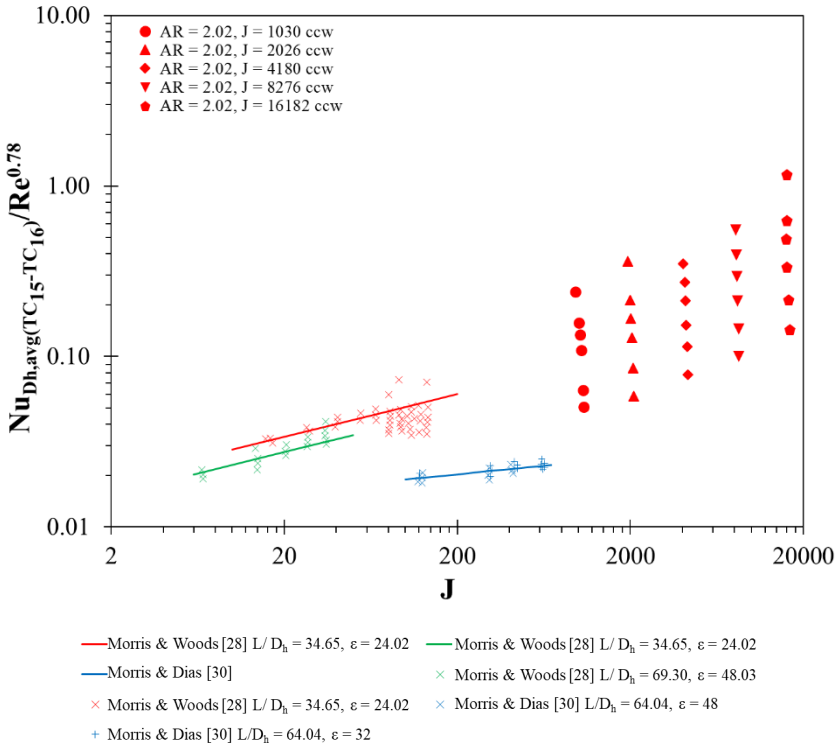

Figure A-40 AR = 2.02 Comparison, Nu_{Dh} vs J ccw

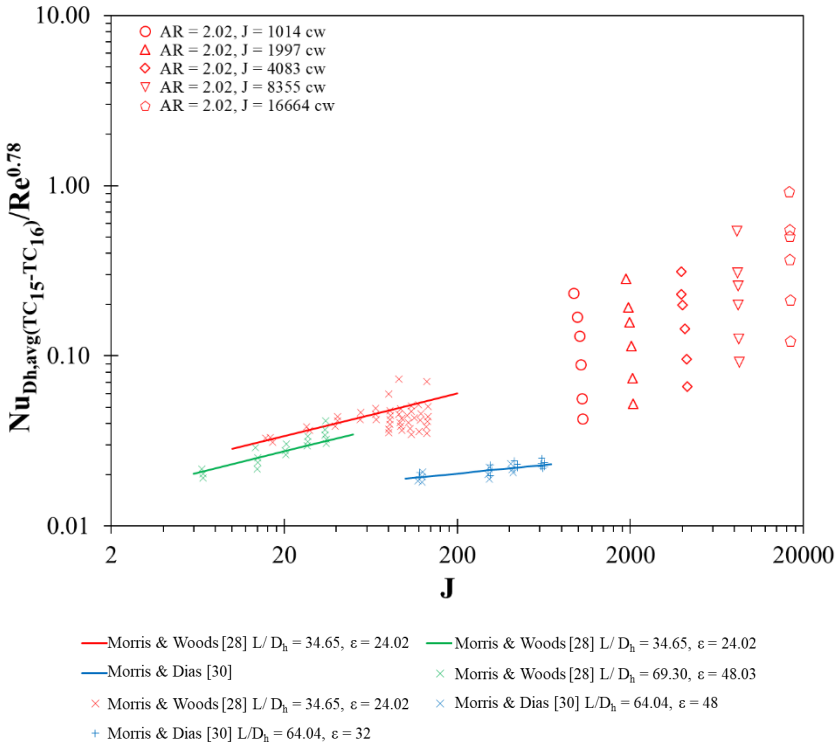

Figure A-41 AR = 2.02 Comparison, Nu_{Dh} vs J cw

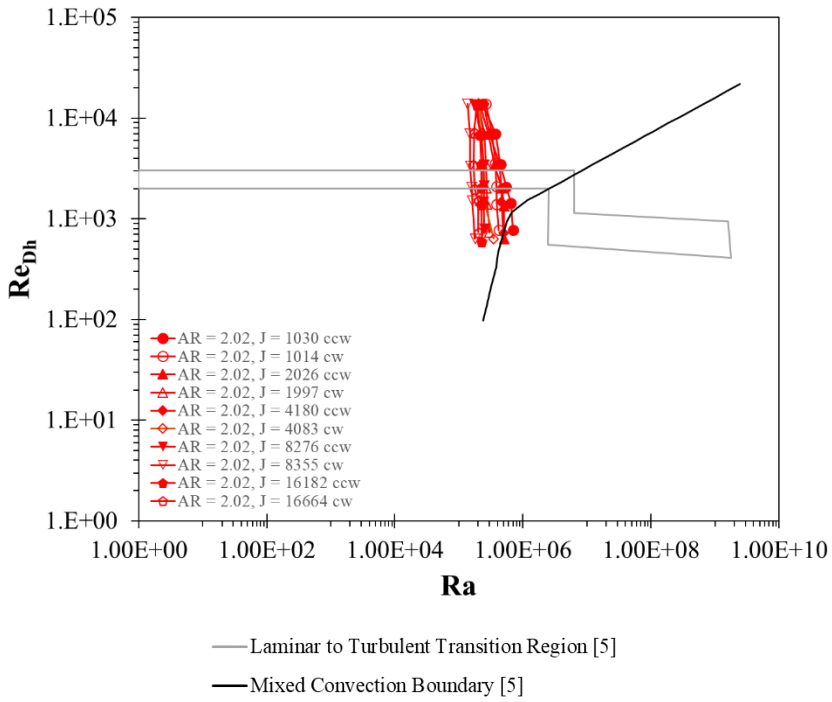

Figure A-42 AR = 2.02 Comparison, Re_{Dh} vs Ra

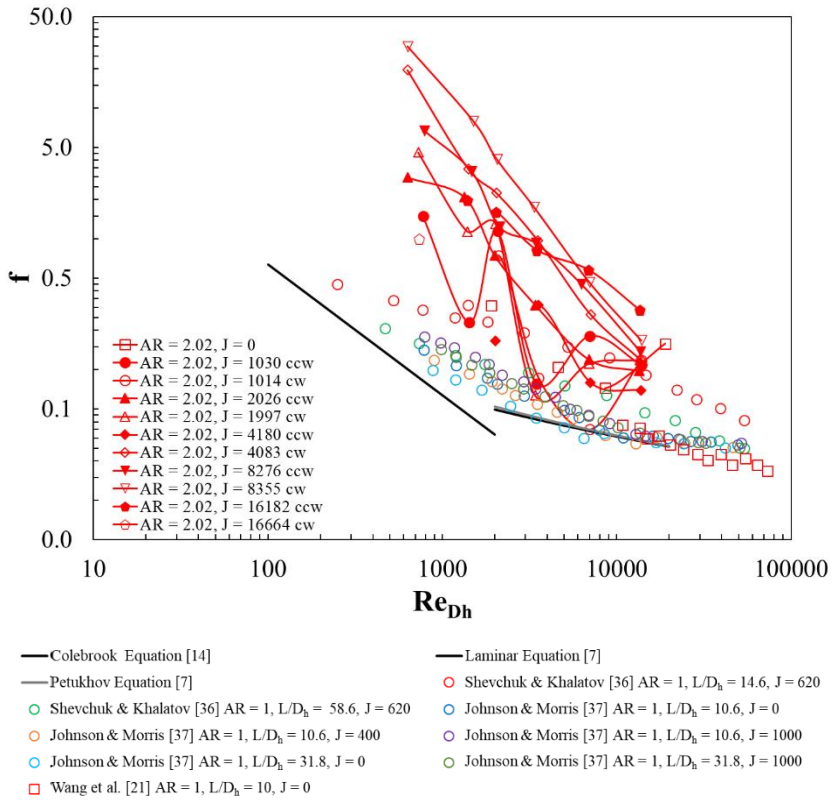

Figure A-43 AR2 Comparison, Friction Factor

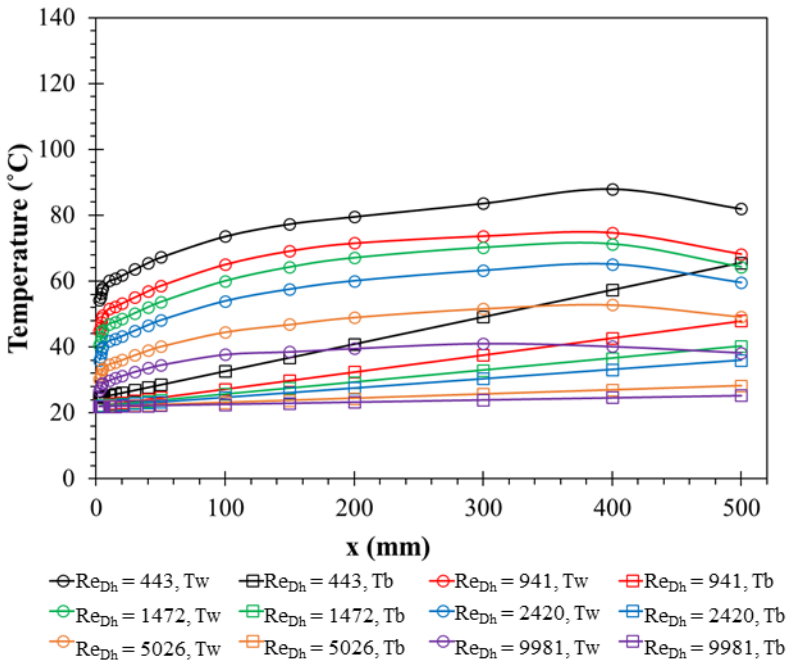

Figure A-44 AR = 3.93 J = 0, 31.4 V, (06/01/21), Temperature Profile

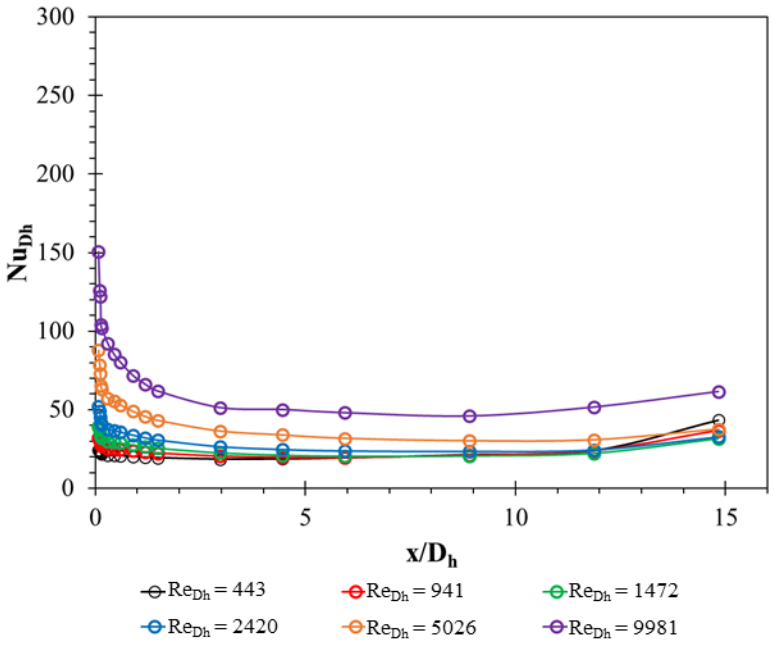

Figure A-45 AR = 3.93 J = 0, 31.4 V, (06/01/21), Nu_{Dh} Profile

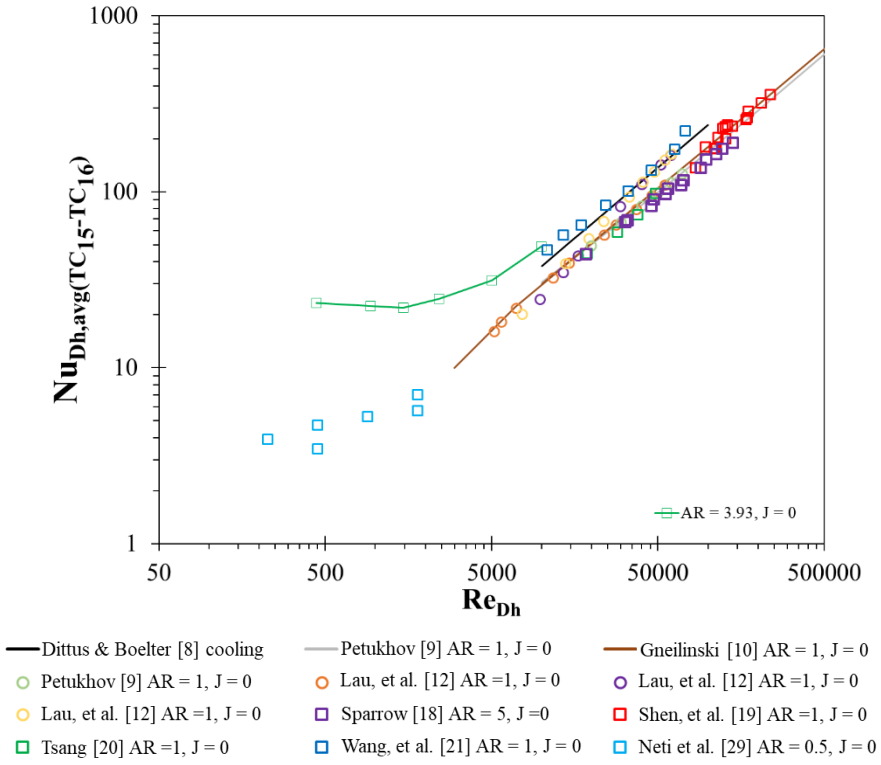

Figure A-46 AR = 3.93 J = 0, Nu_{Dh} vs Re_{Dh}

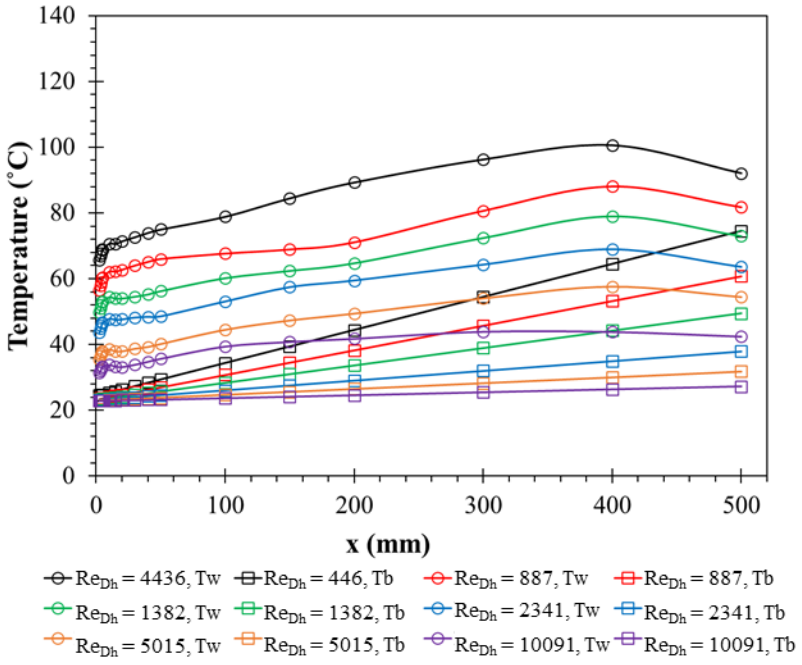

Figure A-47 AR = 3.93 J = 366 ccw, 35 V, (06/01/21), Temperature Profile

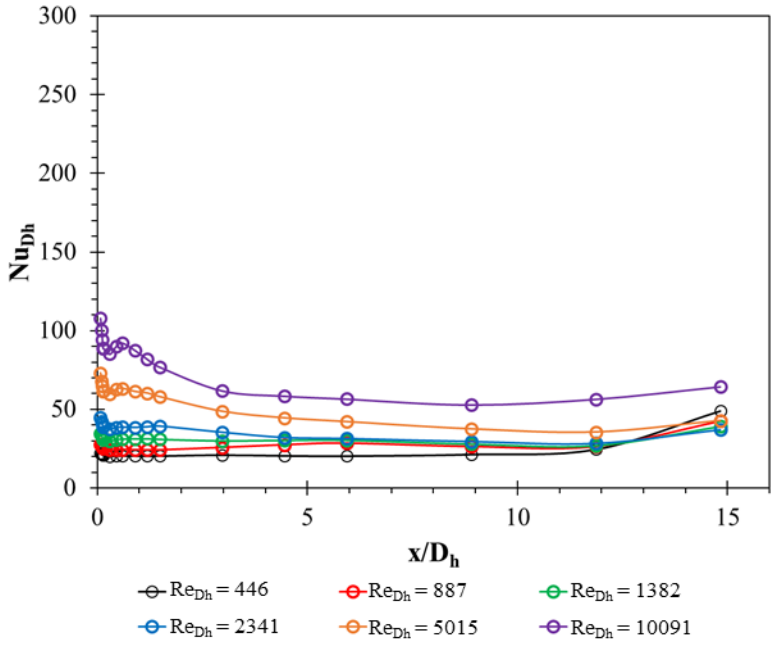

Figure A-48 AR = 3.93 J = 366 ccw, 35 V, (06/01/21), Nu_{Dh} Profile

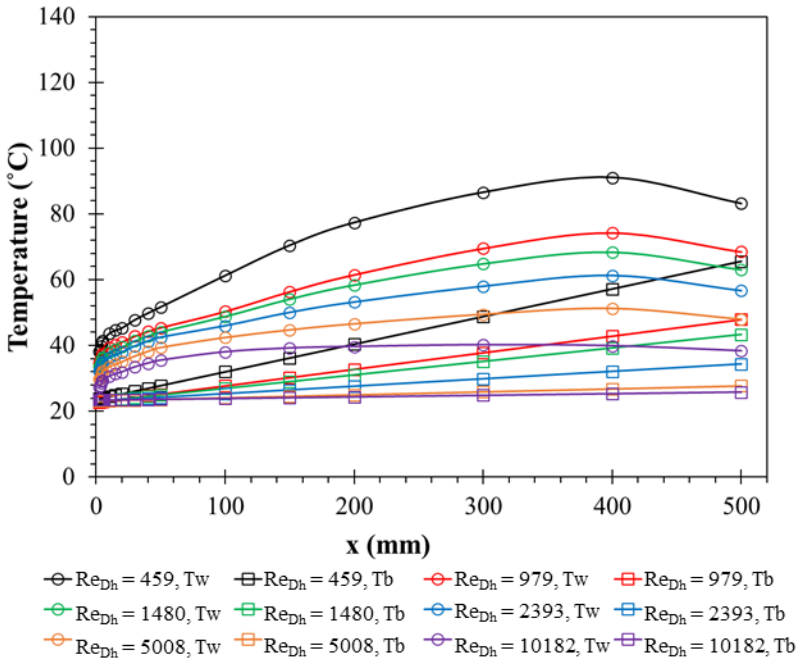

Figure A-49 AR = 3.93 J = 373 cw, (06/01/21), Temperature Profile

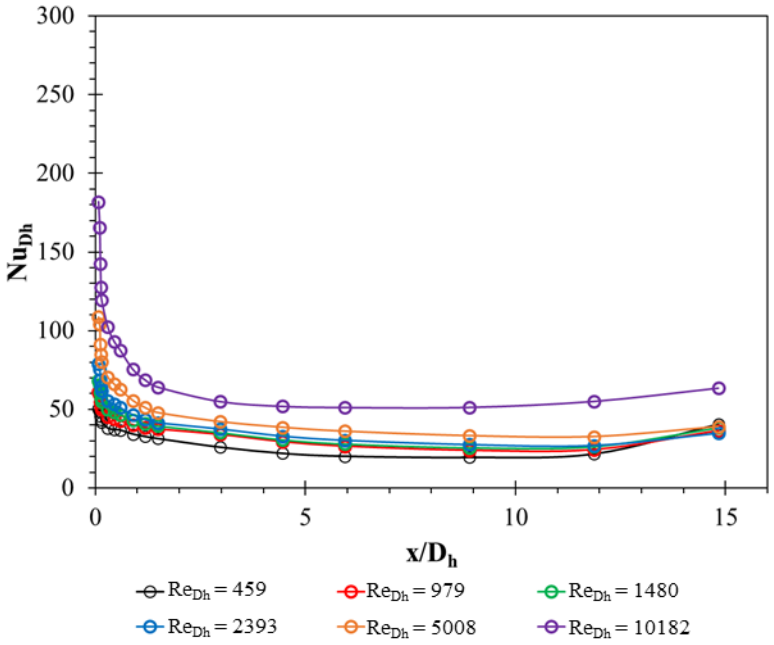

Figure A-50 AR = 3.93 J = 373 cw, 31.4 V, (06/01/21), Nu_{Dh} Profile

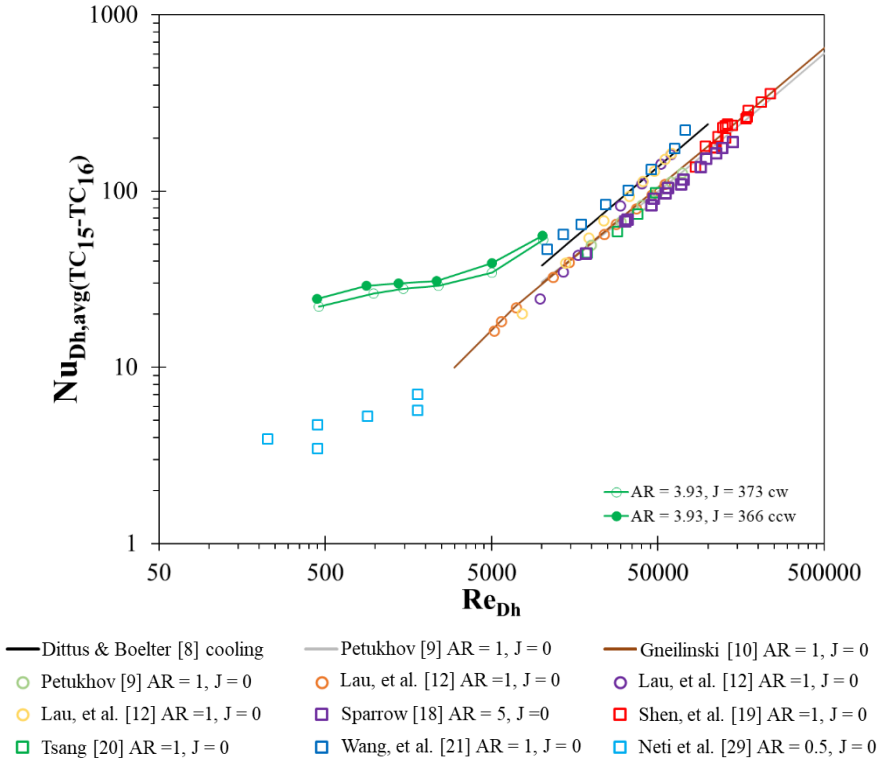

Figure A-51 AR = 3.93 J = 373 cw, 366 ccw, Nu_{Dh} vs Re_{Dh}

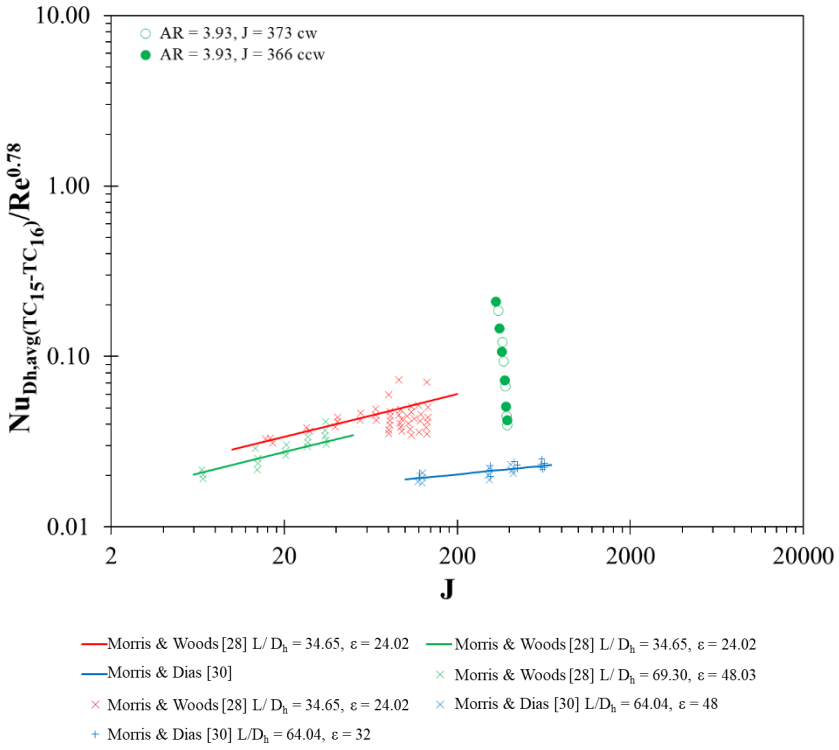

Figure A-52 AR = 3.93 J = 373 cw, 366 ccw, Nu_{Dh} vs J

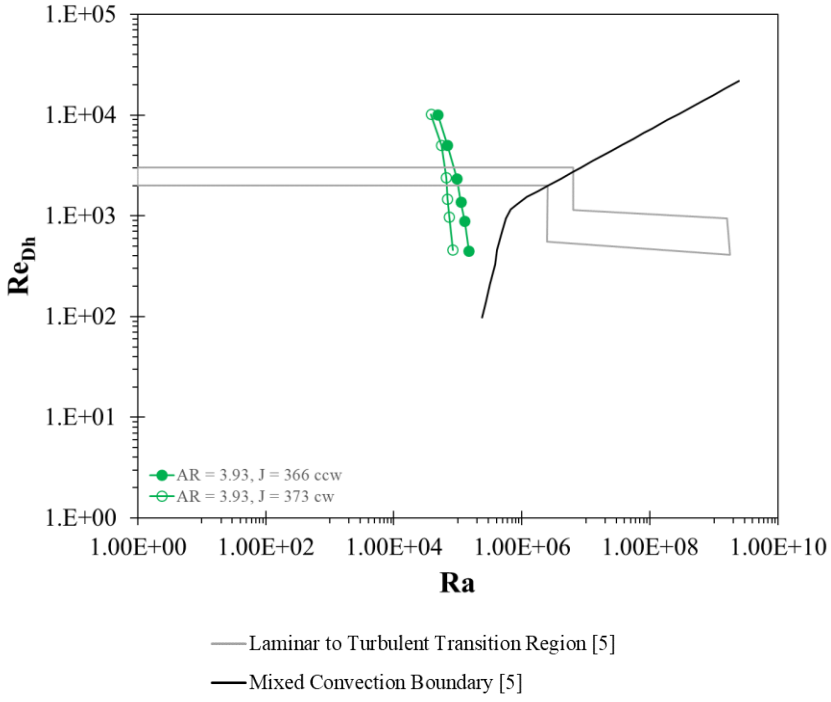

Figure A-53 AR = 3.93 J = 373 cw, 366 ccw, Re_{Dh} vs Ra

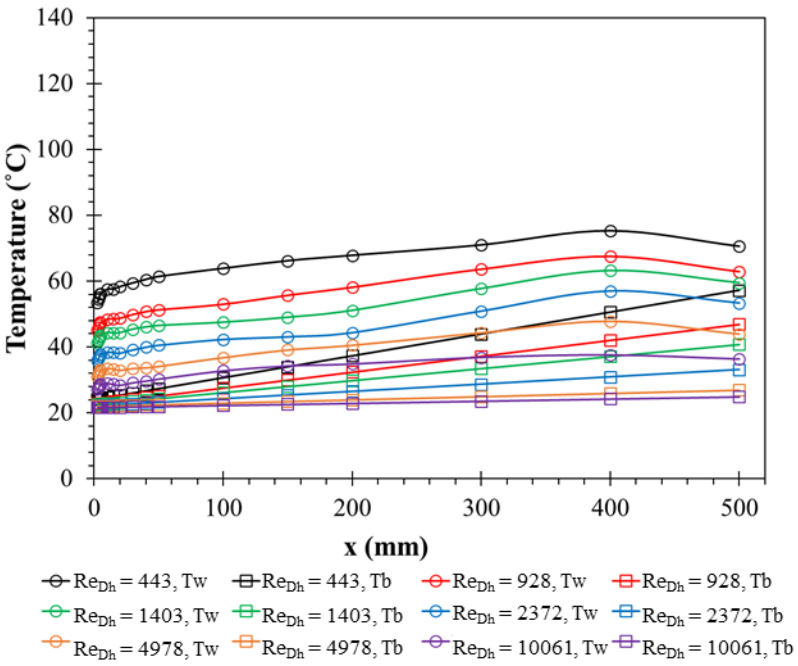

Figure A-54 AR = 3.93, J = 748 ccw, Temperature Profile

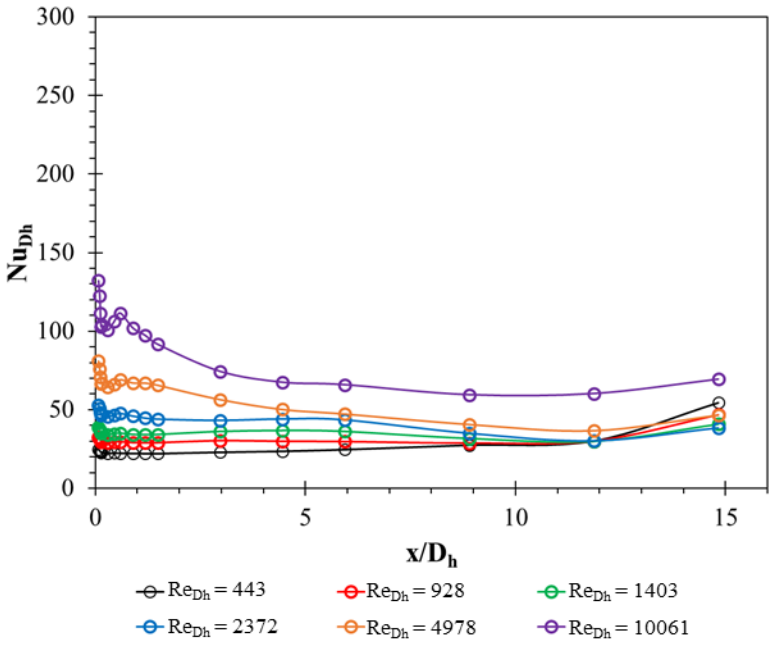

Figure A-55 AR = 3.93, J = 748 ccw, 31.4V, (06/02/21), Nu_{Dh} Profile

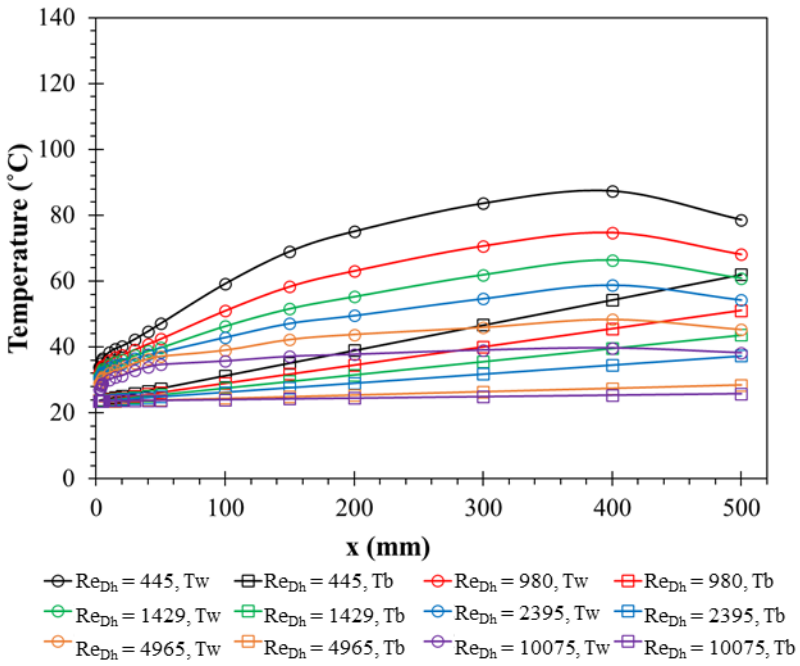

Figure A-56 AR = 3.93, J = 739 cw, 31.4V, (06/02/21), Temperature Profile

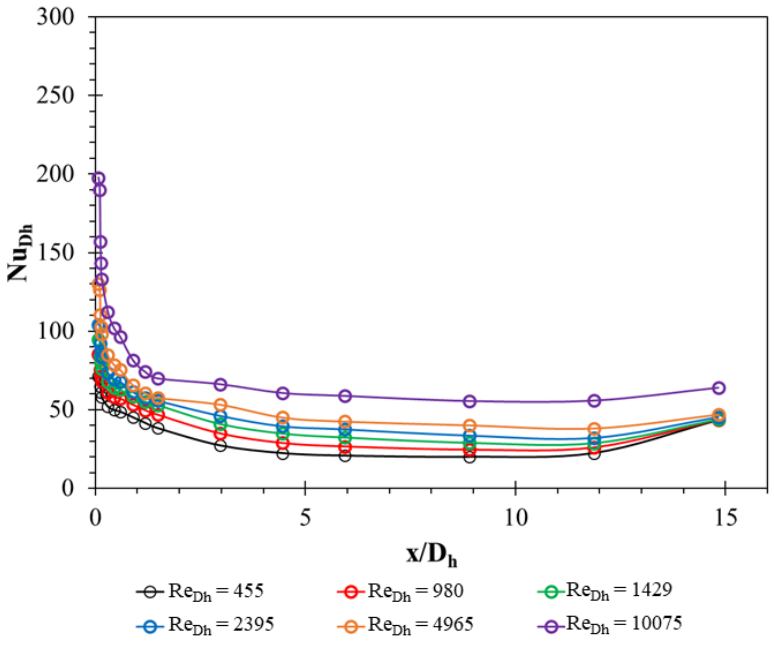

Figure A-57 AR = 3.93, J = 739 cw, 31.4V, (06/02/21), Nu_{Dh} Profile

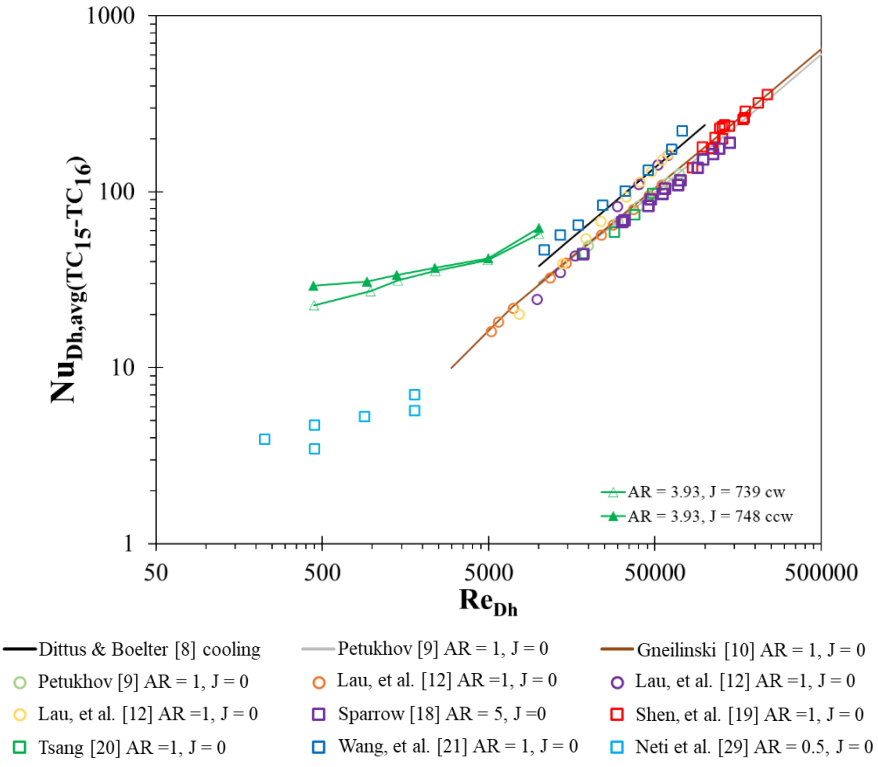

Figure A-58 AR = 3.93, J = 739 cw, 748 ccw, Nu_{Dh} vs Re_{Dh}

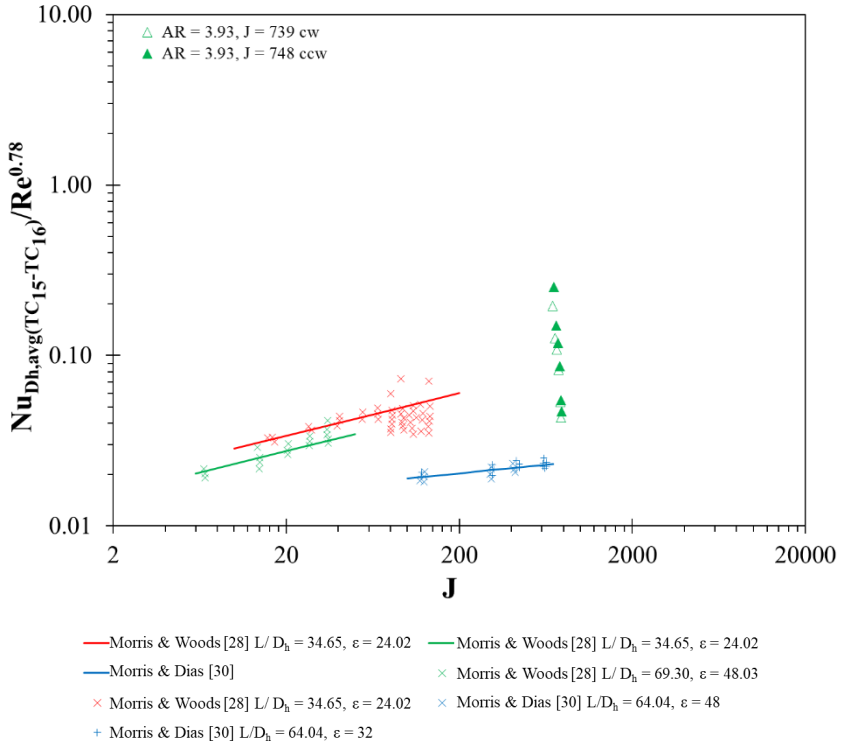

Figure A-59 AR = 3.93, J = 739 cw, 748 ccw, Nu_{Dh} vs J

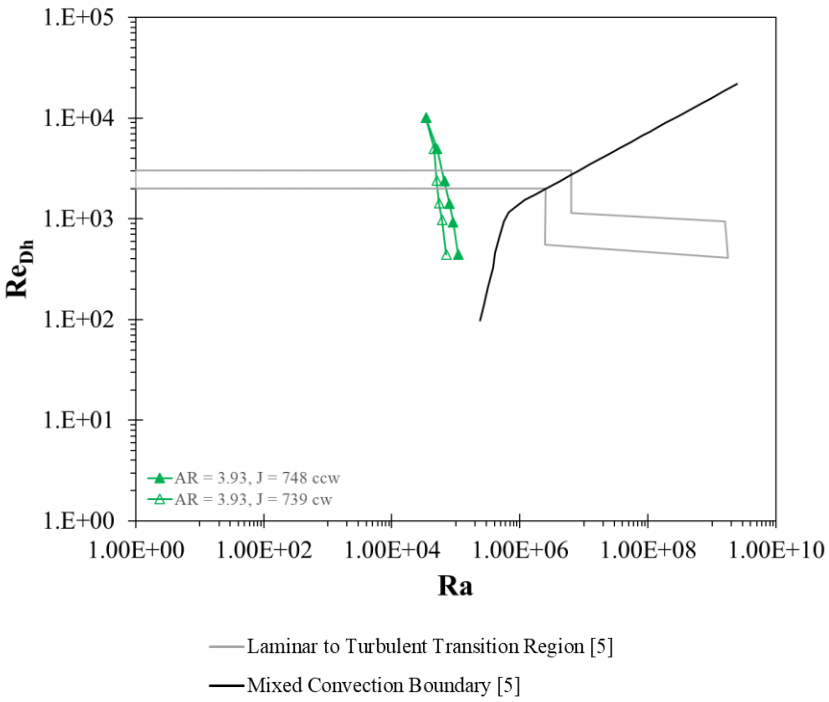

Figure A-60 AR = 3.93, J = 739 cw, 748 ccw, Re_{Dh} vs Ra

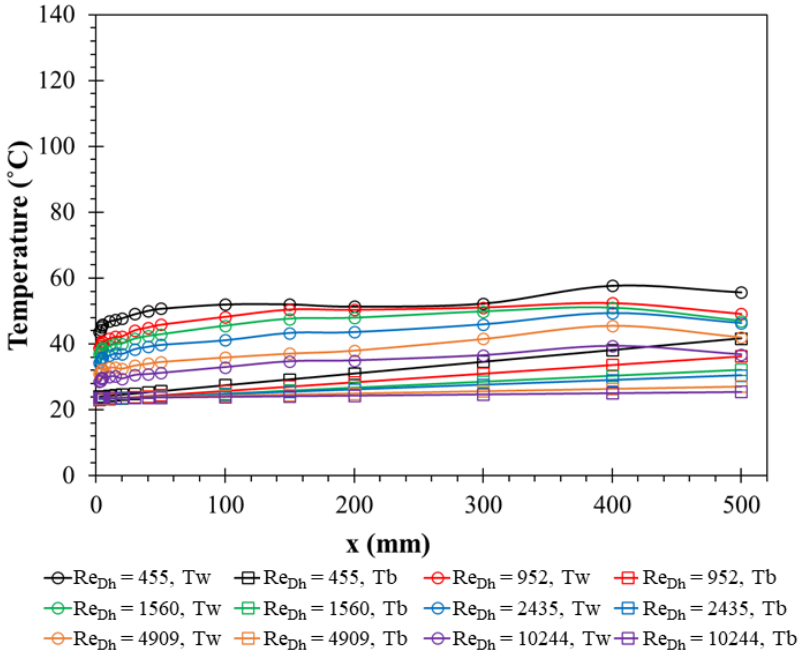

Figure A-61 AR = 3.93, J = 1518 ccw, 40V, (06/02/21), Temperature Profile

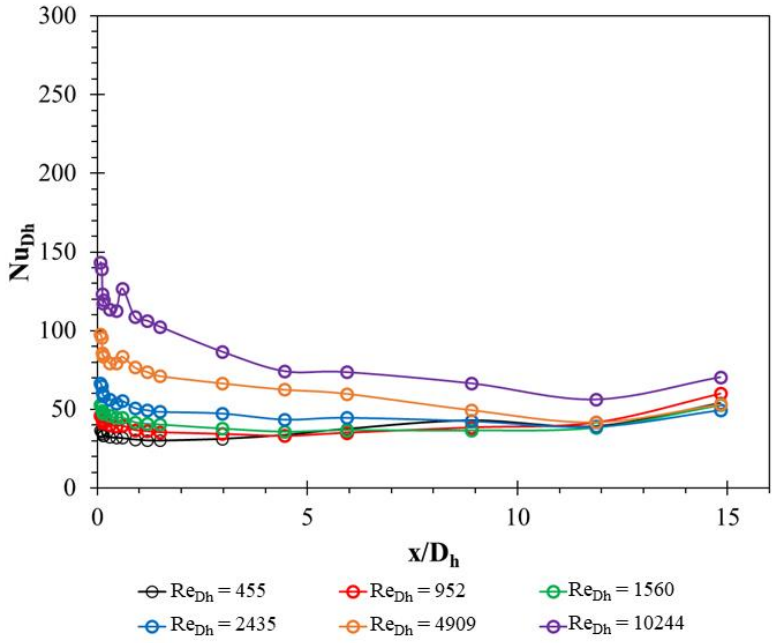

Figure A-62 AR = 3.93, J = 1518 ccw, 40V, (06/02/21), Nu_{Dh} Profile

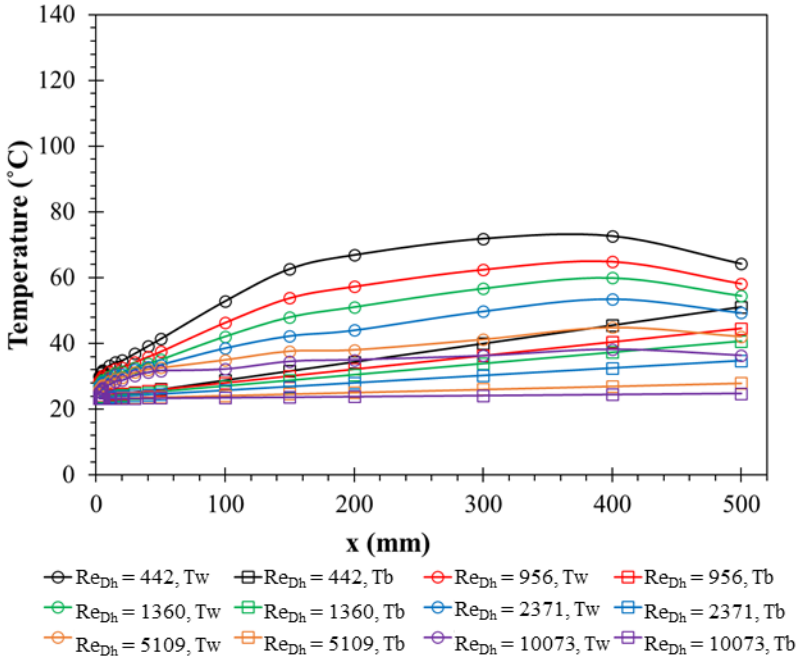

Figure A-63 AR = 3.93, J = 1495 cw, 31.4V, (06/03/21), Temperature Profile

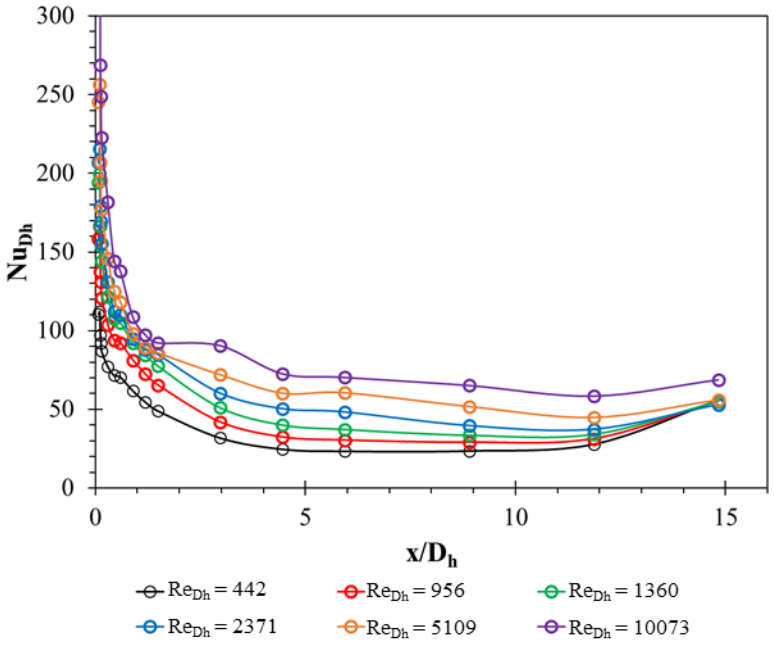

Figure A-64 AR = 3.93, J = 1495 cw, 31.4V, (06/03/21), Nu_{Dh} Profile

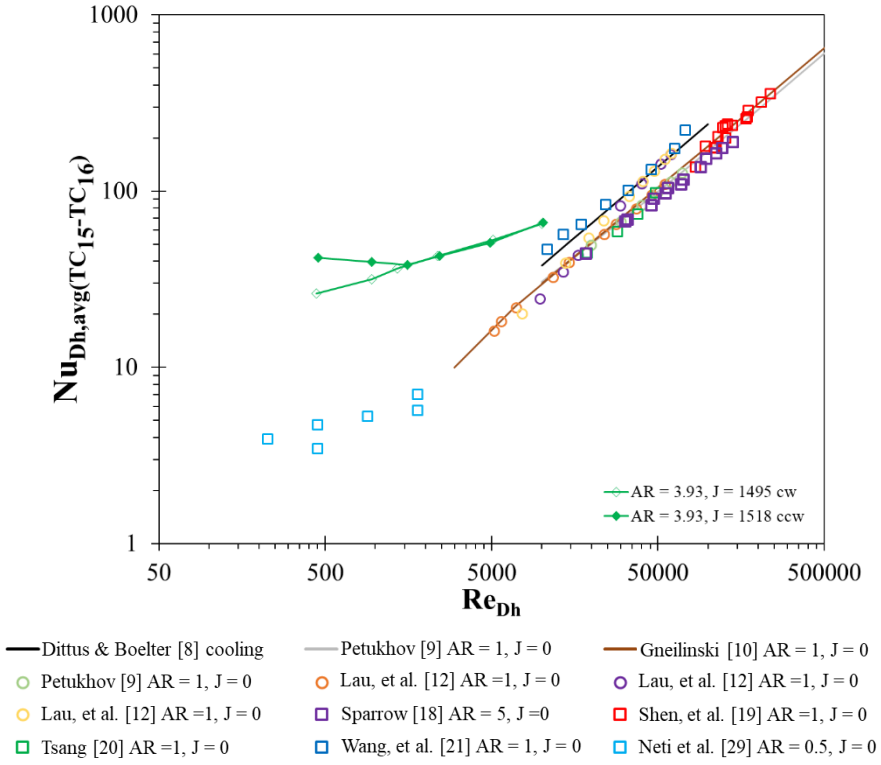

Figure A-65 AR = 3.93, J = 1495 cw, 1518 ccw, Nu_{Dh} vs Re_{Dh}

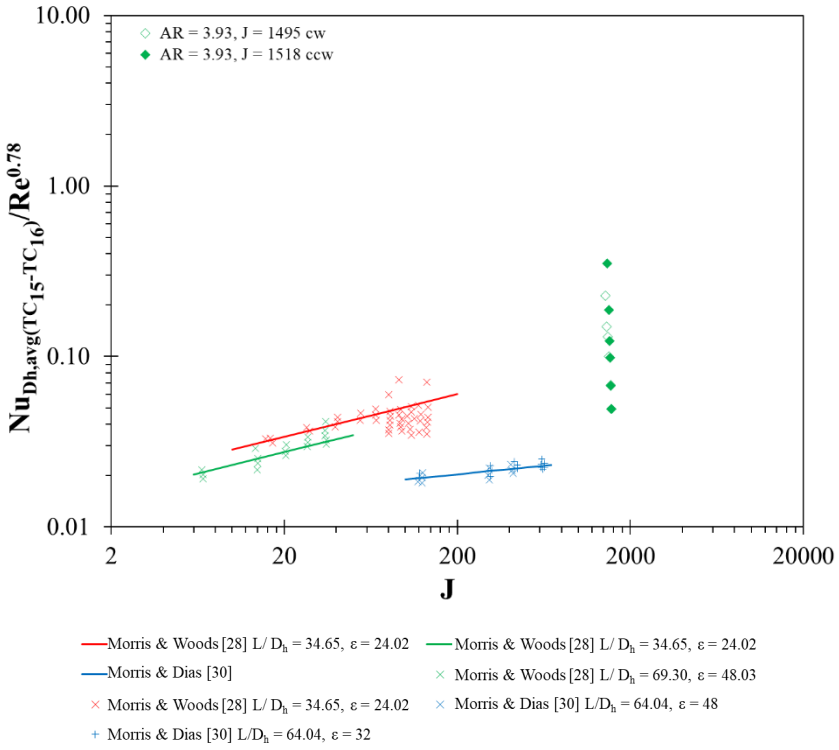

Figure A-66 AR = 3.93, J = 1495 cw, 1518 ccw, Nu_{Dh} vs J

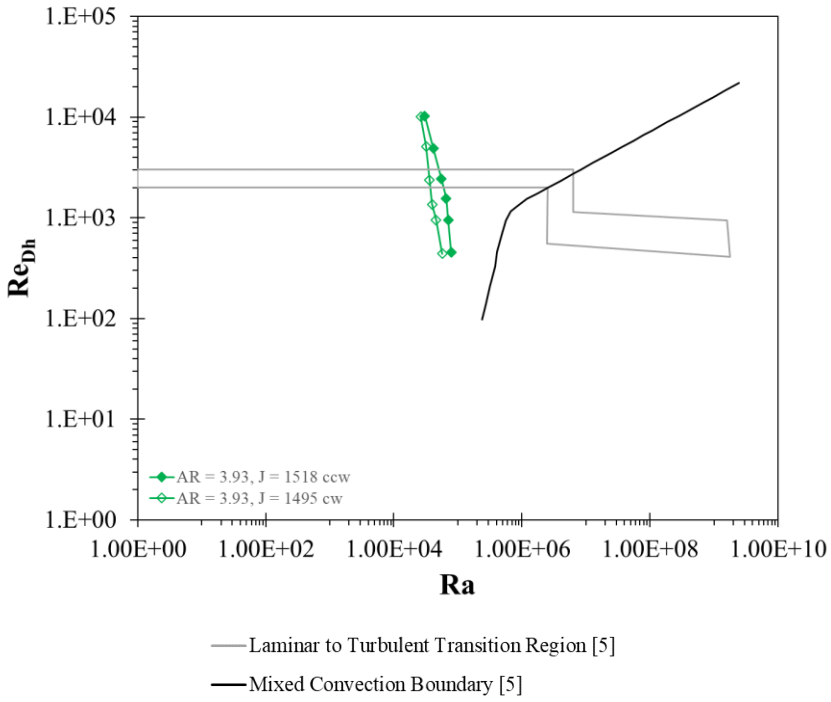

Figure A-67 AR = 3.93, J = 1495 cw, 1518 ccw, Re_{Dh} vs Ra

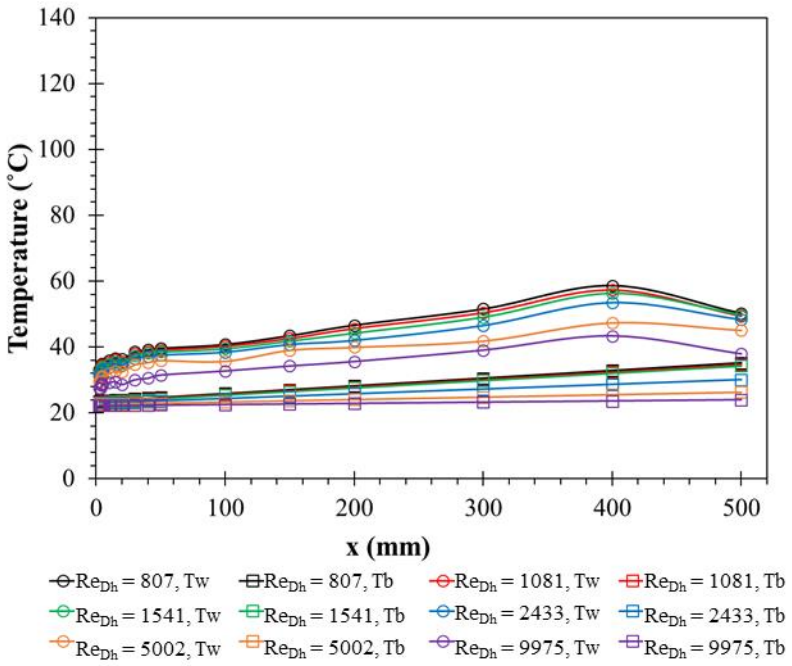

Figure A-68 AR = 3.93, J = 3057 ccw, 40V, (06/03/21), Temperature Profile

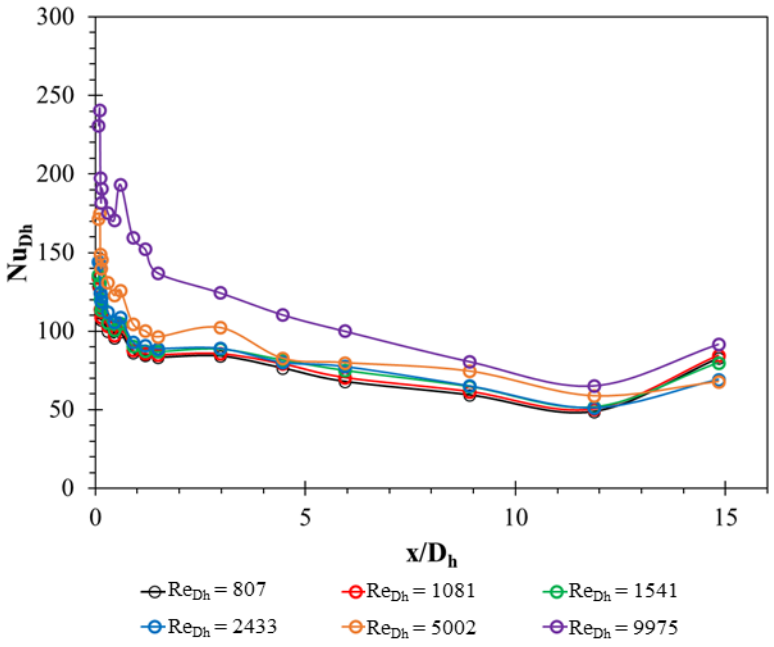

Figure A-69 AR = 3.93, J = 3057 ccw, 40V, (06/03/21), Nu_{Dh} Profile

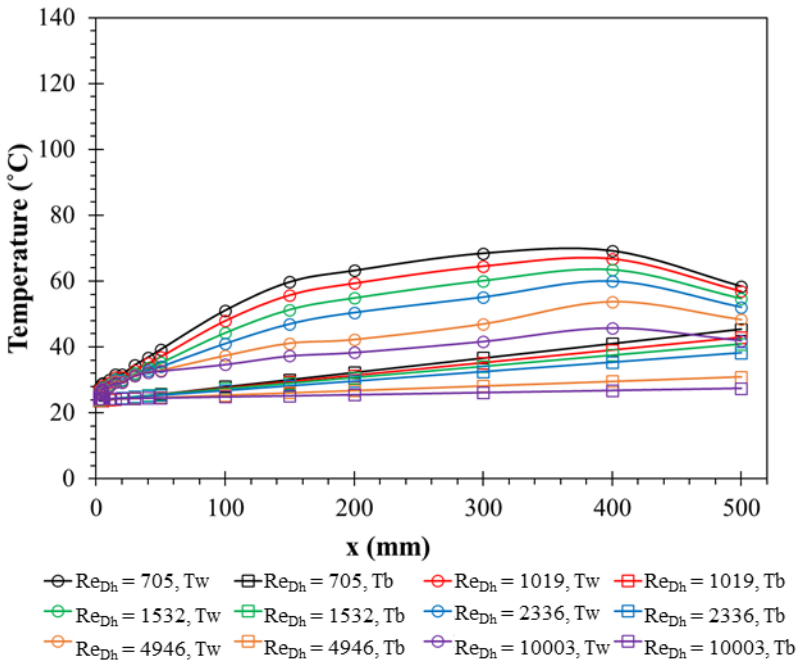

Figure A-70 AR = 3.93, J = 2985 cw, 40V, (06/03/21), Temperature Profile

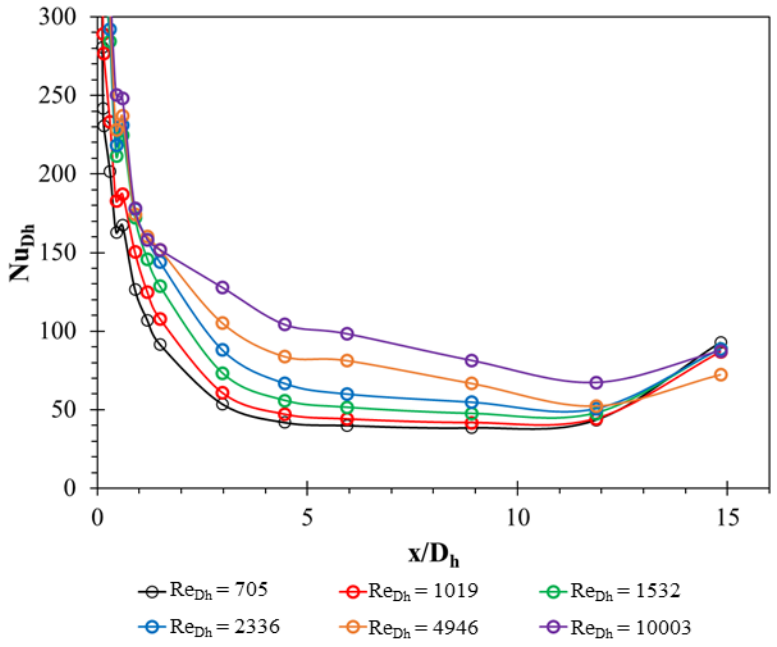

Figure A-71 AR = 3.93, J = 2985 cw, 40V, (06/03/21), Nu_{Dh} Profile

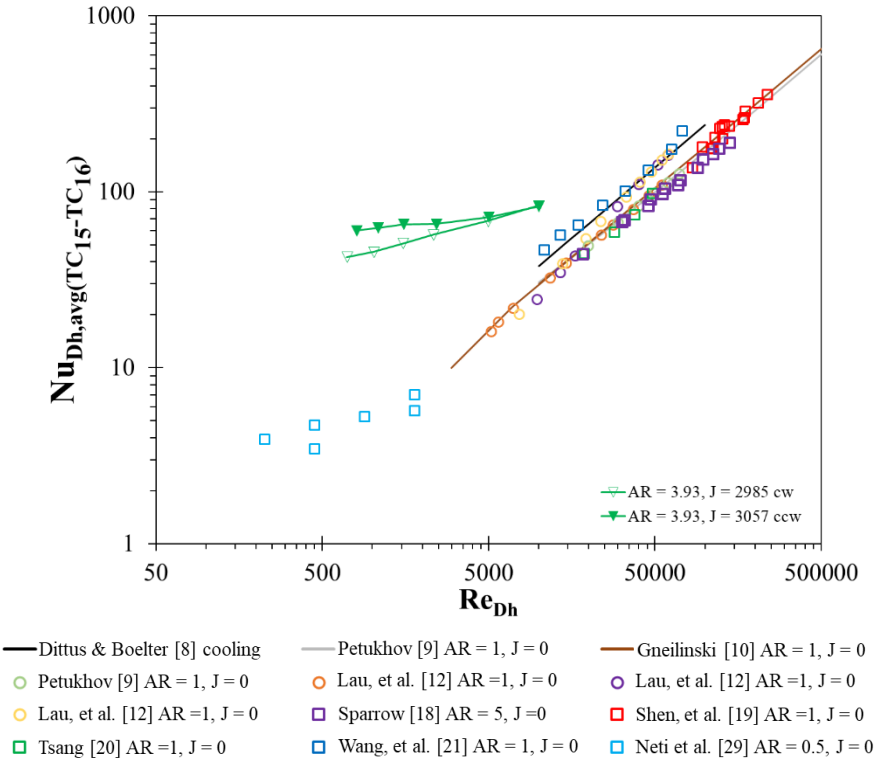

Figure A-72 AR = 3.93, J = 2985 cw, 3057 ccw, Nu_{Dh} vs Re_{Dh}

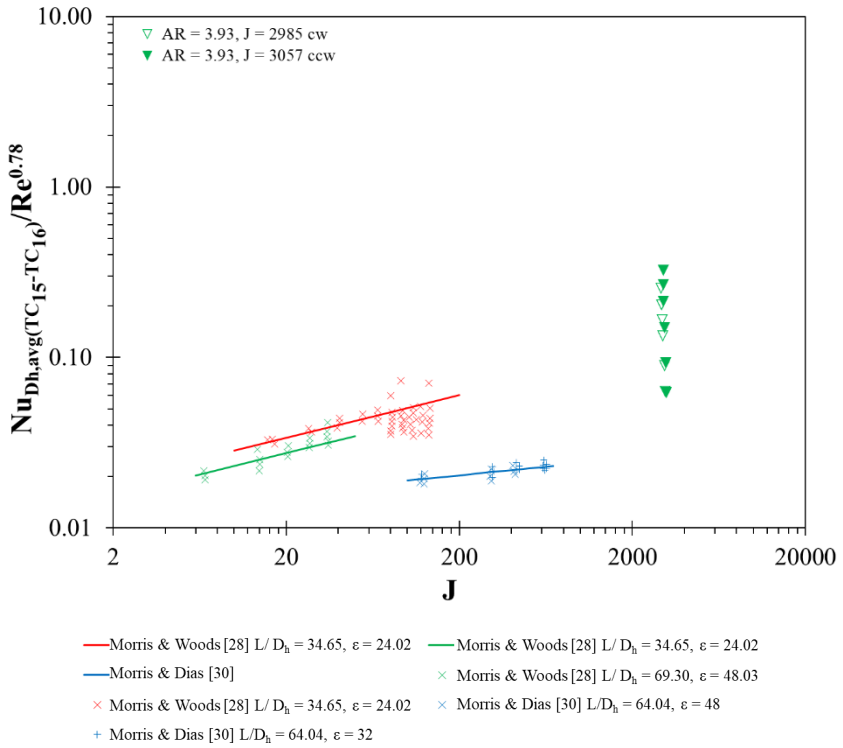

Figure A-73 AR = 3.93, J = 2985 cw, 3057 ccw, Nu_{Dh} vs J

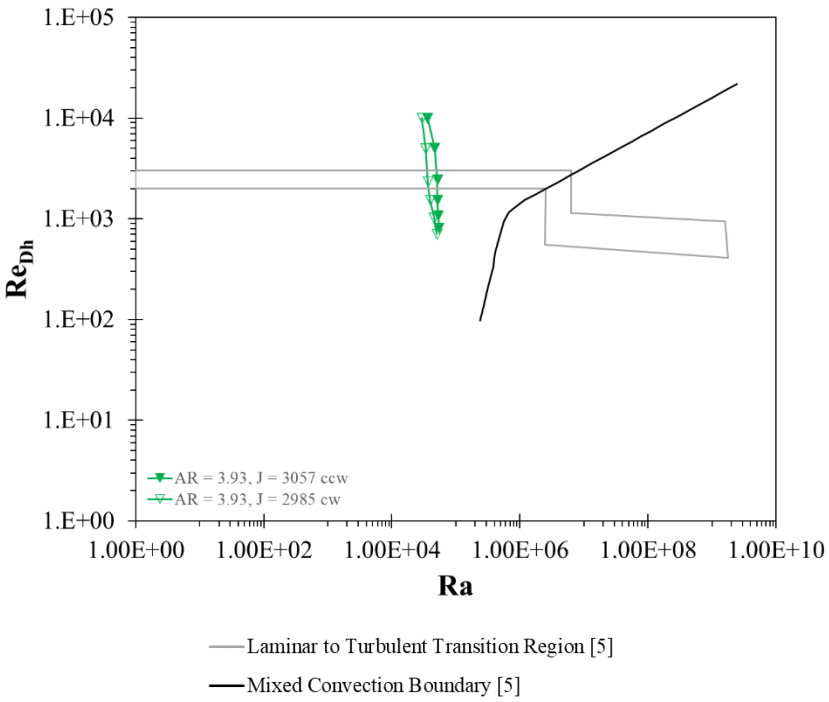

Figure A-74 AR = 3.93, J = 2985 cw, 3057 ccw, Re_{Dh} vs Ra

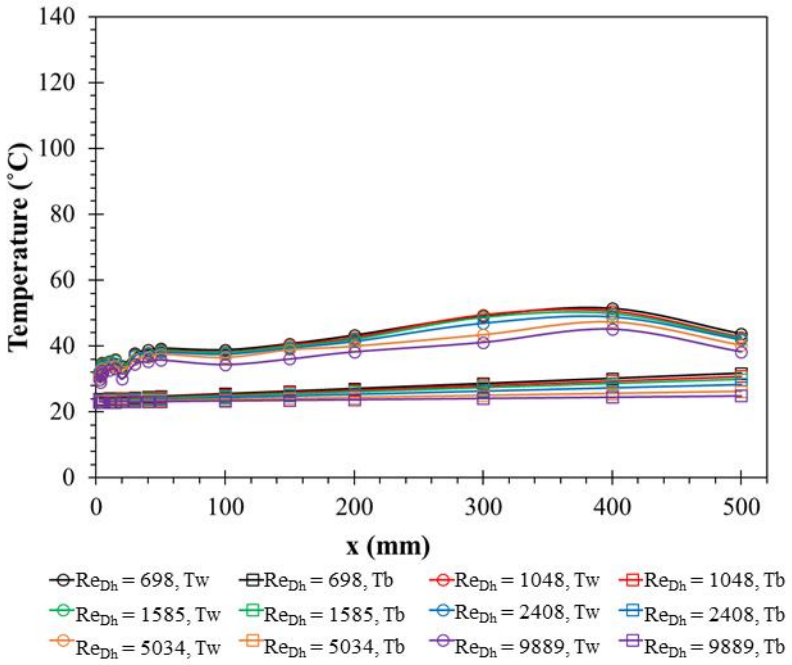

Figure A-75 AR = 3.93, J = 6149 ccw, 50V, (06/04/21), Temperature Profile

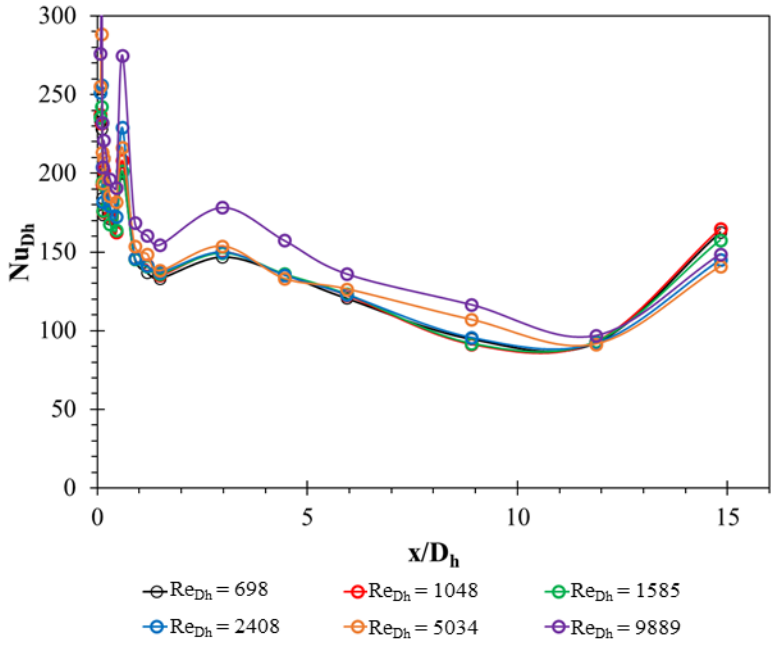

Figure A-76 AR = 3.93, J = 6149 ccw, 50V, (06/04/21), Nu_{Dh} Profile

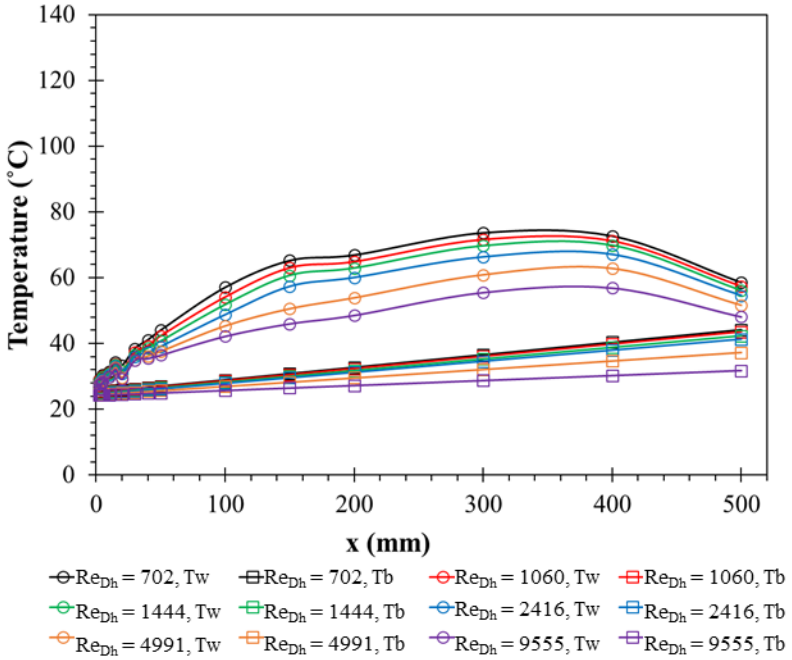

Figure A-77 AR = 3.93, J = 5918 cw, 60V, (06/04/21), Temperature Profile

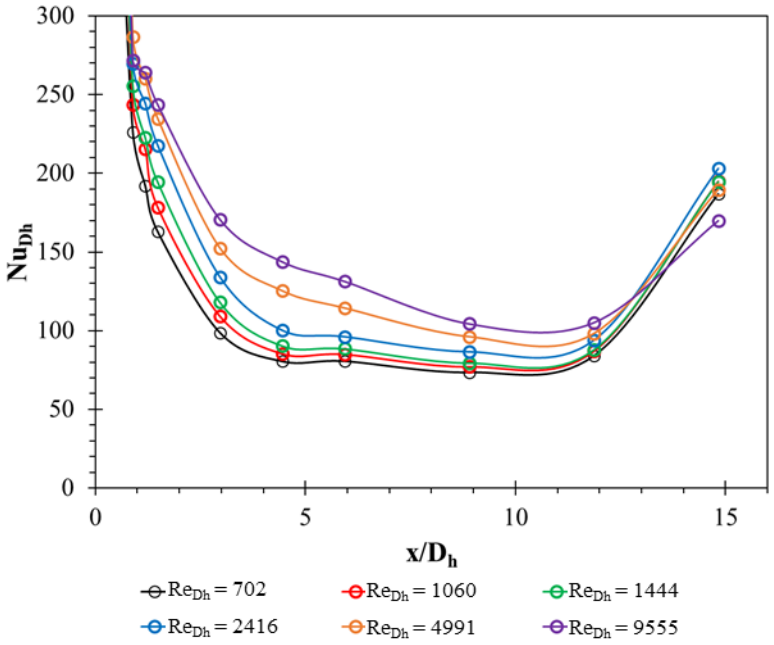

Figure A-78 AR = 3.93, J = 5918 cw, 60V, (06/04/21), Nu_{Dh} Profile

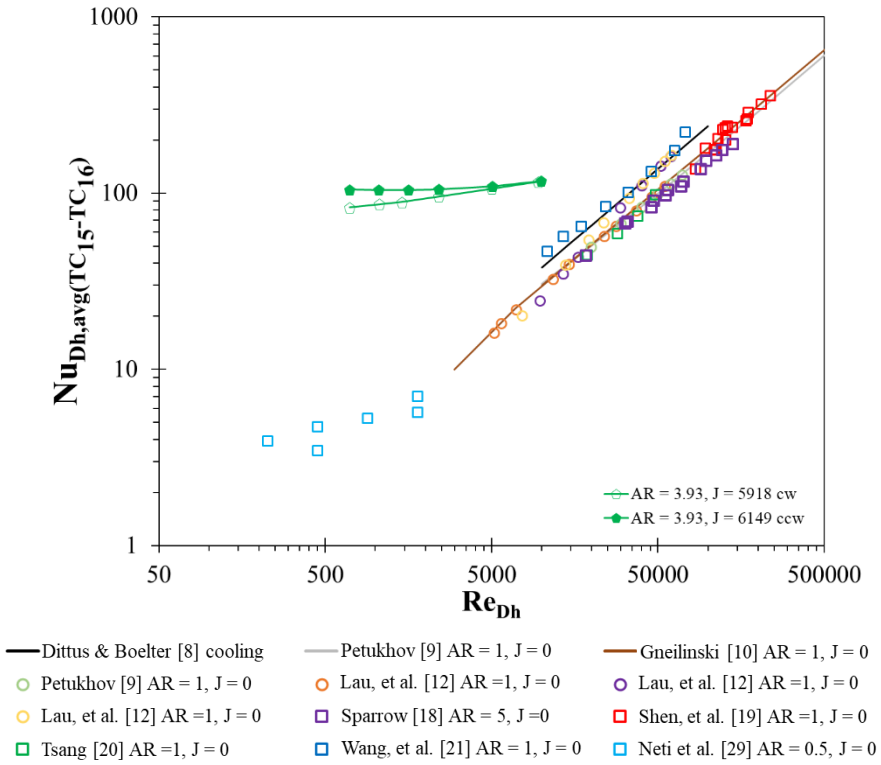

Figure A-79 AR = 3.93, J = 5918 cw, 6149 ccw, Nu_{Dh} vs Re_{Dh}

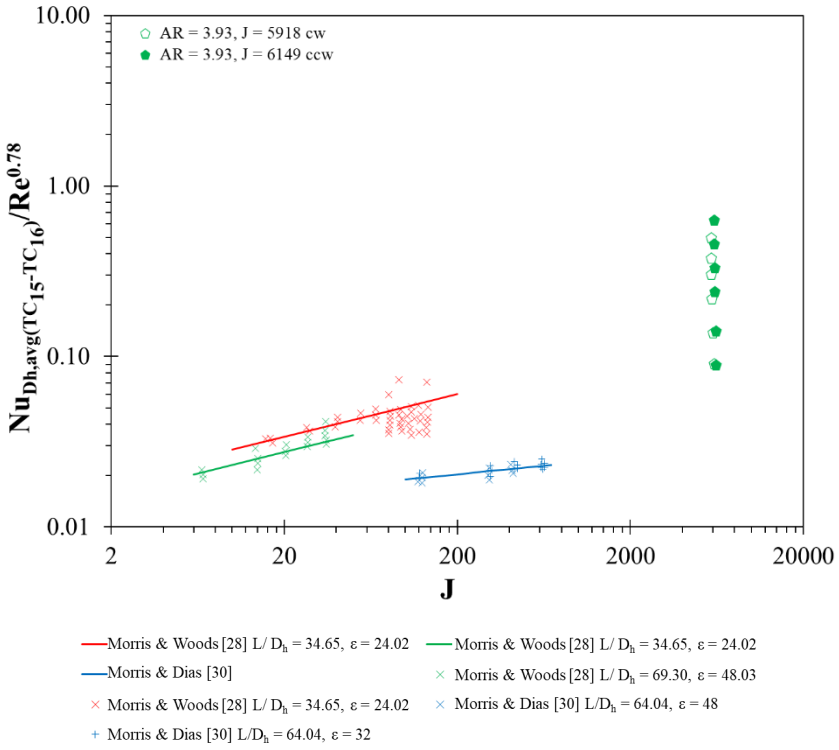

Figure A-80 AR = 3.93, J = 5918 cw, 6149 ccw, Nu_{Dh} vs J

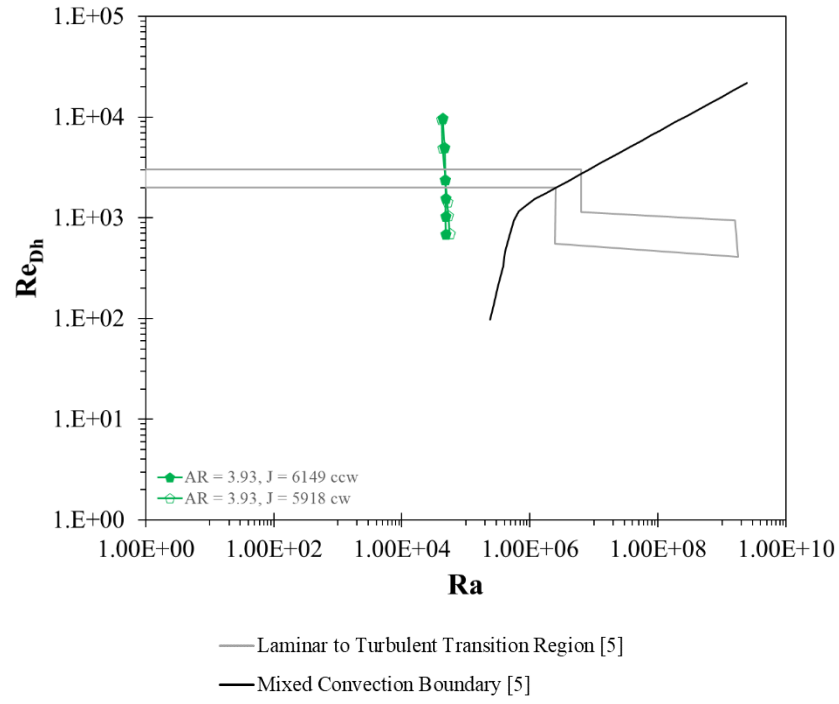

Figure A-81 AR = 3.93, J = 5918 cw, 6149 ccw, Re_{Dh} vs Ra

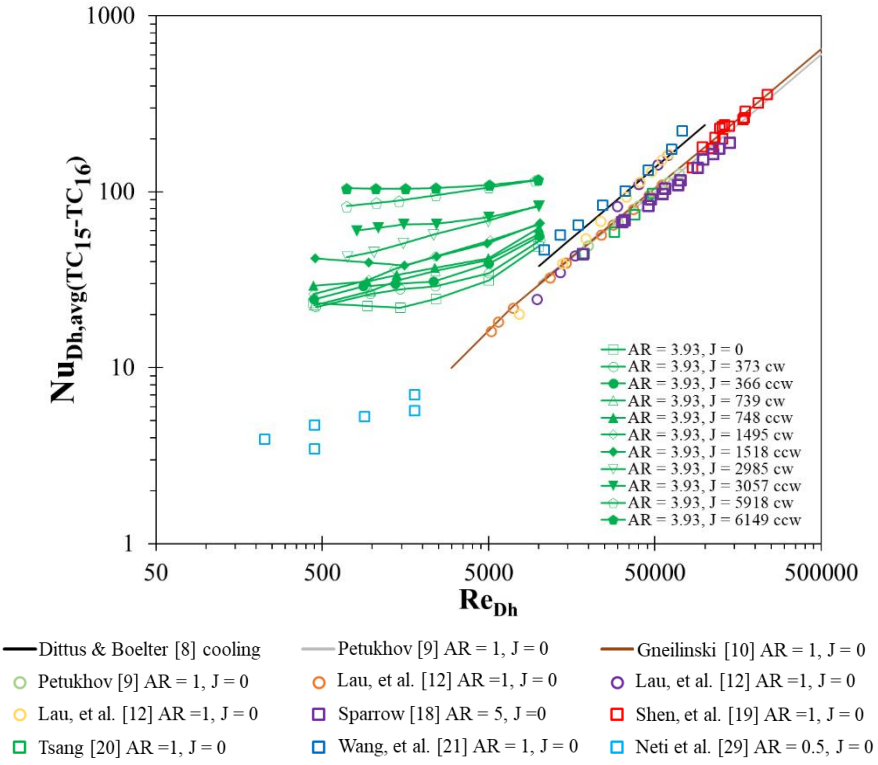

Figure A-82 AR = 3.93 Comparison, Nu_{Dh} vs Re_{Dh}

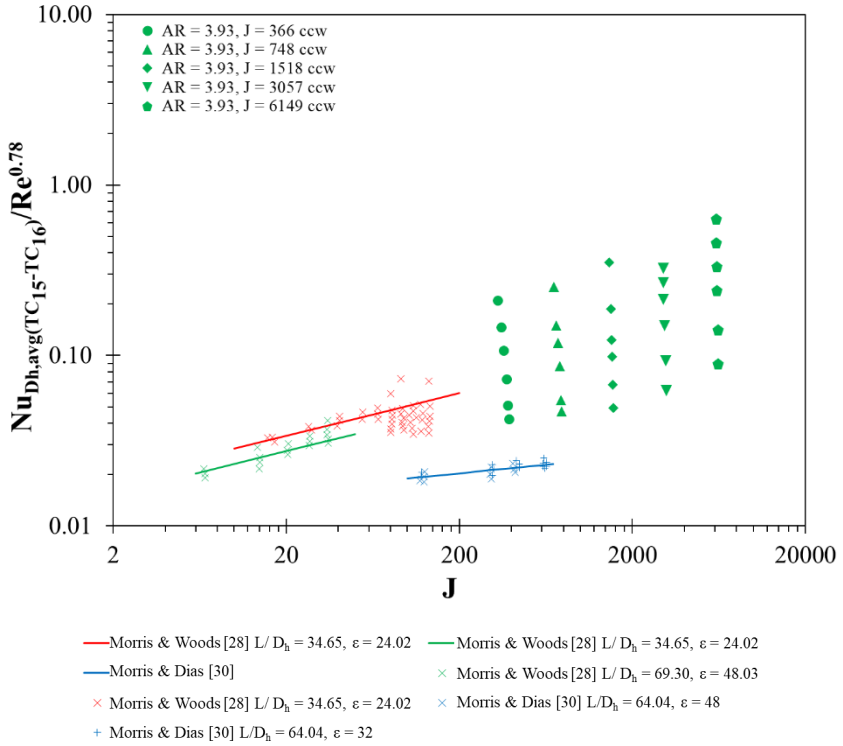

Figure A-83 AR = 3.93 Comparison, Nu_{Dh} vs J ccw

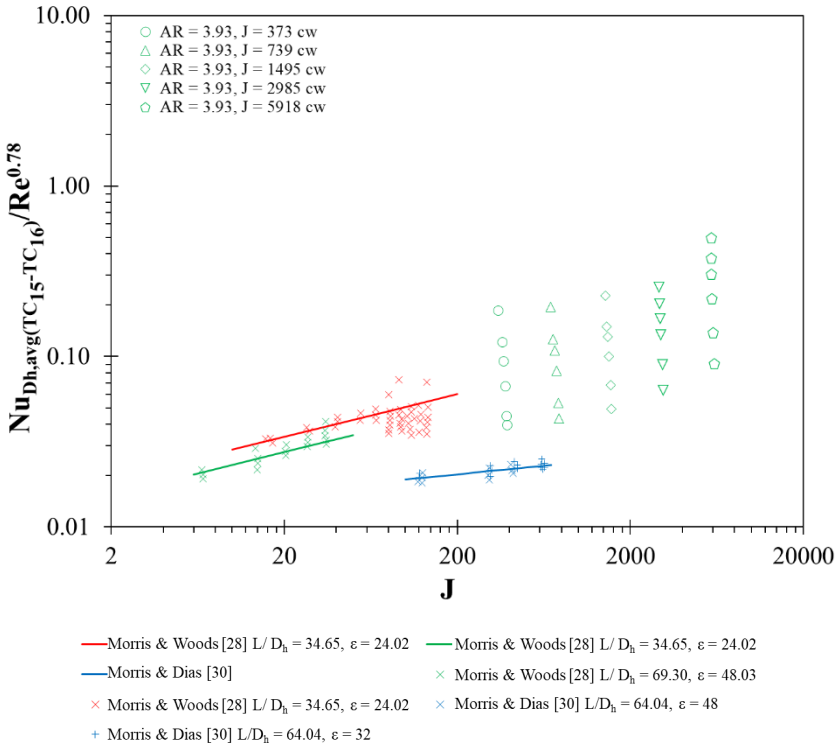

Figure A-84 AR = 3.93 Comparison, Nu_{Dh} vs J cw

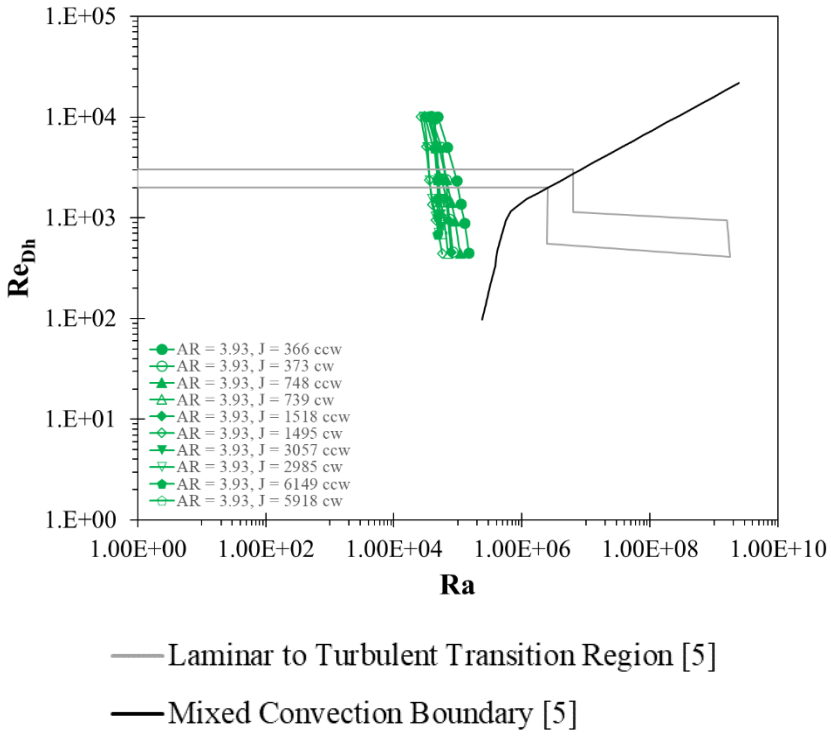

Figure A-85 AR = 3.93 Comparison, Re_{Dh} vs Ra

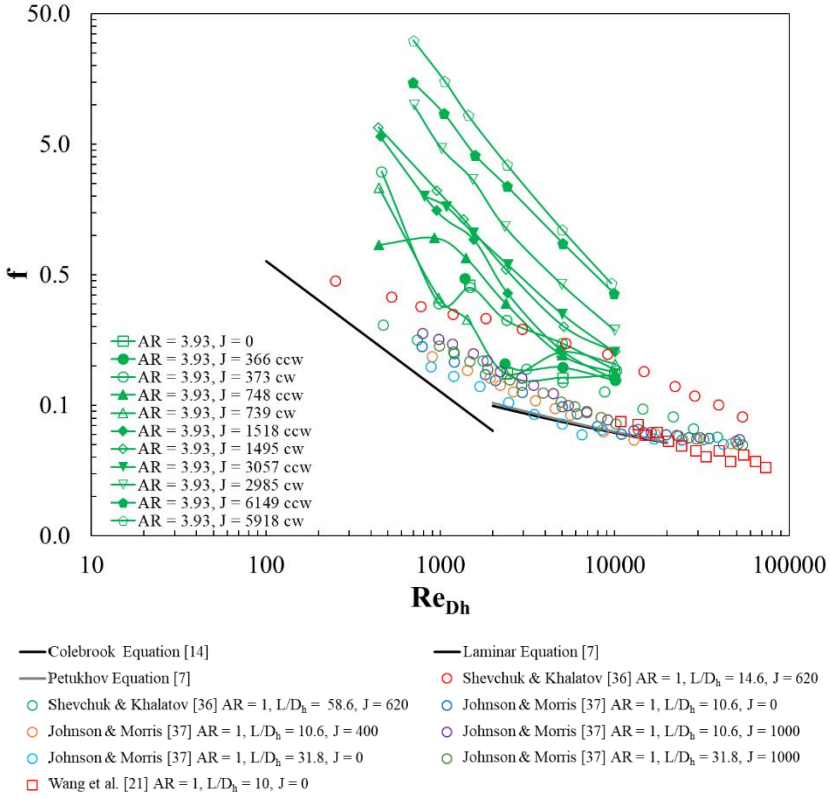

Figure A-86 AR = 3.93 Comparison, Friction Factor

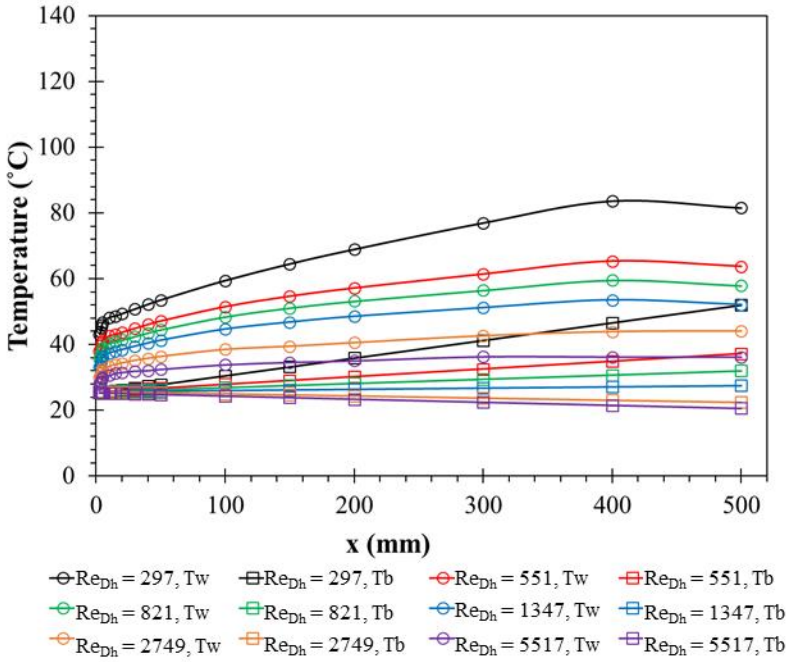

Figure A-87 AR = 8.81, J = 0, 25V, (06/09/21), Temperature Profile

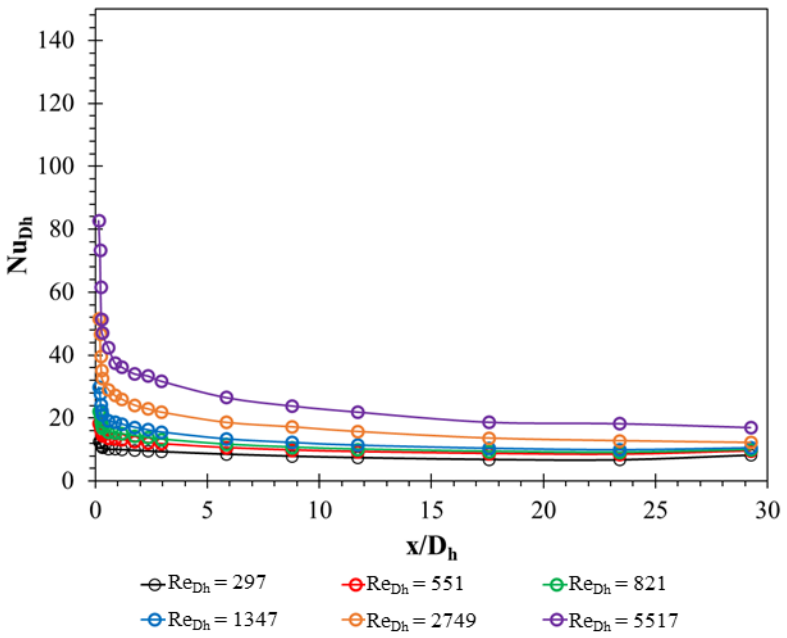

Figure A-88 AR = 8.81, J = 0, 25V, (06/09/21), Nu_{Dh} Profile

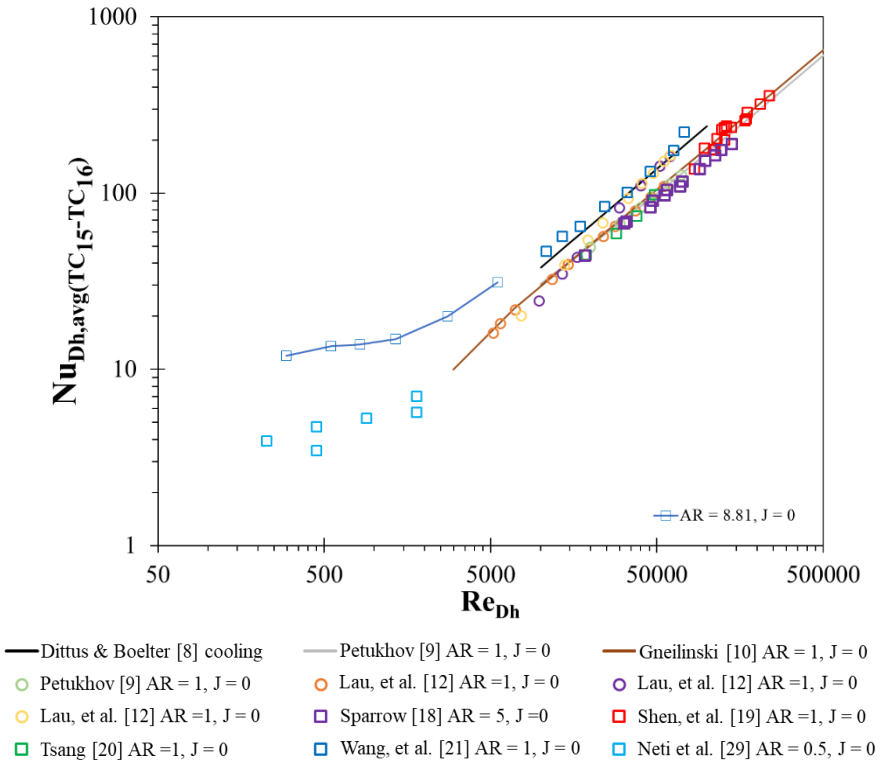

Figure A-89 AR = 8.81, J = 0, Nu_{Dh} vs Re_{Dh}

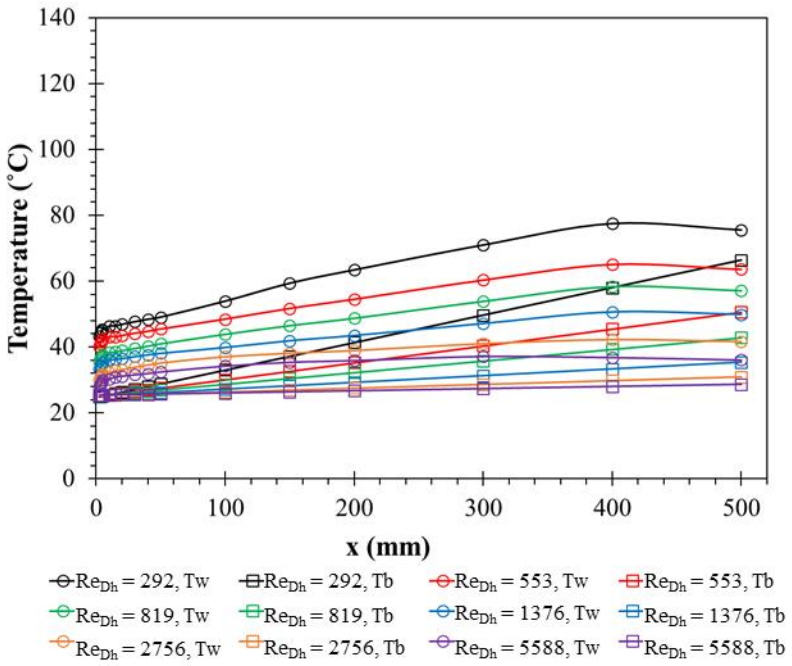

Figure A-90 AR = 8.81, J = 95 ccw, (06/09/21), Temperature Profile

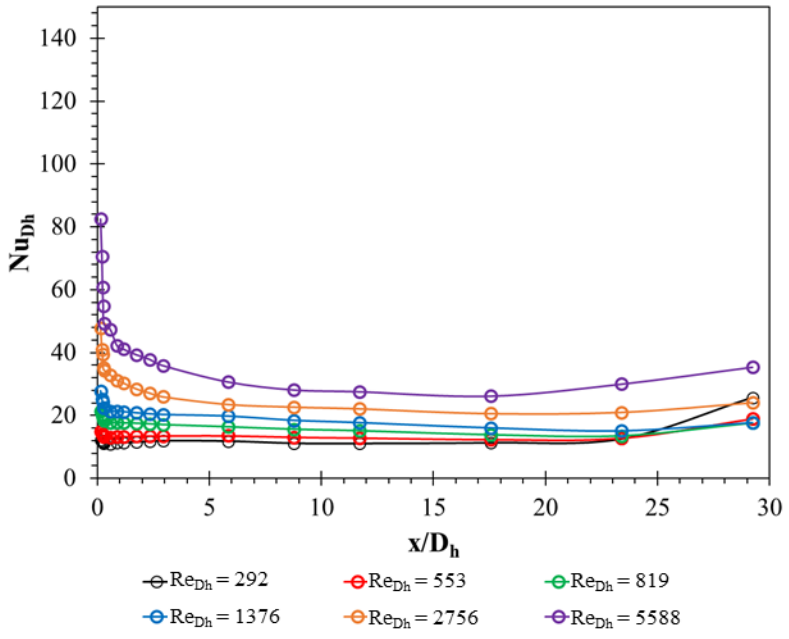

Figure A-91 AR = 8.81, J = 95 ccw, 25V, (06/09/21), Nu_{Dh} Profile

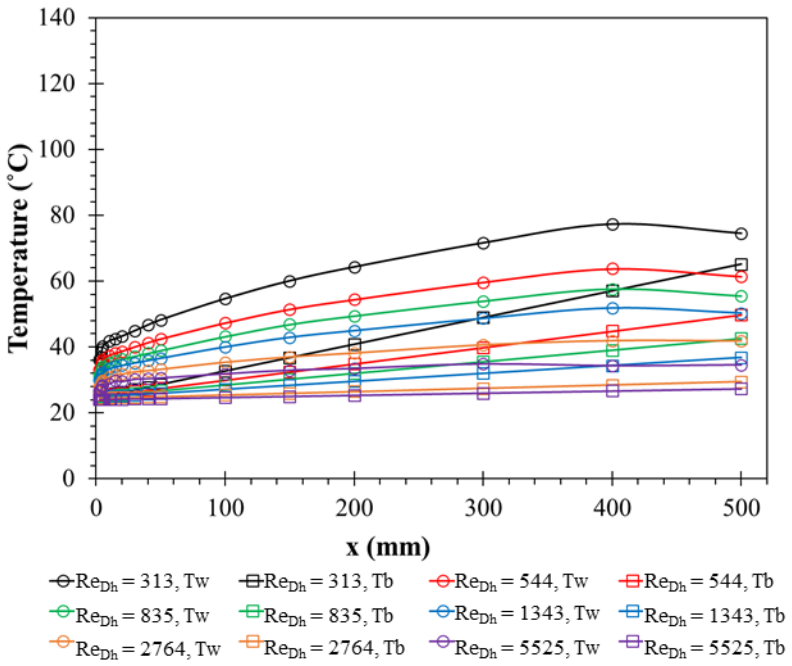

Figure A-92 AR = 8.81, J = 95 cw, (06/09/21), Temperature Profile

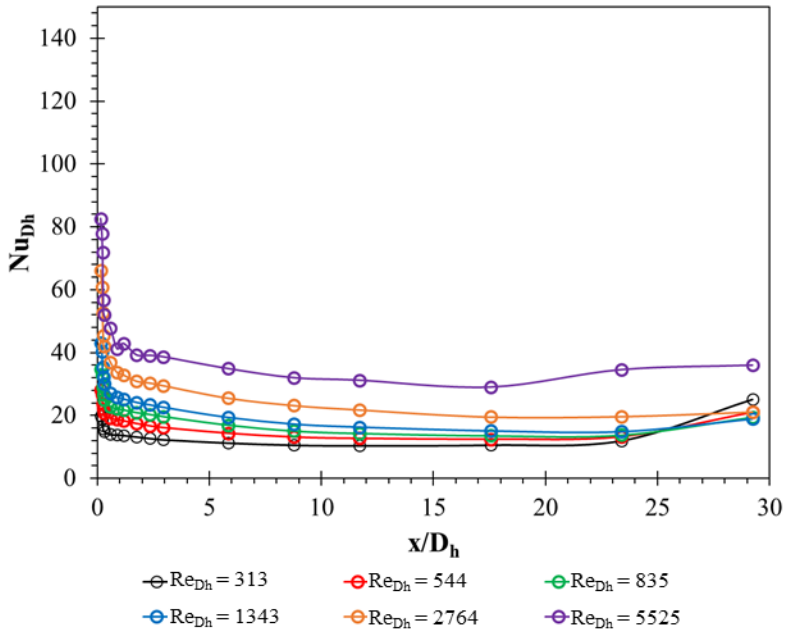

Figure A-93 AR = 8.81, J = 95 cw, 25V, (06/09/21), Nu_{Dh} Profile

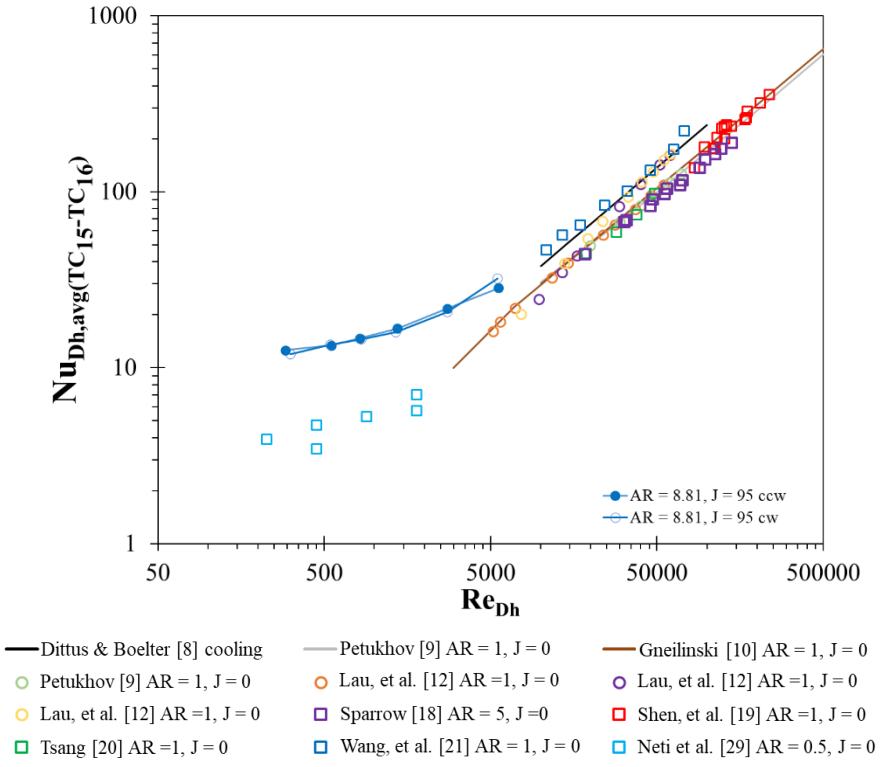

Figure A-94 AR = 8.81, J = 95, Nu_{Dh} vs Re_{Dh}

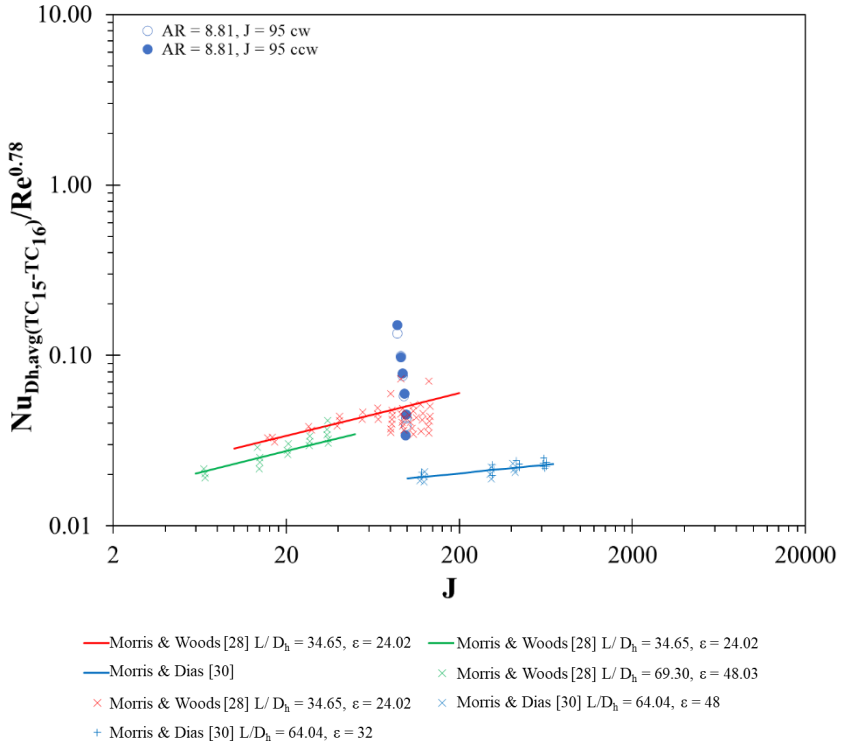

Figure A-95 AR = 8.81, J = 95, Nu_{Dh} vs J

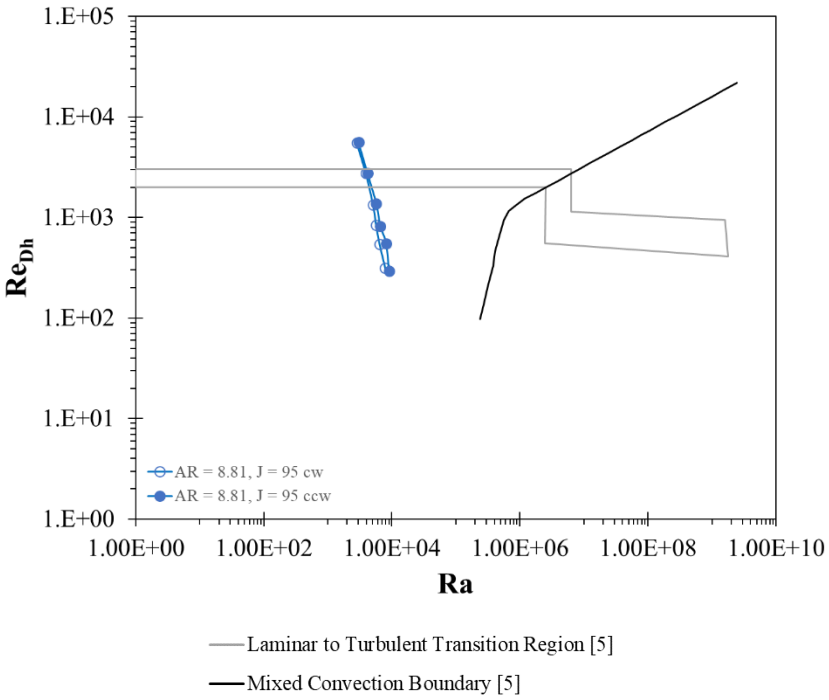

Figure A-96 AR = 8.81, J = 95, Re_{Dh} vs Ra

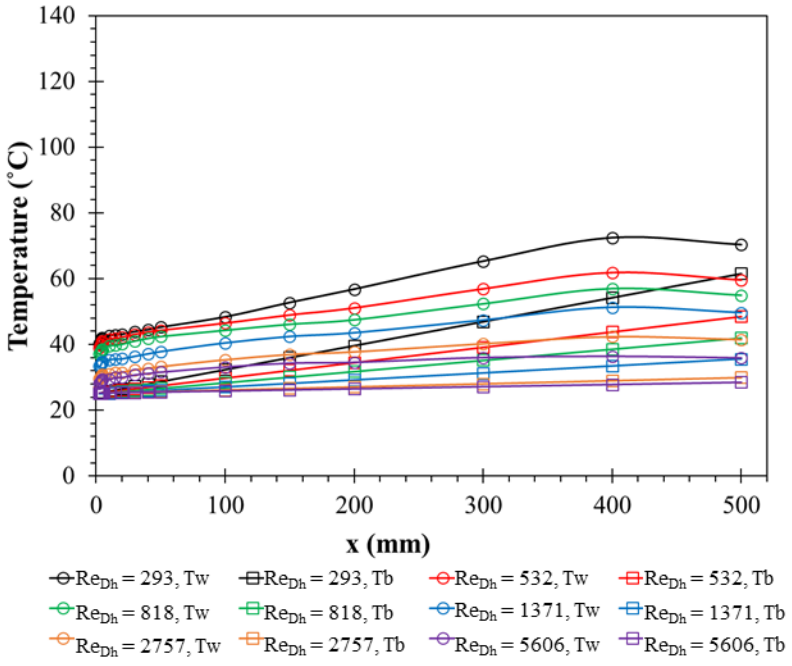

Figure A-97 AR = 8.81, J = 190 ccw, 25V, (06/10/21), Temperature Profile

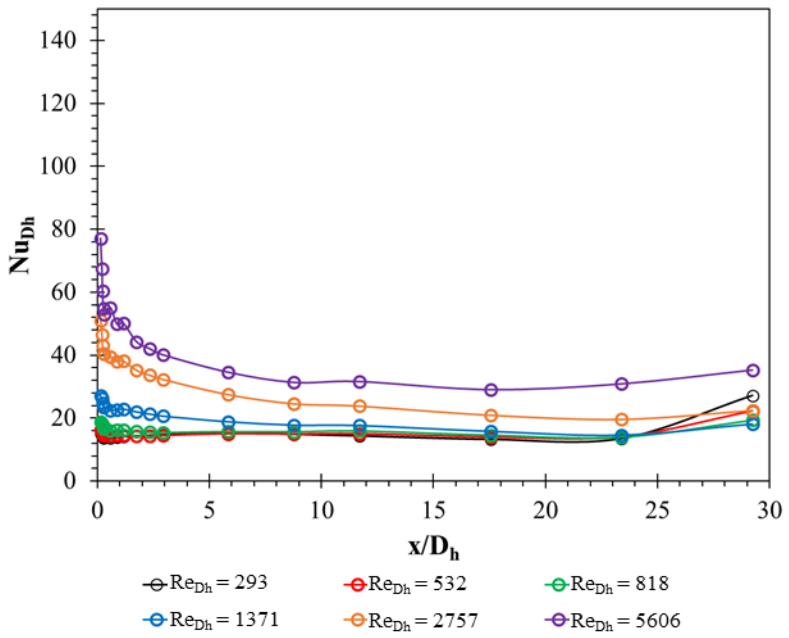

Figure A-98 AR = 8.81, J = 190 ccw, 25V, (06/10/21), Nu_{Dh} Profile

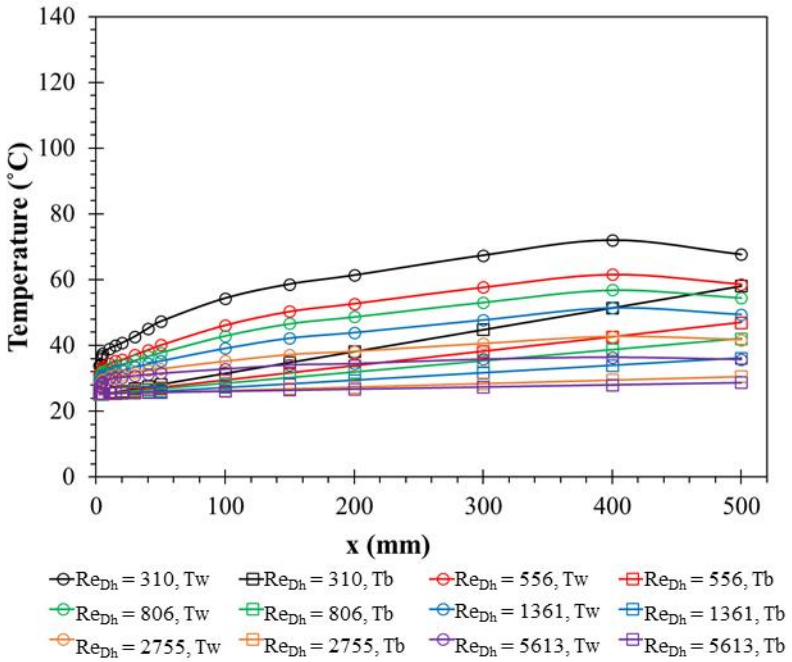

Figure A-99 AR = 8.81, J = 190 cw, 25V, (06/10/21), Temperature Profile

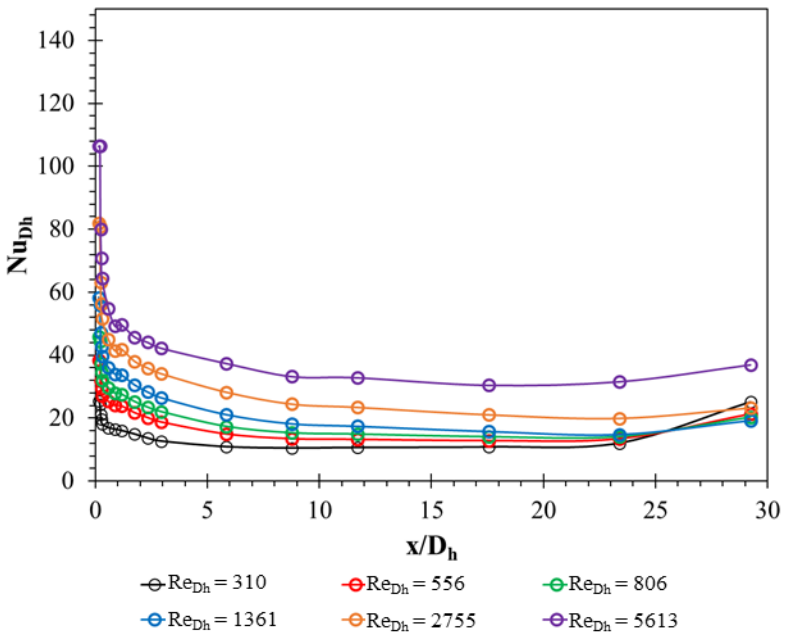

Figure A-100 AR = 8.81, J = 190 cw, 25V, (06/10/21), Nu_{Dh} Profile

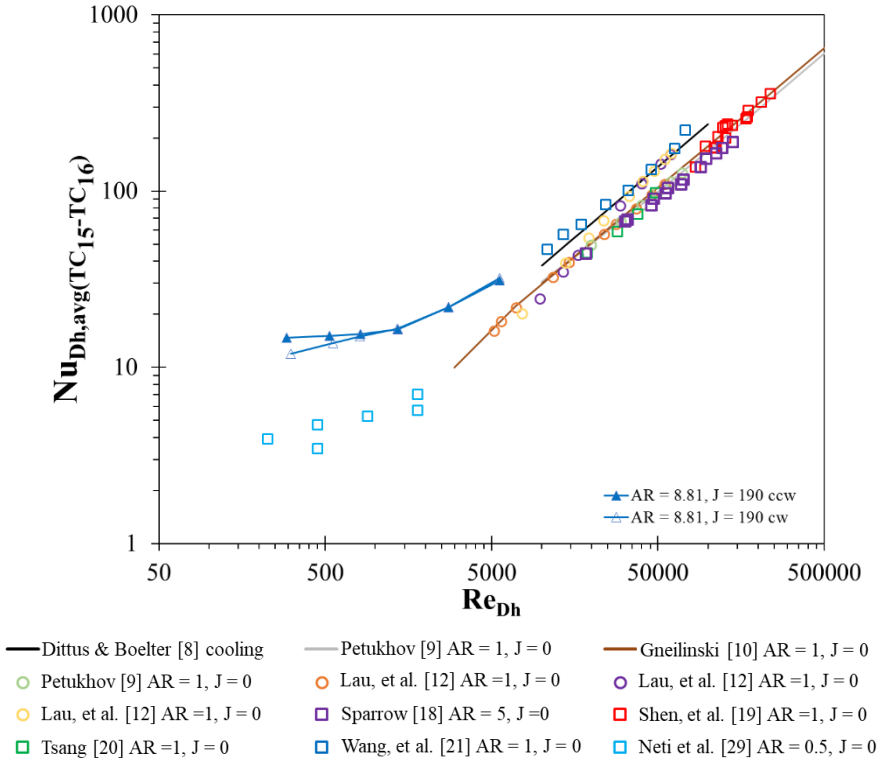

Figure A-101 AR = 8.81, J = 190, Nu_{Dh} vs Re_{Dh}

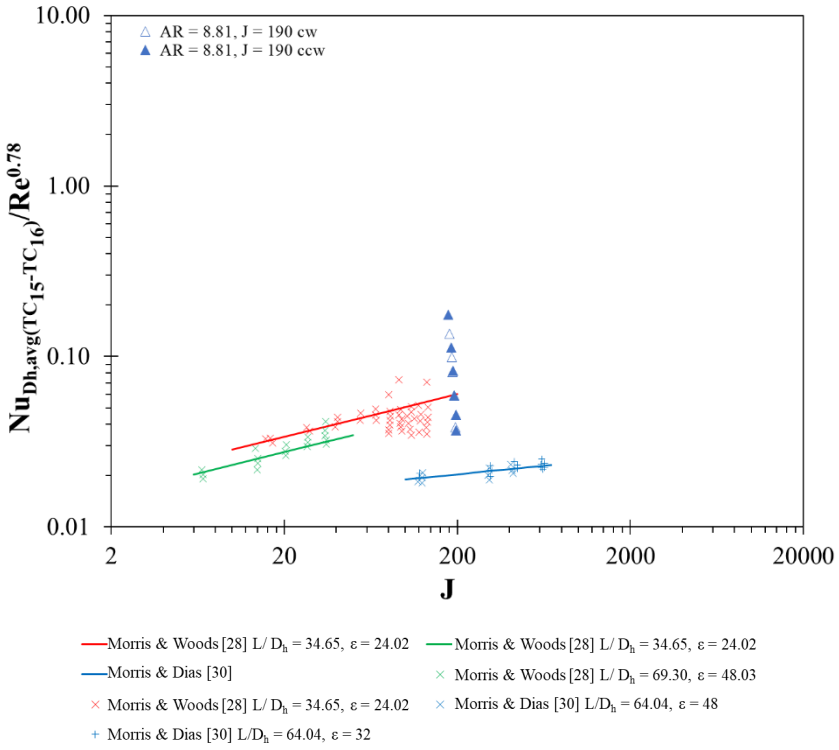

Figure A-102 AR = 8.81, J = 190, Nu_{Dh} vs J

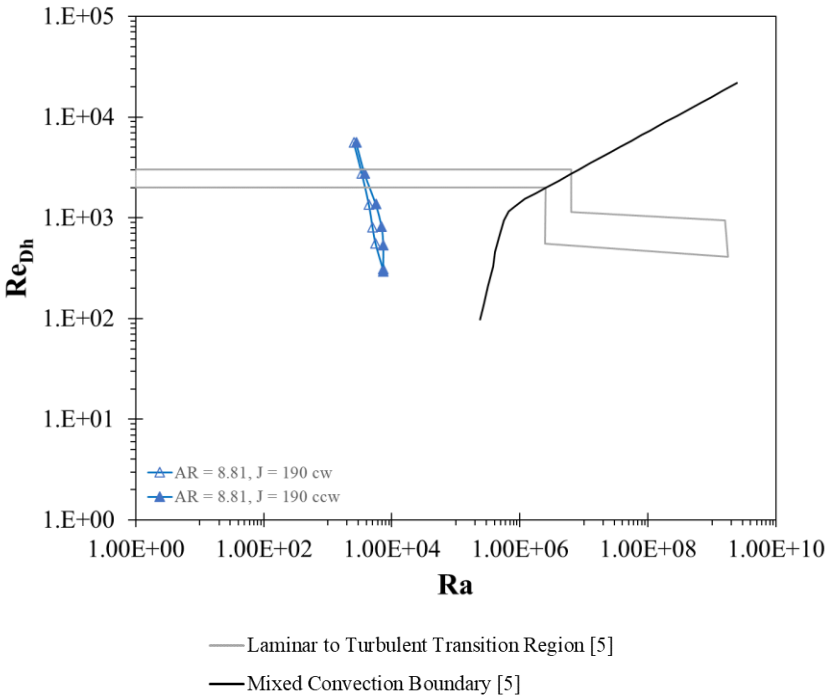

Figure A-103 AR = 8.81, J = 190, Re_{Dh} vs Ra

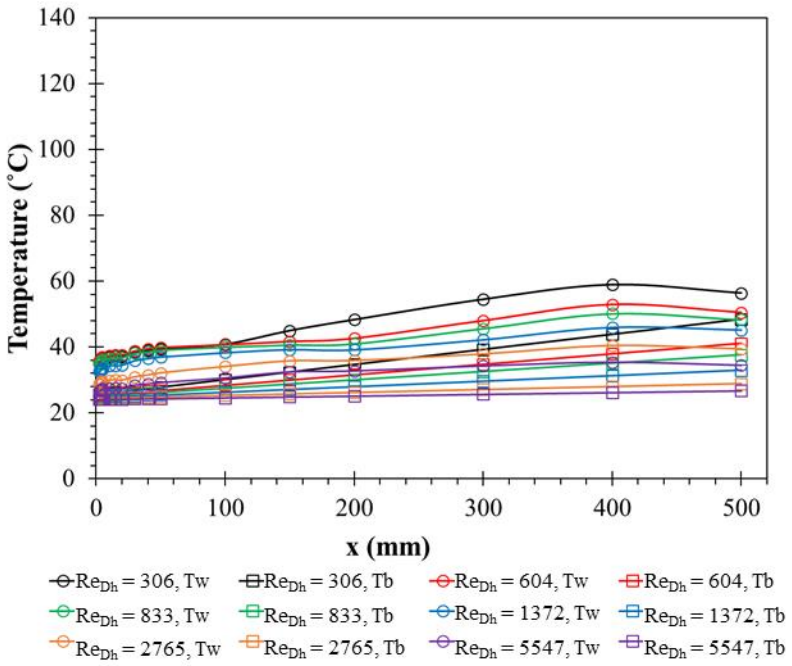

Figure A-104 AR = 8.81, J = 385 ccw, 25V, (06/11/21), Temperature Profile

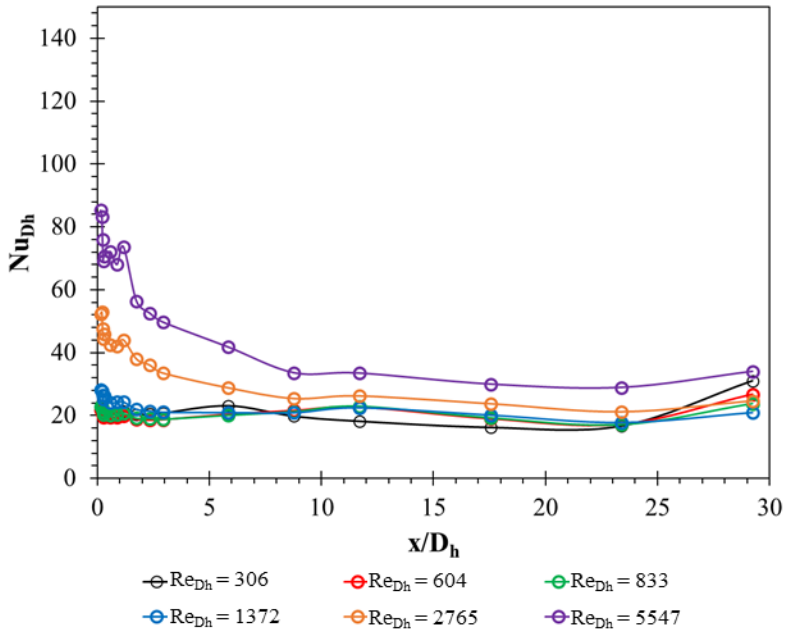

Figure A-105 AR = 8.81, J = 385 ccw, 25V, (06/11/21), Nu_{Dh} Profile

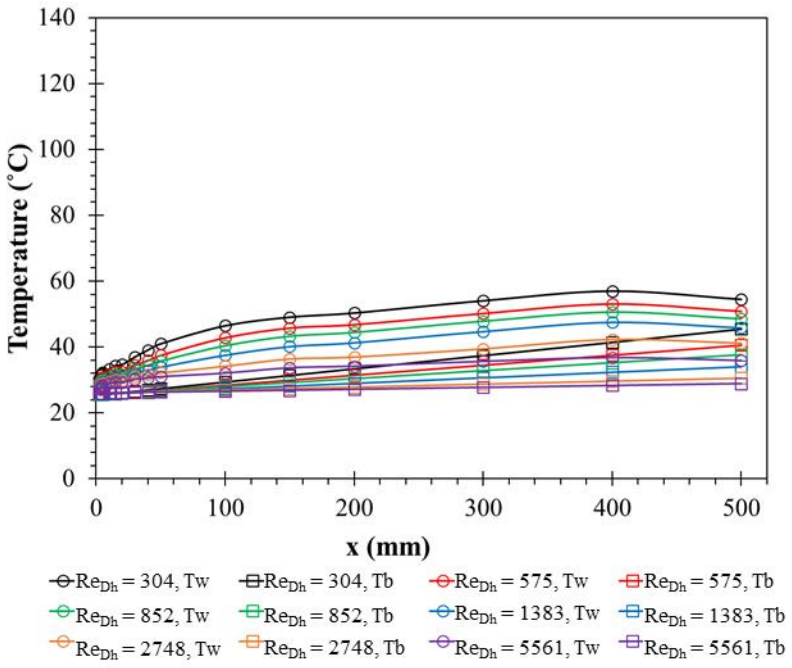

Figure A-106 AR = 8.81, J = 384 cw, 25V, (06/11/21), Temperature Profile

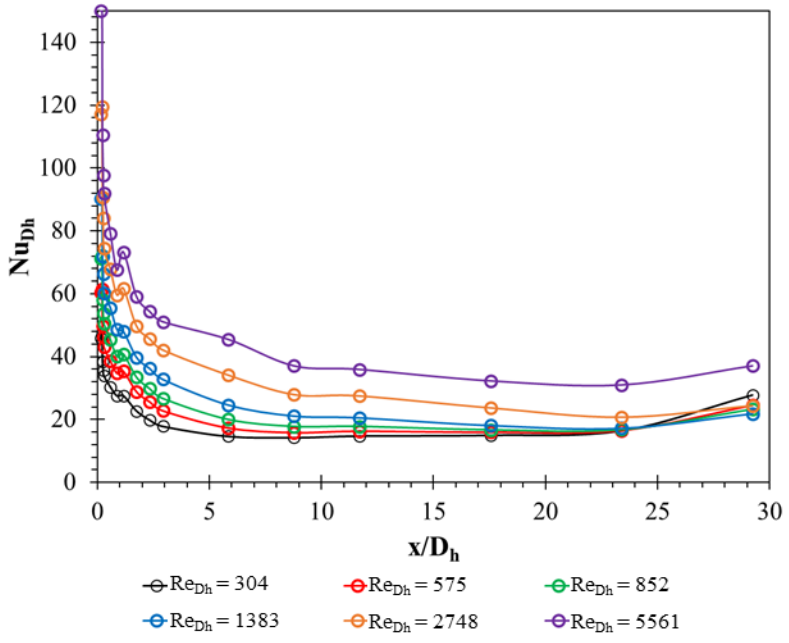

Figure A-107 AR = 8.81, J = 384 cw, 25V, (06/11/21), Nu_{Dh} Profile

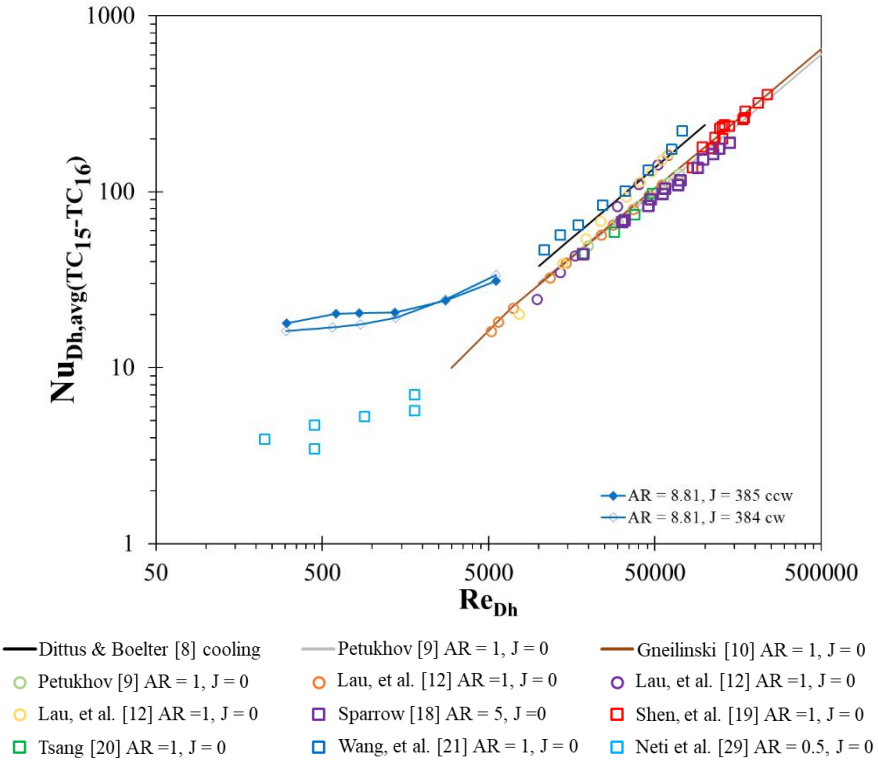

Figure A-108 AR = 8.81, J = 384 cw, 385 cw, Nu_{Dh} vs Re_{Dh}

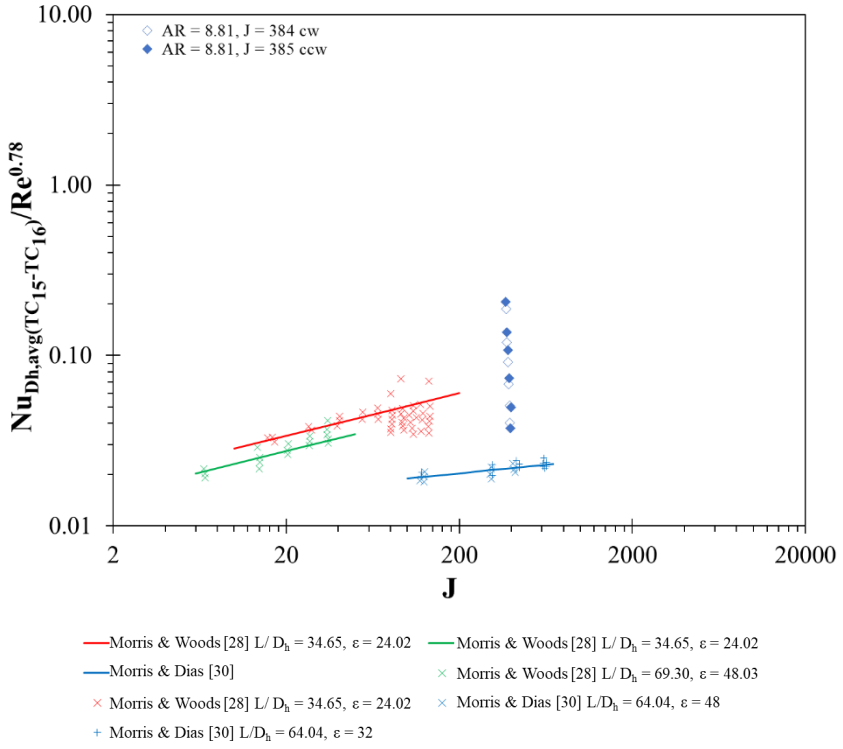

Figure A-109 AR = 8.81, J = 384 cw, 385 cw, Nu_{Dh} vs J

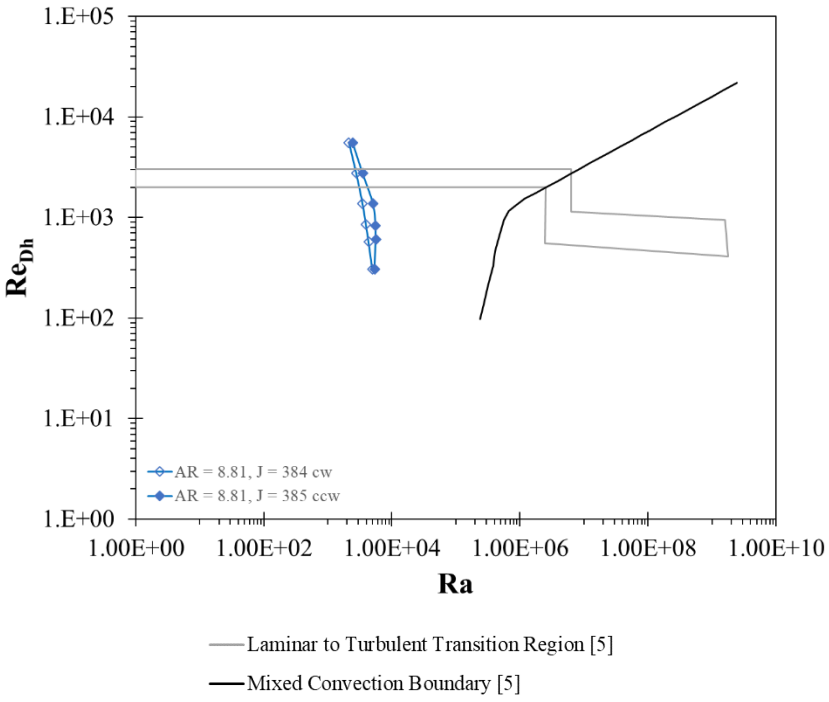

Figure A-110 AR = 8.81, J = 384 cw, 385 cw, Re_{Dh} vs Ra

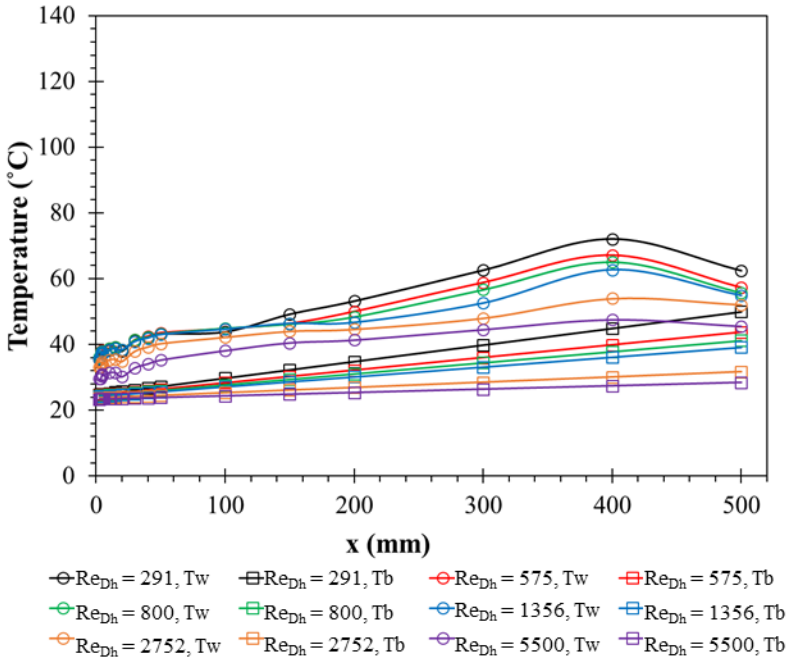

Figure A-111 AR = 8.81, J = 761 ccw, 40V, (06/12/21), Temperature Profile

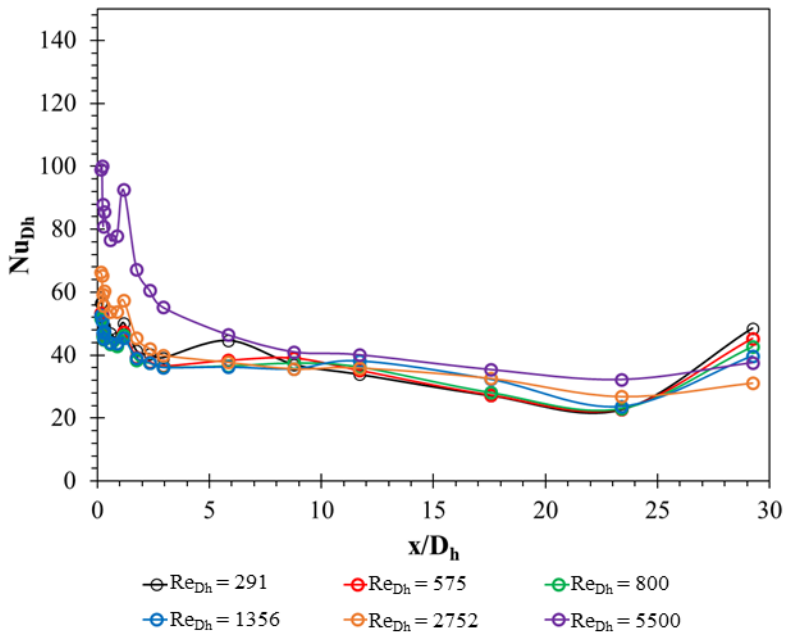

Figure A-112 AR = 8.81, J = 761 ccw, 40V, (06/12/21), Nu_{Dh} Profile

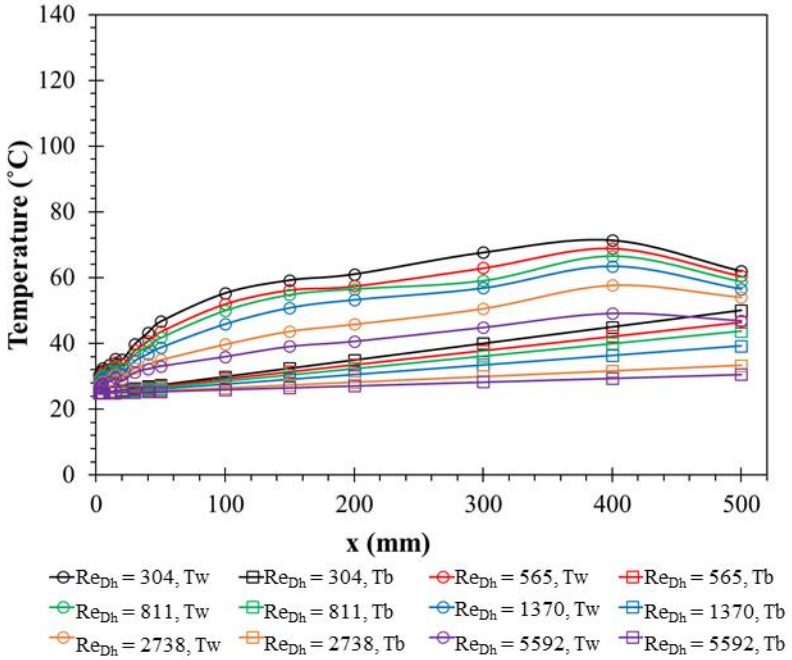

Figure A-113 AR = 8.81, J = 755 cw, 40V, (06/12/21), Temperature Profile

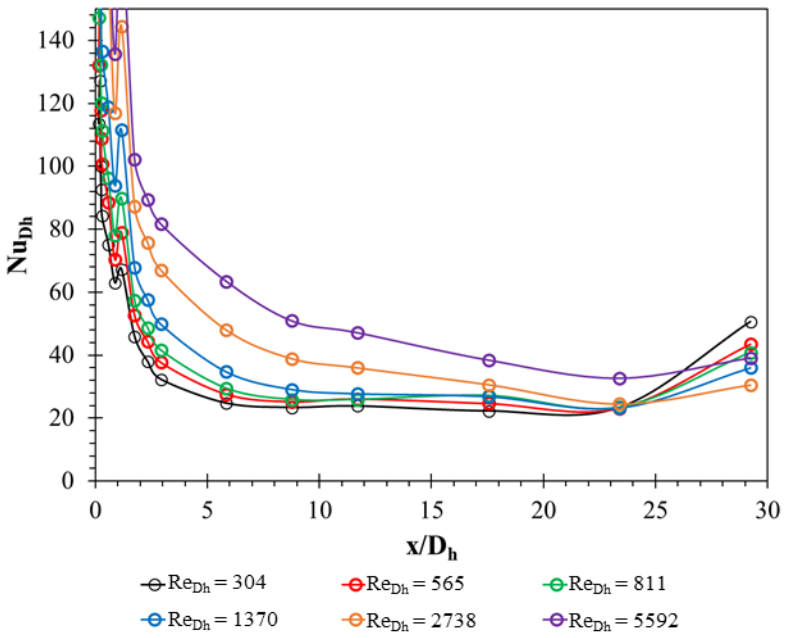

Figure A-114 AR = 8.81, J = 755 cw, 40V, (06/12/21), Nu_{Dh} Profile

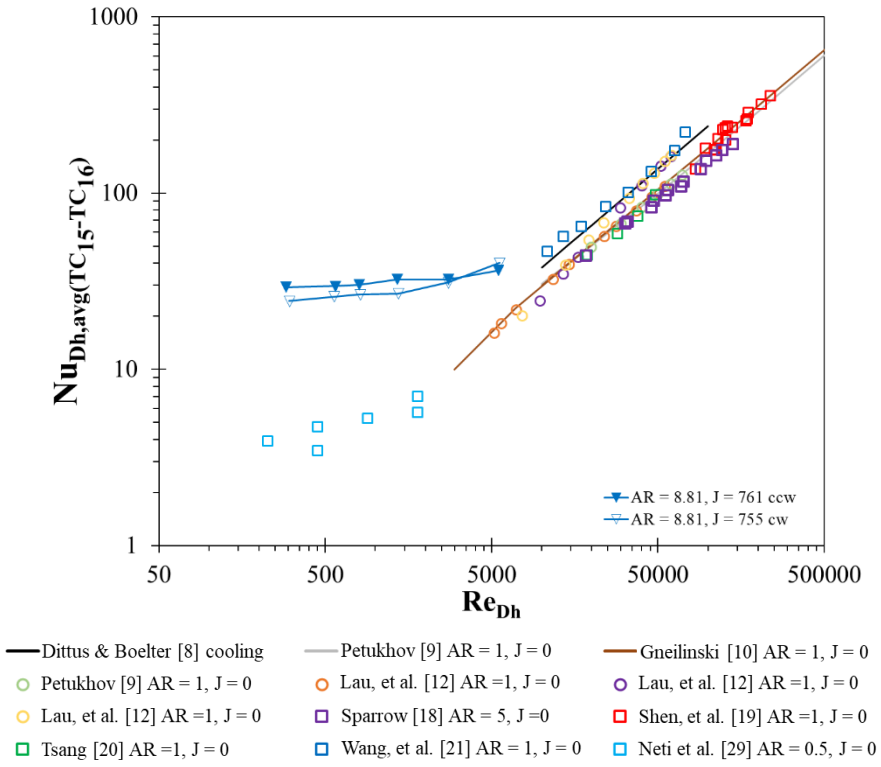

Figure A-115 AR = 8.81, J = 755 cw, 761 ccw, Nu_{Dh} vs Re_{Dh}

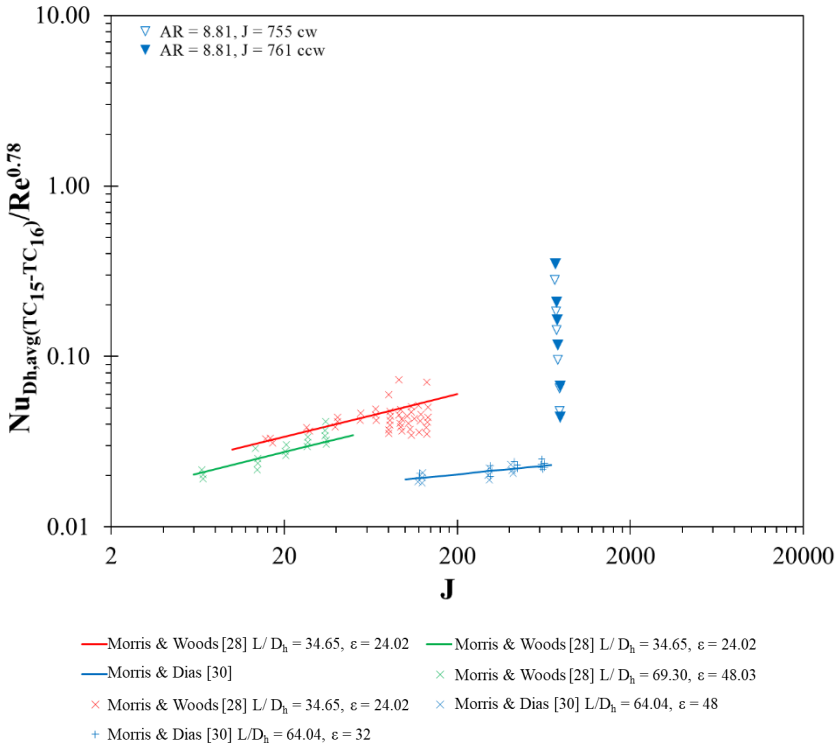

Figure A-116 AR = 8.81, J = 755 cw, 761 ccw, Nu_{Dh} vs J

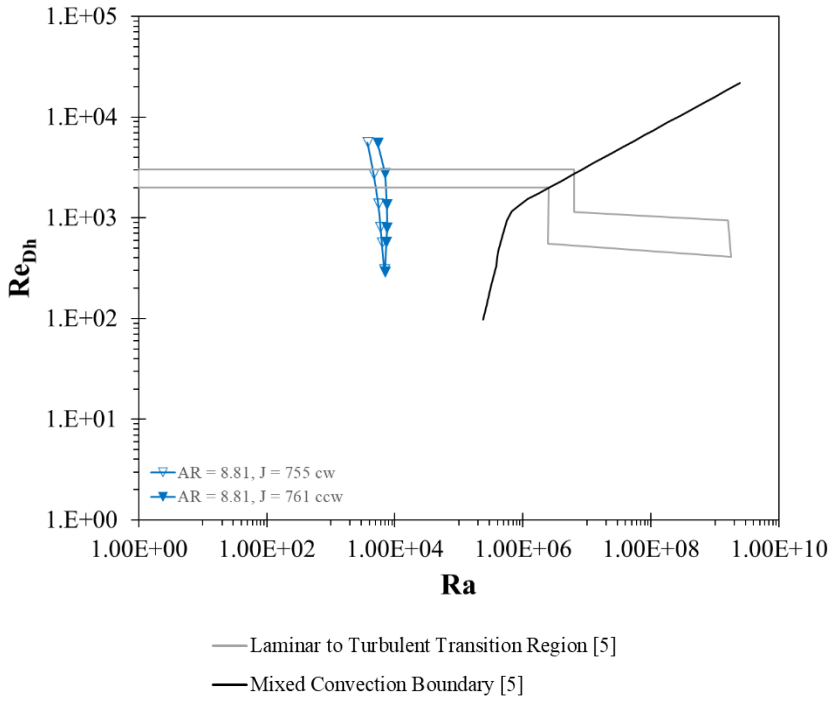

Figure A-117 AR = 8.81, J = 755 cw, 761 ccw, Re_{Dh} vs Ra

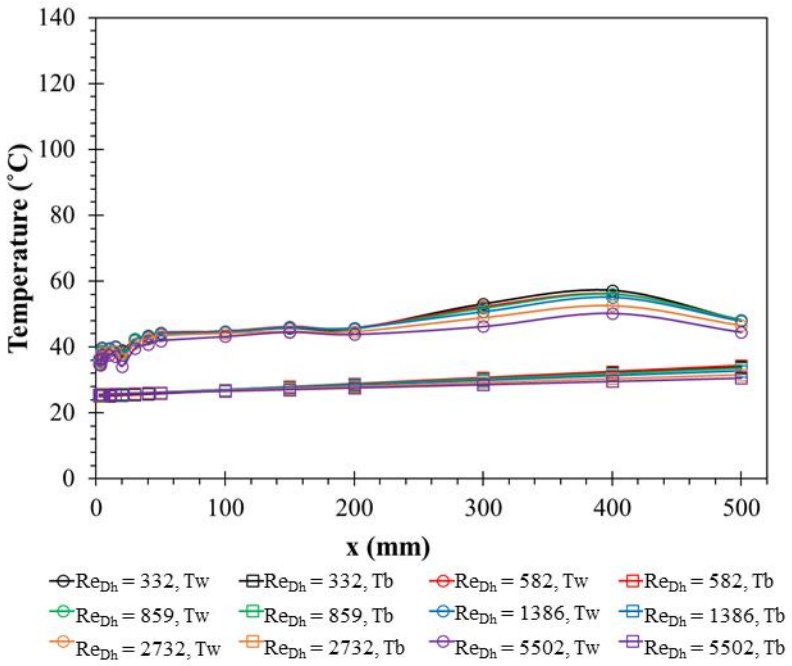

Figure A-118 AR = 8.81, J = 1544 ccw, 50V, (06/12/21), Temperature Profile

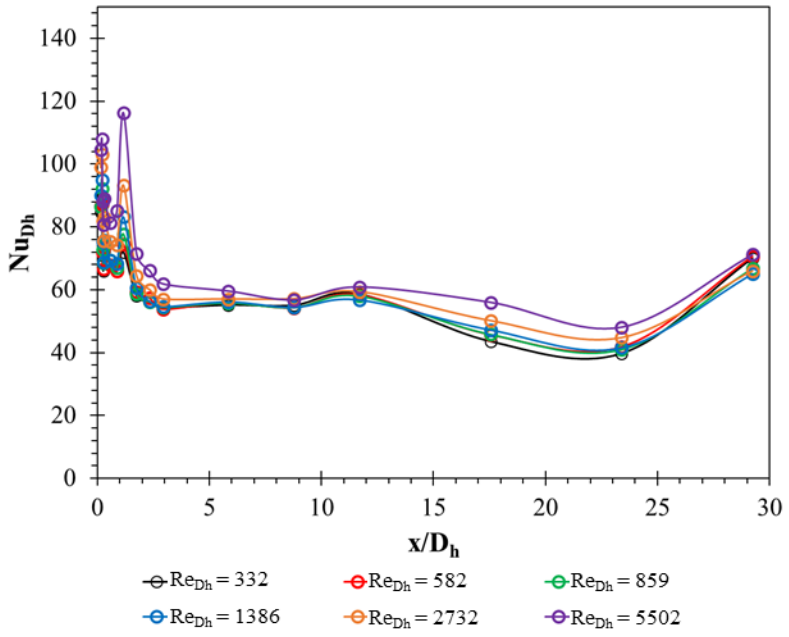

Figure A-119 AR = 8.81, J = 1544 ccw, 50V, (06/12/21), Nu_{Dh} Profile

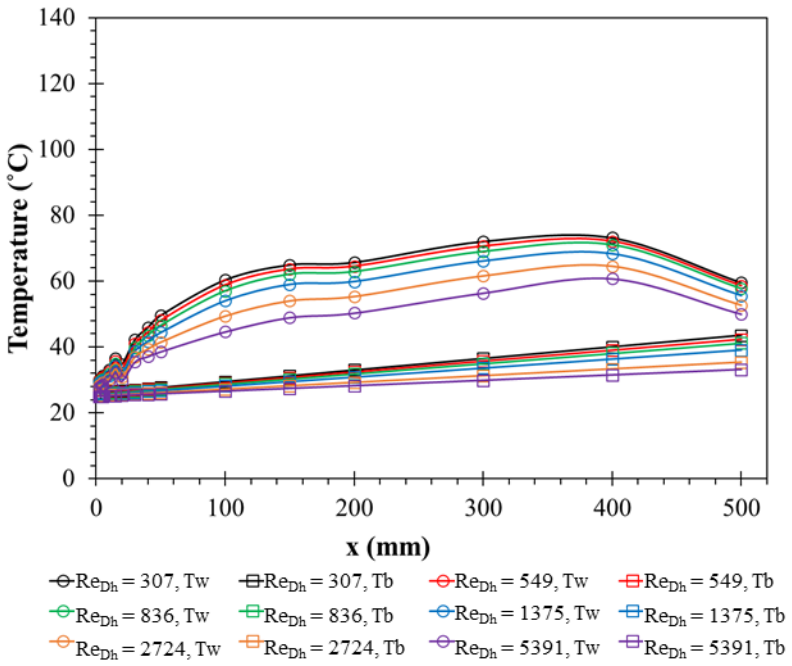

Figure A-120 AR = 8.81, J = 1516 cw, 60V, (06/14/21), Temperature Profile

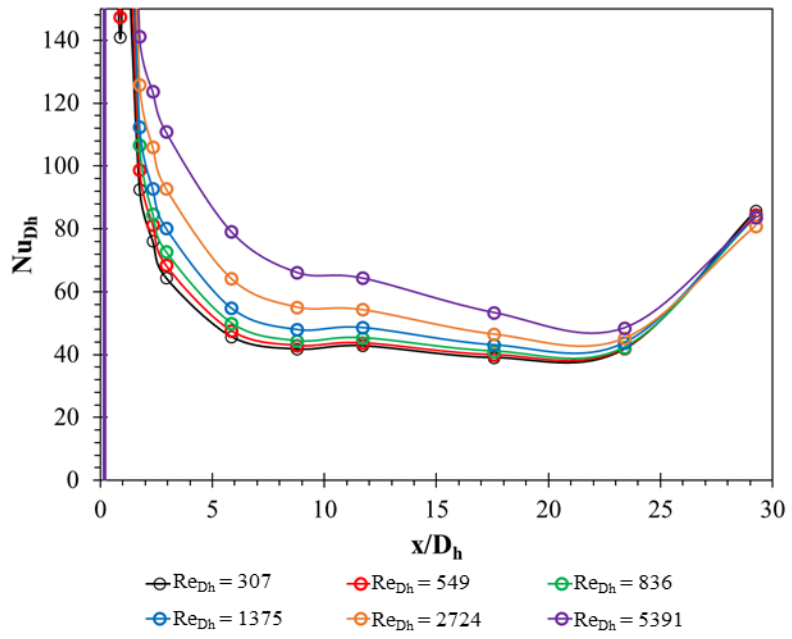

Figure A-121 AR = 8.81, J = 1516 cw, 60V, (06/14/21), Nu_{Dh} Profile

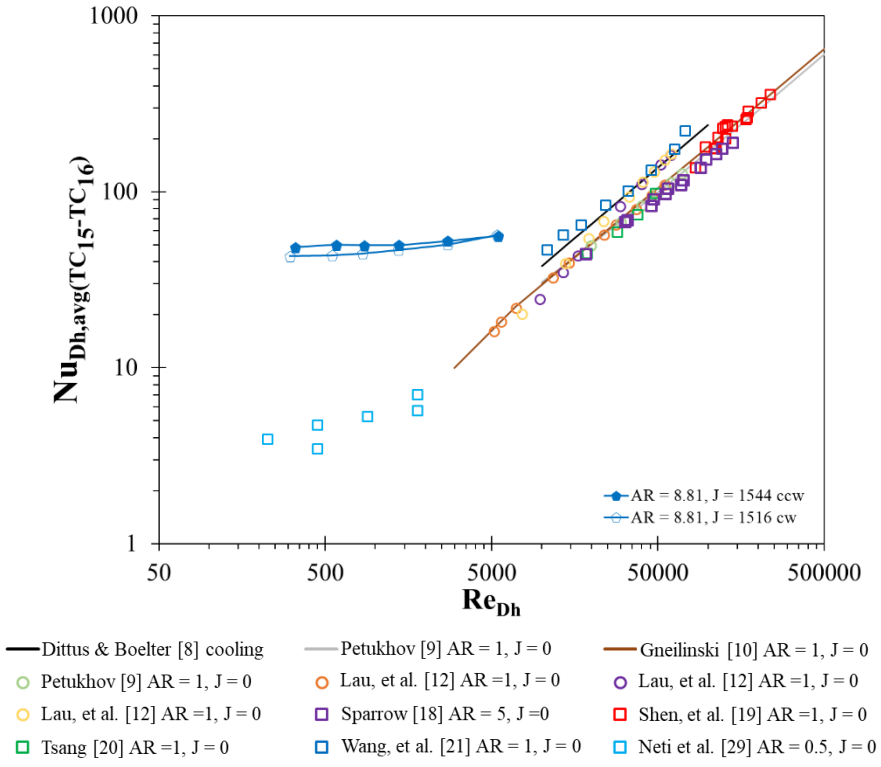

Figure A-122 AR = 8.81, J = 1516 cw, 1544 ccw, Nu_{Dh} vs Re_{Dh}

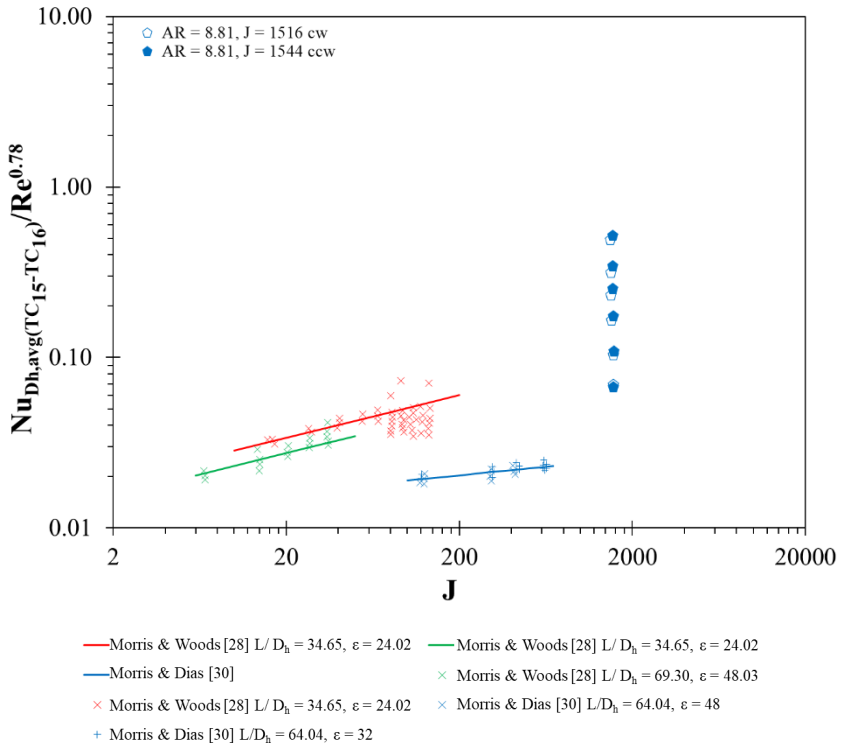

Figure A-123 AR = 8.81, J = 1516 cw, 1544 ccw, Nu_{Dh} vs J

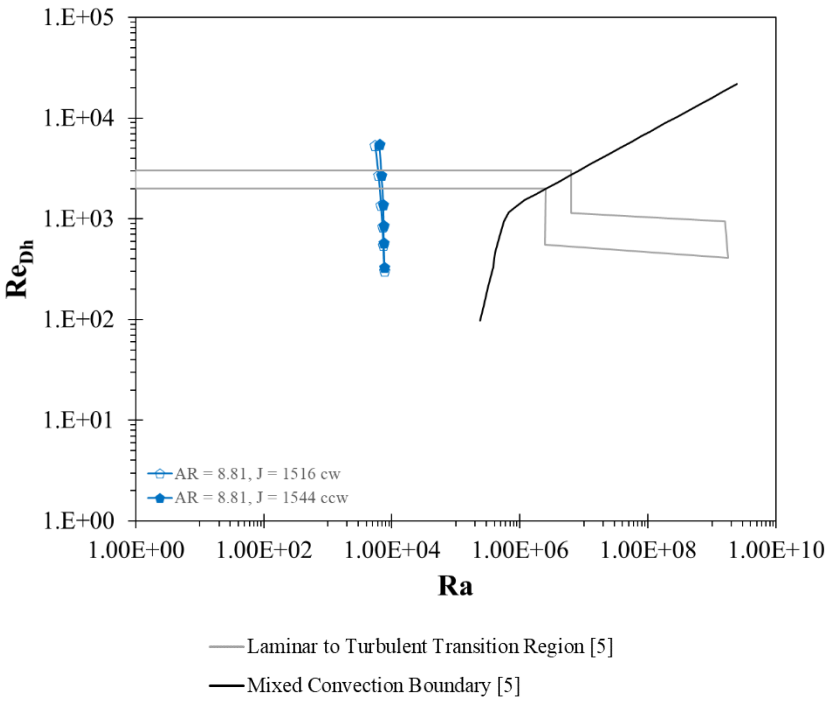

Figure A-124 AR = 8.81, J = 1516 cw, 1544 ccw, Re_{Dh} vs Ra

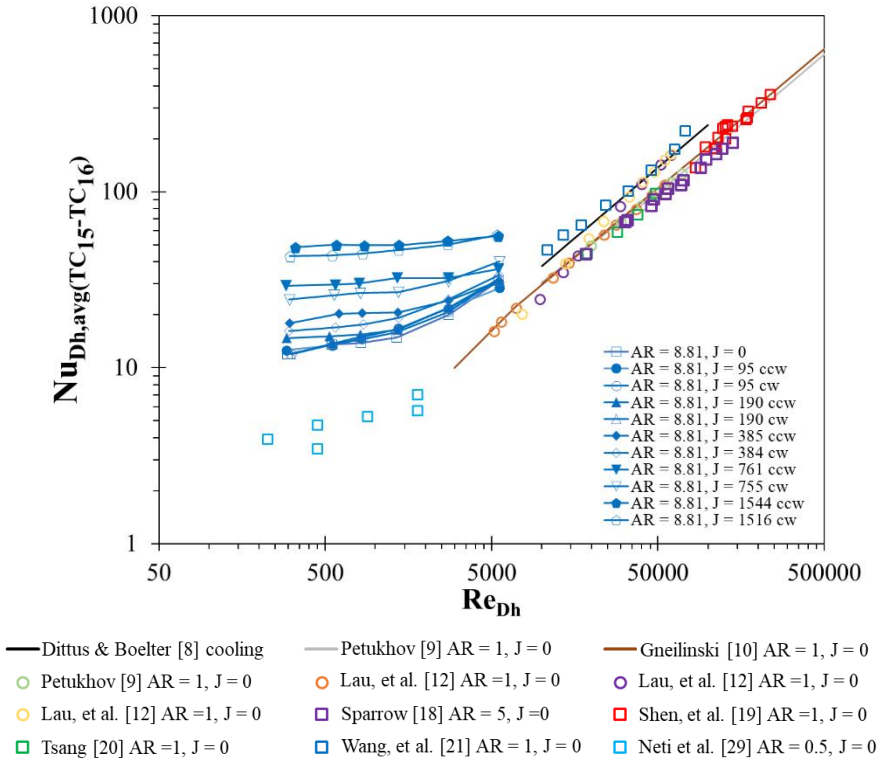

Figure A-125 AR = 8.81 Comparison, Nu_{Dh} vs Re_{Dh}

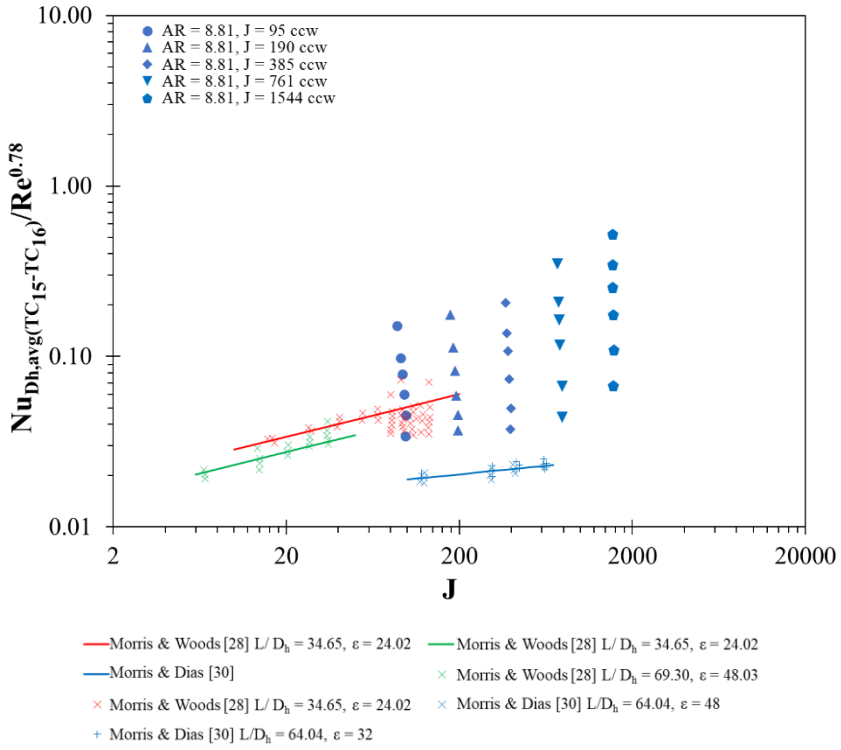

Figure A-126 AR = 8.81 Comparison, Nu_{Dh} vs J ccw

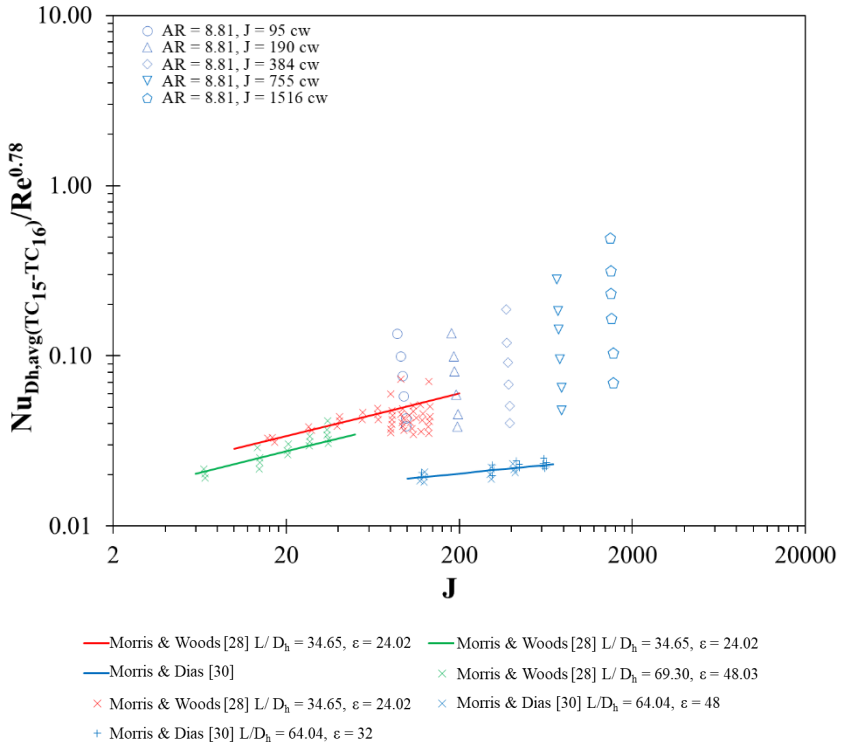

Figure A-127 AR = 8.81 Comparison, Nu_{Dh} vs J cw

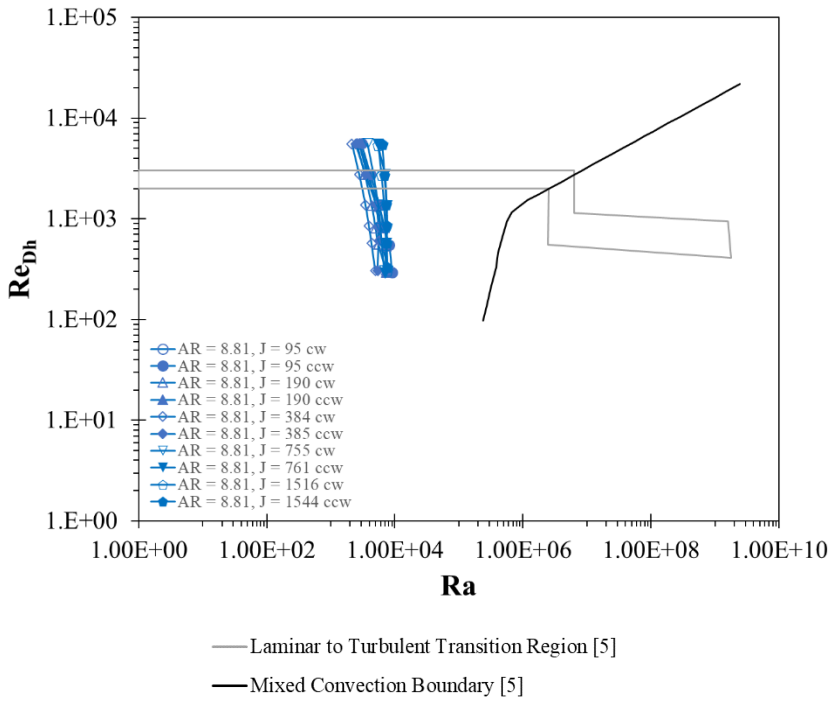

Figure A-128 AR = 8.81 Comparison, Re_{Dh} vs Ra

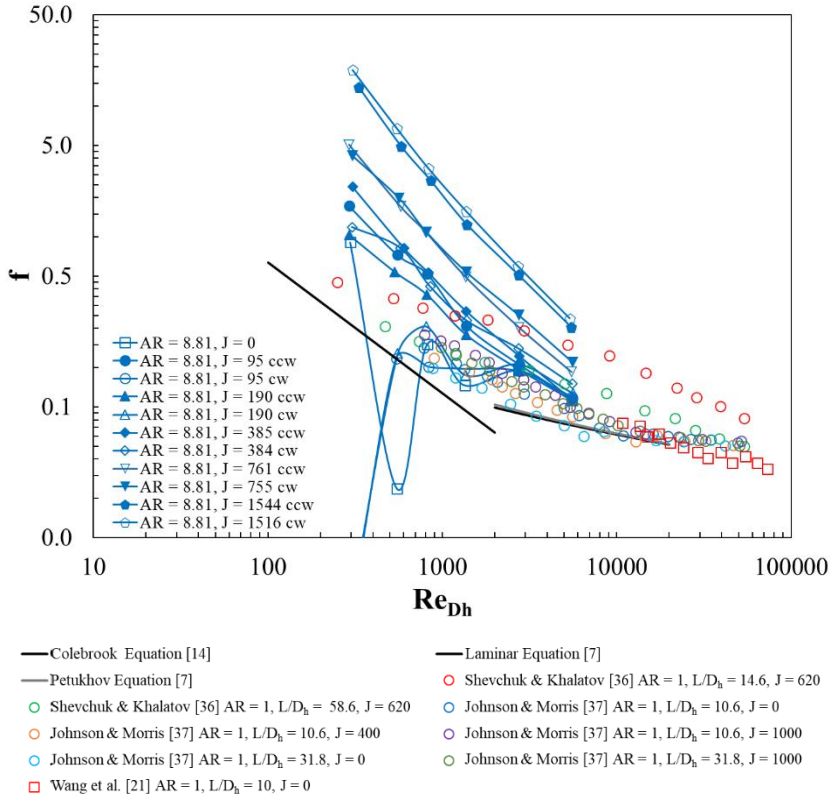

Figure A-129 AR = 8.81 Comparison, Friction Factor

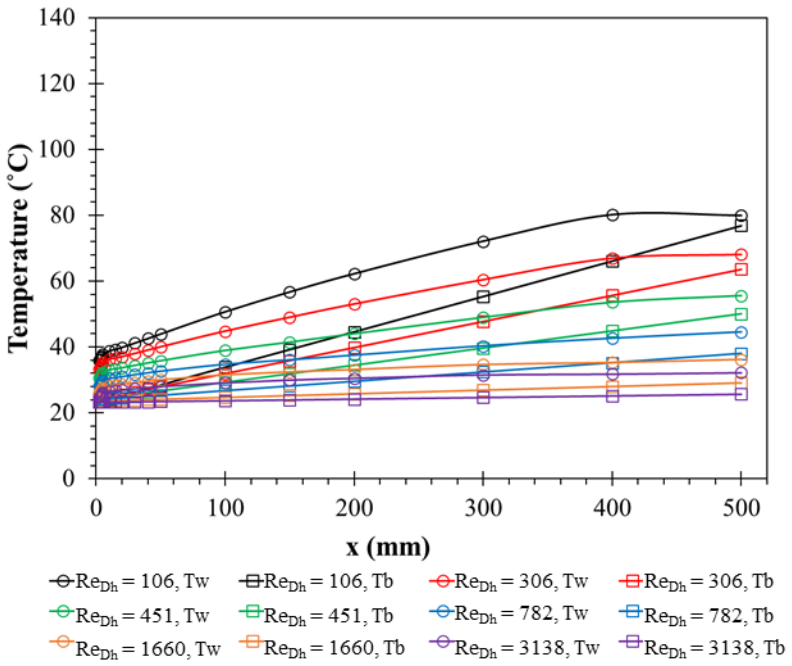

Figure A-130 AR = 17.33, J = 0, 20V, (06/15/21), Temperature Profile

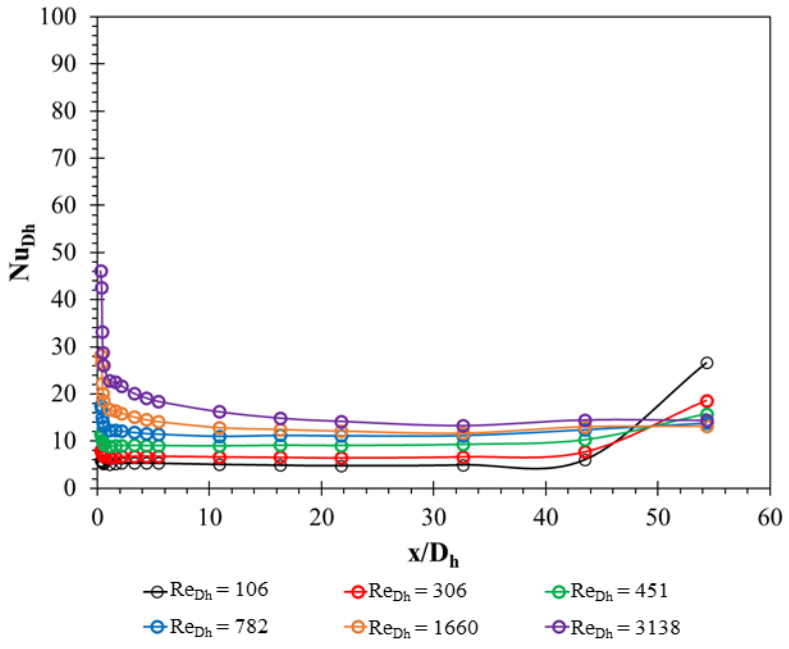

Figure A-131 AR = 17.33, J = 0, 20V, (06/15/21), Nu_{Dh} Profile

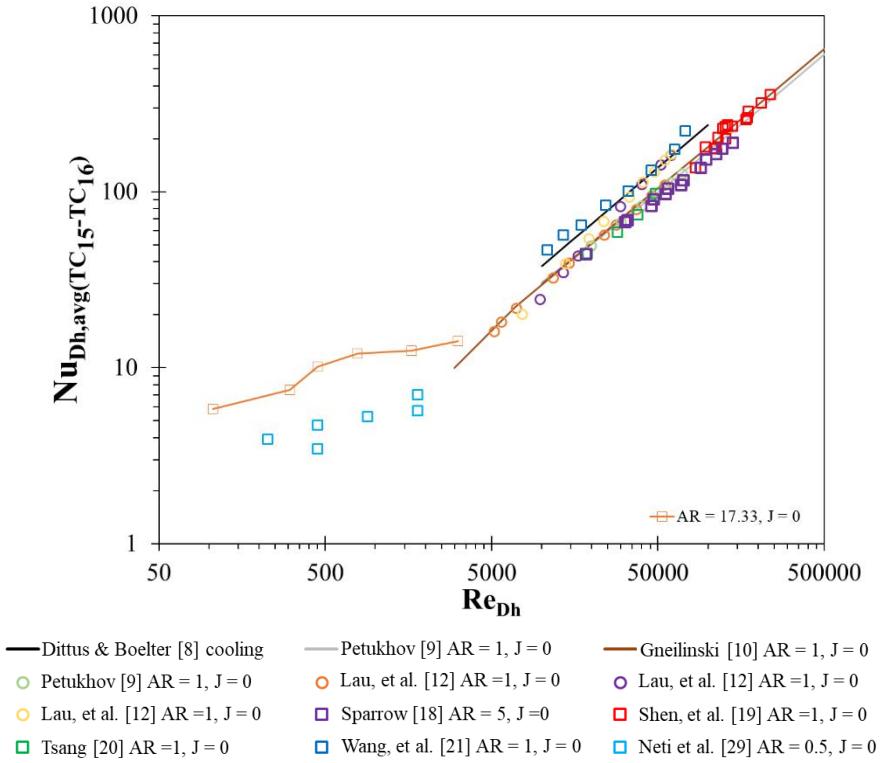

Figure A-132 AR = 17.33, J = 0, Nu_{Dh} vs Re_{Dh}

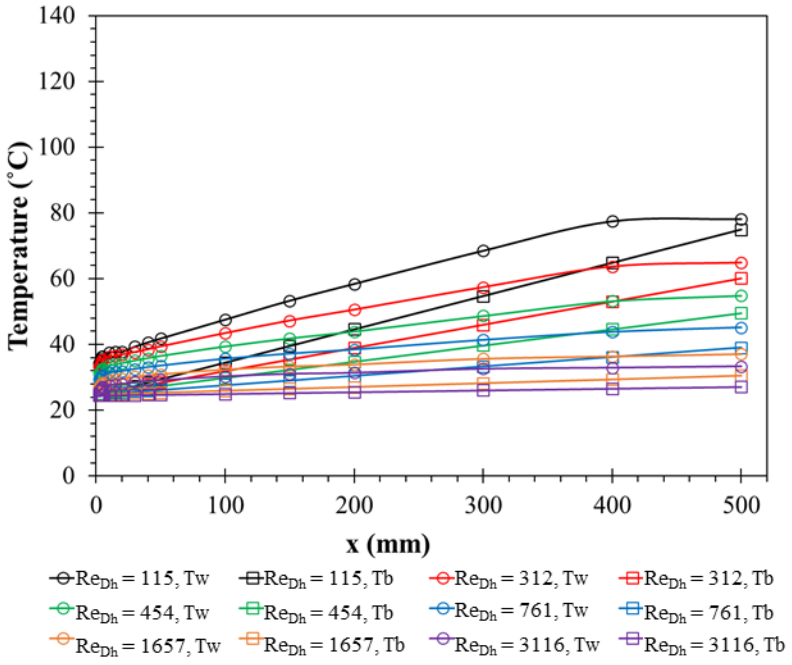

Figure A-133 AR = 17.33, J = 27 ccw, 20V, (06/15/21), Temperature Profile

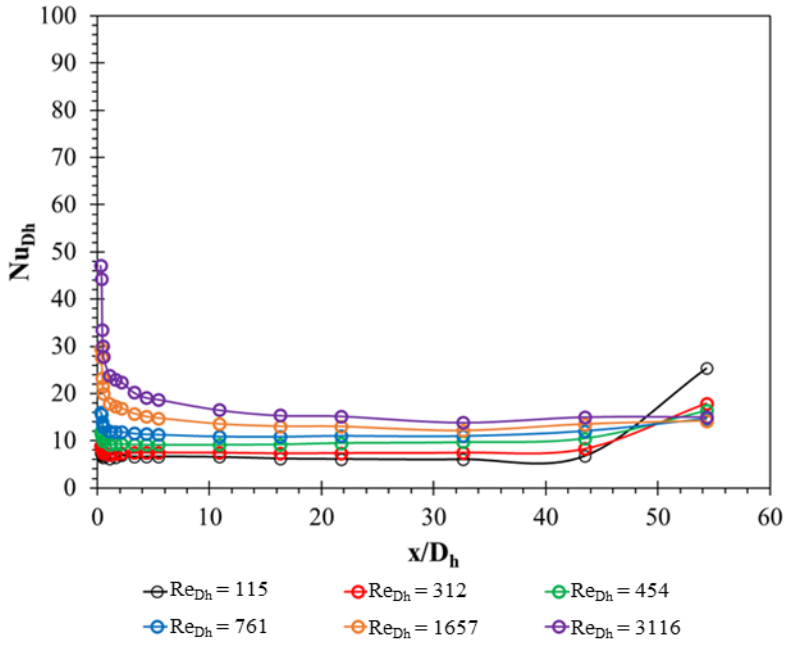

Figure A-134 AR = 17.33, J = 27 ccw, 20V, (06/15/21), Nu_{Dh} Profile

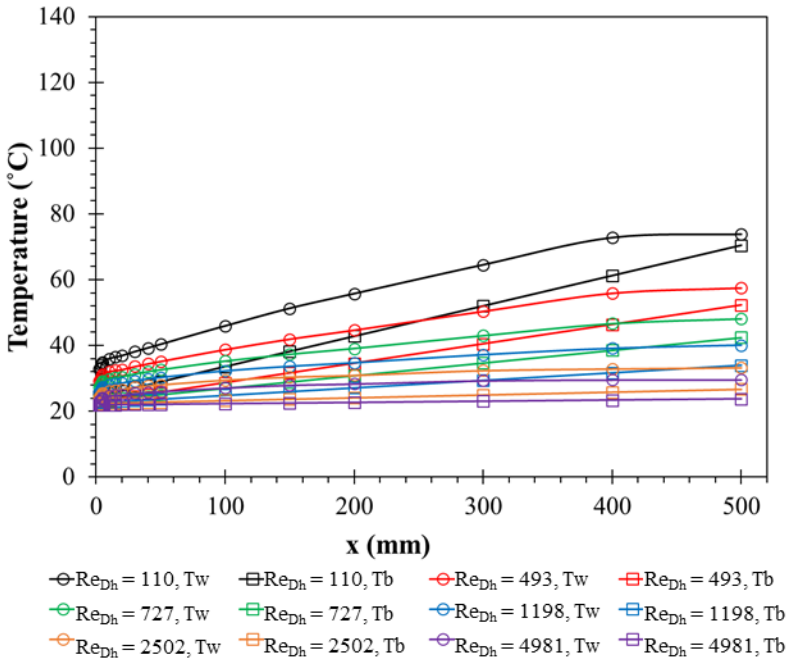

Figure A-135 AR = 17.33, J = 28 cw, 20V, (06/16/21), Temperature Profile

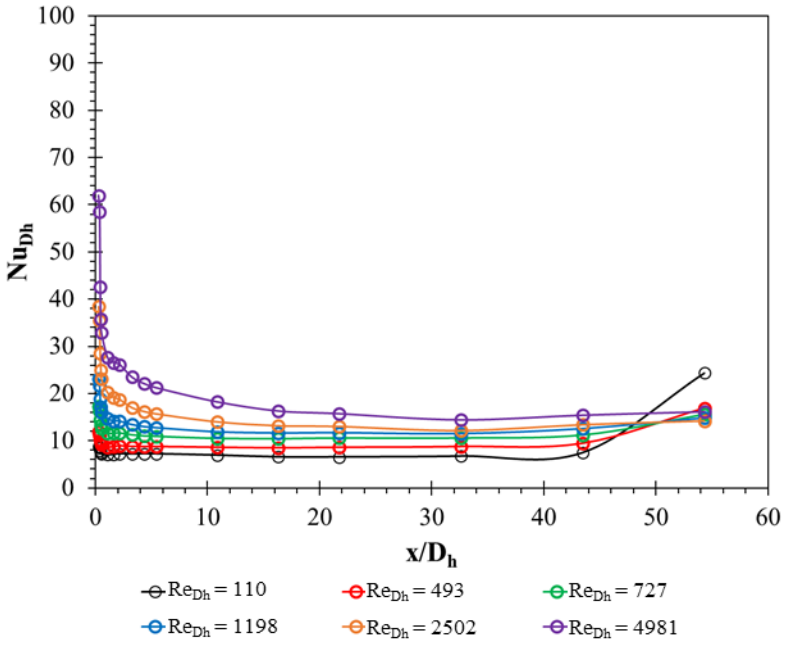

Figure A-136 AR = 17.33, J = 28 cw, 20V, (06/16/21), Nu_{Dh} Profile

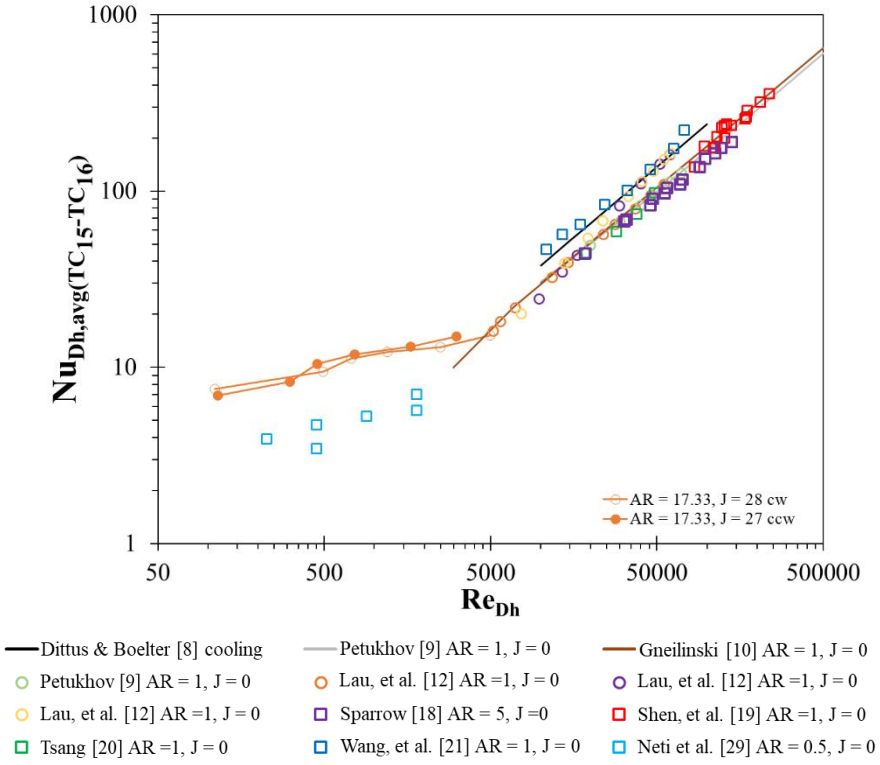

Figure A-137 AR = 17.33, J = 28 cw, 27 ccw, Nu_{Dh} vs Re_{Dh}

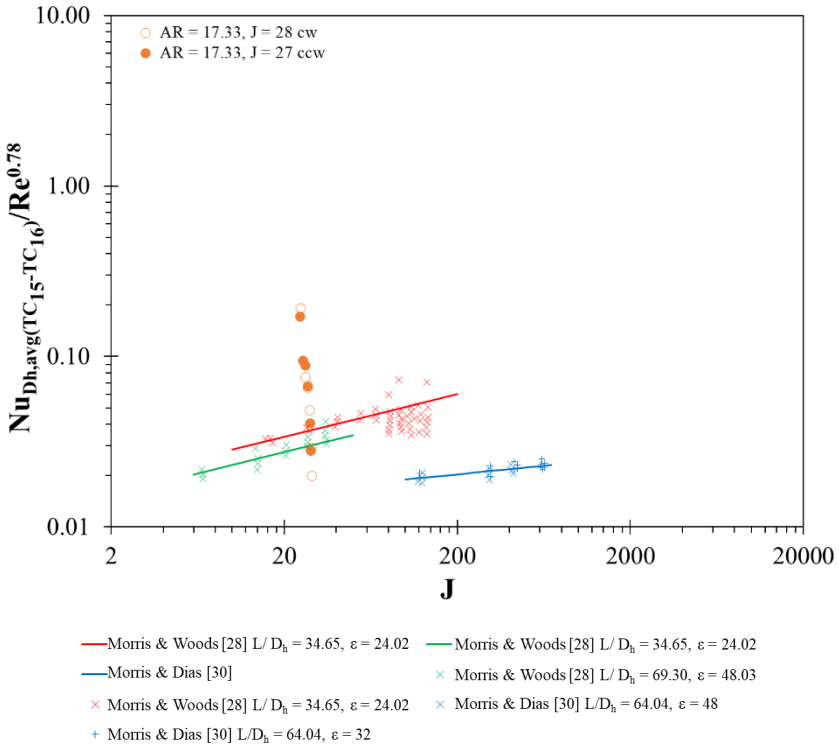

Figure A-138 AR = 17.33, J = 28 cw, 27 ccw, Nu_{Dh} vs J

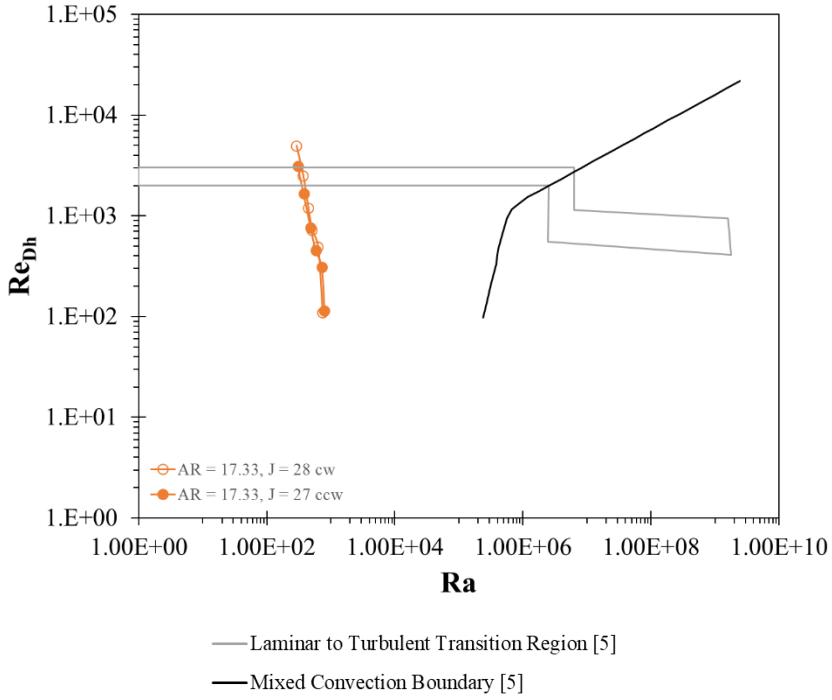

Figure A-139 AR = 17.33, J = 28 cw, 27 ccw, Re_{Dh} vs Ra

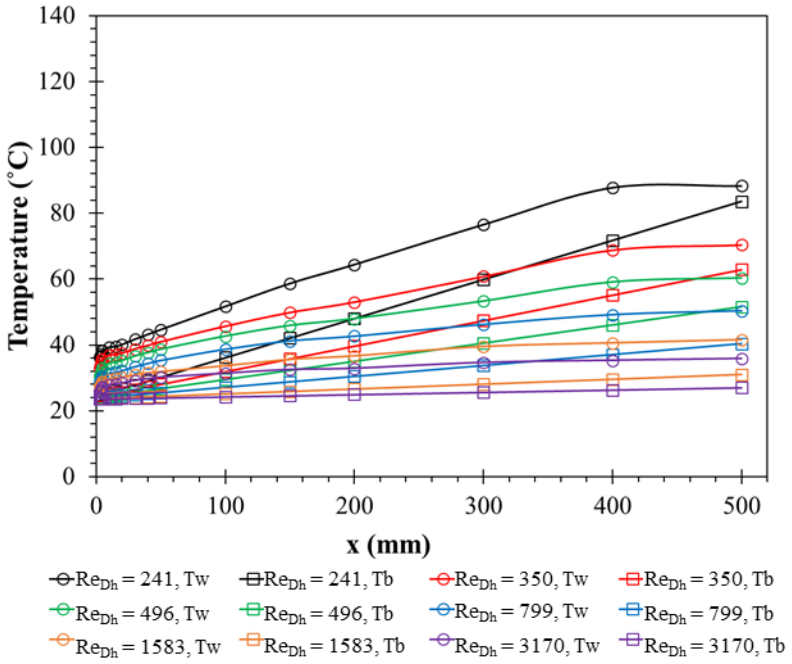

Figure A-140 AR = 17.33, J = 54 ccw, 25V, (06/16/21), Temperature Profile

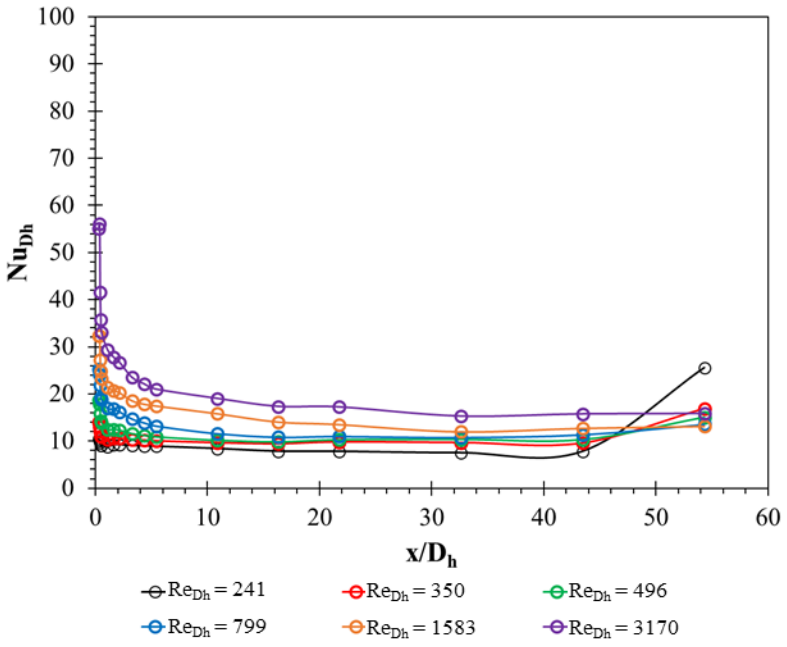

Figure A-141 AR = 17.33, J = 54 ccw, 25V, (06/16/21), Nu_{Dh} Profile

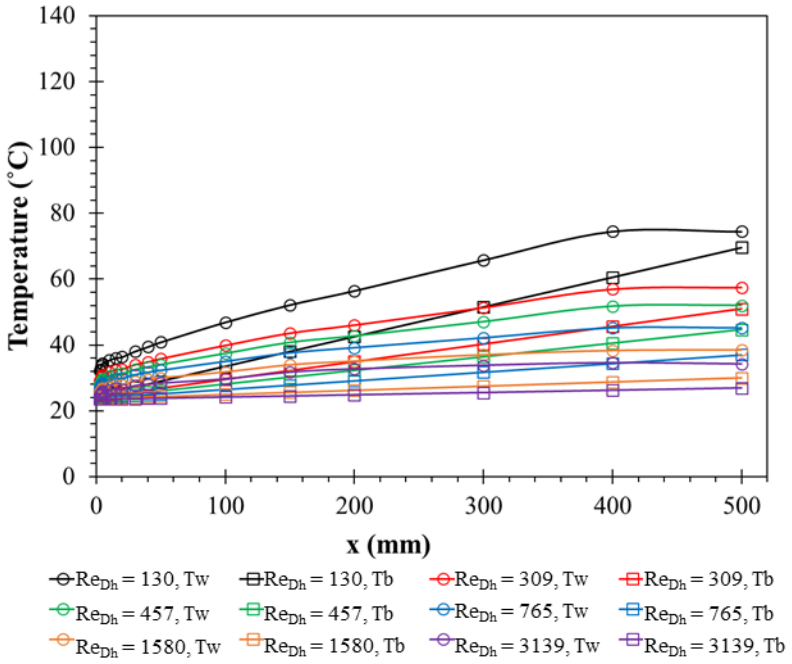

Figure A-142 AR = 17.33, J = 55 cw, 22.5V, (06/24/21), Temperature Profile

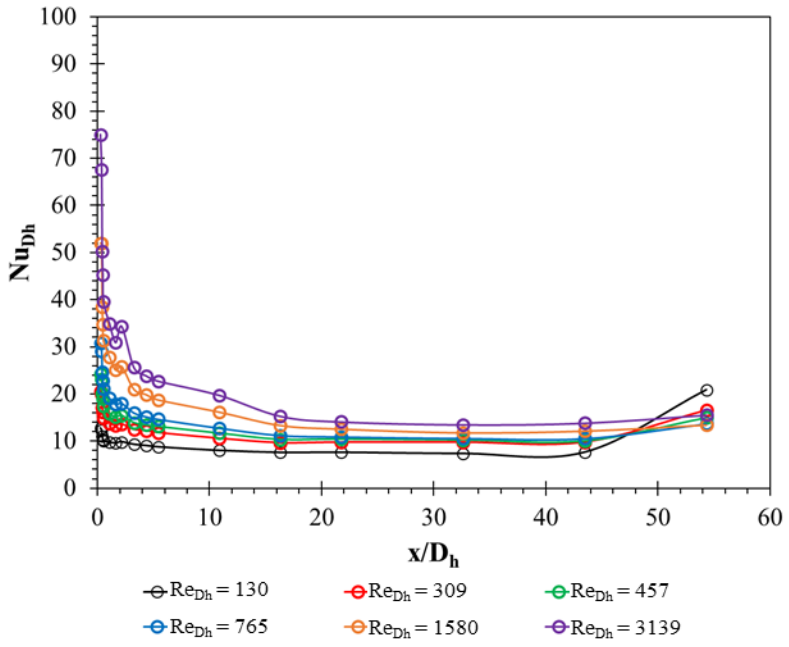

Figure A-143 AR = 17.33, J = 55 cw, 22.5V, (06/24/21), Nu_{Dh} Profile

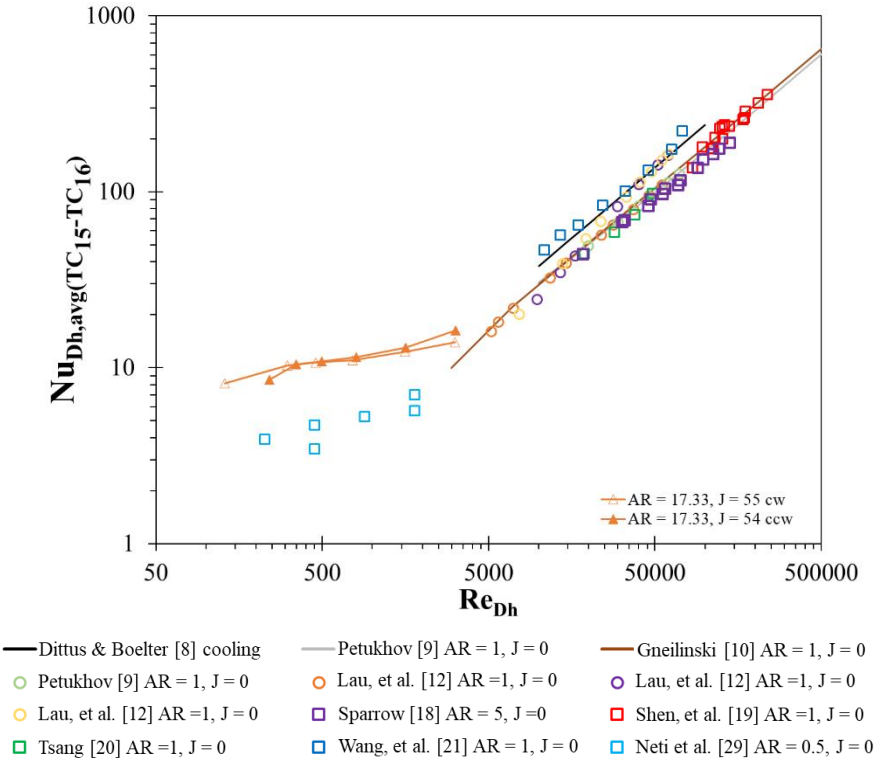

Figure A-144 AR = 17.33, J = 55 cw, 54 ccw, Nu_{Dh} vs Re_{Dh}

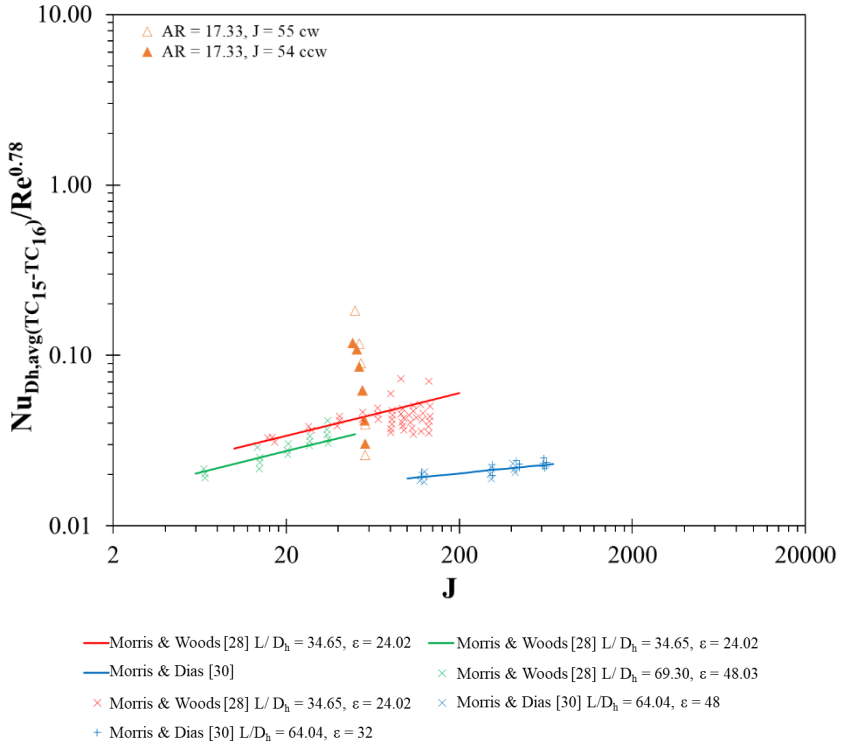

Figure A-145 AR = 17.33, J = 55 cw, 54 ccw, Nu_{Dh} vs J

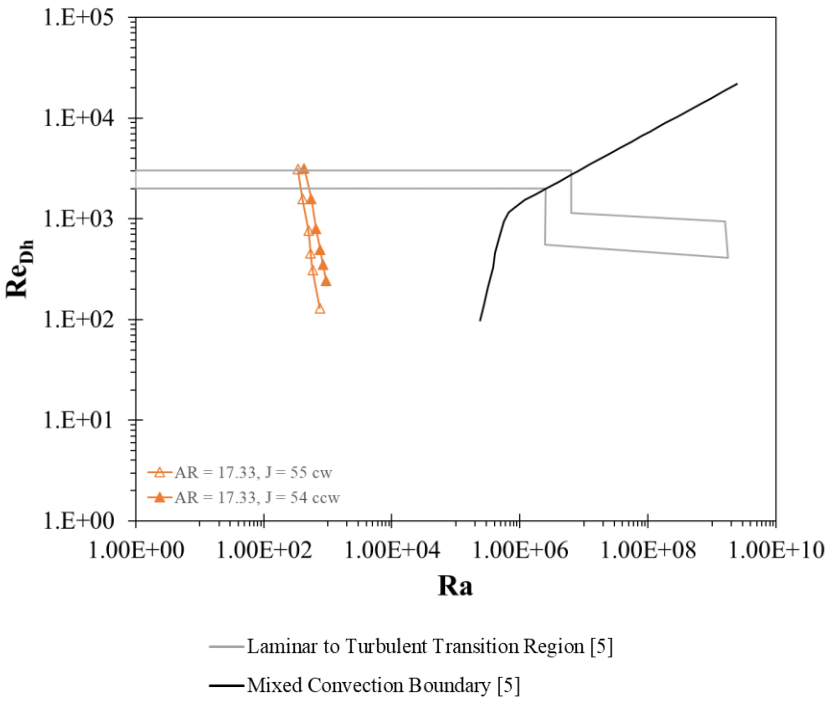

Figure A-146 AR = 17.33, J = 55 cw, 54 ccw, Re_{Dh} vs Ra

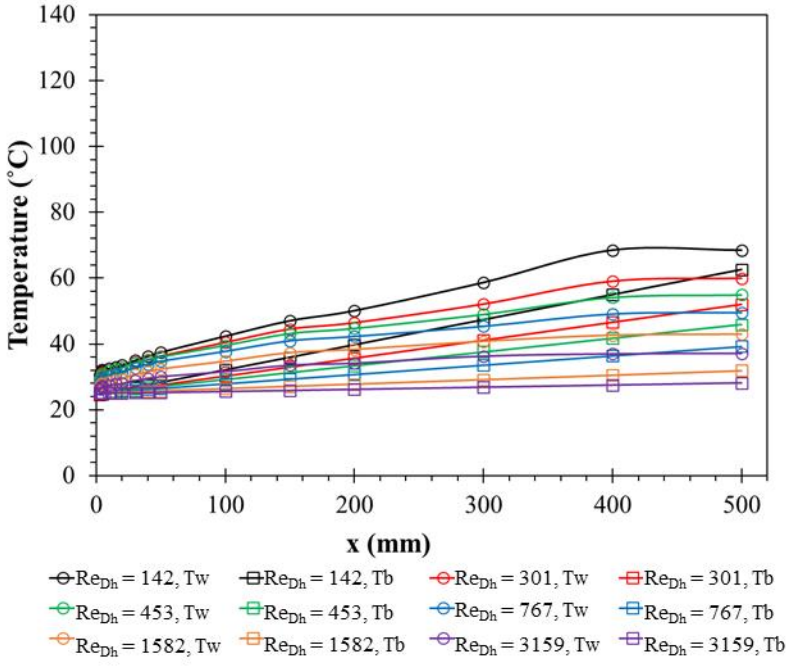

Figure A-147 AR = 17.33, J = 109 ccw, 25V, (06/22/21), Temperature Profile

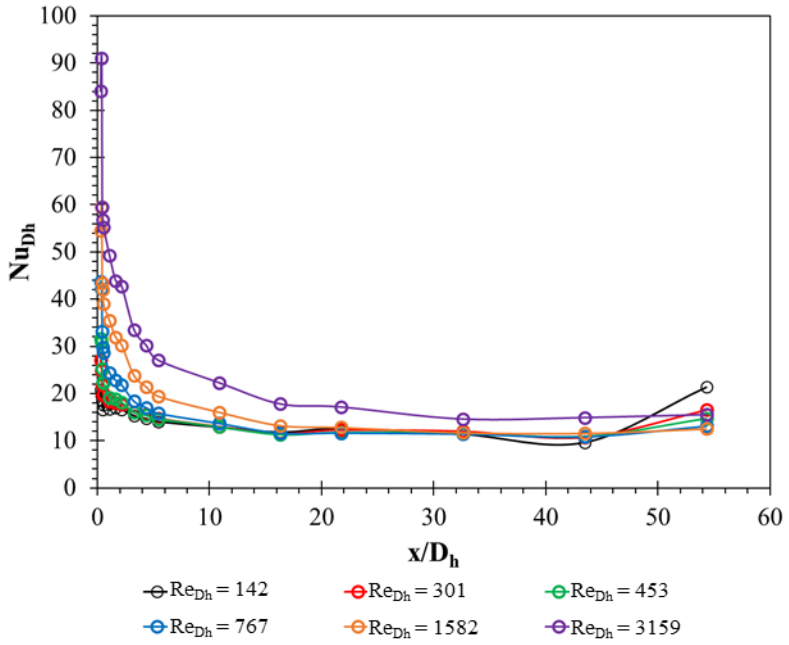

Figure A-148 AR = 17.33, J = 109 ccw, 25V, (06/22/21), Nu_{Dh} Profile

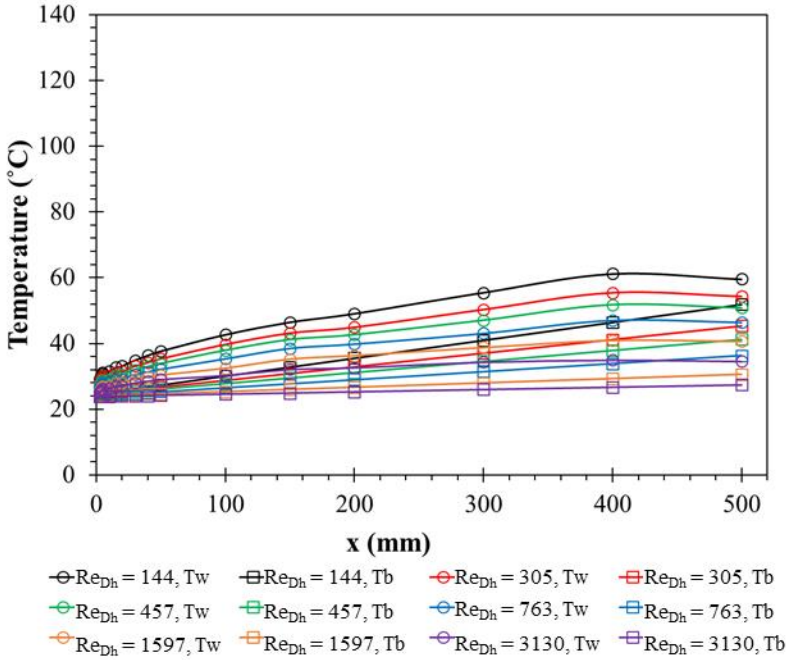

Figure A-149 AR = 17.33, J = 111 cw, 25V, (06/2/21), Temperature Profile

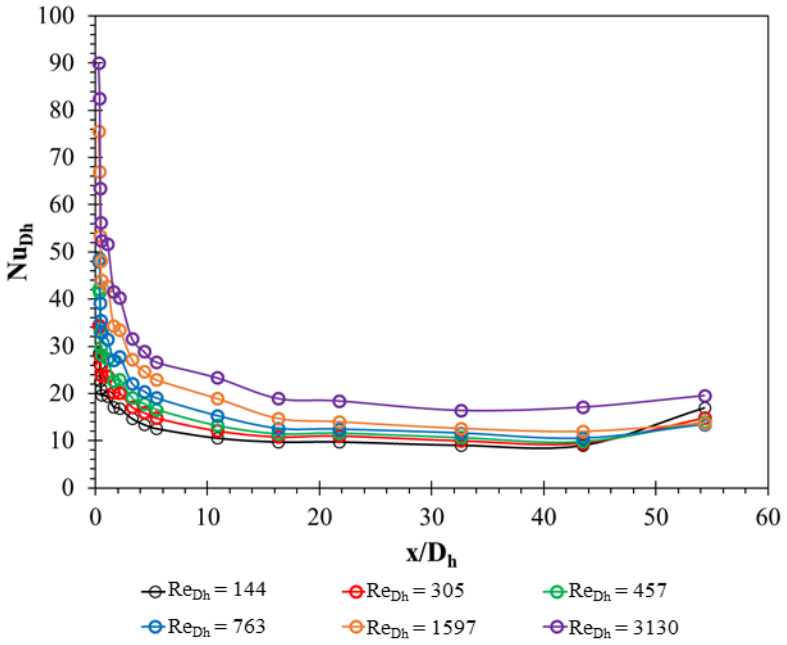

Figure A-150 AR = 17.33, J = 111 cw, 25V, (06/2/21), Nu_{Dh} Profile

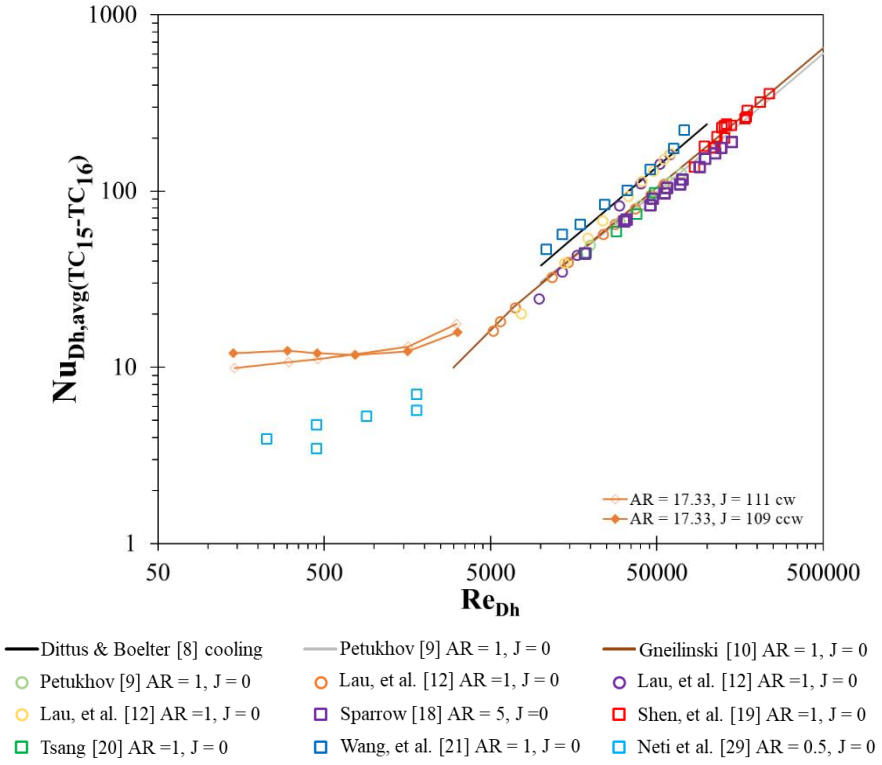

Figure A-151 AR = 17.33, J = 111 cw, 109 ccw, Nu_{Dh} vs Re_{Dh}

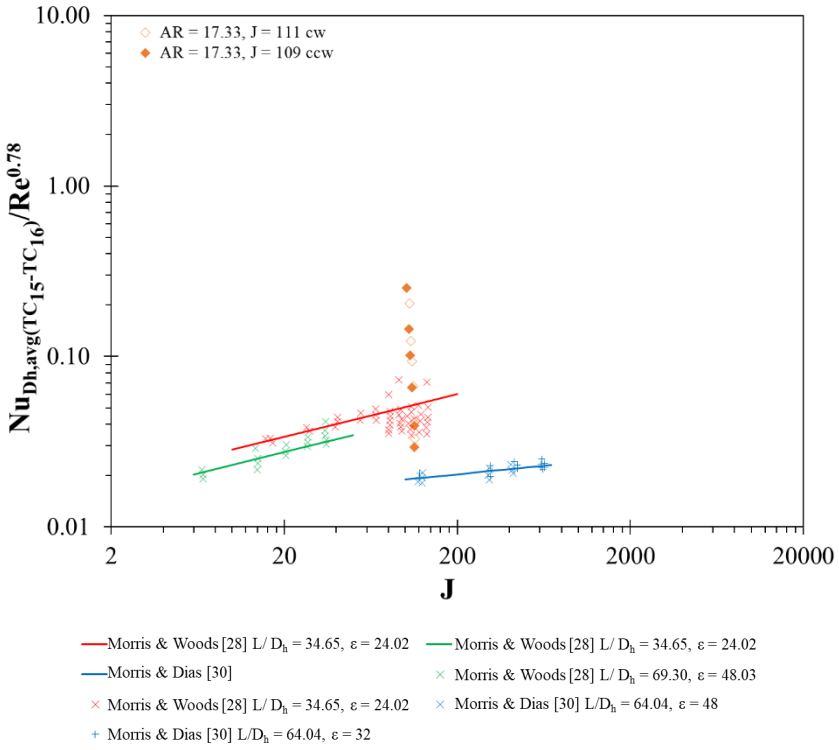

Figure A-152 AR = 17.33, J = 111 cw, 109 ccw, Nu_{Dh} vs J

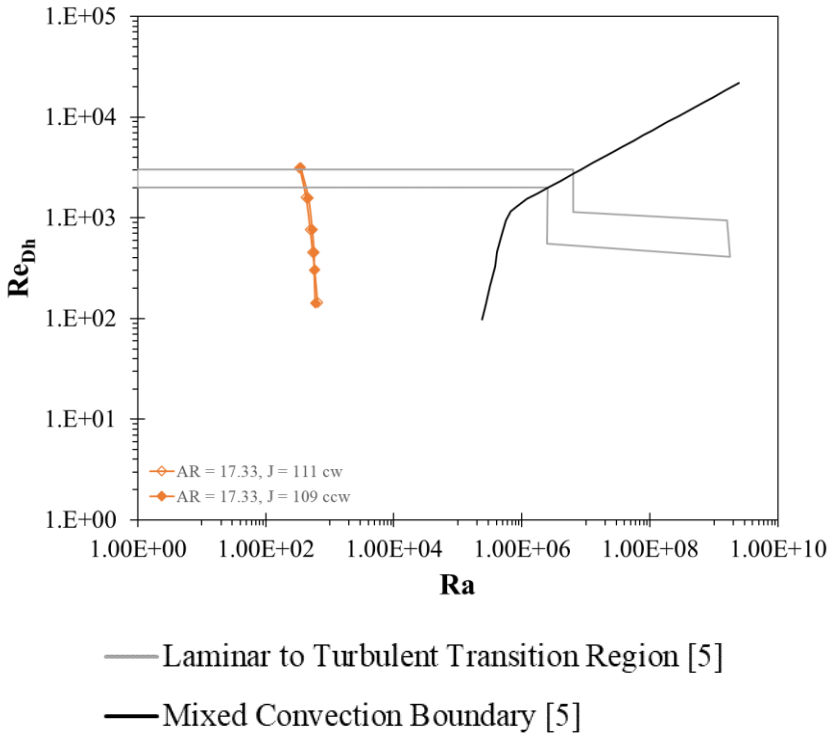

Figure A-153 AR = 17.33, J = 111 cw, 109 ccw, Re_{Dh} vs Ra

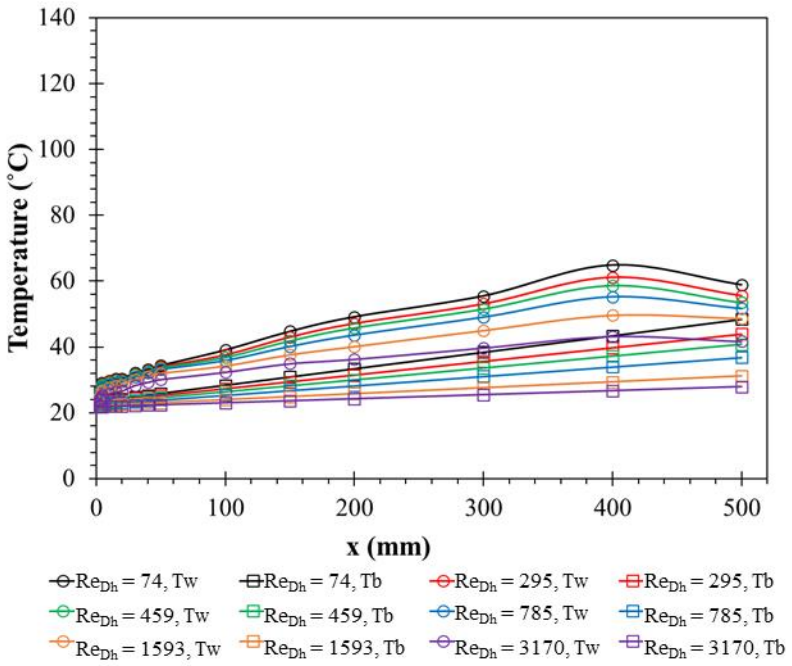

Figure A-154 AR = 17.33, J = 223 ccw, 40V, (06/23/21), Temperature Profile

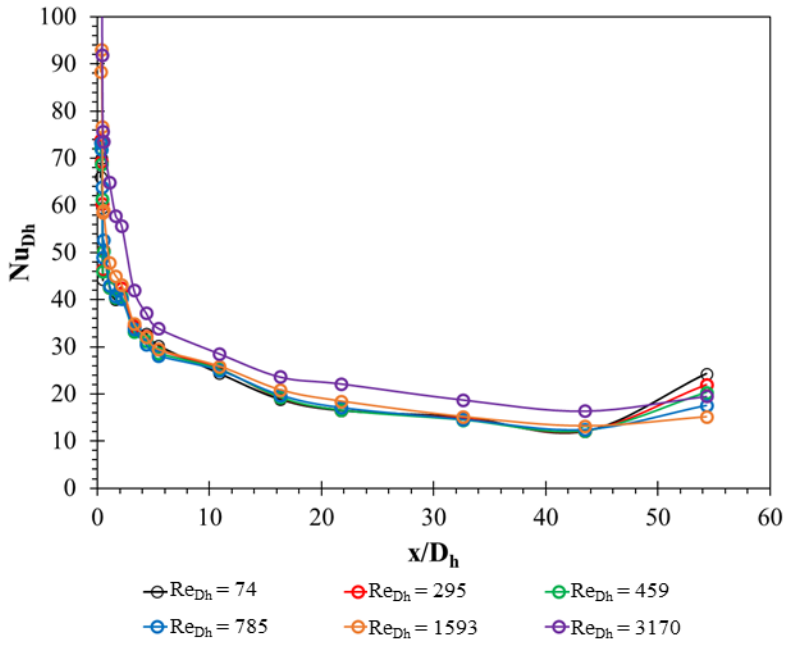

Figure A-155 AR = 17.33, J = 223 ccw, 40V, (06/23/21), Nu_{Dh} Profile

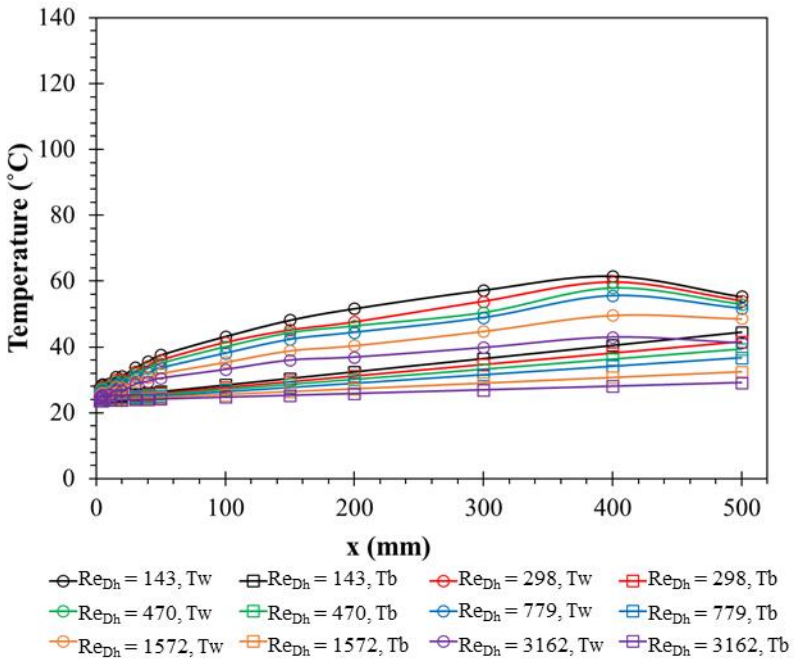

Figure A-156 AR = 17.33, J = 223 cw, 25V, (06/23/21), Temperature Profile

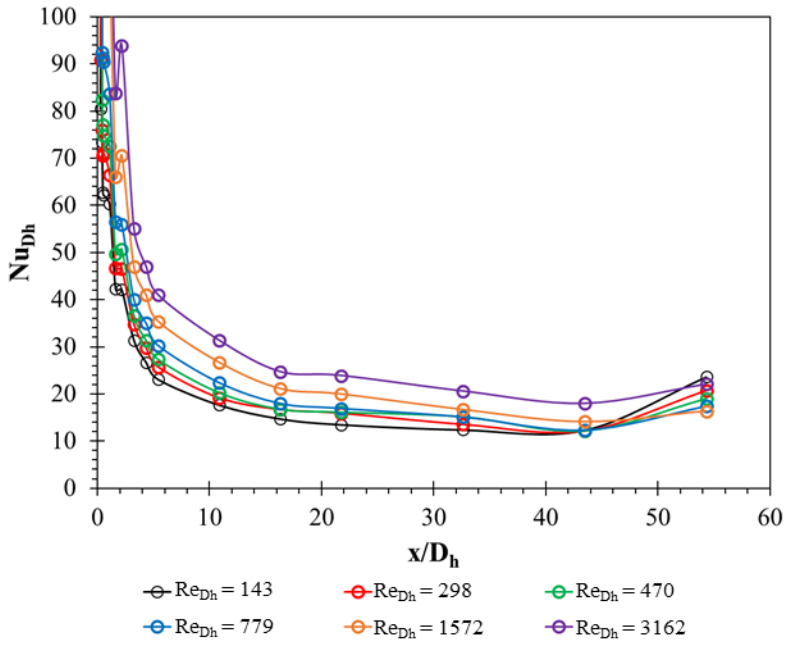

Figure A-157 AR = 17.33, J = 223 cw, 25V, (06/23/21), Nu_{Dh} Profile

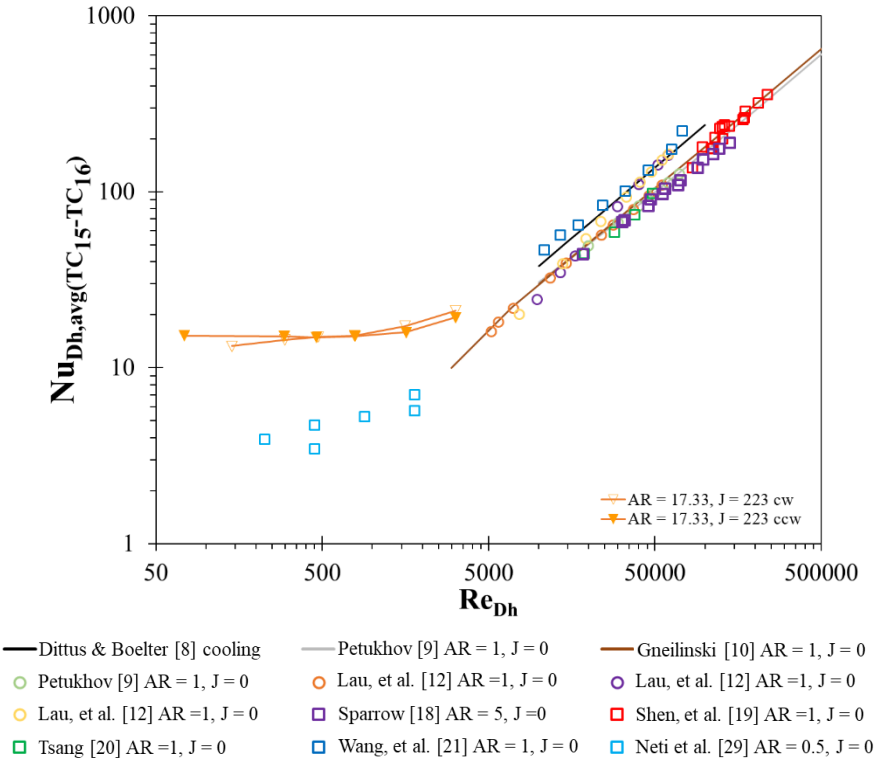

Figure A-158 AR = 17.33, J = 223, Nu_{Dh} vs Re_{Dh}

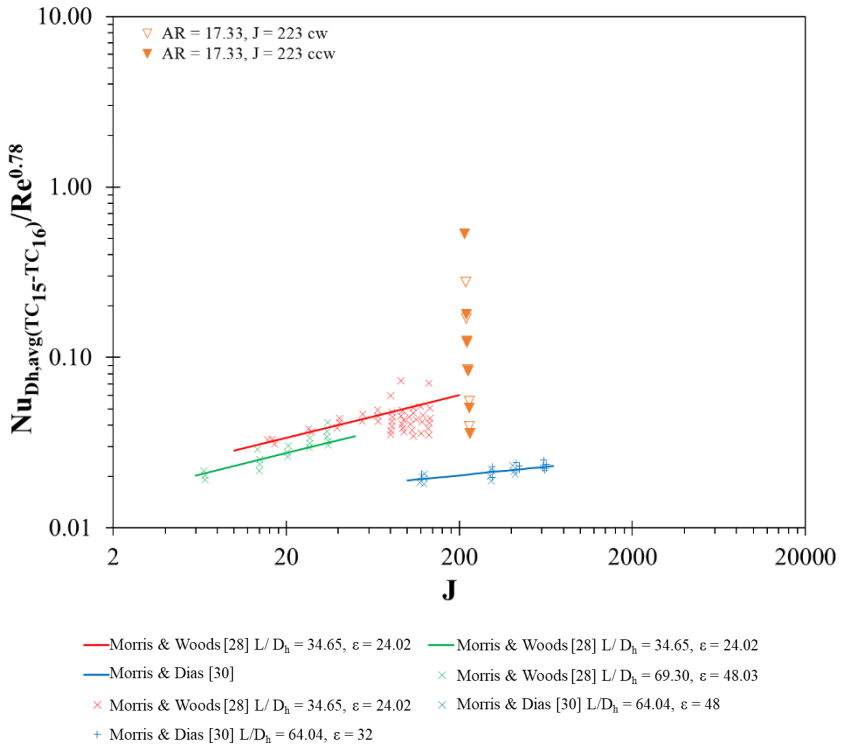

Figure A-159 AR = 17.33, J = 223, Nu_{Dh} vs J

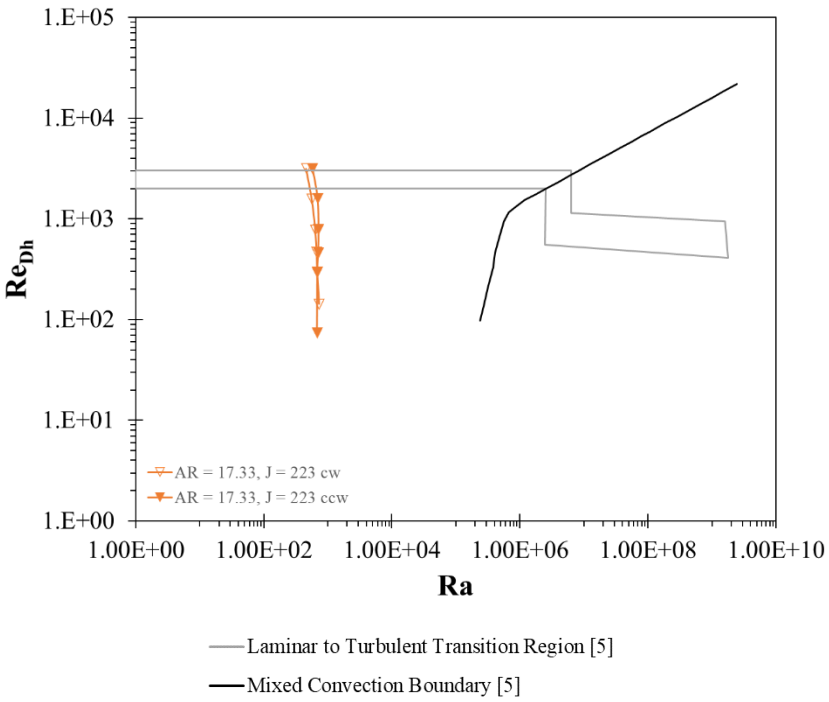

Figure A-160 AR = 17.33, J = 223, Re_{Dh} vs Ra

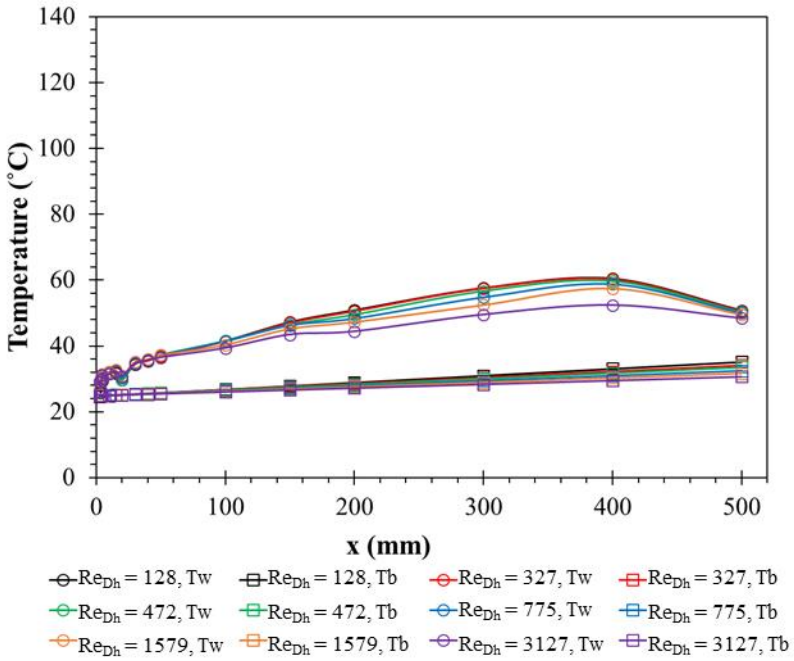

Figure A-161 AR = 17.33, J = 451 ccw, 50V, (06/23/21), Temperature Profile

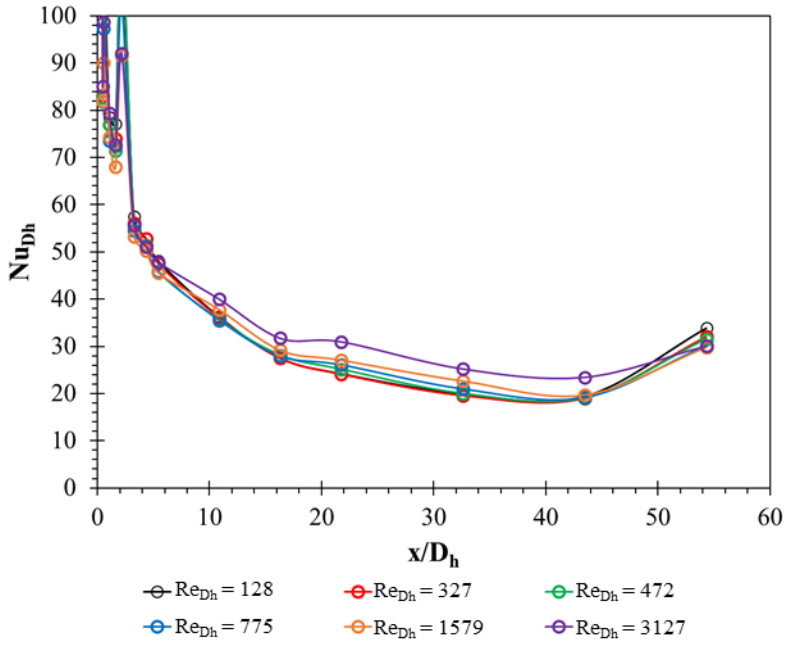

Figure A-162 AR = 17.33, J = 451 ccw, 50V, (06/23/21), Nu_{Dh} Profile

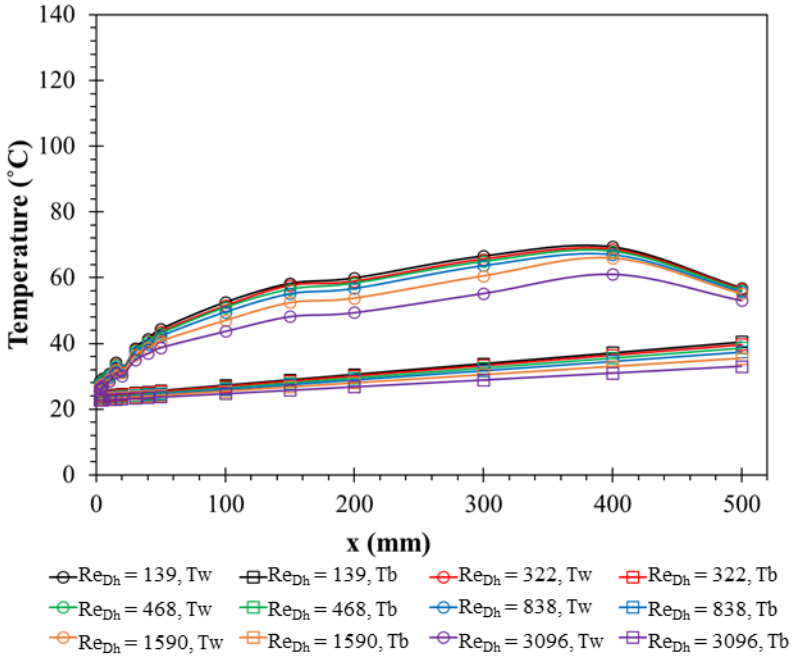

Figure A-163 AR = 17.33, J = 443 cw, 60V, (06/24/21), Temperature Profile

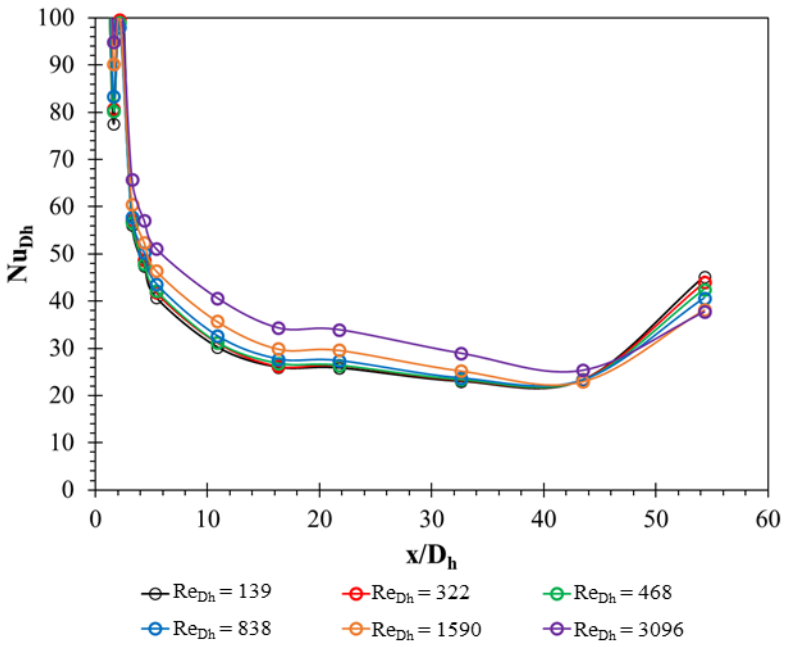

Figure A-164 AR = 17.33, J = 443 cw, 60V, (06/24/21), Nu_{Dh} Profile

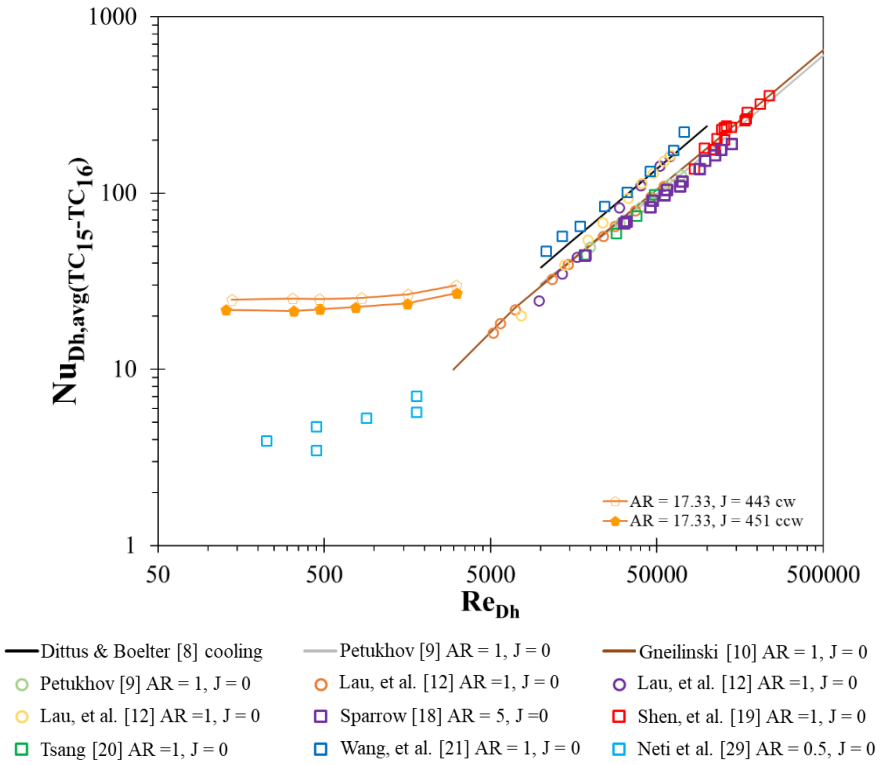

Figure A-165 AR = 17.33, J = 443 cw, 451 ccw, Nu_{Dh} vs Re_{Dh}

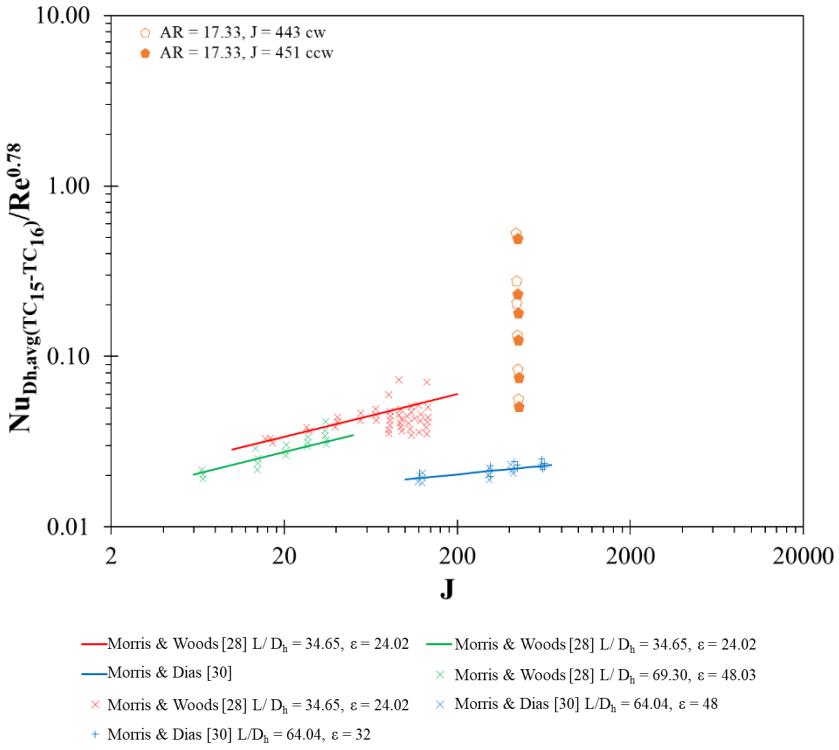

Figure A-166 AR = 17.33, J = 443 cw, 451 ccw, Nu_{Dh} vs J

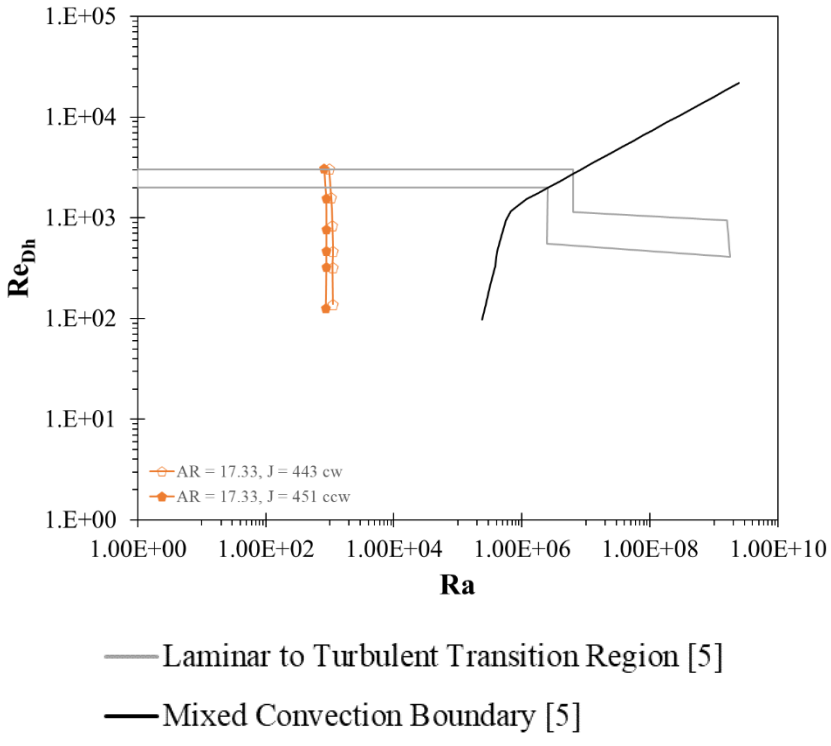

Figure A-167 AR = 17.33, J = 443 cw, 451 ccw, Re_{Dh} vs Ra

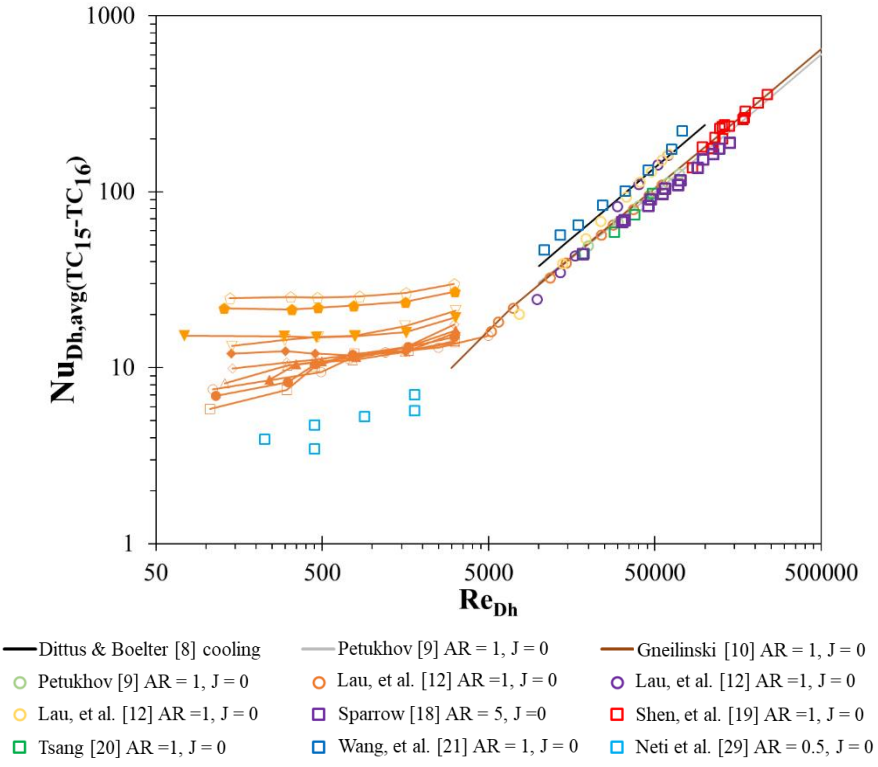

Figure A-168 AR = 17.33, Nu_{Dh} vs Re_{Dh}

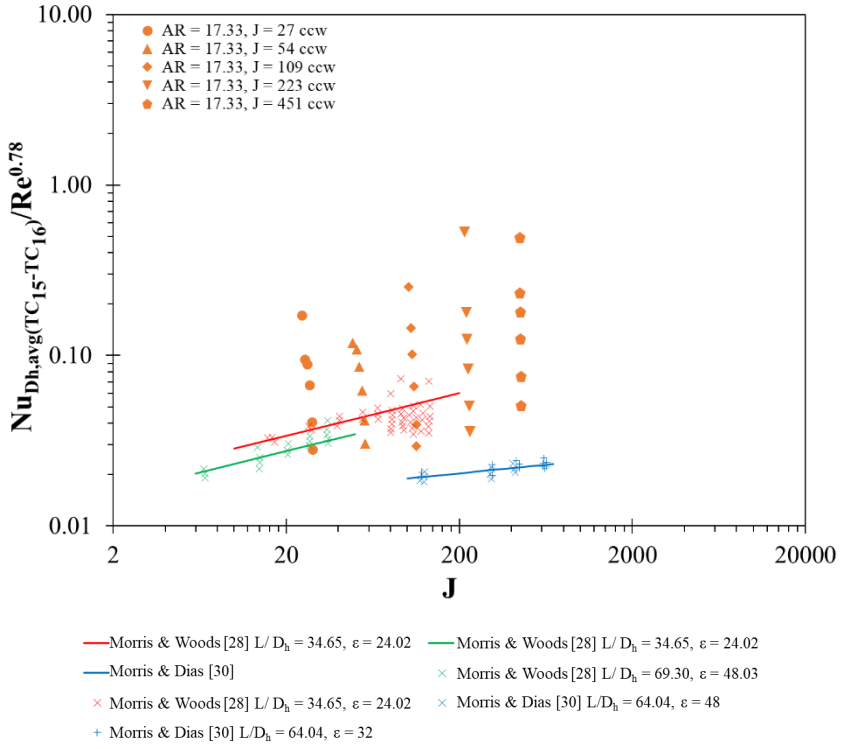

Figure A-169 AR = 17.33, Nu_{Dh} vs J ccw

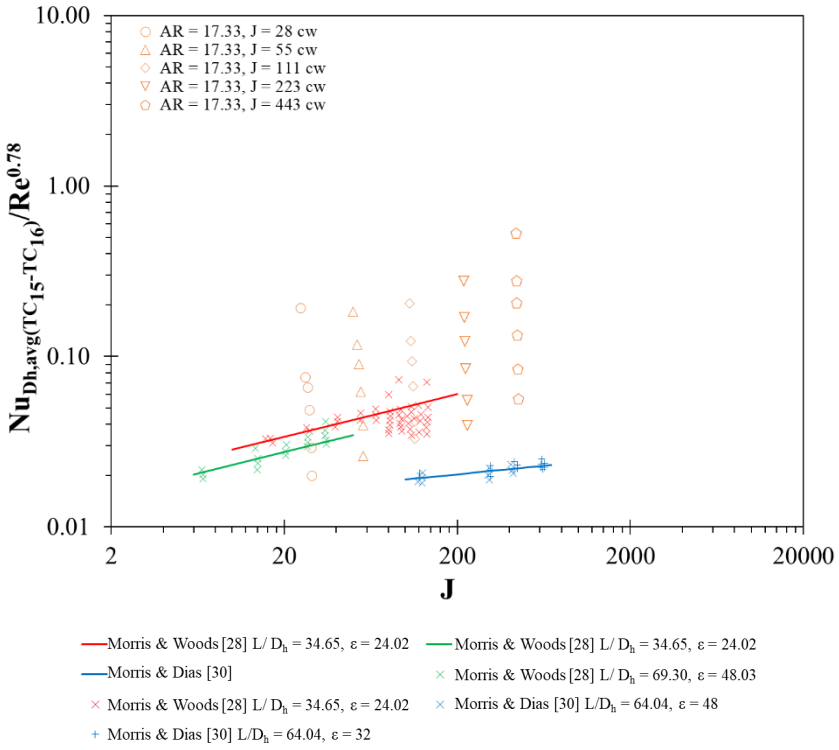

Figure A-170 AR = 17.33, NuDh vs J cw

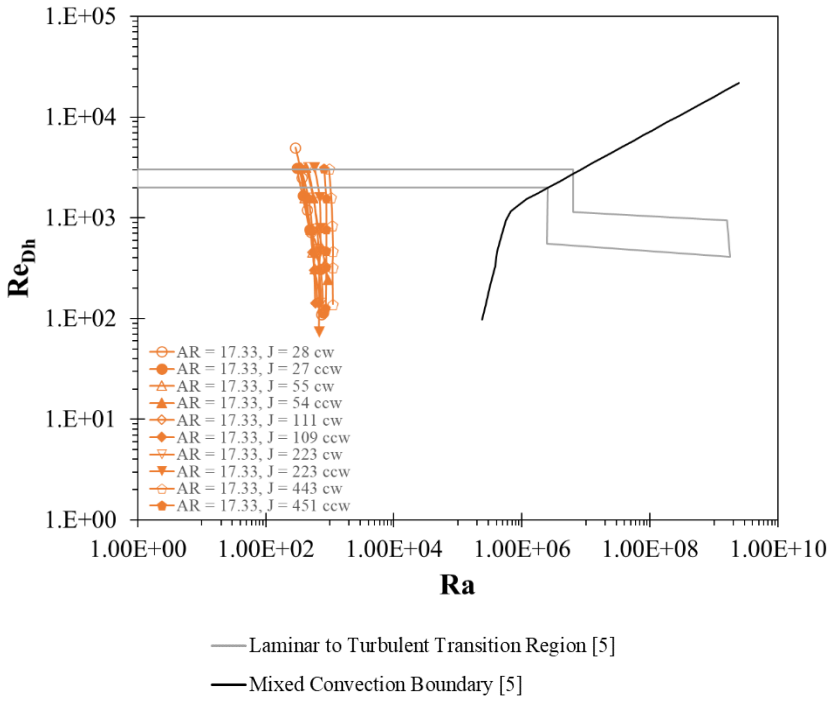

Figure A-171 AR = 17.33 Comparison, Re_{Dh} vs Ra

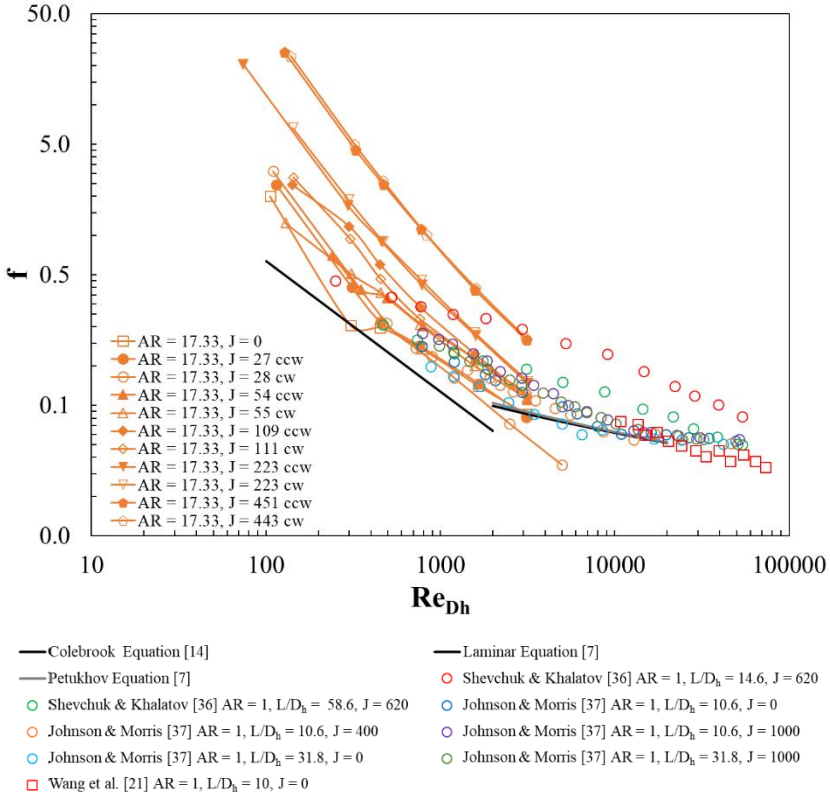

Figure A-172 AR = 17.33 Comparison, Friction Factor

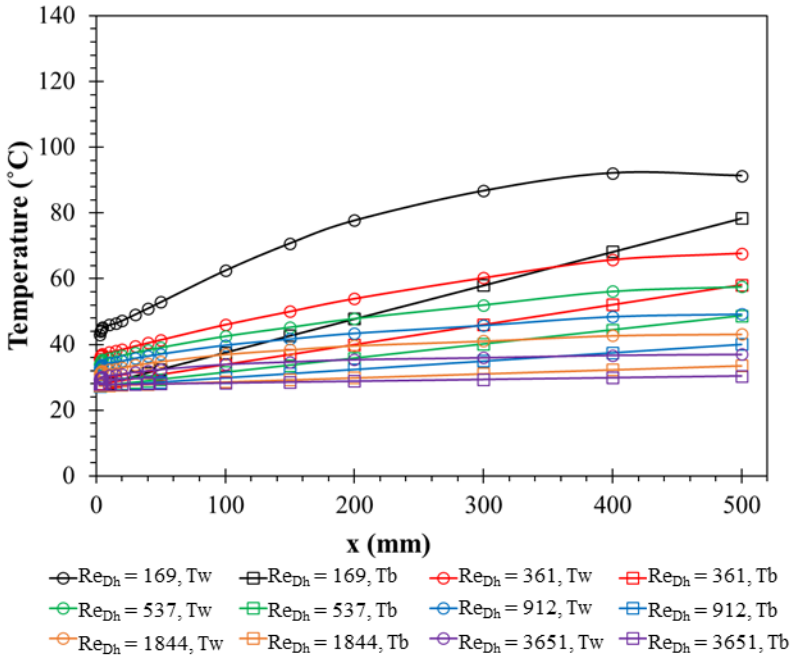

Figure A-173 Realistic S-shaped Model, J = 0, 20V, (06/30/21), Temperature Profile

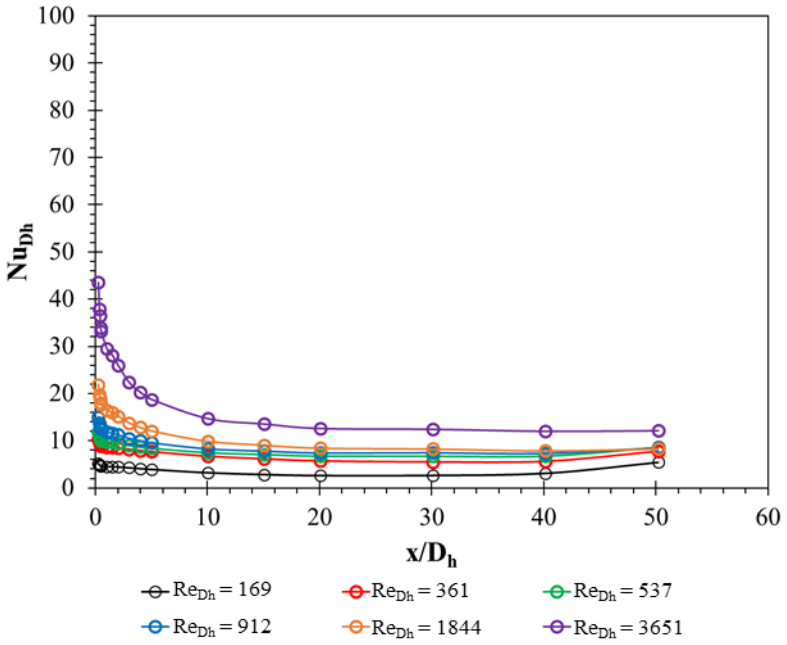

Figure A-174 Realistic S-shaped Model, J = 0, 20V, (06/30/21), Nu_{Dh} Profile

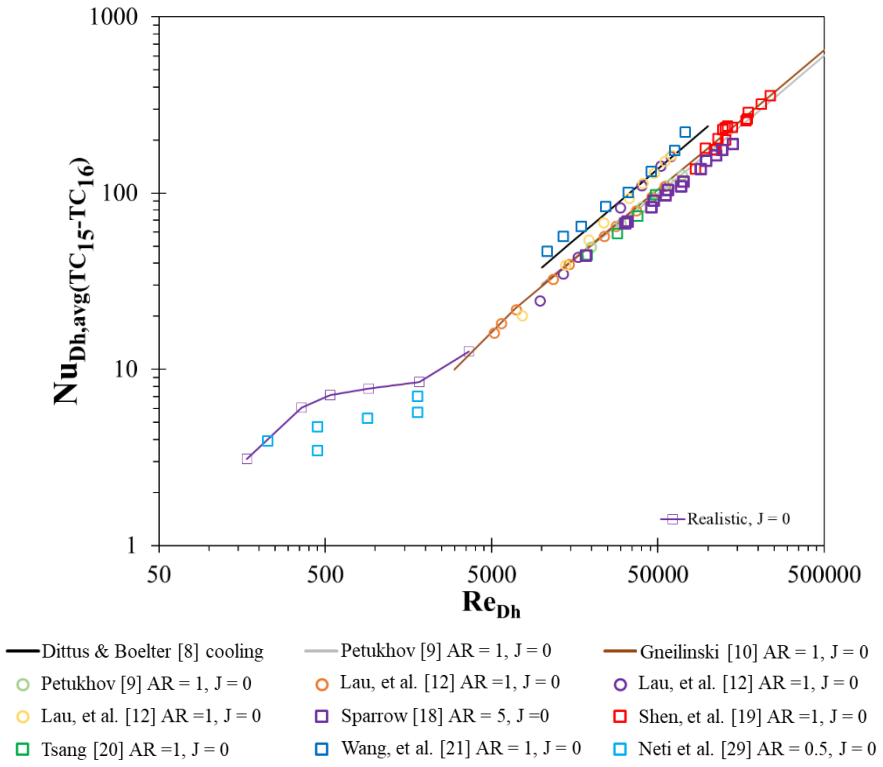

Figure A-175 Realistic S-shaped Model, J = 0, Nu_{Dh} vs Re_{Dh}

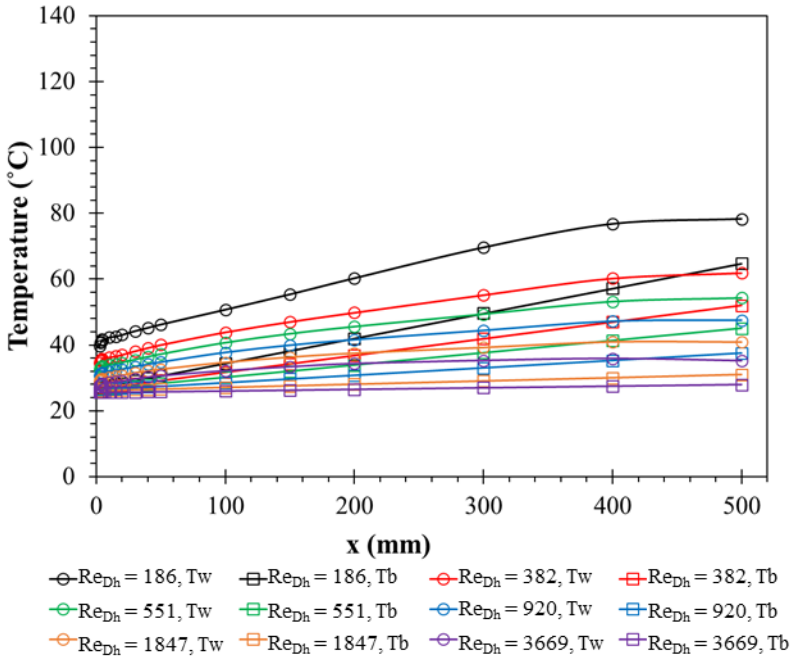

Figure A-176 Realistic S-shaped Model, J = 32 ccw, 20V, (07/01/21), Temperature Profile

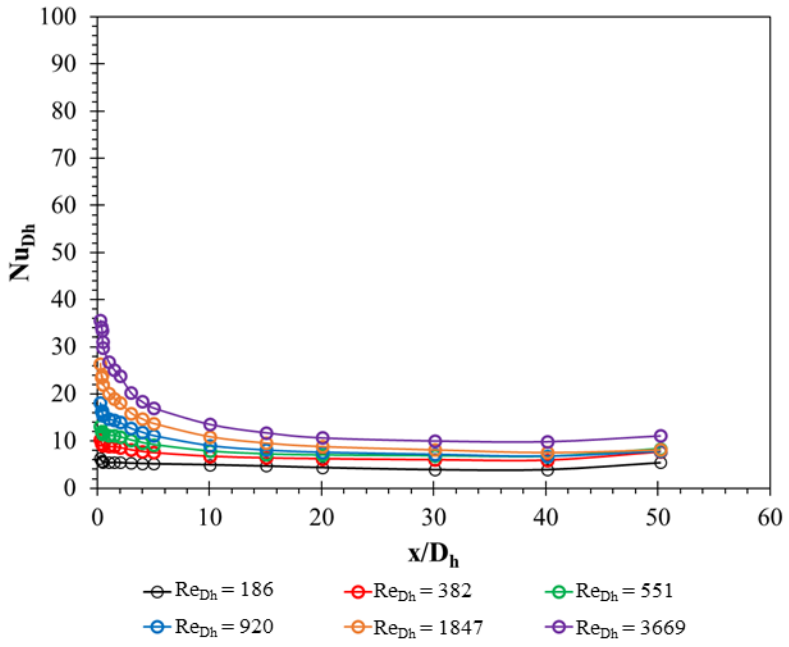

Figure A-177 Realistic S-shaped Model, J = 32 ccw, 20V, (07/01/21), Nu_{Dh} Profile

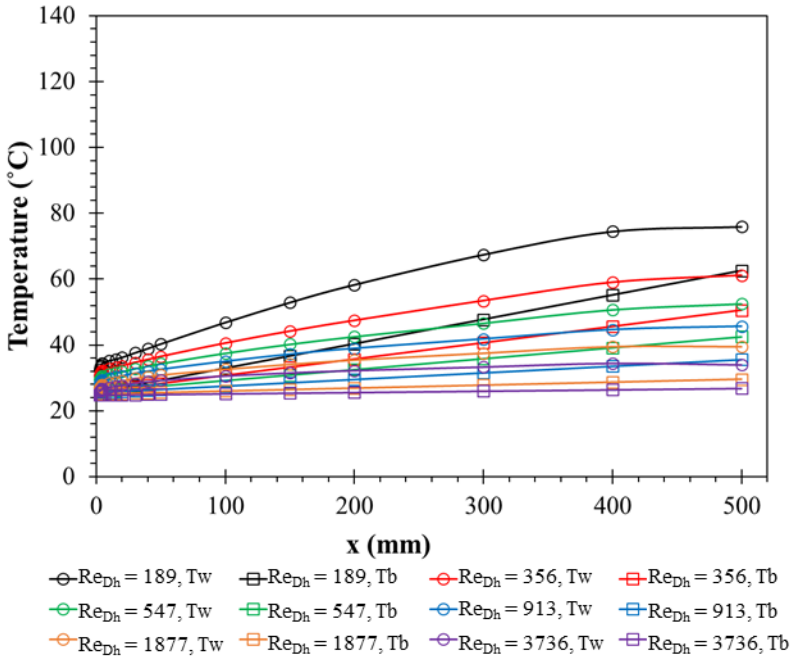

Figure A-178 Realistic S-shaped Model, J = 33 cw, 20V, (07/01/21), Temperature Profile

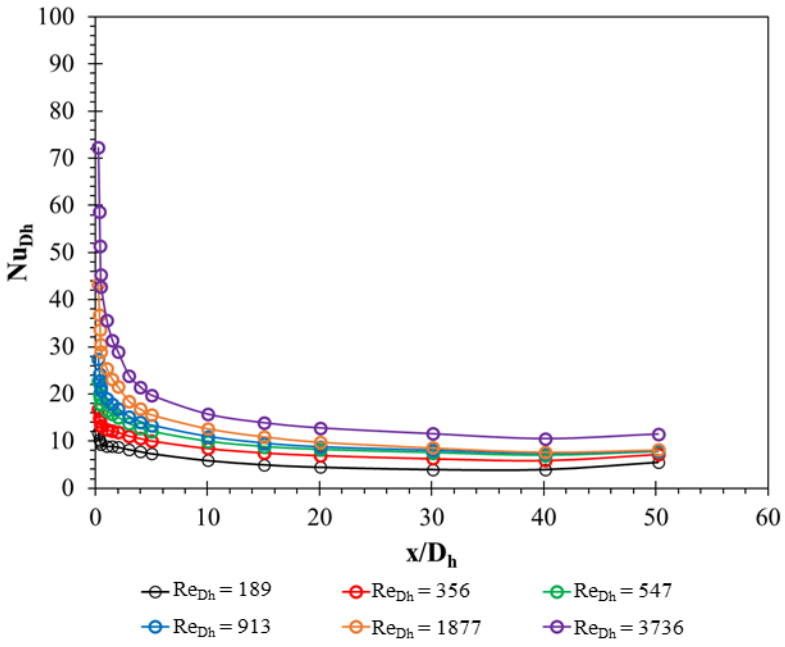

Figure A-179 Realistic S-shaped Model, J = 33 cw, 20V, (07/01/21), Nu_{Dh} Profile

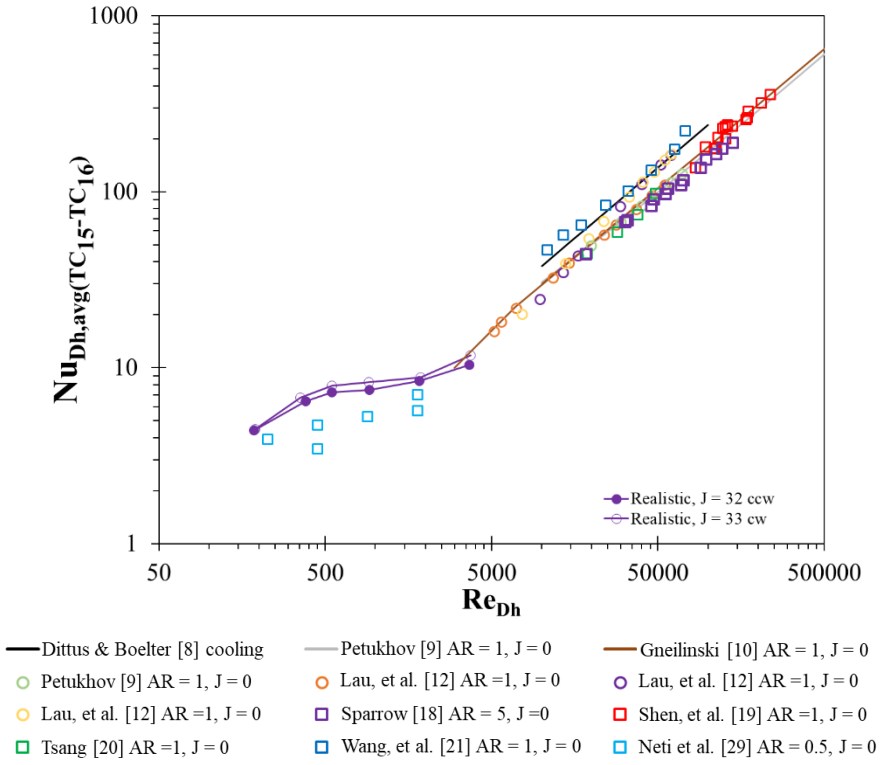

Figure A-180 Realistic S-shaped Model, J = 33 cw, 32 ccw, Nu_{Dh} vs Re_{Dh}

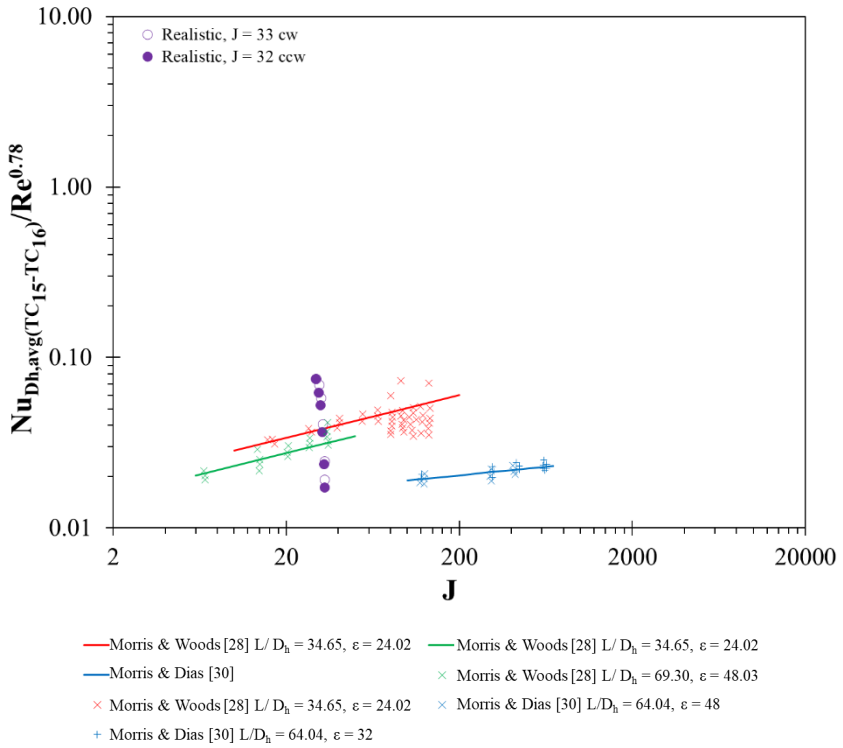

Figure A-181 Realistic S-shaped Model, J = 33 cw, 32 ccw, Nu_{Dh} vs J

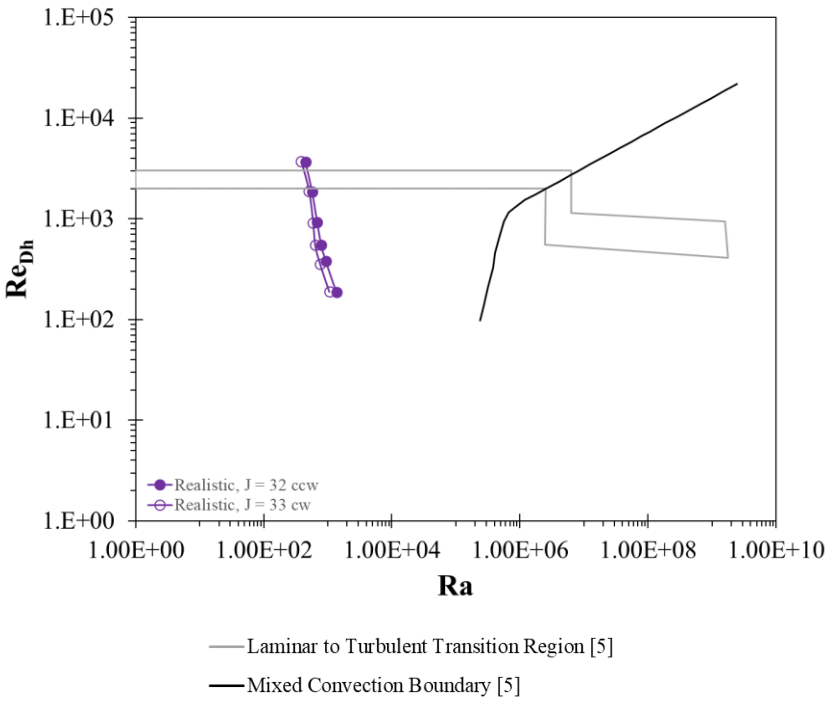

Figure A-182 Realistic S-shaped Model, J = 33 cw, 32 ccw, Re_{Dh} vs Ra

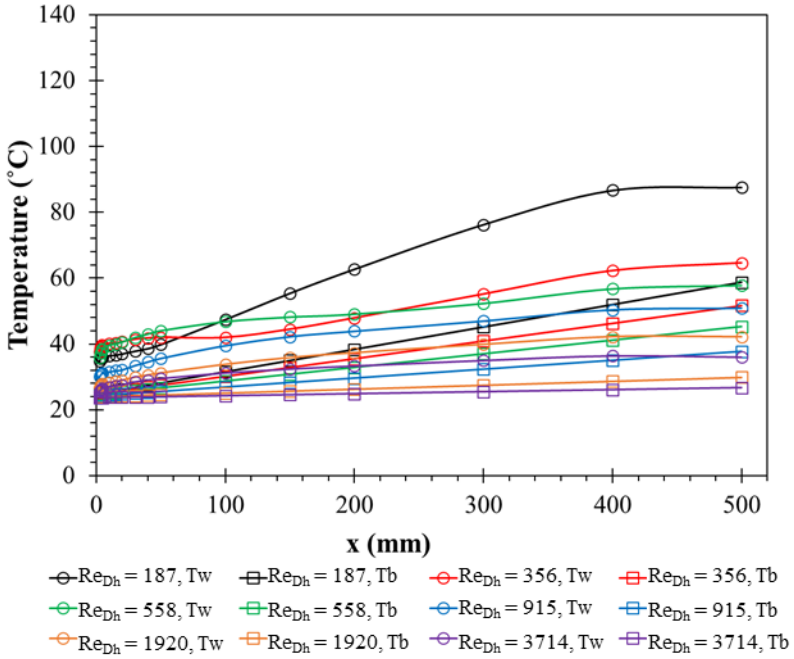

Figure A-183 Realistic S-shaped Model, J = 65 ccw, 22.5V, (07/02/21), Temperature Profile

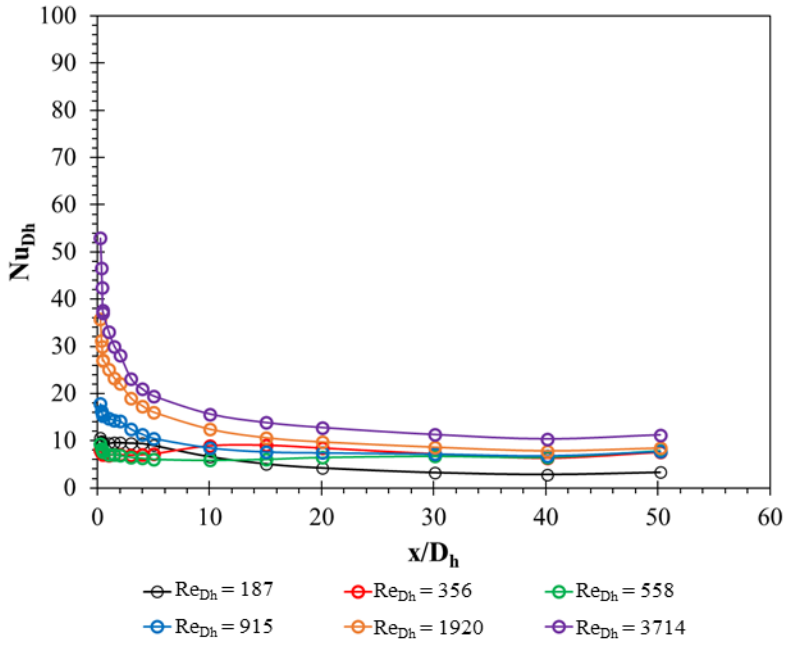

Figure A-184 Realistic S-shaped Model, J = 65 ccw, 22.5V, (07/02/21), Nu_{Dh} Profile

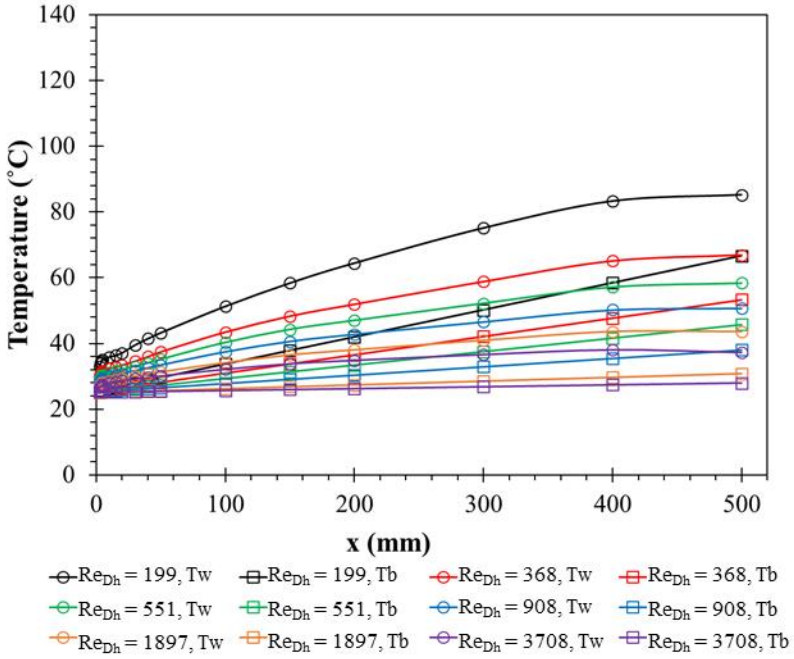

Figure A-185 Realistic S-shaped Model, J = 64 cw, 22.5V, (07/02/21), Temperature Profile

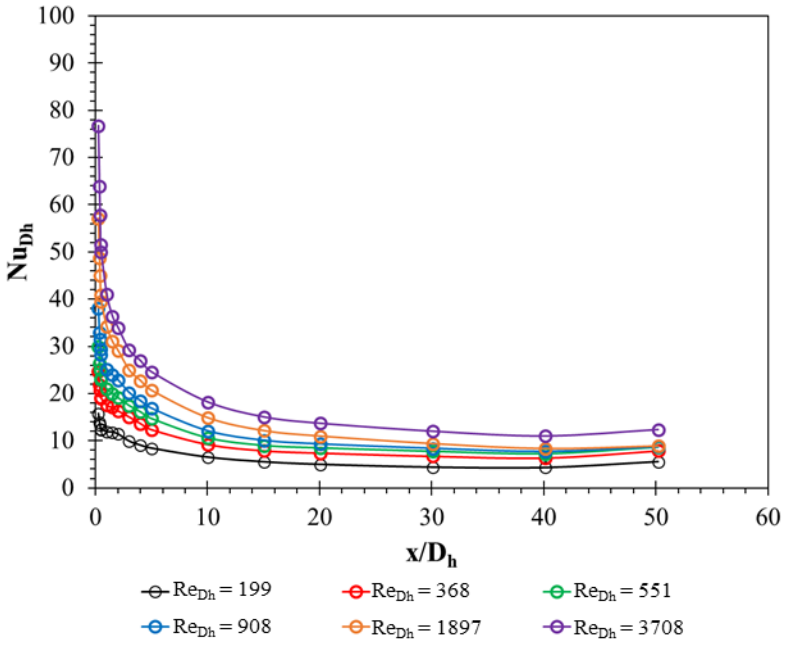

Figure A-186 Realistic S-shaped Model, J = 64 cw, 22.5V, (07/02/21), Nu_{Dh} Profile

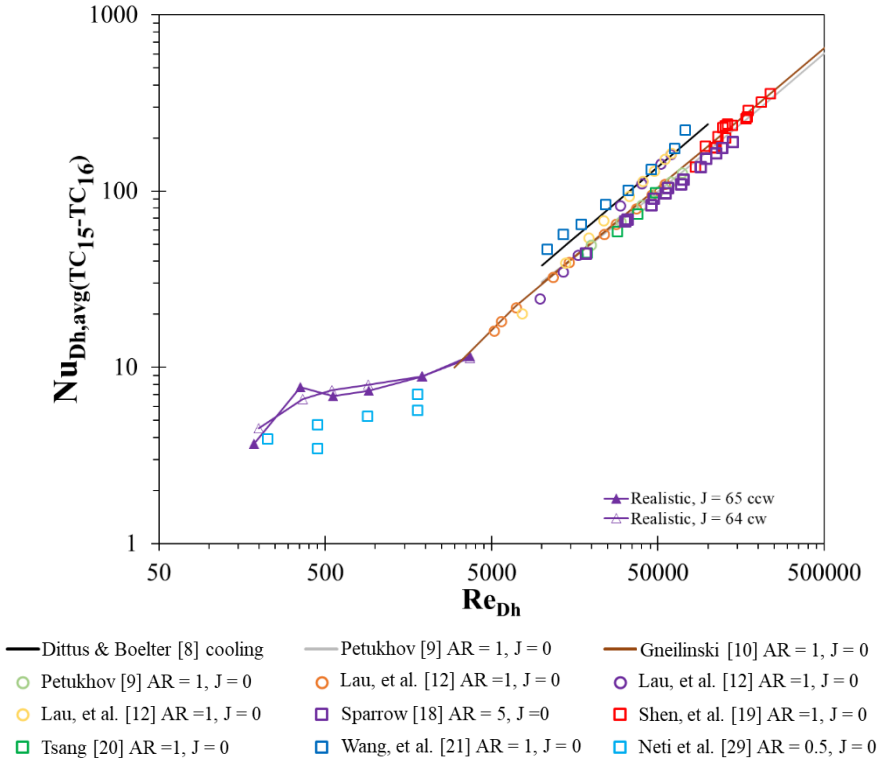

Figure A-187 Realistic S-shaped Model, J = 64 cw, 65 ccw, Nu_{Dh} vs Re_{Dh}

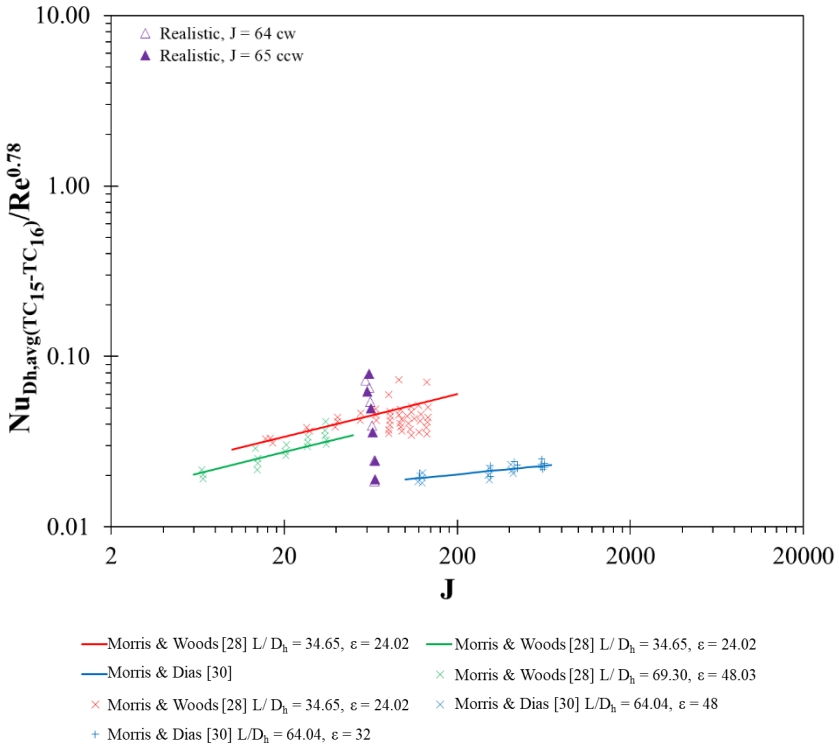

Figure A-188 Realistic S-shaped Model, J = 64 cw, 65 ccw, Nu_{Dh} vs J

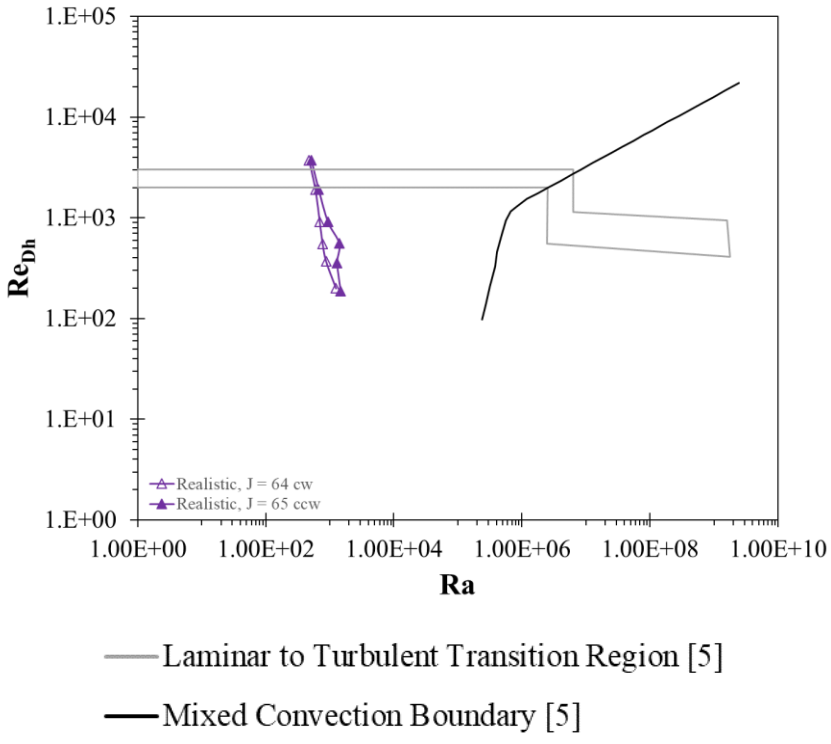

Figure A-189 Realistic S-shaped Model, J = 64 cw, 65 ccw, Re_{Dh} vs Ra

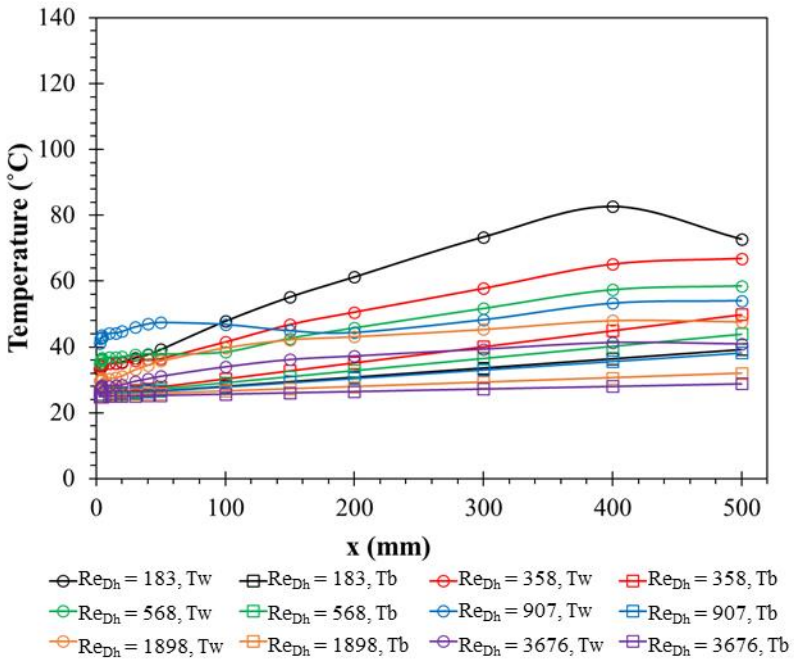

Figure A-190 Realistic S-shaped Model, J = 129 ccw, 25V, (07/02/21), Temperature Profile

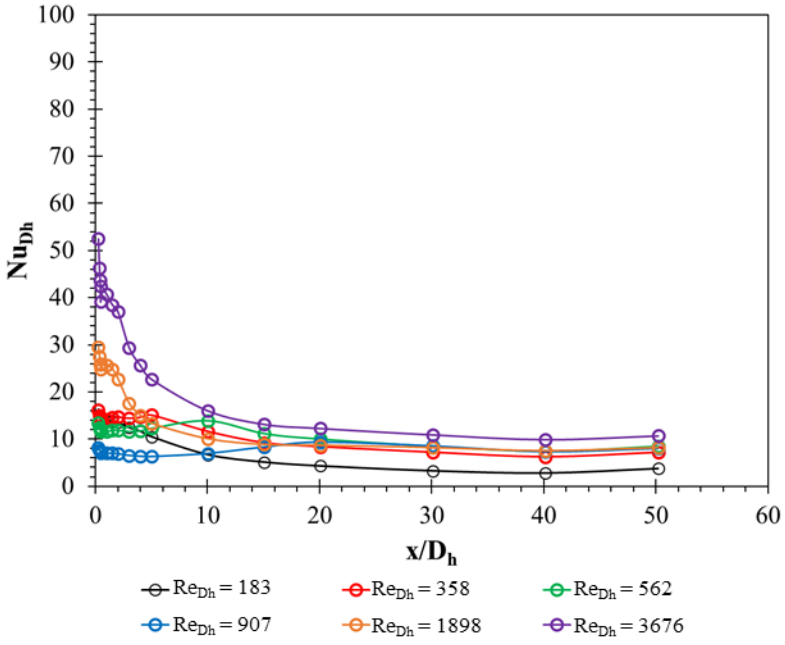

Figure A-191 Realistic S-shaped Model, J = 129 ccw, 25V, (07/02/21), Nu_{Dh} Profile

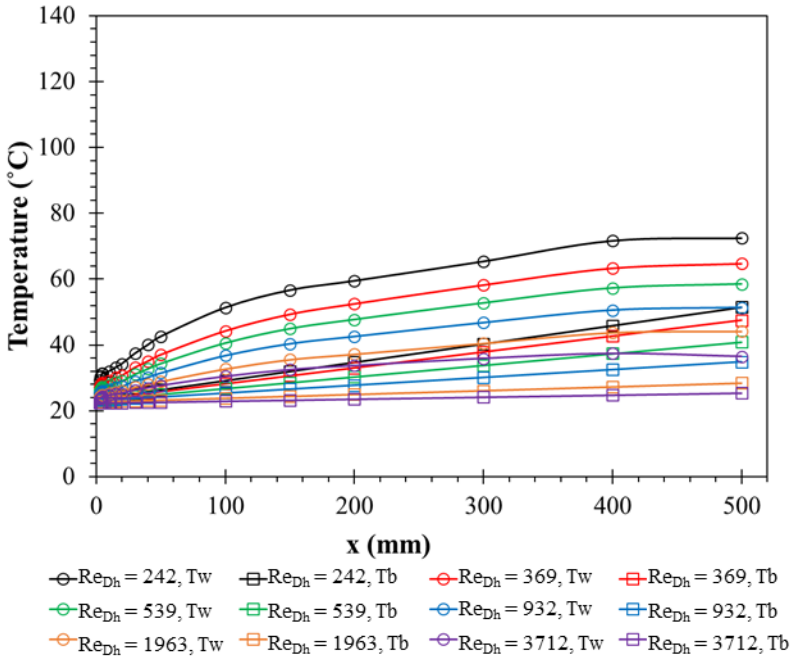

Figure A-192 Realistic S-shaped Model, J = 131 cw, 25V, (07/03/21), Temperature Profile

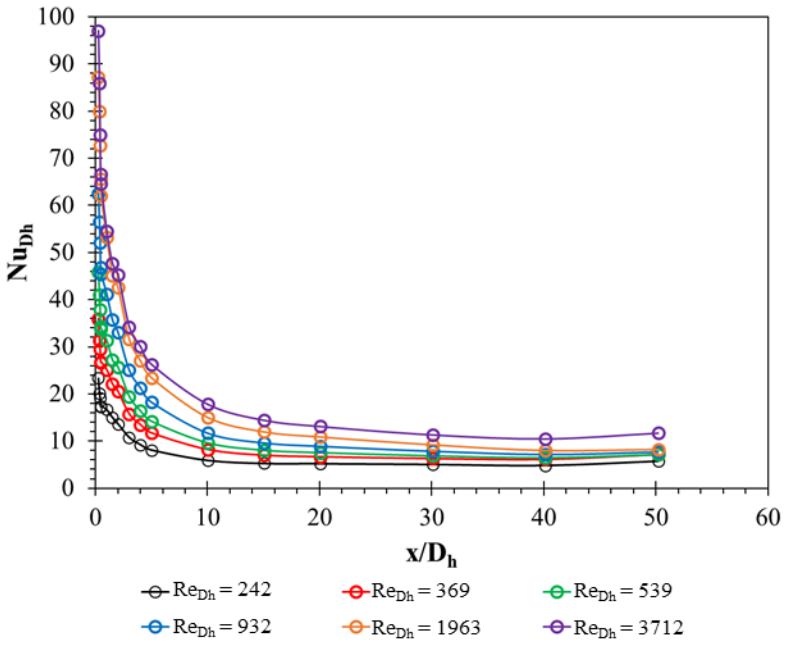

Figure A-193 Realistic S-shaped Model, J = 131 cw, 25V, (07/03/21), Nu_{Dh} Profile

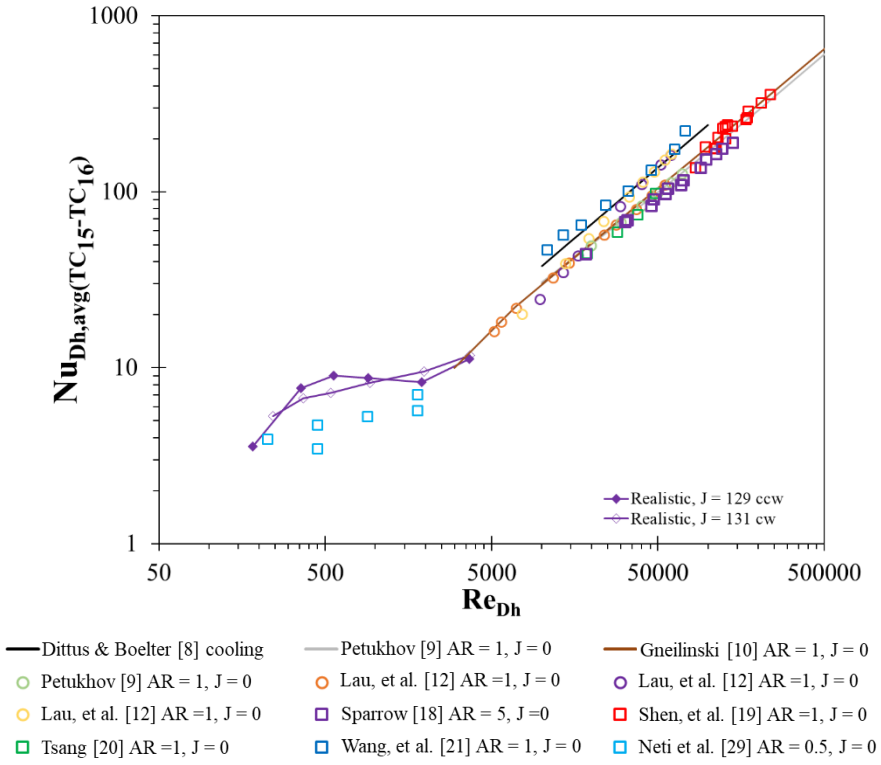

Figure A-194 Realistic S-shaped Model, J = 131 cw, 129 ccw, Nu_{Dh} vs Re_{Dh}

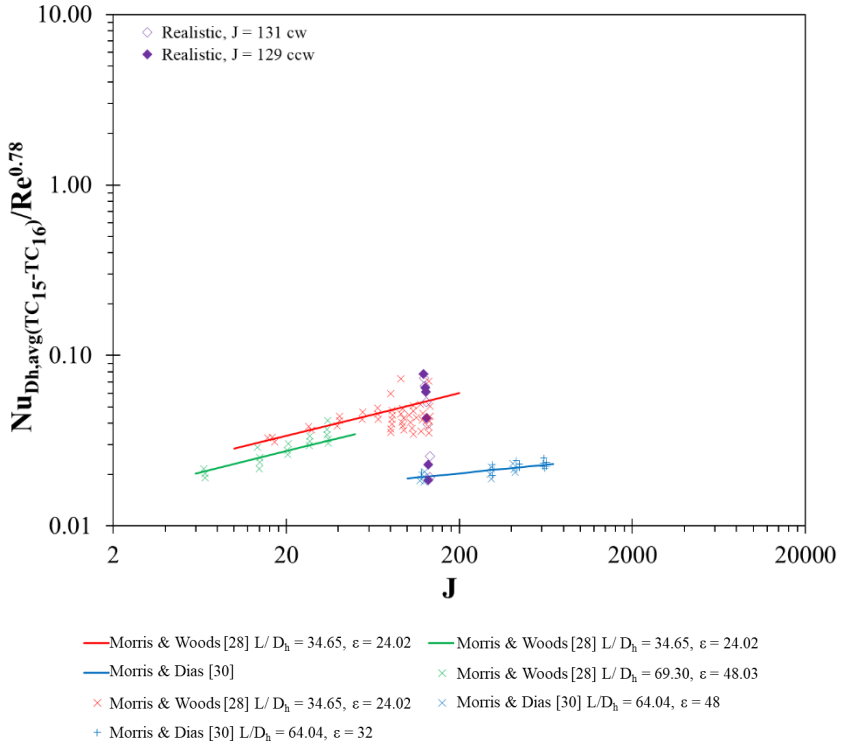

Figure A-195 Realistic S-shaped Model, J = 131 cw, 129 ccw, Nu_{Dh} vs J

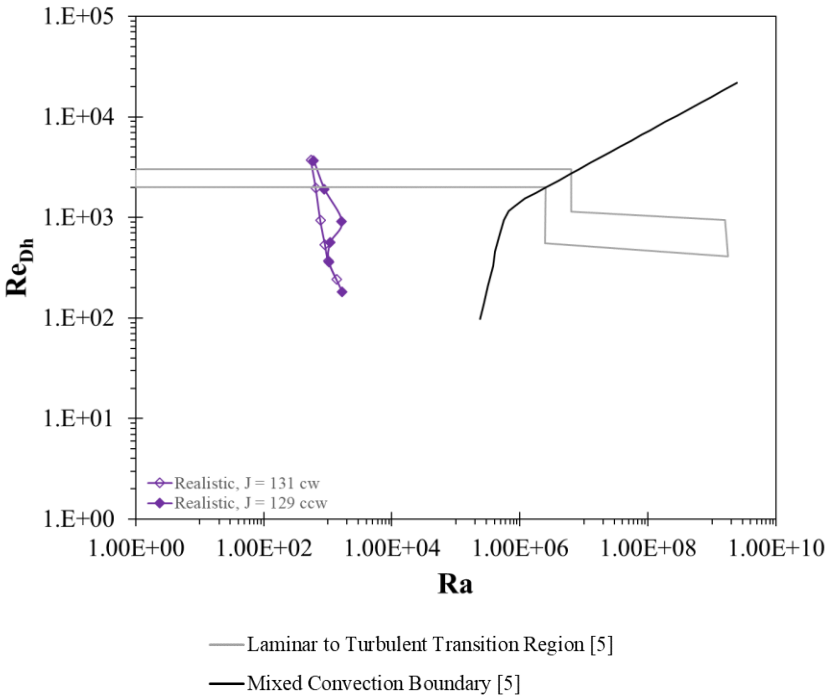

Figure A-196 Realistic S-shaped Model, J = 131 cw, 129 ccw, Re_{Dh} vs Ra

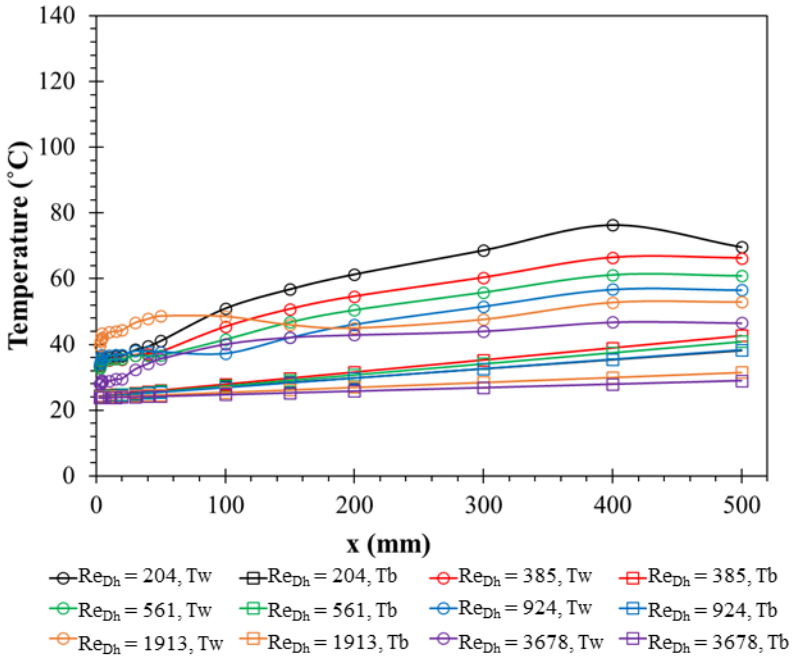

Figure A-197 Realistic S-shaped Model, J = 262 ccw, 31.4V, (07/03/21), Temperature Profile

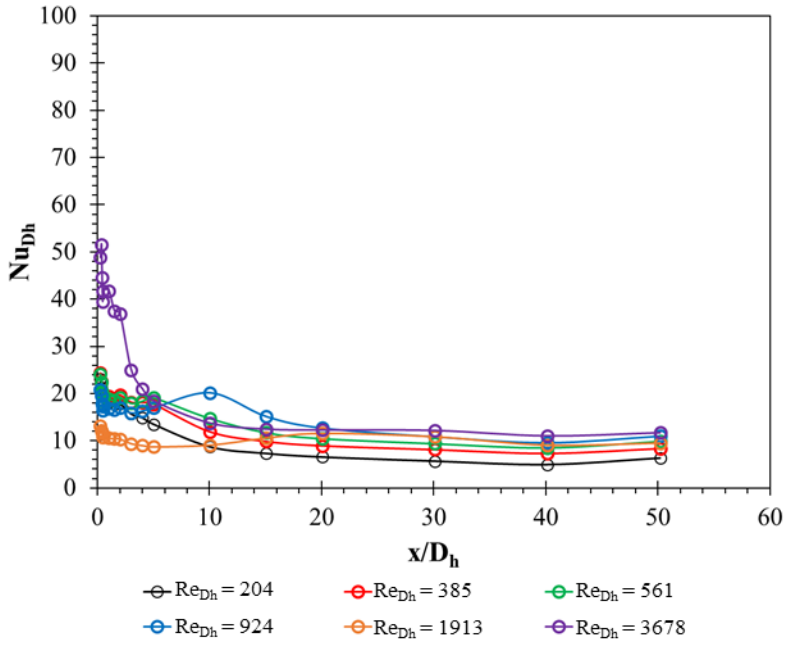

Figure A-198 Realistic S-shaped Model, J = 262 ccw, 31.4V, (07/03/21), Nu_{Dh} Profile

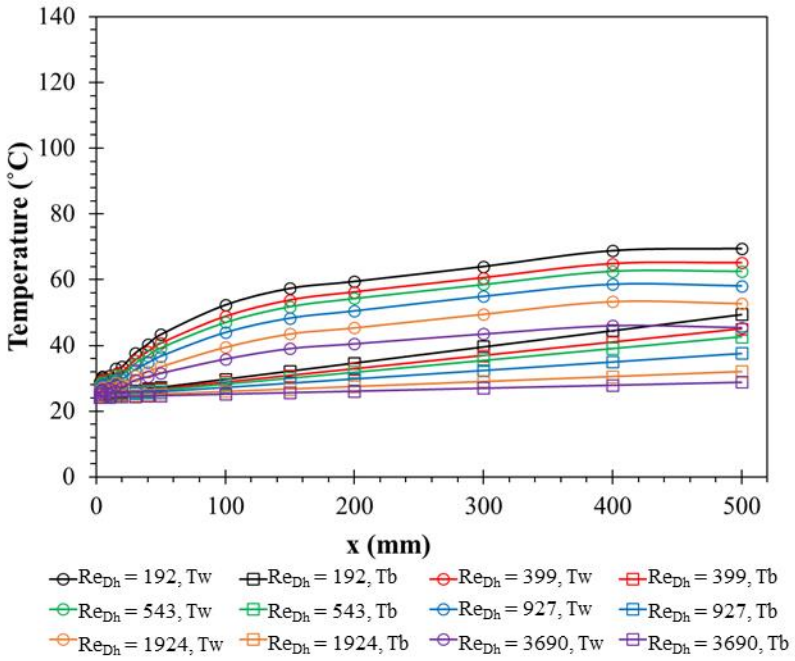

Figure A-199 Realistic S-shaped Model, J = 260 cw, 31.4V, (07/03/21), Temperature Profile

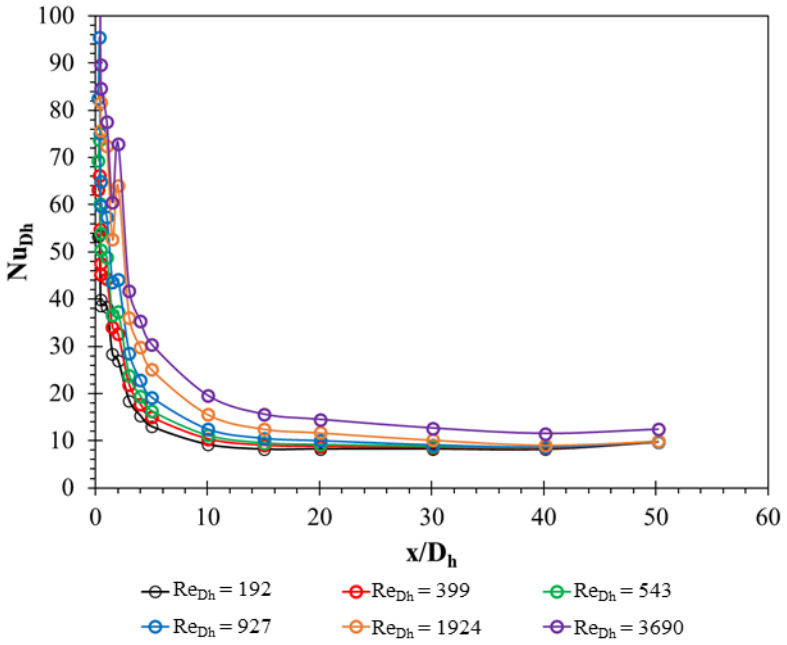

Figure A-200 Realistic S-shaped Model, J = 260 cw, 31.4V, (07/03/21), Nu_{Dh} Profile

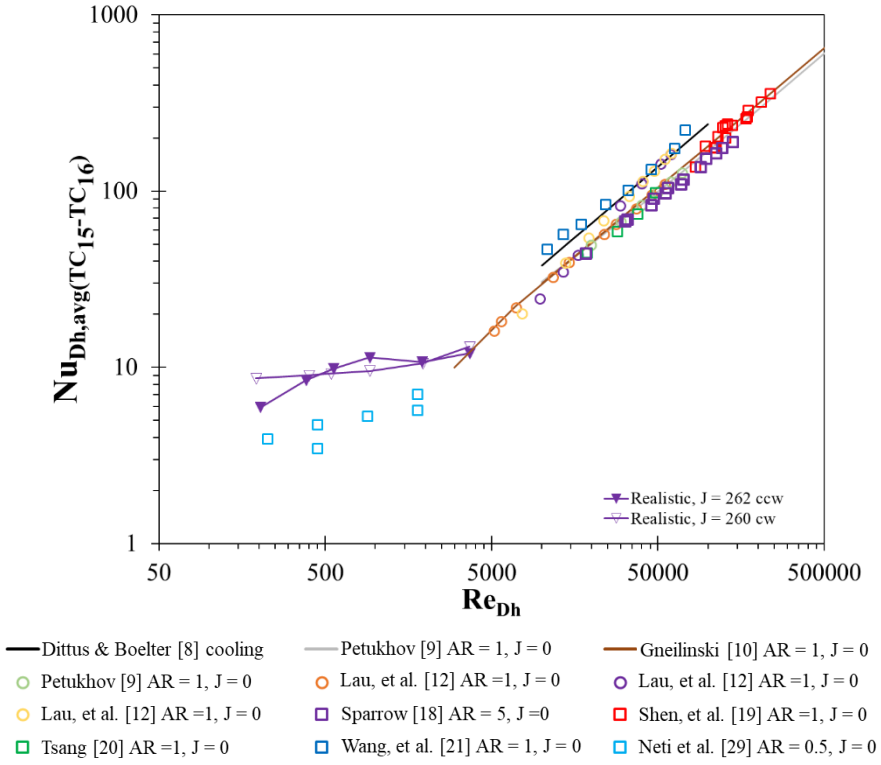

Figure A-201 Realistic S-shaped Model, J = 260 cw, 262 ccw, Nu_{Dh} vs Re_{Dh}

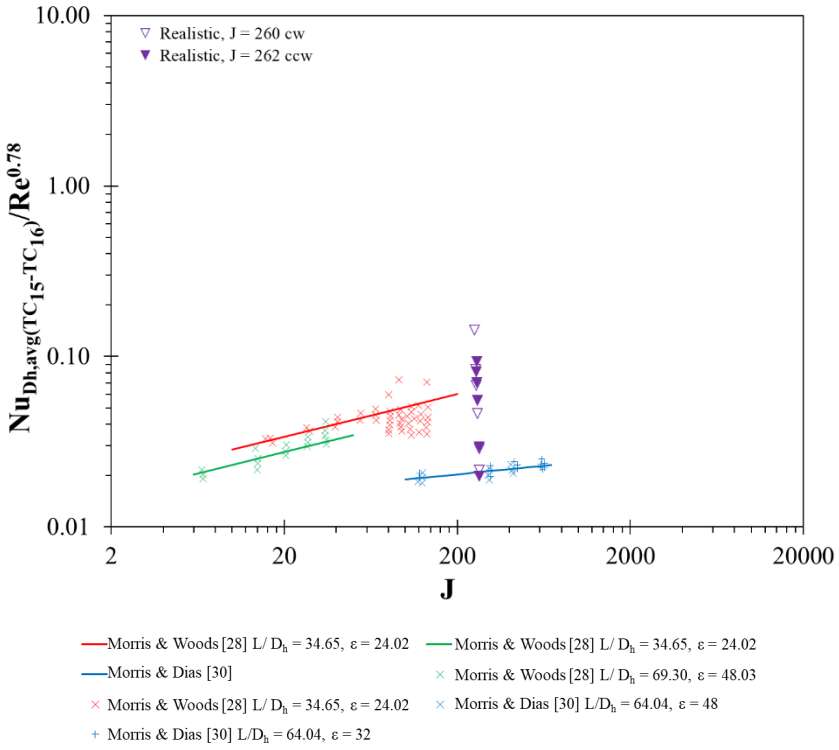

Figure A-202 Realistic S-shaped Model, J = 260 cw, 262 ccw, Nu_{Dh} vs J

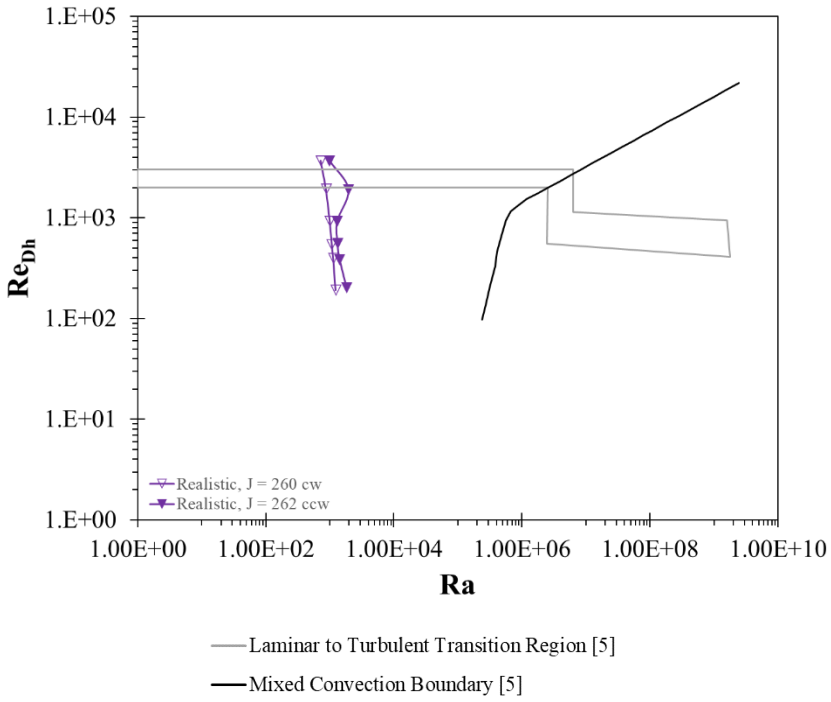

Figure A-203 Realistic S-shaped Model, J = 260 cw, 262 ccw, Re_{Dh} vs Ra

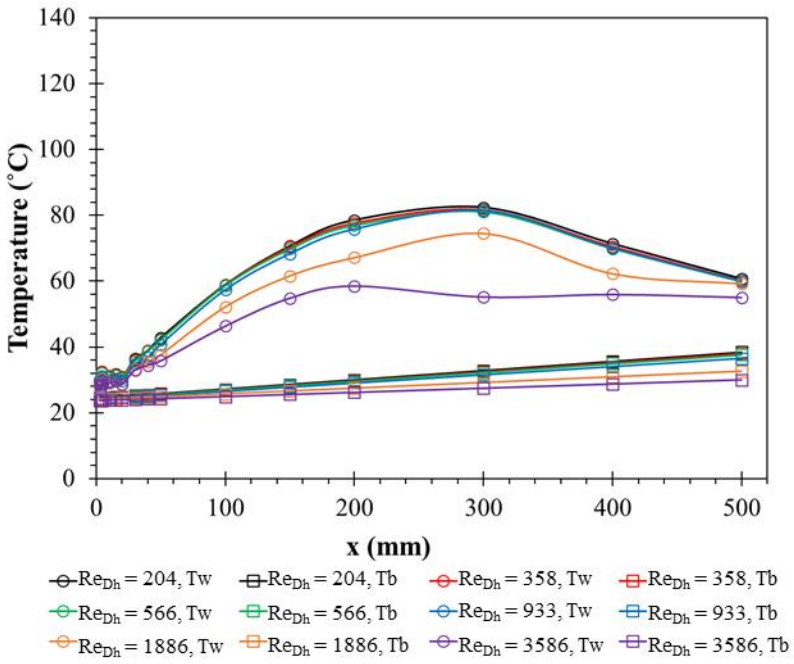

Figure A-204 Realistic S-shaped Model, J = 523 ccw, 35V, (07/06/21), Temperature Profile

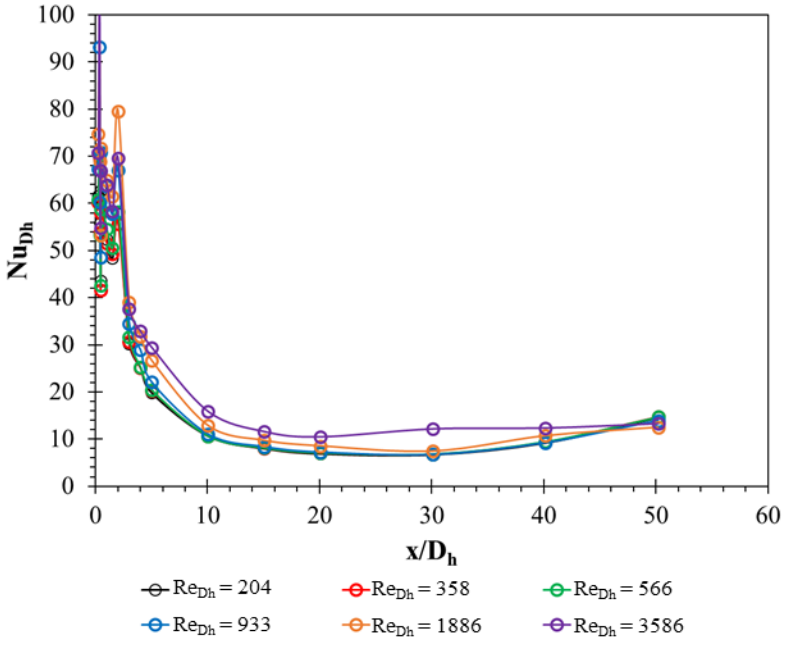

Figure A-205 Realistic S-shaped Model, J = 523 ccw, 35V, (07/06/21), Nu_{Dh} Profile

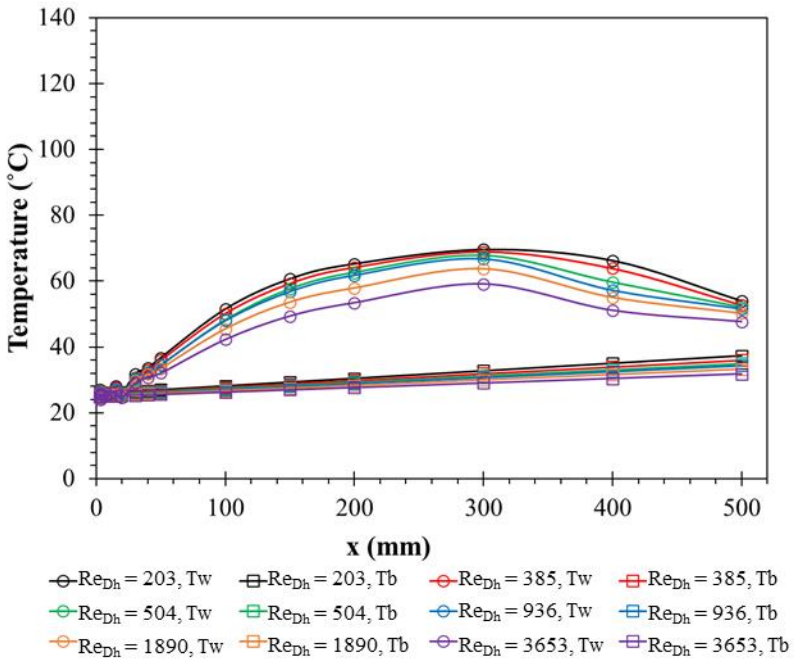

Figure A-206 Realistic S-shaped Model, J = 523 cw, 35V, (07/06/21), Temperature Profile

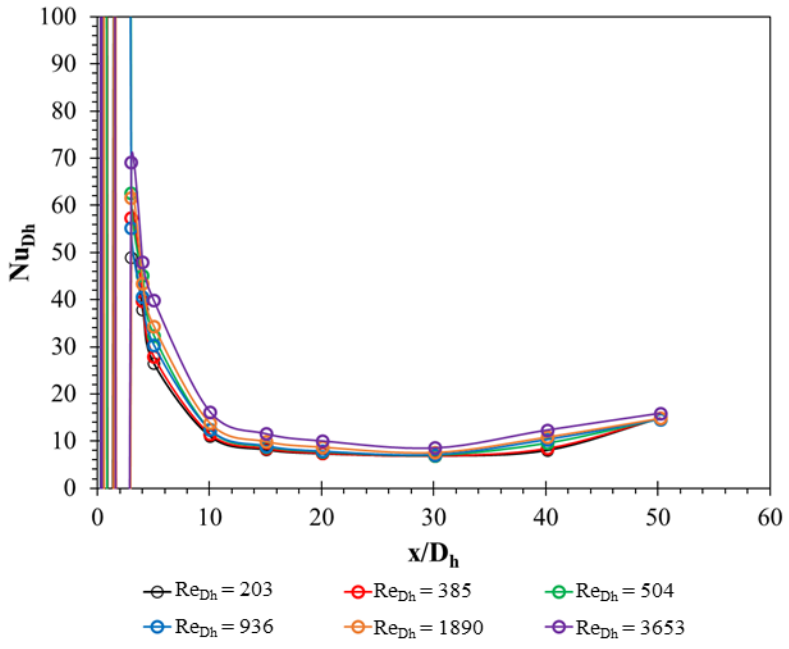

Figure A-207 Realistic S-shaped Model, J = 523 cw, 35V, (07/06/21), Nu_{Dh} Profile

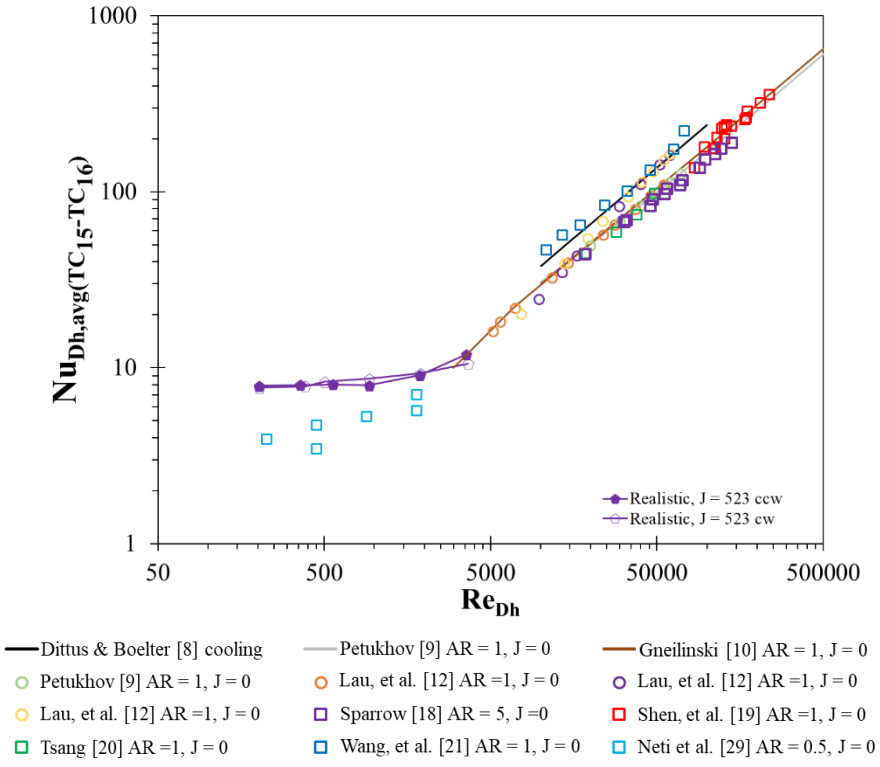

Figure A-208 Realistic S-shaped Model, J = 523, Nu_{Dh} vs Re_{Dh}

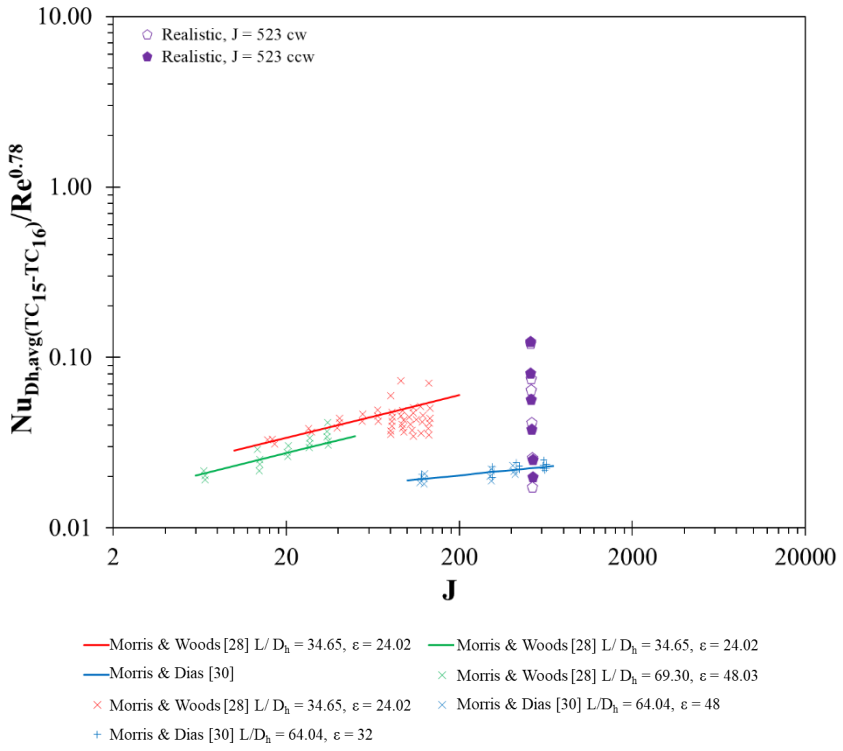

Figure A-209 Realistic S-shaped Model, J = 523, Nu_{Dh} vs J

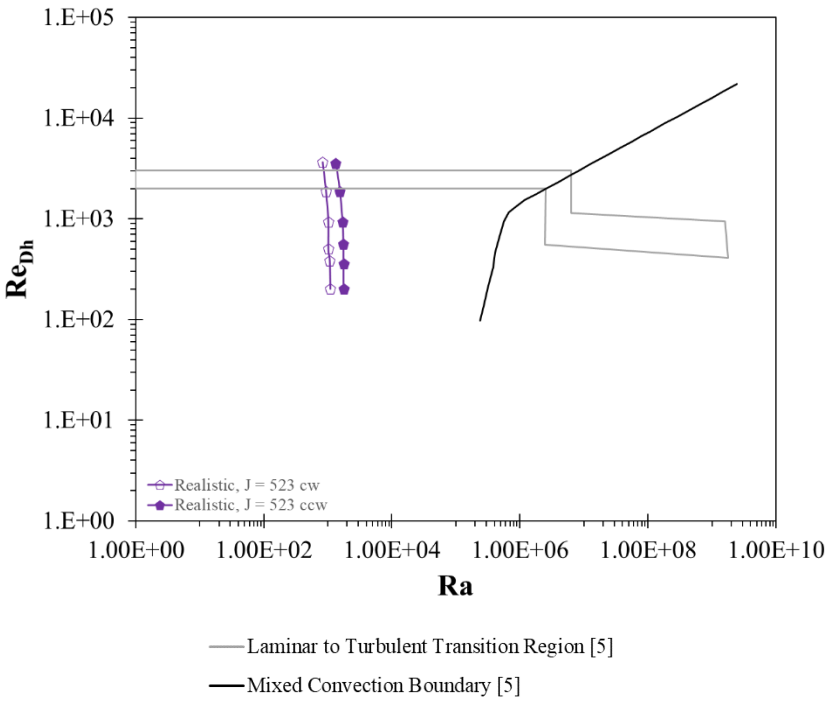

Figure A-210 Realistic S-shaped Model, J = 523, Re_{Dh} vs Ra

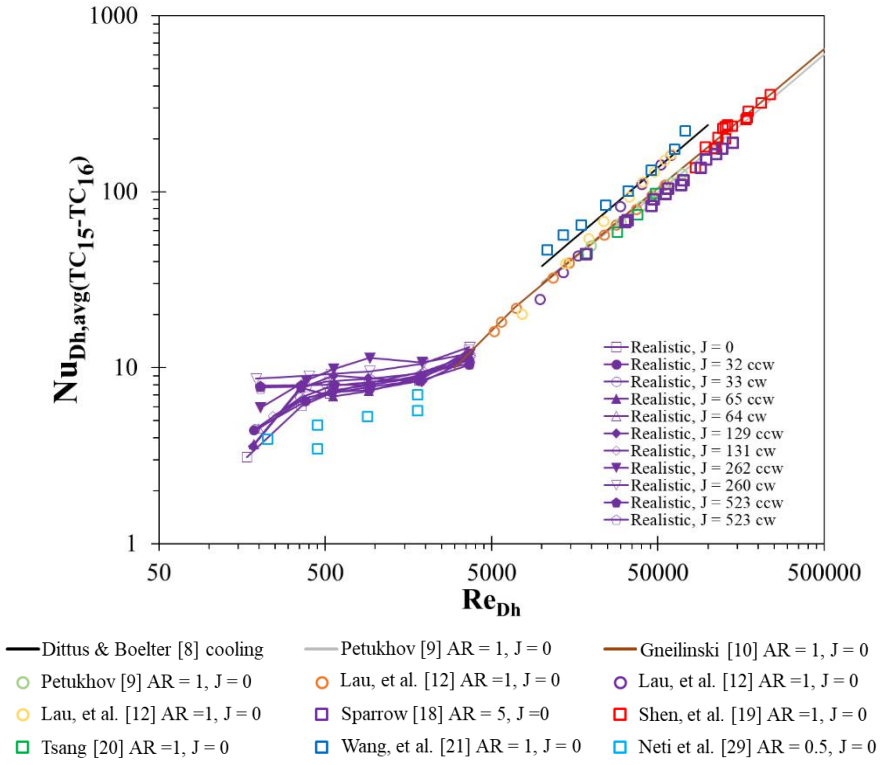

Figure A-211 Realistic S-shaped Model Comparison, Nu_{Dh} vs Re_{Dh}

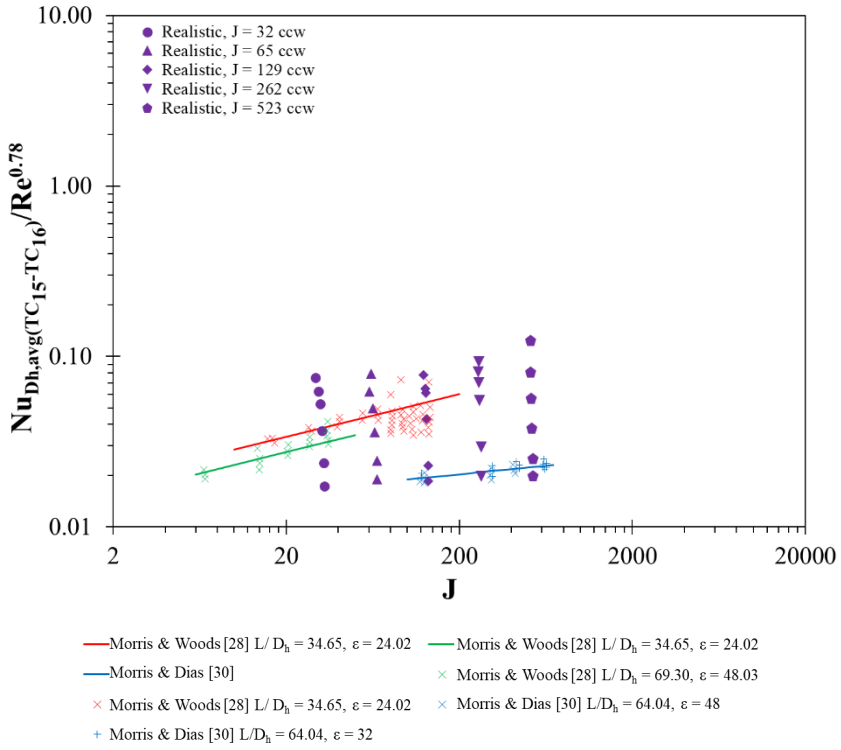

Figure A-212 Realistic S-shaped Model Comparison, Nu_{Dh} vs J ccw

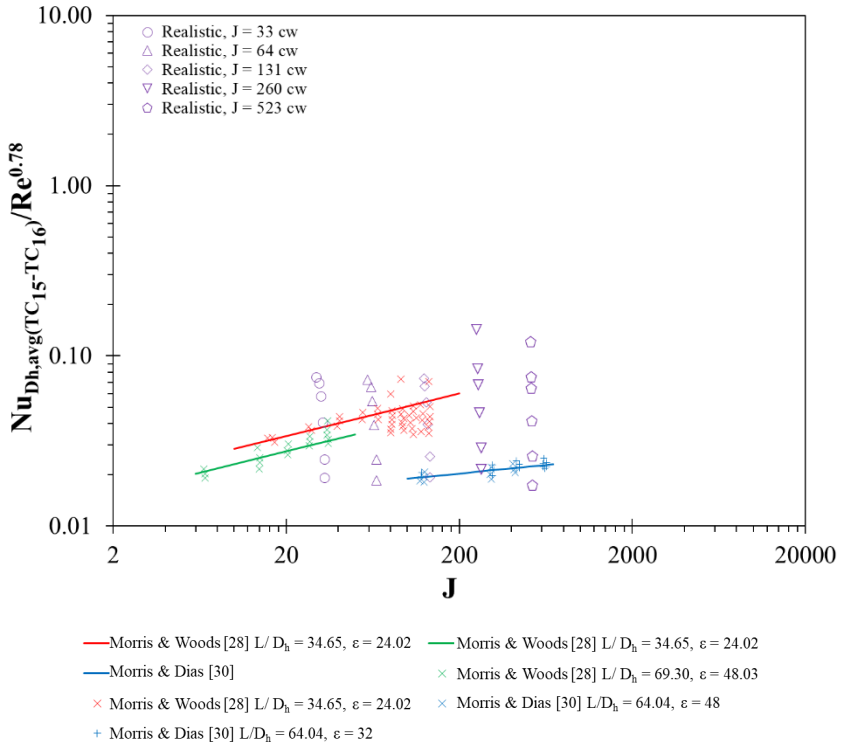

Figure A-213 Realistic S-shaped Model Comparison, Nu_{Dh} vs J cw

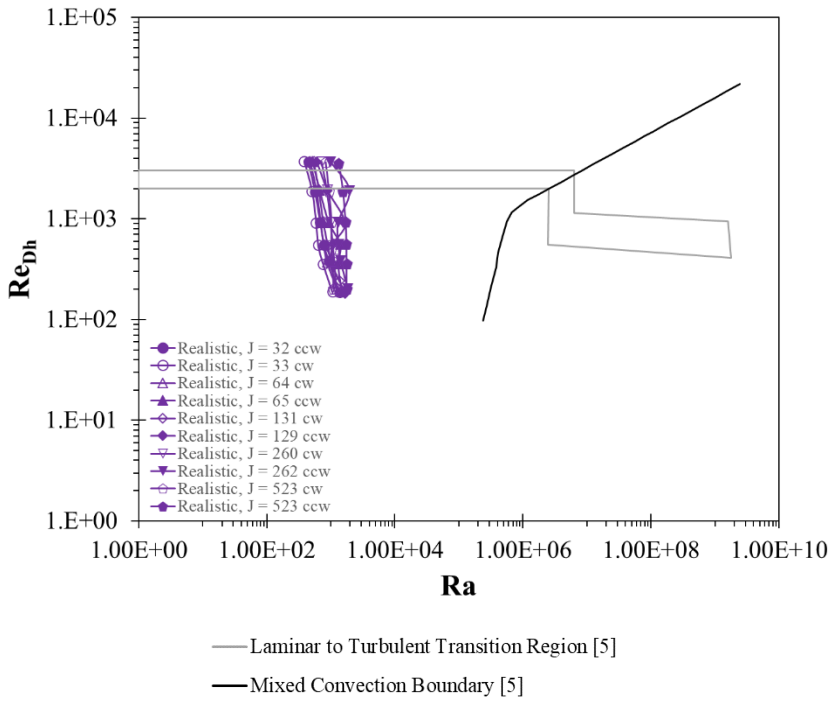

Figure A-214 Realistic S-shaped Model Comparison, Re_{Dh} vs Ra

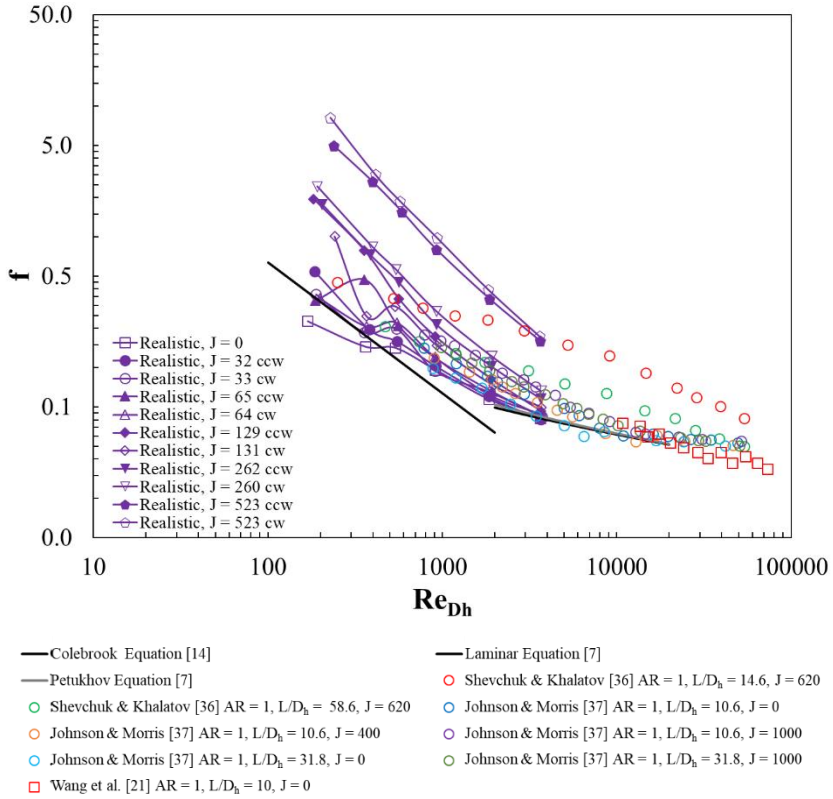

Figure A-215 Realistic S-shaped Model Comparison, Friction Factor

Appendix B: Annular Duct Data

Table B-2 Annular Duct Test Matrix

ω (rpm)	$\Delta r/r_1 = 0.05$	$\Delta r/r_1 = 0.1$	$\Delta r/r_1 = 0.3$	$\Delta r/r_1 = 0.6$
0	O	O	O	O
100	O	O	O	O
200	O	O	O	O
400	O	O	O	O
800	O	O	O	O
Re_{Dh}	7792 ~ 10296, 20767 ~ 22771, 40488 ~ 41689 Clockwise (from rear view)			

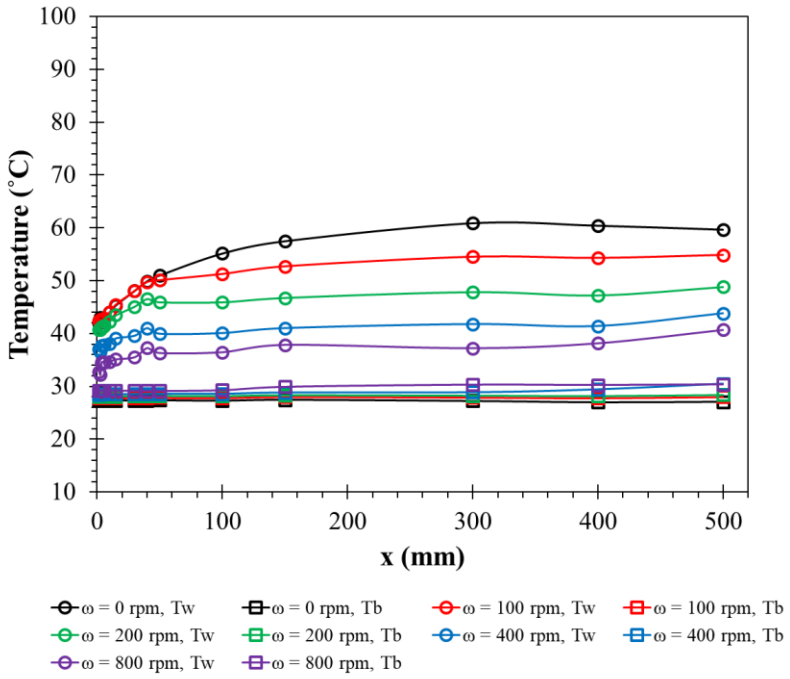

Figure B-1 $\Delta r/r_1 = 0.05$, Re_{Dh} = 7698-7986, 50V, (07/28/21), Temperature Profile

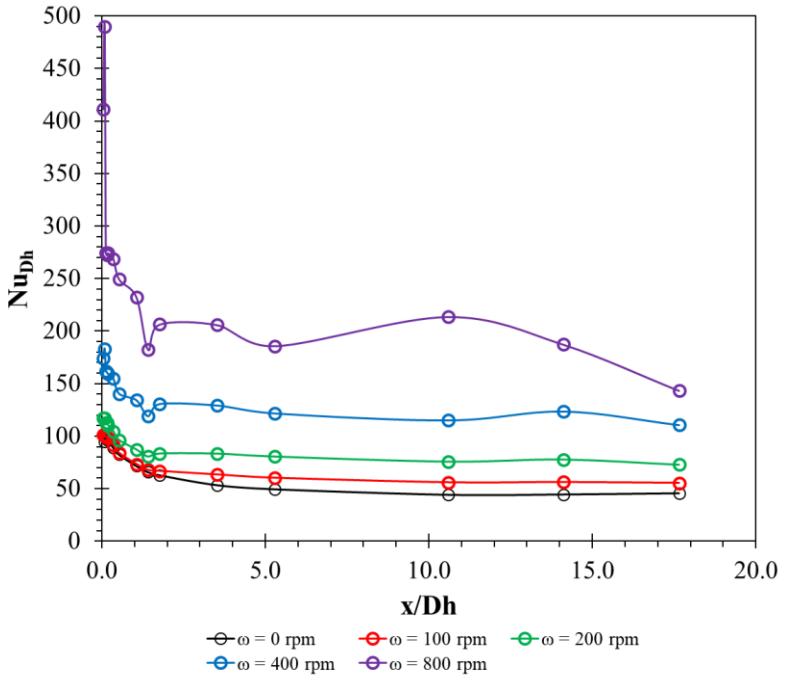

Figure B-2 $\Delta r/r_1$ = 0.05, Re_{Dh} = 7698-7986, 50V, (07/28/21), Nu_{Dh} Profile

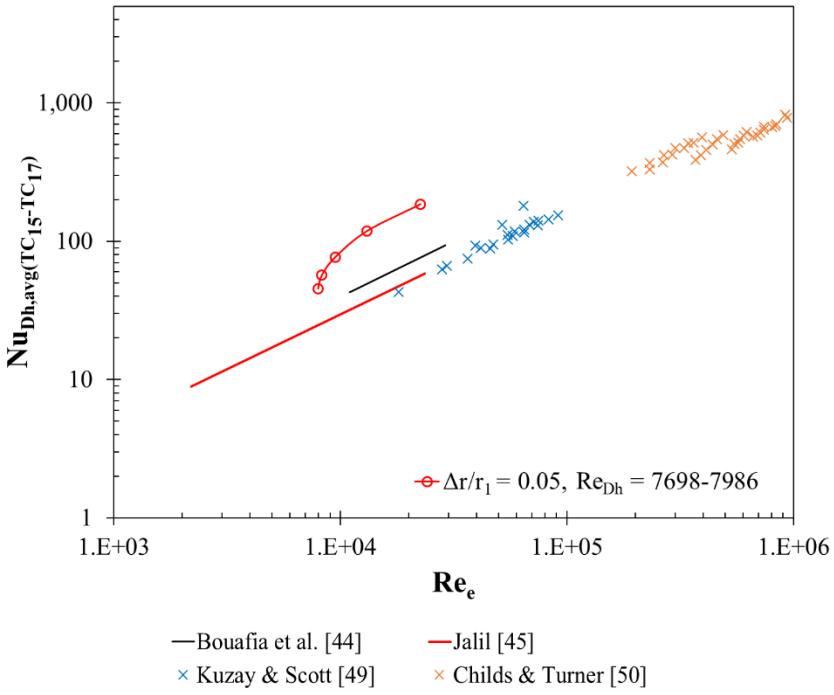

Figure B-3 $\Delta r/r_1$ = 0.05, Re_{Dh} = 7698-7986, Nu_{Dh} vs Re_e

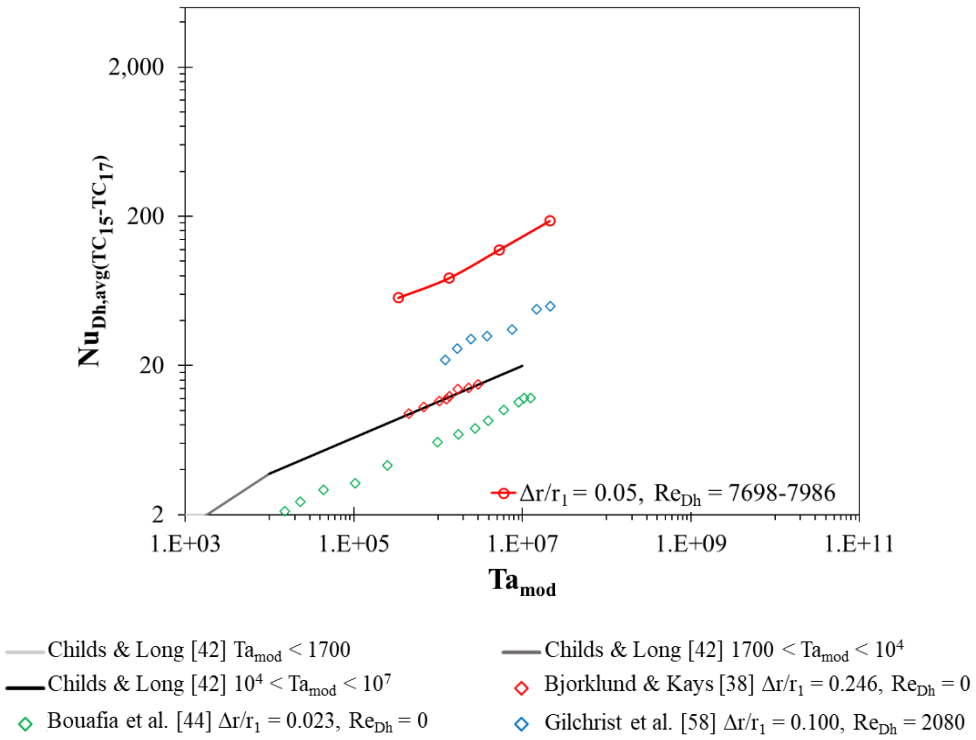

Figure B-4 $\Delta r/r_1 = 0.05$, $Re_{Dh} = 7698\text{-}7986$, Nu_{Dh} vs Ta

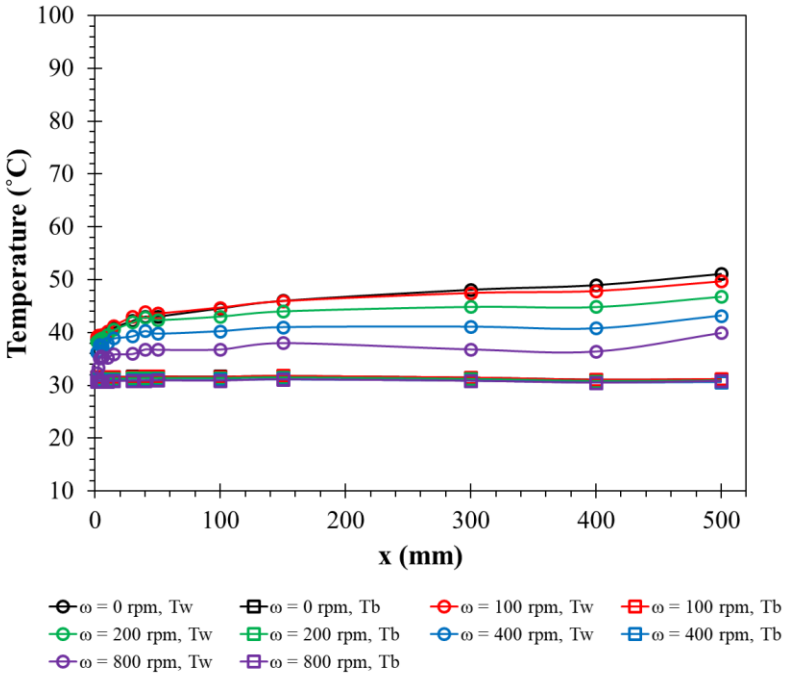

Figure B-5 $\Delta r/r_1 = 0.05$, $Re_{Dh} = 22576\text{-}23144$, (07/28/21), Temperature Profile

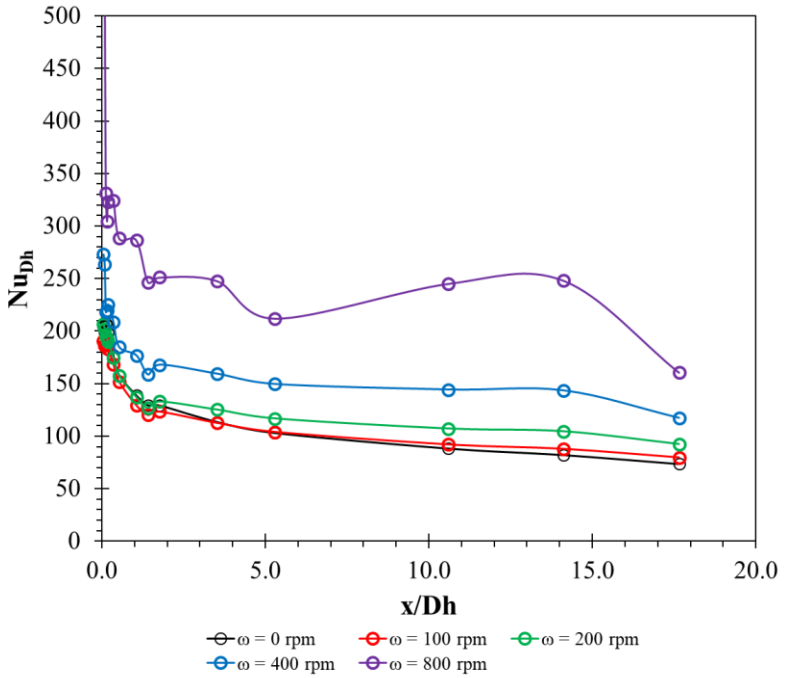

Figure B-6 $\Delta r/r_1 = 0.05$, Re_{Dh} = 22576-23144, 50V, (07/28/21), Nu_{Dh} Profile

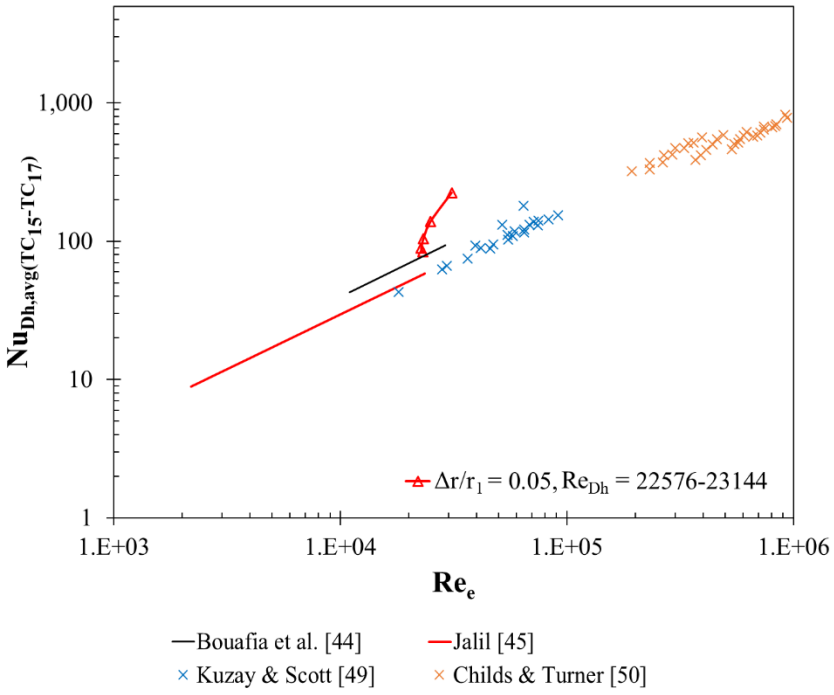

Figure B-7 $\Delta r/r_1 = 0.05$, Re_{Dh} = 22576-23144, Nu_{Dh} vs Re_e

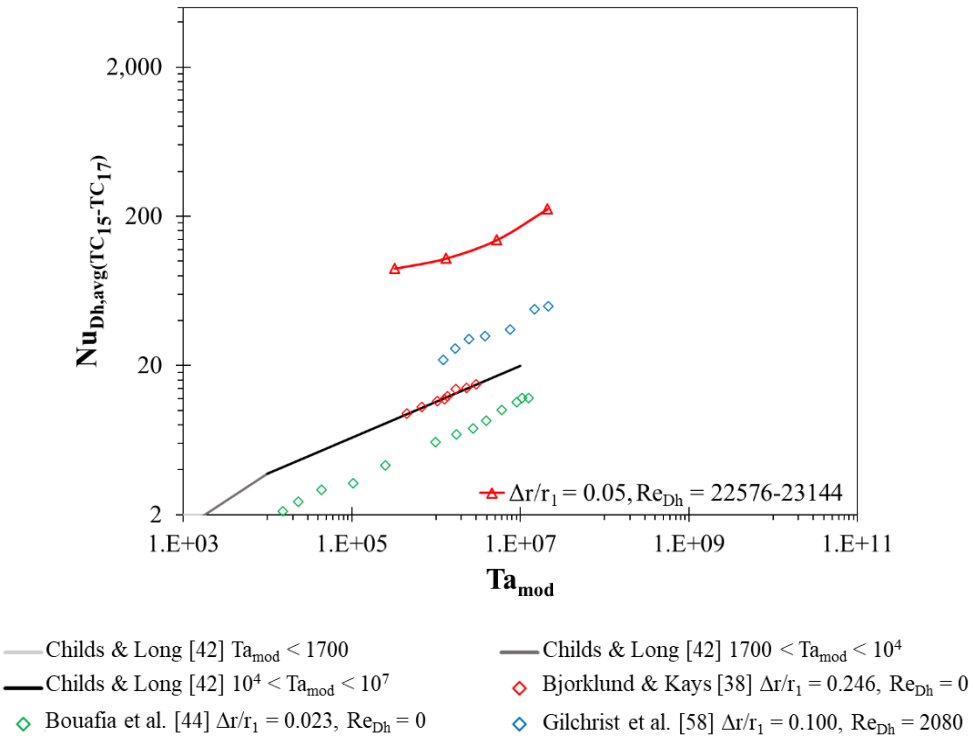

Figure B-8 $\Delta r/r_1 = 0.05$, $Re_{Dh} = 22576\text{-}23144$, Nu_{Dh} vs Ta

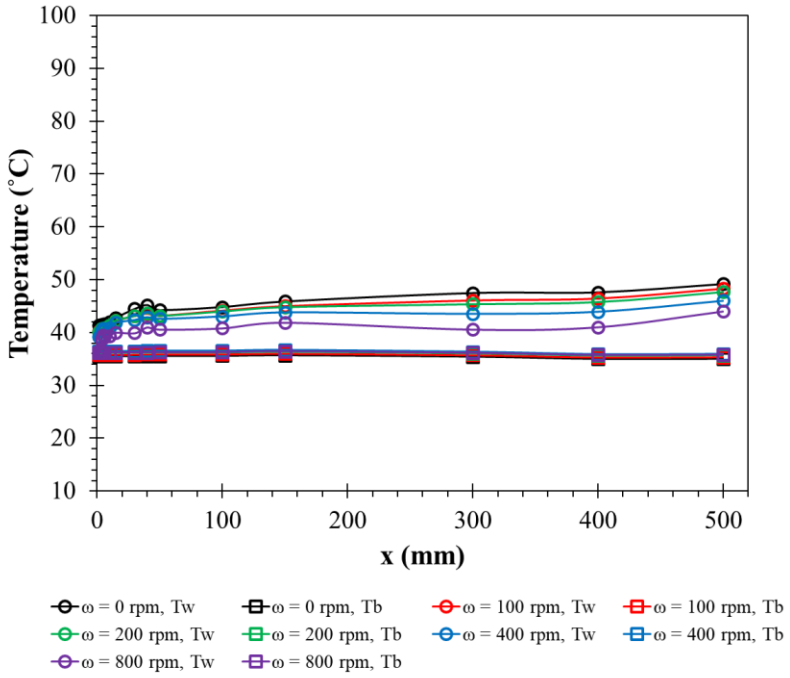

Figure B-9 $\Delta r/r_1 = 0.05$, $Re_{Dh} = 41600\text{-}41726$, 50V, (07/28/21), Temperature Profile

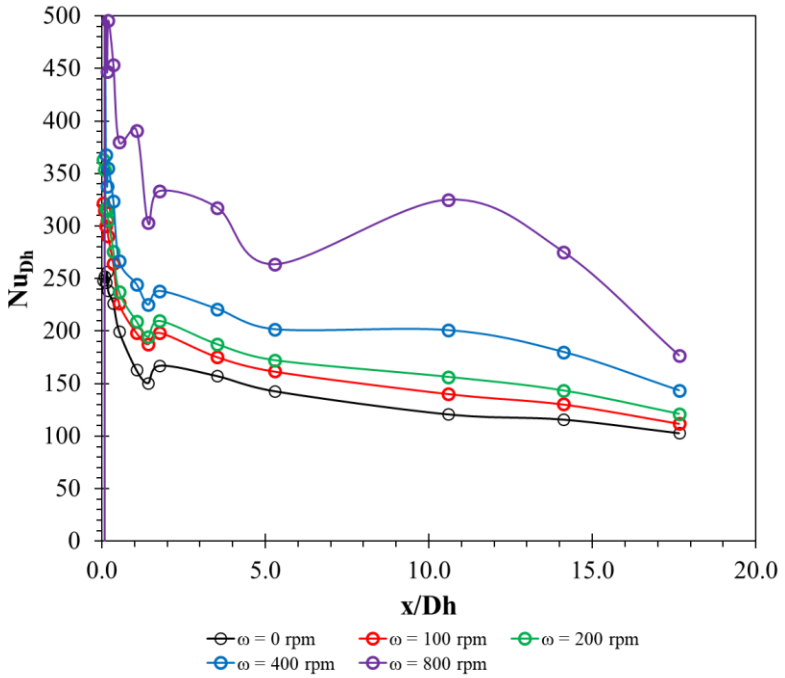

Figure B-10 $\Delta r/r_1$ = 0.05, Re_{Dh} = 41600-41726, 50V, (07/28/21), Nu_{Dh} Profile

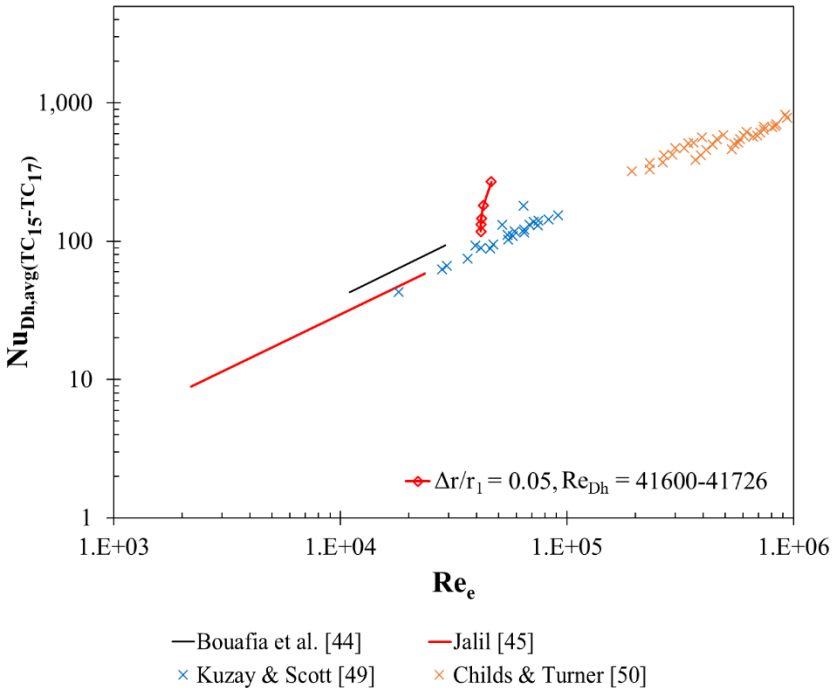

Figure B-11 $\Delta r/r_1$ = 0.05, Re_{Dh} = 41600-41726, Nu_{Dh} vs Re_e

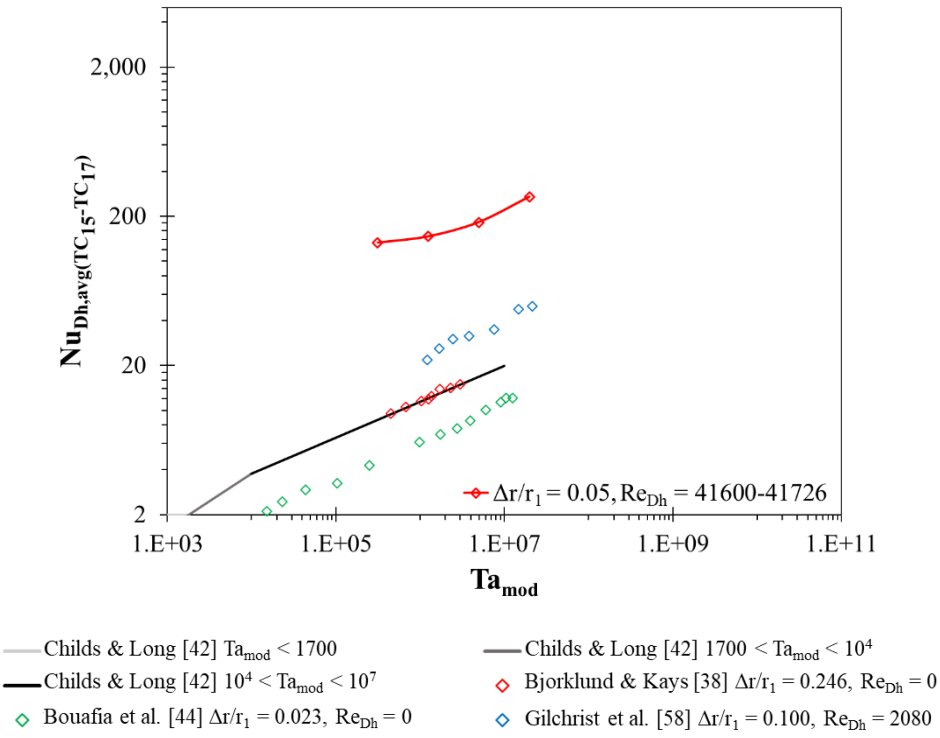

Figure B-12 $\Delta r/r_1 = 0.05$, $Re_{Dh} = 41600\text{-}41726$, Nu_{Dh} vs Ta

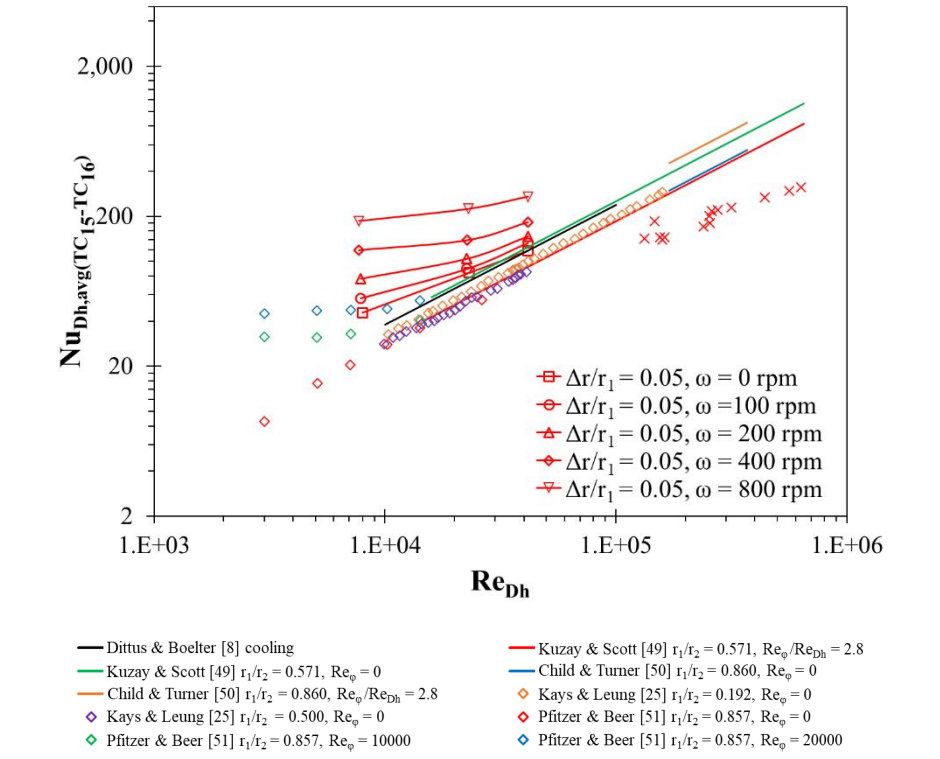

Figure B-13 $\Delta r/r_1 = 0.05$ Comparison, Nu_{Dh} vs Re_{Dh}

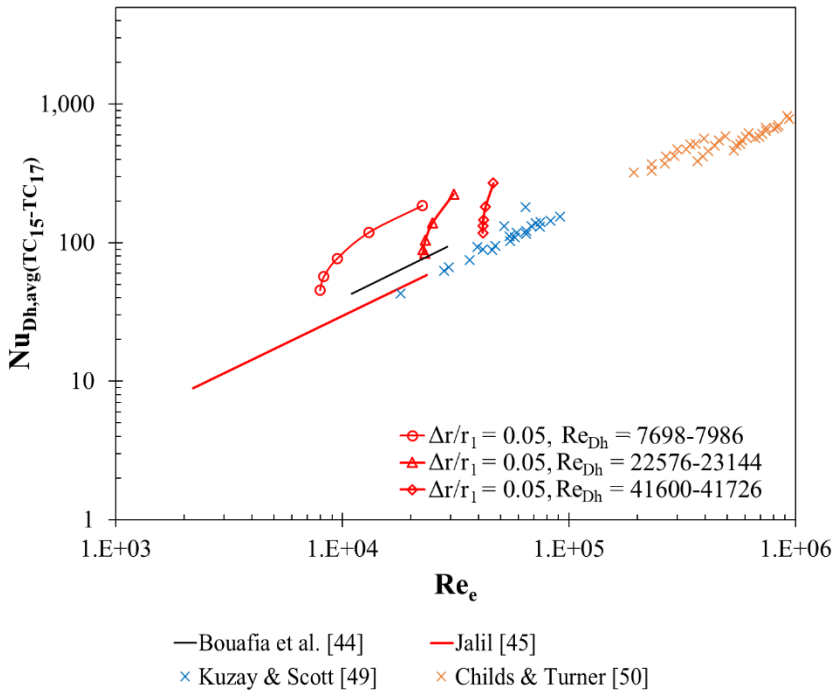

Figure B-14 $\Delta r/r_1 = 0.05$ Comparison, Nu_{Dh} vs Re_e

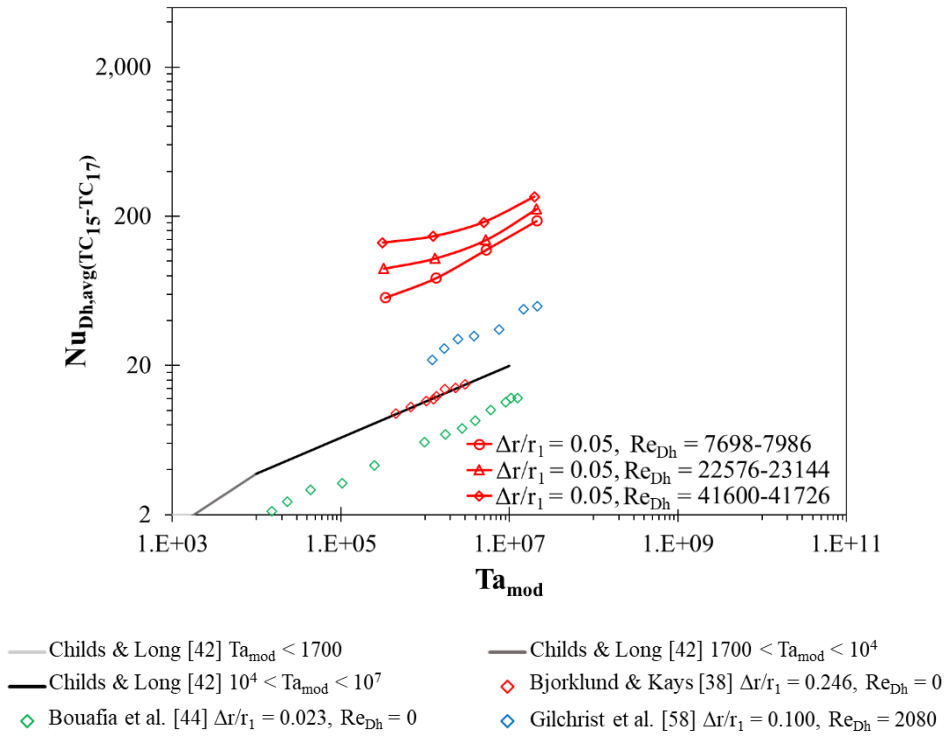

Figure B-15 $\Delta r/r_1 = 0.05$ Comparison, Nu_{Dh} vs Ta

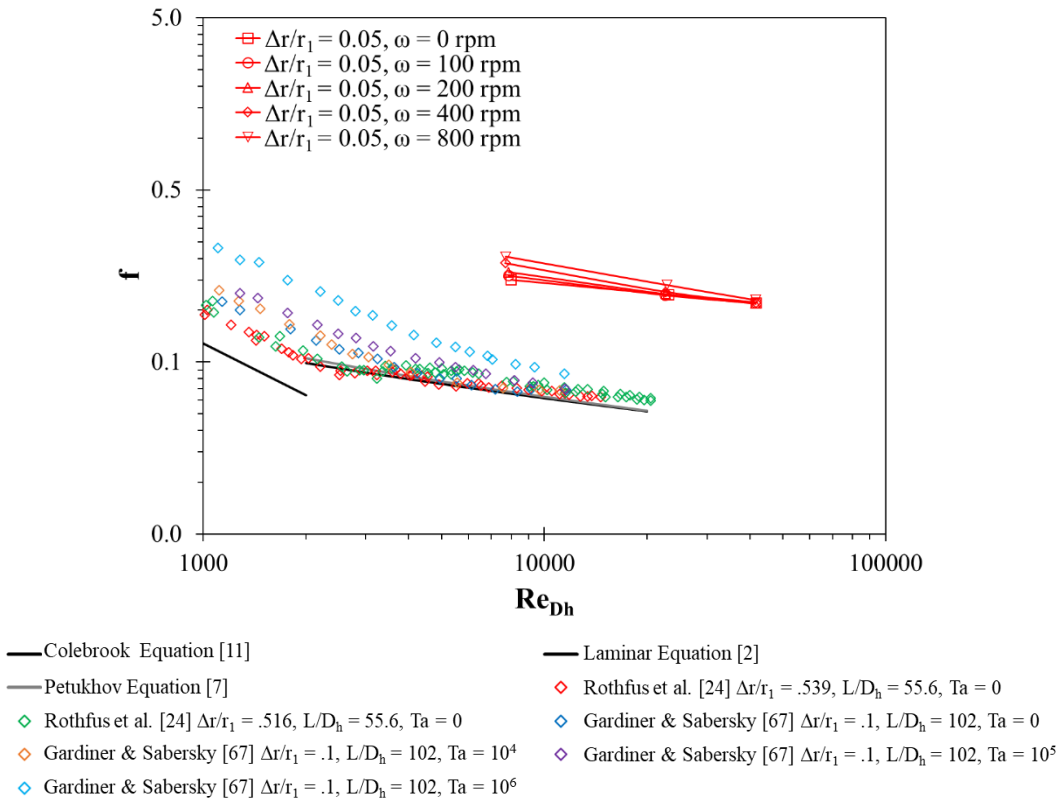

Figure B-16 $\Delta r/r_1$ = 0.05 Comparison, Friction Factor vs Re_{Dh}

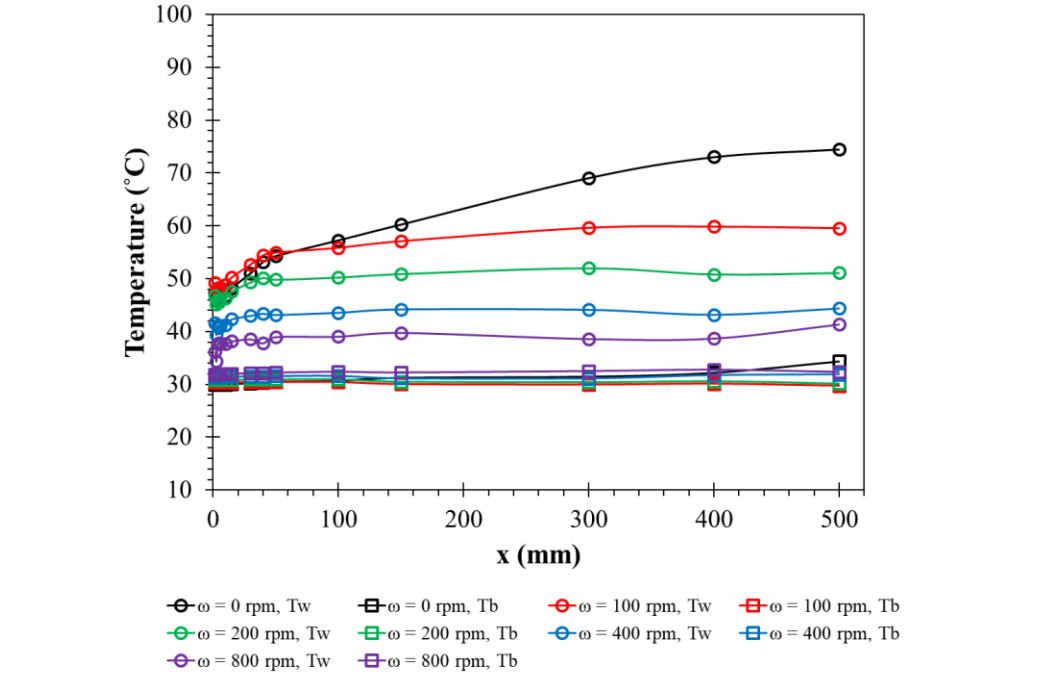

Figure B-17 $\Delta r/r_1$ = 0.1, Re_{Dh} = 10062-10464, 50V, (07/29/21), Temperature Profile

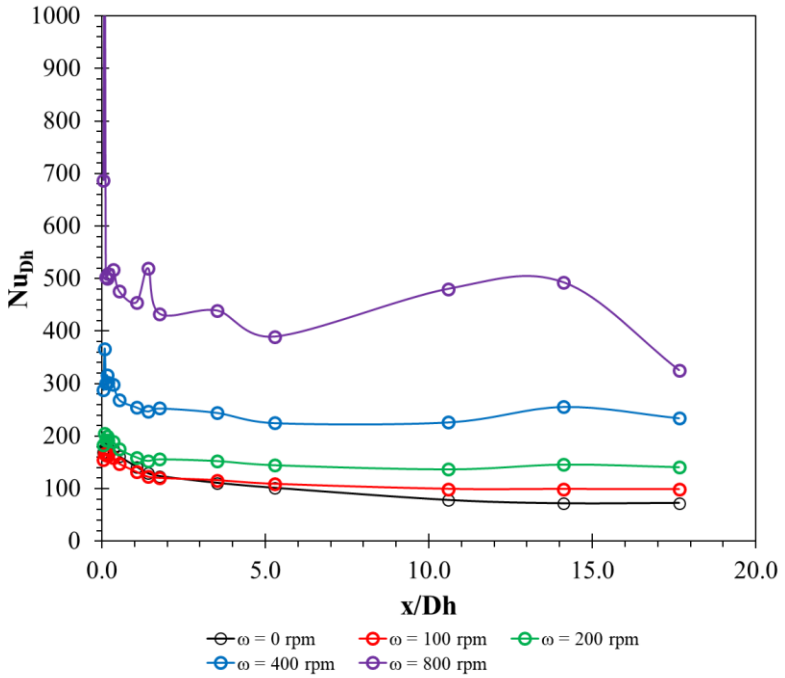

Figure B-18 $\Delta r/r_1$ = 0.1, Re_{Dh} = 10062-10464, 50V, (07/29/21), Nu_{Dh} Profile

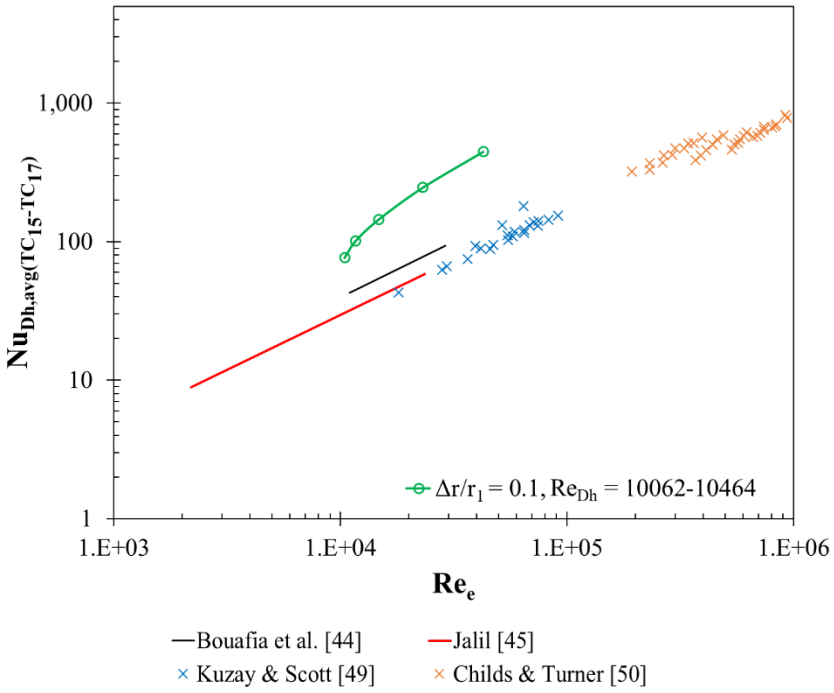

Figure B-19 $\Delta r/r_1$ = 0.1, Re_{Dh} = 10062-10464, Nu_{Dh} vs Re_e

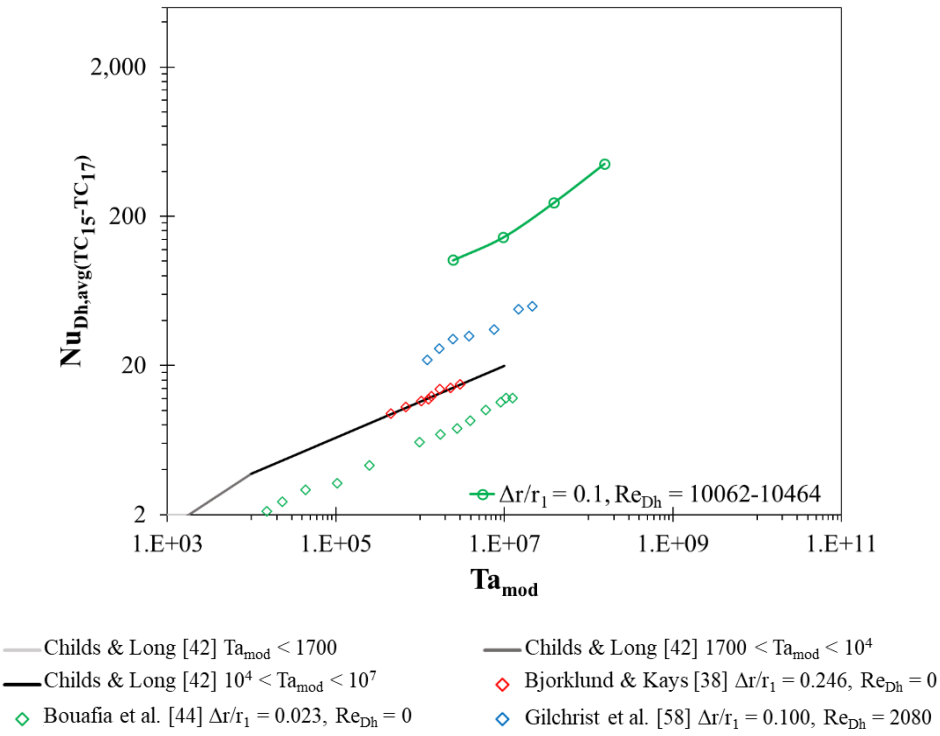

Figure B-20 $\Delta r/r_1 = 0.1$, Re_{Dh} = 10062-10464, Nu_{Dh} vs Ta

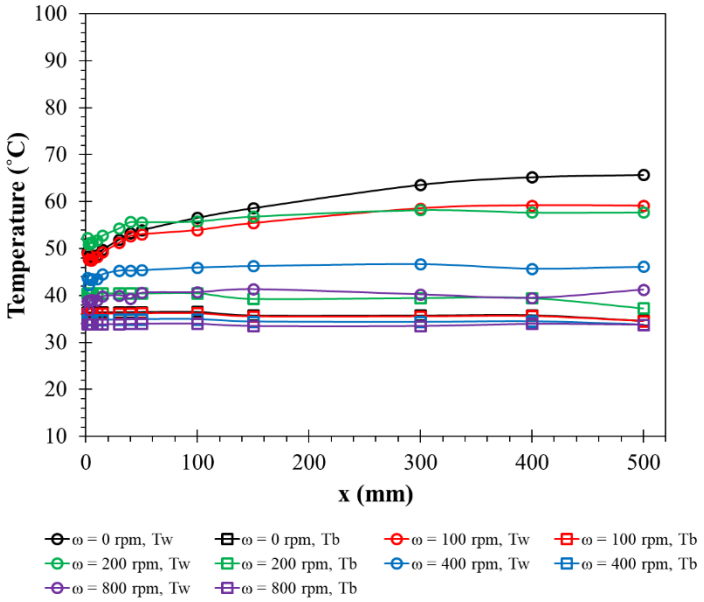

Figure B-21 $\Delta r/r_1 = 0.1$, Re_{Dh} = 20126-21616, 50V, (07/29/21), Temperature Profile

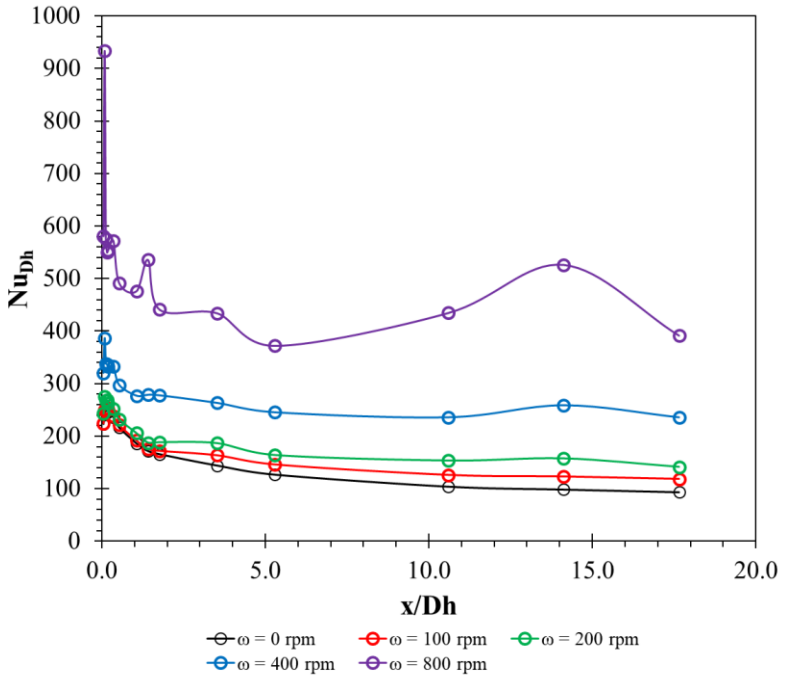

Figure B-22 $\Delta r/r_1$ = 0.1, Re_{Dh} = 20126-21616, 50V, (07/29/21), Nu_{Dh} Profile

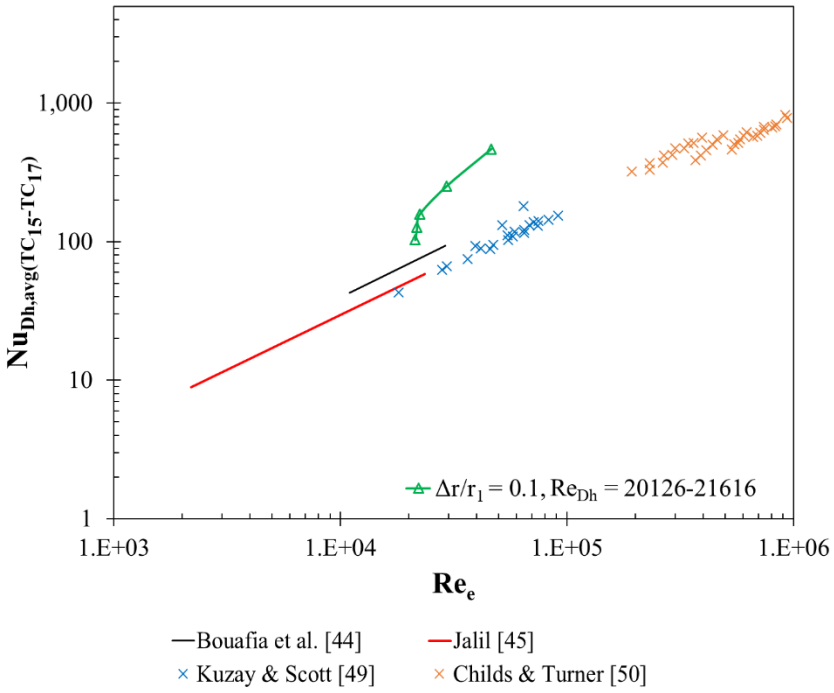

Figure B-23 $\Delta r/r_1$ = 0.1, Re_{Dh} = 20126-21616, Nu_{Dh} vs Re_e

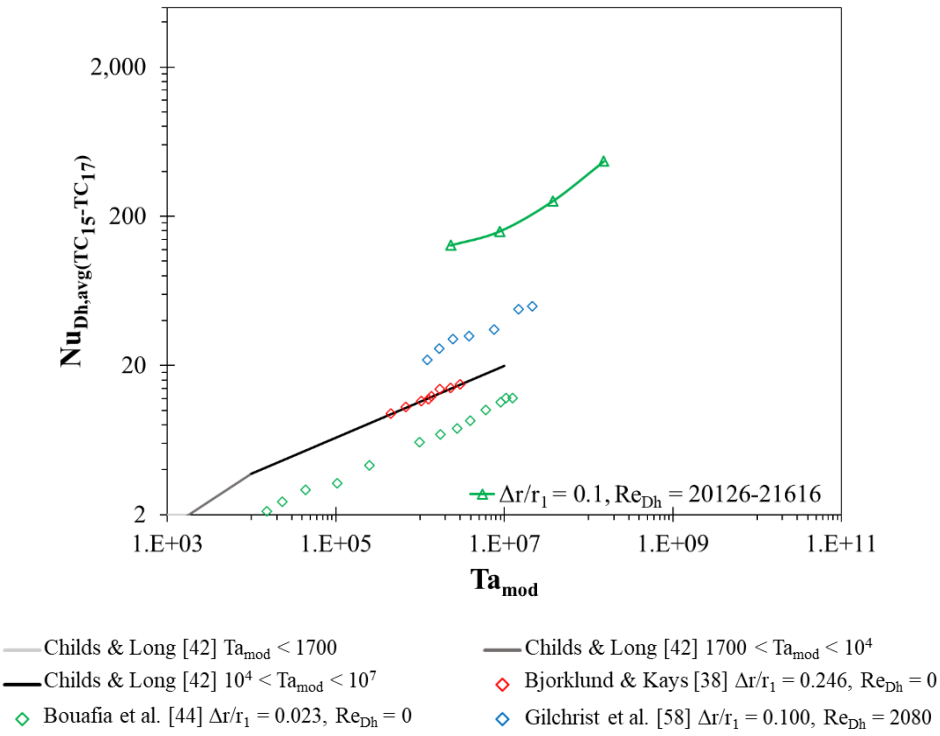

Figure B-24 $\Delta r/r_1 = 0.1$, $Re_{Dh} = 20126\text{-}21616$, Nu_{Dh} vs Ta

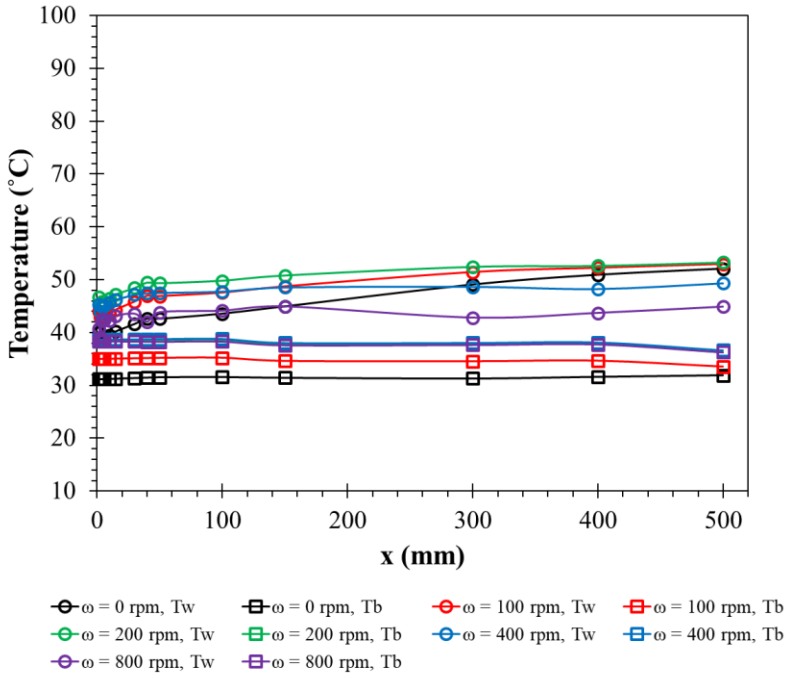

Figure B-25 $\Delta r/r_1 = 0.1$, $Re_{Dh} = 40202\text{-}40968$, 50V, (07/29/21), Temperature Profile

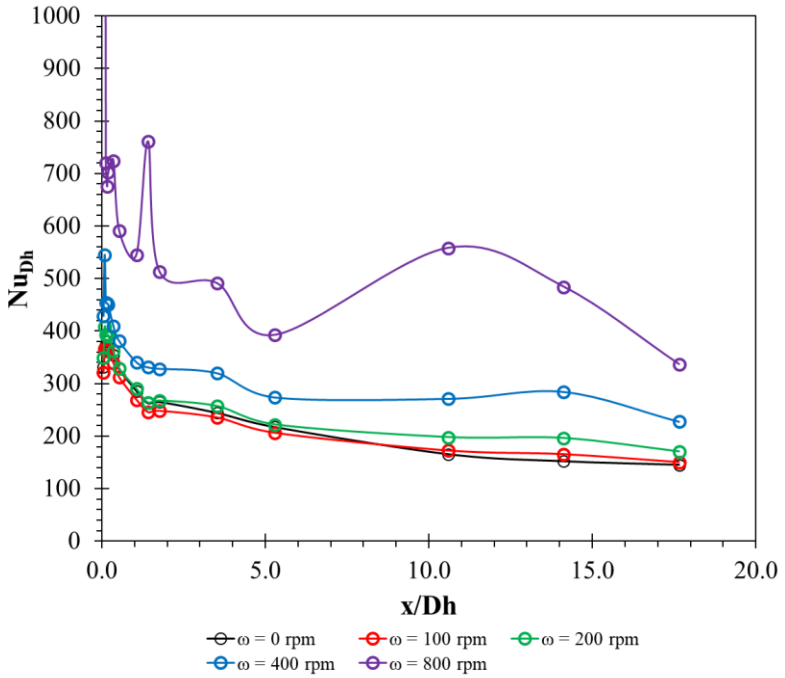

Figure B-26 $\Delta r/r_1$ = 0.1, Re_{Dh} = 40202-40968, 50V, (07/29/21), Nu_{Dh} Profile

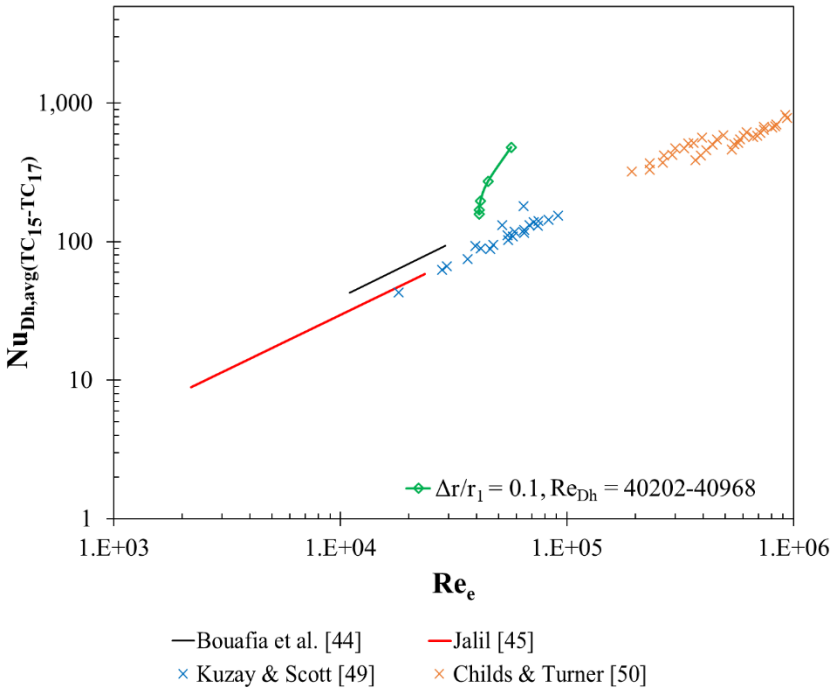

Figure B-27 $\Delta r/r_1$ = 0.1, Re_{Dh} = 40202-40968, Nu_{Dh} vs Re_e

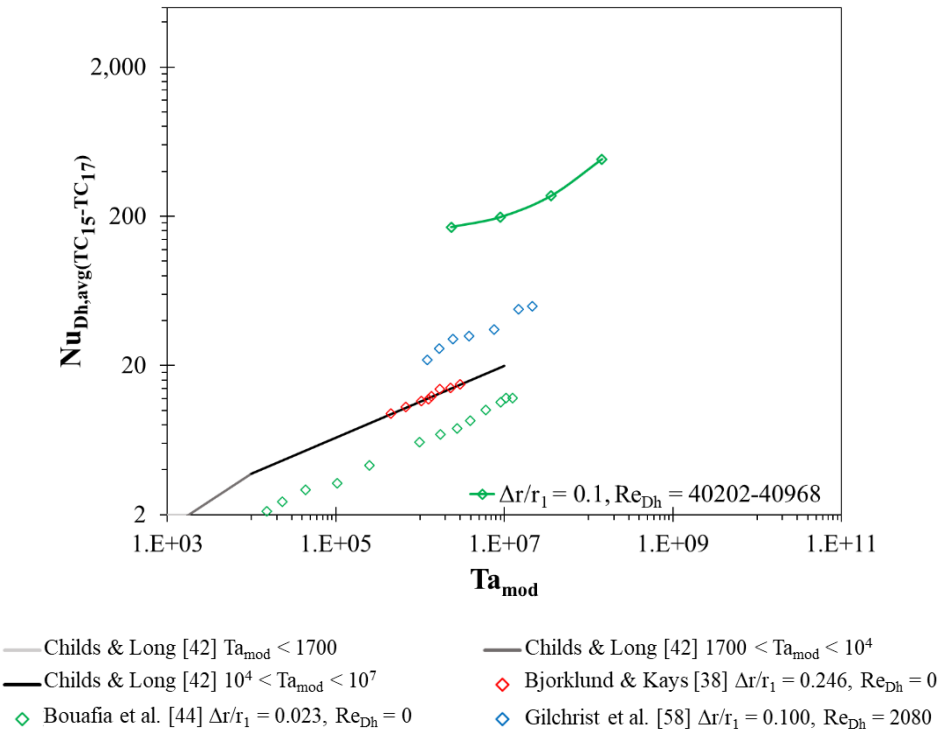

Figure B-28 $\Delta r/r_1 = 0.1$, $Re_{Dh} = 40202\text{-}40968$, Nu_{Dh} vs Ta

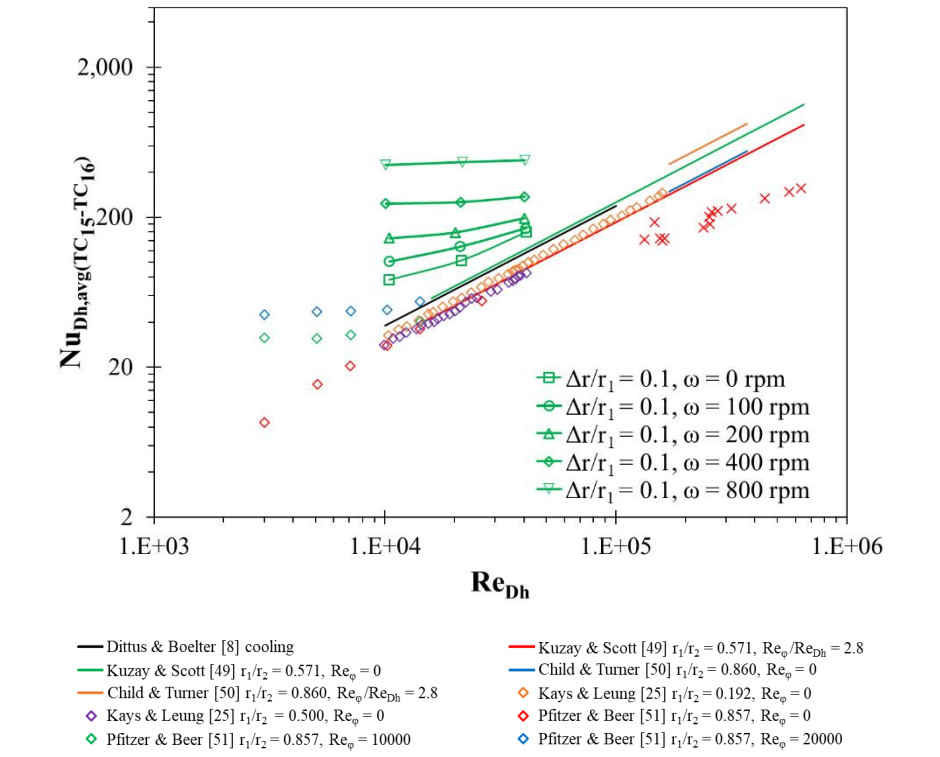

Figure B-29 $\Delta r/r_1 = 0.1$ Comparison, Nu_{Dh} vs Re_{Dh}

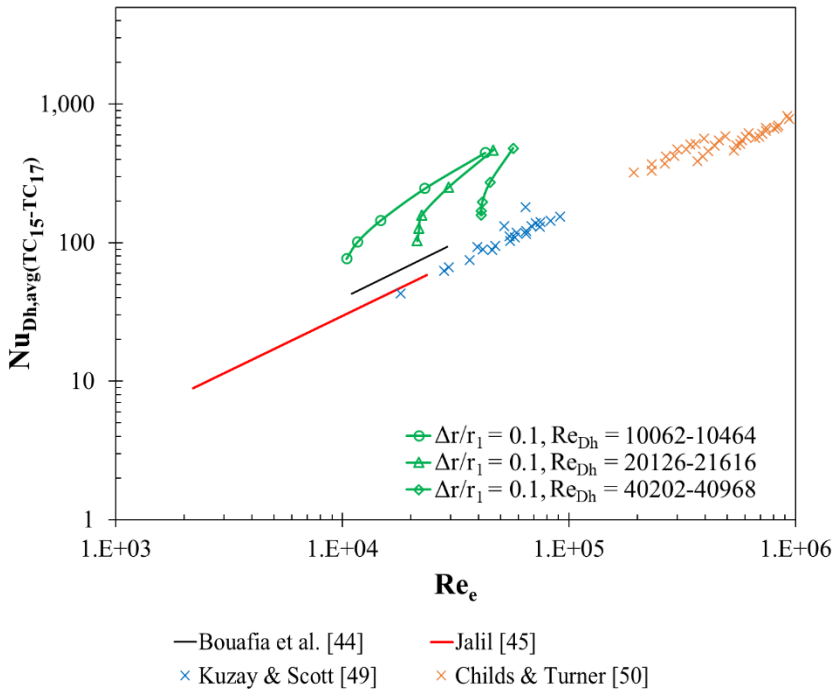

Figure B-30 $\Delta r/r_1 = 0.1$ Comparison, Nu_{Dh} vs Re_e

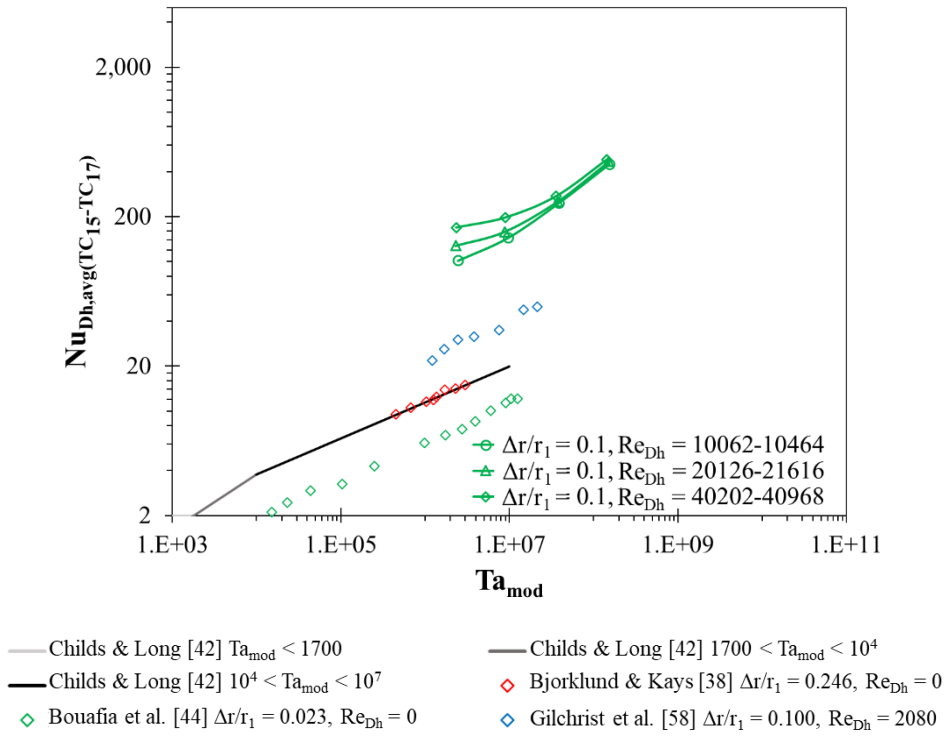

Figure B-31 $\Delta r/r_1 = 0.1$ Comparison, Nu_{Dh} vs Ta

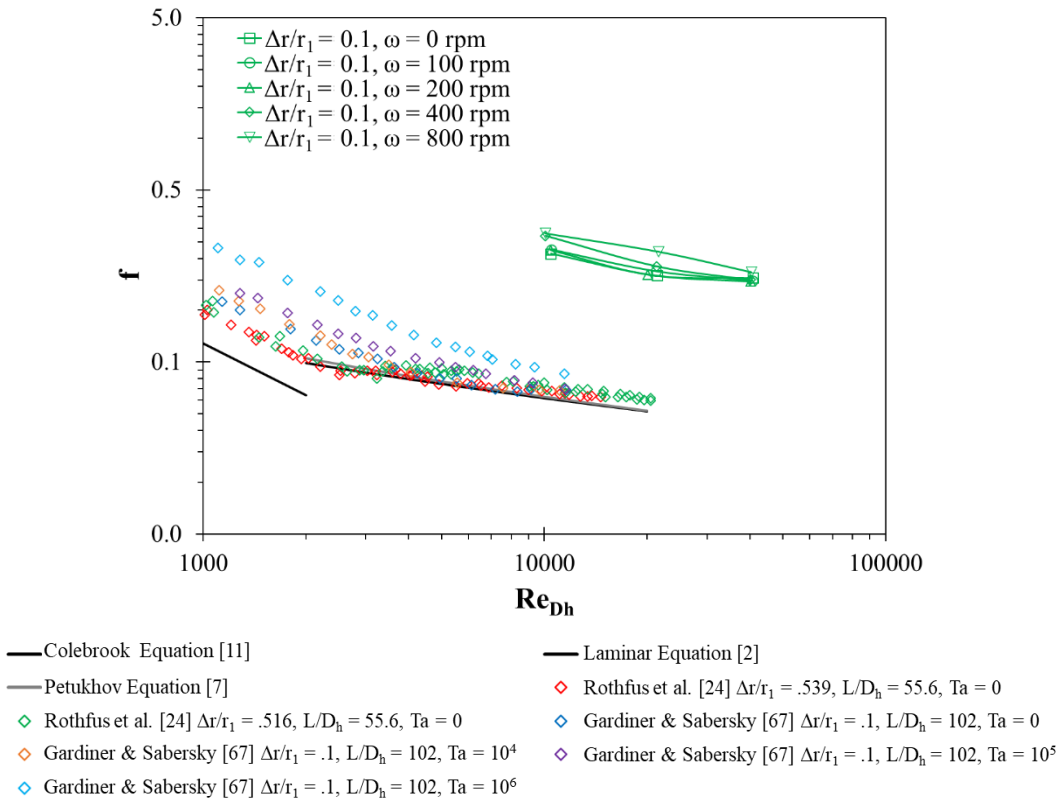

Figure B-32 $\Delta r/r_1 = 0.1$ Comparison, Friction Factor vs Re_{Dh}

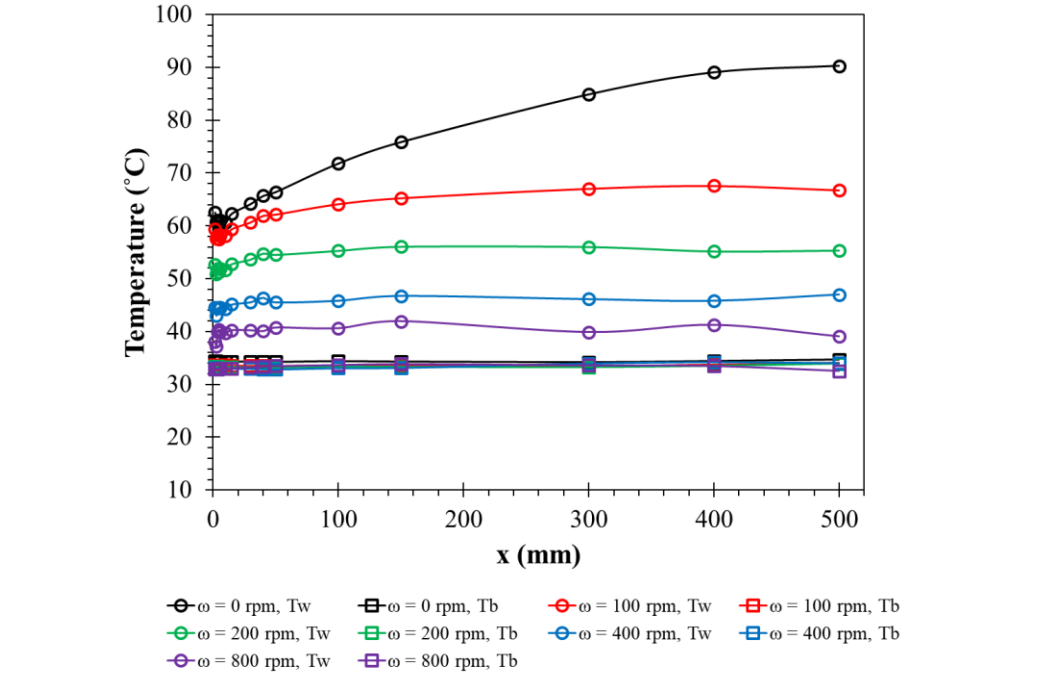

Figure B-33 $\Delta r/r_1 = 0.3$, Re_{Dh} = 9766-9944, 50V, (07/30/21), Temperature Profile

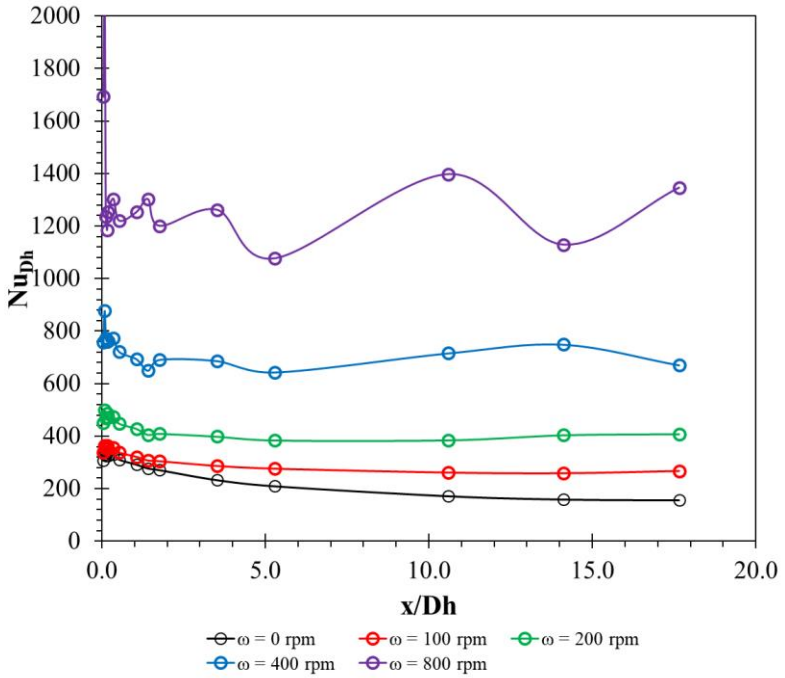

Figure B-34 $\Delta r/r_1$ = 0.3, Re_{Dh} = 9766-9944, 50V, (07/30/21), Nu_{Dh} Profile

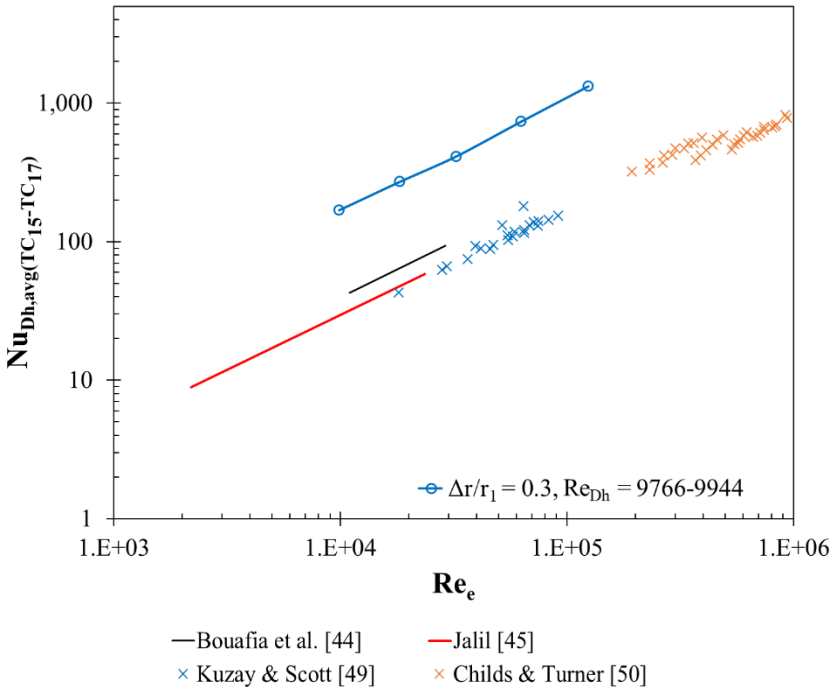

Figure B-35 $\Delta r/r_1$ = 0.3, Re_{Dh} = 9766-9944, Nu_{Dh} vs Re_e

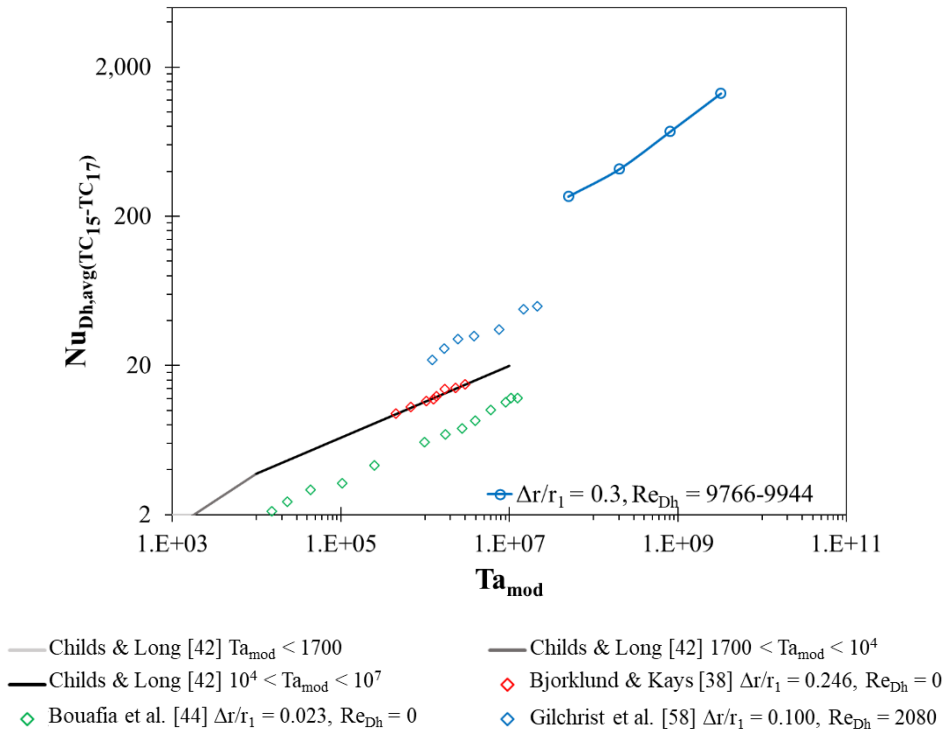

Figure B-36 $\Delta r/r_1 = 0.3$, Re_{Dh} = 9766-9944, Nu_{Dh} vs Ta

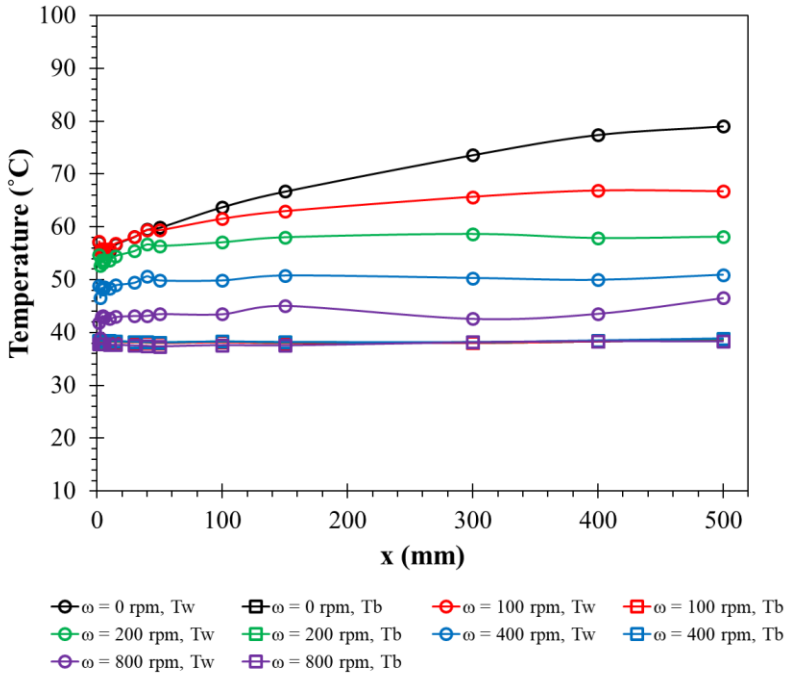

Figure B-37 $\Delta r/r_1 = 0.3$, Re_{Dh} = 20716-21162, 50V, (07/30/21), Temperature Profile

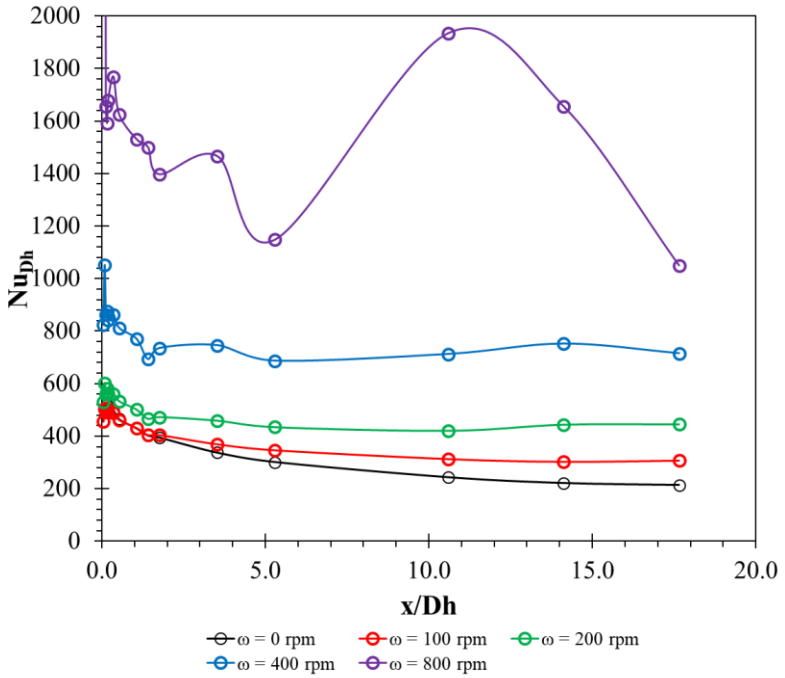

Figure B-38 $\Delta r/r_1$ = 0.3, Re_{Dh} = 20716-21162, 50V, (07/30/21), Nu_{Dh} Profile

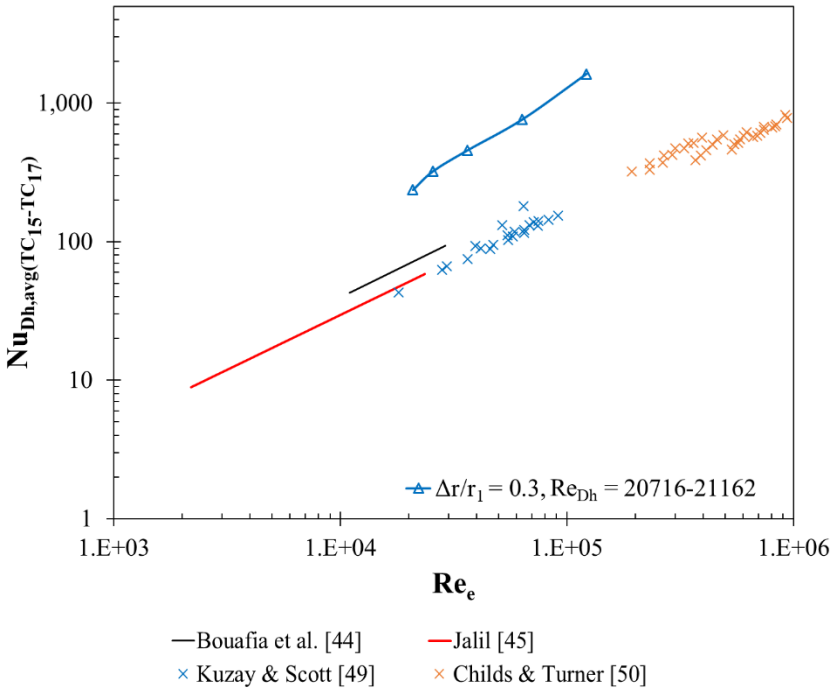

Figure B-39 $\Delta r/r_1$ = 0.3, Re_{Dh} = 20716-21162, Nu_{Dh} vs Re_e

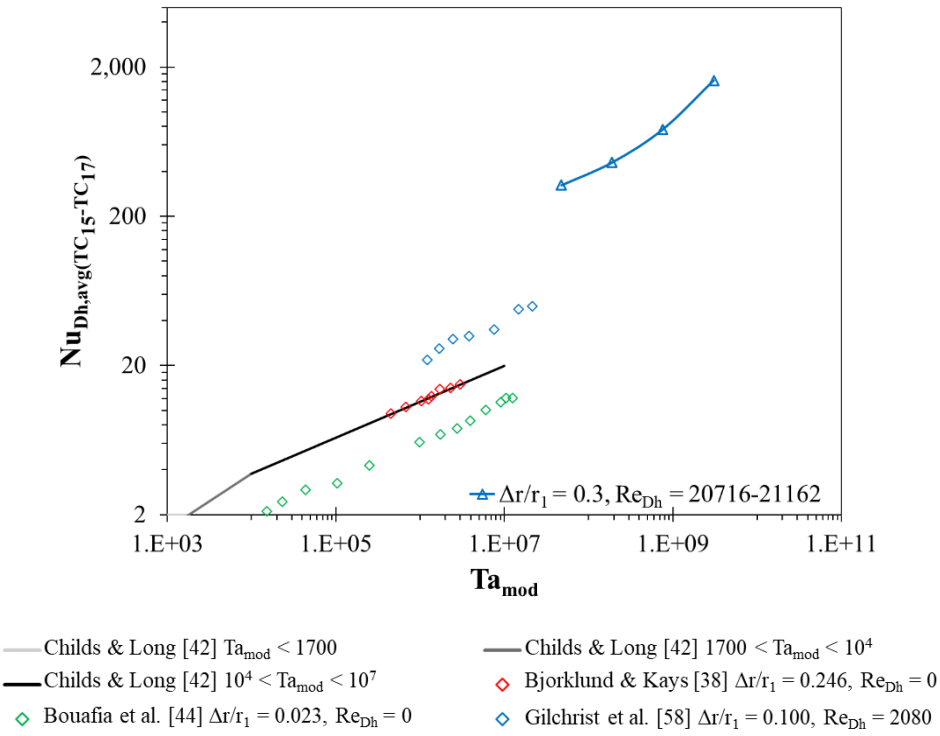

Figure B-40 $\Delta r/r_1 = 0.3$, Re_{Dh} = 20716-21162, Nu_{Dh} vs Ta

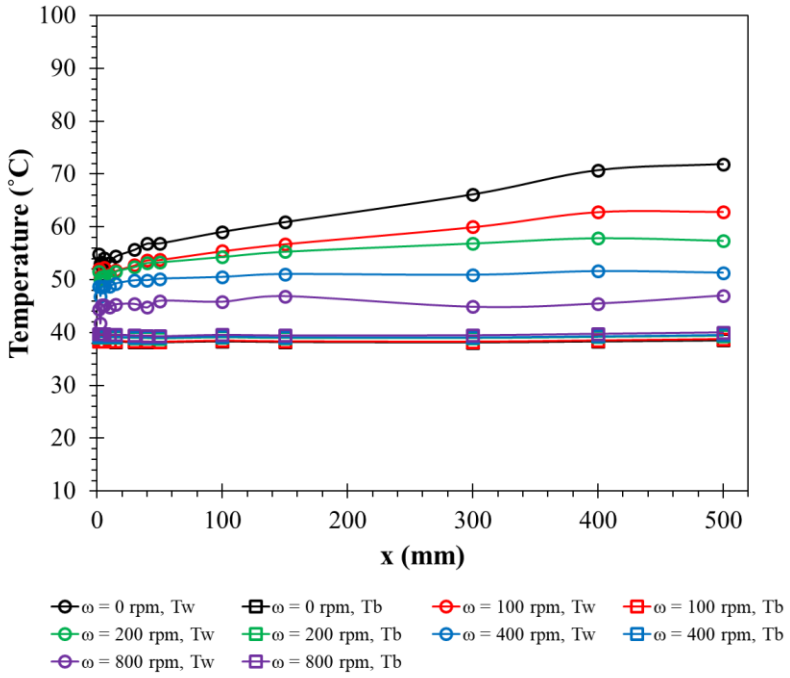

Figure B-41 $\Delta r/r_1 = 0.3$, Re_{Dh} = 40672-41014, 50V, (07/30/21), Temperature Profile

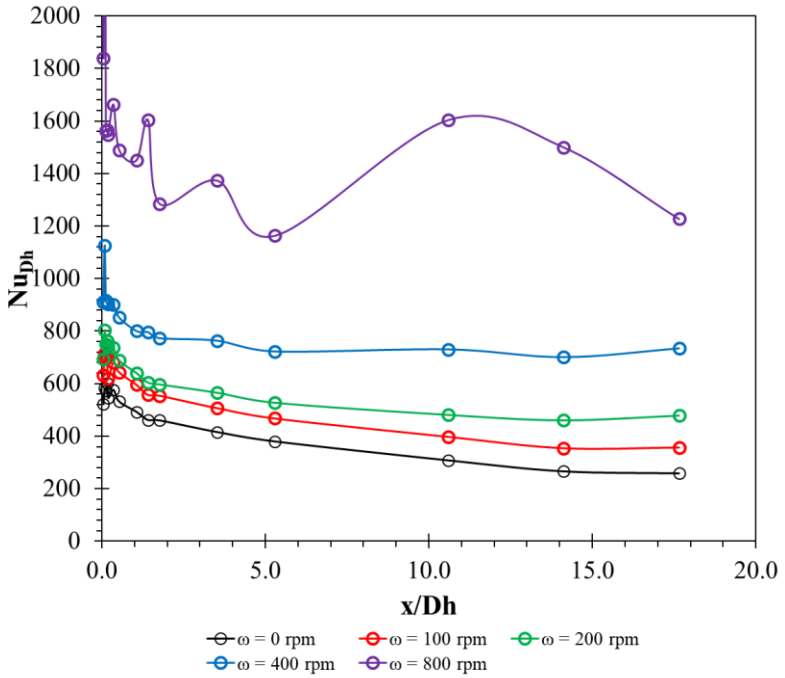

Figure B-42 $\Delta r/r_1 = 0.3$, $Re_{Dh} = 40672\text{-}41014$, (07/30/21), Nu_{Dh} Profile

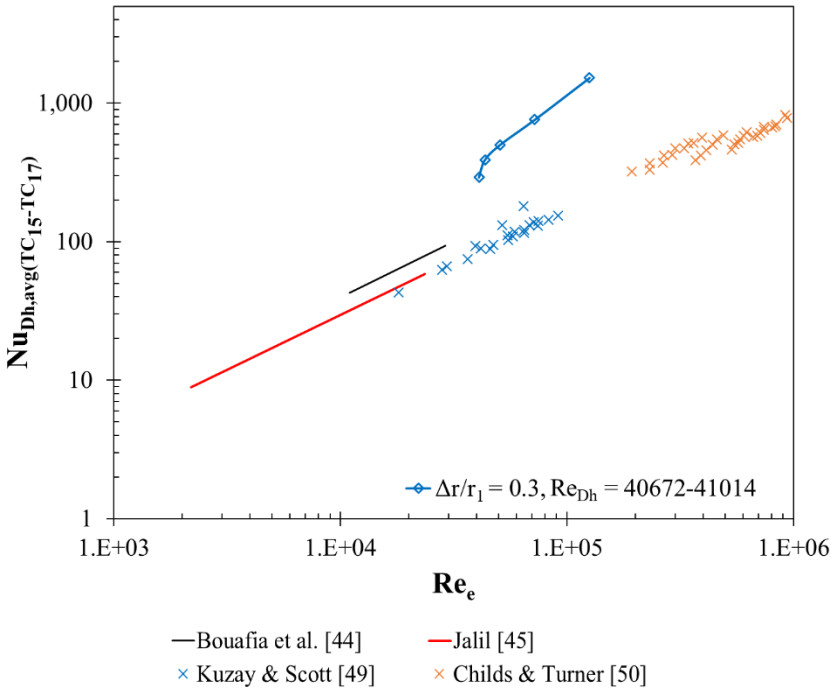

Figure B-43 $\Delta r/r_1 = 0.3$, $Re_{Dh} = 40672\text{-}41014$, Nu_{Dh} vs Re_e

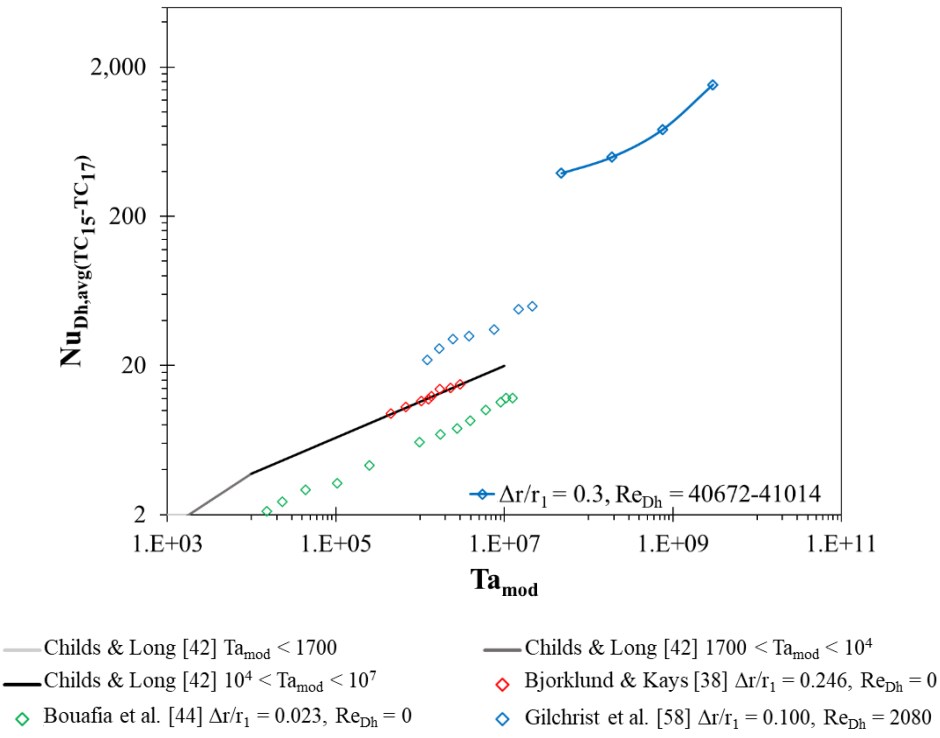

Figure B-44 $\Delta r/r_1 = 0.3$, $Re_{Dh} = 40672\text{-}41014$, Nu_{Dh} vs Ta

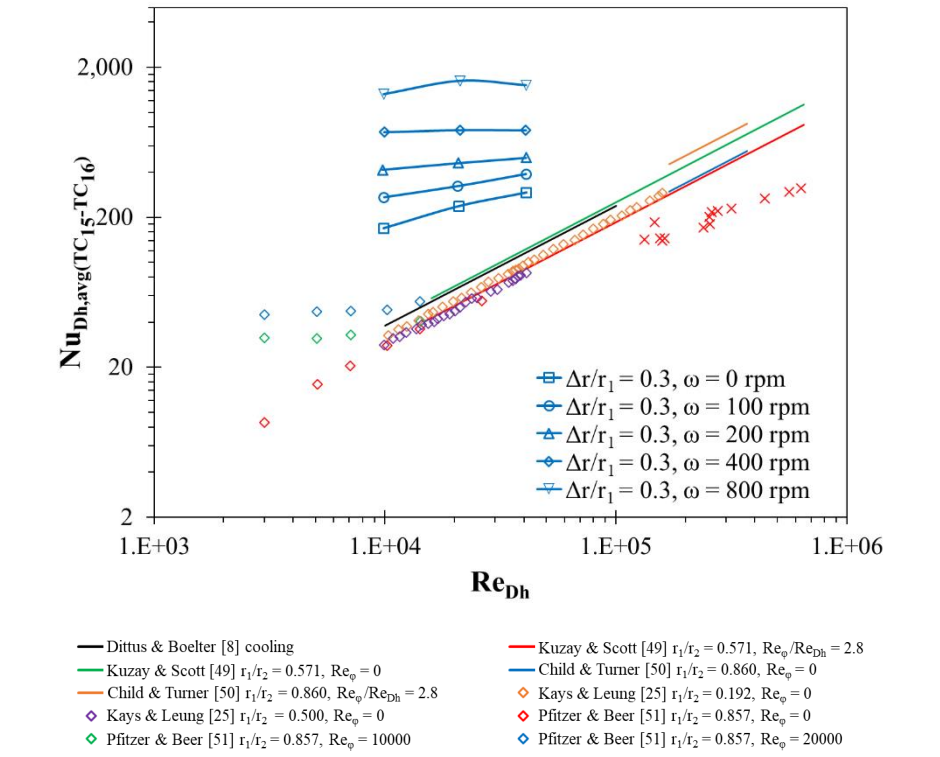

Figure B-45 $\Delta r/r_1 = 0.3$ Comparison, Nu_{Dh} vs Re_{Dh}

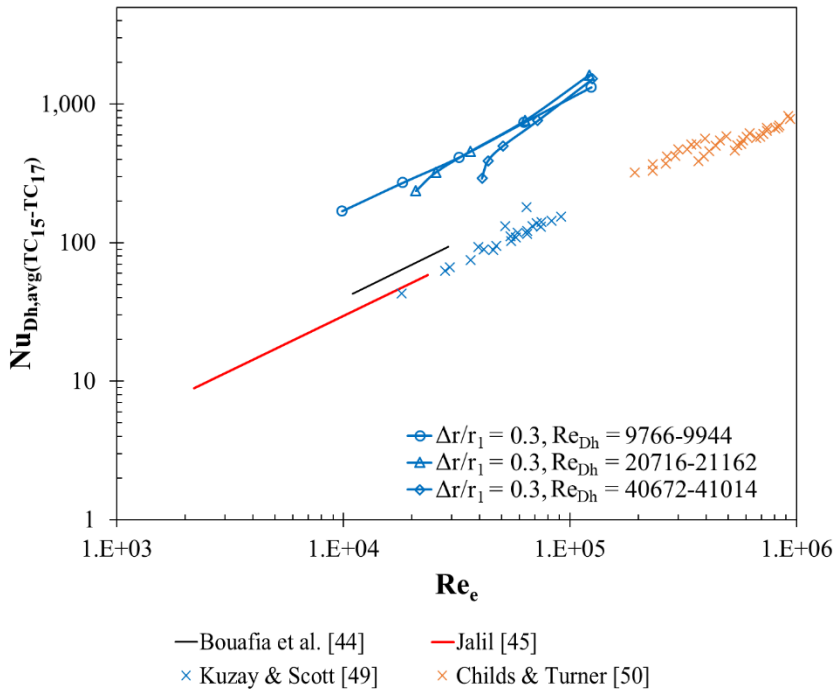

Figure B-46 $\Delta r/r_1 = 0.3$ Comparison, Nu_{Dh} vs Re_e

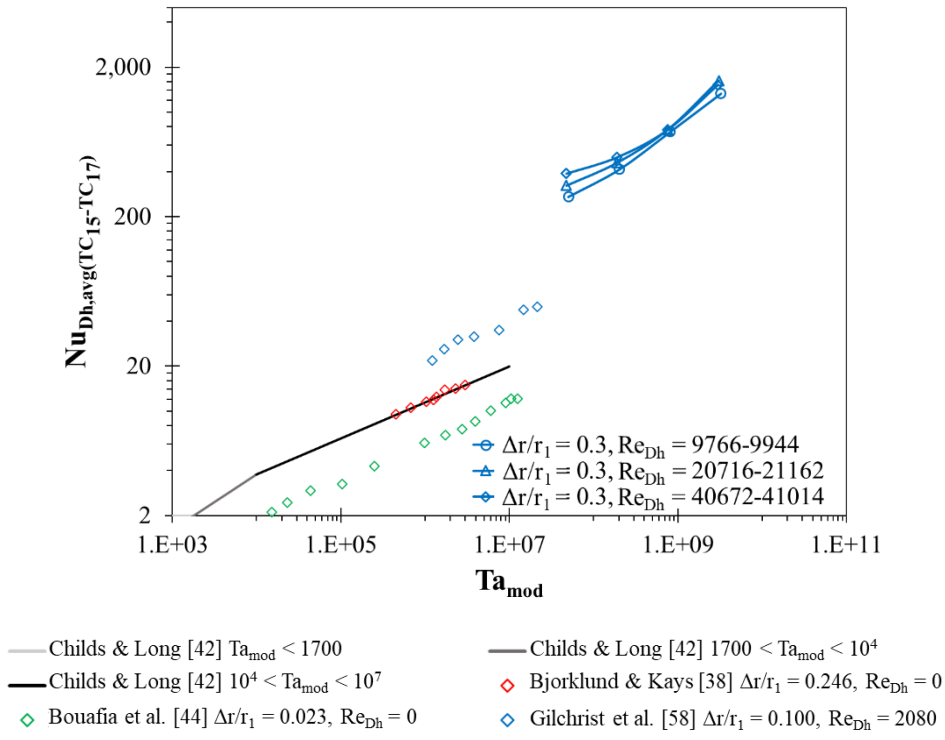

Figure B-47 $\Delta r/r_1 = 0.3$ Comparison, Nu_{Dh} vs Ta

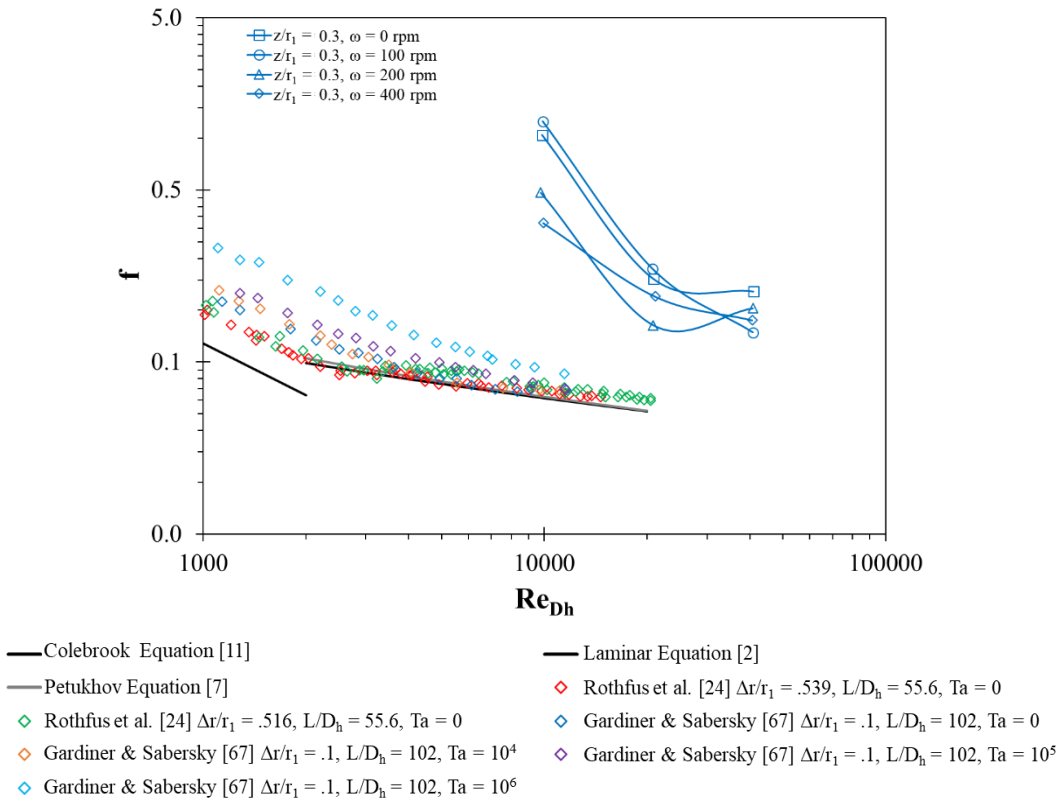

Figure B-48 $\Delta r/r_1 = 0.3$ Comparison, Friction Factor vs Re_{Dh}

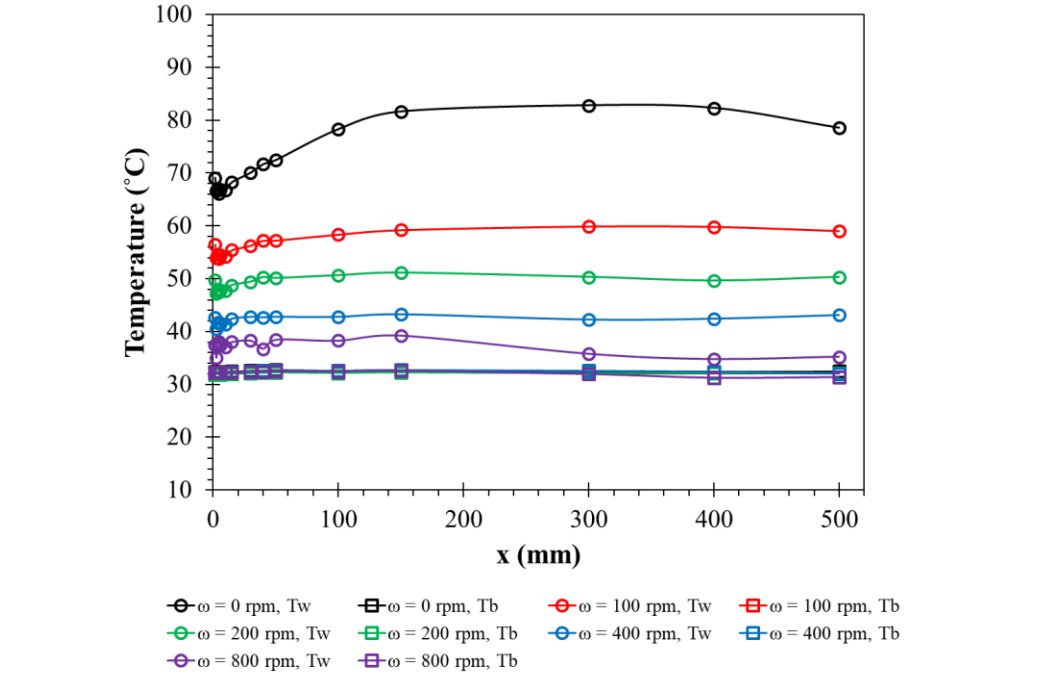

Figure B-49 $\Delta r/r_1 = 0.6$, Re_{Dh} = 9794-9856, 45V, (07/31/21), Temperature Profile

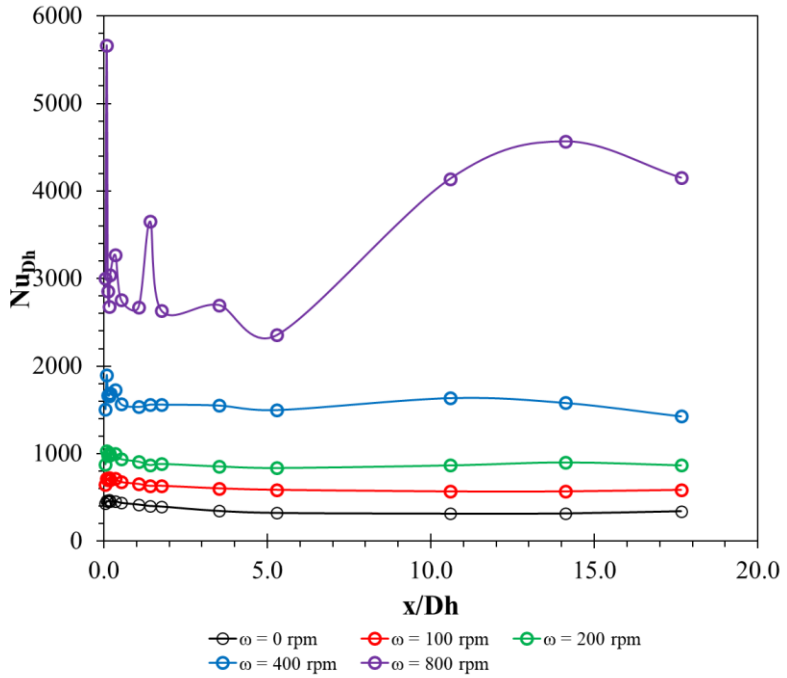

Figure B-50 $\Delta r/r_1$ = 0.6, Re_{Dh} = 9794-9856, 45V, (07/31/21), Nu_{Dh} Profile

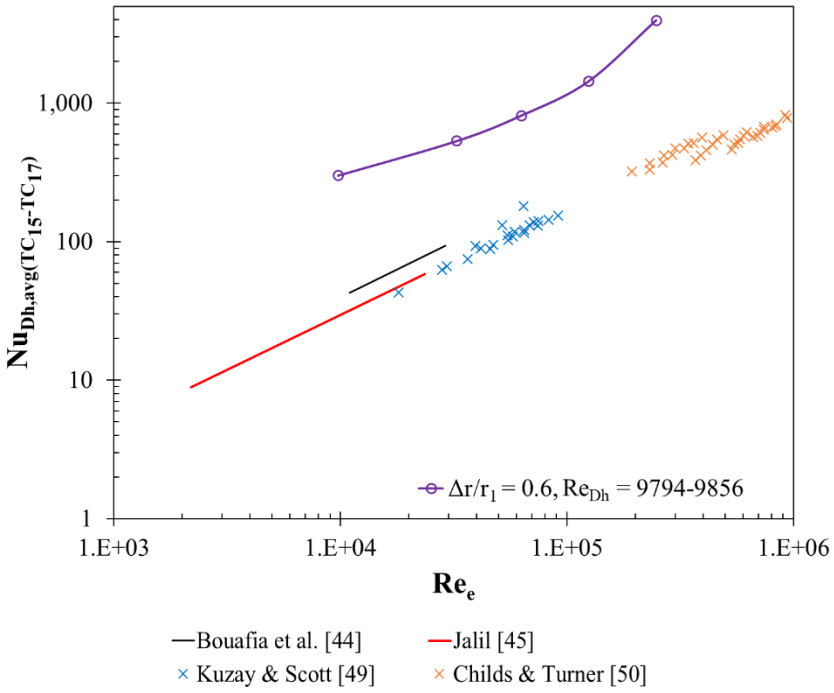

Figure B-51 $\Delta r/r_1$ = 0.6, Re_{Dh} = 9794-9856, Nu_{Dh} vs Re_e

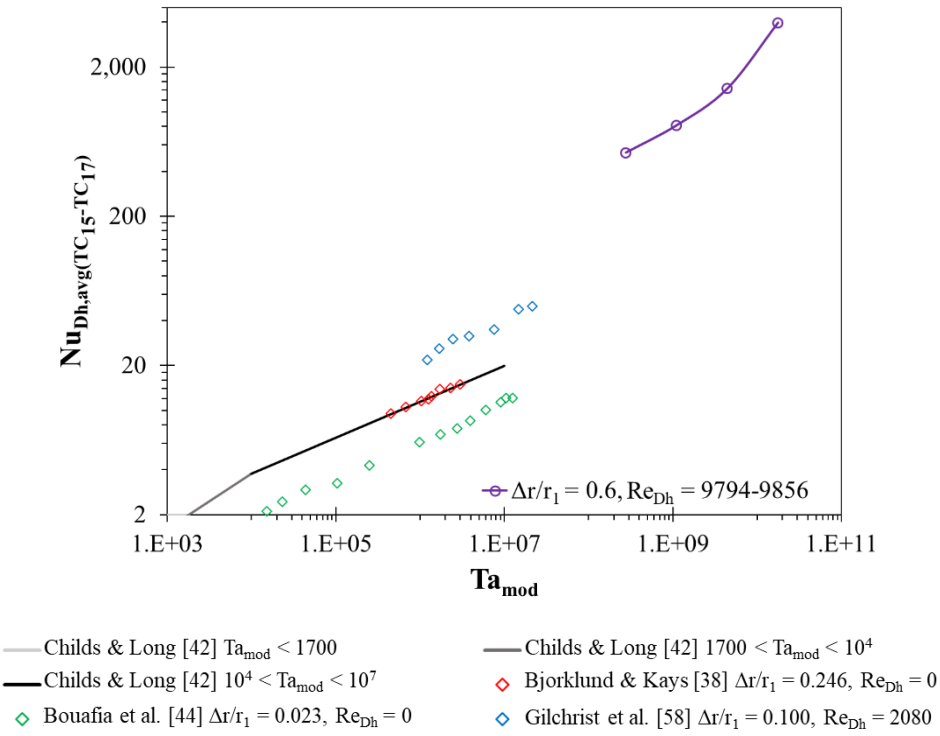

Figure B-52 $\Delta r/r_1 = 0.6$, Re_{Dh} = 9794-9856, Nu_{Dh} vs Ta

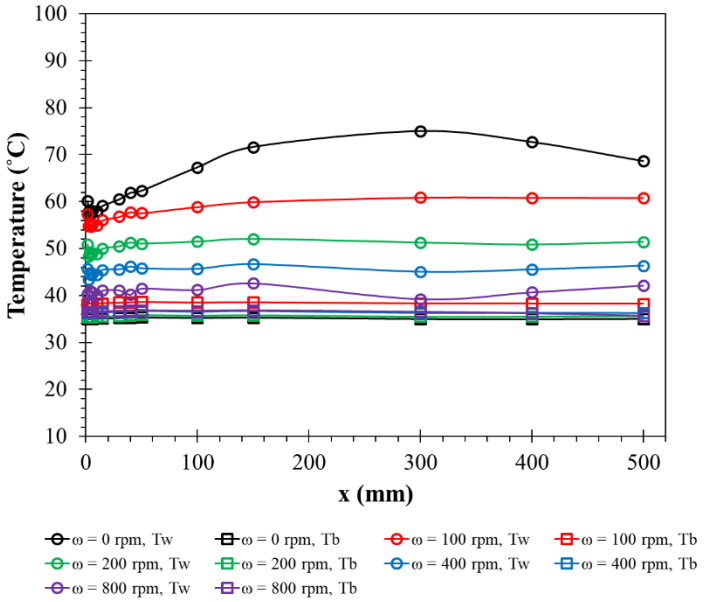

Figure B-53 $\Delta r/r_1 = 0.6$, Re_{Dh} = 20498-20884, 45V, (07/31/21), Temperature Profile

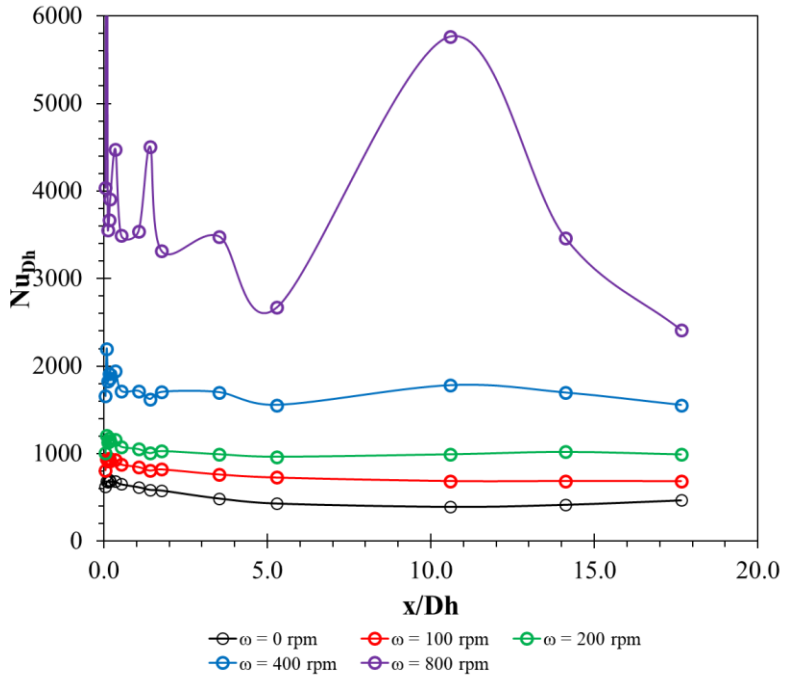

Figure B-54 $\Delta r/r_1$ = 0.6, Re_{Dh} = 20498-20884, 45V, (07/31/21), Nu_{Dh} Profile

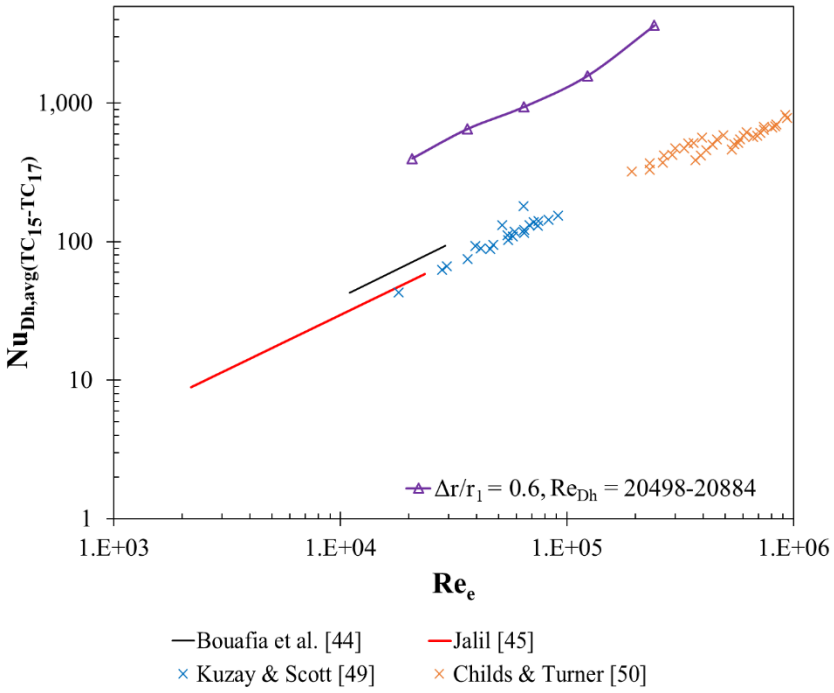

Figure B-55 $\Delta r/r_1$ = 0.6, Re_{Dh} = 20498-20884, Nu_{Dh} vs Re_e

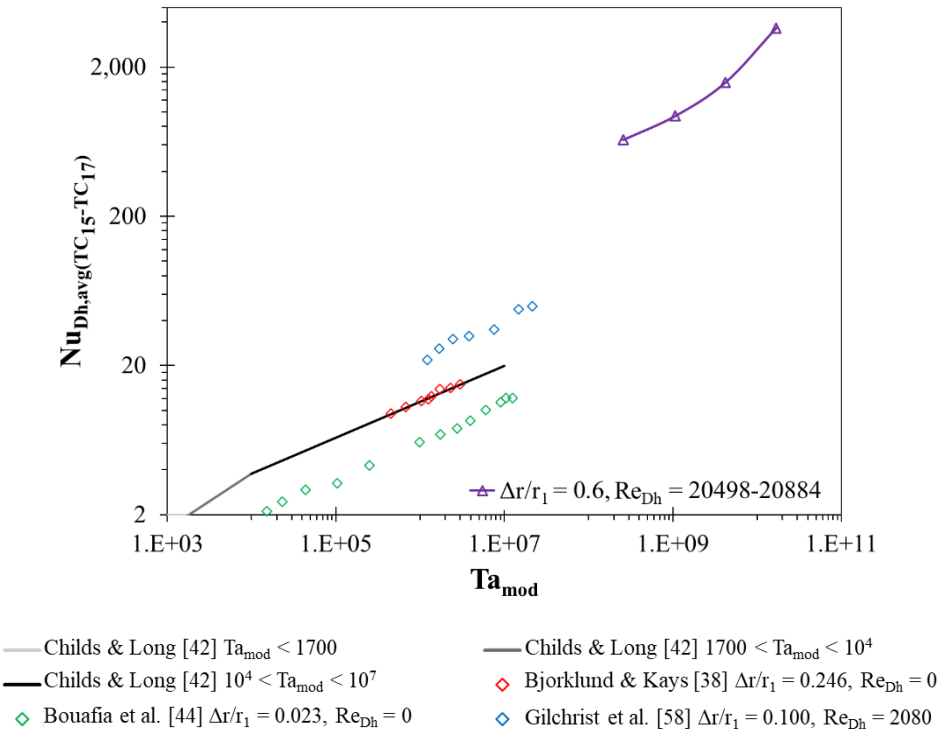

Figure B-56 $\Delta r/r_1 = 0.6$, $Re_{Dh} = 20498\text{-}20884$, Nu_{Dh} vs Ta

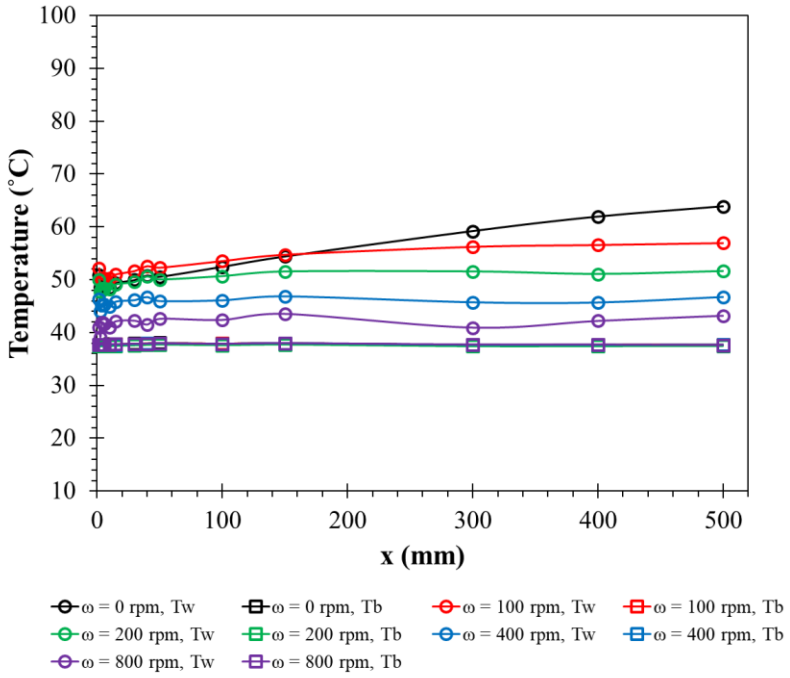

Figure B-57 $\Delta r/r_1 = 0.6$, $Re_{Dh} = 41588\text{-}41810$, 45V, (07/31/21), Temperature Profile

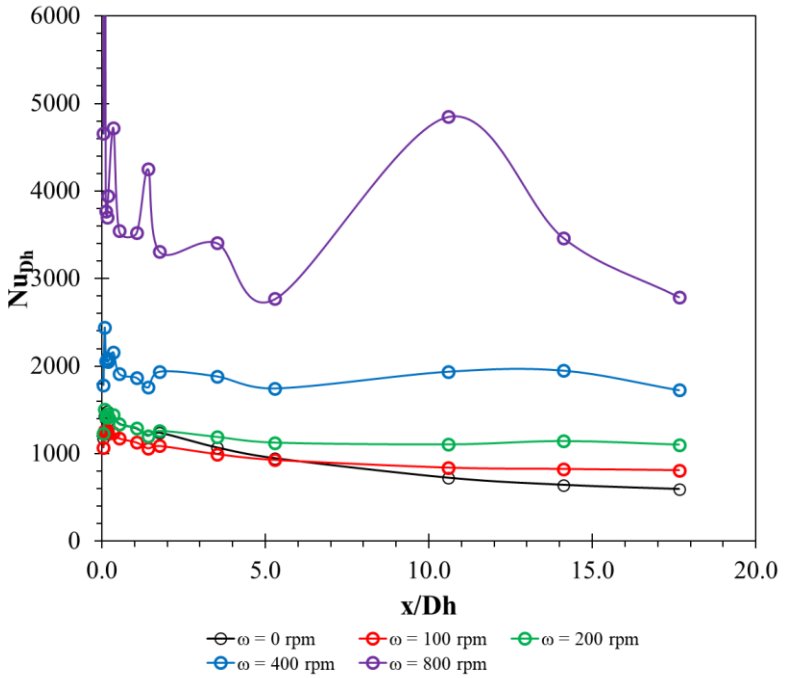

Figure B-58 $\Delta r/r_1$ = 0.6, Re_{Dh} = 41588-41810, 45V, (07/31/21), Nu_{Dh} Profile

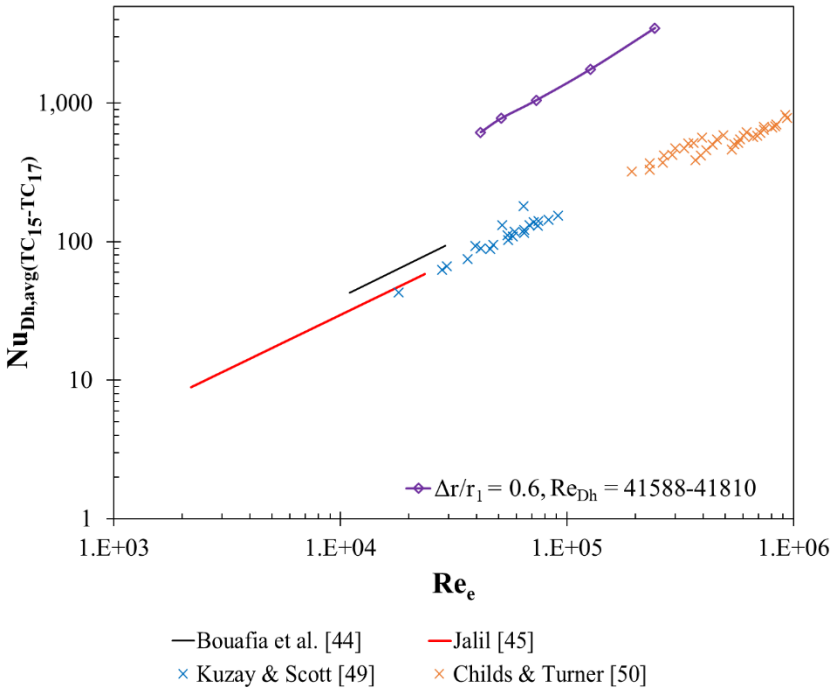

Figure B-59 $\Delta r/r_1$ = 0.6, Re_{Dh} = 41588-41810, Nu_{Dh} vs Re_e

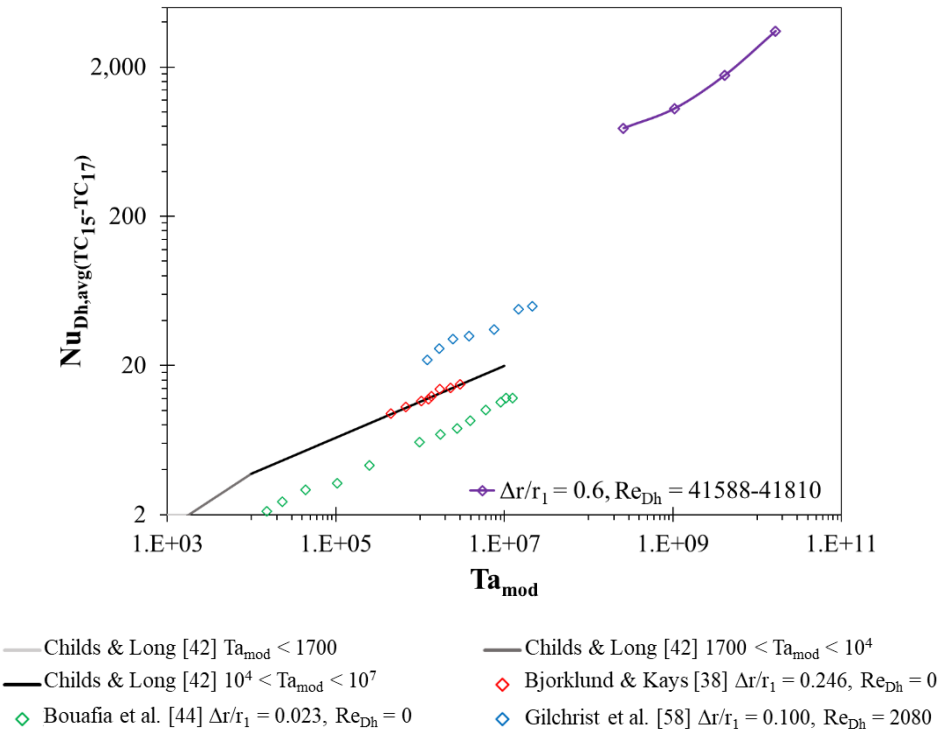

Figure B-60 $\Delta r/r_1 = 0.6$, $Re_{Dh} = 41588\text{-}41810$, Nu_{Dh} vs Ta

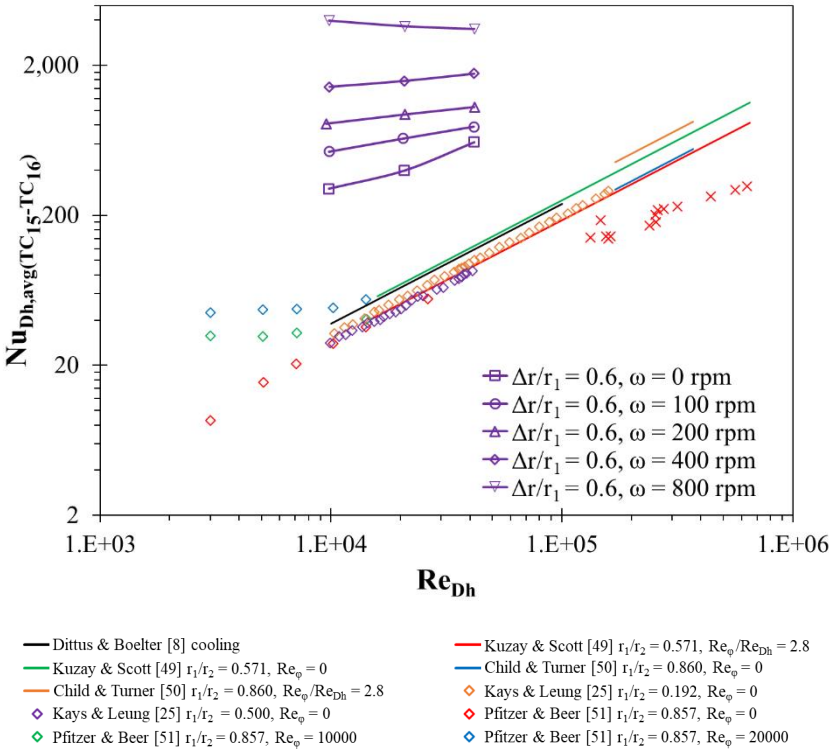

Figure B-61 $\Delta r/r_1 = 0.6$ Comparison, Nu_{Dh} vs Re_{Dh}

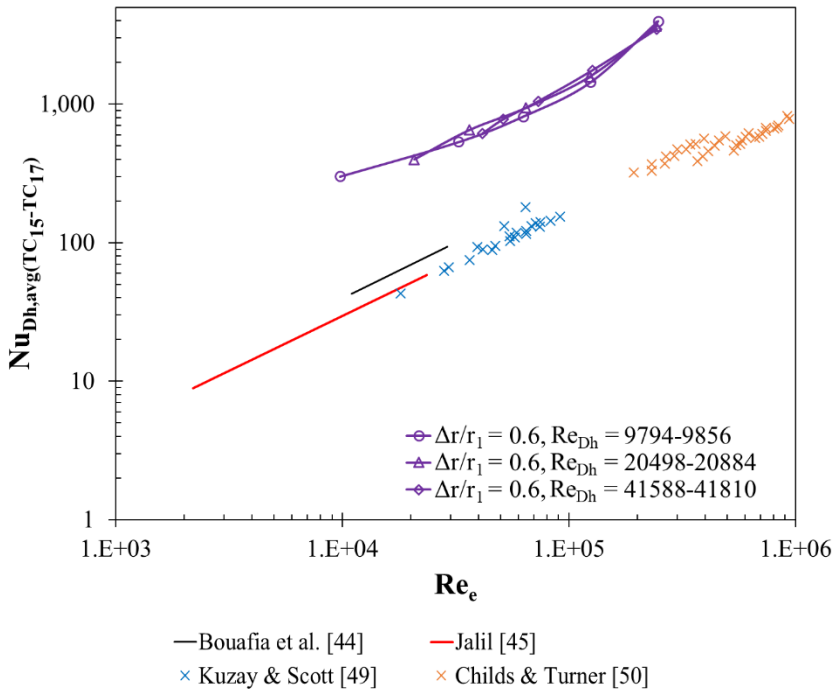

Figure B-62 $\Delta r/r_1 = 0.6$ Comparison, Nu_{Dh} vs Re_e

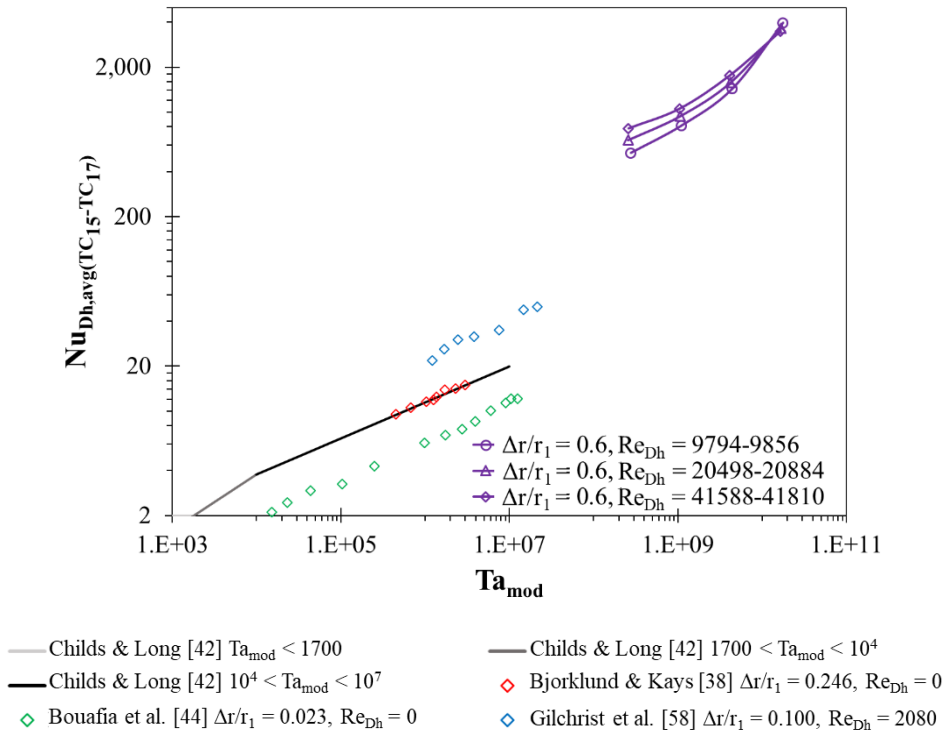

Figure B-63 $\Delta r/r_1 = 0.6$ Comparison, Nu_{Dh} vs Ta